High-Enthalpy Shock/Boundary-Layer Interaction on a Double Wedge

Thesis by

Jean-Paul Davis

In Partial Fulfillment of the Requirements

for the Degree of

Doctor of Philosophy

California Institute of Technology

Pasadena, California

1999

(Submitted September 29, 1998)

Acknowledgements

Many people contributed in some way to the completion of this work. Firstly, I would like to thank Professor Bradford Sturtevant for providing important guidance while at the same time giving me the freedom to follow my own intuition. I would also like to thank Professor Hans Hornung who managed somehow to impart in me a portion of his extensive knowledge in high-enthalpy aerodynamics. Gratitude is also due Professors Anatol Roshko, Toshi Kubota, and Joseph Shepherd for their insights, as well as Professors Dale Pullin and David Goodwin for taking the time to read through and critique this rather long thesis.

Running experiments in the T5 Hypervelocity Shock Tunnel Laboratory is always a group effort. Special thanks are due Bahram Valiferdowsi for help with the hardware, and Michael Kaneshige who was responsible for the timely completion of my second experimental campaign over the Christmas holiday. The following graduate students, past and present, have also assisted me in the lab to varying degrees; (in alphabetical order) Philippe Adam, Jacques Bélanger, Eric Cummings, Patrick Germain, Patrick Lemieux, Ivett Leyva, Adam Rasheed, Bernard Rousset, Simon Sanderson, Stefan Schlamp, and Chihyung Wen. In addition, Jan Martinez-Schramm of the DLR was essential at the beginning of my second experimental campaign, and also performed thermocouple calibrations for me at his own lab in Germany.

Considerable thanks go to Joseph Olejniczak who provided the computational Navier Stokes code along with much invaluable advice on using it and modifying it to my own needs. Cray supercomputer resources were provided through funding by NASA Offices of Mission to Planet Earth, Aeronautics, and Space Science. Experiments were funded by the Air Force Office of Scientific Research under grant F49629-93-1-0338. Additional funding was provided by Caltech.

Abstract

Interaction between a shock wave and a boundary layer at a compression corner can produce a region of separated flow. The length of separation is important in determining aerodynamic forces, and the heat transfer at reattachment is important for the design of thermal protection systems. The effects of high-enthalpy flow on these phenomenon, particularly separation length, are not well known. Experiments to measure separation length and reattachment heating are performed in the T5 Hypervelocity Shock Tunnel using nitrogen test gas and a double-wedge geometry which allows greater control over local flow conditions at separation and, at high incidence angle, may produce real-gas effects due to dissociation behind the leading shock. Local external flow conditions were found by computational reconstruction of the inviscid nonequilibrium flow field.

Application of results from asymptotic theory to a simple model for separation leads to a new scaling parameter which approximately accounts for wall temperature effects on separation length for a laminar nonreacting boundary layer and extends previous results to arbitrary viscosity law. A classification is introduced which divides mechanisms for real-gas effects into those acting internal and external to viscous regions of the flow, with internal mechanisms further subdivided into those arising upstream and downstream of separation. Application of the ideal dissociating gas model to a scaling law based on local external flow parameters and a nonreacting boundary layer shows that external mechanisms due to dissociation decrease separation length at low incidence but depend on the free-stream dissociation at high incidence, and have only a small effect on peak heating. A limited numerical study of reacting boundary layers shows that internal mechanisms due to recombination in the upstream boundary layer cause a slight decrease in separation length and a large increase in heat flux relative to a nonreacting boundary layer with the same external conditions.

Correlations are presented of experimentally measured separation length using local external flow parameters computed for reacting flow, which scales out external mechanisms but not internal mechanisms. These show the importance of the new scaling parameter in high-enthalpy flows, a linear relationship between separation length and reattachment pressure ratio as found previously for supersonic interactions, and a Reynolds-number effect for transitional interactions. A significant increase in scaled separation length is observed for high-enthalpy data in the laminar regime, and this is attributed to an internal recombination mechanism occurring in the separated shear layer. Experimental data for reattachment heat flux are found to agree roughly with existing correlations and to exhibit an increase due to an internal recombination mechanism, but cannot provide further insight due to large scatter.

Contents

List of Figures

List of Tables

Nomenclature

Roman characters

a	speed of sound; constant in triple-deck scaling (Equation 4.39)
A_e/A_*	ratio of nozzle exit area to nozzle throat area
AR	full aspect ratio of a test model (span divided by total chord length); cell aspect ratio on numerical grid
b	span of a test model; constant in triple-deck scaling (Equation 4.39)
c	specific heat capacity of a solid material; constant in triple-deck scaling (Equation 4.39)
c_f	constant of proportionality in Arrhenius forward reaction rate expressions
c_p	specific heat capacity of a gas at constant pressure
c_v	translational–rotational specific heat capacity of a gas at constant volume $c_{v_{tr}} + c_{v_r}$
C	Chapman–Rubesin parameter $\rho\mu/\rho_e\mu_e$, equivalent to constant in Chapman linear viscosity law $\mu/\mu_e = CT/T_e$; constant of proportionality in IDG reaction rate expression
C_f	skin friction coefficient based on local boundary-layer edge conditions (Equation 4.13)
C_{f,x_1}	skin friction coefficient an undisturbed boundary layer would have at $x = x_1$
C_P	pressure coefficient based on free-stream conditions (Equation 2.14)
d	constant in triple-deck scaling (Equation 4.39); relative root-square deviation (Equation 6.1)
D	determinant in quadratic equation for density ratio across IDG shock (Equation 5.8)
$D_{11_{N_2}}$	self-diffusion coefficient for molecular nitrogen
D_{12}	binary diffusion coefficient
e	total specific energy (per unit mass of gas mixture) including kinetic, internal, and chemical energies
e_r	specific internal energy from rotational modes (per unit mass of gas mixture)
e_{tr}	specific internal energy from translational modes (per unit mass of gas mixture)

e_v specific internal energy from vibrational modes (per unit mass of N_2)

E Eckert number $u_e^2/(h_e - h_w)$

f frequency

f_c cutoff frequency for spectral filter

$f'(\eta)$ similar boundary-layer velocity profile $u(\eta)/u_e$

$F_0'(\tilde{\eta})$ profile of scaled velocity through shear layer, from multi-deck asymptotic solution downstream of separation

$g(\eta)$ similar boundary-layer total-enthalpy profile $h_T(\eta)/h_{T_e}$

$g(t)$ unit impulse response function for temperature in a semi-infinite solid

h specific enthalpy

h_0 stagnation enthalpy in the nozzle reservoir

h_s° chemical enthalpy of formation for species s

h_T local total (stagnation) enthalpy

$\hbar$ Planck constant, 6.626196×10^{-34} J·s

H_0 ratio of stagnation enthalpy to dissociation energy (Equation 5.4)

I intensity of light

k thermal conductivity

k_b backward (recombination) reaction rate

k_f forward (dissociation) reaction rate

k_v thermal conductivity for conduction of vibrational energy in a gas

K ratio of kinetic to dissociation energy (Equation 5.3)

K_1 hypersonic similarity parameter $M_\infty \sin\theta_1$

K_{eq} equilibrium constant for the reaction $N_2 + M \rightleftarrows 2N + M$

K_s Gladstone–Dale constant for refractive index of a gaseous species s

L model length scale, usually either the front plate chord (10 cm) or full model chord (15cm)

Le Lewis number $\rho D_{12} c_p/k$

L_h distance from leading edge to hingeline

L_{pk} growth length of reattaching boundary layer at location of peak heating (Equation 1.14)

L_{sep} distance along dividing streamline from separation point to reattachment point

L_u distance from hingeline to separation point

m mass of single atom in binary gas mixture

M Mach number u/a

$\mathcal{M}_s$ molecular weight of species s

n general exponent for power-law dependence

$n(t)$ noise component of a measured signal

p static pressure

p_0 stagnation pressure in the nozzle reservoir

p_{2R} initial pressure in the secondary reservoir

p_4 shock tube driver pressure; primary diaphragm burst pressure

p_{CT} initial pressure in the compression tube

p_{inc} inviscid wedge pressure p_3 at incipient separation condition

p_{inv} pressure on first wedge from inviscid computation

p_R experimental pressure averaged over transducers downstream of reattachment

p_{ST} initial pressure in the shock tube

p_T local total (stagnation) pressure; pitot pressure in supersonic flow

P ratio of static to dynamic pressure (Equation 5.2); probability

Pr Prandtl number $\mu c_p/k$

$\dot{q}$ normal heat flux at the wall, from the fluid to the body

$\dot{q}_1$ experimental heat flux averaged over thermocouples just upstream of separation

$\dot{q}_j$ heat flux in j-direction due to conduction of translational and rotational internal energy

$\dot{q}_{pk}$ peak value of heat flux in flap region

$\dot{q}_R$ experimental heat flux averaged over thermocouples just downstream of reattachment

$\dot{q}_{v_j}$ heat flux in the j-direction due to conduction of vibrational internal energy

Q^s_{el} electronic partition function for species s

Q_{T-V} source term for internal energy exchange from translational to vibrational modes

r recovery factor for heating due to viscous dissipation in a boundary layer

R reattachment point in two-dimensional flow; specific gas constant

Re Reynolds number $\rho u L/\mu$

Re_{x_1} Reynolds number at separation based on distance from leading edge

$s(t)$ noisy measured signal, *e.g.* for thermocouple measurements, $\Delta T(t) + n(t)$

S separation point in two-dimensional flow

Sc Schmidt number $\mu/\rho D_{12}$

St Stanton number based on local boundary-layer edge conditions (Equation 4.14)

St_∞ Stanton number based on free-stream conditions (Equation 2.12)

t time during a shot, referenced to time of shock reflection in nozzle reservoir; in 1-D heat conduction equations, time from initial temperature rise at thermocouple surface; test value for Student's t-distribution (Equation 6.2)

t_{dgc} time at which onset of significant driver gas contamination occurs

t_{est} time at which steady separated flow is established on the double wedge

t_{las} time at which laser is fired for flow visualization

T temperature characterizing translational and rotational internal energy

T_{amb} ambient room temperature

T^* reference temperature (Equation 4.17)

T_v temperature characterizing vibrational internal energy

u mass-averaged gas velocity (typically in the x-direction) or speed

u_s incident shock speed in shock tube

U_0 velocity profile of undisturbed boundary layer in triple-deck theory

v mass-averaged gas velocity in y-direction

v_s diffusion velocity of species s

$\bar{V}_\infty$ free-stream viscous interaction parameter $M_\infty/\sqrt{Re_\infty}$

w_s chemical production rate of species s in kg/m^3·s

x distance along double-wedge surface from leading edge; distance along nozzle centerline from exit plane; distance normal from surface of thermocouple

x_1 distance from leading edge to separation point

X transverse coordinate in triple-deck theory scaled to be of order unity $\epsilon^{-3}(x - x_1)$.

X_s mole fraction of species s

y distance normal to surface of first wedge; distance above nozzle centerline

Y normal coordinate in triple-deck theory scaled to be of order unity in each deck (Y_L, Y_M, and Y_U defined by Equations 4.35–4.37).

Y_s mass fraction of species s

z spanwise distance from the model centerline

$z_s(\eta)$ similar boundary-layer species concentration profile $Y_s(\eta)/Y_{s_e}$

Greek characters

α mass fraction of atoms in a binary dissociating gas; thermal diffusivity $k/\rho c$

β oblique shock angle relative to upstream flow direction

$\hat{\beta}$ pressure gradient parameter for similar compressible boundary-layer

γ ratio of specific heats c_p/c_v

Γ Damköhler number for gas-phase recombination in the boundary layer (Equation 5.22)

δ boundary-layer thickness, defined where $u = 0.99u_e$

δ^* boundary-layer displacement thickness

δ_{ij} Kronecker delta used with index summing notation

δ_s thickness of shear layer above dividing streamline at reattachment

Δ uncertainty or change in the following variable; Damköhler number for oblique shock on a wedge (Equation 5.19)

ΔT rise in temperature at the model surface during an experiment

ΔV thermocouple voltage signal corresponding to ΔT

ϵ small parameter $Re_{x_1}^{-1/8}$ in triple-deck theory

η grid-aligned coordinate in the body-normal direction; transformed normal coordinate in boundary-layer theory (Equations 4.2 and 4.9); temperature exponent in Arrhenius reaction rate expressions

θ flow deflection angle downstream of an oblique shock relative to upstream flow direction

θ_1 incidence angle of first wedge with respect to free stream

θ_d characteristic temperature for dissociation

θ_{ff} angle of finite fringes with respect to horizontal

θ_{inc} flap deflection angle for incipient separation

θ_r characteristic temperature for molecular rotation

θ_{sep} angle between separation streamline and first wedge

θ_v characteristic temperature for molecular vibration

θ_w deflection angle of second wedge (flap) with respect to first wedge

λ wall-shear parameter for compressible boundary layer ($f''(0)/\sqrt{2}$ for a self-similar boundary layer); wavelength

Λ scaling factor describing wall temperature effect on separation length (Equation 4.49)

μ viscosity

ν kinematic viscosity μ/ρ; degrees-of-freedom parameter in Student's t-distribution

ξ grid-aligned coordinate in the streamwise (body-parallel) direction; transformed streamwise coordinate in boundary-layer theory (Equations 4.1 and 4.8)

ρ mass density

ρ_d characteristic density in IDG model

σ standard deviation (sample or population)

τ shear stress $\mu(\partial u/\partial y)$

τ_{ij} shear stress tensor for two-dimensional flow

τ_v characteristic time for vibrational relaxation

ϕ phase shift due to changes in optical path length along a ray through the test section flow; function in Wilke's mixing rule (Equation 4.34)

$\Phi(f)$ optimal spectral filter giving least-squares estimate of true signal when convolved with noisy signal

$\bar{\chi}$ viscous interaction parameter $M^3\sqrt{C^*/Re_x}$

ψ^* dividing streamline between fluid which remains in recirculation region and fluid which continues downstream of reattachment

Subscripts

0 stagnation conditions in the nozzle reservoir; undisturbed boundary-layer profile in triple-deck theory

1 inviscid region downstream of leading shock; location just upstream of separation at boundary-layer edge; upstream state of a single shock in general

2 inviscid region downstream of separation shock; downstream state of a single shock in general

3 inviscid region downstream of reattachment shock

aw conditions at an adiabatic wall

CJ pertaining to the Chapman Jouget limit

e local conditions at the edge of a boundary layer

eq equilibrium-flow solution

ff pertaining to finite-fringe pattern in an interferogram

fp undisturbed flat-plate flow

fr frozen-flow solution

i, j directional indices in either Cartesian coordinates or grid coordinates

inc condition for incipient separation

m index for third-body species in reaction

max	maximum value corresponding to shock detachment
min	minimum value corresponding to C–J limit
n	component normal to an oblique shock; time-step index for a discretized variable
N_2	pertaining to molecular nitrogen
N	pertaining to atomic nitrogen
pk	peak value at reattachment, or location of peak value
r	pertaining to rotational internal energy modes; secondary species index
ref	reference point for describing finite-fringe pattern in an interferogram; flat plate conditions without flap deflection for reference heating
R	local conditions at, or just downstream of, the reattachment point
s	species index
S	local conditions at, or just upstream of, the separation point
tr	pertaining to translational internal energy modes
v	pertaining to vibrational internal energy modes
w	conditions at the wall
ψ^*	conditions along the dividing streamline
∞	free-stream conditions on nozzle centerline at axial position corresponding to either the nozzle exit plane or the model leading edge; free-stream conditions for flat-plate boundary layer
$*$	sonic conditions (at throat of nozzle)

Superscripts

$*$	evaluation at reference-temperature conditions

Acronyms

2R	secondary reservoir (holds compressed air to drive T5 piston)
C–J	Chapman–Jouget
CFD	computational fluid dynamics

CT	compression tube (driver section of T5)
DAS	data acquisition system
DT	dump tank (collects gases after shot in T5)
EMF	electromotive force
ESTC	Equilibrium Shock Tube Calculation (computer program)
IBL	interacting boundary-layer (computational method)
IDG	ideal dissociating gas
N-S	Navier-Stokes
NIST	National Institute of Standards and Technology
PNS	parabolized Navier-Stokes (computational method)
PT	pressure transducer
ST	shock tube (driven section of T5)
SURF	SUpersonic Reacting Flow (computer program)
TC	thermocouple
TDT	triple-deck theory
TS	test section

(This page was intentionally left blank.)

Chapter 1 Introduction

1.1 General Description of Phenomenon

The qualifier "high-enthalpy" in the title of this thesis refers to a gaseous flow with stagnation enthalpy high enough to cause dissociation of a molecular gas. A common example is the flow seen by a vehicle entering the atmosphere at sub-orbital velocity. In the frame of reference of the vehicle, the kinetic energy of the free-stream gas is comparable to its characteristic dissociation energy. Such flows are labeled hypervelocity flows to distinguish them from cold hypersonic flows, in which the Mach number is high but the free-stream speed of sound is very low and the free-stream kinetic energy is small compared to the dissociation energy of the gas. A cold hypersonic flow is also called a perfect-gas flow because the composition remains constant, the energy in vibrational modes of molecules is negligible, and thus the gas can be described using a single perfect-gas equation of state with constant specific heats. A high-enthalpy flow is locally in chemical equilibrium where the characteristic time for dissociation is much greater than the characteristic flow time, which may occur, for example, in the stagnation region of a large blunt body. The flow is chemically frozen where the characteristic time for dissociation is much smaller than the characteristic flow time; this is often the case downstream of weak oblique shock waves. Where the characteristic chemical and flow times are of similar magnitude, the flow is in chemical nonequilibrium. Recombination reactions may also be important where dissociated gas encounters a region of lower velocity and temperature (*e.g.* near a cold wall). In addition, a hypervelocity flow field may include thermal nonequilibrium, where the internal energy in molecular vibrational modes is out of equilibrium with the energy in translational and rotational modes. Ionization of atoms or molecules, however, is insignificant for the flows investigated in this work.

Direct interaction between a shock wave and a boundary layer occurs in many practical high-speed flows. Such interactions on a real flight vehicle are often three-dimensional in nature, but here we consider only two-dimensional interactions, where a planar oblique shock wave is generated by an upstream-facing corner (Figure 1.1, commonly referred to as a "compression corner") or is generated externally and impinges on a boundary layer (Figure 1.2a). The viscous no-slip condition of a boundary layer requires a finite region of subsonic flow near the wall, through which the presence of the shock can be felt upstream of the shock location. The pressure rise across the shock is spread out by the boundary layer as shown schematically in Figure 1.1a. For sufficiently high shock strength (sufficiently high ramp angle in corner flows), the low-speed fluid in the boundary layer cannot

negotiate the imposed pressure rise. Then the boundary layer separates upstream of the shock location and reattaches to the wall downstream of the shock location, producing the configuration shown in Figures 1.1b and 1.2. A free-shear layer between the separation and reattachment locations (S and R in Figure 1.1b) encloses a region of slow-moving, recirculating fluid with reversed flow near the wall. Other names for this region are separation bubble, recirculating region, and dead-air region. The pressure reaches a plateau level between separation and reattachment in well separated flows, as indicated in Figure 1.1b. The separated flow accomplishes two things; the overall pressure rise is split into two smaller jumps, and the free-shear layer transports momentum from the high-speed external fluid to the low-speed fluid which must negotiate reattachment. Two other related flow configurations not considered here are the upstream-facing and downstream-facing steps. Unlike the compression-corner and shock-impingement flows, step flows force a fixed location for either the separation point or reattachment point.

The double-wedge configuration shown in Figure 1.2b is obtained by simply rotating the flat plate in Figure 1.1b to some incidence angle with respect to the free-stream flow direction. The upstream plate becomes the first wedge, and the downstream ramp becomes the second wedge, which will also be referred to as a ramp or flap (*e.g.* the flap deflection angle is the angle of the second wedge with respect to the first wedge). Double-wedge flow is an abstraction of the flow on a reentry vehicle that is flying at angle of attack and using a trailing body flap for longitudinal control. Though the free-stream flow is hypersonic, the interaction at the corner may see only supersonic flow ($M_1 < 5$) for even moderate incidence angles of the first wedge. A laminar supersonic interaction is indicated in Figure 1.2b by coalescence of compressive waves from the interaction to form a shock well outside the boundary layer; in a hypersonic interaction or in a turbulent interaction, the shock may form inside the boundary layer. At high angles of attack in hypervelocity flow, nonequilibrium dissociation behind the leading-edge shock becomes important, and this is one reason the double-wedge geometry was chosen for the present study.

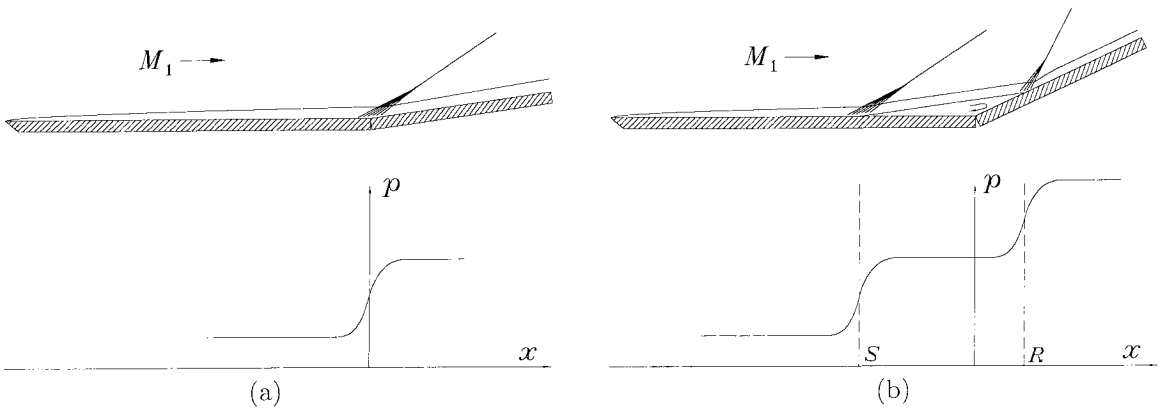

Figure 1.1: Sketch of supersonic viscous flow past an upstream-facing corner and corresponding pressure distributions for (a) attached flow and (b) well separated flow.

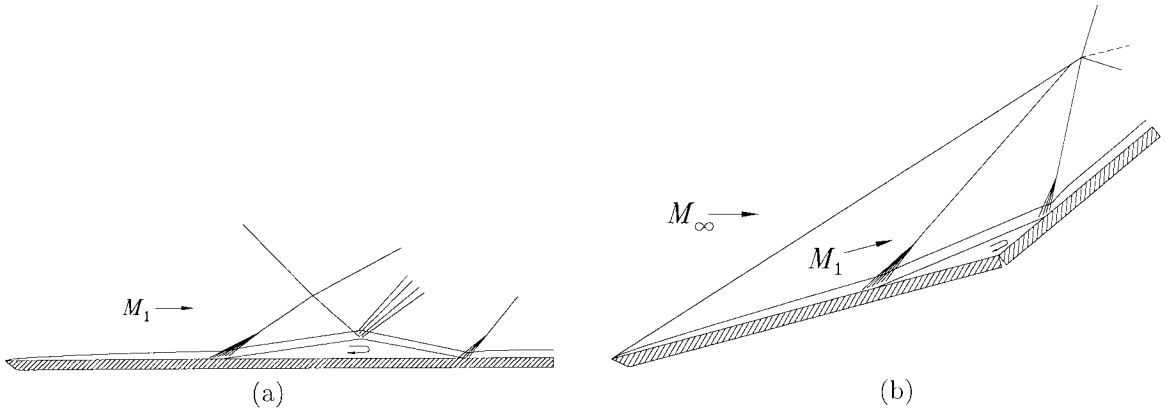

Figure 1.2: Sketch of shock-induced boundary-layer separation for the case of (a) a shock wave impinging on a boundary layer and (b) high-speed flow on a double wedge.

The main topic of this thesis is real-gas effects on the phenomenon of shock/boundary-layer interaction. The phrase "real-gas effects" used throughout this work is here defined as changes in a hypervelocity flow field due to chemical reactions and thermal nonequilibrium, with respect to the same flow without reactions and without vibrational relaxation (*i.e.* a perfect-gas flow in which reactions and vibrational–translational energy exchanges are artificially turned off).

1.2 Motivation and Objective

High-enthalpy shock/boundary-layer interaction can be important in practical high-speed flows such as external flow over a control surface on a hypervelocity vehicle flying at angle of attack, or internal flow in a hypersonic air-breathing propulsion system. The size of the separation bubble effects the distribution of aerodynamic forces, which has implications for effectiveness of control surfaces. The high local wall heating where the boundary layer reattaches is of concern for the design of thermal protection systems. Knowledge gained from the present work pertaining to length of separation in shock/boundary-layer interaction also has application to separation length downstream of a body in high-speed flow; this is an important factor in determining the drag on spacecraft during aerobraking maneuvers.

An infamous example of the importance of shock-induced boundary-layer separation and real-gas effects on a hypervelocity flight vehicle is the pitching-moment anomaly experienced during first flight of the U.S. Space Shuttle Orbiter. During the high Mach-number portion ($M_\infty > 10$) of the reentry flight, when the orbiter flies at greater than 35° angle of attack, the body-flap deflection required to maintain trimmed flight was twice the predicted value. Half of the discrepancy is likely due to the fact that the boundary-layer flow was laminar at high Mach number; predictions assumed a turbulent boundary layer in this regime and thus a much smaller separation bubble at the base of the control flap (Woods *et al.*, 1983). The remaining differences can largely be accounted for

by real-gas effects on the pressure distribution over the body, particularly over the aft expansion region (Weilmuenster *et al.*, 1994). Additional contributions come from high Mach-number effects incorrectly extrapolated from wind tunnel data and viscous drag effects (Griffith *et al.*, 1983; Maus *et al.*, 1984).

The mechanisms by which real-gas effects act in high-enthalpy shock/boundary-layer interaction, and the resulting changes in the extent of separation and the wall heating at reattachment, are poorly understood. Very little research has been performed on this subject. Previous experiments have either explored regimes where real-gas effects are insignificant or have not found conclusive results, and although several computational studies have found different real-gas effects under different conditions, nowhere in the existing literature is there presented a unified explanation of the mechanisms involved (*cf.* Section 1.5.4). The objective of the present work is to develop such a framework for describing mechanisms for real-gas effects in shock/boundary-layer interaction, and where possible, to validate these mechanisms by experiments in a high-enthalpy shock tunnel and by comparison to previous results in the literature. The experimental work is carried out in the T5 Hypervelocity Shock Tunnel at Caltech.

1.3 Scope of Present Work

Separated flow produced by shock/boundary-layer interaction encompasses many different physical phenomena. The present work, however, is limited to the study of those phenomena which are amenable to experimental investigation under high-enthalpy flow conditions using the diagnostics available in the T5 Hypervelocity Shock Tunnel. Thus we consider only the length of the separated region in fully separated flows, which can be measured by flow visualization, and the wall heating at reattachment, which can be measured by heat flux instrumentation.

Phenomena not considered in the present work include upstream influence, plateau pressure, and incipient separation. Upstream influence is the distance upstream of separation (or upstream of the corner for attached flows) over which a pressure disturbance is felt (*i.e.* to the left of S in Figure 1.1b). The low density of pressure measurement instrumentation used in the present experimental work is entirely insufficient for obtaining information on upstream influence. Plateau pressure is the constant pressure reached in a well separated flow with a large separation region, as shown in Figure 1.1b. Measurement of plateau pressure (and pressure upstream of separation) also suffers from sparse instrumentation in the present work. Incipient separation is the state between attached and separated flows; for an upstream-facing corner, the incipient separation angle is the maximum ramp angle to maintain attached flow. To study this phenomenon experimentally requires many repeated experiments with the same free-stream conditions but small increments in flap deflection angle, which was deemed infeasible for the present work in T5.

Furthermore, the present study is limited to two-dimensional shock/boundary-layer interactions, and the present experiments are limited to interactions generated by an upstream-facing corner on a double wedge. To remove as many complications as possible, we consider only double wedges with a sharp leading edge, and we work with a simple binary gas consisting of atoms and molecules of the same element. While the experiments in T5 do include transitional and turbulent interactions, the emphasis in this work is on laminar interactions.

The present experiments are not designed to simulate actual flight conditions. In fact, it is not possible to precisely duplicate hypervelocity flight conditions on a scaled test model in a shock tunnel, due to two different phenomena. One is partial free-stream dissociation at high-enthalpy conditions; the dissociated gas in the nozzle reservoir does not fully recombine before the nozzle expansion flow becomes chemically frozen. The other is a difference in the dependence on density of reaction rates for dissociation (a binary reaction) and recombination (a tertiary reaction). For nonequilibrium flows in which both reactions are important, only one of the reactions can be properly scaled. The approach taken in the present work is to use the capabilities of the T5 Hypervelocity Shock Tunnel to explore the physics of the problem, regardless of whether the flow conditions correspond to a portion of a particular reentry flight trajectory.

1.4 Physical Description of Separated Flow

Before considering real-gas effects, it is important to understand the physical processes which control the phenomena of separation length and reattachment heating. The present notation for separated flow geometry on a double wedge, used throughout this work, is shown in Figure 1.3. The boundary layer separates upstream of the corner (also referred to as the hingeline) at S and reattaches downstream at R. Between S and R, the dividing streamline ψ^* (approximated here by a straight line) is defined as the streamline through which there is no mass flux; the gas inside ψ^* remains in the recirculation region while the gas outside ψ^* continues downstream of reattachment. Only the angle of the first wedge, θ_1, is measured with respect to the free-stream flow direction; the separation angle

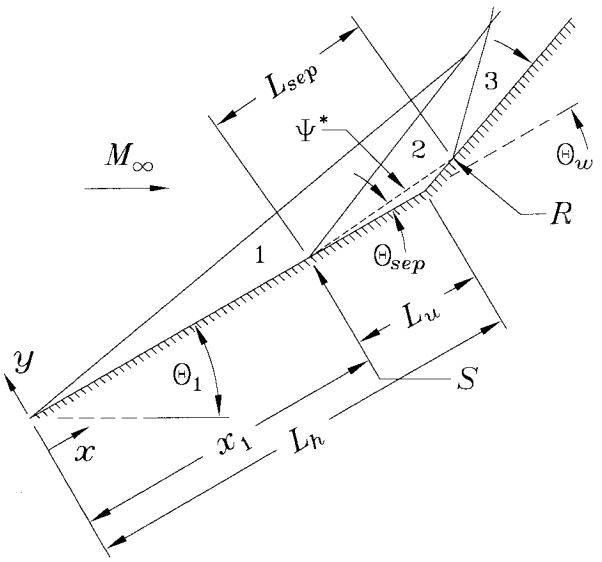

Figure 1.3: Schematic of separated flow on a double wedge with definitions for the notation used throughout this work.

θ_{sep} and ramp deflection angle θ_w are measured with respect to the first wedge. Separation length L_{sep} is the distance from S to R along ψ^*. The distance L_u between S and the corner is not to be confused with the upstream influence defined in Section 1.3. (The term "upstream influence" is sometimes used in the literature to refer to the length defined here as L_u, which can cause confusion because the two lengths are due to different physical phenomena.) Other horizontal length parameters are measured from the leading edge (L_h to the hingeline and x_1 to the separation point), and y is distance perpendicular to the first wedge surface. The subscripts ∞ and 1–3 refer to different inviscid flow regions. In general, these flow regions are not uniform as implied by Figure 1.3, and hence we take the following restricted definitions when discussing experimental results: ∞ refers to free-stream conditions on the nozzle centerline at an axial location corresponding to the leading edge of the double wedge; 1 refers to the edge of the boundary layer just upstream of S; 2 and 3 refer to consistently defined locations based on either experimental or computational data (*cf.* Section 3.3.4). Note that the subscript e refers to boundary-layer edge conditions in general.

The local flow around the separation point S has been found to depend only on local conditions (*e.g.* M_1 and Re_{x_1}), and not on the downstream agency producing separation; see, for example, the early work of Gadd *et al.* (1954). This part of the flow is determined by a coupling of the pressure/flow-deflection relationship at the edge of the boundary layer and the momentum equation at the wall, and was dubbed "free interaction" by Chapman *et al.* (1958). Although the point S moves upstream for increasing θ_w, the shape of the pressure rise to separation and then to the pressure plateau in the separated region is determined locally by an interaction between the supersonic flow outside the boundary layer and the thickening of the low-speed region of the boundary layer near the wall. In fact, the separation angle θ_{sep} and resulting plateau pressure are analogous to the ramp angle θ_w and resulting inviscid pressure rise for incipient separation on an upstream-facing corner. Note that the free interaction is not entirely independent of the downstream condition; the position of S can have a small effect on the local parameters controlling free interaction, particularly for nonuniform external flow.

The physical process which determines separation length L_{sep} has been elegantly described by Glick (1962) as follows: an element of fluid at S just outside the dividing streamline ψ^* has essentially zero velocity and a total pressure p_T equal to the local static pressure p_S, but when this element reaches R, it must have $p_T = p_R > p_S$; the increase in mechanical energy is accomplished by viscous transport of momentum from the outer flow towards ψ^*. Thus as θ_w is increased, p_R is increased and the separated shear layer must extend over a longer distance in order to impart the momentum required to overcome the pressure rise at reattachment. In addition, there is a weak coupling between the flow at R and the flow at S; θ_{sep} depends on the position of S which depends on p_3/p_2, which itself depends on θ_{sep}.

Different ideas related to the general physical picture described above have led to different ap-

proaches for modeling the separation bubble. In order to explain the effect of transition to turbulence on separation length, Chapman *et al.* (1958) considered an equilibrium balance between the mass flow entrained into the low-speed side of the separated shear layer from the dead-air region and the mass flow injected back into the dead-air region at reattachment. Similarly, Hakkinen *et al.* (1959) found a scaling for L_{sep} by considering a momentum balance between forward and reverse flow across the line of zero velocity embedded in the recirculating region. A well known theory for the plateau pressure (also applicable to the determination of L_{sep}), put forth by Chapman *et al.* (1958) for laminar flows and by Korst (1956) for turbulent flows, requires that the total pressure along the dividing streamline ψ^* as it approaches R is equal to the static pressure p_3 downstream of R. The analysis assumes an isentropic compression process along ψ^* close to R, neglects the fact that the pressure at reattachment, p_R, is typically much lower than p_3, and neglects the initial thickness of the boundary layer at separation. While the errors tend to cancel each other for flows with incoming boundary-layer thickness small compared to separation length (Chapman and Korst, 1957), the effect of initial thickness was shown to be important in some cases (McDonald, 1964; Nash, 1963).

In the present work, we focus on a model that uses a momentum balance between shear forces acting on ψ^* and the pressure rise at reattachment, an idea due originally to Sychev (1982) and applied by Roshko (1995) to the problem of separation length in supersonic base flow. The balance of stresses acting on the boundary of the separation bubble can be written

$$\int_0^{y_R} (p_{\psi^*} - p_2)\, \mathrm{d}y \;=\; \int_{x_1}^{x_R} \tau_{\psi^*}\, \mathrm{d}x\,, \tag{1.1}$$

where the small shear stress along the wall is neglected, and the separation geometry of Figure 1.3 is approximated for small θ_{sep} as an upstream facing step of height y_R equal to the perpendicular distance of R from a line tangent to the first wedge surface. Note that for laminar interactions, p_{ψ^*} is essentially constant and equal to the plateau pressure over much of the separated region, increasing only close to R. This model shows that L_{sep} is determined by a balance between the reattachment pressure rise and the evolution of shear stress along the dividing streamline.

In all the approaches discussed above, information is required about the development of the velocity profile in the free-shear layer, and it is this information which is most difficult to obtain. The theoretical approach discussed in Section 4.2 essentially relates the shear stress along ψ^* to the wall shear stress of the incoming boundary layer undisturbed by separation.

The length of separation is also very sensitive to the location of transition to turbulence. If transition occurs in the free-shear layer upstream of reattachment, then τ_{ψ^*} is increased over part of the separation region due to the fuller velocity profile in a transitional or turbulent viscous layer, resulting in a decreased L_{sep} compared to a purely laminar interaction (*cf.* Section 1.5.2.1). Such a

transitional interaction is likely to occur even if the incoming boundary layer is far from transition, because the free-shear layer is much less stable than a boundary layer. A purely turbulent interaction refers to cases where the incoming boundary layer is turbulent; this can be further subdivided into cases where transition occurs somewhere between the leading edge and separation, and cases where the boundary layer is turbulent from the leading edge. The present work concentrates on purely laminar interactions, where the theory presented in Section 4.2.1 might be useful for ascertaining real-gas effects on separation length.

We now turn briefly to the phenomenon of increased heat flux on the second wedge (flap) compared to the first wedge. The physics involved is rather straightforward. Even for incompressible flow, impingement of an incoming boundary layer or shear layer will increase heating on the flap by a stagnation process. Considering compressible flow, the heating increases due to the effects of shock compression; the increased density, increased temperature, and decreased velocity all result in higher heat transfer to the ramp wall. In addition, the boundary layer initially experiences a reduction in thickness on the wedge due to compression of the boundary layer; this phenomenon is shown schematically in Figures 1.1 and 1.2. The "necked" region can induce higher heat loads on the wall. The pressure at reattachment in a fully separated flow may be slightly higher than the inviscid ramp pressure for attached flow at the same ramp angle; the external flow in the separated case reaches the same deflection angle as for the attached case, but has been processed by two oblique shocks instead of one, and thus has smaller losses. (The inviscid ramp pressure is restored via an expansion emanating from the shock intersection point.) The increased pressure recovery for separated flows can result in increased wall heat flux as well. Transition of the free-shear layer can cause large increases in the heat flux at reattachment over purely laminar interactions.

1.5 Review of Previous Work

While there have been few results published for real-gas effects on shock/boundary-layer interaction, the phenomenon has been studied quite extensively for perfect-gas flows. The review of perfect-gas work in this section is not exhaustive, but is meant to provide an overview of the various methods that have been used to attack the problem, plus salient results (from both experiment and analysis) relevant to separation length and reattachment heating. More attention is given to the problem of separation length than to reattachment heating. Previous work in high-enthalpy flows are discussed in detail at the end of this section.

1.5.1 Methods for Predicting Interaction Flows

Some of the earlier attempts at analysis of shock-induced separation flows relied on simple models of separation, free-shear layers, and reattachment. Chapman (1950) developed a laminar mixing layer

theory which gave the velocity along the dividing streamline, which was then applied to a criterion for total pressure on the dividing streamline (*cf.* Section 1.4) to obtain the plateau pressure for leading-edge separation (Chapman *et al.*, 1958). As detailed by Needham (1965), other workers have extended this idea to include the effects of finite boundary-layer thickness upstream of separation, temperature of the dead-air region, and nonisentropic compression at reattachment. McDonald (1965) considered turbulent separation at a compression corner. Results of such shear-layer modeling methods depend on the form of the shear layer profiles, and have shown only limited success at accurately predicting features of separated compression-corner flows.

1.5.1.1 Momentum Integral Techniques

Much use has been made of momentum integral methods to predict laminar separated flows, whereby the boundary-layer equations are applied to the entire interaction region, with reversed-flow profiles in the separation region. The equations are reduced to ordinary differential equations by transforming to incompressible form and integrating across the boundary layer; these are coupled to the inviscid outer flow and integrated downstream from an initial pressure perturbation, the position of which is iterated upon to match the downstream boundary condition. Introduced originally by Crocco and Lees (1952) as a "mixing theory," the method has been extended upon and improved by, among others, Glick (1962) who linked Crocco's mixing-rate correlation function to experimental results, Lees and Reeves (1964) who included an equation for moment of momentum and linked the profile shape parameter to similarity solutions of Cohen and Reshotko (1956), Klineberg and Lees (1969) who included the energy equation, and Georgeff (1974) who improved and simplified Klineberg's method. The method has even been used to study control effectiveness on real vehicles (Ikawa, 1977). Nielsen *et al.* (1970) used a different transformation, used analytic functions for the profiles, and employed a different downstream boundary condition; compared to Klineberg's method, Nielsen's method matches experiment better near reattachment but worse near separation. Hunter and Reeves (1971) applied a momentum integral method to turbulent separation with limited success in predicting experimental results. A major drawback of all these methods is that they neglect pressure gradients normal to the wall, which can be important near separation and reattachment where the boundary layer is curved. Bloy and Georgeff (1974) found that the critical stability behavior of these methods depends on the particular formulation of the equations and is due to the neglect of normal pressure gradients, having no other physical significance. Holden and Moselle (1968) developed an integral technique which included an equation for momentum in the normal direction and found reasonable agreement with experiment. These momentum integral techniques have proven to be a useful, though approximate, method for prediction of shock-induced separated flows.

Two other methods are mentioned here because they are related to the momentum integral

approach. One is the interaction boundary-layer (IBL) method introduced by Werle and Vatsa (1974). They used transformed boundary-layer equations and viscous/inviscid coupling, but these are instead solved implicitly over the entire interaction by a relaxation technique. The comparison with experiment was fair, but the results appear to depend on mesh size. In a method presented by Igarashi *et al.* (1988), the shock-wave/boundary-layer interaction flow is solved numerically by applying the momentum integral method to a viscous sub-layer near the wall and applying the (inviscid) Euler equations to the outer part of the boundary layer. Agreement with experiment was fair.

1.5.1.2 Asymptotic Theory

Attempts to develop a more exact technique for analysis of separated flows led to asymptotic methods in which viscous flow is represented by a multi-layer structure. Lighthill (1953) first introduced the idea for a supersonic boundary layer, with a viscous, incompressible sub-layer near the wall, an inviscid, compressible layer in the main part of the boundary layer, and supersonic, isentropic external flow at the outer edge of the boundary layer. These ideas were formalized in a nonlinear triple-deck theory (TDT) by Stewartson and Williams (1969), who considered separation as a perturbation to an undisturbed boundary layer. The approach consists of expanding variables in the small parameter $\epsilon = Re_{x_1}^{-1/8}$, finding dominant balances in the Navier Stokes equations for each layer, and asymptotically matching across all three decks. By use of Chapman's linear viscosity law $\mu/\mu_e = CT/T_e$, the velocity distribution is made independent of the energy equation so that only perturbations to the momentum equation need be considered. Subsequent authors have looked at nonisentropic flow conditions for the upper deck; Neiland (1971a) used the tangent-wedge approximation, Brown and Stewartson (1975) applied the full inviscid Euler equations for $M_1 \gg 1$, and Brown *et al.* (1975) presented an approximate theory bridging the supersonic and hypersonic regimes. The energy equation was first introduced to TDT by Rizzetta (1979), while more recent work by Brown *et al.* (1990) and Kerimbekov *et al.* (1994) focuses on the effects of wall temperature. Inger (1996) presented a simplified formulation including the energy equation, valid for both supersonic and hypersonic flows. The asymptotic form of the solution downstream of separation, where additional layers must be introduced for the reversed flow, was considered by Neiland (1971b) and Stewartson and Williams (1973). Burggraf (1975) extended these results for the plateau region to the reattachment region, and by using Chapman's hypothesis regarding total pressure on the dividing streamline (*cf.* Section 1.4), derived a scaling for the length of the plateau region in well separated flows.

Unlike simpler boundary-layer theory, triple-deck theory includes normal pressure gradients in the main deck. The multi-deck structure allows an interaction between the thickening of the viscous sub-layer and the pressure gradients in the outer layer, with the middle layer simply displaced from

the wall at separation. The theory is, however, strictly valid only in the limit of $Re_{x_1} \rightarrow \infty$, a fact commonly cited to explain discrepancies between TDT results and experimental data at lower Re_{x_1}. Rizzetta *et al.* (1978), Brown *et al.* (1990), and Burggraf *et al.* (1979) have made comparisons between numerical TDT solutions and IBL solutions (*cf.* Section 1.5.1.1), finding that as Re_{x_1} increases to very high values ($\sim 10^8$), the IBL solution approaches the TDT solution. Despite its shortcomings, triple-deck theory has been found capable of reproducing scaling laws previously found by purely empirical methods. Inger (1994a,b) used TDT to corroborate an empirical relation for incipient separation, and as described below in Section 1.5.2, Katzer (1989) noticed a striking similarity between his empirical result for separation length scaling and the theoretical result of Burggraf (1975) based on TDT. Asymptotic theory seems to provide information regarding the functional dependence of gross interaction quantities such as separation length, probably because it incorporates the essential physics.

1.5.1.3 Navier–Stokes Computations

With modern high-speed digital computers, it is possible to attempt solution of the full Navier–Stokes equations (or rather, their discretized version) for shock/boundary-layer interaction flows. Cheng (1993) gives a review of Navier–Stokes computation methods prior to 1993, discussing the parabolized Navier Stokes (PNS) approach where the equations are made parabolic by dropping many streamwise-dependent terms, the thin-layer Navier–Stokes approach which uses the unsteady PNS equations in a time-marching technique to recover some upstream influence effects, and more recent techniques to solve the full Navier–Stokes equations. The comparisons made between computation and experiment in the existing literature do not show consistent results, particularly with regard to the extent of separation. In most cases, computations underpredict the length of separation (Fay and Sambamurthi, 1992; Hung and MacCormack, 1976; Leyland, 1996; Power and Barber, 1988; Ramakrishnan *et al.*, 1991), but some authors report predictions that both underestimate and overestimate experimental L_{sep} (Grasso *et al.*, 1994; Grasso and Marini, 1996; Rizzetta and Mach, 1989; Simeonides *et al.*, 1994), depending on the numerical grid or depending on the experiment simulated. Thomas (1992) noted that the computed position of separation generally moves upstream with increased grid resolution, and Simeonides *et al.* (1994) suggest that a convergence criterion for computation of separated flows be based on the steady location of separation with respect to both grid refinement and iteration.

True convergence with respect to grid refinement, however, is not a simple matter to obtain; both Grasso *et al.* (1994) and Rizzetta and Mach (1989) clearly show that the solution depends not just on the overall grid resolution, as characterized by the number of cells in each spatial direction, but also on exactly how those cells are distributed. Results can be extremely sensitive to such parameters as the spatial distribution of cells in the interaction region, and the aspect ratio of cells at the leading

edge, at separation, and at reattachment. One common problem is that grids are refined near the leading edge and near the corner, but in well separated flow, the steady-state separation point is located in between. Rizzetta and Mach (1989) also showed large differences between results obtained using different numerical methods. In fact, the different methods exhibited different dependencies on the grid cell distribution. To make matters even worse, some of the experiments commonly used for comparison utilize wind tunnel models of aspect ratio less than unity (Coët and Chanetz, 1993; Holden and Moselle, 1968) for which centerline measurements are not necessarily free from three-dimensional flow (*cf.* Section 2.7.5). Rudy *et al.* (1989) could only obtain good agreement with experiment for a well separated compression-corner flow by computing the full three-dimensional solution, but Lee and Lewis (1993) were able to match the same experimental data using a two-dimensional method.

The accurate prediction of separated flows by numerical solution of the Navier–Stokes equations remains an important topic for research. In particular, there is a clear need for systematic, exhaustive study of the dependency of solutions on grid cell distribution and on numerical method (such a study is well beyond the scope of the present work). On the other hand, computational techniques are still useful as an aide to understanding the physics of shock/boundary-layer interaction, and it is mainly in this capacity that viscous computations are utilized in the present work.

1.5.2 Separation Length

The length of separation in perfect-gas flow depends upon the parameters which govern the incoming boundary layer, the free-shear layer, and the reattachment pressure rise; these include the local Reynolds number Re_{x_1} and Mach number M_1 at separation, the wall temperature ratio T_w/T_1, the flap deflection θ_w, and the ratio of specific heats γ_1. Separation length must also depend on a length scale, and as long as the downstream edge of the ramp does not influence the reattachment region (*i.e.* if the ramp is long enough), the only length scales are the distance from the leading edge x_1 and the boundary-layer thickness δ_1, itself a function of x_1. Since the interaction at separation is a local phenomenon, boundary-layer thickness, characterized by the better-defined displacement thickness δ_1^*, is often used to scale L_{sep}. Thus L_{sep} should obey a correlation in the form

$$\frac{L_{sep}}{\delta_1^*} \propto f\left(Re_{x_1},\, M_1,\, \frac{T_w}{T_1},\, \theta_w,\, \gamma_1\right) . \tag{1.2}$$

Note that δ_1^* itself depends on Re_{x_1}, M_1, T_w/T_1, and γ_1.

1.5.2.1 Qualitative Results

Clearly, L_{sep} is expected to increase with increasing flap deflection θ_w, or equivalently, with increasing pressure rise at reattachment p_3/p_2. This has been confirmed numerous times both by experiments

(Anders, 1970; Bloy and Georgeff, 1974; Coleman and Stollery, 1972; Elfstrom, 1972; Ferguson and Schaefer, 1962; Gadd *et al.*, 1954; Harvey, 1968; Hayakawa and Squire, 1982; Holden, 1978; Kumar and Stollery, 1994; Miller *et al.*, 1964; Needham, 1965; Roshko and Thomke, 1970; Settles and Bogdonoff, 1982; Settles *et al.*, 1979) and by computations (Bloy and Georgeff, 1974; Fay and Sambamurthi, 1992; Grasso and Leone, 1992; Katzer, 1989; Nielsen *et al.*, 1970; Rizzetta *et al.*, 1978), regardless of whether the interaction is laminar, transitional, or turbulent. L_{sep} has also been shown without exception to increase with decreasing M_1, experimentally and computationally (Anders and Edwards, 1968; Elfstrom, 1972; Gadd *et al.*, 1954; Hayakawa and Squire, 1982; Holden, 1971a, 1972; Katzer, 1989; Miller *et al.*, 1964; Needham, 1965; Roshko and Thomke, 1976). This behavior with M_1 might be expected because the growth rate of a free-shear layer decreases with increasing Mach number, resulting in higher shear stress along the dividing streamline and hence a decrease in L_{sep}. The Mach-number influence is actually more complicated; both the separation angle θ_{sep} and reattachment pressure rise p_3/p_2 depend on M_1 independently of the shear layer development.

The effect of wall temperature on L_{sep} for laminar and turbulent interactions has been shown by experiments and computation (Brown *et al.*, 1990; Coët and Chanetz, 1993; Curle, 1961; Elfstrom, 1972; Ferguson and Schaefer, 1962; Georgeff, 1974; Holden, 1972; Lewis *et al.*, 1968; Needham, 1965; Nielsen *et al.*, 1970); L_{sep} increases with increasing T_w/T_1, so that cooling the wall causes a decrease in the extent of separation. The effect is much stronger for laminar interactions than for turbulent interactions, and may be due to changes in boundary-layer and shear-layer thickness with T_w/T_1. There are conflicting results in the literature for transitional flows. Experiments by Johnson (1968) show L_{sep} increasing with T_w/T_1, while experiments by Coët and Chanetz (1993) show the opposite trend. The latter result was attributed to the stabilizing effect on the shear layer of lowering T_w/T_1, so that transition was delayed. (The location of transition has a strong influence on L_{sep}.)

For purely laminar interactions, L_{sep} increases with increasing Re_{x_1}, as shown by both experiment and computation (Anders and Edwards, 1968; Holden, 1971a; Johnson, 1968; Lewis *et al.*, 1968; Miller *et al.*, 1964; Needham and Stollery, 1966a; Nielsen *et al.*, 1970). Since the wall shear stress of a laminar boundary layer decreases with increasing Re_{x_1}, this behavior is consistent with the physical picture presented in Section 1.4 where L_{sep} is governed by shear stress. Experiments with transitional interactions all show L_{sep} decreasing with increasing Re_{x_1}, due to upstream movement of transition in the shear layer (Ferguson and Schaefer, 1962; Gadd *et al.*, 1954; Johnson, 1968; Needham and Stollery, 1966a; Todisco and Reeves, 1970). Results for purely turbulent interactions depend on the range of Re_{x_1} investigated; some experiments show L_{sep} increasing with Re_{x_1} (Coleman and Stollery, 1972; Elfstrom, 1972; Holden, 1972; Todisco and Reeves, 1970) while others show the opposite (Roshko and Thomke, 1970, 1976; Settles and Bogdonoff, 1982). Hunter and Reeves (1971) found by computation that L_{sep} increases with Re_{x_1} for transition occurring upstream of separation

but downstream of the leading edge, with the trend reversing when transition reaches the leading edge. In the first regime, thickening of the boundary layer at transition dominates, while in the second regime, increasing Re_{x_1} results in decreased thickness for a fully turbulent boundary layer. Both turbulent regimes produce much smaller separation bubbles than the laminar regime, due to increased skin friction.

The importance of the incoming boundary-layer profile in determining L_{sep} was shown clearly by Hayakawa and Squire (1982), who found that injecting gas through a porous wall upstream of a turbulent interaction had the effect of reducing skin friction and increasing separation length. They indicate only that transition is well upstream of the injection location, but one must assume their experiments were in the first turbulent regime discussed above, because the experiments of Roshko and Thomke (1976) in the second turbulent regime show separation length increasing with skin friction. The latter result is not consistent with the view taken in Section 1.4, so that there must be a different mechanism dominating the behavior of L_{sep} in the second turbulent regime. This discrepancy is not considered further here because analysis for the present work (*cf.* Section 4.2.1) is concerned only with laminar interactions.

The effect of leading-edge bluntness on separation length is important in most practical situations; reentry vehicles have blunt, not sharp, leading edges, in order to reduce the local wall heating. Although this aspect is left out of the present study to simplify the problem, some results from the literature are mentioned here. Most studies showed L_{sep} decreasing with increasing bluntness (Coët and Chanetz, 1994; Grasso and Marini, 1996; Kumar and Stollery, 1996). Holden (1971a) showed this trend occurs in hypersonic flows only for large nose radius where the increased favorable pressure gradient due to bluntness increases skin friction and dominates the behavior L_{sep}, whereas for smaller nose radius, L_{sep} actually increases with bluntness due to a decrease in M_1 and an increase in Re_{x_1}.

1.5.2.2 Scaling Results

Despite the extensive observations of separation length behavior in shock/boundary-layer interaction, there are relatively few published results concerning the quantitative functional dependence of L_{sep} on the parameters of interest. Two likely reasons for this are that (1) the models and techniques used to predict separated flow often do not admit closed-form expressions for L_{sep} and (2) most experimental studies do not provide enough data for meaningful correlation of L_{sep}. In this section we discuss previous results for scaling of L_{sep} in laminar interactions; some information on scaling for turbulent interactions can be found in Roshko and Thomke (1976) and Settles and Bogdonoff (1982). These are presented in roughly chronological order.

Hakkinen *et al.* (1959) presented a simple model of separation length for shock impingement on a laminar boundary layer with an adiabatic wall, in which an approximate momentum balance is

applied to the reversed flow. Their result, written using the current notation and with some liberty taken concerning the reference length, is

$$\frac{L_{sep}}{x_1} \propto \left(1 + \frac{\gamma_1 - 1}{2}\sqrt{Pr}M_1^2\right)^{3/2} \left(\frac{C_{f,x_1}}{\sqrt{M_1^2 - 1}}\right)^{1/4} \left(\frac{p_3 - p_{inc}}{\frac{1}{2}\rho_1 u_1^2}\right), \tag{1.3}$$

where the skin friction coefficient for an undisturbed boundary layer is defined as $C_f = 2\tau_w/\rho_e u_e^2$, and the Prandtl number Pr appears as the recovery factor for a laminar boundary layer. The pressure rise is taken with respect to the inviscid wedge pressure under incipient separation conditions, p_{inc}, which is practically identical to the plateau pressure p_2 according to the analogy discussed in Section 1.4. It should also be noted that the definition of L_{sep} is slightly different for shock-impingement flows; instead of the distance along the dividing streamline as for wedge flows, L_{sep} is defined as the distance along the straight wall from separation to reattachment. The correlation worked reasonably well for their experimental data, though the experiments covered a limited range in Re_{x_1} and only one Mach number ($M_1 = 2$). Thus the very weak predicted dependence on Re_{x_1} (through C_{f,x_1}) was impossible to verify.

Anders and Edwards (1968) developed an expression for scaling of L_u in laminar compression-corner interactions by combining a result of Chapman *et al.* (1958) for scaling of the upstream influence at separation with empirical correlation to computed results from an analytical technique. In the present notation this scaling is

$$\frac{L_u}{x_1} \propto Re_{x_1}^{1/5} \sqrt{\frac{C_{f,x_1}}{(M_1^2 - 1)^{1/2}}} \left(\cos\theta_{sep} + \frac{\sin\theta_{sep}}{\tan(\theta_w - \theta_{sep})}\right)^{-1}. \tag{1.4}$$

The derivation of this result appears to have incorrectly applied the expression from Chapman *et al.* (1958), but nevertheless, it roughly matches their experimental data. The experiments encompassed only a factor of two variation in Re_{x_1} and a very small range in Mach number (with nominal $M_1 = 12$).

A purely empirical correlation of experimental separation length data for laminar interactions on compression corners was given by Needham (1965) as

$$\frac{L_{sep}}{x_1} \propto \frac{\sqrt{Re_{x_1}}}{M_1^3} \left(\frac{p_3}{p_2}\right)^2. \tag{1.5}$$

The data considered in this correlation are mostly in the hypersonic Mach-number regime ($7 \lesssim M_1 \lesssim 15$) and cover a wide range in Re_{x_1}. The small variation with T_w/T_1 found in the experiments was neglected in this scaling. The dependence on $\sqrt{Re_{x_1}}$ is consistent with an inverse proportionality between L_{sep} and C_{f,x_1} of the undisturbed boundary layer, as expected by the physical view given in Section 1.4.

A theoretical scaling law was derived by Burggraf (1975) based on the triple-deck theory of Stewartson and Williams (1969) and Neiland (1971b) (*cf.* Section 1.5.1.2). His formulation is somewhat coded, but a direct translation to the present notation gives

$$\frac{L_{sep}}{x_1} \propto \left[\frac{(T_w/T_1)\theta_w}{\lambda^{3/4}\left(M_1^2-1\right)^{1/2}} - 1.55\,\frac{C^{1/4}(T_w/T_1)}{\lambda^{5/6}\left(M_1^2-1\right)^{1/4} Re_{x_1}^{1/4}} \right]^{3/2}, \tag{1.6}$$

where λ is the wall-shear constant of the undisturbed boundary layer ($\lambda = 0.332$ for a compressible Blasius boundary layer), and $C = \rho\mu/\rho_e\mu_e$ is the Chapman–Rubesin parameter from compressible boundary-layer theory. Katzer (1989) reinterpreted this result in a slightly different fashion,

$$\frac{L_{sep}}{\delta_1^*} \propto \left[\frac{(T_w/T_1)^{3/2}}{1.72 + 1.11(\gamma_1 - 1)M_1^2} \right] \frac{\sqrt{Re_{x_1}/C}}{M_1^3} \left(\frac{p_3 - p_{inc}}{p_1} \right)^{3/2}, \tag{1.7}$$

where the denominator of the first factor and the numerator of the second factor on the right hand side come from Katzer's expression for δ_1^*, not from triple-deck theory.

Hayakawa and Squire (1982) suggested a simple scaling law based on the ideas of Chapman *et al.* (1958) regarding free interaction:

$$\frac{L_u}{\delta_1} \propto \frac{1}{C_{f,x_1} M_1^2} \left(\frac{p_h}{p_1} - 1 \right), \tag{1.8}$$

where the pressure rise is characterized by the pressure at the hingeline p_h instead of the pressure downstream of reattachment, and boundary-layer thickness is used to normalize L_u. This formula had mild success in correlating their experimental results for turbulent interactions at supersonic Mach number where C_{f,x_1} was varied by gas injection upstream of separation. Grasso and Marini (1996) modified and extended this scaling for hypersonic interactions, giving the following result:

$$\frac{L_u}{\delta_1} \propto \frac{2}{\gamma_1 M_1^3 C_{f,x_1}} \left(\frac{p_3}{p_1} - 1 \right). \tag{1.9}$$

Note that the use of δ_1 to normalize L_{sep} in both Equations 1.8 and 1.9 results in cancelation of Reynolds-number effects entering via C_{f,x_1} for laminar flows, since δ_1 and C_{f,x_1} are both proportional to $Re_{x_1}^{-1/2}$.

For the shock-impingement problem in laminar, supersonic flow, Katzer (1989) found the following empirical correlation from results of Navier–Stokes computations:

$$\frac{L_{sep}}{\delta_1^*} \propto \frac{\sqrt{Re_{x_1}/C}}{M_1^3} \left(\frac{p_3 - p_{inc}}{p_1} \right), \tag{1.10}$$

where, again, C is the Chapman–Rubesin parameter and p_{inc} is the wedge pressure for incipient separation. Note that the dependence on Re_{x_1} is due to normalization by δ_1^*. The computations

encompassed a limited range in Re_{x_1} and considered only an adiabatic wall. The Mach-number range was $1.4 \leq M_1 \leq 3.4$. The numerical data correlated very well to this formula, with little scatter.

Kumar (1995) correlated experimental data from a number of sources over a range of Reynolds numbers in the hypersonic regime ($7 \lesssim M_1 \lesssim 19$), using the form

$$\frac{L_{sep}}{\delta_1^*} \propto \frac{1}{\bar{\chi}_1} \left(\frac{p_3}{p_1} \right)^n . \tag{1.11}$$

The parameter $\bar{\chi}_1$ is the viscous interaction parameter upstream of separation ($\bar{\chi} = M^3 \sqrt{C/Re_x}$). The exponent n on the pressure ratio was approximately 2 for laminar interactions and 1 for transitional and turbulent interactions. Correlation against Re_{x_1} was not performed.

A simplified expression for hypersonic laminar interactions was suggested by Mallinson *et al.* (1995, 1996b), whereby the tangent-wedge approximation (see Anderson, 1989) is used to give the pressure rise at reattachment:

$$\frac{L_{sep}}{\delta_1} \propto \frac{(M_1 \theta_w)^2}{\bar{\chi}_1} . \tag{1.12}$$

This same functional form was assumed for the distance L_u, which with rather large scatter, gave a rough correlation of experimental data.

The scaling of separation length in terms of physical parameters clearly remains an unresolved problem, as evidenced by the wide range of results, spanning almost 40 years, given in Equations 1.3–1.12. One fairly consistent finding is that L_{sep} is inversely proportional to M_1^3. The power-law dependence on pressure ratio appears to be different for supersonic (*cf.* Equations 1.3, 1.8, and 1.10) and hypersonic (*cf.* Equations 1.5 and 1.11) laminar interactions, with the theoretical triple-deck result falling in between (*cf.* Equation 1.7). Almost every result, unfortunately, shows a different dependence on Reynolds number or skin friction; in this regard, Equation 1.5 is the most convincing because it correlates data from multiple sources over a reasonable range in Re_{x_1}. The effect of wall temperature is only considered in Equations 1.6 and 1.7. As mentioned in Section 1.5.1.2, Katzer (1989) recognized that the application of triple-deck theory by Burggraf (1975) resulted in a scaling (Equation 1.7) with the same dependence on Mach number and the same construction of the pressure ratio factor $(p_3 - p_{inc})/p_1$ (though with different power-law dependence) as his purely empirical result (Equation 1.10). He also suggests that TDT will give the correct scaling for wall temperature effects. For these reasons, we will turn to triple-deck theory in Section 4.2 to help develop a new scaling for separation length.

1.5.3 Reattachment Heating

For the reasons discussed in Section 1.4, heat flux near reattachment is higher than the heat flux at the same location on an undeflected flap, and may also be higher than for an attached flow with the same flap deflection. For example, Coleman and Stollery (1972) found that for turbulent separated flows, the maximum heat flux at reattachment, also called the peak heating $\dot{q}_{pk}$, could increase beyond that expected for a stagnation point. Very few works on shock/boundary-layer interaction attempt correlation of $\dot{q}_{pk}$ to determine the scaling laws which govern its behavior; those that do are experimental in nature. If the boundary-layer edge conditions are known downstream of reattachment, then the heat flux can always be computed using various theories or models (*cf.* Section 4.1). The trouble arises, however, in determining an appropriate origin for the reattached boundary layer that accounts for the compression it experiences at reattachment; simply using the distance from the leading edge will not reproduce the peak heating at reattachment.

Early work was concerned with correlations to predict the maximum reattachment heat flux, given the external inviscid flow conditions downstream of reattachment in region 3. Holden (1966) was able to correlate peak heating in laminar compression corner flows using

$$M_3^3 \, St_{pk,w} \;\propto\; \bar{\chi}_{3,pk} \,,$$

which is more simply written

$$St_{pk,w} \;\propto\; Re_{x_{pk}}^{-1/2} \,. \tag{1.13}$$

The Stanton number St is defined by Equation 4.14; the subscript w here refers to evaluation of the density in the denominator of St at the local wall conditions instead of the edge conditions. The Reynolds number is based on the length scale x_{pk}, the distance from the leading edge to the location of peak heating. This empirical result for a limited range in hypersonic Mach number is perhaps fortuitous, but use of the wall density is consistent with the idea that reattachment heating is determined by growth of a sublayer from the stagnation point on the dividing streamline, developing underneath the compressed outer part of the boundary layer. Bushnell and Weinstein (1968) correlated laminar data over a larger range in Mach number by including an estimate for L_{pk}, the growth length of the sublayer to the point of maximum heat transfer. From the geometry shown in Figure 1.4, they suggest

$$L_{pk} \;=\; \frac{\delta_s}{\sin\left(\theta_w - \theta_{sep}\right)} \,, \tag{1.14}$$

where δ_s is the thickness of the shear layer at reattachment outside the dividing streamline, assumed to be equal to the incoming boundary-layer thickness at separation plus the growth of a zero-initial-thickness shear layer between separation and reattachment. The correlation is otherwise similar to

Equation 1.13 above, but using wall conditions in the Reynolds number as well;

$$St_{pk,w} \propto \left(\frac{\rho_w u_3 L_{pk}}{\mu_w}\right)^n, \qquad n = \begin{cases} -0.5 & \text{for laminar interactions, and} \\ -0.2 & \text{for turbulent interactions.} \end{cases} \tag{1.15}$$

The peak heating is often correlated with the peak pressure that occurs at the same location, and nondimensionalized by a reference value. In this manner, a prediction might be made requiring only knowledge of the pressure in region 3. For turbulent interactions on compression corners, the correlation

$$\frac{\dot{q}_{pk}}{\dot{q}_1} \simeq \left(\frac{p_{pk}}{p_1}\right)^{0.85} \tag{1.16}$$

was found by Holden (1972) (see also Hankey and Holden, 1975) to work well over a large range of Mach numbers (in the hypersonic regime) and Reynolds numbers. Note that the heat flux and pressure are referenced to the undisturbed boundary layer just upstream of separation. For laminar interactions, however, Holden (1978) found that the data do not collapse very well using this form of correlation, the exponent in Equation 1.16 varying between 0.5 and 0.7. Hung and Barnett (1973) give the following correlations in terms of Stanton number:

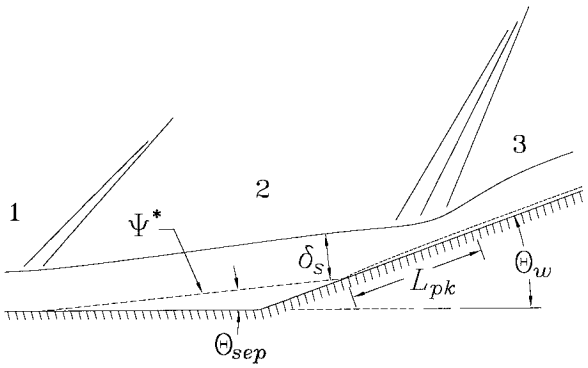

Figure 1.4: Schematic of growth length for reattaching boundary layer.

$$\frac{St^*_{pk}}{St^*_{fp}} \simeq \begin{cases} 0.13\left(\dfrac{p_{pk}}{p_{fp}}\right)^{1.13} & \text{for laminar interactions,} \\ 0.468\left(\dfrac{Re_{L_h}}{10^6}\right)^{1.85}\left(\dfrac{p_{pk}}{p_{fp}}\right)^{1.13} & \text{for transitional interactions, and} \\ \left(\dfrac{p_{pk}}{p_{fp}}\right)^{0.8} & \text{for turbulent interactions.} \end{cases} \tag{1.17}$$

The $*$ refers to evaluation at the Eckert reference temperature (*cf.* Section 4.1.1.3), and *fp* indicates the reference heat flux and pressure are taken for an undisturbed flat-plate flow but at the same location as the peak heating, *i.e.* at a distance $x = x_{pk}$ from the leading edge. For transitional interactions, when transition to turbulence occurs between separation and reattachment, $\dot{q}_{pk}$ has a significant dependence on the location of transition and hence the Reynolds number. Again, though the correlation for turbulent interactions works well, the laminar interaction data maintain a rather

large scatter.

Reasonable success was achieved correlating a very wide range of data by Simeonides *et al.* (1994), who incorporated the growth length given by Equation 1.14 into expressions of the same form as Equation 1.17 (see also Simeonides and Haase, 1995). Their result is as follows:

$$\frac{\dot{q}_{pk}}{\dot{q}_{fp}} \simeq \begin{cases} \left(\dfrac{p_{pk}u_{pk}x_{pk}}{p_{fp}u_{fp}L_{pk}}\right)^{0.5} & \text{for laminar interactions,} \\ 0.072\left(Re^{*}_{x_{pk}}\right)^{0.3}\left(\dfrac{p_{pk}u_{pk}}{p_{fp}u_{fp}}\right)^{0.8}\left(\dfrac{x_{pk}}{L_{pk}}\right)^{0.2} & \text{for transitional interactions, and} \\ \left(\dfrac{p_{pk}u_{pk}}{p_{fp}u_{fp}}\right)^{0.8}\left(\dfrac{x_{pk}}{L_{pk}}\right)^{0.2} & \text{for turbulent interactions.} \end{cases} \tag{1.18}$$

For transitional interactions, the Reynolds number is based on the edge conditions in region 3 and evaluated at the reference temperature T^*. Experimental peak heating data from from a number of different shock/boundary-layer interaction flows covering five decades in $Re^{*}_{x_{pk}}$ and $5 < M_1 < 20$ have been correlated to $\pm 20\%$ using Equation 1.18.

In passing we mention that Holden (1971a), Coët and Chanetz (1994), and Kumar and Stollery (1994) all found peak heating to decrease with increasing bluntness of the leading edge.

1.5.4 Real-Gas Effects

The presence of real-gas effects in shock/boundary-layer interaction flow introduces new parameters to the problem, namely stagnation enthalpy and reaction rate. While an appropriate nondimensional enthalpy parameter is the stagnation enthalpy normalized by a characteristic dissociation energy of the gas, we follow convention and refer to dimensional stagnation enthalpy h_0 in this section. A nondimensional reaction rate is the ratio of characteristic reaction time to characteristic flow time, or Damköhler number; this parameter is difficult to define in a global sense for high-enthalpy, viscous separating flow on a compression corner or double wedge.

Unlike in the review of perfect-gas results above (Sections 1.5.1–1.5.3), here we can afford to be more exhaustive, covering all published work known to the present author. There simply have not been very many studies undertaken that concern real-gas effects on shock/boundary-layer interaction in the types of flow of interest to the present work; only four different experimental studies, and little more than twice that number of published computational results. Most of the work is fairly recent, and it all considers flows of air or nitrogen. As before, we will subdivide the discussion into results bearing on separation length and on reattachment heating.

1.5.4.1 Separation Length

Two studies of compression-corner flows have been carried out in the T3 Shock Tunnel at the Australian National University using air for the test gas. The first, conducted by Rayner (1973), considered only a single configuration, that of a double wedge with $\theta_1 = 18.5°$ and $\theta_w = 30°$, where the flap span and L_h could each be varied. Separation length was found to initially decrease with increasing h_0 and then increase again at high enthalpy; the behavior with h_0, however, was not correlated independently of the behavior with other parameters. For shock tunnel flows, both M_∞ and Re_∞ tend to decrease with increasing h_0, while T_w/T_1 decreases due to higher free-stream temperatures. Thus, in view of the trends observed for perfect-gas flows (*cf.* Section 1.5.2), and disregarding chemical processes, L_{sep} for these experiments may be dominated by the changes in Re_{x_1} and T_w/T_1 as h_0 increases. The very high-enthalpy conditions ($h_0 > 25$ MJ/kg) in T3, where L_{sep} was observed to increase, have subsequently been shown to produce flows with significant contamination by the helium used to drive the shock tube (Crane and Stalker, 1977). Rayner (1973) had some success correlating his separation length data using the analysis of Hakkinen *et al.* (1959) (*cf.* Equation 1.3) modified to account for a nonadiabatic wall condition, though the skin friction and reversed-flow properties were computed assuming an equilibrium dissociated condition, which is probably not realistic (see below).

The second study in T3, by Mallinson (1994), dealt with a flat plate ($\theta_1 = 0°$) followed by a compression corner of variable ramp angle ($5° \leq \theta_w \leq 24°$). The main conclusion was that real-gas effects on the interaction were negligible under the conditions investigated (Mallinson *et al.*, 1996b, 1997b). This result is to be expected, because the reaction rates for dissociation downstream of an oblique shock in high-enthalpy flow remain insignificant for moderate shock angles (as has been shown by Sanderson (1995) using a simple model). Dissociation in the boundary layer for these experiments was found to be negligible even at high enthalpy (Mallinson *et al.*, 1996a). The partially dissociated free stream at the high-enthalpy condition ($h_0 \simeq 20$ MJ/kg) might be expected to cause some effect on separation length if there is recombination occurring near the wall, but either the density was too low to produce significant recombination rates, or possibly the simple expression (for hypersonic interactions neglecting wall temperature effects, Equation 1.12) used to correlate L_{sep} was insufficient to bring out any differences due to recombination.

Other experimental studies (Davis, 1996; Krek *et al.*, 1996) have looked at axisymmetric configurations abstracted from the windward centerline geometry of either the Hermes reentry vehicle (the hyperboloid–flare geometry) or the Space Shuttle Orbiter (the HAC geometry). These geometries correspond to flight at high angle of attack (30–35°) with a trailing body flap deflected 20°. Experiments were performed on the hyperboloid–flare geometry in the HEG shock tunnel at DLR in Germany by Krek *et al.* (1996), using air. With separation length correlated against the free-stream viscous interaction parameter $\bar{V}_\infty = M_\infty/\sqrt{Re_\infty}$, they found an apparent reduction in L_{sep}

with increasing h_0 at constant $\bar{V}_\infty$. Experiments by the present author (Davis, 1996) on the HAC geometry in the T5 Shock Tunnel at GALCIT using nitrogen, however, showed no such trend with enthalpy when correlated in the same manner. A reduction in L_{sep} due to real-gas effects at high enthalpy might be explained by dissociation occurring immediately downstream of the reattachment shock, if the reaction rates there are appreciable. Compared to a chemically frozen flow, this would reduce the reattachment pressure rise and hence reduce L_{sep}; correlation against $\bar{V}_\infty$ cannot verify this because it does not properly account for the Mach-number and wall temperature effects on L_{sep}.

The earliest calculated results for separation length in high-enthalpy compression-corner flows are those of Anders and Edwards (1968), who applied an analytical procedure to equilibrium air flows with $M_1 \approx 12$ and $h_0 \lesssim 12$ MJ/kg. They found that chemical equilibrium resulted in smaller L_{sep} compared to chemically frozen flow at the same conditions. For most of the equilibrium results, L_{sep} increased with increasing h_0; this trend reversed at $h_0 \lesssim 5$ MJ/kg for large separation regions (high θ_w).

The result that separation length decreases for reacting flows relative to frozen flows is found in a number of computational studies on compression-corner flows (Grasso and Leone, 1992), axisymmetric hyperboloid-flare flows (Brenner *et al.*, 1993; Kordulla *et al.*, 1992; Oswald *et al.*, 1995), and shock-impingement flows (Furumoto *et al.*, 1997). When there is negligible dissociation in regions 1 and 2 upstream of reattachment (as in Furumoto *et al.* (1997) and Grasso and Leone (1992)), this behavior is clearly due to the lower pressure in region 3 caused by dissociation behind the reattachment shock. An explanation is not so obvious for the results of Oswald *et al.* (1995), Brenner *et al.* (1993), or Kordulla *et al.* (1992), who compared frozen flow to full chemical equilibrium flow on the hyperboloid flare. To complicate matters, the comparison by Oswald *et al.* was between an equilibrium flight condition at $M_\infty = 25$ and a perfect-gas wind tunnel condition at $M_\infty = 10$. In all of these studies, dissociation occurs in region 1 due to the bow shock, which increases M_1 and actually results in higher p_3 compared to frozen flow. The behavior of L_{sep} may be dominated by the change in M_1, or there may be an unknown effect due to reactions occurring in the viscous regions of the flow.

Ikawa (1979) also found a reduction in L_{sep} for reacting flow, but using a very different analysis. He extended Klineberg's momentum integral method (*cf.* Section 1.5.1.1) to include the species conservation equation for a binary dissociating gas and considered the difference between fully dissociated and fully recombined boundary-layer edge conditions with a fully recombined condition at the wall. The approach assumes that binary diffusion dominates production of molecules by recombination. The case with dissociation at the boundary-layer edge showed a thinner boundary layer (which Ikawa attributes to the diffusion circuit set up in the boundary layer) and a smaller separation bubble.

Real-gas effects on separated shock-impingement flows were also studied computationally by

Ballaro and Anderson (1991) and Grumet *et al.* (1994) for dissociated upstream conditions corresponding to air flow that has expanded around a blunt body after being processed by a Mach 25 normal shock. Both restricted themselves to $T_w/T_1 = 1$. For the separation length in nonequilibrium flow compared to frozen flow, Ballaro and Anderson (1991) found a slight decrease at the two Reynolds numbers investigated, while Grumet *et al.* (1994) found a slight decrease at low pressure and a large increase at high pressure. In the latter case, the large increase in L_{sep} was attributed to strong recombination in the recirculation region at high pressure. Reasons for the decrease in L_{sep} under other conditions are not obvious; only Ballaro and Anderson give pressure results, and those show increased p_3 for nonequilibrium flow. Both of these studies have separation occurring close to the leading edge of the grid, which raises the question of whether or not the separation point is being artificially (and unintentionally) fixed. Grumet *et al.* (1994) also considered the effect of wall catalyticity, and found that L_{sep} was larger for a fully noncatalytic than for a fully catalytic wall, and the difference was less pronounced at the high-pressure condition where gas-phase recombination dominates.

Brenner *et al.* (1993) performed computations comparing a flight condition to a high-enthalpy condition in the HEG shock tunnel for the hyperboloid–flare geometry, and found larger L_{sep} for the tunnel condition than the flight condition. The tunnel condition has a partially dissociated free stream which might account for the higher L_{sep} according to the above result of Grumet *et al.* (1994), but it also has lower Mach number than the flight condition, which could cause the same behavior.

It should be noted that high-enthalpy studies have also been performed on other types of separated flows; three examples are a downstream-facing step (Gai *et al.*, 1989), a three-dimensional interaction due to a vertical fin (Stacey and Simmons, 1992), and the wake of a blunted cone (Eitelberg and Kastell, 1997).

1.5.4.2 Reattachment Heating

Of the experimental studies mentioned in the previous section, only Mallinson *et al.* (1996b) looked at the peak reattachment heating. They found that the ratio $\dot{q}_{pk}/\dot{q}_{fp}$ was reasonably well predicted using the correlation of Simeonides *et al.* (1994) in Equation 1.18. Mallinson *et al.* (1997b) also advanced a theory for real-gas effects on heat transfer due to dissociation in the boundary layer, which showed slightly increased peak heating for equilibrium chemistry over frozen chemistry.

All of the computational studies cited in the previous section show increased reattachment heat flux for reacting flows, except the study by Furumoto *et al.* (1997). This work considers full nonequilibrium shock-impingement flow with a nondissociated free stream at $M_1 = 7$ and a relatively high wall temperature, and its results show significant oxygen dissociation occurring at the wall beginning downstream of separation. At reattachment, the temperature inside the boundary layer is

much higher than outside the boundary layer. The reacting compression-corner flow computations of Grasso and Leone (1992), also with a nondissociated free stream but with a much colder wall temperature, were performed under chemical equilibrium. These showed increased reattachment heat flux compared to frozen flow. The wall temperature appears to be the most important difference between these two cases, suggesting that the behavior of heat flux with chemistry depends on whether dissociation or recombination dominates the near-wall flow. The equilibrium-air computations of Brenner *et al.* (1993) and Oswald *et al.* (1995) for hyperboloid–flare flows both used moderately cool wall temperatures and both showed increased heat flux at reattachment over frozen-flow computations.

The computational results of Ballaro and Anderson (1991) and Grumet *et al.* (1994) for shock-impingement flows with partially dissociated free stream both show increased heat transfer at reattachment, attributed to the energy release of recombination, except for the low-pressure case of Grumet *et al.* (1994) with a noncatalytic wall boundary condition. The results of Ikawa (1979) also show increased heat flux, which in his restricted analysis, can only be due to a diffusion circuit between the fully dissociated boundary-layer edge and fully recombined wall condition.

1.6 Overview

The present work seeks to advance scientific understanding of the phenomenon of unconfined separation and reattachment in reacting flow, particularly regarding the aspects of separation length and reattachment heating. Even with the restrictions on scope introduced in Section 1.3, this phenomenon is very complex. In fact, as discussed in Section 1.5.2.2, the functional dependence of separation length is not entirely known even for perfect-gas flows, despite the extensive work that has been performed by numerous authors over the past four decades. Even less is known about how the molecular dissociation and recombination found in practical hypervelocity flows affects separation phenomena.

Experimental measurements from separated double-wedge flows in the T5 hypervelocity shock tunnel may provide insight to real-gas effects on separation length and reattachment heating, but only after extensive analysis; analysis to reconstruct properties of the flow field which cannot be measured and analysis to understand expected real-gas behavior from a theoretical standpoint. Thus, while Chapter 2 is devoted to the methods used to obtain experimental measurements pertinent to separation length and reattachment heating, these are not directly used to show any results until Chapter 6. The computational methods used to reconstruct the external inviscid flow field in the experiments and to study viscous aspects of the flow are described in Chapter 3, and theoretical results pertaining to boundary layers and separation length in nonreacting flow are presented in Chapter 4. The latter includes development of a new scaling law for separation length based on the

application of triple-deck theory to the model for separation introduced in Section 1.4. In Chapter 5, a framework is presented for discussing real-gas effects on separation length and reattachment heating, and the individual mechanisms are investigated independently of each other using various simplified models and more advanced computational techniques. Finally, in Chapter 6, the computational methods, theoretical results, and framework for real-gas effects from Chapters 3–5 are applied to the experimental measurements of separation length and reattachment heating discussed in Chapter 2 to see what may be learned from them.

Chapter 2 Experimental Methods

The goal of the present experimental study is to discern real-gas effects on shock-induced separation in compression-corner flow. To achieve this goal, use is made of the T5 Hypervelocity Shock Tunnel at Caltech. This facility can produce short-duration, high-speed flows of high enough stagnation enthalpy ($h_0 > 20$ MJ/kg with air or nitrogen test gas) to cause significant real-gas effects due to dissociation downstream of strong shocks. The standard flat-plate/trailing-flap configuration (*cf.* Figure 1.1b) does not produce shocks strong enough to cause dissociation (*cf.* Section 1.5.4). Therefore, we use a double-wedge geometry for the test model; at high angles of attack and high enthalpy, the oblique shock from the leading edge of a double wedge causes significant dissociation of the free-stream gas. A two-dimensional geometry, as opposed to an axisymmetric double cone, is selected for two reasons. First, the incidence angle and flap deflection angle can easily be made adjustable on a 2-D model, while an axisymmetric model would require separate realizations of the hardware for each angle investigated. Second, a two-dimensional geometry increases the sensitivity of line-integrated flow visualization techniques, because the optical path length through flow features is much longer than for the equivalent axisymmetric geometry. The disadvantage of a double-wedge configuration is that the flow on the model is inherently three-dimensional; this fact is addressed in Section 2.7.5. The test model is instrumented with surface thermocouples to measure heat flux and piezoelectric transducers to measure static pressure. Separation length is measured using flow visualization. The experiments encompassed approximately 125 shots in T5 during two separate campaigns, the first in July–August 1996 (T5 shots 1276–1325), the second in November–December 1997 (T5 shots 1725–1799).

The subsequent sections in this chapter describe the shock tunnel facility (Section 2.1), the test model (Section 2.2), tunnel flow conditions (Section 2.3), and diagnostic techniques including flow visualization (Section 2.4), heat flux measurement (Section 2.5), and pressure measurement (Section 2.6). Issues regarding flow quality are addressed in Section 2.7.

2.1 T5 Hypervelocity Shock Tunnel

The idea of using a free piston to drive a shock tunnel was pursued by Stalker (1967) in Australia, culminating in the operational facilities T3 at the Australian National University in 1969, T4 at the University of Queensland in 1987, and T5 at Caltech in 1990. Later free-piston tunnels include HEG in Germany (1992) and the G2 Range at AEDC (1995), as well as HEK (1996) and HIEST (1997) in Japan. These facilities, often referred to as "Stalker tubes," all operate on the same principle; a

free piston is driven by high-pressure air to adiabatically compress the driver gas for a shock tube, with the reflected shock region of the shock tube then acting as the reservoir for a nozzle expansion to the desired flow conditions. A schematic of T5, without the test section, is shown in Figure 2.1, along with information regarding its size and performance characteristics. The reservoir holding compressed air to drive the piston is referred to as the secondary reservoir (2R) to distinguish it from the primary reservoir which stores compressed air between shots. The compression tube (CT) initially holds driver gas at low pressure and room temperature; after piston compression by a volume ratio of 40–70, the stainless steel primary diaphragm bursts, sending a very strong shock wave into the test gas held initially at low pressure and room temperature in the shock tube (ST). Because the effective driver section is so short, continued motion of the piston after the diaphragm bursts is necessary to maintain a relatively constant pressure for a duration of a few milliseconds. Tuned piston operation includes both this goal as well as the goal of safely stopping the piston against elastic bumpers at the end of the CT. For low-enthalpy operation, argon is added fractionally to the driver gas in order to lower the temperature after piston compression. The test section (TS), and the dump tank (DT) used to collect the driver and driven gases at low pressure after a shot, are not shown in Figure 2.1. A secondary diaphragm (made of thin mylar sheet) situated on the supersonic side of the nozzle throat initially separates the test gas in the shock tube from a rough vacuum in the nozzle and test section; it is vaporized by reflection of the incident shock. Useful test time is on the order of 1–2 ms. The CT, ST, and nozzle all recoil together in response to the piston motion. The inertial mass is required to reduce the recoil distance to approximately 6–10 cm. Further information regarding the T5 facility can be found in Hornung and Bélanger (1990), Hornung *et al.* (1991), and Hornung (1992).

The present investigation makes use of both the heavy (120 kg) and light (90 kg) pistons to achieve a wide range of primary diaphragm burst pressures (from around 15 MPa up to 110 MPa) with piston trajectories tuned for safe operation. (The characteristics-based computer codes by Bélanger (1990, 1993) were an invaluable aid to the design of tuned piston operation for new conditions.) We also rely exclusively on the conical nozzle, which provides uniform (but not parallel) exit flow at all area ratios and all enthalpies, unlike the contoured nozzle (Rousset, 1995). The conical nozzle has a 7° half-angle and three interchangeable throat sections of minimum diameter 1.5 cm, 2 cm, and 3 cm, providing nozzle exit area ratios of 400, 225, and 100, respectively. These throat sections were designed by the present author (Davis, 1996) with continuous curvature along the wall to minimize flow disturbances which can focus on the nozzle centerline.

Diagnostics for the shock tunnel consist of linear voltage displacement transducers (LVDT) to measure recoil movements of the CT and the 2R, and piezoelectric pressure transducers (PCB model no. 119M44) to measure pressures in the shock tube. For the present work, pressure measurements included two redundant stations in the driver section to measure the primary diaphragm burst

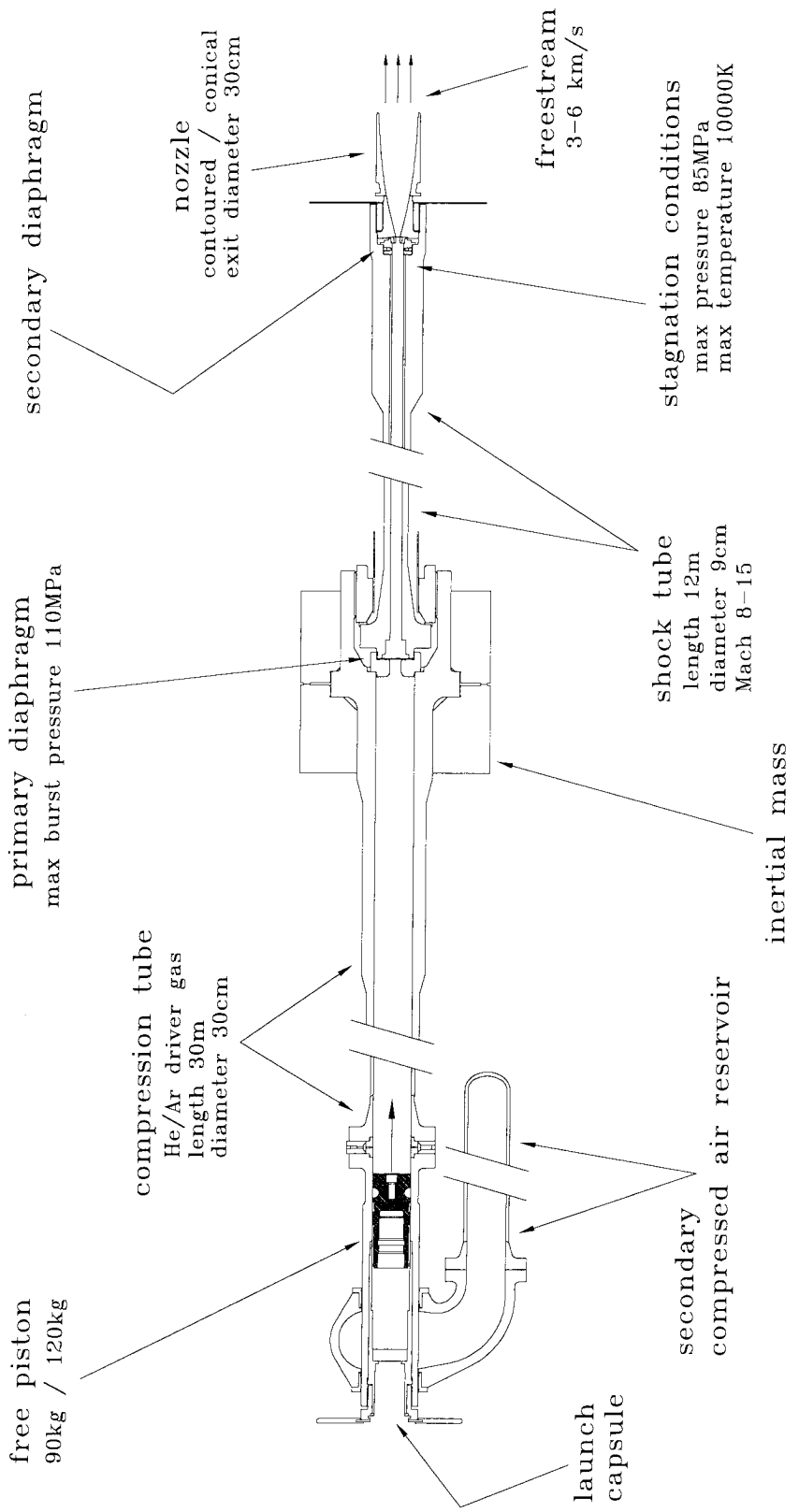

Figure 2.1: Schematic of the T5 Hypervelocity Shock Tunnel and information on its size and performance. The test section and dump tank are not shown.

pressure p_4, two redundant stations in the shock tube 4.8 cm from the end wall to measure nozzle reservoir pressure p_0, and two stations further upstream in the shock tube (2.37 m and 4.77 m from the end wall) to measure the incident shock speed u_s. The redundant stations are placed at identical positions on opposite sides of the tunnel and referred to by the compass directions north and south; north is to the right when facing downstream. An accelerometer placed near the launch end of the CT provides a trigger signal approximately 200 ms before shock reflection, which is needed to operate the flow visualization system.

Analog voltage signals from both shock tunnel and test model instrumentation are recorded using a high-speed data acquisition system (DAS) consisting largely of DSP Technology components; three CAMAC-standard crates with 60 digitizer channels (12-bit resolution on ± 5 V), 50 amplifiers, and a trigger generator. Eight of the digitizer channels reside on four independently controllable modules, and these are used to record signals from shock tunnel instrumentation at various sample rates (5–250 kHz). The remaining digitizer channels typically record signals from test model instrumentation at 200 kHz. Acquisition is triggered by a signal from the transducers measuring p_0, thus throughout this work, time $t = 0$ corresponds to the time of shock reflection. Additional modules in the crate include a digital counter and a laser controller with digital delay generation, both built in-house. A bank of 24 PCB power supplies for piezoelectric instrumentation is also mounted on the same rack. The DAS is controlled by computer using software designed in-house.

2.2 Double-Wedge Test Model

2.2.1 Description

Two views of the test model installed in the test section of T5 are shown in Figure 2.2. The model consists of two main sections; a forward plate (the first wedge) of approximately 10 cm chord and 20 cm span, and a trailing plate (the second wedge, often referred to as the flap) of approximately 5 cm chord and 20 cm span (detailed information on the model dimensions can be found in Appendix A). The flap chord length of half the front plate chord length ensures complete reattachment on the flap for separated flows, so that the flap length does not influence the length of separation. Each plate has its own instrumentation enclosure and wiring conduit. As indicated in Figure 2.3, the rear enclosure fits between the extended side walls of the forward enclosure, and the desired deflection angle of the trailing plate relative to the forward plate is obtained by inserting a keyed positioning wedge between the two enclosures. A set of positioning wedges were machined for $\theta_w = 5$–$40°$ in $5°$ increments. The incidence angle of the entire assembly is adjustable to five discrete values ($\theta_1 = 0°$, $15°$, $30°$, $35°$, and $40°$). At each position, threaded holes in the side walls of the forward enclosure line up with holes in the support beams. Bolts through these holes provide positive locking at the desired incidence angle. Additional resistance to rotation about the pivot

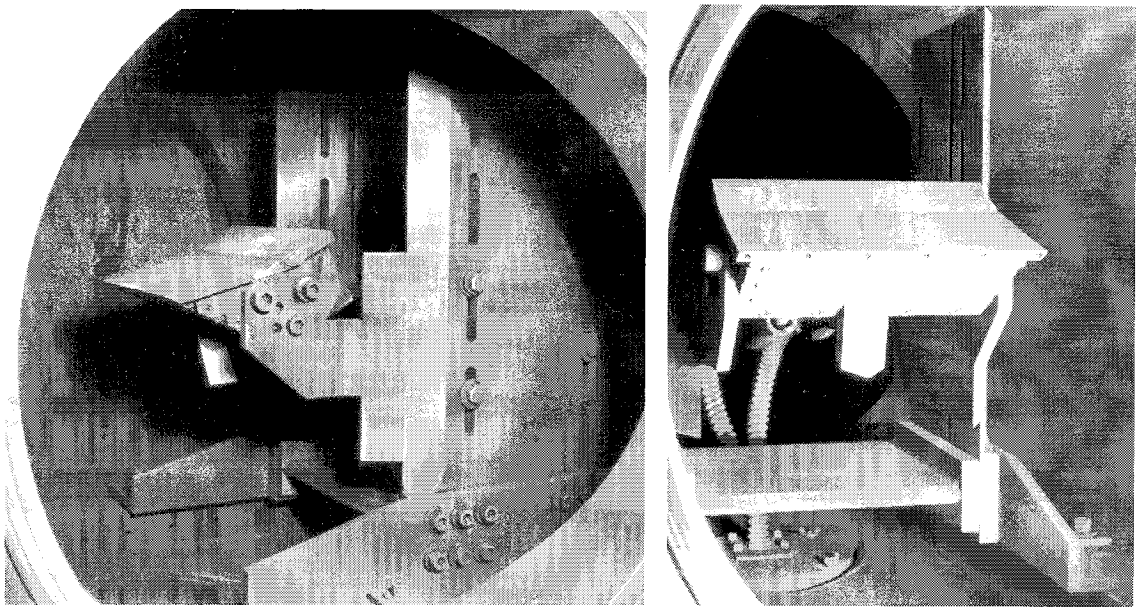

Figure 2.2: Two views of the double-wedge test model installed in T5.

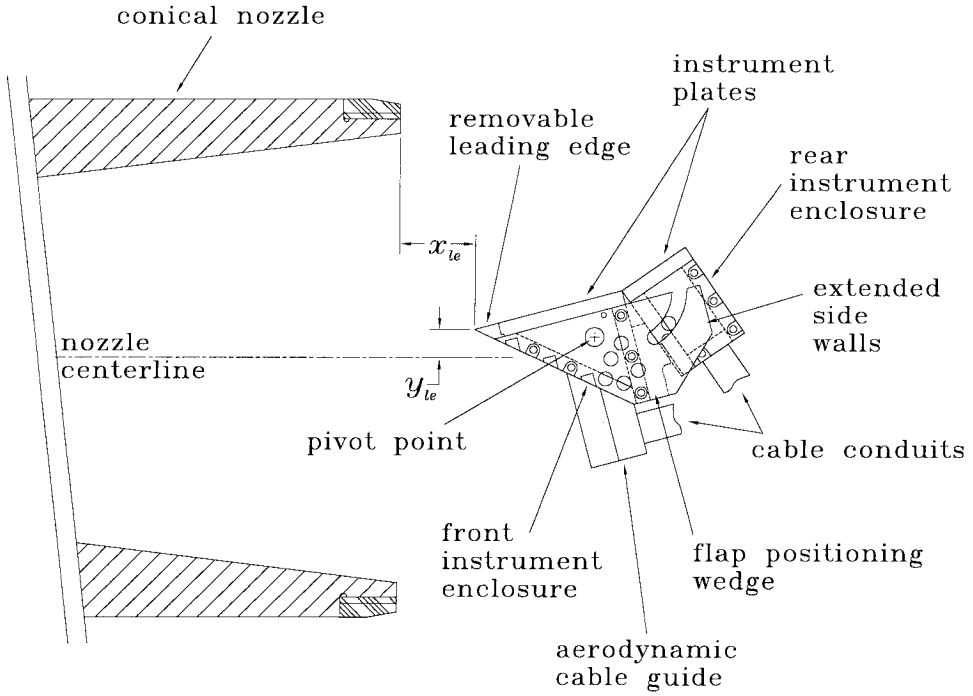

Figure 2.3: Sketch of model showing size and position relative to nozzle exit.

point under aerodynamic loading is given by small angle positioning blocks, keyed to the top of the side support beams and located behind the pivot point, that transfer loads directly from the forward instrument plate to the side support beams. The support structure, which can be seen in Figure 2.2 but is not shown in Figure 2.3, utilizes the double-fin model support designed by Sanderson (1995), which allows vertical translation of the model to maintain a constant vertical position of its leading

edge while varying the incidence angle.

The front wall (which is also the bottom wall) of the forward enclosure is sloped 40° to the front plate surface, resulting in an attached shock at the leading edge for all θ_1 investigated. A cable guide below the forward enclosure protects the forward wiring conduit from heat and pressure loading, and has a sharp leading edge of 40°half-angle to reduce shock standoff. The leading edge of the forward plate is removable for repair or replacement. Once during each experimental campaign, the underside of the leading edge was machined to remove damage caused by debris from the shock tube. This was only deemed necessary when a deep nick in the sharp leading edge occurred close to the model centerline where heat flux measurements are taken. Each operation slightly shortened the length L_h of the forward plate; the total change after two test series was less than 1 mm, smaller than the uncertainty in measurements of separation location. Between machining operations, the leading edge remained essentially sharp, with radius stabilized at less than 100 μm.

While the enclosures and supports were fabricated from cold-rolled 1018 steel, the instrumentation plates and leading edge were made from 303 stainless steel because its thermal product $\sqrt{\rho c k}$ (which determines the wall temperature rise for a given heat flux) better matches $\sqrt{\rho c k}$ of the thermocouple materials. This avoids local nonuniformities in the wall temperature which could effect the boundary-layer flow. In addition, the excellent corrosion resistance of stainless steel makes the flow surfaces much easier to keep clean. The internal cavities of the enclosures were not isolated from the

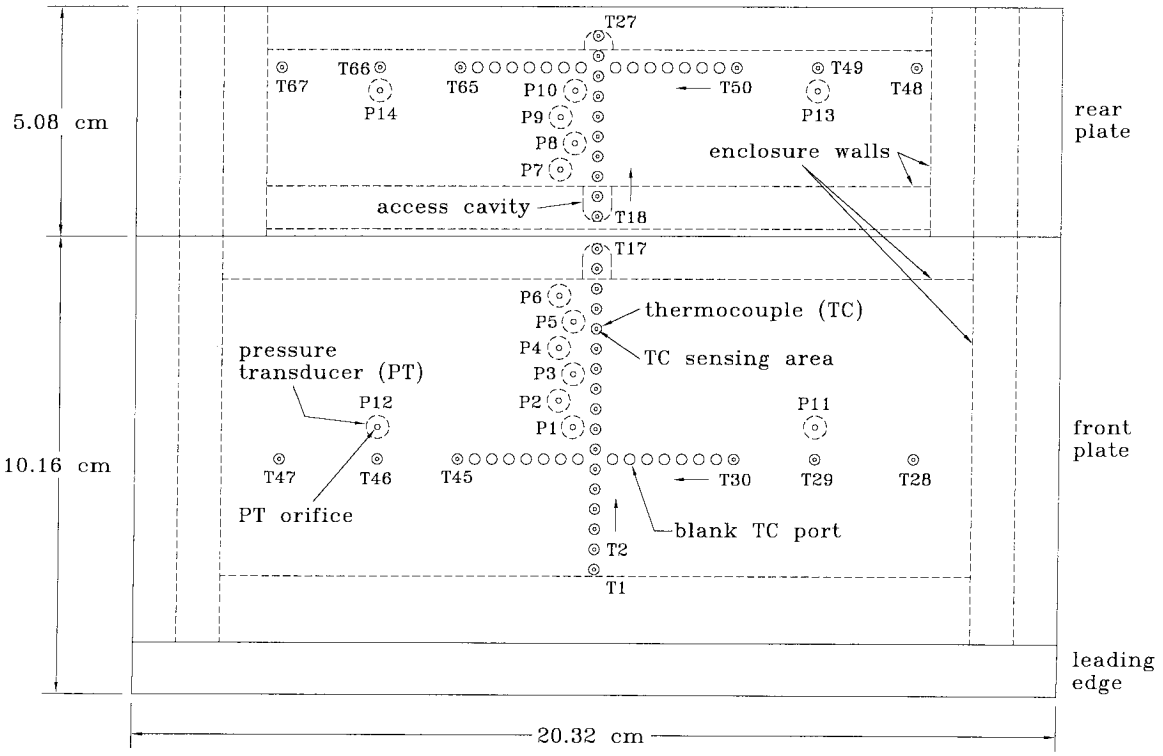

Figure 2.4: Layout of instrumentation plates, including labels for port locations.

test section vacuum. Silicone sealant and epoxy, however, were used to block most pathways so that very little soot reached internal cavities when the dump tank was vented to atmospheric pressure after each shot. Each enclosure had its own wiring harness, consisting of bundles of 30 AWG wire in twisted pairs passed through flexible metal conduits connected to an electrical feedthrough plate in the test section floor. Miniature D-type connectors inside the enclosures allowed removal of the instrumentation plates while leaving the wiring harnesses in place.

The layout for instrumentation on both plates is shown in Figure 2.4. Though the plates and wiring harnesses were designed for 14 pressure transducers (PT's) and 67 thermocouples (TC's), only 39 thermocouples were installed for the present study, and only 37 of these could be used simultaneously due to limitations of the DAS. The unused TC ports were plugged by flush-mounted stainless steel dowel. The TC numbering scheme of the original design is kept in the present study, with T1–27 arrayed streamwise along the model centerline, and with T28–47 and T48–67 arrayed spanwise across the front and rear plates respectively. The streamwise PT ports P1–10 are staggered in two planes slightly offset from the centerline. Detailed information on the instrument port locations can be found in Appendix A.

2.2.2 Position and Alignment

The vertical and streamwise horizontal position of the model relative to the nozzle is defined by y_{le} and x_{le} as shown in Figure 2.3. The distance y_{le} was measured to approximately ± 1 mm accuracy by reference to the test section floor. The leading edge was typically positioned above the nozzle centerline ($y_{le} > 0$) to avoid possible centerline flow disturbances. As mentioned in Sections 2.4.4 and 2.5, measurements were difficult for the $\theta_1 = 0°$ configuration with $y_{le} > 0$. Unfortunately, an oversight in the model design prevented vertical positioning at $y_{le} < 0.6$ cm for $\theta_1 = 0°$. The distance x_{le} was measured to approximately ± 0.5 mm accuracy by noting the tunnel position which corresponds to $x_{le} = 0$, and for each shot recording the tunnel position as it recoils; during the test time of interest, the nozzle remains stationary at its maximum recoiled position. Due to poor alignment of the fixed test section rails on which the symmetric model support is mounted, the model centerline was positioned approximately 7 mm from the nozzle centerline in the spanwise horizontal direction towards the north side of the test section. The model was aligned about its pitch and roll axes by shimming underneath the support structure until the front instrument plate was level to gravity in the $\theta_1 = 0°$ position. The model support did not allow adjustment about the yaw axis, but the leading edge was parallel to the nozzle exit plane within $\pm 1°$. This is sufficient alignment in yaw because the nozzle flow is conically diverging in any case.

Some minor difficulties were experienced with alignment of the hingeline between the front and rear instrument plates. Though the positioning wedges are keyed for automatic hingeline alignment, machining and assembly tolerances prevented exact alignment across the full

span. Best results were obtained by clamping the rear plate/enclosure by hand in the correct position while tensioning the side bolts which hold the rear enclosure between the extended side walls of the front enclosure; typically this gave good alignment at one end of the hingeline but a slight downstream-facing step (< 40 μm) at the other end. For a few shots in the first experimental campaign, there occurred a more severe upstream-facing step on the order of 500 μm, an example of which is shown in Figure 2.5. It has been shown by Needham and Stollery (1966b) that the effect of such a step on separated corner flow is to simply shift the effective corner location. The outer flow behaves as if the flap surface extended all the way to the upstream surface. For some shots, the hingeline also had a small gap at one end of not more than 25 μm, which could conceivably reduce the extent of separation by suction. According to the results of Ball and Korkegi (1968), a gap this size should have very little effect on the length of separation for high Mach-number interactions but may be of significance for the low Mach-number interactions found at $\theta_1 > 30°$ in the present experiments.

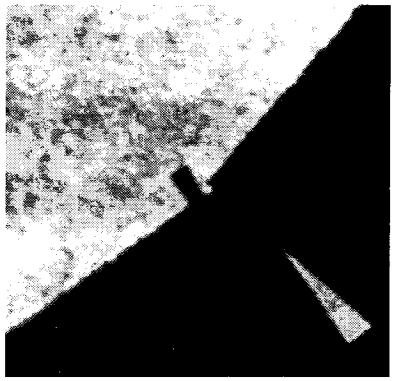

Figure 2.5: Worst case of upstream-facing step at the hingeline (preshot 1291).

Misalignment was also of concern at the joint between the removable leading edge and the front instrument plate. Flow visualization near the leading edge performed at the beginning of the second experimental campaign revealed a measurable disturbance emanating from this joint, as shown in

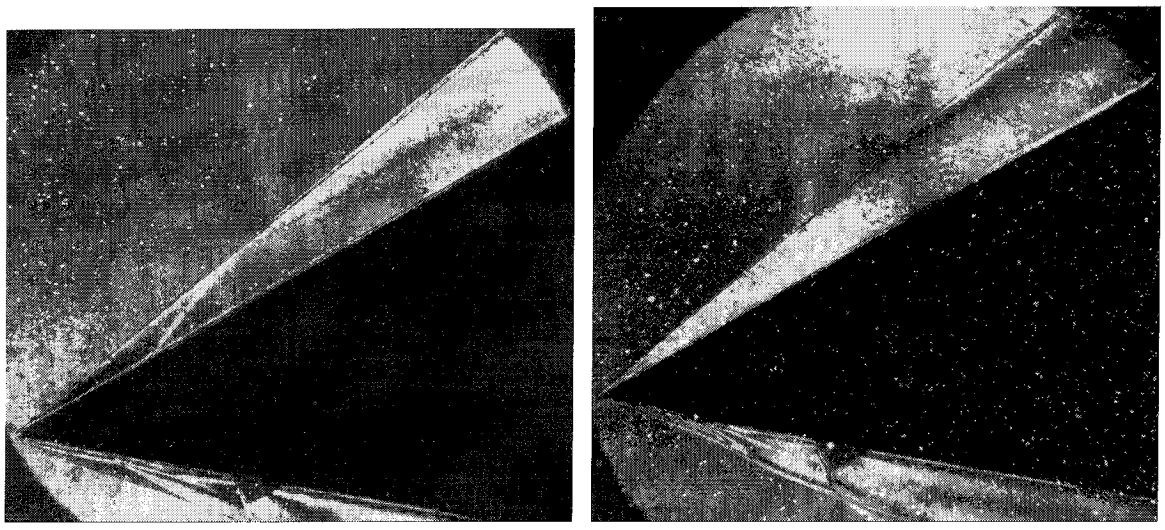

(a) (b)

Figure 2.6: Interferograms of flow near leading edge showing effect of misalignment at leading-edge joint; (a) 64 μm downstream-facing step at joint prior to addition of shims (shot 1729), (b) 6.4 μm upstream-facing step at joint after shims were added (shot 1798). Condition B1, $A_e/A_* = 100$, $\theta_1 = 30°$.

Figure 2.6a. The joint was found to have a downstream-facing step (64 μm high near the centerline) due in part to machining tolerances. Between shots 1736 and 1737, shims were added in the tongue-and-groove key between the leading edge and the front plate (see side view in Figure 2.3) to lower the leading edge with respect to the front plate. The step size was reduced by an order of magnitude, and as shown in Figure 2.6b, any remaining disturbance to the flow could not be observed in the flow visualization. Heat flux measurements taken before and after installation of the shims, at nominally the same flow condition, do not show any significant effect due to a step at the leading-edge joint (see shots 1729 and 1798 in Appendix F). A similar problem occurs at the hingeline when the flap is set to $\theta_w = 0°$, but this could not be corrected by shims.

2.3 Flow Conditions

Three different parameters in the experiments can be varied to control the local flow conditions ahead of separation. These parameters are the nozzle reservoir conditions (characterized by p_0 and h_0), the nozzle area ratio (A_e/A_*), and the incidence angle θ_1 of the first wedge. The computations required to obtain nozzle free-stream and wedge flow conditions are described in Chapter 3. Flow conditions on the wedge are given in Appendix E for each experiment. Nozzle reservoir and free-stream conditions are discussed below in Sections 2.3.1 and 2.3.2 respectively. Only experiments using nitrogen test gas are considered here (eight shots were performed using carbon dioxide, and these are discussed in Appendix G).

2.3.1 Nozzle Reservoir Conditions

The nozzle reservoir conditions, in the reflected shock region of the shock tube, are determined by the tunnel operating conditions. The latter can be described by the initial filling pressures in the ST (p_{ST}) and CT (p_{CT}), the primary diaphragm burst pressure p_4, the driver gas composition (a mixture of He and Ar), and to a lesser extent by the piston driving pressure ($p_{2\mathrm{R}}$, which primarily influences the piston trajectory). The experiments encompassed ten different tunnel operating conditions as shown in Table 2.1. These are divided into three groups A, B, and C according to stagnation enthalpy. The experiments relied heavily on conditions B1, B2, C2, and C4. Conditions A1 and C1 correspond to conditions A and C in Sanderson (1995). Conditions A2 and A3 were designed to obtain high free-stream Reynolds number in an attempt to produce fully turbulent interactions. Conditions B2 and B3 were found after the first experimental campaign to produce transitional interactions, hence condition B1 was developed to obtain lower Reynolds number and fully laminar interactions at low enthalpy. This new condition represents an extension of previous operation of T5; use was made of the new light piston to obtain a very low burst pressure with tuned piston trajectory and tailored shock tube interface. Condition C3 is close to the design condition of the

	h_0 MJ/kg	p_0 MPa	u_s km/s	p_{ST} kPa	p_4 MPa	p_{CT} kPa	He %	p_{2R} (psig)	m_p (kg)
A1	3.89 ±0.49	11.6 ±1.1	1.97 ±0.18	75	32.4 ±8.5	46	75	280	120
A2	4.91 ±0.12	38.9 ±1.9	2.17 ±0.02	160	86.3 ±3.0	61	30	620	120
A3	4.42 ±0.20	41.0 ±1.4	2.12 ±0.06	230	(110)	91	15	925	120
B1	6.96 ±0.60	6.28 ±1.05	2.68 ±0.14	20	17.7 ±1.6	24	78	140	90
B2	8.33 ±0.61	20.0 ±2.5	2.88 ±0.12	45	39.2 ±4.5	55	78	400	120
B3	10.6 ±0.9	57.3 ±4.1	3.21 ±0.17	85	81.9 ±3.6	116	85	1110	120
C1	20.6 ±2.2	27.8 ±2.7	4.58 ±0.26	20	48.8 ±12.6	95	100	600	120
C2	24.1 ±1.1	16.7 ±1.2	5.06 ±0.14	12	47.3 ±3.7	43	100	325	90
C3	24.4 ±1.3	47.9 ±4.8	4.88 ±0.11	22.5	87.6 ±5.7	104	100	1000	120
C4	28.2 ±2.9	23.1 ±2.3	5.33 ±0.32	10	58.7 ±6.2	61.5	100	440	120

Table 2.1: Shock tunnel operating conditions for the present study. Uncertainties describe only the 2σ variation over each set of shots. m_p is the piston mass. For Condition A3, p_4 exceeded the transducer range and was not measured accurately.

T5 contoured nozzle, and was used only in two shots comparing attached flow for the two different nozzles at roughly the same nozzle exit area ratio. As discussed below in Section 2.7.2.2, condition C4, which was used extensively during the first experimental campaign, came under suspicion for contamination by driver gas, and thus condition C2 was developed for the second campaign to provide a noncontaminated high-enthalpy condition.

The reservoir pressure p_0 is measured directly, by first averaging each of the two transducer signals over a period during which they remain relatively constant, then taking the average of the two results. The averaging period is typically 1 ms at low enthalpy and less than 0.5 ms at high enthalpy, and in all cases, encompasses the time of interest for measurements on the model (taking into account the propagation time from the reservoir to the model). Other reservoir properties are obtained by calculation using the computer program ESTC (Equilibrium Shock Tube Calculation, described by McIntosh (1979)). Given the initial pressure and temperature in the shock tube and the measured incident shock speed u_s, this program computes inviscid equilibrium reflected shock conditions (assuming an ideal driver) followed by an isentropic expansion to the measured stagnation pressure p_0. Note that the measured pressure is lower than the theoretical inviscid pressure due to viscous losses in the shock tube boundary layer, expansion waves propagating from the short, unsteady driver section, and flow of the gas into the nozzle. The reservoir conditions for each experiment are listed in Appendix D. Shots which significantly deviate from the nominal conditions in Table 2.1 are marked A0, B0, or C0 in Appendix D.

Uncertainty in measured p_0 for each shot is estimated to be about ±5% based on discrepancies between the redundant transducers due to uncertainty in, and changes in, their factory-calibrated sensitivities. A measurement accuracy of ±1.5% is obtained for the average shock speed between the measurement stations, which translates to ±3% accuracy in h_0 since $h_0 \propto u_s^2$. The uncertainty

in h_0, however, is larger because in fact the incident shock speed is not constant along the shock tube, so that measuring u_s between different stations would result in different computed values for h_0. For lack of a more rigorous estimate, an uncertainty of $\pm 8\%$ in h_0 is assumed for the present experiments. These single-shot uncertainties in p_0 and h_0 are not included in Table 2.1. Instead, Table 2.1 gives the mean and variation (corresponding to twice the standard deviation σ, a 95% confidence level if the data is normally distributed) over each set of shots, indicating repeatability of each condition.

2.3.2 Nozzle Free-Stream Conditions

For each of the reservoir conditions given in Table 2.1, three different free-stream conditions, corresponding to three different nozzle area ratios A_e/A_*, can be obtained by changing the conical nozzle throat. Free-stream conditions for the combinations used in the present experiments are shown in Table 2.2. Note that α is the mass fraction of atomic nitrogen (also called the dissociation fraction) and T_v is a temperature characterizing the vibrational excitation of N_2. The nozzle flow is computed for each shot using a Navier–Stokes solver which includes full thermochemical nonequilibrium and approximates the boundary-layer displacement effect by assuming a laminar boundary layer (the true nozzle flow is expected to be turbulent or transitional). Details on the computational method, the propagation of reservoir condition uncertainties, and experimental validation are given in Sections 3.1 and 3.2. The exit flow of the conical nozzle varies in the axial direction; for purposes of comparison, the free-stream conditions in Table 2.2 are defined as the flow properties on the nozzle centerline at the nozzle exit plane and averaged over results from the number of shots indicated. When used in analysis of individual shots, the free-stream conditions instead refer to flow properties on the nozzle centerline at the axial position of the double-wedge leading edge. The values in Table 2.2 are averaged over the shots at each condition. The length scale for Re_∞ is taken as the front plate chord length, 10 cm.

For T5, the present experiments encompass a large range in free-stream Reynolds number, from 0.5×10^6/meter to 13×10^6/meter. Of particular importance is the new condition B1, which has successfully produced low-enthalpy flows with low Re in the same range as the high-enthalpy conditions C2 and C4. This development allowed comparison of purely laminar interactions on the double wedge at both low- and high-enthalpy conditions. A small range in Mach number is obtained by varying the nozzle area ratio; note, however, that M_∞ cannot be varied independently of Re_∞ and h_0.

	A_e/A_*	M_∞	Re_∞ $L = 10$cm	α_∞	T_∞ K	T_{v_∞} K	ρ_∞ kg/m^3	u_∞ m/s	p_∞ kPa	# of shots
A1	100	6.8	4.5×10^5	9.8×10^{-12}	340	2200	0.034	2500	5.4	7
A2	100	6.6	1.1×10^6	1.4×10^{-8}	450	2100	0.087	2900	20	2
	225	7.9	7.3×10^5	1.2×10^{-8}	330	2200	0.048	2900	8.1	2
	400	9.0	5.3×10^5	9.1×10^{-10}	260	2300	0.029	3000	4.1	2
A3	100	6.6	1.3×10^6	9.6×10^{-10}	410	2000	0.10	2700	4.1	2
B1	100	6.5	1.1×10^5	0.0014	680	3000	0.0098	3400	4.1	4
	225	7.8	8.7×10^4	5.1×10^{-4}	450	3100	0.0059	3400	1.2	6
	400	8.8	6.2×10^4	4.8×10^{-4}	380	3200	0.0037	3500	0.72	9
B2	100	6.3	2.8×10^5	0.0013	840	2800	0.026	3700	12	4
	225	7.6	2.0×10^5	0.0015	590	2900	0.015	3800	3.8	5
	400	8.6	1.5×10^5	0.0015	470	3000	0.0094	3800	2.3	6
B3	400	8.2	3.2×10^5	0.0016	670	3000	0.023	4300	7.1	3
C1	400	7.2	8.1×10^4	0.059	1300	3900	0.0070	5600	4.1	3
C2	100	5.0	7.3×10^4	0.11	2700	4000	0.011	5700	12	6
	225	6.3	6.1×10^4	0.11	1800	4100	0.0065	5800	6.8	6
	400	7.3	4.8×10^4	0.12	1400	4200	0.0041	5900	2.5	5
C3	100	4.7	1.7×10^5	0.063	3400	3900	0.029	5800	37	2
C4	100	4.8	8.3×10^4	0.13	3200	4100	0.013	6000	17	2
	225	6.0	6.3×10^4	0.15	2200	4200	0.0073	6200	11	12
	400	7.0	5.7×10^4	0.15	1700	4300	0.0052	6300	8.1	2

Table 2.2: Nominal free-stream conditions for the present study (centerline at nozzle exit).

2.4 Flow Visualization

For the present work, flow visualization offered the most accurate means of measuring separation length. The primary technique used was holographic interferometry, though some use was also made of shadowgraphy. Both techniques rely on a Nd:YAG laser light source (frequency doubled to 532 nm wavelength) with duration on the order of 2 ns to effectively "freeze" the high-speed flow field. They also both rely on an interference filter to block broadband emission from high-temperature regions of the flow. A digital controller in the DAS keeps the laser thermally stabilized prior to a shot by cycling the flash lamps at 10 Hz, stops the cycling and opens an electromechanical shutter upon receiving a trigger from the CT accelerometer, and fires the laser at a predetermined time t_{las} (given in Appendix D for each shot). The following sections briefly describe each visualization system (Sections 2.4.1 and 2.4.2), the methods for aligning the laser beam to the test model (Section 2.4.3), and the methods for measuring separation length from the photographic records (Section 2.4.4). Flow visualization photographs for each shot are reproduced in Appendix F.

2.4.1 Shadowgraphy

During the first experimental campaign, the standard optical system of T5 was utilized in shadowgraph mode for a number of shots. This system, originally designed by Arndt Schmücker and built by Eric Cummings (priv. comm.), consists of a conventional single-pass folded-Z arrangement with 3.05 m focal-length spherical mirrors used off-axis. The mirrors provide a 20 cm field of view, approximately the same diameter as the test section windows and large enough to visualize flow over the entire upper surface of the double-wedge model. Collection optics minify and image the beam onto 4×5 inch Kodak TMAX (ASA 400) film, from which 8×10 inch prints are developed normally. Schlieren visualization was attempted on a few shots by placing the edge of a razor blade at the focus of the collecting-side spherical mirror. Good schlieren results could not be obtained with this system, however, due to use of a coherent light source and to nonnegligible astigmatism. The one advantage this shadowgraphy system has over the holographic system described below is visualization of the full flow field. The principle disadvantage is that the shadowgraph technique is not sensitive enough to discern a separated shear layer except at high-density conditions. The system described here was primarily useful on shots for which a very large separation region was expected, for example at small θ_1 and large θ_w (see shadowgraphs for shots 1307 1316 in Appendix F). In order to provide an accurate length scale for photographic measurements, a no-flow shadowgraph was taken with a grid printed on a transparency and affixed to one of the test section windows.

2.4.2 Holographic Interferometry

The T5 holographic interferometer system designed and built by Simon Sanderson provides increased sensitivity to density gradients and increased resolution of flow features, compared to the shadowgraphy system described above. The only drawback is a reduced field of view, with diameter of approximately 7 cm. A sketch of the apparatus is shown in Figure 2.7, and additional details concerning the system are given by Sanderson (1995). The device is typically used in a double-pulse mode. Each pulse is split into an object beam which passes through the test section and a holographic reference beam which passes around the test section. The two beams are brought together, with a 5° included angle and equal path lengths, at an image plane of the test section, and the interference pattern thus created is recorded as a hologram. The first (no-flow) pulse is recorded before a shot, and the second pulse is recorded during the test time of interest. The two holograms are recorded on the same piece of 35 mm Kodak SO-253 film. White light is used to reconstruct both object beams simultaneously from the developed holographic film. The resulting interference pattern, equivalent to a Mach-Zehnder interferogram, is recorded on 35 mm Kodak TPAN film, from which enlarged prints are made. In single-pulse mode, the reconstructed object beam can be used for shadowgraphy or schlieren photography (see shots 1283 and 1288 in Appendix F for ex-

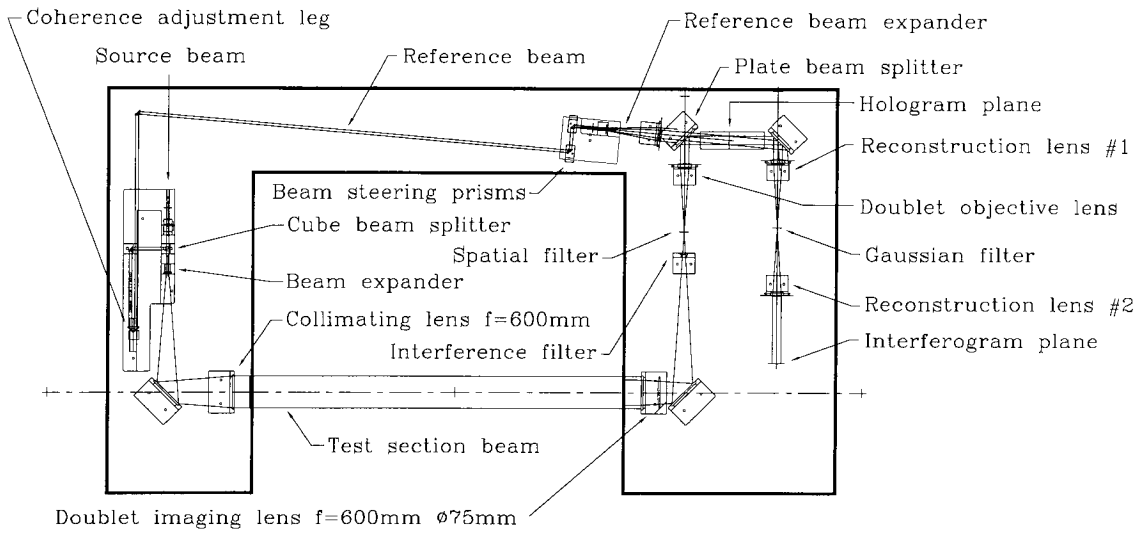

Figure 2.7: Sketch of the holographic interferometer, from Sanderson (1995).

amples of holographic shadowgraphy, and Figure 2.22 for a comparison between shadowgraphy and interferometry).

The fringes in an interferogram show phase shift of the during-flow object beam relative to the no-flow object beam, and are related to contours of density in the flow field. Because the phase shift is integrated along a line of sight and the flow in the experiments is three-dimensional (*cf.* Section 2.7.5), the relationship to density contours in the nominally two-dimensional centerline plane cannot be quantified. The apparatus in Figure 2.7 is designed to perform infinite-fringe interferometry, but many of the interferograms in Appendix F show finite-fringe patterns of arbitrary angle and spacing in the free-stream region, where only a very small phase shift is expected. A finite-fringe pattern can only result from some uncontrolled motion of the laser beam or optics components during the time between pulses. The problem was partially traced to mechanical instability of the camera mounting hardware. Vibrations from operation of the shock tunnel are a potential cause for uncontrolled motions of the laser beam, though the supporting optical tables incorporate some vibrational isolation from the floor. An accelerometer placed on the floor underneath the ST frame for shot 1321 showed vibration beginning approximately 1 ms after shock reflection.

Most of the interferograms from the second experimental campaign show an abundance of white specks which were probably caused by a dusty dark room environment during construction work in the same building. Though cosmetically unappealing, these specks in no way detract from the quantitative measurements of flow geometry described in Section 2.4.4. An accurate length scale for photographic measurements was provided by mounting two small pins on the side of the model just upstream of the hingeline. A double image of the model is apparent in many interferograms, which can only occur due to deflection of the model support under aerodynamic loading (hence the worst

deflection occurs for high pressure condition B3; for example, see shot 1322 in Appendix F). Areas blocked by the model during the no-flow pulse show a shadowgraph instead of an interferogram.

2.4.3 Laser Beam Alignment

Accurate alignment of the laser beam to the coordinate system of the test model is important for accurate measurement of flow field geometry relative to the model. There are a number of diagnostic methods to check this alignment. The best test for alignment parallel to a flat surface such as an instrument plate is to place a sharp object (such as the corner of a razor blade) against the surface, first on one outboard side and then the other, and compare the resulting silhouettes. If the beam and the surface plane are nonparallel, the sharp point in one silhouette will be cut off by shadow. Other methods are to look for reflections off the flat surface, or to look for a shadow cast by the beam-incident edge on a screen placed against the far edge. Alignment was always performed to the front plate, leaving a slight beam misalignment to the rear plate surface due to the hardware misalignment mentioned in Section 2.2.2. None of these techniques, however, will check alignment of the beam parallel to the hingeline. During the first experimental campaign, small pieces of reflective glass were glued to the side of the front and rear instrument plates and the beam was aligned to bring their reflections close to the beamline at the beam expander. This method had only marginal success. A much better technique, applied often during the second campaign, is to inspect the silhouette of the corner region, in particular the triangular "hole" below and behind the hingeline, between the back side of the front plate and the front side of the rear plate. If the beam is aligned to the hingeline, then the upper point of the triangle in the silhouette will coincide with the apparent corner location, as shown by the no-flow photograph in Figure 2.8b.

Note that for the misaligned case in Figure 2.8a, a line coincident with rear side of the triangle silhouette passes through the apparent corner but a line coincident with the front side falls behind the apparent corner. Thus the primary misalignment is within a plane parallel to the front surface. In fact, an angular misalignment within this plane of approximately 0.4° can be measured from Figure 2.8a. This misalignment was never worse than 0.5° during the first experimental campaign, and in any case could be accounted for as follows: the apparent corner formed by intersection of the front and rear plate surfaces corresponds to the corner location at one edge of the model, and the intersection point between the front plate surface and the front side of the triangle corresponds to the corner location at the opposite edge of the model, so that the corner location at the centerline of the model falls halfway between these two points. Aside from this shift of the corner, a small beam misalignment within the plane of the front plate surface will not significantly alter the apparent location of separation. The flow is three-dimensional, and the leading edge of separation is bowed, with the upstream extremity occurring only near the model centerline (*cf.* Section 2.7.5).

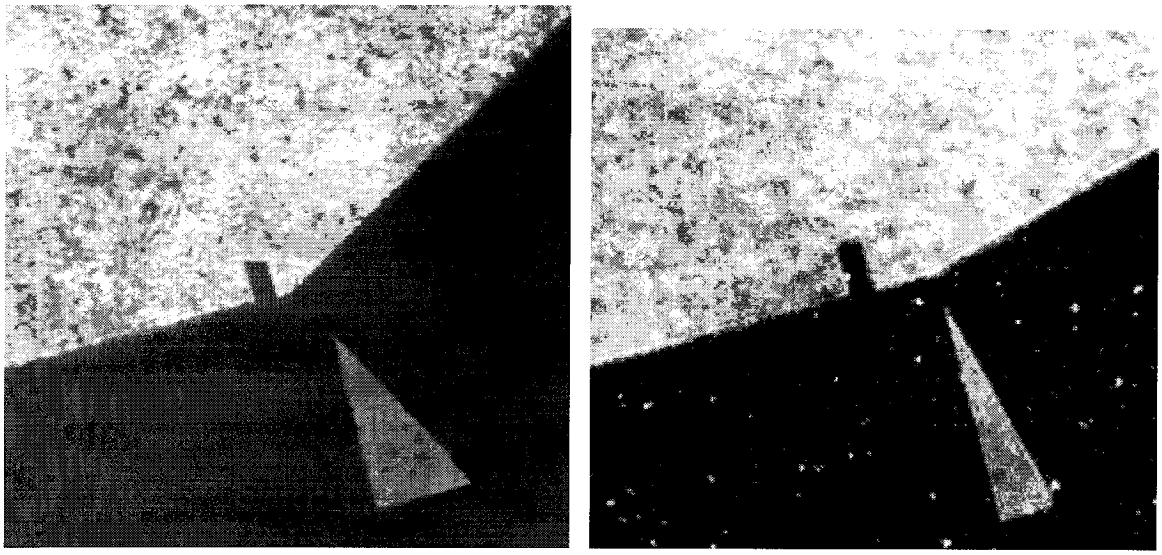

(a) (b)

Figure 2.8: Silhouette of corner region showing alignment of the laser beam to the model; (a) aligned parallel to the front plate surface, but not to the hingeline (preshot 1317), (b) well aligned (preshot 1774)

2.4.4 Separation Length Measurement

The primary purpose for flow visualization in the present work is to measure the separation geometry, in particular L_{sep}. Because it is difficult to assess with any accuracy the location R of reattachment from the interferograms, we instead measure the distance L_u from the corner to the separation point S and the angle θ_{sep} of the dividing streamline. Then L_{sep} is given by the geometry in Figure 1.3 as

$$L_{sep} = \frac{L_u \sin(\theta_w)}{\sin(\theta_w - \theta_{sep})}. \tag{2.1}$$

Viscous computations of separated flow on a double wedge were undertaken in order to understand the relationship between the the interferometric fringe pattern and the dividing streamline, so that a consistent algorithm could be developed for measuring L_u and θ_{sep} from the experimental interferograms. Because separation in two-dimensional flow is commonly defined to occur at a point of zero wall shear stress τ_w, it is also of interest to look at the relationship between the fringe pattern and the skin friction. The computations, including the method for computing interferograms, are described in Section 3.5. The computed interferograms assume a purely two-dimensional flow across the full span of the model, and are not expected to match the experimental interferograms. Differences due to an uncontrolled finite-fringe effect in the experimental interferograms, however, are mitigated by including the finite-fringe phase shift in the corresponding interferogram computation.

The computational result in Figure 2.9 shows a finite-fringe interferogram under purely two-dimensional flow conditions corresponding to shot 1783, which has a relatively thick boundary layer on a low-incidence wedge. The dividing streamline ψ^*, represented by a thick black line, is clearly

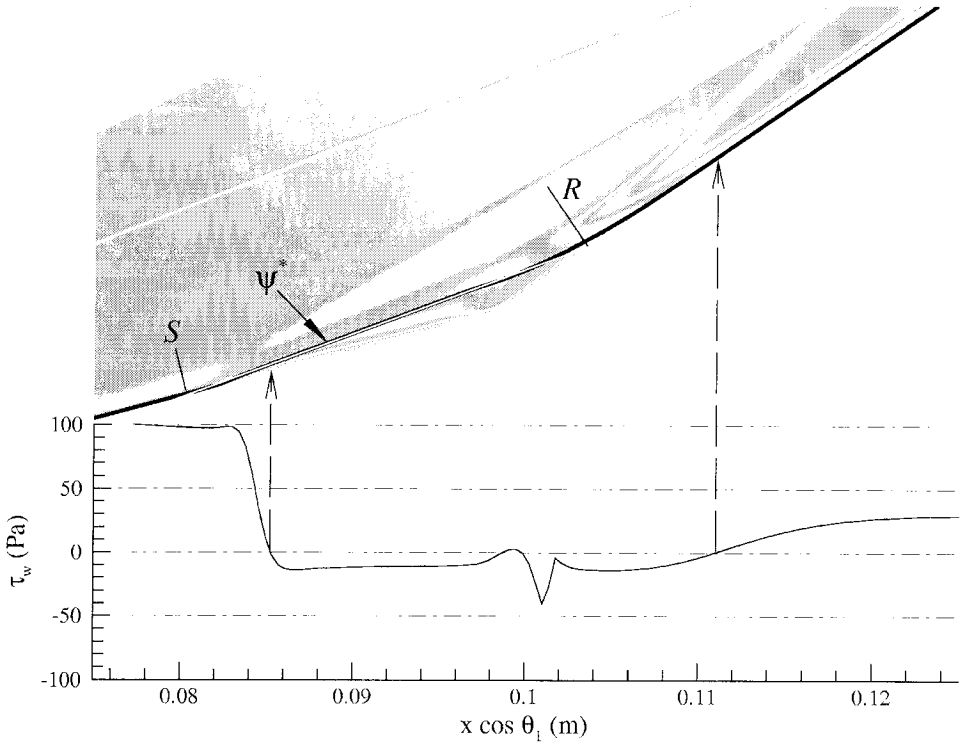

Figure 2.9: Computational results showing relationship between interferometric fringe shift, dividing streamline ψ^* (thick black line), and skin friction for condition of shot 1783. Thin white line is present approximation to ψ^*. Note that ψ^* is parallel to outer fringe of shear layer.

curved near separation and reattachment for a viscous flow. On approach to reattachment, it curves first towards the wall, then slowly the other direction to meet the wall tangentially. The model of separation presented in Section 1.4, however, assumes ψ^* can be represented by a straight line between S and R. In Figure 2.9, such a straight-line approximation is shown by the thin white line drawn tangent to the central part of ψ^*, which intersects the wall at the points labeled S and R. These locations for separation and reattachment defined by the straight line approximation to ψ^* are very different from the locations defined by $\tau_w = 0$. For consistency with Figure 1.3 and Equation 2.1, and since the points of $\tau_w = 0$ are not discernible from the interferometric fringe pattern in any case, we must rely on the straight-line approximation to define S, R, L_u, θ_{sep}, and L_{sep} in the present experimental study. In Figure 2.9, S is situated upstream of where the separation shock intersects the fringe at the boundary-layer edge, but slightly downstream of where it intersects the wall. The position is more accurately determined by where the fringe next to the wall first turns away from the wall, assuming this fringe can be seen in the experimental interferogram. The dividing streamline ψ^* appears parallel to the outer-most fringe of the separated shear layer, indicating that θ_{sep} can be measured using that outer-most fringe.

Experimental interferograms were digitized to facilitate measurements using a computer with a pointing device. Figure 2.10 shows an example of the measurements made on shot 1783 (the

same condition as in Figure 2.9). Lines drawn parallel to a fringe in the separated shear layer and to the front plate surface are used to measure θ_{sep}. The shear-layer fringes in the experimental interferogram diverge slightly in the downstream direction, probably due to three-dimensional end effects. This introduces some subjectivity to the measurement algorithm for θ_{sep}, accounted for by assigning an appropriate uncertainty to the measured value. The point S is placed where the fringe in the sublayer immediately adjacent to the wall turns away from the wall, with subjectivity again accounted for by uncertainty. The distance L_u is then measured between S and the corner, taking into account any known beam misalignment effect (*cf.* Section 2.4.3). The same measurement technique is shown applied to shot 1741 in Figure 2.11. In this case, the boundary layer is too thin to discern its structure, and the computational result shows S occurring below the point where the separation shock intersects the boundary layer. Compared to Figure 2.10, the divergence of fringes in the shear layer for the experimental interferogram is more pronounced. Though the flow is three-dimensional, the apparent locations of both S and the outer edge of the shear layer should correspond closely to the actual locations near the centerline of the model where the separation region is expected to be largest.

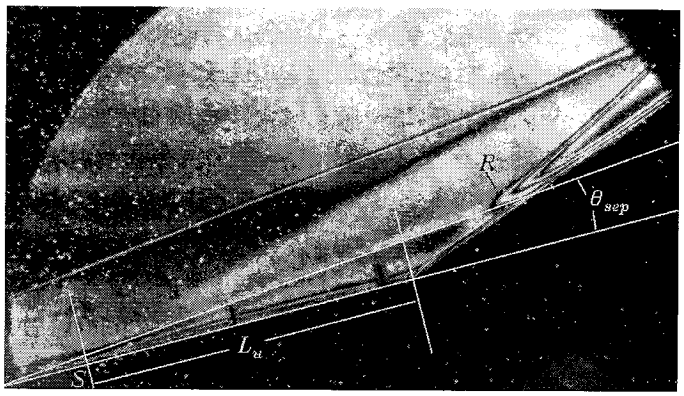

Figure 2.10: Experimental interferogram for shot 1783 (B1, $A_e/A_* = 225$, $\theta_1 = 15°$, $\theta_w = 20°$) showing measurement technique for obtaining L_u and θ_{sep}.

Interferometric measurements of L_u were converted to physical length by a scale determined from pegs placed on the side of the model, which can be seen in all the interferograms. The physical distance between the leading edge of the front peg and the downstream edge of the rear peg was 15.8 ± 0.06 mm for shots 1286–1785 and 14.8 mm for shots 1786–1799. The scale was often measured using photographs reconstructed from single-pulse no-flow holograms, for which the peg silhouettes are not obscured by a double image (*cf.* Section 2.4.2). Uncertainties ΔL_u and $\Delta\theta_{sep}$ assigned to the measurements of L_u and θ_{sep} respectively are used to determine the uncertainty ΔL_{sep} in L_{sep} by the usual formulation for propagation of errors (Bevington, 1969),

$$(\Delta L_{sep})^2 = (\Delta L_u)^2 \left(\frac{\partial L_{sep}}{\partial L_u}\right)^2 + (\Delta\theta_{sep})^2 \left(\frac{\partial L_{sep}}{\partial \theta_{sep}}\right)^2 , \tag{2.2}$$

where the errors ΔL_u and $\Delta\theta_{sep}$ are assumed to be uncorrelated. Applied to Equation 2.1,this yields

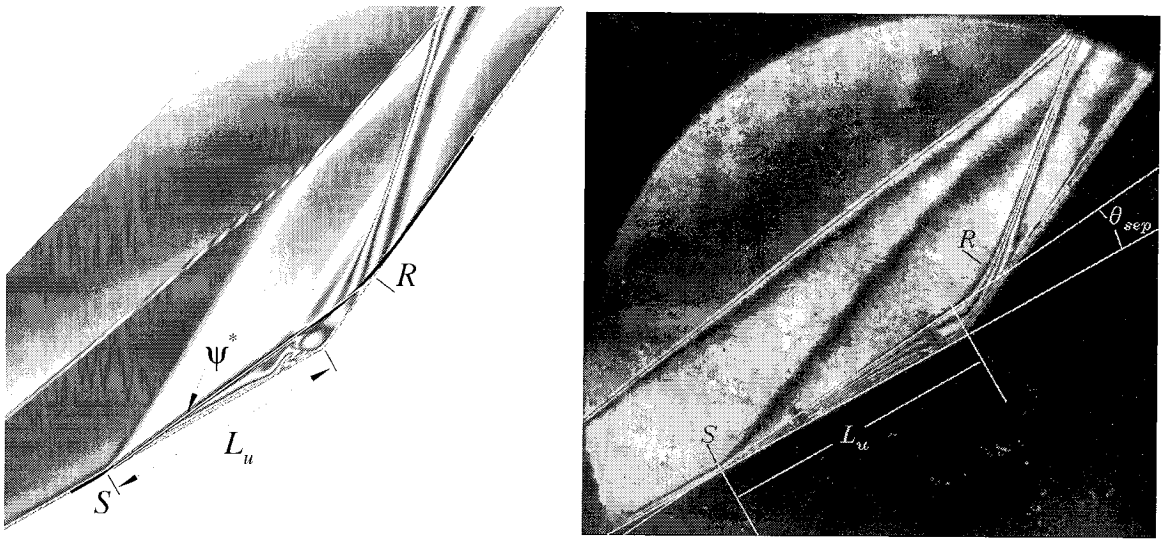

Figure 2.11: Measurement technique for separation length applied to shot 1741 (C2, $A_e/A_* = 225$, $\theta_1 = 30°$, $\theta_w = 25°$); (a) computational interferogram showing dividing streamline ψ^* (thick black line) and straight-line approximation to it (thin white line), (b) experimental interferogram showing measurement of L_u and θ_{sep}.

$$\frac{\Delta L_{sep}}{L_{sep}} = \sqrt{\left(\frac{\Delta L_u}{L_u}\right)^2 + \left(\frac{\Delta\theta_{sep}}{\tan(\theta_w - \theta_{sep})}\right)^2}. \tag{2.3}$$

Values for θ_{sep}, L_u, L_{sep}, and their corresponding uncertainties are given in Appendix D from all shots on which they could be measured. Measurements of the leading-edge shock angle β_1 are presented there as well.

For the rare interferogram in which separation appeared to occur slightly upstream of the field of view (*e.g.* shot 1320 in Appendix F), an estimate for S was made by extending lines coincident with the separation shock and the shear layer to an intersection point outside the field of view. Measurements of L_u and θ_{sep} could not be made for shots with $\theta_1 = 0°$; at low density, the interferometric technique was too insensitive to adequately discern a separation shock and separated shear layer (see shots 1764–1773 in Appendix F), and at high density, the separation region was much too large to be captured in the field of view (see shots 1759–1762 in Appendix F). Both problems were exacerbated by the restriction on vertical model position mentioned in Section 2.2.2, which causes an expansion at the leading edge. The two experiments performed at condition A3 (shots 1748 and 1751) appear to exhibit attached flow despite a rather large ramp angle in one case. Measurements of L_u and θ_{sep} for several shots were made using a shadowgraph instead of an interferogram, under conditions where the density gradient across the shear layer was strong enough to produce a discernible shadow from which to measure θ_{sep} (*e.g.* shot 1316 in Appendix F). The separation point S in these cases was placed at the intersection of the separation shock and the body.

2.5 Heat Flux Measurement

In order to study reattachment heating, coaxial thermocouples were used in the present experiments to measure time-resolved surface temperatures on the double-wedge model, from which surface heat flux could be deduced. Next to flow visualization, this is the most common and robust type of measurement made in T5. The following sections describe the hardware (Section 2.5.1), the method used to obtain time-resolved heat flux from a measured voltage signal (Section 2.5.2), and some examples of heat flux spatial distributions (Section 2.5.3). Details not covered in this section are given in Appendix B.

2.5.1 Coaxial Surface Thermocouples

The coaxial type E (constantan–chromel) thermocouples were built in-house based on the design of Sanderson (1995). An essential feature of the design is that the center electrode is tapered where it contacts the outer electrode. This results in a very thin junction (in the form of a 0.8 mm diameter circle on the surface of the model) and very fast response time on the order of 1 μs. Figure 2.12 shows a sketch of a thermocouple installed in an instrument plate. Wire leads are soldered to each electrode, then the two electrodes are assembled with epoxy adhesive to electrically insulate them except at the junction, and an epoxy bead is later added to the rear for strain relief. Leads of thermocouple material (constantan and chromel) were used in the present work, but copper leads will work just as well because the entire thermal gradient of interest occurs very close to the surface, and the solder joints remain at constant temperature (thermal penetration depth is less than 0.5 mm during an experiment). The assembled thermocouple is mounted in the instrument plate using cyanoacrylate adhesive, such that the outer electrode is flush with the surface. The protruding stub of the center electrode is then cut off, and any remaining material is removed by filing and sanding to assure a flat surface with good contact between the electrodes.

The thermoelectric EMF generated by the temperature rise at the model surface is on the order of 1 mV, and thus the signal must be highly amplified to obtain reasonable dynamic range at the 2.4 mV resolution of the digital recorder. The amplification factors were changed from shot to shot to make full use of the available recording range under different test conditions and model configurations, relying partly on trial and error and partly on a rule of thumb that gives $\Delta V \propto \rho_\infty h_0^{3/2}$ for constant geometry at different free-stream conditions (which holds for constant Stanton number with $\dot{q} \propto \Delta T \propto \Delta V$ and $h_0 \propto u_\infty^2$). Only the differential voltage between the two electrodes was amplified and recorded, so that any EMF generated by the junction between the outer electrode and the instrument plate does not affect the measurement. The model was connected to a common ground with the DAS, effectively shielding thermocouple lead pairs from external electromagnetic disturbances but not from each other. The lead pairs were also twisted to reduce noise. The original

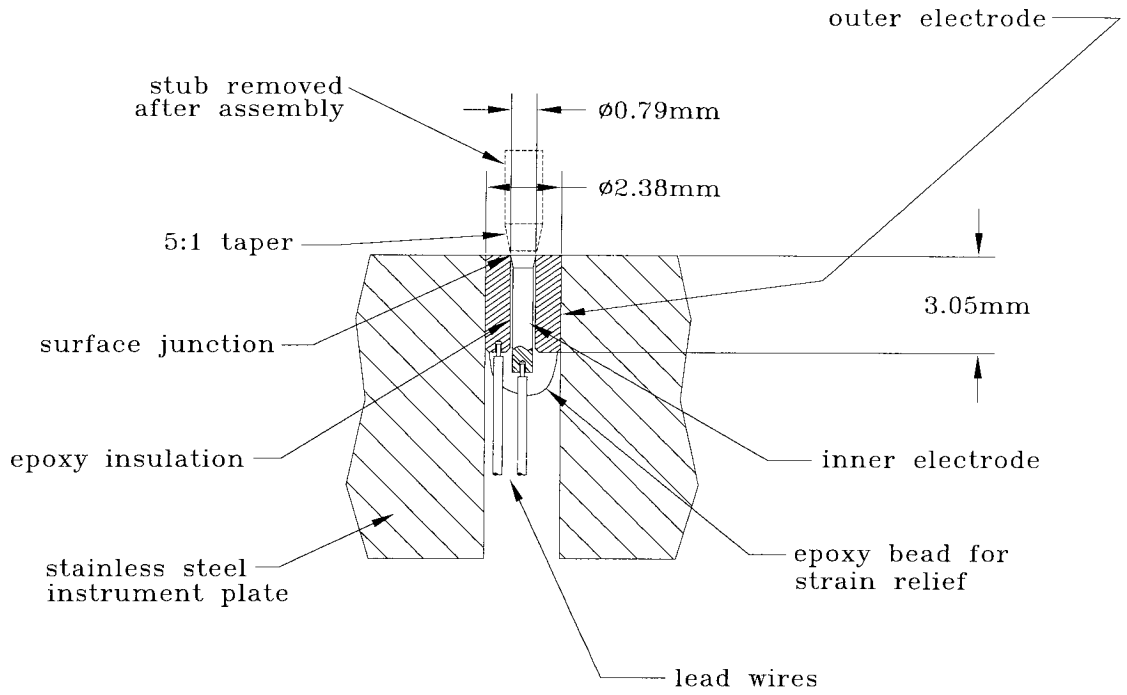

Figure 2.12: Sketch of a coaxial surface thermocouple shown mounted in an instrument plate.

thermocouple design used chromel for the inner electrode and constantan for the outer electrode, but later the design was changed to switch these materials; both designs were used in the model simultaneously without affecting the measurements (aside from changing the sign of ΔV). The reference junction of each thermocouple circuit is effectively formed at the wiring harness connector inside the model enclosures. The temperature at the reference junctions does not change during an experiment, and was assumed to be the same as the ambient room temperature T_{amb}.

Whereas the present experiments used commercial amplifier modules mounted in crates external to the test section, some previous experiments in T5 (Sanderson, 1995) have used custom amplifier circuits mounted inside a cavity in the model support, this cavity being sealed from the test section and open to the room *via* tubular conduit feedthroughs. The latter technique may reduce noise by avoiding transmission of very small signals on long cables outside the test section. To alleviate any concern that the present experiments may suffer unnecessarily from poor signal-to-noise ratio, a comparison is made in Figure 2.13 between signals recorded under nominally the same free-stream condition using the present double-wedge test model and using the apparatus of Sanderson (1995). The latter configuration consists of a 4 cm diameter cylinder. Where the local inclination angle is the same on the two models, the local flow conditions are similar in the sense of Newtonian hypersonic flow theory. Thus we compare a signal from the present experiments at $\theta_1 = 30°$ (Figure 2.13a) with a signal from a thermocouple on the cylinder located 60° from the stagnation line (Figure 2.13b). The noise levels, evident in the signal before flow starting, are approximately the same for both cases. (The resolution in temperature is smaller for the cylinder case due to a smaller amplifier gain.) The

signal spectra also show no significant difference aside from a peak near 47 kHz for the cylinder case due to an unknown source of interference; this frequency is evident upon close inspection of the preflow signal and is therefore not related to the flow. Similar types of noise occurred intermittently for certain thermocouples in the present experiments as well. We can conclude that the signal-t-noise ratio in general is not adversely affected by placing the amplifiers outside the test section.

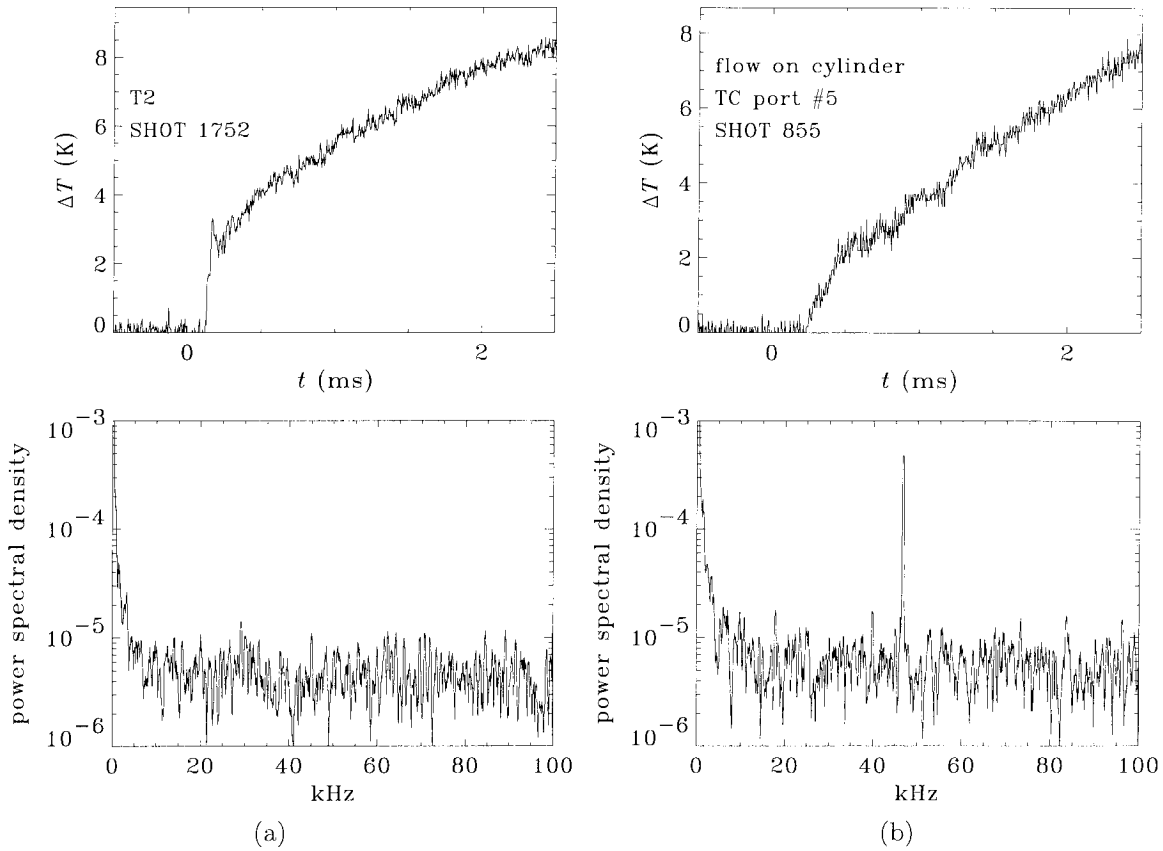

Figure 2.13: Comparison between thermocouple signal from a present experiment and an experiment of Sanderson (1995); (a) T2 on shot 1752, condition A1, $A_e/A_* = 100$, $\theta_1 = 30°$, (b) TC port #5 (60° from stagnation line of cylinder) on shot 855, condition A1, $A_e/A_* = 109$ (contoured nozzle). For clarity, the spectra have been smoothed using $\simeq$ 400 Hz boxcar average.

2.5.2 Signal Processing

The amplified voltage signal from each thermocouple was digitally sampled at 200 kHz over a 20.5 ms record length. The first step in processing the digital data is to apply reverse amplification to recover the actual voltage. Then the average initial preflow voltage level is subtracted to give only the change in voltage during an experiment. The initial voltage, which varies from shot to shot, is due to uncontrolled thermal gradients in the DAS equipment where each thermocouple circuit is completed, and does not change during the test time. The voltage rise ΔV is converted to temperature rise

ΔT (with respect to the initial model temperature) using cubic-spline interpolation of the standard tabulated temperature-EMF relationship for type E thermocouples from NIST (ASTM, 1993). The initial temperature is assumed equal to the reference-junction temperature T_{amb}, and since this is not 0°C as required by the standard table, a compensating voltage, corresponding to the EMF generated at T_{amb} with respect to a fictional 0°C reference junction, must be added to the signal before converting to temperature. T_{amb} is then subtracted from the signal to obtain ΔT.

From the temperature rise, time-resolved heat flux $\dot{q}$ is obtained by a spectral deconvolution technique. This technique is based upon the theory of one-dimensional unsteady heat transfer in a semi-infinite solid, which for constant thermal properties is described by the linear partial differential equation

$$\frac{\partial^2 T}{\partial x^2} = \frac{1}{\alpha}\frac{\partial T}{\partial t}\,. \tag{2.4}$$

Here, x is distance normal from the surface and α is thermal diffusivity of the solid; note that $\alpha = k/\rho c$, where k is thermal conductivity and c is specific heat of the solid. The boundary conditions corresponding to the experiments are

$$T(x,0) = T_i\,, \qquad T(0,t) = T_i + \Delta T(t)\,, \tag{2.5}$$

$$\left.\frac{\partial T(t)}{\partial x}\right|_{x\to\infty} = 0\,, \qquad \left.\frac{\partial T(t)}{\partial x}\right|_{x=0} = \dot{q}(t)\,. \tag{2.6}$$

The solution $T(x,t)$ of this system is given by

$$\Delta T(x,t) = \int_0^t g(x,t-t')\,\dot{q}(t')\,dt' \tag{2.7}$$

where the kernel of the convolution integral, $g(x,t)$, is the unit impulse response function

$$g(x,t) = \sqrt{\frac{\alpha}{\pi k^2 t}}\exp\frac{-x^2}{4\alpha t}\,; \qquad t>0\,. \tag{2.8}$$

Deconvolution of Equation 2.7 to obtain $\dot{q}(t)$ from noisy, discretized, temperature data is relatively straightforward using fast Fourier transform techniques (see Press *et al.*, 1992). The noisy measured signal $s(t)$ is assumed to consist of two uncorrelated components, the "true" temperature $\Delta T(t)$ and the noise $n(t)$. Denoting the fast Fourier transform of a quantity by upper case symbols, the time resolved heat flux is given by

$$\dot{q}(t) = FFT^{-1}\left[\frac{S(f)\,\Phi(f)}{G(f)}\right]\,, \tag{2.9}$$

where the optimal (in the least-squares sense) filter in the frequency domain, $\Phi(f)$, is given by

$$\Phi(f) = \frac{|S(f)|^2 - |N(f)|^2}{|S(f)|^2}\,. \tag{2.10}$$

Some estimate of the noise spectrum $|N(f)|^2$ is required, and this is typically based on the behavior of the signal spectrum at high frequencies. The high-frequency spectra of the current measurements, however, are nonsmooth, nonwhite, and nonrepeatable, preventing consistently reliable estimates of $|N(f)|^2$. Therefore we opt to use a square cutoff filter which removes the entire high-frequency portion of the signal above a specified cutoff frequency f_c,

$$N(f) = \begin{cases} 0, & f < f_c \\ \max\left[S(f)\right], & f \geq f_c \end{cases}, \tag{2.11}$$

eliminating susceptibility of the result to occasional high-frequency interference found in some measurements. This works well because the temperature signal of interest consists almost entirely of low frequencies. Note that the 3 dB bandwidth of the amplifiers is only 50 kHz in any case. When applying Equation 2.9 to the digital data, the time series $s(t)$ and $g(t)$ must be padded with zeros to four times their original length, as detailed in Section B.1, to minimize acausal corruption of the data.

It remains to specify the parameters x, α, and k. The temperature is effectively measured at a distance x below the surface, corresponding to the depth of the junction. Based on microscopy results (*cf.* Section B.2), the junction depth was assumed to be approximately 1 μm for all thermocouples on all experiments. The thermal properties α and k for each of the thermocouple materials (constantan and chromel) are given by Sundqvist (1992), but it is not clear how these relate to the effective thermal properties at the junction. Here we assume that an adequate representation is given by simply averaging the properties of constantan and chromel, which gives reasonable agreement with the limited calibration results available (*cf.* Section B.3). Variation of the thermal properties with temperature can be significant, violating the constant-property assumption of Equation 2.4. For the present work, the effect of temperature-dependent properties is approximated by using constant properties evaluated for each signal at an average temperature, the average being taken between the time of flow starting and the time of flow visualization. The validity of this approximation is shown in Section B.3. An example of the deconvolution process is presented in Figure 2.14.

2.5.3 Heat Flux Results

All thermocouple signals were processed as above with a filter cutoff at $f_c = 20$ kHz, and these were each averaged over a 100 μs time period centered on t_{las} to obtain spatial distributions of heat flux. This time period was chosen to encompass two cycles at the filter cutoff frequency. Two examples of streamwise distributions (TC ports 1–27) are shown in Figure 2.15. The heat flux is made nondimensional by a Stanton number based on free-stream conditions (on the nozzle axis at the model leading edge),

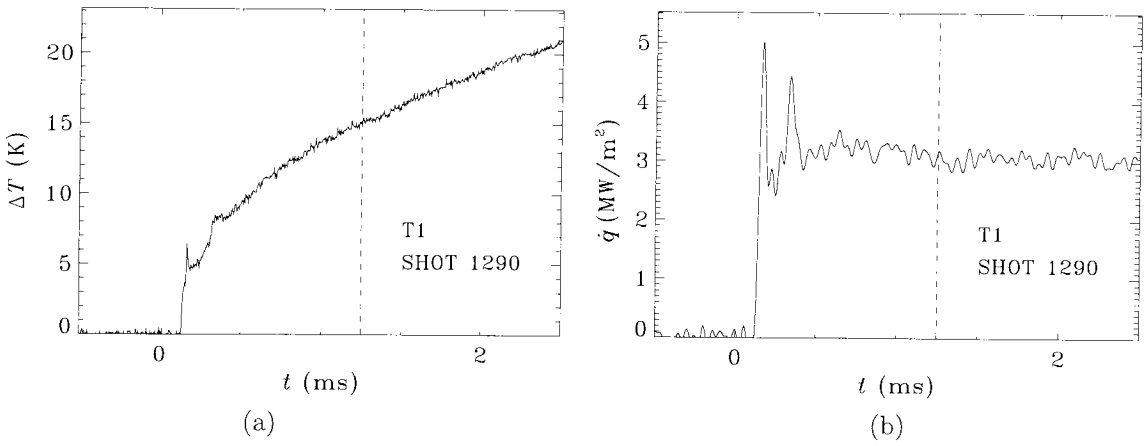

Figure 2.14: Example of temperature signal deconvolution from shot 1290 (condition B2, $A_e/A_* = 225$, $\theta_1 = 35°$, $\theta_w = 20°$); (a) temperature history, (b) deconvolved heat flux using $f_c = 20$ kHz. Dashed line indicates time of flow visualization.

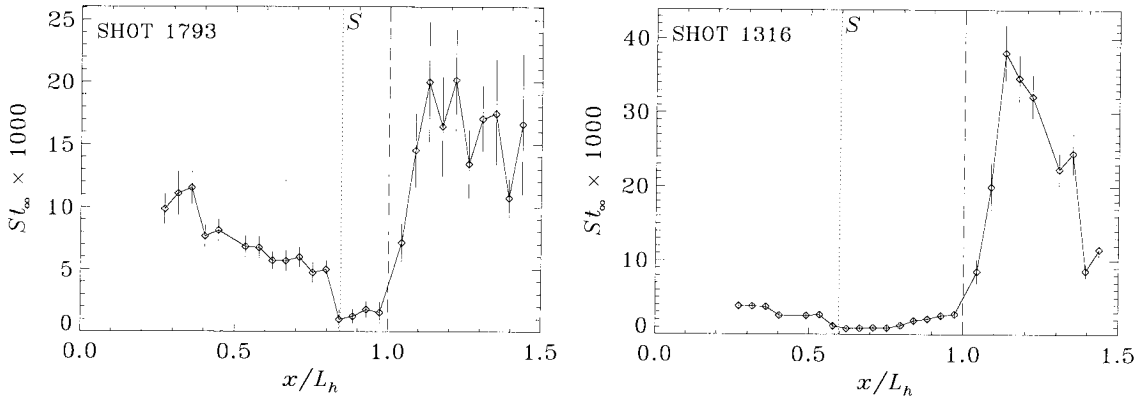

Figure 2.15: Two examples of streamwise distribution of Stanton number for shot 1793 (condition B1, $A_e/A_* = 225$, $\theta_1 = 40°$, $\theta_w = 15°$) and shot 1316 (condition B2, $A_e/A_* = 225$, $\theta_1 = 15°$, $\theta_w = 30°$). Dashed line is hingeline location, dotted line is separation location measured from flow visualization, $\diamond$ are experimental measurements, and solid connecting line serves only as a visual aid.

$$St_\infty = \frac{\dot{q}}{\rho_\infty u_\infty (h_0 - c_{p_\infty} T_w)} \tag{2.12}$$

where T_w is the wall temperature, assumed constant at 300 K, and vibrational excitation in the free stream is ignored when computing $c_{p_\infty} = R_\infty + c_{v_\infty}$ since it is negligible at the wall. This normalization does not collapse data from different double-wedge configurations and different test conditions, but serves only to show the magnitude of wall heat flux relative to energy flux in the free stream.

Thermocouple signals are discarded if they saturate the digitizer output during the test time of interest (due to overpredicted amplifier gains), if they clearly suffer from a poor connection, if the uncertainty in the result is larger than the heat flux value, or if the result is nonsensical based on results from neighboring thermocouples. Note in Figure 2.15 that T6 is missing for shot 1793 while

T5 and T23 are missing for shot 1316. The error bars include estimated uncertainties from several sources, combined to obtain the total uncertainty under the assumption that they are noncorrelated, *i.e.* total $\Delta = \left(\sum_i \Delta_i^2\right)^{1/2}$. The following list describes the various sources.

1. There is some uncertainty in the voltage-to-temperature conversion; a standard tolerance of $\pm 1.7°$C applies to the NIST table, due to small differences in thermocouple material from different manufacturers. Any such bias error will vary slowly with temperature, and since we measure relative temperature instead of absolute temperature, this tolerance is taken to be a "full scale error" where the "full scale" is arbitrarily set at 100°C. In other words, a relative uncertainty of $\pm 1.7\%$ is assumed for all ΔT measurements, which carries through directly to a $\pm 1.7\%$ uncertainty in $\dot{q}$.

2. The contribution to $\Delta\dot{q}$ from uncertainty in the thermal properties of the thermocouple arises from the proportionality $\dot{q} \propto \sqrt{\rho c k}$ (*cf.* Equations 2.9 and 2.8, noting that $k/\sqrt{\alpha} = \sqrt{\rho c k}$ and that the exponential factor gives negligible contribution from $\Delta\alpha$ because x is so small). Based on uncertainty in the published thermal property values and comparison to limited calibration results (*cf.* Section B.3), the relative uncertainty in $\sqrt{\rho c k}$ is assumed to be $\pm 8\%$ for the present experiments.

3. Unsteadiness of the heat flux time history during the 100 μs averaging period is accounted for by an uncertainty equal to twice the standard deviation of the signal over that averaging period.

Upstream of separation, the heat flux distributions in Figure 2.15 fall gradually with increasing distance, as expected for viscous flat-plate flow away from the leading edge. There is, however, significant scatter about the mean decline. This scatter is very repeatable and does not change with vertical repositioning of the model, and therefore must be due to the thermocouples themselves. Erroneous heat flux could be measured if a thermocouple was not mounted exactly flush with the surface, but this problem rarely occurred during the present experiments. The most likely cause is large scatter in the effective thermal product $\sqrt{\rho c k}$ of the thermocouples. Calibration of individual thermocouples, though it could not be performed for the present study, may reduce the scatter.

Both distributions in Figure 2.15 also show a sudden drop in heat flux near separation, consistent with previous observations of laminar boundary-layer separation (*e.g.* Needham, 1965). There is a very strong rise in $\dot{q}$ at reattachment downstream of the hingeline. For shot 1316, this is followed by a strong expansion. Measurements in the flap region often have larger uncertainties as seen for shot 1793, which may be due in part to three-dimensional instabilities arising from the concave flow at reattachment flow (*cf.* Section 2.7.5). Note that $\dot{q}$ for shot 1316 begins to rise slowly in the middle of the separation bubble, well ahead of reattachment. This behavior has previously been observed when transition occurs in the separated shear layer (*e.g.* Kumar and Stollery, 1994). Streamwise

and spanwise distributions of St_∞ are presented for each shot in Appendix F. Note that, for the same reasons discussed in Section 2.4.4, heat flux measurements for configurations with $\theta_1 = 0°$ suffered very poor signal-to-noise ratio, due to the extremely small temperature rise (sometimes less than 0.25 K). For shots with a measurable separation length and $\theta_1 > 0°$, an experimental value for reattachment heat flux $\dot{q}_R$ was obtained by averaging over appropriate, manually selected thermocouple results in the flap region between the sharp rise at reattachment and any large change further downstream due to a strong expansion or to shock–shock interaction. Similarly, the heat flux just upstream of separation, $\dot{q}_1$, was obtained by averaging over three thermocouples upstream of the separation location observed from flow visualization. Appendix D gives results for $\dot{q}_1$ and $\dot{q}_R$, as well as $\dot{q}_{pk}$, the maximum observed heat flux from a single thermocouple in the flap region.

2.6 Pressure Measurement

Transducers to measure surface pressure were not a primary feature of the test-model design. The only instrumentation available in T5 that could fit within the size constraints of the model had unproven reliability, and as mentioned in Section 1.3, the limits on spacing and number of pressure transducers prevented detailed measurements of the pressure rise at separation and reattachment. Nevertheless, pressure data was acquired during the present experiments for comparison with results from flow computation in Section 3.3.3.

2.6.1 Piezoelectric Pressure Transducers

Pressure instrumentation on the double-wedge model consisted of fourteen miniature transducers, PCB model no. 105B12. These transient devices operate on the piezoelectric effect, by which a quartz disc produces output charge (converted to a voltage signal by the powered transducer circuitry) proportional to the compressive force acting on it. The sensors have a 2 μs response time and a 1 s discharge time constant, so that negligible degradation of the signal occurs during the test time.

The recessed mounting configuration, shown in Figure 2.16, was designed to protect the gauge head from the harsh flow environment while maintaining a reasonable response time to the initial flow starting process and avoiding cavity resonance. A thin layer of RTV-type silicone sealant over the gauge head insulates it from thermal loads. Though they are acceleration-compensated to reduce erroneous signals due to vibration, previous use of these transducers in T5 yielded very poor signal-to-noise ratios. Significant improvement in this regard was obtained for the present experiments by filling the mounting threads with silicone sealant and leaving the transducer slightly loose; when the sealant dries, it provides some measure of vibrational damping between the model and the transducer.

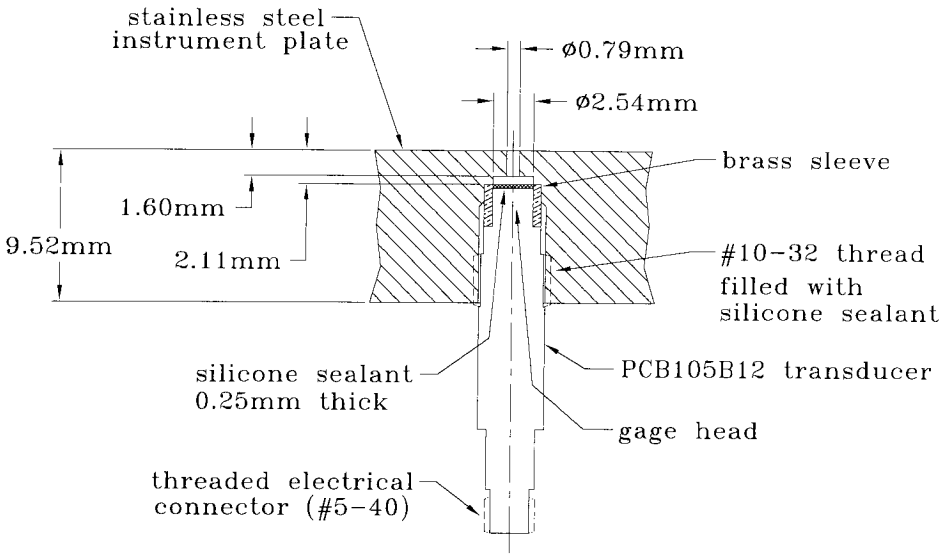

Figure 2.16: Sketch of recessed mounting configuration for pressure transducers.

2.6.2 Signal Processing

Voltage signals from the pressure transducers were sampled at 200 kHz over a 20.5 ms record length. These are converted to pressure by the gauge sensitivities which have been individually calibrated; details are given in Appendix C. The spectral filtering method described in Section 2.5.2 for thermocouple measurements can also be applied to pressure measurements, *i.e.*

$$p(t) \;=\; FFT^{-1}\left[S(f)\,\Phi(f)\right], \tag{2.13}$$

where $S(f)$ is the transform of a noisy pressure signal and $\Phi(f)$ is again given by Equation 2.10. A simple cutoff filter suffices to remove all high-frequency noise due to vibration or cavity resonance. An example of pressure signal filtering is presented in Figure 2.17.

2.6.3 Pressure Results

As for the heat flux measurements, all pressure signals were filtered at $f_c = 20$ kHz and averaged over a 100 μs time period centered on t_{las} to produce distribution plots like those in Figure 2.18, which show streamwise distributions (PT ports 1–10). The nondimensional pressure coefficient C_P gives the magnitude of local static pressure relative to the free-stream dynamic pressure, and is given by (under the assumption that $p \gg p_\infty$)

$$C_P \;=\; \frac{p}{\frac{1}{2}\rho_\infty u_\infty^2}, \tag{2.14}$$

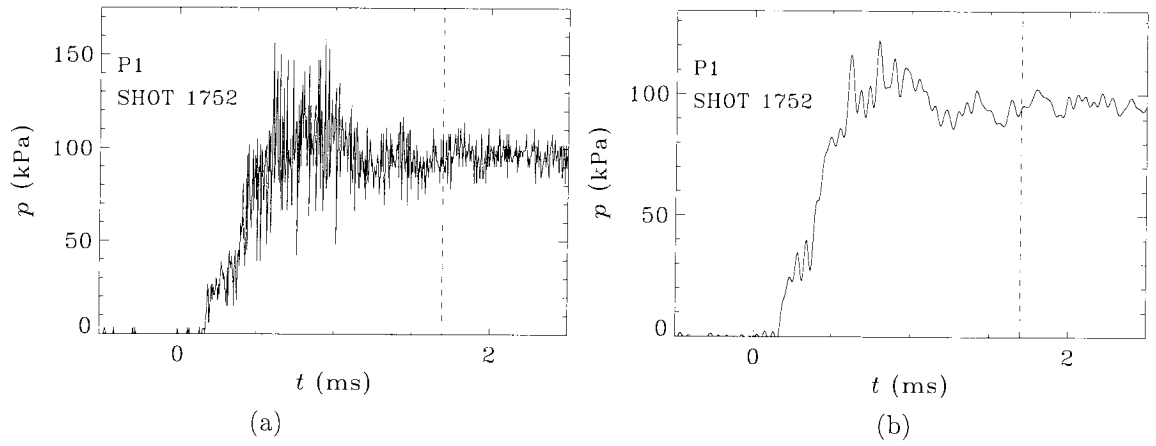

Figure 2.17: Example of pressure signal processing from shot 1752 (condition A1, $A_e/A_* = 100$, $\theta_1 = 30°$, $\theta_w = 25°$); (a) raw pressure history, (b) processed by square cutoff filter, $f_c = 20$ kHz. Dashed line indicates time of flow visualization.

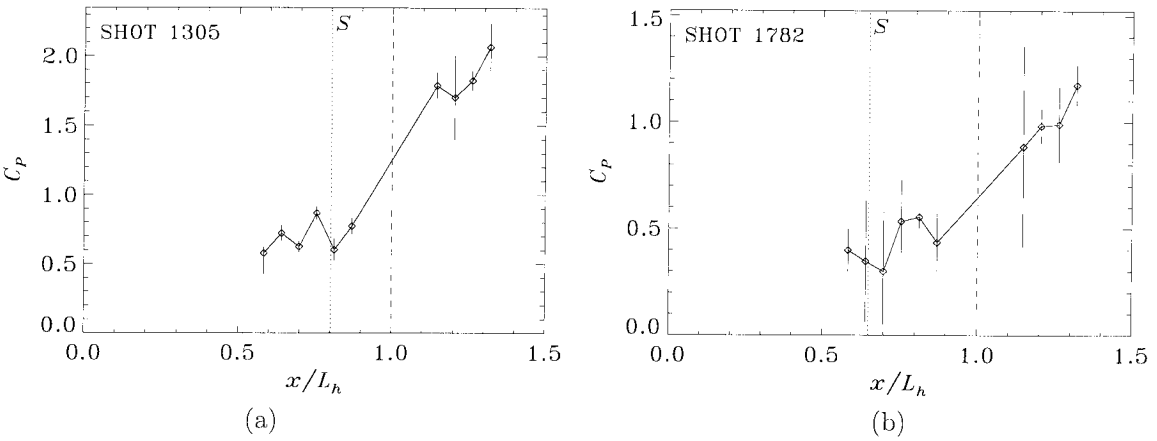

Figure 2.18: Two examples of streamwise distribution of pressure coefficient for shot 1305 (condition B2, $A_e/A_* = 400$, $\theta_1 = 30°$, $\theta_w = 20°$) and shot 1782 (condition B1, $A_e/A_* = 400$, $\theta_1 = 15°$, $\theta_w = 20°$). Dashed line is hingeline location, dotted line is separation location measured from flow visualization, $\diamond$ are experimental measurements, and solid connecting line serves only as a visual aid.

where the free-stream conditions are again taken on the nozzle centerline at the model leading edge. The same criteria described in Section 2.5.3 for heat flux measurements are used to discard poor pressure signals. The error bars in this case represent combined uncertainty from two sources; uncertainty in transducer sensitivities (*cf.* Appendix C) and unsteadiness over the averaging period.

Both distributions in Figure 2.18 show an increased pressure downstream of reattachment on the flap, but only the distribution for shot 1782 suggests the slightly increased pressure expected in the separated region with respect to the pressure upstream of separation. The rather large scatter prevents accurate measurements in this region. Many results show large uncertainties as seen for shot 1782 in Figure 2.18. Data in the flap region, however, tends to exhibit relatively less scatter, and

may be useful for comparison to results from computational methods (*cf.* Section 3.3.3). Streamwise and spanwise distributions of pressure coefficient are presented in Appendix F for each shot. Given in Appendix D are experimental values for the reattachment pressure p_R obtained by averaging over appropriate, manually selected results from transducers P7 P10.

2.7 Flow Quality

Addressed in this section are issues regarding quality of the double-wedge flow in the present experiments; nozzle disturbances (Section 2.7.1), establishment of separation (Section 2.7.2.1), contamination by driver gas (Section 2.7.2.2), shock–shock interaction (Section 2.7.3), unsteadiness (Section 2.7.4), and three-dimensionality (Section 2.7.5).

2.7.1 Nozzle Flow Disturbances

Turbulence in the nozzle boundary layer may cause unsteady acoustic disturbances in the free-stream flow. This might affect transition of a boundary layer or separated shear layer on the double-wedge model, but is not considered in the present work. Small misalignments at the joints in the nozzle may cause some disturbance to the free-stream flow, but these should be very weak as long as the boundary layer is thick compared to the step. Sources near the throat, where the boundary layer is thin, are of particular concern. The profiles of the throat walls were designed to have continuous curvature from the shock tube end wall through the minimum area to the conical section. According to results of Dumitrescu *et al.* (1996), this should eliminate disturbances in the throat region. At the downstream end of the throat insert, however, there is a joint where the secondary diaphragm is placed, and this may cause a significant disturbance which focuses on the nozzle centerline. Comparison of measured heat flux distributions on a wedge from two shots at nominally the same free-stream condition, but with vertical translation of the model by 2.2 cm moving the leading edge from above to below the nozzle centerline, shows no effect that can be attributed to stationary disturbances in the nozzle flow. The comparison used the $A_e/A_* = 100$ throat, and therefore no conclusions can be drawn regarding the $A_e/A_* = 400$ throat, for which the joint in question falls further downstream of the minimum area, well into the supersonic flow region. Apart from disturbances generated by the nozzle, the free stream may be subjected to unsteadiness in the reservoir conditions.

In Figure 2.19, spectra from pressure signals in the nozzle reservoir and on the test model are compared. There are only minor similarities, such as the peak near 20 kHz. The strong peak at 7.5 kHz in Figure 2.19a cannot be explained by cavity resonance in the transducer mounts, and must be due to disturbances propagating from the moving piston in the driver section of the shock tube. This disturbance is typically increased in magnitude at low-enthalpy conditions. It is not clear at what frequency one should look for the same disturbance in the spectrum for static pressure on the

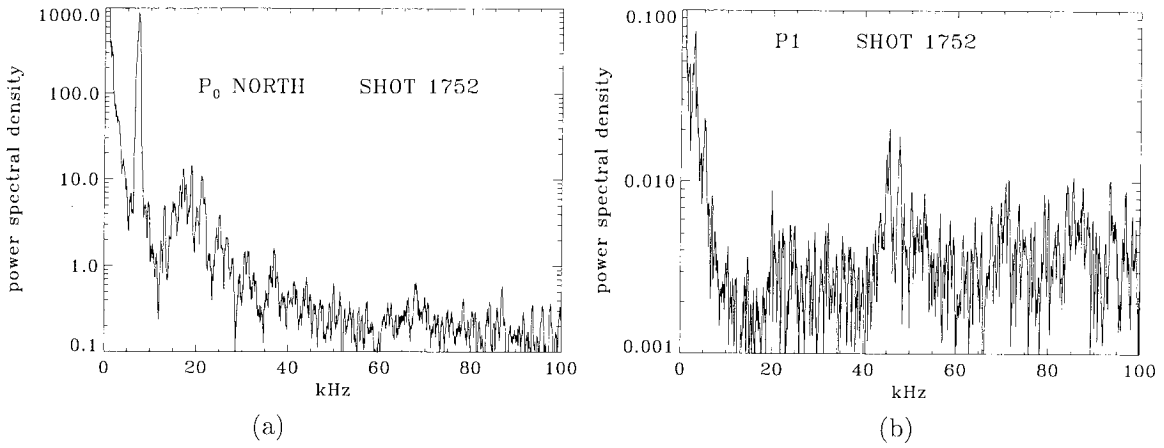

Figure 2.19: Comparison of power spectral density distributions on shot 1752 (condition A1, $A_e/A_* = 100$, $\theta_1 = 30°$, $\theta_w = 25°$); (a) nozzle reservoir pressure, (b) pressure on test model. For clarity, both spectra are smoothed using $\simeq 400$ Hz boxcar average.

wedge. Two peaks near 45 kHz in Figure 2.19b are probably due to vibration of the model.

2.7.2 Limits to Test Time

The test time for the present experiments in T5 is effectively defined as the time during which there is steady, viscous flow of nitrogen on the model. This time is limited on the low end by the establishment of steady separated flow on the model, and on the high end by the arrival of a significant amount of driver gas from the CT at the model. The existence of any test time at all is an issue for high-enthalpy conditions C1-C4. The lower and upper limits are considered separately below. In summary, all conditions except C4 are expected to have sufficient test time between establishment and contamination, during which flow visualization was performed. Condition C4 is suspected of significant contamination at an early time prior to flow visualization. Recall that all absolute values for time are given with respect to the time of the pressure rise in the nozzle reservoir.

2.7.2.1 Flow Establishment

Steady separated flow on a double wedge in shock tunnel flow is established only after several processes have completed. First, the nozzle starting flow takes some finite time to reach a steady state. Then a boundary layer must develop on the model. Finally, a separated region appears at the corner and grows in size until reaching an equilibrium state. In reality, these processes will overlap to some extent, but a conservative estimate of establishment time is obtained by summing the times required for each process separately. Such an estimate is made in Table 2.3 for each part of the establishment process by considering the maximum observed values over the experiments at low-enthalpy (A1–B3) and high-enthalpy (C1–C4) conditions. The times required for propagation of the leading shock wave from the nozzle reservoir to the test model, for passage of the nozzle

starting shock system, and for passage of the unsteady upstream-facing expansion were estimated from heat flux time histories, an example of which is shown in Figure 2.20. (Pressure time histories were not useful for this exercise because initial response of the recessed cavity obscures evidence of the external starting flow.) Davies and Bernstein (1969) showed that the time required to establish steady boundary-layer flow on a flat plate behind a shock wave is given by $3.33L/u$, where L is the plate length and u is the external flow speed. Here we take $L = 15$ cm, the full chord length of the model, and $u = u_1$, the post-shock velocity on the first wedge. The latter depends strongly on θ_1 and h_0, but only weakly on A_e/A_*. The lowest values of u_1 are used in Table 2.3 to assure a conservative estimate of the development time. Evidence of the boundary-layer establishment process can be seen in Figure 2.20.

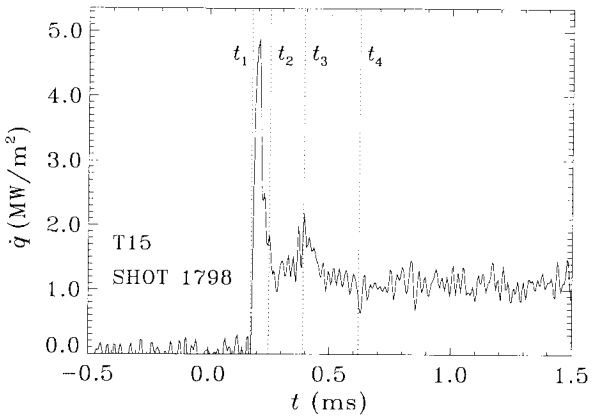

Figure 2.20: Heat flux time history showing the flow starting process on shot 1798 (condition B1, $A_e/A_* = 100$, $\theta_1 = 30°$, $\theta_w = 0°$). Times t_1–t_4 are defined in Table 2.3. Signal processed using a filter cutoff at $f_c = 50$ kHz.

		low h_0	high h_0
propagation delay for leading shock	t_1	260 μs	180 μs
passage of starting shock system	$t_2 - t_1$	50 μs	30 μs
passage of unsteady upstream-facing expansion	$t_3 - t_2$	200 μs	150 μs
development of boundary layer (Davies & Bernstein)	$t_4 - t_3 = 3.33L/u_1$	240 μs	130 μs
establishment of separation (Holden)	$t_{est} - t_4 = L_{sep}/a_w$	170 μs	170 μs
establishment of separation (Hung & MacCormack)	$t_{est} - t_3 = 7L/u_1$	520 μs	280 μs
total establishment time (Holden)	t_{est}	920 μs	660 μs
total establishment time (Hung & MacCormack)	t_{est}	1030 μs	640 μs

Table 2.3: Estimates for the maximum time required to establish steady separated flow at low- and high-enthalpy conditions in the present experiments. L is taken as the full chord length, 15 cm.

Holden (1971b) found by experiment that the time to establish separated flow is well correlated by L_{sep}/a_w, where a_w is the speed of sound at the wall. Physically, this corresponds to propagation of an acoustic disturbance forward from reattachment. In Table 2.3, the largest observed values of L_{sep} are used and a_w is computed based on the composition α_1 near separation. A different criterion for establishment time was suggested by Hung and MacCormack (1976) based on a computational study. They noted that the time for numerical convergence of a separated flow solution was approximately $7L/u$, which includes the time to develop a boundary layer. Mallinson *et al.* (1997a)

found slightly better agreement with their experiments using the latter result. The maximum time for establishment of separated flow, t_{est}, is estimated in Table 2.3 using both the Holden criterion and the Hung and MacCormack criterion. In either case, establishment is predicted to occur well before the time of interest; flow visualization is typically performed at 850 μs for high-enthalpy conditions and 1250–1700 μs for low-enthalpy conditions. Verification of the predictions in the present experiments is difficult due to unsteady motions of the separation and reattachment locations apart from the establishment process (*cf.* Section 2.7.4).

2.7.2.2 Driver-Gas Contamination

Significant contamination of the test section flow by helium and argon driver gases can occur at a time earlier than expected by assuming only drainage of the test gas through the nozzle. The phenomenon has been shown (Mark, 1958) to arise from interaction between the reflected shock and the shock tube boundary layer; the reflected shock bifurcates near the wall, and upon interaction with the driver-driven gas interface, causes jetting of driver gas near the wall ahead of the interface. A simple model of this process due to Davies and Wilson (1969) has shown good agreement with experimental results for the onset of contamination in T5 under nominally tailored interface conditions (Sudani and Hornung, 1998). The model assumes perfect gases and uses measured values for speeds and pressure ratios of the incident and reflected shocks. Results of the model for the present nominal operating conditions are given in Table 2.4, where the time t_{dgc} should correspond to less than 5% contamination by driver gas, assuming a tailored interface.

condition	A1/A2/A3	B1/B2	B3	C1/C3	C2	C4
t_{dgc} (μs)	> 2300	~ 1800	~ 1700	~ 1100	~ 950	~ 840

Table 2.4: Estimates based on the Davies and Wilson (1969) model for the time t_{dgc} of onset of driver gas contamination, including the propagation delay time between reservoir and test model.

A tailored interface condition means that when the reflected shock interacts with the interface, no waves are reflected back towards the end wall. Slightly off-tailored conditions are common in operation of a shock tunnel. In the undertailored case, an expansion wave reflects back towards the end wall because the acoustic impedance decreases and the shock speed increases across the interface. In the overtailored case, compressive waves are reflected from the interface. Evidence for the tailoring condition of a given shot can be found in the time history of the nozzle reservoir pressure, a drop in pressure corresponding to an undertailored interface and a rise in pressure corresponding to an overtailored interface. Two examples are shown in Figure 2.21. The tailoring condition has been shown to effect the time at which driver gas contamination occurs in T5 for medium-enthalpy ($h_0 \simeq 14$ MJ/kg) and high-enthalpy ($h_0 \simeq 20$ MJ/kg) conditions (Sudani and Hornung, 1997; Sudani *et al.*, 1998). In both cases, the onset of 12.5% driver-gas contamination was delayed (450 μs at

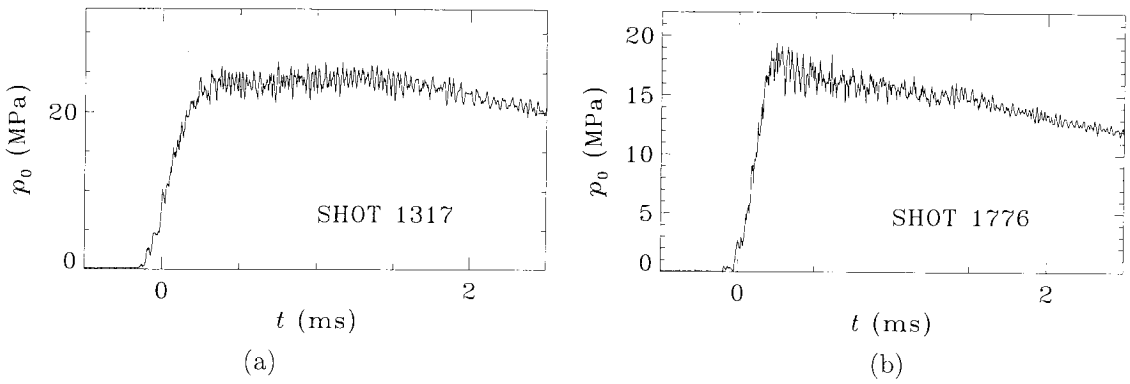

Figure 2.21: Effect of interface tailoring on reservoir pressure signal; (a) slightly overtailored (condition C4), (b) slightly undertailored (condition C2).

medium h_0 and 100 μs at high h_0) by slight undertailoring, and advanced (almost 1000 μs at both enthalpy levels) by slight overtailoring. At low enthalpy ($h_0 \simeq 8$ MJ/kg), tailoring had very little effect on the arrival time of driver gas (Sudani *et al.*, 1998). The tailoring condition was ascertained for each shot in the present study from p_0 signals and is given in Appendix D.

With flow visualization typically performed at $t_{las} = 850$ μs for high-enthalpy conditions, we see in Table 2.4 that condition C4 is expected to be marginally contaminated even with a tailored interface. In fact, condition C4, used exclusively during the first experimental campaign, consistently suffered from slight overtailoring as shown in Figure 2.21a, and is therefore suspected of being highly contaminated ($> 15\%$ driver gas). During the second campaign, attempts were made to develop a consistently undertailored version of this condition with $h_0 \simeq 28$ MJ/kg by increasing the driver compression ratio and using the light piston. A slightly undertailored condition was attainable, but not repeatable. Thus we reverted to condition C2 at lower enthalpy ($h_0 \simeq 24$ MJ/kg) with repeatable slight undertailoring; a typical p_0 signal is shown in Figure 2.21b. With the delay due to slight undertailoring, condition C2 is expected to have driver gas contamination of no more than a few percent until $t_{dgc} > 1000$ μs, plenty of test time for measurements to be taken after establishment of separated flow. The only other condition which may be marginal is condition B1, for which flow visualization was typically performed at $t_{las} = 1700$ μs, and which often had a slightly overtailored interface. Based on the results of Sudani *et al.* (1998) for $h_0 \simeq 8$ MJ/kg, condition B1 is expected to be less than 5% contaminated at 1700 μs.

2.7.3 Shock–Shock Interaction

Interaction between the leading-edge shock and the reattachment shock on a double wedge can lead to several different flow configurations, depending on the strength of the shocks. Based on computational results, Olejniczak *et al.* (1997) have identified five different configurations, four of these analogous to the Edney (1968) classification types I, IV, V, and VI for shock impingement on

the bow shock of a blunt body (see also Olejniczak and Candler, 1996). Viscous flow complicates matters by introducing a weak shock from separation and by moving the reattachment shock origin downstream, but the analogy still holds in many cases. The most common case in the present experiments is of type VI, in which the flow field remains entirely supersonic, and an expansion fan emanates from the intersection point towards the flap (see, for example, the interferogram for shot 1305 in Appendix F). At higher flap deflection, the second wedge angle with respect to the free stream ($\theta_w + \theta_1$) may require a detached shock, resulting in a strong shock–shock interaction.

An example of the strong shock–shock interaction commonly observed for a number of shots in the present work is shown in Figure 2.22. According to the results of Olejniczak *et al.* (1997), a type VI interaction transitions to a type V interaction as θ_w is increased. The interaction in Figure 2.22, however, does not appear to fit the type V classification which includes three triple points, nor does it correspond to a type IV interaction which occurs only for inviscid flow with Mach reflection off the first wedge. Only two triple points are obvious in Figure 2.22, the lower one on the oblique shock from reattachment and the upper one on the leading-edge shock with a nearly normal shock above it. Between the triple points is an oblique shock which produces a supersonic jet directed towards the flap wall. Instead of being bounded on both sides by subsonic flow as in the blunt body type IV configuration, here the jet is is bounded on its lower side by the supersonic flow downstream of the reattachment shock. The two supersonic streams stagnate together on the wall, then reexpand downstream to form a supersonic jet along the wall, bounded by the shear layer

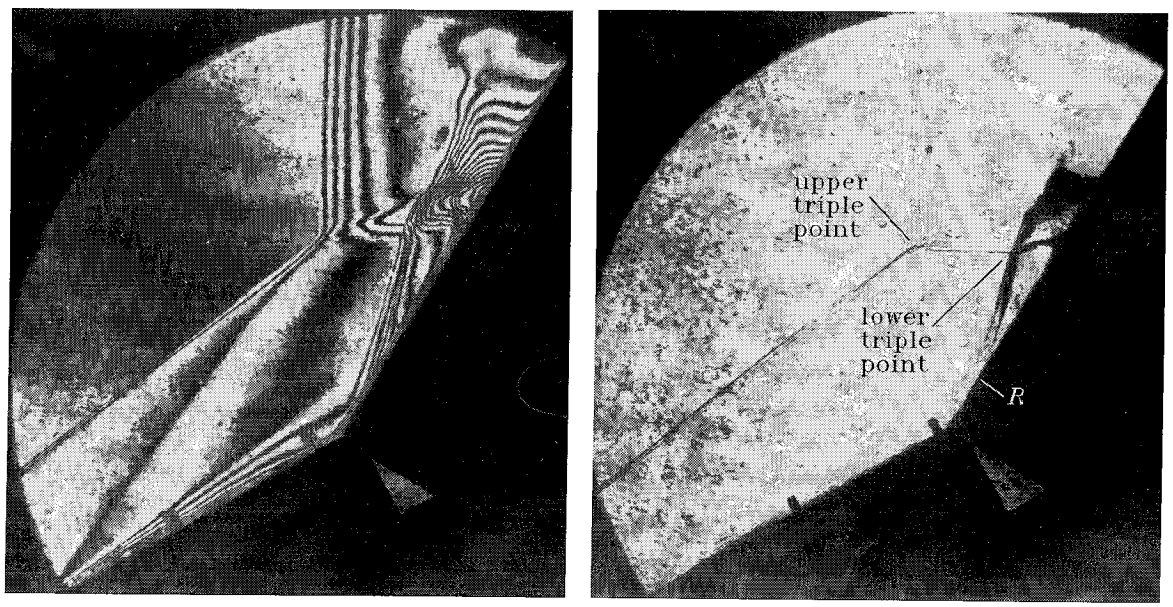

(a) (b)

Figure 2.22: Example of strong shock–shock interaction on a double wedge; (a) holographic interferogram (shot 1306), (b) holographic shadowgraph (shot 1288) at nominally the same condition (C4, $A_e/A_* = 225$, $\theta_1 = 30°$, $\theta_w = 30°$).

which originated at the upper triple point. Very high heat transfer and pressure have been observed in the jet stagnation region. Both a shadowgraph and an interferogram of the same nominal flow field are shown in Figure 2.22 to aid interpretation. An interaction fitting the type V classification is evident in shots 1750-1752 (see interferograms in Appendix F), where the lower triple point becomes two triple points with a normal shock between them. The subsonic region behind this normal shock keeps the upper supersonic jet away from the wall.

The existence of a strong shock shock interaction does not hinder measurements regarding separation and reattachment as long as the interaction only influences the flow downstream of the reattachment region. Clearly, this is the case for the condition in Figure 2.22, where the supersonic reattachment flow remains unaffected by the interaction until it encounters the reflected shock from the lower triple point, far enough downstream of reattachment to avoid influencing the reattachment region. This is also the case for nearly all the experiments in which strong shock–shock interaction was observed. (A notable exception is shot 1299, see interferogram in Appendix F.) Such interactions can, however, obscure measurements of the peak reattachment heating. They may also introduce additional flow unsteadiness due to, for example, shear-layer instabilities feeding disturbances through the subsonic region to the upper bow shock, causing oscillations in the upper triple point and hence in the lower triple point. Experimental evidence is given below in Section 2.7.4 for upstream movement of the interaction shock system during the test time of interest, after establishment of a steady separation region. There is also computational evidence for this motion, discussed in Section 3.3.

2.7.4 Unsteadiness

Compared to the flow one can attain in a continuous wind tunnel or even in most short-duration cold hypersonic facilities, the flow in T5 is inherently unsteady. Even during the short period between flow establishment and the onset of contamination (*cf.* Section 2.7.2), unsteady disturbances from the shock tube propagate to the test model. The nozzle reservoir region can be highly nonuniform (see, for example, the computations by Chue and Itoh, 1996). Further unsteady phenomenon can arise from instabilities of a boundary layer or separated shear layer in the flow over a test model. Thus when analyzing the present experiments, an implicit assumption is made that as long as variations in the flow properties are relatively small compared to their mean values over some "steady period" about the time of interest, then the mean flow closely resembles a truly steady flow of the same mean flow properties.

The time-resolved heat flux measurements often show evidence of large-scale unsteadiness. Two examples from the separated-flow region are given in Figure 2.23 (see Figure 2.4 for the TC port locations T9-T18). Considering first the low-enthalpy case in Figure 2.23a, we see that during the separated-flow establishment process, the drop in heat flux characteristic of laminar separation moves

upstream quickly at first, but then rather slowly from T13 to T11. Well after the separated region is expected to be fully established, the separation point appears to approach T10, then reverse direction and move downstream of T11 for a very brief time. Such motion is presumably not connected with establishment but with other mechanisms for unsteady flow. Because the magnitude of the motion is fairly small relative to the overall size of the separation region (TC ports are spaced approximately 4.5 mm apart), measurements taken at the time of flow visualization are assumed indicative, within measurement error bounds, of the corresponding steady flow field. For the high-enthalpy condition in Figure 2.23b, separation again moves at first quickly upstream, then more slowly as it approaches a position between T12 and T13 corresponding to established flow. Note that steady flow near the hingeline takes almost as long to establish as flow near separation. The forward motion of separation at much later times ($t > 2$ ms) is likely due to the arrival of large amounts of driver gas. The heat flux signal at T15 in Figure 2.23a shows significant unsteady features of unknown origin. This type of low frequency noise is more generally observed in flows with a transitional shear layer. Disturbances anywhere at reattachment or in the separated shear layer can propagate throughout the subsonic recirculating region. The heat flux upstream of separation at port T9 appears very steady.

Another example of large-scale unsteady flow is shown in Figure 2.24 which gives heat flux time histories for TC's along the ramp downstream of reattachment during a shot with strong shock-shock interaction (*cf.* Section 2.7.3). A rise in heat flux, associated with the reflected shock from the lower triple point and the jet impingement stagnation region immediately downstream of it, moves upstream during the shot. The same behavior is evident in the pressure time histories measured on the flap, in Figure 2.25. It is not clear whether this motion is due to inherent unsteadiness of the shock shock interaction or to an unusually long time scale for establishment of the interaction flow pattern. In either case, it does not affect the reattachment region during the time of interest (TC port T19 is downstream of reattachment).

Much of the higher frequency unsteadiness seen in Figures 2.23 and 2.24 represents electrical noise (which is amplified by the deconvolution process), and not any feature of the flow. Where the boundary layer is turbulent, one might expect to see some evidence of this in the high-frequency component of the signal (as seen, for example, by Simeonides and Haase, 1995). Unfortunately, the frequency corresponding to convection of large scale structures in the boundary layer is at least 300 kHz for even the lowest-velocity conditions, and the present measurements cannot discern frequencies higher than 100 kHz. While there may occur fluctuations at measurable frequencies, these are difficult to separate from electrical noise. Attempts to classify the boundary-layer state by analysis of thermocouple signal spectra for the present experiments failed to produce results consistent with other more credible criteria (such as comparing measured heat flux to laminar and turbulent predictions, *cf.* Section 4.1.3).

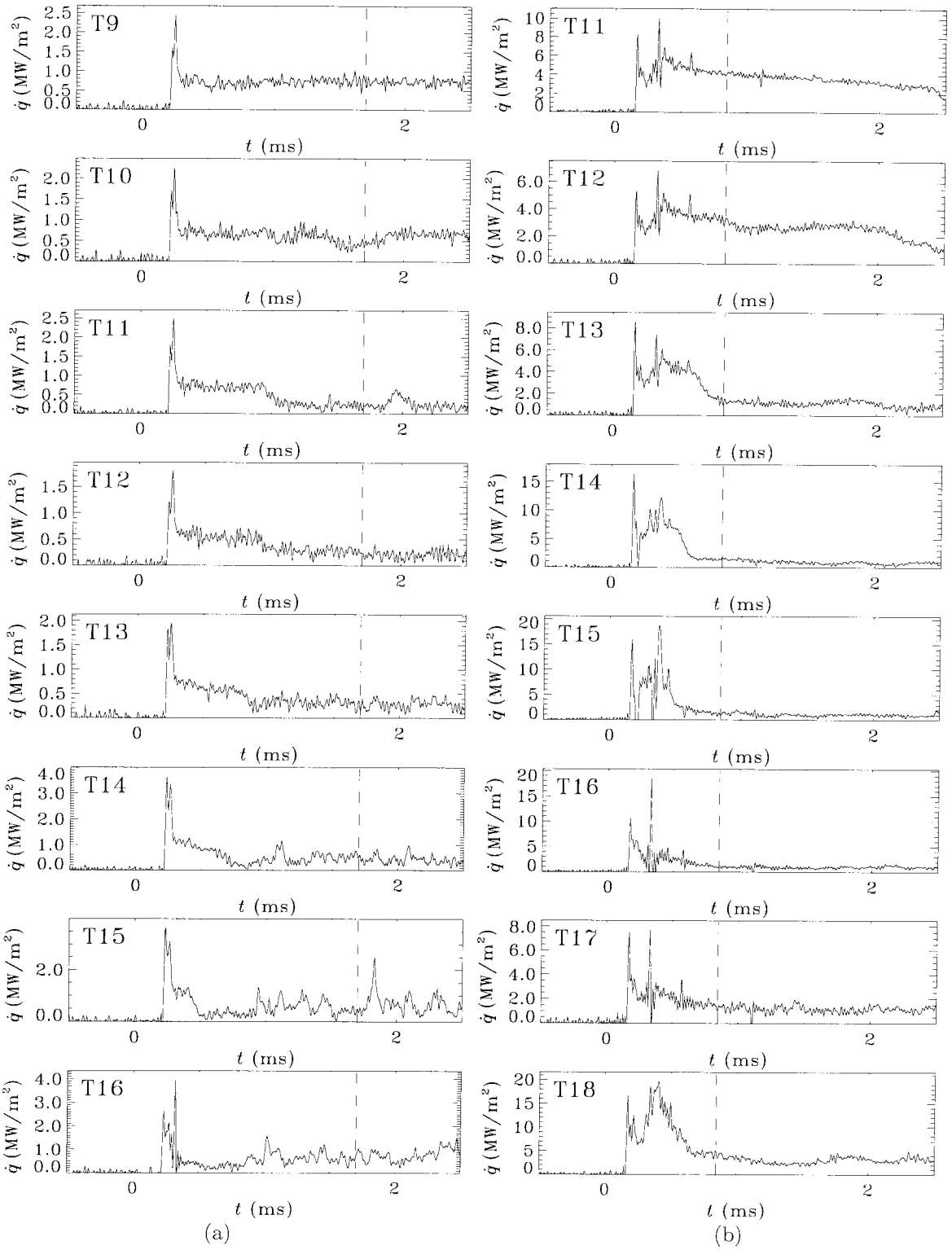

Figure 2.23: Heat flux time histories showing upstream movement of separation; (a) shot 1787 (condition B1, $A_e/A_* = 225$, $\theta_1 = 40°$, $\theta_w = 20°$), (b) shot 1788 (condition C2, $A_e/A_* = 400$, $\theta_1 = 40°$, $\theta_w = 20°$). Flow visualization was performed at time indicated by dashed line. Signals processed using filter cutoff at $f_c = 50$ kHz.

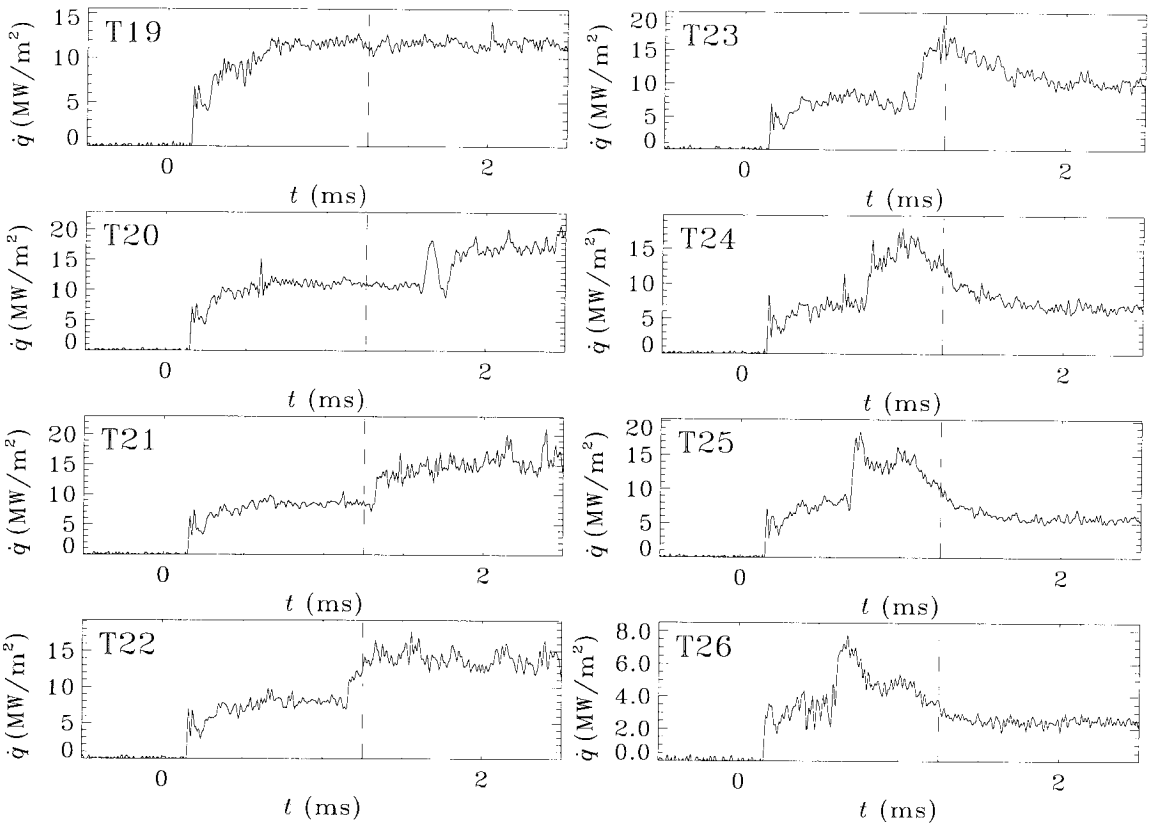

Figure 2.24: Heat flux time histories showing upstream movement of jet impingement from strong shock–shock interaction on shot 1290 (condition B2, $A_e/A_* = 225$, $\theta_1 = 35°$, $\theta_w = 20°$). Dashed line and f_c as in Figure 2.23.

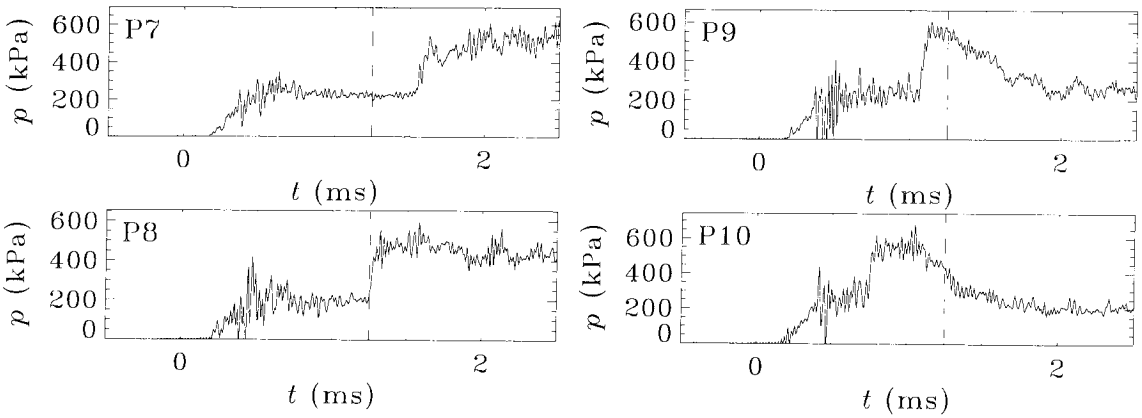

Figure 2.25: Pressure time histories showing upstream movement of jet impingement from strong shock–shock interaction on shot 1290 (condition B2, $A_e/A_* = 225$, $\theta_1 = 35°$, $\theta_w = 20°$). Dashed line and f_c as in Figure 2.23.

2.7.5 Three-Dimensionality

Flow on the double wedge in the present experiments is essentially three-dimensional; the axisymmetric free stream is conically diverging and the finite model span causes end effects. Analysis and computations, however, must rely on the assumption of two-dimensional flow to obtain results with reasonable effort. Ideally, this would require that the flow field within a vertical plane near the centerline of the model closely resembles a purely two-dimensional flow field, where the free-stream variation within a vertical streamwise plane remains independent of spanwise location. The experiments cannot attain this ideal, but do offer a reasonable approximation that allows two-dimensional analysis to illuminate important results in the data relevant to the physics of the problem.

Neglecting, for the moment, three-dimensionality of the incoming free stream, finite span effects are expected to reduce the size of separation due to end spillage. In previous studies, the common methods for minimizing these end effects were to either add fences to the sides of the model, or increase the span of the model until the centerline flow became independent of aspect ratio. The addition of side fences to models of low aspect ratio invariably increases the separation length (Chanetz and Coët, 1993; Holden, 1971a; Johnson, 1968; Miller *et al.*, 1964), which is consistent with the idea that they prevent spillage. Kornilov (1997), however, found with shock-impingement experiments in a variable-width channel that sidewalls cause significant increase in separation length for a span $b \lesssim 85\delta$, where δ is the thickness an undisturbed boundary layer would have at the hingeline. This behavior probably influences results for hypersonic flat plate studies with side fences and aspect ratio $AR < 1$ (for example, see Chanetz and Coët, 1993 or Johnson, 1968), particularly because the boundary layer is not very thin relative to the span under these conditions. Note that AR is defined here as the full aspect ratio of the model, not just the portion upstream of the hingeline. In fact, Hankey and Holden (1975) found that adding side fences to the narrowest configuration ($AR = 0.5$) increased separation length beyond the nominally two-dimensional value found at the widest configuration ($AR = 1$). Lewis *et al.* (1968) found that side fences had negligible effect for $AR \geq 1$.

Hence we might expect $AR \geq 1$ to be a good criterion for necessary span to obtain two-dimensional centerline flow without fences. But Holden (1971a) reports no significant changes going from $AR = 0.75$ to $AR = 1$, and Miller *et al.* (1964) similarly going from $AR = 0.6$ to $AR = 1$. Again, as found by Kornilov (1997) with side walls, the extent of end effects without side fences should depend on the ratio b/δ, not AR. Ball (1971) studied a large-span flat plate with a finite-span trailing flap and found that three-dimensionality as evidenced in the separation length encroached only a distance of $10\delta_1$ from the sides of the flap, where δ_1 is the boundary-layer thickness at separation. The double-wedge test model used in the present experiments has an aspect ratio of 1.33 and typically a very thin boundary layer (for $\theta_1 > 0°$) with b/δ_1 on the order of 100–200. Therefore, at least under uniform two-dimensional free-stream conditions, this test model is expected to produce

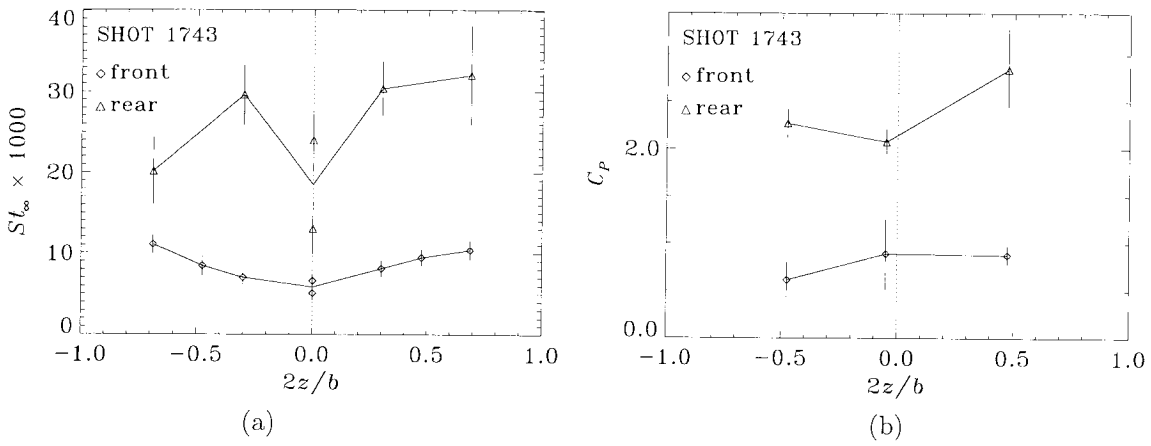

Figure 2.26: Example of spanwise distributions for shot 1743 (condition B1, $A_e/A_* = 400$, $\theta_1 = 30°$, $\theta_w = 20°$); (a) Stanton number, (b) pressure coefficient. Dotted line is model centerline, z is distance from centerline, Symbols are experimental measurements ($\diamond$ for the front plate, $\triangle$ for the rear plate), and solid lines are for visual aid. See Sections 2.5.3 and 2.6.3 for description of error bars.

two-dimensional flow at the centerline, and additional experiments with side fences or increased span were deemed unnecessary.

Another method for checking two-dimensionality is to measure spanwise distributions of pressure or heat flux on the model. Lewis *et al.* (1968) showed that uniform spanwise distributions were a necessary condition, but not a sufficient condition for two-dimensionality. Limited spanwise measurements were made in the present experiments, and an example is given in Figure 2.26. The chordwise position for these distributions is shown in Figure 2.4; they were generally upstream of separation and downstream of reattachment. The centerline thermocouples are offset in the streamwise direction from the outboard ones, so two centerline measurements, corresponding to the adjacent upstream and downstream TC's, are included in each distribution of Figure 2.26a. The slight increase in Stanton number away from the centerline on the front plate is found rather consistently throughout the experiments. The pressure distribution, however, does not show consistent results; on some shots the outboard measurements are higher, on others they are lower or skewed. In the flap region, both heat flux and pressure measurements generally show increased scatter. Spanwise distributions for each shot are presented in Appendix F.

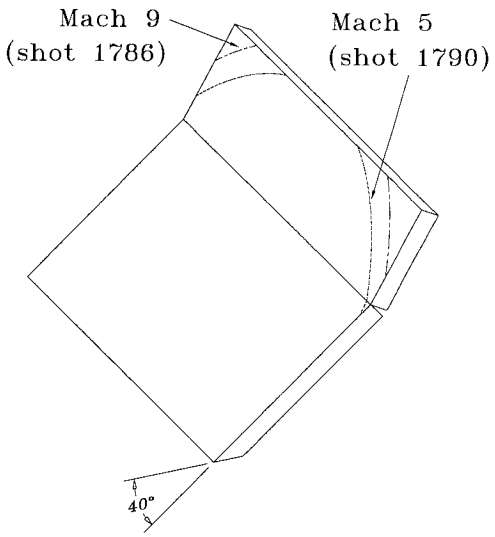

Figure 2.27: Intersection between test model and leading expansion from the nozzle exit, for the worst case configuration ($\theta_1 = 40°$, $\theta_w = 20°$) at two extremes of Mach number.

Though the model span seems sufficient to produce two-dimensional flow on the model centerline for a two-dimensional incoming free stream, the actual free stream is three-dimensional. One potential problem stems from end effects, due to the finite extent of the undisturbed flow core. This core consists of flow that has not been disturbed by the nozzle exit expansion, and its boundary can be estimated by considering a Mach cone emanating from the lip of the nozzle exit. Because the model span is relatively large compared to the nozzle exit diameter and the model is typically positioned entirely above the nozzle centerline, there are some configurations for which this Mach cone intersects the model. Accounting for the model position relative to the nozzle, the worst case of such an intersection is shown in Figure 2.27 for the available range in Mach number. The nozzle expansion is seen to impinge on the outboard edges of the flap under these conditions, only approaching the model centerline at the downstream edge of the flap, well downstream of reattachment. While this will certainly alter the model end effects in the flap region, it is not expected to affect two-dimensionality of flow at the model centerline.

A potentially more insidious three-dimensional aspect of the flow is the conically diverging free stream. The conical source point for the free-stream flow is approximately 1.25 m from the model leading edge, and therefore the local flow direction at the sides of the model is less than 5° from the nozzle centerline direction. We assume that this divergence has a very minor effect on the spanwise uniformity of the double-wedge flow field. The divergence does, however, produce significant axial gradients in the free stream; for example, ρ_∞ can drop 25% between the leading and trailing edges of the model. An experimental comparison was made between the conical and contoured nozzles to ascertain the effect these free-stream gradients have on the double-wedge flow. The contoured nozzle was designed to produce parallel uniform exit flow at a high-enthalpy, high-pressure condition

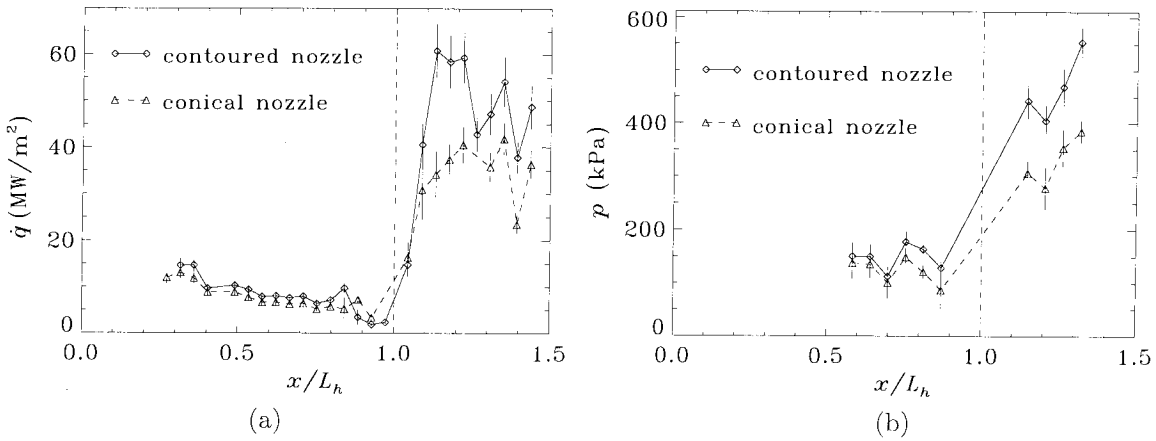

Figure 2.28: Comparison between conical and contoured nozzles at same nominal condition (C3, $A_e/A_* = 100$–conical/110–contoured, $\theta_1 = 15°$, $\theta_w = 5°$); (a) streamwise heat flux distribution, (b) streamwise pressure distribution. Symbols are experimental measurements; ◊ with the contoured nozzle, △ with the conical nozzle, and vertical dashed line is the hingeline. Connecting solid and dashed lines are visual aid only. See Sections 2.5.3 and 2.6.3 for description of error bars.

(condition C3 in Table 2.2). Results for streamwise distribution of heat flux and pressure are shown in Figure 2.28. The conical nozzle gives lower heat flux and pressure than the contoured nozzle, the difference increasing with streamwise distance from the leading edge and becoming more pronounced in the flap region. Thus the expanding free stream must be accounted for during analysis of the present experiments. As described in Section 3.2, it is accounted for approximately by assuming two-dimensional flow in a vertical streamwise plane through the nozzle axis, extracted from the three-dimensional expansion. Spanwise distributions of measurements also show lower values for the conical nozzle, but no difference in shape between the two nozzles. In fact, the contoured nozzle result also shows the characteristic increase in heat flux away from the centerline, seen in Figure 2.26a, indicating that this nonuniformity is not connected to free-stream flow divergence.

An additional three-dimensional effect can occur in the reattaching boundary layer and may be responsible for the large scatter of heat flux measurements in the flap region (*cf.* Figure 2.26a). The concave boundary-layer curvature at reattachment can induce three-dimensional instabilities that take the form of streamwise vortices. Extensive evidence for such instabilities was found for supersonic separated flow by Ginoux (1965), who noted coherent spanwise variations in static pressure and heat flux corresponding to striations observed in sublimation patterns at reattachment, and pitot probe survey results consistent with the existence of counter-rotating pairs of streamwise vortices downstream of reattachment. In hypersonic flows, Coët and Chanetz (1993) found similar evidence using heat-sensitive paint and heat flux instrumentation, as did Henckels *et al.* (1993) using infrared thermography, oil flow techniques, and pitot probe surveys. Miller *et al.* (1964) observed striation in the scorch patterns at reattachment. The heat flux variations due to this phenomenon can reach 50% of the mean value (Coët and Chanetz, 1993).

Some indication of three-dimensional effects can be seen in the soot pattern left on the model after a shot. In a few cases, the location of reattachment was evident in this soot pattern, and as seen in Figure 2.29, it clearly moves upstream towards the hingeline near the sides of the model

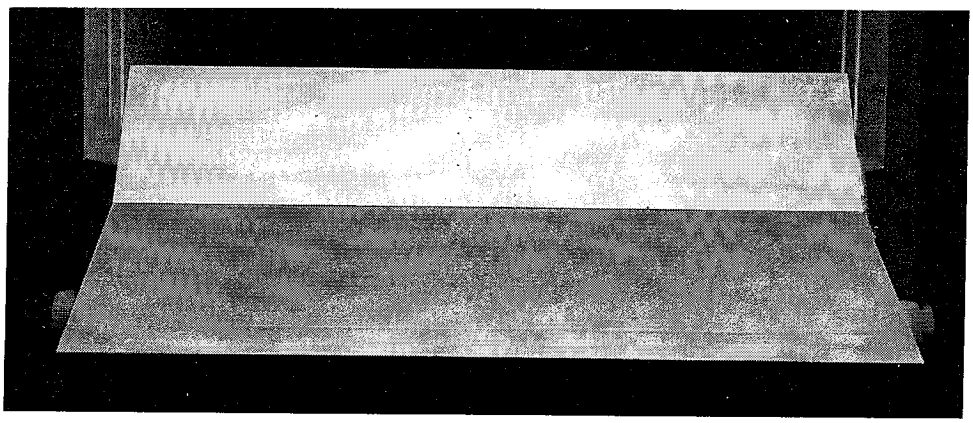

Figure 2.29: Post-shot photograph of soot pattern on model showing three-dimensional reattachment.

but remained constant over the middle of the model. A striation pattern at reattachment could also be observed in the soot pattern after some shots at large θ_w, suggesting the presence of three-dimensional instabilities. The separation line could not be discerned from the soot pattern, but it is interesting to note that soot on the front plate tended to collect more at the sides of the model near the hingeline and near the leading edge. Care must be taken in interpreting any such soot patterns because the tunnel run-down flow lasts much longer than the test flow of interest.

2.8 Summary

The experiments on a double-wedge test model configuration in the T5 hypervelocity shock tunnel described in this chapter allowed measurement of separation length and reattachment heating under both low- and high-enthalpy flow conditions. Flow visualization was used to measure separation length and coaxial surface thermocouples were used to measure heat flux at an array of locations on the model surface. In addition, pressure measurements were made at a limited number of locations using piezoelectric transducers. Many issues arise regarding the flow quality, and these have been addressed thoroughly in the present chapter. In particular, it was found reasonable to approximate flow near the center of the model as two-dimensional despite the generally three-dimensional nature of the flow field. Other important aspects of the flow cannot be measured and must be deduced from theoretical or computational methods; the presence of nonuniform flow due to a conical nozzle expansion and of thermochemical nonequilibrium in the nozzle and wedge flows necessitates the use of computational methods which are described in the next chapter. Some of the experimental heat flux and pressure measurements are used in Chapters 3 and 4 to partially validate computational methods and theoretical results, but consideration of the experimental measurements of separation length and peak heating is delayed until Chapter 6.

Chapter 3 Computational Methods

The present study makes heavy use of advanced computational techniques, because many flow parameters of interest cannot be measured experimentally, nor can they be predicted with reasonable accuracy by simple analysis (due to the nonuniform, nonequilibrium nature of the flow). The nozzle reservoir conditions, obtained as described in Section 2.3.1, serve as the basis for all further flow computations. For each shot in which the separation geometry is measured, a single computer code is used to compute both the viscous nozzle flow and the inviscid external flow on the test model. The latter is referred to as a triple-wedge computation; the experimentally measured separated region is replaced by a third wedge. Further calculations performed for some shots include viscous single-wedge computations to compare with heat flux measurements and viscous double-wedge computations for aiding interpretation of flow visualization. In addition, the same code is used to study flat-plate boundary layers in reacting flow. Section 3.1 describes the computational code, and Sections 3.2–3.6 describe each type of computation undertaken; nozzle-flow, inviscid triple-wedge, viscous and inviscid single-wedge, viscous double-wedge, and viscous flat-plate computations. Resolution and convergence issues are considered for the computations in Sections 3.3 and 3.6. Comparisons to experimental pressure and heat flux measurements are presented for the computations in each of Sections 3.2–3.5. These serve as our only means of testing the code for simulation of flow in T5.

3.1 Navier–Stokes Nonequilibrium Code

The computer code, obtained from Olejniczak (1997) and based on the work of Candler (1988), solves a finite-volume representation of the Reynolds-averaged Navier Stokes equations including thermochemical nonequilibrium. It is referred to in this document as the N–S code, even when discussing inviscid computations. The code is set up to simulate only two-dimensional (planar or axisymmetric) flows of nitrogen. Vibrational modes for internal energy of nitrogen molecules are considered separable from rotational modes and characterized by a vibrational temperature T_v, while rotational modes are assumed in equilibrium with translational modes. Electronic excitation and ionization are neglected. The code does not include models for turbulence and thus all viscous calculations are for laminar flow. The fundamental equations, transport and source term models, numerical method, and boundary conditions are each described briefly in Sections 3.1.1–3.1.4.

3.1.1 Fundamental Equations

The equations for unsteady nonequilibrium flow are written here in general differential form using standard index summing notation with $j = 1, 2$ referring to the x and y directions respectively. For each species s (in the present case, there are two, atomic and molecular nitrogen), the mass conservation equation is

$$\frac{\partial \rho_s}{\partial t} + \frac{\partial}{\partial x_j}(\rho_s u_j) = -\frac{\partial}{\partial x_j}(\rho_s v_{s_j}) + w_s \,, \tag{3.1}$$

where v_s are diffusion velocities, ρ_s are partial densities, and w_s are production rates from chemical reactions. The mass-averaged momentum conservation equations in the x and y directions ($i = 1, 2$) are given by

$$\frac{\partial}{\partial t}(\rho u_i) + \frac{\partial}{\partial x_j}(\rho u_i u_j) = -\frac{\partial p}{\partial x_i} - \frac{\partial \tau_{ij}}{\partial x_j} \,, \tag{3.2}$$

where τ_{ij} is the shear stress tensor and no external forces have been included. Conservation of vibrational energy for the single molecular species N_2 is written as

$$\frac{\partial}{\partial t}(\rho_{N_2} e_v) + \frac{\partial}{\partial x_j}(\rho_{N_2} e_v u_j) = -\frac{\partial}{\partial x_j}(\rho_{N_2} e_v v_{N_{2_j}}) - \frac{\partial \dot{q}_{v_j}}{\partial x_j} + Q_{T-V} + e_v w_{N_2} \,, \tag{3.3}$$

where e_v is the molecular vibrational energy per unit mass of N_2, $\dot{q}_{v_j}$ is the heat flux due to conduction of vibrational energy, and Q_{T-V} is a source term representing the transfer of energy from translational to vibrational modes. The last term in Equation 3.3 represents vibrational energy removed or added by dissociation or recombination (respectively) of N_2. Finally, there is an equation for conservation of the total internal energy e per unit mass of the gas mixture;

$$\frac{\partial}{\partial t}(\rho e) + \frac{\partial}{\partial x_j}(\rho e u_j) = -\frac{\partial}{\partial x_j}(p u_j) - \frac{\partial}{\partial x_j}(\tau_{ij} u_i) - \frac{\partial \dot{q}_j}{\partial x_j} - \frac{\partial \dot{q}_{v_j}}{\partial x_j} - \frac{\partial}{\partial x_j}\sum_s \rho_s h_s v_{s_j} \,. \tag{3.4}$$

Note that $\dot{q}_j$ is the heat flux due to conduction of translational and rotational energy, and the species enthalpy includes formation enthalpy, vibrational energy, and rotational energy;

$$h_s = h_s^\circ + e_{tr_s} + p_s/\rho_s + e_{v_s} + e_{r_s} \,. \tag{3.5}$$

Thus the last term in Equation 3.4 represents heat flux due to mass diffusion of internal and chemical energies.

In addition to the above conservation equations, we require equations of state relating the conserved quantities (mass, momentum, vibrational and total energies) to nonconserved quantities (pressure, vibrational and translational temperatures). The pressure depends on translational temperature according to a mixture of ideal gases,

$$p = \sum_s \rho_s R_s T \,, \tag{3.6}$$

where R_s is the gas constant for each species. Though the code has options for more detailed theoretical models, for the present work we rely on the simple harmonic oscillator model to relate the vibrational temperature T_v to the energy e_v of the N_2 molecules;

$$e_v = \frac{R_{N_2}\theta_v}{\exp\left(\theta_v/T_v\right) - 1} \,, \tag{3.7}$$

where $\theta_v = 3393$ K is the characteristic temperature for vibration of N_2. Then e_v is related to the translational–rotational temperature T by subtracting the vibrational, kinetic, and chemical energies from the total energy;

$$\sum_s \rho_s c_{v_s} T = \rho e - \frac{1}{2}\rho u_j u_j - \rho_{N_2} e_v - \rho_N h_N^\circ \,, \tag{3.8}$$

where c_{v_s} are specific heat capacities at constant volume for translational and rotational internal energy modes. Note that $h_{N_2}^\circ = 0$ J/kg and $h_N^\circ = 33.6216$ MJ/kg.

The shear-stress tensor is given by

$$\tau_{ij} = -\mu\left(\frac{\partial u_i}{\partial x_j} + \frac{\partial u_j}{\partial x_i}\right) + \frac{2}{3}\mu\frac{\partial u_k}{\partial x_k}\delta_{ij} \,, \tag{3.9}$$

where μ is the mixture viscosity and δ_{ij} is the Kronecker delta. Under the dilute-gas assumption, bulk viscosity is neglected. The conduction heat flux terms are defined by Fourier's Law,

$$\dot{q}_j = -k\frac{\partial T}{\partial x_j} \qquad \text{and} \qquad \dot{q}_{v_j} = -k_v\frac{\partial T_v}{\partial x_j} \,, \tag{3.10}$$

and the diffusion velocities are assumed to follow a simplified version of the model given by Bartlett *et al.* (1968);

$$\rho_s v_{s_j} = -\frac{\rho D_{11_{N_2}}\bar{\mu}_2}{\mathcal{M}_{mix}\bar{\mu}_1}\left(\frac{\partial Z_s}{\partial x_j}\right) \,, \tag{3.11}$$

where

$$Z_s = \frac{\rho_s/F_s}{\sum_r \rho_r/F_r} \,, \qquad \bar{\mu}_1 = \sum_s X_s F_s \,, \qquad \text{and} \qquad \bar{\mu}_2 = \mathcal{M}_{mix}\sum_s \frac{Y_s}{F_s} \,, \tag{3.12}$$

$\mathcal{M}_{mix}$ is the molecular weight of the gas mixture, Y_s are mass fractions, X_s are mole fractions, $D_{11_{N_2}}$ is the self-diffusion coefficient for molecular nitrogen, and the diffusion factors for nitrogen are given by $F_{N_2} = 1$ and $F_N = 0.625$. Note that the binary diffusion coefficient is defined here as $D_{12} = D_{11_{N_2}}/F_{N_2}F_N$, and if both diffusion factors were unity, Equation 3.11 would reduce to Fick's Law for a binary gas mixture, $\rho_s v_{s_j} = -\rho D_{12}(\partial Y_s/\partial x_j)$.

3.1.2 Transport and Source Term Models

To close the conservation, state, and flux equations given in the previous section, we need appropriate models to evaluate the transport coefficients μ, k, k_v, and $D_{11_{N_2}}$ as well as the source terms w_s and Q_{T-V}. The validity and limitations of these models are discussed by Olejniczak (1997).

The mixture viscosity and translational–rotational conductivity are computed using a complex mixing rule given by Gupta *et al.* (1990) based on curve fits to collision cross-sections of the different interaction pairs (N_2–N_2, N_2–N, N–N). The necessary equations, too lengthy to reproduce here, can also be found in the thesis by Olejniczak (1997). The vibrational thermal conductivity of N_2 is given by

$$k_v = \rho_{N_2} D_{11_{N_2}} c_{v_v} , \tag{3.13}$$

where the specific heat for vibrational modes is defined by use of Equation 3.7;

$$c_{v_v} = \frac{\partial e_v}{\partial T_v} = R_{N_2} \left(\frac{\theta_v}{T_v} \right)^2 \frac{e^{\theta_v/T_v}}{\left(e^{\theta_v/T_v} - 1 \right)^2} . \tag{3.14}$$

The self-diffusion coefficient $D_{11_{N_2}}$ is found from kinetic theory, again using the curve fits of Gupta *et al.* (1990) for the N_2–N_2 collision cross section. Note that for inviscid computations using the N–S code, the transport coefficients μ, k, k_v, and D_{12} are effectively all set to zero.

The vibrational relaxation process, describing the exchange of energy between translational and vibrational modes, is assumed to be given by the Landau–Teller formulation,

$$Q_{T-V} = \rho_{N_2} \frac{e_v^*(T) - e_v}{\tau_v} , \tag{3.15}$$

where e_v^* is the vibrational energy, Equation 3.7, evaluated at the translational–rotational temperature instead of the vibrational temperature, and τ_v is a characteristic vibrational relaxation time. The latter is computed as the molar average of the relaxation times for each collision partner,

$$\tau_v = \frac{\sum_s X_s}{\sum_s X_s / \tau_{v_s}} . \tag{3.16}$$

The vibrational relaxation time for each collision partner s is given by the semi-empirical result of Millikan and White (1963),

$$\tau_{v_s} = \frac{1}{p} \exp \left[0.00116 \bar{\mu}_s^{1/2} \theta_v^{4/3} \left(T^{-1/3} - 0.015 \bar{\mu}_s^{1/4} \right) - 18.42 \right] , \tag{3.17}$$

where the pressure p is in atm and $\bar{\mu}_s = \mathcal{M}_s \mathcal{M}_{N_2} / \left(\mathcal{M}_s + \mathcal{M}_{N_2} \right)$ is the reduced mass for each pairing. The mass source terms w_s arise from dissociation and recombination of nitrogen, *i.e.* the chemical reaction

$$\mathrm{N_2 + M} \rightleftarrows \mathrm{2N + M}, \tag{3.18}$$

where the third body M is either N or N_2. The forward (dissociation) and backward (recombination) reaction rates are k_f and k_b respectively, and are different for each third body m. The source terms are then given by

$$w_{\mathrm{N}} = -w_{\mathrm{N_2}} = \mathcal{M}_{\mathrm{N_2}} \sum_m \left[k_{f_m} \frac{\rho_m}{\mathcal{M}_m} \frac{\rho_{\mathrm{N_2}}}{\mathcal{M}_{\mathrm{N_2}}} \right] - \mathcal{M}_{\mathrm{N_2}} \sum_m \left[k_{b_m} \frac{\rho_m}{\mathcal{M}_m} \left(\frac{\rho_{\mathrm{N}}}{\mathcal{M}_{\mathrm{N}}} \right)^2 \right]. \tag{3.19}$$

The forward rates are assumed to adhere to an Arrhenius form with a modified temperature according to the vibration–dissociation coupling model of Park (1988a),

$$k_{f_m} = c_{f_m} \left(\sqrt{T T_v} \right)^{\eta_m} \exp\left(-\theta_{d_m} / \sqrt{T T_v} \right), \tag{3.20}$$

where the constants c_f, η, and θ_d from Park (1988b) are reproduced in Table 3.1. The backward reaction rates are then evaluated for each reaction using a definition of the equilibrium constant K_{eq},

$$k_{b_m} = \frac{k_{f_m}(T)}{K_{eq}(T)}, \tag{3.21}$$

where k_f and K_{eq} have been evaluated at the translational temperature T because there is no dependency of recombination on vibrational excitation. K_{eq} is obtained from a seven-parameter curve fit to the high-temperature Gibbs free-energy data of Gupta *et al.* (1990) (see Olejniczak, 1997). Note that for frozen-flow computations using the N–S code, the source terms w_s and Q_{T-V} are effectively set to zero so that chemical composition and vibrational excitation remain constant throughout the flow field. It should also be emphasized that the thermochemical model described here has unknown accuracy, and is not adequately tested by the few comparisons between computation and experiment in Sections 3.2–3.5.

third body m	c_f $\mathrm{m^3/(kgmol{\cdot}s)}$	η	θ_d K
N	3.0×10^{19}	-1.6	113200
N_2	7.0×10^{18}	-1.6	113200

Table 3.1: Constants in Equation 3.20 for forward (dissociation) reaction rates, from Park (1988b).

3.1.3 Numerical Method

The fundamental equations given in Section 3.1.1 can be written in a general, vectorized conservation form as

$$\frac{\partial \vec{U}}{\partial t} + \frac{\partial \vec{F}}{\partial x} + \frac{\partial \vec{G}}{\partial y} = \vec{W}. \tag{3.22}$$

The vector of conserved quantities $\vec{U}$ is $[\rho_N,\ \rho_{N_2},\ \rho u,\ \rho v,\ e_v,\ e]$, where here u and v are the mass-averaged velocities in the x and y directions. $\vec{F}$ and $\vec{G}$ are the x-direction and y-direction fluxes, respectively, and $\vec{W}$ consists of the source terms. This equation set is solved in a finite-volume approximation on a body-fitted numerical grid with generally non-Cartesian coordinates ξ (the streamwise direction along the body) and η (the body-normal direction). The method employed to accomplish this is described in detail by Candler (1988). The technique uses upwind differencing with modified Steger–Warming flux splitting (MacCormack and Candler, 1989), a type-dependent method that captures shocks well but is modified in viscous shear regions to avoid excess numerical dissipation. From the resulting finite-volume representation, a steady-state solution is obtained by Gauss–Seidel line relaxation, a fully implicit iterative technique in which block-tridiagonal matrix inversion is applied to individual η-gridlines during backward and forward sweeps in the ξ-direction.

Note that this method is not time-accurate. A steady-state solution for a particular grid (*i.e.* an iteration-converged but not necessarily grid-converged solution) is assumed to be obtained when there are negligible changes in the solution during the previous 50 iterations. This required anywhere from 600 iterations and 4 hours for inviscid triple-wedge computations performed on an Intel Pentium machine, to more than 60000 iterations and 550 hours for one of the viscous double-wedge computations performed on a CRAY J-90 supercomputer.

3.1.4 Boundary Conditions

Each boundary of the grid can be handled in one of several different ways. At a supersonic inflow boundary, the variables are simply held fixed at their initial values corresponding to the free-stream or inlet flow. Zero-gradient extrapolation is applied to the outflow boundary, which is arranged always to be supersonic (except inside a boundary layer). Boundaries at an inviscid wall or at a line of symmetry (*e.g.* the nozzle axis) both require the same conditions; zero normal pressure gradient and zero normal fluxes of mass, momentum, and energy.

For viscous computations, the conditions enforced at a wall boundary include zero normal pressure gradient, zero velocity (the no-slip condition), and specified constant wall temperature taken to be 300 K in the present study. The vibrational temperature is assumed in equilibrium with the wall temperature. The original code enforced a fully noncatalytic viscous wall boundary condition, or zero normal gradients of species concentrations ($|\partial Y_s/\partial\eta|_w = 0$). For the present work, an option was added to the N–S code to implement a fully catalytic viscous wall boundary condition wherein the gas is assumed to be completely recombined at the wall ($\alpha_w = 0$). If a viscous wall boundary intersects an inflow boundary, then an inviscid wall condition must be applied to the first few cells of the wall boundary in order to accurately compute the leading edge of the boundary layer. Application of these boundary conditions to particular grids is described for different types of computations in each of the following sections.

3.2 Nozzle Free-Stream Computations

Thermochemical nonequilibrium flow through the conical nozzle is computed using the N–S code for each experiment, based on the reservoir conditions estimated as described in Section 2.3.1. The displacement effect of the nozzle boundary layer on the nozzle centerline flow is approximately accounted for by assuming a laminar boundary layer, though the real nozzle boundary layer is expected to be transitional or turbulent. The results of these computations are used to initialize the various wedge computations. The method is identical to that used by Olejniczak (1997). The following sections discuss the computational grid and initialization (Section 3.2.1), present comparisons to experimental pitot pressure data (Section 3.2.2), and describe the use of nozzle-flow computations to initialize wedge-flow computations (Section 3.2.3).

3.2.1 Grid and Initialization

The numerical grid used for axisymmetric, viscous nozzle flow computations is shown in Figure 3.1. AB is the centerline (axis) of the nozzle and has a symmetry boundary condition, CD is the wall of the nozzle and has a viscous wall boundary condition, BC is located downstream of the test model and has a supersonic outflow condition, and DA is located just downstream of the nozzle throat minimum area and has a supersonic inflow boundary condition. Note that in order to obtain the conically diverging free-stream flow over the double-wedge model, it is necessary to artificially extend the nozzle beyond the actual location of the nozzle exit as indicated in Figure 3.1. Thus the computed results cannot account for any interference between the nozzle lip expansion and the flow about the model (*cf.* Section 2.7.5). The grid consists of 200 cells in the ξ-direction clustered at the inlet end and 100 cells in the η-direction clustered at the axis and at the wall. The clustering is obtained by exponential distribution of the cell spacing to match a specified minimum cell size. The cell distribution through the boundary layer is not adequate for accurate computation of wall fluxes, but we are only interested in the displacement effect of the boundary layer. The viscous wall boundary condition in this case is applied all the way to the leading edge of the grid; this is no worse than other approximations made in this region (see below), and the real flow has some finite boundary-layer thickness at this location in any case.

The equilibrium-flow option of the Supersonic Reacting Flow (SURF) code by Rein (1989, 1991) is used to perform a quasi-one-dimensional equilibrium nozzle-flow computation from the reservoir to a short distance (typically 2–5 mm) downstream of the throat minimum area where the flow is supersonic. The result is used to initialize the inflow boundary of the computational grid in Figure 3.1, assuming the velocity components along DA are given by a pure conical flow with source point defined by the nozzle walls. Then the entire grid is initialized to correspond to an equilibrium conical expansion. From this state, the N–S code converges quickly on a steady-state nonequilibrium

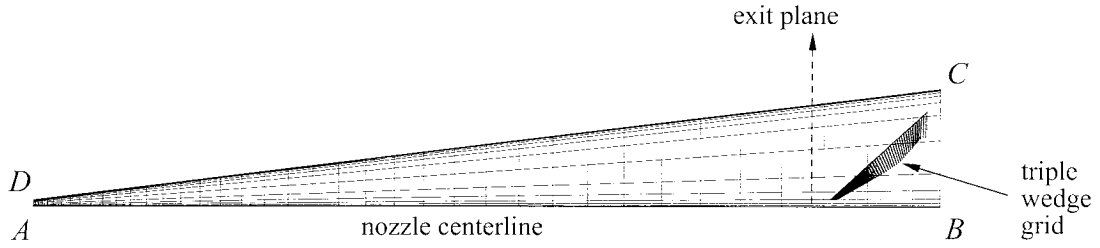

Figure 3.1: Finite-volume grid for nozzle computations (every fifth gridline is shown). A triple-wedge computational grid is overlaid to show its position and size relative to the nozzle computational domain.

solution. Neither the SURF calculation nor the N–S calculation accounts for deviation of the nozzle wall profile from strictly conical near the minimum area.

3.2.2 Comparison to Experiment

The only measurements available of the nozzle free stream in T5 are those taken using a rake of pitot pressure probes (Rousset, 1995). Unfortunately, the pitot pressure is fairly insensitive to the thermochemical state of the free-stream gas. Thus comparison between computed and experimental pitot pressures cannot validate the thermochemical models used in the code, but can still serve to verify that the code reproduces the correct overall fluid mechanics. To that end, nozzle-flow computations were performed at two test conditions from a previous experimental study in T5 by the present author (Davis, 1996) for which free-stream pitot surveys of the conical nozzle had been undertaken. Both viscous and inviscid computations were performed in order to verify the boundary-layer displacement effect. The code gives results for the free-stream flow properties upstream of the normal shock on the pitot probe; to obtain local pitot pressure from these results, a secondary calculation of the normal-shock process is required. The expected degree of nonequilibrium downstream of this shock is not clear from the pitot probe geometry. Calculating the pitot pressure for both a chemically–vibrationally frozen shock and an equilibrium shock provides an upper and lower limit. The equation set which must be solved for equilibrium downstream conditions $(p_2, \rho_2, u_2, T_2, \alpha_2)$ with chemical–vibrational nonequilibrium upstream state $(p_1, \rho_1, u_1, T_1, \alpha_1, T_{v_1})$ is as follows: thermal equation of state for a mixture of ideal gases,

$$p_2 \;=\; \rho_2 \left(1 + \alpha_2\right) R_{\mathrm{N}_2} T_2 \,; \tag{3.23}$$

conservation of mass,

$$\rho_1 u_1 \;=\; \rho_2 u_2 \,; \tag{3.24}$$

conservation of momentum,

$$p_1 + \rho_1 u_1^2 \;=\; p_2 + \rho_2 u_2^2\,; \tag{3.25}$$

conservation of total enthalpy,

$$h_1 + \frac{1}{2}u_1^2 \;=\; h_2 + \frac{1}{2}u_2^2\,, \tag{3.26}$$

where

$$h \;=\; \alpha\left(3R_{\mathrm{N}_2}T + h_{\mathrm{N}}^{\circ}\right) + (1-\alpha)\left(\frac{5}{2}R_{\mathrm{N}_2}T + e_v\right) + \frac{p}{\rho} \tag{3.27}$$

with $e_v(T_v)$ given by Equation 3.7 and $T_{v_2} = T_2$ for equilibrium downstream state; equilibrium law of mass action (Vincenti and Kruger, 1965)

$$\frac{\alpha_2^2}{1-\alpha_2} \;=\; \frac{e^{-\theta_d/T_2}}{\rho_2}\left[m\left(\frac{\pi m k}{\hbar^2}\right)^{3/2}\theta_r\sqrt{T_2}\left(1-e^{-\theta_v/T_2}\right)\frac{\left(Q_{el}^{\mathrm{N}}\right)^2}{Q_{el}^{\mathrm{N}_2}}\right]\,, \tag{3.28}$$

where θ_r is the characteristic temperature for rotational modes (2.9 K for N_2), m is the mass of one N atom (2.3246×10^{-26} kg), k and $\hbar$ are the Boltzmann and Planck constants respectively, and Q_{el} are the electronic partition functions (here assumed constant with temperature, $Q_{el}^{\mathrm{N}} = 4$ and $Q_{el}^{\mathrm{N}_2} = 1$). For a frozen pitot probe shock, only Equations 3.23–3.26 are solved, setting $\alpha_2 = \alpha_1$ and $T_{v_2} = T_{v_1}$.

Computational results for the free-stream pitot pressure are compared to experimental results in Figure 3.2 for the two test conditions. The calculated distributions appear to have low spatial resolution because they are based on a limited number of data extracted from the N–S computational result, evenly spaced along the nozzle radius. The viscous-flow computation with equilibrium-shock assumption falls closest to the experimental data, but still slightly lower, which suggests that the laminar viscous computation only partially accounts for the boundary-layer displacement effect. The effect of assuming a turbulent boundary layer was not investigated because turbulence modeling was not available in the N–S code used for the present work. On the other hand, Olejniczak (1997) found good agreement with pitot pressure measurements at his high-enthalpy condition (similar to the present condition C4) using a laminar viscous computation and assuming a frozen shock. Pitot survey results in the free stream of the contoured nozzle at HEG (Hannemann *et al.*, 1996) appear to match turbulent calculations for low-pressure conditions and laminar calculations for high-pressure conditions (with $p_{T_\infty} = 0.92\rho_\infty u_\infty^2$ assumed instead of a computed shock). In addition, the error bars in Figure 3.2 do not include the $\pm 5\%$ uncertainty in p_0 (*cf.* Section 2.3.1), which could give significantly more overlap with the computed result. (Note that normalization by p_0 scales this uncertainty out of the computed data which depends on the measured p_0, but brings the uncertainty into the experimental data which is independent of the measured p_0.) Thus it is not clear by exactly how much the nozzle computations for the present experiments underpredict the free-stream pressure (and hence density) in general. From the results in Figure 3.2, we might

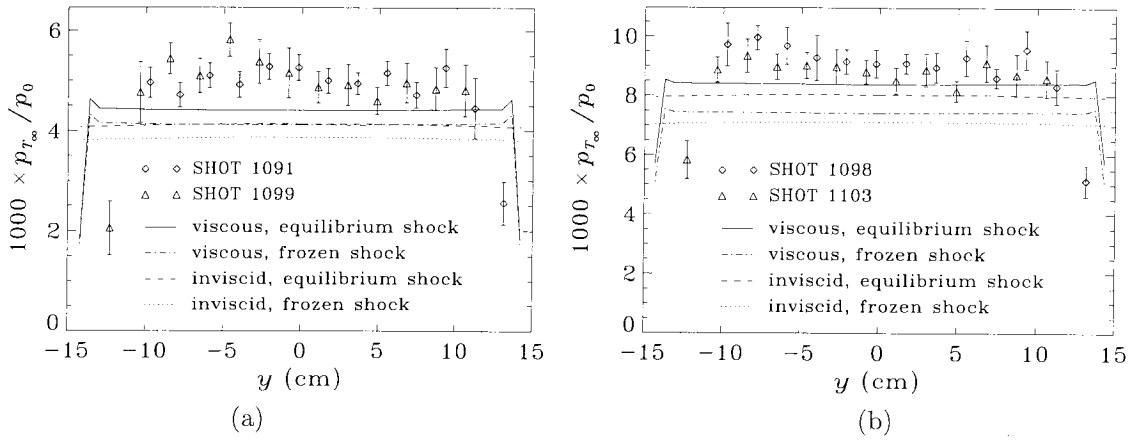

Figure 3.2: Two examples of comparisons between experimentally measured pitot pressure distributions (normalized by p_0) from Davis (1996) and conical nozzle-flow computations; (a) a low-enthalpy condition $h_0 \simeq 9.6$ MJ/kg, $p_0 \simeq 19.4$ MPa, $A_e/A_* = 400$, (b) a high-enthalpy condition $h_0 \simeq 25$ MJ/kg, $p_0 \simeq 21.1$ MPa, $A_e/A_* = 225$. $\diamond$ and $\triangle$ are experimental measurements from two different shots at nominally the same condition, different curves are computational results for various combinations of viscous or inviscid nozzle flow with frozen or equilibrium probe shock assumption as indicated, error bars include only standard deviation of pressure time history over averaging period, and the y-coordinate is defined in Figure 2.3.

expect no more than a 5–10% discrepancy. Another important observation from Figure 3.2 is that the pitot-pressure distribution is slightly nonuniform, having lobes on either side of the nozzle centerline, and this nonuniformity is not included in the computations. (Note that $y > 0$ is above the nozzle centerline, where the double-wedge test model resides.)

Uncertainty in the computed nozzle free-stream properties due to the measurement uncertainty in reservoir conditions was estimated by recomputing one high-enthalpy case (condition C2, $A_e/A_* = 225$) with modified reservoir conditions corresponding to $\pm 5\%$ in p_0 and $\pm 8\%$ in h_0. Overall, this showed errors of $\pm 6\%$ in p_∞, $\pm 7.8\%$ in ρ_∞, $\pm 5.6\%$ in T_∞, $\pm 3\%$ in u_∞, $\pm 20\%$ in α_∞, and $\pm 1.6\%$ in T_{v_∞}. These uncertainties do not include the discrepancy due to the laminar boundary-layer assumption discussed above, or any discrepancy due to uncertainty in the thermochemical modeling; the latter has not been quantified in the present work.

3.2.3 Initialization of Wedge Computations

For various (single-, double-, triple-) wedge computations corresponding to particular shots in T5, the numerical grid is initialized using results from the nozzle-flow computation. The free-stream flow is assumed to be purely conical, an approximation to the extent that growth of the nozzle boundary-layer displacement thickness is not exactly linear. The computed speed, density, and temperatures (translational and vibrational) along the nozzle centerline, between the nozzle exit and the downstream edge of the nozzle grid, are curve-fit with parabolas as a function of the distance from the virtual source point. These curve fits are then used to initialize the wedge computation;

the speed, density, and temperatures at each grid cell are given by the cell's distance from the source point, and the flow direction is given by the angle of a ray from the source point to the cell. The distance calculation includes the measured position of the wedge with respect to the nozzle, given by x_{le} and y_{le}. Chemical reactions are frozen in the nozzle free stream and hence the composition does not change with axial distance. The wedge grids are initialized to the composition computed on the nozzle centerline at the axial location of the wedge leading edge.

Note that the planar wedge computations are initialized using the solution from an axisymmetric nozzle computation. Thus the axisymmetric free-stream expansion is forced to become a planar expansion in the steady-state solution of the wedge computation. The implications of this fact are discussed below in Section 3.3.2, where it is shown that the inaccuracy introduced by this method of initialization is not large. The only way to account more exactly for an axisymmetric free stream is to rely on three-dimensional wedge computations, for which the computational expense becomes unreasonable.

3.3 Inviscid Triple-Wedge Computations

It is shown in Chapter 4 that in order to analyze the experimentally measured separation length or heat flux, knowledge is required of the local flow parameters at the edge of the boundary layer. To this end, an inviscid computation of the external flow over the test model was performed for each shot in which separation length was measured (which includes only cases with $\theta_1 \geq 15°$). The double-wedge body profile is modified to include a third wedge across the hingeline between separation and reattachment, corresponding to the experimentally measured separation bubble. An example of such an inviscid computation is presented in Figure 3.3. Mach contours in the free stream are due to initialization of the computation using the conical nozzle-flow results as described above. These inviscid computations neglect any viscous–inviscid interaction between the boundary layer and the shock layer. The interaction effect is addressed later in Section 3.4.2 and is found to be small in the present experiments. In this section, the triple-wedge computational grid is described (Section 3.3.1), resolution and convergence issues are addressed (Section 3.3.2), and comparisons are made to experimental data for wall pressure and shock angles (Section 3.3.3). Presented in Section 3.3.4 is the method for extracting external flow parameters from the triple-wedge computations.

3.3.1 Grid

A typical numerical grid used for the inviscid triple-wedge computations is shown in Figure 3.4. The configuration is called a triple wedge because the experimentally measured separation region on a double wedge is represented by an impermeable surface between S and R, and thus the inviscid

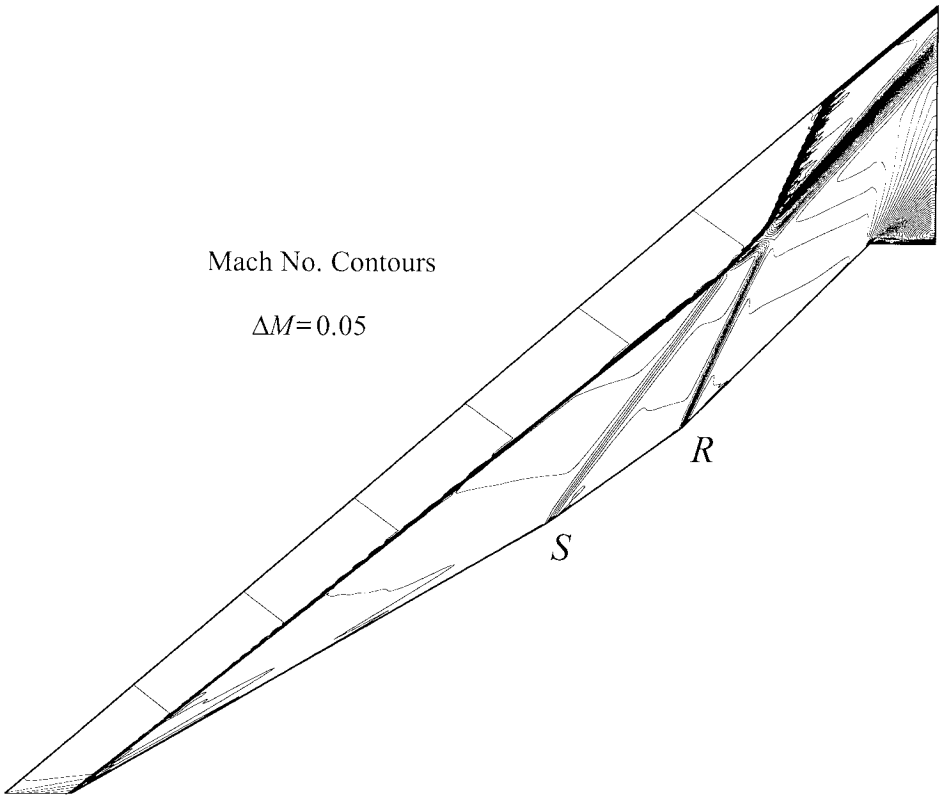

Figure 3.3: Example of inviscid triple-wedge computational result showing contours of Mach number (shot 1302, condition B2, $A_e/A_* = 400$, $\theta_1 = 30°$, $\theta_w = 15°$).

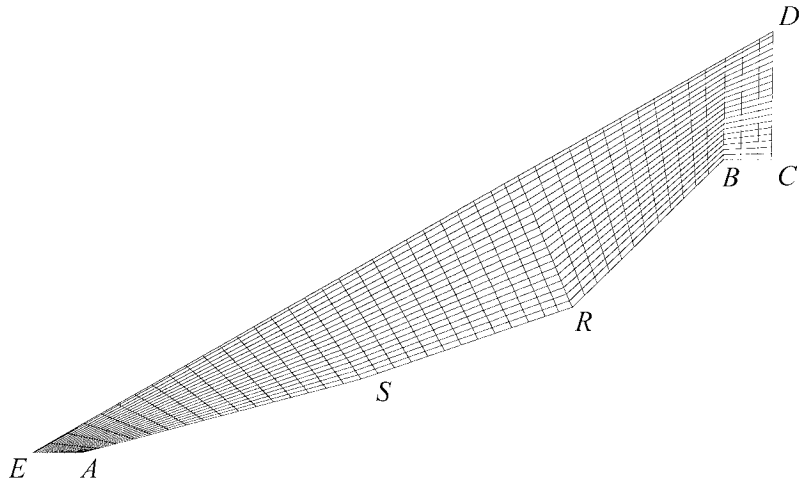

Figure 3.4: Finite-volume grid for inviscid triple-wedge computations (every fifth gridline is shown).

flow sees a succession of three wedges. The first wedge AS deflects the flow to an angle θ_1, the second wedge SR deflects it further to an angle $\theta_1 + \theta_{sep}$, and the third wedge RB brings the flow to a deflection angle of $\theta_1 + \theta_w$. The tail section BC, though it does not mimic the experimental configuration for which $\angle RBC = 90°$, serves to assure an expansion to supersonic outflow conditions

at CD, and is particularly necessary for cases with strong shock–shock interaction. Segments CD and EA are typically set to a length $0.1L_h$. The length of segment CD is set automatically according to experimentally measured shock angles for each shot in an (only partially successful) attempt to prevent shocks from impinging on the free-stream boundary DE. The grid consists of 220 cells in the ξ-direction and 100 cells in the η-direction, distributed uniformly without clustering.

An inviscid wall boundary condition is applied along $ASRBC$, and a supersonic outflow condition along CD. Supersonic inflow is assumed along DE. For a number of the computations, the steady-state solution results in impingement of the reattachment shock on the boundary DE, as seen for example in Figure 3.3. Where this occurs, the boundary condition on DE produces a locally unphysical solution. The only region of the solution in which we are interested, however, is the flow along the wedge wall near S and R, well outside the domain of influence of the anomaly, even in cases of strong shock–shock interaction involving a subsonic flow region adjacent to DE. The upstream segment EA is treated with a symmetry boundary condition (identical to an inviscid wall condition). This condition is proper if the wedge leading edge is positioned on the centerline of the nozzle where the flow velocity is horizontal. In fact, the leading edge is generally positioned above the nozzle centerline, and initialization of the computational grid includes a vertical component of velocity along EA. The resulting disturbance to the steady-state flow solution consists of a weak expansion wave emanating from point E, which can be seen in Figure 3.3. Comparison of inviscid results on this type of grid geometry to results on the corrected geometry used for single-wedge computations (*cf.* Section 3.4) show that the leading-edge anomaly has negligible effect on the flow properties of interest.

3.3.2 Resolution and Convergence Issues

The present computations do not employ any refinement of the grid near sharp gradients, and as can be seen in Figure 3.3, the computed shocks are not very thin. The grid introduces an additional length scale which has a noticeable affect on the computational results near shock–shock interactions, as can be seen, for example, in Figure 3.3. We are only interested, however, in the flow properties along the wall. To ascertain the effect of grid refinement on the wall flow, computations were performed for a uniform free-stream condition at various grid resolutions from 110×50 to 275×125 cells. The results, shown in Figure 3.5 in terms of the pressure coefficient, clearly indicate that a locally grid-converged solution is obtained along the wall at locations away from the shocks for the 220×100 grid size used in the present work. Use of a uniform free stream for these computations makes clear the extent of shock spreading due to the numerical technique; the theoretical result consists of pure step discontinuities between regions of constant pressure. Note that in Figure 3.5, as in all plots in this work that include triple-wedge computational results, the distance ordinate is given along the wall of the corresponding double wedge, not the artificial wall of the triple wedge.

For many of the shots showing strong shock–shock interaction, the steady solution seriously overestimates the upper shock standoff distance. This results in a significantly different shock interaction pattern, often corrupting reattachment so that it can no longer be considered uninfluenced by the shock interaction, as it appears to be in the experimental interferograms. An example of this problem is presented in Figure 3.6. The discrepancy cannot be accounted for by uncertainties in the thermochemical modeling because it occurs at low-enthalpy (essentially nonreacting) as well as high-enthalpy conditions. Uncertainty in the free-stream conditions also could not cause such a large error, and recomputing with a grid of higher resolution (440 × 200) had no effect on the error. The phenomenon may be explained, however, if the experimental flow has not in fact reached a steady state at the time of flow visualization. Additional evidence of an unsteady forward motion of the shock interaction structure, long after the expected establishment time for a steady separation bubble, is seen in pressure and heat flux time histories from downstream of reattachment (*cf.* Section 2.7.4).

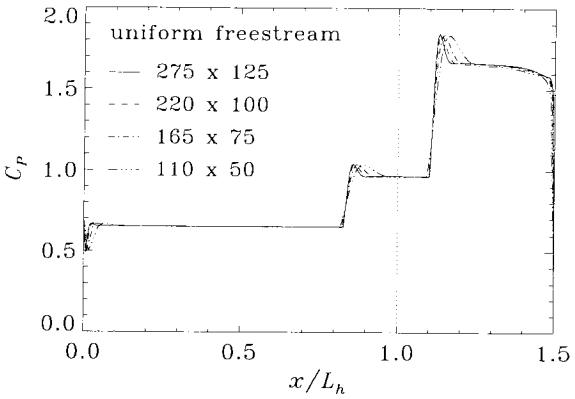

Figure 3.5: Effect of grid refinement on wall pressure for inviscid triple-wedge computations with a uniform free stream based on condition B2 with $A_e/A_* = 400$. Various curves correspond to different grid resolutions as indicated by the number of ξ-direction and η-direction cells.

In order to obtain flow properties along the wall for a configuration that corresponds to that seen in the flow visualization, triple-wedge computations with strong shock–shock interactions are halted before reaching a global steady state. The solutions utilized in such cases are globally nonconverged, but are locally converged on the forebody and along the wall past reattachment, *i.e.* the solution in the latter regions of the grid is not changing with iteration. At much later time, the solution at reattachment does change if the shock interaction structure moves forward enough. Although the code is strictly not time-accurate, we assume here that a locally steady solution corresponds to a temporally converged prediction for the same locally defined area in the experimental flow. The code cannot, however, provide temporal information on motion of the shock interaction structure beyond the fact that it moves upstream.

Figure 3.7 shows the initial free-stream flow field, obtained from nozzle computation results as described in Section 3.2.3, overlaid on the triple-wedge computational result. The initialization corresponds to a three-dimensional axisymmetric flow field, but the triple-wedge computation is carried out assuming two-dimensional planar flow for consistency with the two-dimensional double-wedge test model, *i.e.* the flow on the wedge downstream of the shock is certainly not axisymmetric.

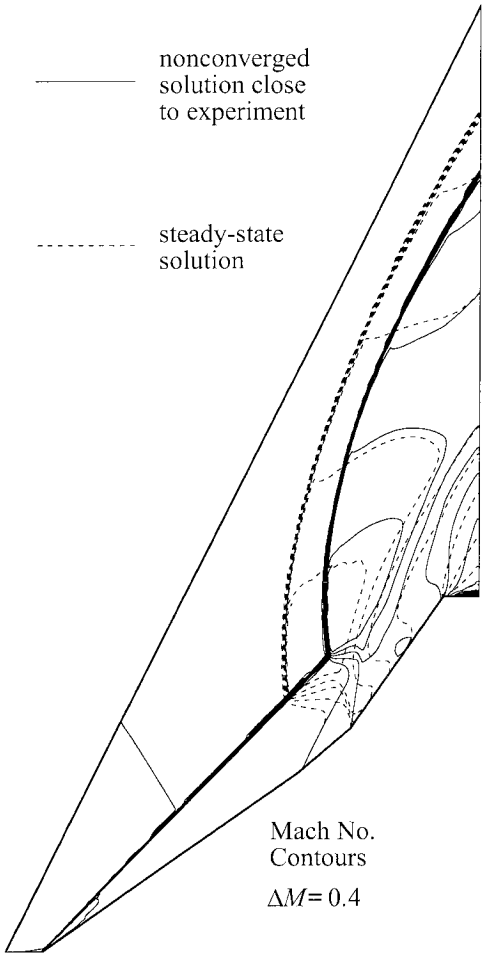

Figure 3.6: Comparison of steady and unsteady (temporally nonconverged) solutions for a strong shock–shock interaction case (shot 1290, condition B2, $A_e/A_* = 225$, $\theta_1 = 35°$, $\theta_w = 20°$). The unsteady solution better matches experiment.

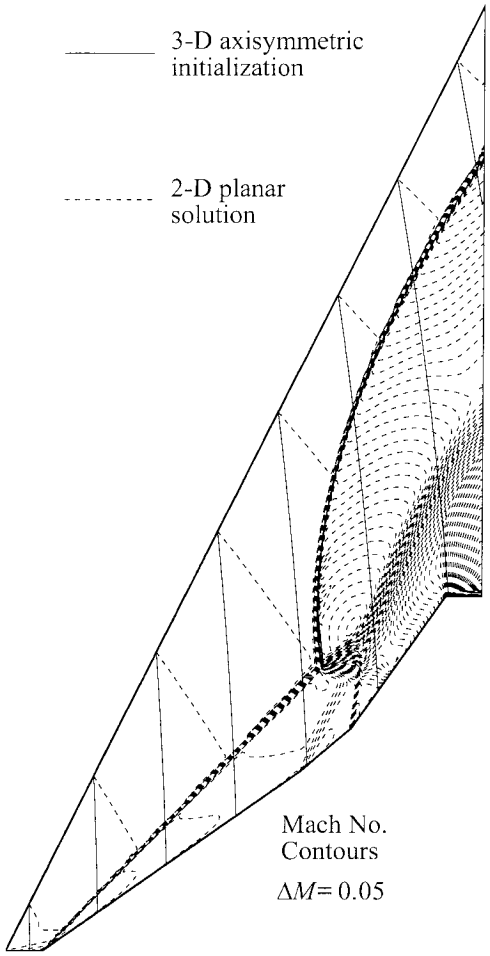

Figure 3.7: Error induced in free-stream flow by initialization of the two-dimensional planar computation with a three-dimensional axisymmetric flow field (shot 1290, condition B2, $A_e/A_* = 225$, $\theta_1 = 35°$, $\theta_w = 20°$).

Not only is the initial axisymmetric free-stream flow modified to a planar flow, but the free-stream boundary of the grid is maintained at the axisymmetric initial condition, resulting in an unrealistic planar expansion. The error induced by this mismatching of flow fields is reasonably small, as evident in Figure 3.7; at points just upstream of the leading shock, the planar free-stream Mach number is not more than one contour level lower than the axisymmetric free-stream Mach number, corresponding to only a 0.5% decrease in Mach number for the case shown. Investigation of the two flow fields in Figure 3.7 at a single point near the shock indicates that the error affects only the thermal expansion and not the kinematic expansion. The velocity is unaffected in both magnitude and direction, while small increases are found in the pressure (3%), density (2%), and temperature

(<1%). Note that the error diminishes as the leading shock approaches the free-stream boundary of the grid.

3.3.3 Comparison to Experiment

Pressure measurements from the double-wedge test model can be compared to the wall pressure distributions computed from the inviscid triple-wedge computations. Two examples of such comparisons are shown in Figure 3.8 for shots 1295 and 1790. Experiment and computation roughly agree near separation for shot 1295, but this is rare; usually, the pressure measurements in this region ($x < L_h$) have large scatter and uncertainty, and in many cases the computational result appears to underpredict the pressure, as seen in Appendix F where comparisons are shown for all shots with corresponding triple-wedge computations. In the flap region downstream of reattachment, there is a tendency for the computation to underpredict the pressure, but again, this behavior is not found consistently throughout all cases computed. For shot 1790, the computed pressure approximately matches experiment at reattachment, but is too low further downstream because the computation fails to reproduce the experimental location of jet impingement from a strong shock–shock interaction. No trends can be discerned from the data in Appendix F regarding particular conditions that result in underpredicted pressures.

A slight underprediction of pressure on the entire double-wedge model, however, might be expected from the results in Section 3.2.2 concerning comparison between computed and experimental pitot pressure in the nozzle free stream. That is, the wedge pressure is underpredicted if the free-stream pressure is underpredicted, whether due to assumption of a laminar nozzle boundary layer or to other phenomena unaccounted for such as nonuniformities in the free stream. The computational

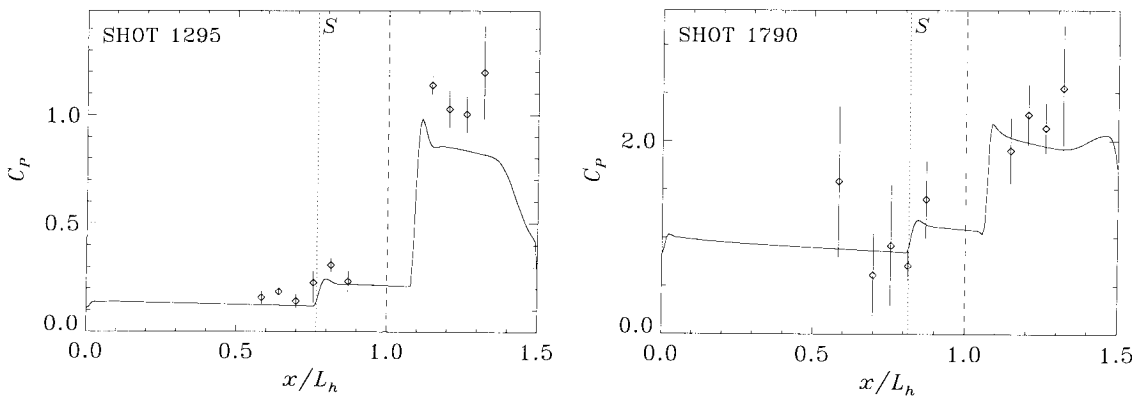

Figure 3.8: Two examples of comparisons between experimentally measured pressure and inviscid triple-wedge computations; shot 1295 (condition B3,$A_e/A_* = 400$, $\theta_1 = 15°$, $\theta_w = 20°$) and shot 1790 (condition C2,$A_e/A_* = 100$, $\theta_1 = 40°$, $\theta_w = 20°$). Solid curve is computational result, $\diamond$ are experimental measurements, dashed line is hingeline location, dotted line is separation location measured from flow visualization, C_P is defined by Equation 2.14, and error bars are described in Section 2.6.3.

results of Brück and Hannemann (1997) for hypersonic nozzle flow and hyperboloid–flare flow in the RWG Ludwieg tube facility at DLR provide some insight to these issues. They computed the nozzle flow with a turbulent boundary layer using an accurately measured profile for the geometry that includes real disturbances in the wall curvature. The computed pressure in the flare region was found to be sensitive not only to free-stream nonuniformities but also to the location of boundary-layer transition on the model. For a low-pressure condition, computation with the nonuniform free stream matched experimental flare pressure, but computation assuming a uniform free stream significantly overpredicted experiment. For a high-pressure condition, both methods underpredicted experimental flare pressure, but good agreement was found by forcing a turbulent boundary layer to start near reattachment in the computations, presumably due to sudden growth of the boundary layer. Another potential source of error in the computed free-stream pressure level is the uncertainty in reservoir pressure (*cf.* Section 3.2.2). As shown below in Section 3.4.2, the inviscid computations can underpredict the wedge pressure for cases with $\theta_1 = 15°$ due to neglect of viscous inviscid interaction. In addition, there is the small error mentioned in Section 3.3.2 due to grid initialization, though this acts to increase the computed flap pressure.

Comparison between computed and experimental shock angles may provide further insight; this is done in Figure 3.9 for the two shots shown in Figure 3.8. For shot 1295 in Figure 3.9a, all three shock angles (for the leading-edge, separation, and reattachment shocks) are matched well by the inviscid triple-wedge computational results, shown as thick white lines. For shot 1790 in Figure 3.9b, however, the computed shock angle at reattachment is higher than in the experiment. Though not shown here, the computational results do exhibit some shock curvature, but significantly less than

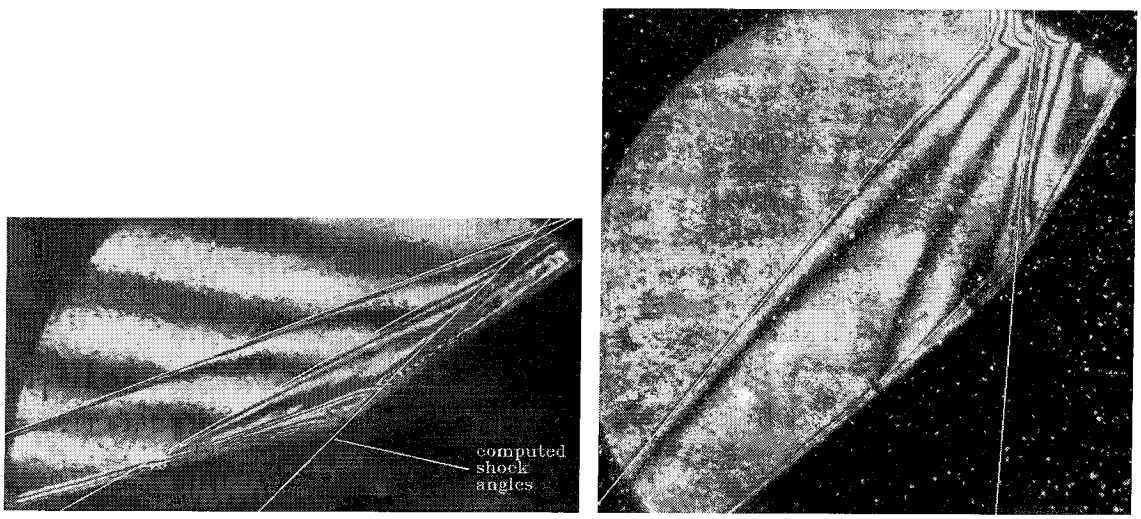

(a) (b)

Figure 3.9: Two examples of comparisons between computed shock angles and experimental interferograms, for the same conditions as in Figure 3.8; (a) shot 1295, (b) shot 1790. The thick white lines are parallel to shocks seen in the computational results.

is seen in the experimental interferogram for the reattachment shock and for the leading edge shock just upstream of the triple point. Some other shots at high incidence show worse agreement for the reattachment shock angle. The mechanisms described above for underpredicting pressure all have an affect on computed shock angle. A more important source of error, particularly for the high-incidence cases which have lower supersonic Mach numbers in region 2, is the measurement uncertainty in θ_{sep}, a parameter that defines the geometry of the inviscid triple-wedge computations. The measured separation angle θ_{sep} has rather large uncertainty (*cf.* Section 2.4.4) that in a few cases even exceeds $\pm 30\%$. This value for θ_{sep} used in the computations certainly affects the resulting shock angles at separation and reattachment, and may also affect the pressure level immediately downstream of reattachment as the compression process is distributed differently between the two shocks.

Thus there are at least five mechanisms for producing nonnegligible errors in computed flap pressure;

1. incorrect free-stream pressure level,
2. neglected or incorrect free-stream nonuniformity,
3. neglected viscous inviscid interaction when $\theta_1 = 15°$,
4. boundary-layer transition near reattachment, and
5. uncertainty in the measured separation angle θ_{sep}.

With each mechanism having different trends depending on the flow conditions, and the large scatter found in experimental pressure measurements, it is not surprising that there is little consistency in comparisons of the computed flap pressure results to experiment.

3.3.4 External Flow Parameters

Flow properties at the boundary-layer edge at particular stations corresponding to flow regions 1, 2, and 3 in Figure 1.3 are obtained from the triple-wedge computations as shown by the example in Figure 3.10. Stations 1 and 2 are taken just upstream of the pressure rise at separation and reattachment respectively. Care must be taken in defining station 3 downstream of reattachment because the lateral extent of the artificial overshoot from numerics is obscured by the nonuniform ramp flow. The pressure may drop quickly due to an expansion, or as in Figure 3.10, it may rise again due to jet impingement from a strong shock–shock interaction. For consistency, we take station 3 offset a fixed distance downstream of the peak computed pressure. This distance is based on the result in Figure 3.5 for a 220×100 grid with uniform flow, for which the extent of the artificial overshoot can clearly be identified. Values of flow properties that are relevant to results in Chapters 5 and 6, obtained in the manner described above, are given in Appendix E for each shot that was computed.

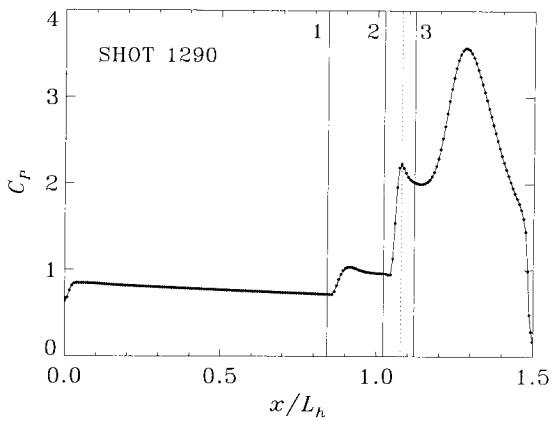

Figure 3.10: Example of obtaining external flow parameters at stations 1, 2, and 3 from inviscid triple-wedge computation (shot 1290, condition B2, $A_e/A_* = 225$, $\theta_1 = 35°$, $\theta_w = 20°$). Dotted line is at peak pressure, from which solid line 3 is offset a fixed amount to avoid numerical overshoot, and points are cell centers from computational grid.

3.4 Single-Wedge Computations

Viscous computations using the N–S code were desired for a few shots in order to (1) ascertain the error made by neglecting the boundary layer in the triple-wedge computations and (2) verify that the code can reproduce experimentally measured values of heat flux. Numerical calculation of the separated region is computationally expensive and was not needed for these purposes; therefore, these computations were performed on a single-wedge geometry corresponding to only the front part of the test model, or the entire model when $\theta_w = 0°$. The computational grid is described in Section 3.4.1, viscous interaction effects are considered in Section 3.4.2, and comparisons to experimental heat flux are presented in Section 3.4.3.

3.4.1 Grid

An example of the numerical grid used for viscous single-wedge computations is shown in Figure 3.11. The grid wraps around the leading edge; ABC is given a viscous wall boundary condition (both noncatalytic and catalytic conditions are considered), while CD and FA are given supersonic outflow boundary conditions. The supersonic inflow boundary DEF is held at the initial free-stream conditions. The distance EB is typically set to $0.05L_h$ and the distance CD is set, according to the measured shock angle, to ensure the shock crosses the outflow boundary and not DE. The wedge length BC is either L_h or $1.5L_h$. The leading edge is positioned relative to the conical nozzle free stream according to the measured values of x_{le} and y_{le} as for the triple-wedge computations. In the ξ-direction the grid has 218 cells, clustered at the leading edge with exponential distribution of the cell spacing. In the η-direction the grid has 100 cells, clustered at the wall using an iterative grid-smoothing technique, akin to a solution technique for Poisson's equation in two dimensions with cell

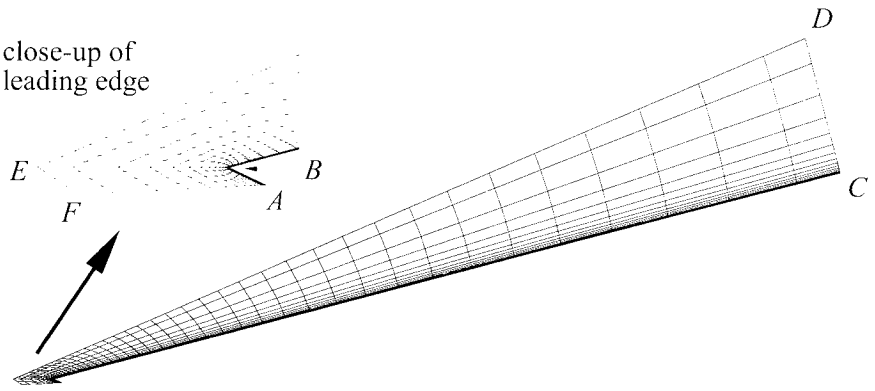

Figure 3.11: Finite-volume grid for viscous single-wedge computations (every fifth gridline is shown), with magnified view of leading-edge region.

spacing in ξ and η as the independent variables. The iterations are stopped once 35 cells fall within the boundary-layer displacement thickness estimated from perfect-gas theory (*cf.* Equation 4.25) at the downstream edge. In addition, the η-lines are forced to approach normal to the wall boundary, causing them to be curved as seen in Figure 3.11. Though this grid produces solutions with a thick shock wave away from the leading edge, this has no effect on the results close to the wall where the boundary layer is well resolved.

3.4.2 Viscous Interaction Effect

Single-wedge computations can be used to verify the magnitude of the viscous interaction effect due to boundary-layer growth, which is neglected in the triple-wedge computations. The strength of the interaction in flow region 1 depends on the viscous interaction parameter $\bar{\chi}_1 = M_1^3\sqrt{C^*/Re_{x_1}}$, with strong interactions identified by $\bar{\chi}_1 \geq 4$ (Hayes and Probstein, 1959). The strongest interactions in the experiments presently under computational investigation (which excludes cases with $\theta_1 = 0°$) occur on shots with $A_e/A_* = 400$ and $\theta_1 = 15°$, for which $\bar{\chi}_1 \leq 0.55$. These are well within the weak interaction regime. Two examples of the interaction effect are shown in Figure 3.12 by comparing pressure distributions from viscous and inviscid computations on a single-wedge geometry. The inviscid computations were carried out on a grid similar to the viscous computations, wrapped around the leading edge but with straight η-lines and uniform cell spacing in the η-direction.

With $\theta_1 = 30°$, as for shot 1737 in Figure 3.12, the viscous interaction effect is negligible. For a worst-case situation represented by shot 1774 in Figure 3.12 (which has $\theta_1 = 15°$ and $\bar{\chi}_1 = 0.54$), the inviscid computation underpredicts the pressure near the hingeline by less than 5%. (Note that the additional discrepancy for $x/L_h > 0.8$ is due to a numerical anomaly at the downstream boundary.) Investigation of the two flow solutions for shot 1774 at a point outside the boundary layer in the viscous case shows that the inviscid computation also underpredicts the temperature by 6%, and

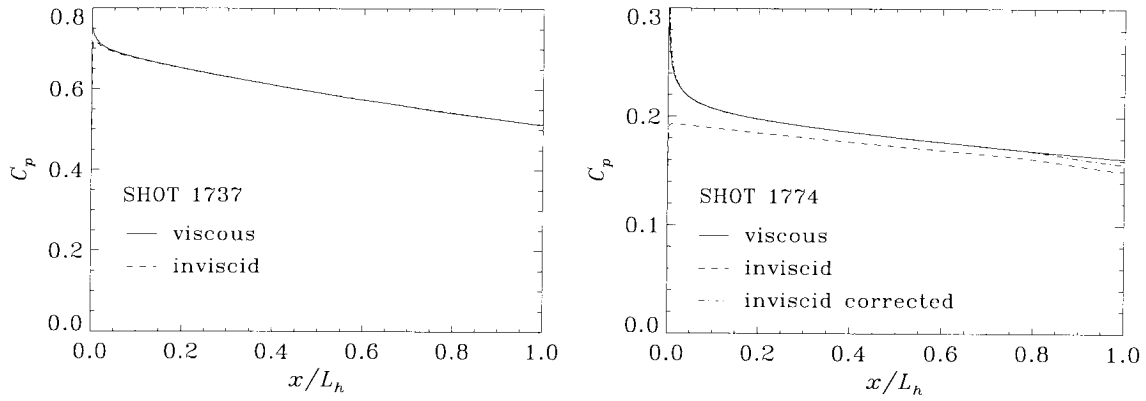

Figure 3.12: Comparisons between viscous (solid curve) and inviscid (dashed curve) single-wedge computational results showing viscous interaction effect on pressure distribution for shot 1737 (condition C2, $A_e/A_* = 100$, $\theta_1 = 30°$, $\bar{\chi}_1 = 0.09$) and shot 1774 (condition B1, $A_e/A_* = 400$, $\theta_1 = 15°$, $\bar{\chi}_1 = 0.54$) with correction from weak interaction theory applied to inviscid result (dash–dot curve).

overpredicts the density by 2%, the Mach number by 4%, and the velocity by less than 1%. A curve is plotted for shot 1774 in Figure 3.12 showing application of the weak viscous interaction theory from Hayes and Probstein (1959) to the inviscid pressure distribution p_{inv} to obtain a corrected pressure distribution;

$$\frac{p}{p_{inv}} \simeq 1 + \gamma \left(M_\infty \frac{\mathrm{d}\delta^*}{\mathrm{d}x} \right) J_1 + \frac{\gamma(\gamma+1)}{4} \left(M_\infty \frac{\mathrm{d}\delta^*}{\mathrm{d}x} \right)^2 J_2 \,, \tag{3.29}$$

where J_1 and J_2 are complicated functions of p_∞/p_{inv}, γ, and $K_1 = M_\infty \theta_1$ from tangent-wedge theory, and $\mathrm{d}\delta^*/\mathrm{d}x$ is evaluated for a perfect gas using Equation 4.25. The pressure thus corrected closely matches the viscous computational result. This perfect-gas theory works well even for high-enthalpy conditions with $\theta_1 = 15°$, because the wedge flow remains essentially frozen (chemically and vibrationally) for such a weak oblique shock; it is only necessary to use the correct γ to account for the partial free-stream dissociation and vibrational excitation,

$$\gamma = 1 + \frac{R}{c_v + (1-\alpha) c_{v_v}} \,, \tag{3.30}$$

with c_{v_v} given by Equation 3.14, and with R and c_v mass-averaged over the gas mixture. Hayes and Probstein (1959) suggest correcting for other flow properties by assuming an isentropic process and using the compressible form of Bernoulli's equation, but this fails to recover the viscous results for shot 1774. Thus in the present work we neglect the viscous interaction effect on all shots, with the knowledge that this introduces a small error as described above for cases with $\theta_1 = 15°$.

3.4.3 Comparison to Experiment

In addition to the previous comparisons to measured values of free-stream pitot pressure (*cf.* Section 3.2.2) and wall pressure on the double-wedge model (*cf.* Section 3.3.3), comparisons can be made between viscous computational results and experimental heat flux measurements on the double-wedge model. This is perhaps a more stringent test of the code's ability to reproduce flow in T5, because the heat flux measurements are more sensitive to the flow thermochemistry and generally more reliable than pressure measurements. Four different experiments were considered; two shots at high and low enthalpy with $\theta_1 = 30°$ and $\theta_w = 0°$ which were specifically performed to obtain heat flux data on an inclined flat plate over a longer distance without separation (shots 1737 and 1799), and two shots at lower density with $\theta_1 = 15°$ (shot 1774 because it was used for the viscous interaction study in Section 3.4.2, and shot 1775 for the reason given below). Results are shown in Figure 3.13. Though the single-wedge computations for shots 1774 and 1775 encompass only $x \leq L_h$ because $\theta_w > 0°$, the entire experimental heat flux distributions are shown including the flap region. For the high-enthalpy cases with dissociation in the free stream and behind the leading shock, two computations were performed, one with a catalytic and one with a noncatalytic wall boundary condition. Wall-normal heat flux obtained from the computations includes both $\dot{q}$ and $\dot{q}_v$ (*cf.* Equation 3.10), plus the heat transfer due to mass diffusion (the summation in the last term of Equation 3.4) for cases with a catalytic-wall boundary condition.

Note that for shot 1737 in Figure 3.13, there is only a small difference between catalytic and noncatalytic results; this is because the density is high enough to cause strong recombination near the wall even in the noncatalytic case, which also increases heat transfer, though by a different mechanism than the catalytic mechanism of mass diffusion (*cf.* Section 5.2.3). The high-enthalpy shot 1775 was chosen to produce a significant difference in heat flux for catalytic and noncatalytic wall conditions due to the low density. Unfortunately, the dissociation fraction at the boundary-layer edge, which limits the difference between catalytic and noncatalytic results, remains close to the free-stream value ($\alpha \simeq 0.1$) for this low-incidence case. The difference turns out to be of the same order as the scatter in experimental data, and much of the data fall between the two computed results. From this comparison we cannot infer the presence or absence of a catalytic effect in the experiments. The test model surface of dirty stainless steel is not expected, however, to be catalytic to nitrogen recombination.

Shot 1774 in Figure 3.13 shows the best agreement between computation and experiment, but it also has the largest experimental uncertainty. The high-enthalpy shot 1737 shows slight overprediction of the heat flux where it is better matched in the other cases, over much of the forebody (TC ports T4–T15). It is clear from the repeatable scatter in the experimental data that the thermocouple measurements include systematic error, and that this error is not entirely accounted for by the error bars which were calculated as described in Section 2.5.3. The measured heat flux for

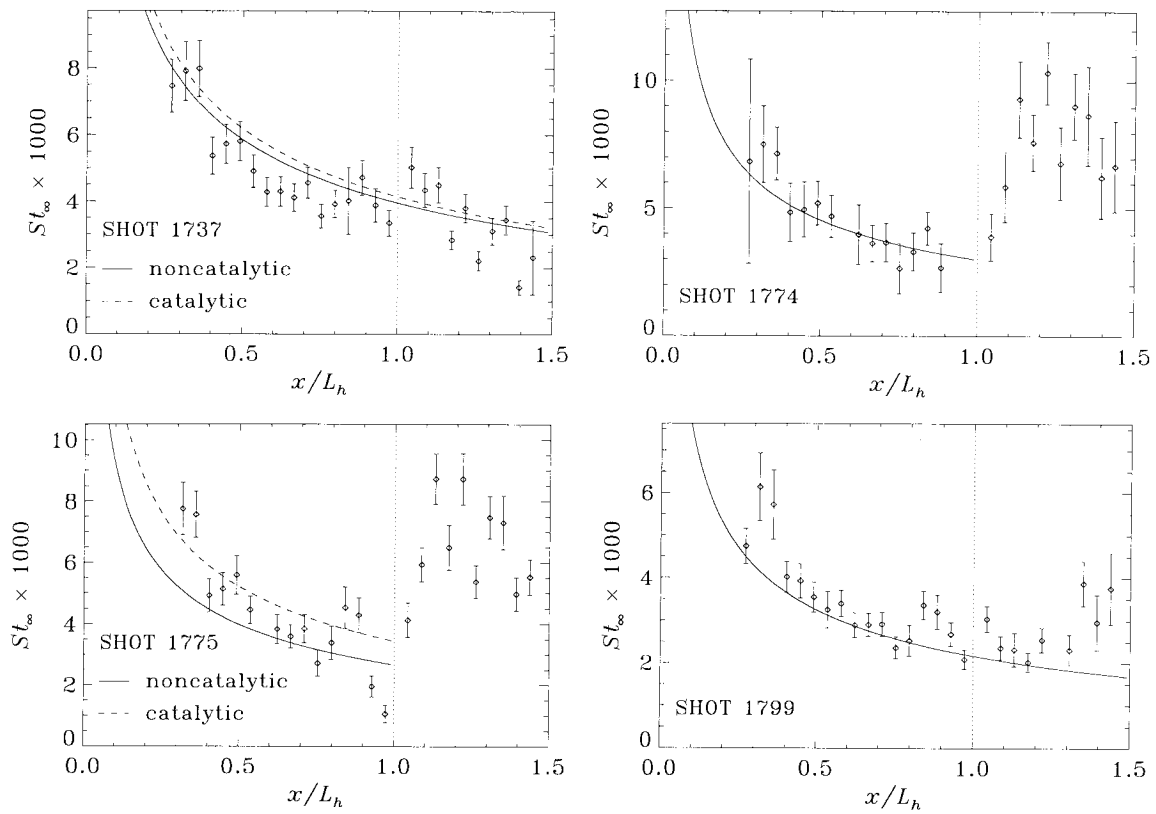

Figure 3.13: Comparisons between experimentally measured heat flux and viscous single-wedge computations; shot 1737 (condition C2, $A_e/A_* = 100$, $\theta_1 = 30°$, $\theta_w = 0°$), shot 1774 (condition B1, $A_e/A_* = 400$, $\theta_1 = 15°$, $\theta_w = 15°$), shot 1775 (condition C2, $A_e/A_* = 400$, $\theta_1 = 15°$, $\theta_w = 15°$), and shot 1799 (condition B2, $A_e/A_* = 100$, $\theta_1 = 30°$, $\theta_w = 0°$). Curves are computational results (solid curve for noncatalytic wall and dashed curve for catalytic wall), $\diamond$ are experimental measurements, dotted line is hingeline location, St_∞ is defined by Equation 2.12, and error bars are described in Section 2.5.3.

$x > L_h$ in shots 1737 and 1799 might also be affected by a step in the wall at the hingeline between the instrument plates (*cf.* Section 2.2.2). Uncertainty in the nozzle reservoir conditions, and hence in the free-stream conditions, produces uncertainty in the dimensional computed heat flux. This uncertainty is not shown in the plots. As explained in Section 3.2.2, the normalization (here to obtain Stanton number) effectively places the additional uncertainty on the locations of the normalized experimental data in Figure 3.13. The normalizing factor $\rho_\infty u_\infty h_0$ from Equation 2.12 has an expected uncertainty of $\pm 7.5\%$ based on the nozzle-flow sensitivity to reservoir uncertainty (*cf.* Section 3.2.2). Overall, good agreement is found between computation and experiment in Figure 3.13, inspiring confidence in the computational techniques used for the present study.

3.5 Viscous Double-Wedge Computations

A very limited number of viscous double-wedge computations, in which the separated flow region is actually calculated, were undertaken using the N S code in order to aid the interpretation of experimental interferograms. The goal was to verify the relationship between the fringe pattern used to measure separation length and other physical aspects of the separation region which are not accessible in the present experiment but which are typically used to define separation and reattachment in a theoretical sense, *e.g.* skin friction and the dividing streamline. These computations also allow comparisons with the measured heat flux downstream of reattachment, which could not be accomplished with the single-wedge computations in Section 3.4, and investigation of real-gas effects in the separated shear layer (*cf.* Section 5.2.2.2). As discussed in Section 1.5.1.3, prediction of separated flows is a state-of-the-art problem in computational fluid dynamics and is particularly prone to grid-convergence problems. Thus the present computations, though performed at reasonably high resolution, are not expected to match experimental results in terms of separation length. They are, however, expected to provide solutions which incorporate the relevant physics of separated flow, and therefore be useful for interpretation of experimental results. Section 3.5.1 describes the computational grid, Section 3.5.2 gives the technique for obtaining computional interferograms, and Section 3.5.3 presents comparisons to experimental heat flux data.

3.5.1 Grid

A typical numerical grid used for viscous double-wedge computations is shown in Figure 3.14. A viscous noncatalytic wall condition is applied to AHC, where point H corresponds to the hingeline on the double-wedge test model. Line CD has a supersonic outflow condition, and its length is again determined by the measured shock angles. An expansion tail, as used for the triple-wedge computations (*cf.* Section 3.3), is not required here because strong shock–shock interaction cases are not considered. Supersonic inflow is assumed along DE, and a symmetry condition is applied on EA. As for the triple-wedge computations, the condition on EA produces an anomaly when the grid is initialized with a vertical velocity component on EA due to the offset position of the test model ($y_{le} \neq 0$), but its effect on the boundary-layer flow further downstream has been shown to be negligible. The length of segment EA is set to $0.025L_h$. The grid consists of 400 cells in the ξ-direction distributed uniformly and 200 cells in the η-direction clustered at the wall using the same technique as for the single-wedge computations (*cf.* Section 3.4), except without forcing of η-lines normal to the wall boundary and with only 25 cells inside the estimated boundary-layer displacement thickness (*cf.* Equation 4.25). For reasons mentioned in the introduction to this section, issues of grid-convergence were not addressed for the double-wedge computations.

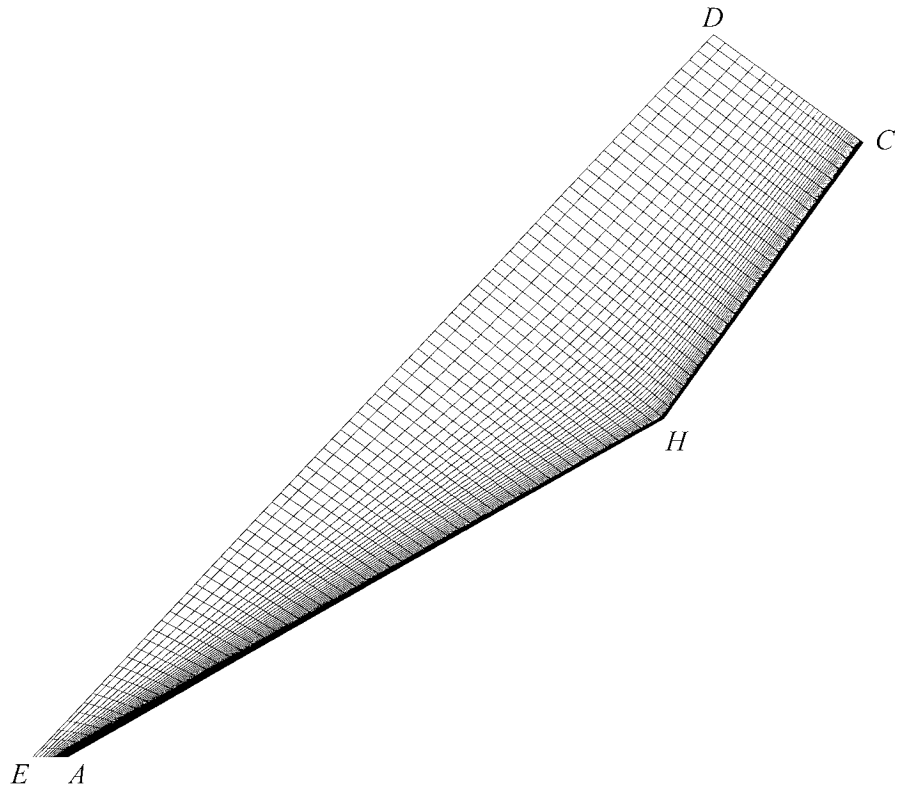

Figure 3.14: Finite-volume grid for viscous double-wedge computations (every fifth gridline is shown).

3.5.2 Computation of Interferograms

From the computed double-wedge flow fields, interferograms are calculated which, because the flow computations are only two-dimensional, correspond to an idealized situation where pure two-dimensional flow exists across the full span of the model and end effects are negligible. Though this prohibits direct comparison to the experimental interferograms where end effects are important, the computed interferograms still prove useful for verifying the experimental measurement technique for separation length, as detailed in Section 2.4.4. The computational interferograms are obtained by first calculating the phase shift ϕ at each cell on the grid with respect to a reference point in the free stream;

$$\phi = \frac{2\pi b}{\lambda}(\rho - \rho_\infty)\left[\alpha K_{\mathrm{N}} + (1-\alpha)K_{\mathrm{N}_2}\right], \tag{3.31}$$

where $K_{\mathrm{N}} = 3.1 \times 10^{-4}$ m^3/kg and $K_{\mathrm{N}_2} = 2.38 \times 10^{-4}$ m^3/kg are the Gladstone-Dale constants for atomic and molecular nitrogen, b is the span of the double-wedge model, and λ is the laser wavelength (532 nm). An additional, linearly varying phase shift ϕ_{ff} corresponding to the finite fringe pattern in the experiment can be computed by taking the reference point for ρ_∞ in Equation 3.31, (x_{ref}, y_{ref}), to be at the center of a dark fringe in the free stream, and applying the following equation:

$$\phi_{ff} = \pi + \frac{2\pi}{\lambda_{ff}} \left[(y - y_{ref}) \cos\theta_{ff} - (x - x_{ref}) \sin\theta_{ff} \right] , \tag{3.32}$$

where λ_{ff} is the spacing and θ_{ff} is the angle with respect to horizontal of the finite fringes in the free stream. The leading term π is added to force the intensity to be zero at the reference point. A scalar proportional to the intensity at each cell is then calculated using

$$I \propto \cos^2 \left(\frac{\phi + \phi_{ff}}{2} \right) . \tag{3.33}$$

Computed interferograms are then obtained by plotting flooded contours of I with gray-scale shading; these are shown for two cases in Section 2.4.4.

3.5.3 Comparison to Experiment

In Section 3.4.3 it was shown that the N S code could reproduce the experimental heat flux on the forebody of the double wedge with reasonable accuracy. It is of interest to make similar comparisons using the double-wedge computations which include heat-flux predictions for the flap region downstream of reattachment, particularly in light of the results in Section 3.3.3 for pressure in the flap region. Such comparisons are shown in Figure 3.15 for the three double-wedge cases computed. As expected, overall agreement with measured heat flux upstream of separation is good. Surprisingly, two of the cases (shots 1741 and 1796) show reasonable agreement with the length of separation. Only shot 1783, however, shows the same heat flux level in the flap region for both computation and experiment, though the location of peak heating in this case is not matched due to the underpredicted separation length in the computation. In the other two cases, the measured flap heat flux is significantly higher than the computed values, suggesting that in the experiments, transition to turbulence is occurring in the boundary layer at or near reattachment. On the other hand, later investigation of the measured separation length (*cf.* Section 6.1) suggests that most high-enthalpy experiments had purely laminar interactions.

Other possible contributors to the discrepancy in heat flux are an underpredicted flap pressure or a catalytic wall effect (the heat flux was computed assuming a noncatalytic wall). The comparisons with pressure from triple-wedge computations in Appendix F show a large underprediction of flap pressure for shot 1741 but a much smaller discrepancy for shot 1783. (Pressure results from double-wedge computations, not shown, are similar to those from triple-wedge computations except that they have finite pressure gradient at reattachment and no numerical overshoot.) Although computation shows that shot 1796 is highly dissociated in the flap region with $\alpha_3 \simeq 0.25$, a neglected catalytic wall effect seems a less likely candidate for the discrepancy because the noncatalytic result matches experiment upstream of separation where $\alpha_1 \simeq 0.15$. The only conclusion we can draw here is that high-enthalpy experiments which otherwise appear to have purely laminar interactions may

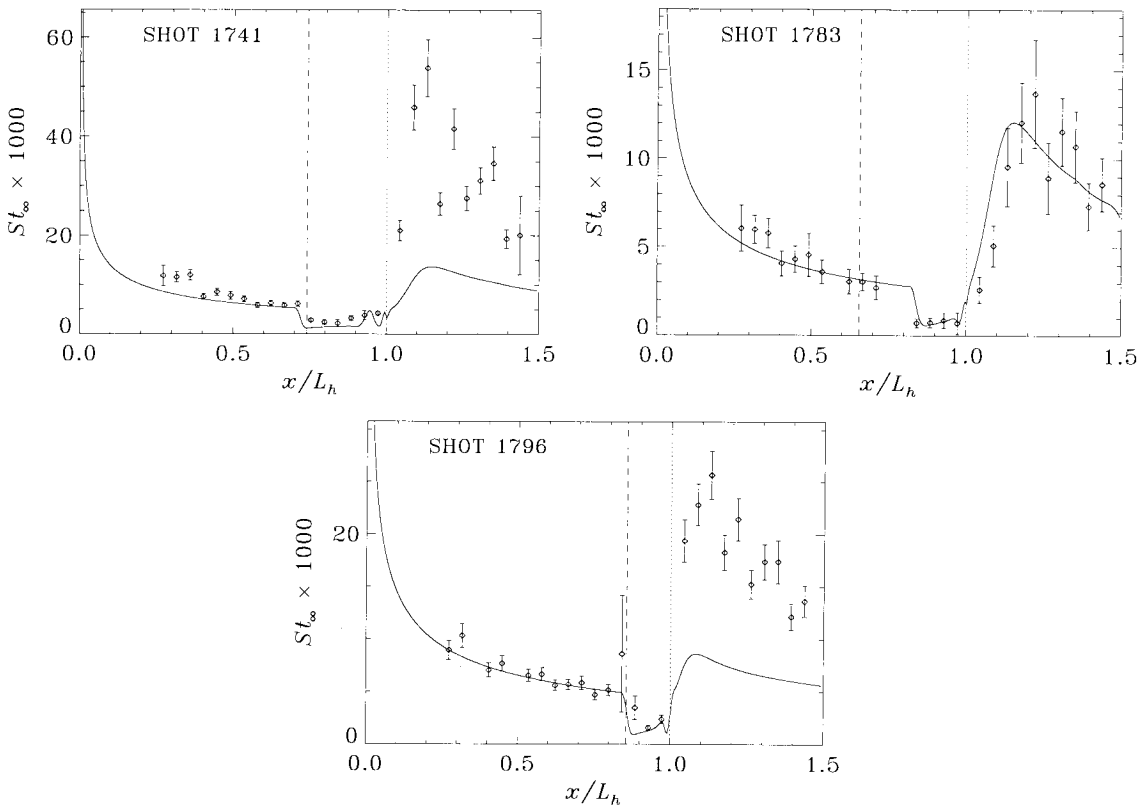

Figure 3.15: Comparisons between experimentally measured heat flux and viscous double-wedge computations; shot 1741 (condition C2, $A_e/A_* = 225$, $\theta_1 = 30°$, $\theta_w = 25°$), shot 1783 (condition B1, $A_e/A_* = 225$, $\theta_1 = 15°$, $\theta_w = 20°$), and shot 1796 (condition C2, $A_e/A_* = 100$, $\theta_1 = 40°$, $\theta_w = 15°$). Curves are computational results, $\diamond$ are experimental measurements, dotted line is hingeline location, dashed line is separation location measured from flow visualization, St_∞ is defined by Equation 2.12, and error bars are described in Section 2.5.3.

in fact have transition starting near reattachment, but that any underprediction of the flap pressure must be considered in making such a determination. This issue is considered further in Section 4.1.2 where turbulent boundary-layer theory is applied to inviscid triple-wedge computational results.

The strange behavior of the computed heat flux just upstream of reattachment for all three cases in Figure 3.15 coincides with similar behavior in the skin friction (see Figure 2.9 for shot 1783) and pressure (not shown), and may be related to a singularity in the reversed-flow region under interactive boundary-layer theory found by Smith (1988) and studied further by Smith and Farid Khorrami (1991). Though these authors used a triple-deck boundary-layer formulation instead of the full two-dimensional Navier–Stokes equations used here, the phenomenon appears often in other published results of N S computations for separated flow in shock/boundary-layer interactions (*e.g.* Ballaro and Anderson, 1991; Brenner and Prinz, 1992; Grasso and Marini, 1996; Grumet *et al.*, 1994; Power and Barber, 1988).

3.6 Boundary-Layer Computations

The N–S code is also employed in the present work to study reacting boundary layers on a simple flat-plate geometry, with free-stream conditions corresponding to the range of local flow conditions in region 1 obtained during the experiments. The goal is to verify the importance of chemistry in the boundary layer upstream of separation by computing each case three times; once with chemically vibrationally frozen flow, once with thermochemical nonequilibrium and a noncatalytic wall condition, and once with thermochemical nonequilibrium and a catalytic wall condition. The different cases studied and their results are given in Section 5.2.1. In this section we briefly discuss execution of the computations and issues relating to convergence.

3.6.1 Grid and Initialization

A rectangular grid like the one shown in Figure 3.16 is used for the boundary-layer computations. The grid is initialized with uniform free-stream conditions based on boundary-layer edge conditions just upstream of separation obtained from triple-wedge computations. For cases where this condition significantly departs from a frozen or equilibrium condition, it is modified slightly in the frozen-flow computation to produce the same boundary-layer edge conditions as the reacting-flow computations at the location of interest (*cf.* Section 5.2.1). It is important to note that these computations are not meant to simulate the wedge boundary layer exactly, which in the experiments often sees a nonuniform edge condition.

Referring to the grid in Figure 3.16, supersonic inflow conditions are applied on DE and supersonic outflow conditions on BC. A viscous wall boundary condition (either catalytic or noncatalytic) is applied on AB, but not along its entire length; an inviscid condition is applied to the first six cells at the leading edge of the grid to avoid interaction between the inflow condition on DA and initial growth of the boundary layer. The upper boundary CD is held at the initial free-stream conditions, which is an unphysical condition where the weak compressive wave from the leading edge intersects CD and for cases where the steady-state solution has streamwise gradients upstream

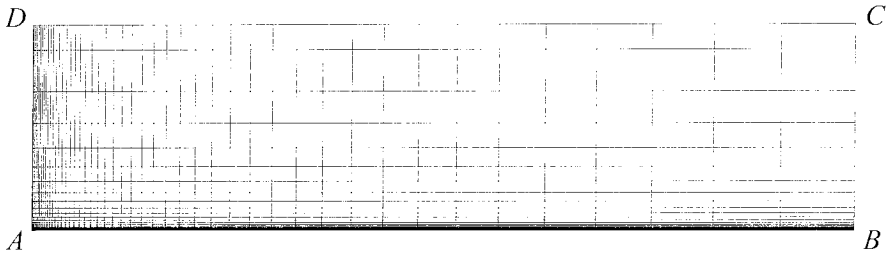

Figure 3.16: Finite-volume grid for flat-plate boundary-layer computations (every second gridline is shown).

of this wave because the prescribed free-stream condition is not frozen or in equilibrium. Since they only influence the flow near the wall downstream of the location of interest, these anomalies are not considered a hindrance. The length of the grid is set to 10 cm, approximately the length L_h, and the height is set to 2.5 cm. Boundary-layer profiles are taken at a location $x = 5$ cm from the leading edge. The grid consists of 100 cells in the ξ-direction clustered at the leading edge and 75 cells in the η-direction clustered at the wall. In both directions, the clustering conforms to an exponential distribution of cell spacing. The minimum cell size in the ξ-direction is 51 μm. In the η-direction, the exponential distribution is fixed by requiring 35 cells inside the boundary-layer displacement thickness estimated from perfect-gas theory (*cf.* Equation 4.25).

3.6.2 Resolution and Convergence Issues

Due to the η-direction clustering of cells near the wall as described above, the boundary-layer profile is expected to be well resolved in the present computations, There is some question, however, concerning the dependence of the solution on the grid refinement at the leading edge. Poor resolution of the initial growth of the boundary layer over the first few cells of viscous wall boundary condition may affect the solution further downstream. Of particular importance is the cell shape in this region, characterized by the cell aspect ratio $AR = \Delta\xi/\Delta\eta$. While the large aspect ratio (due to clustering in the wall-normal direction) works well for most of the boundary layer because streamwise gradients are small, it is not appropriate at the leading edge. To quantify the grid-convergence with respect to cell aspect ratio at the leading edge, one case with a thin boundary layer (and hence a large cell aspect ratio near the wall) was computed three times, each with a different minimum ξ-direction cell size between 30 and 100 μm. The total number of cells was kept constant. Shown in Figure 3.17 is the relative change in the wall shear stress with respect to the result for the smallest aspect ratio. Wall shear stress is a parameter of interest to the study in Section 5.2.1 and is expected to be sensitive to dynamics of the leading edge. Reducing the aspect ratio at the leading edge by a factor of two from 600 to 300 does have a large effect near the leading edge, but causes less than a 0.5% change in τ_w downstream at $x = 5$ cm, the location of interest. Since the computation with $AR = 300$ gives only a 0.2% increase in τ_w

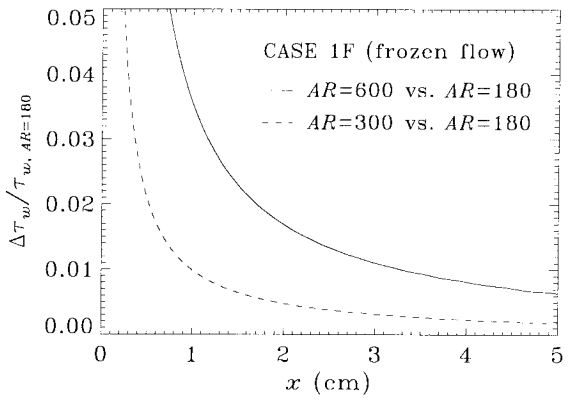

Figure 3.17: Effect of leading-edge grid refinement on wall shear of flat-plate boundary-layer computation; AR is aspect ratio of leading-edge wall-adjacent cell, CASE1F is described in Section 5.2.1.

over the computation with $AR = 180$, it is assumed that further reductions in aspect ratio will not cause significant change. Computations are thus performed with minimum ξ-direction cell size of 51 μm, corresponding to the $AR = 300$ in Figure 3.17; note that the aspect ratio varies case by case depending on the estimated boundary-layer thickness which determines the minimum η-direction cell size.

3.7 Summary

The computational code used in the present study, to compute experimental flow conditions as well as to investigate aspects of chemically reacting viscous flow, solves a finite-volume representation of the Navier–Stokes equations with thermochemical nonequilibrium on a body-fitted grid. For each experiment in which separation length was measured, this code was first used to compute the viscous nozzle flow, then used to compute the inviscid external flow on a triple-wedge geometry determined by the experimentally measured separation geometry, the nozzle-flow result being used to initialize the triple-wedge computation. The approximations involved in this process and sources for error or uncertainty have been discussed in detail, including comparisons to experimental data. A limited number of viscous computations on single-wedge, double-wedge, and flat-plate geometries described in the present chapter were undertaken to provide comparison with experimental heat flux measurements and to aid in the interpretation of the physics of reacting viscous flow, whether to develop an algorithm for measuring separation length from interferograms in Chapter 2, or to understand real-gas effects on boundary layers in Chapter 5. The computational approach described here for obtaining information about each experiment considers only the inviscid flow, but the analysis of experimental results in Chapter 6 also requires some information regarding the boundary layer. In the first part of the next chapter, a simplified theory for nonreacting flow is shown to provide a useful approximation of the boundary layer when applied to the local inviscid computational results.

Chapter 4 Theoretical Analysis and Modeling

By the methods described in Chapters 2 and 3, we have determined many of the flow parameters in each experiment required for analysis of separation length and reattachment heating in high-enthalpy double-wedge flows. The external inviscid flow is known from computation, but for most shots, the only information available regarding viscous regions of the flow consists of experimentally measured heat flux distributions and separation length. In Section 4.1, theories and models are presented for compressible boundary-layer flow, which, although restricted to chemically frozen flow, can provide additional information characterizing the boundary layer approaching separation. Of particular interest is the wall shear stress important for modeling separation length (*cf.* Section 1.4). In Section 4.2, a theoretical scaling law is developed for separation length in nonreacting flow based on asymptotic theory and on the simple model presented in Section 1.4. It is only by understanding the behavior of separation length in a chemically frozen flow that real-gas effects on the phenomenon can be elucidated. In-depth discussion on the effects of reacting flow is not included in this chapter, but is deferred until Chapter 5.

4.1 Compressible Boundary Layers

Section 4.1.1 covers the self-similar, compressible, laminar boundary-layer theory useful for obtaining skin friction and heat flux. A model for turbulent boundary layers is presented in Section 4.1.2 and used in Section 4.1.3 as an aid to interpreting experimental heat flux results downstream of reattachment. The models used to evaluate transport properties are presented in Section 4.1.4.

4.1.1 Laminar Theory

The full self-similar equations for a reacting boundary layer, though not useful for general nonequilibrium flow and not otherwise considered in this chapter, are presented here in Section 4.1.1.1 because (1) they are a superset of the simplified equations considered in this section, and (2) they are useful for discussing the physics of reacting boundary-layer flow in Chapter 5. Simplifications for frozen flow are introduced in Section 4.1.1.2. In Section 4.1.1.3, expressions for skin friction and heat flux are developed and compared to the single-wedge computational results from Section 3.4. Analytical expressions for boundary-layer thickness are given in Section 4.1.1.4.

4.1.1.1 Reacting-Flow Boundary Layer

The most general equations for laminar compressible boundary-layer flow in thermochemical nonequilibrium can be obtained by applying the boundary-layer approximations to Equations 3.1–3.4. Their solution, however, requires a finite-difference numerical technique. To obtain analytical results, one must invoke the concept of similarity, where, by an appropriate transformation of coordinates, the equations are under certain conditions reduced to ordinary differential equations. One condition always necessary is that flow properties are a function only of the transformed normal coordinate. The general transformations for planar flows we use here are often referred to as the Illingworth–Levy or Lees–Dorodnitsyn transformations (Illingworth, 1949; Lees, 1956) obtained by the technique of Li and Nagamatsu (1955);

$$\xi = \int_0^x \rho_e u_e \mu_e \, \mathrm{d}x \,, \tag{4.1}$$

$$\eta = \frac{\rho_e u_e}{\sqrt{2\xi}} \int_0^y \frac{\rho}{\rho_e} \, \mathrm{d}y \,, \tag{4.2}$$

where e denotes the edge of the boundary layer. Applying these transformations to the boundary-layer equations and assuming similar forms for the velocity, total enthalpy, and species concentrations,

$$u = u_e f'(\eta) \,, \qquad h_T = h_{T_e} g(\eta) \,, \qquad \text{and} \qquad Y_s = Y_{s_e} z_s(\eta) \,, \tag{4.3}$$

where prime denotes differentiation with respect to η, results in the following nondimensional similarity equations given by Dorrance (1962): conservation of mass,

$$\left(\frac{C}{Sc} z_s' \right)' + f z_s' = \frac{2\xi f' z_s'}{Y_{s_e}} \frac{\mathrm{d}Y_{s_e}}{\mathrm{d}\xi} - \frac{2\xi w_s}{\rho \rho_e u_e^2 \mu_e Y_{s_e}} \,; \tag{4.4}$$

conservation of momentum,

$$(Cf'')' + f f'' = \frac{2\xi}{u_e} \frac{\mathrm{d}u_e}{\mathrm{d}\xi} \left[(f')^2 - \frac{\rho_e}{\rho} \right] \,; \tag{4.5}$$

and conservation of energy,

$$\left(\frac{C}{Pr} g' \right)' + f g' = \frac{2\xi f' g}{h_{T_e}} \frac{\mathrm{d}h_{T_e}}{\mathrm{d}\xi} + \frac{u_e^2}{h_{T_e}} \left[\left(\frac{1}{Pr} - 1 \right) C f' f'' \right]' + \left[\frac{C}{Sc} \left(\frac{1}{Le} - 1 \right) \sum_s \frac{h_s Y_{s_e}}{h_{T_e}} z_s' \right]' \,. \tag{4.6}$$

Note that $C = \rho\mu / \rho_e \mu_e$ is the Chapman Rubesin parameter, $Pr = \mu c_p / k$ is the Prandtl number, $Sc = \mu / \rho D_{12}$ is the Schmidt number, and $Le = k / \rho c_p D_{12}$ is the Lewis number; all of these parameters are allowed to vary with η. Vibrational energy is not considered in this formulation, though Equation 4.6 does apply to vibrationally frozen flow if the constant vibrational energy is included

in the species enthalpy h_s. Equations 4.4–4.6 are ordinary differential equations as long as

$$\begin{aligned} &\frac{\xi}{u_e}\frac{\mathrm{d}u_e}{\mathrm{d}\xi} = \text{constant}, \quad \frac{\xi}{Y_{s_e}}\frac{\mathrm{d}Y_{s_e}}{\mathrm{d}\xi} = \text{constant}, \quad \frac{\xi w_s}{\rho\rho_e u_e^2 \mu_e Y_{s_e}} = \text{constant}, \\ &\frac{u_e^2}{h_{T_e}} = \text{constant}, \quad \frac{\xi}{h_{T_e}}\frac{\mathrm{d}h_{T_e}}{\mathrm{d}\xi} = \text{constant}, \quad \frac{h_s Y_{s_e}}{h_{T_e}} = \text{constant}, \end{aligned} \tag{4.7}$$

and all profiles are functions of η only (including h_s/h_{s_e} and ρ/ρ_e in addition to those in Equation 4.3). Only for certain special cases will these conditions be satisfied in a real flow. For edge conditions which vary slowly in ξ, however, the local similarity method may be used, whereby the self-similar boundary-layer equations are solved for each ξ-station of interest using the local edge properties. The history of the boundary layer only affects the local solution through the definition of ξ and η (Equations 4.1 and 4.2). It is shown by the computational results in Section 5.2.2.1 that self-similarity cannot be achieved for a general reacting-flow boundary layer, due to serious violation of the third condition in Equation 4.7. The reacting-flow equations given here are not used for further developments in this chapter, but are referred to in Section 5.2 to shed light on the physical mechanisms for real-gas effects on boundary layers.

4.1.1.2 Simplified Frozen-Flow Boundary Layer

In the interest of obtaining simple expressions for skin friction and heat transfer, we restrict ourselves here to chemically frozen boundary layers with a noncatalytic wall, *i.e.* $w_s = 0$ and $z_s(\eta) = 1$, so that Equation 4.4 is identically satisfied. The additional assumption of constant total enthalpy along the boundary-layer edge, h_{T_e} =constant, reduces Equation 4.6 to only three terms. A great simplification is also achieved by assuming a constant value for the Chapman–Rubesin parameter C and including it in the similarity variables,

$$\xi = \int_0^x C\rho_e u_e \mu_e \,\mathrm{d}x\,, \tag{4.8}$$

$$\eta = \frac{\rho_e u_e}{\sqrt{2\xi}} \int_0^y \frac{\rho}{\rho_e}\,\mathrm{d}y\,. \tag{4.9}$$

For an ideal fluid with a linear viscosity law, this assumption is exact; for the more general case where C varies throughout the boundary layer, a constant value might be used corresponding to evaluation of C at an appropriate condition, *e.g.* at the wall when evaluating skin friction which depends on the viscosity there. With these assumptions, the nondimensional momentum and energy equations for a similar boundary layer may be written, following Rogers (1992), as

$$f''' + ff'' = \hat{\beta}\left[(f')^2 - g\right], \tag{4.10}$$

$$g'' + Pr\, f g' = \frac{u_e^2}{h_{T_e}}(1 - Pr)\,(f' f'')' , \tag{4.11}$$

where

$$\hat{\beta} = \frac{h_{T_e}}{h_e}\frac{2\xi}{u_e}\frac{\mathrm{d}u_e}{\mathrm{d}\xi} \tag{4.12}$$

is analogous to the pressure gradient parameter in the Faulkner–Skan equations for an incompressible boundary layer, with $\hat{\beta} < 0$ corresponding to an adverse pressure gradient and $\hat{\beta} > 0$ corresponding to a favorable pressure gradient. The similarity conditions in Equation 4.7 reduce to the requirement that $\hat{\beta}$ =constant and either M_e = constant or $Pr = 1$. A constant value for $\hat{\beta}$ requires a certain Mach-number distribution given by $M_e \propto \xi^{\hat{\beta}/2}$. Again, the assumption of local similarity allows these equations to be applied to a general nonsimilar boundary layer with nonunit Prandtl number and arbitrary Mach-number distribution.

4.1.1.3 Skin Friction and Heat Flux

Two boundary-layer properties of primary importance in the present study are the wall shear stress, also called skin friction, and the wall heat flux. In nondimensional form, these are given by the skin friction coefficient

$$C_f = \frac{\tau_w}{\frac{1}{2}\rho_e u_e^2} = \frac{\mu_w\,(\partial u/\partial y)_w}{\frac{1}{2}\rho_e u_e^2} \tag{4.13}$$

and the Stanton Number

$$St = \frac{\dot{q}}{\rho_e u_e\,(h_e + r u_e^2/2 - h_w)} = \frac{k_w\,(\partial T/\partial y)_w}{\rho_e u_e\,(h_e + r u_e^2/2 - h_w)} \tag{4.14}$$

where r is the recovery factor, approximately $\sqrt{Pr}$ for laminar flow and $\sqrt[3]{Pr}$ for turbulent flow, that determines the adiabatic wall enthalpy $h_{aw} = h_e + r u_e^2/2$.

Consider first the skin friction coefficient, with $\partial u/\partial y$ written in terms of the coordinate transformations (Equations 4.8–4.9) and the similarity profile $f(\eta)$;

$$C_f = \frac{\mu_w \rho_w u_e^2 f''(0)/\sqrt{2\xi}}{\frac{1}{2}\rho_e u_e^2} = f''(0)\left(\frac{\mu_w \rho_w}{\mu_e \rho_e}\right)\sqrt{\frac{2}{C\,Re_x}\frac{\mathrm{d}\ln\xi}{\mathrm{d}\ln x}}\,. \tag{4.15}$$

Then with the constant C evaluated at the wall conditions, $C_w = \mu_w \rho_w/\mu_e \rho_e$, and writing $\lambda = f''(0)/\sqrt{2}$, this becomes

$$C_f = 2\lambda\sqrt{\frac{C_w}{Re_x}\frac{\mathrm{d}\ln\xi}{\mathrm{d}\ln x}}\,. \tag{4.16}$$

Under the local similarity assumption, Equation 4.16 applies to a general nonreacting boundary layer with arbitrary pressure gradient described locally by $\hat{\beta} \neq 0$. The wall shear parameter λ, however, must be found by solving Equations 4.10–4.11 for each desired combination of $\hat{\beta}$, Pr, and

M_e. For $Pr = 1$, the solution depends only on $\hat{\beta}$. Results for this restricted case are presented in the literature (see Rogers, 1992, or the seminal work of Cohen and Reshotko, 1956), from which it can be noted that λ is only a weak function of $\hat{\beta}$ for mild favorable pressure gradients (small positive $\hat{\beta}$) and cold walls (small $g_w = g(0) = h_w/h_{T_e}$). Under these conditions, the zero pressure gradient solution offers a reasonable approximation to the skin friction. The simplification $\hat{\beta} = 0$ explicitly decouples the momentum and energy equations, making Equation 4.10 identical with the Blasius equation for a self-similar, flat-plate incompressible boundary layer. The parameters $\hat{\beta}$ and g_w can be estimated for the present experiments by using the inviscid triple-wedge computational results to evaluate them. We find generally that $0.02 < \hat{\beta} < 0.2$ with $\hat{\beta} > 0.1$ only for a few cases. At low enthalpy, $0.03 < g_w < 0.08$, but at high enthalpy, $0.10 < g_w < 0.35$ if a frozen boundary layer with $\alpha_w = \alpha_e$ is assumed when calculating h_w; the chemical enthalpy of atomic nitrogen at the wall tends to increase g_w. If a fully recombined condition is assumed for the wall, then we obtain $g_w \lesssim 0.015$ for high-enthalpy shots. In either case, the experiments clearly fall within the regime of mild favorable pressure gradient and cold wall where the flat-plate boundary layer with constant edge properties is a reasonable assumption. Thus in Equation 4.16, we can set $\mathrm{d}\ln\xi/\mathrm{d}\ln x = 1$ and $\lambda = 0.332$ from the Blasius solution.

The resulting expression for skin friction on a flat-plate compressible boundary layer, $C_f = 0.664\sqrt{C_w/Re_x}$, works well for adiabatic walls but not for isothermal walls (White, 1991). It has been found empirically (Eckert, 1955) that replacing C_w in this expression by C^*, the Chapman–Rubesin parameter evaluated at a reference temperature T^* which depends on M_e and T_w/T_e, gives reasonably good accuracy for compressible flat-plate flows with hot or cold walls. Dorrance (1962) showed that this reference-temperature method in fact has a basis in similar boundary-layer theory. The generalized formula

$$\frac{T^*}{T_e} = \frac{1}{2}\left(1 + \frac{T_w}{T_e}\right) + \frac{(\gamma - 1)\sqrt{Pr}}{12} M_e^2 \tag{4.17}$$

is exact for $Le = 1$, $Pr = 1$, c_p =constant, and μ =constant, and is very accurate if we allow a power-law for viscosity, $\mu \propto T^n$. With this definition for the reference temperature, the skin friction coefficient is now given by

$$C_f = 0.664\sqrt{\frac{C^*}{Re_x}}. \tag{4.18}$$

Note that this is not the same as substituting C^* for C in Equation 4.15.

The validity of using Equation 4.18 under the conditions of the present experiments can be checked for the single-wedge cases computed in Section 3.4 using the N–S code in both viscous and inviscid modes. The viscous computational result for τ_w is taken as the "exact" solution, to be compared with τ_w calculated from Equations 4.13 and 4.18 using edge properties from the inviscid computational result. In other words, local flat-plate similarity is applied at each grid point on the wall of the inviscid solution. Models used to compute the transport parameters μ and Pr are given

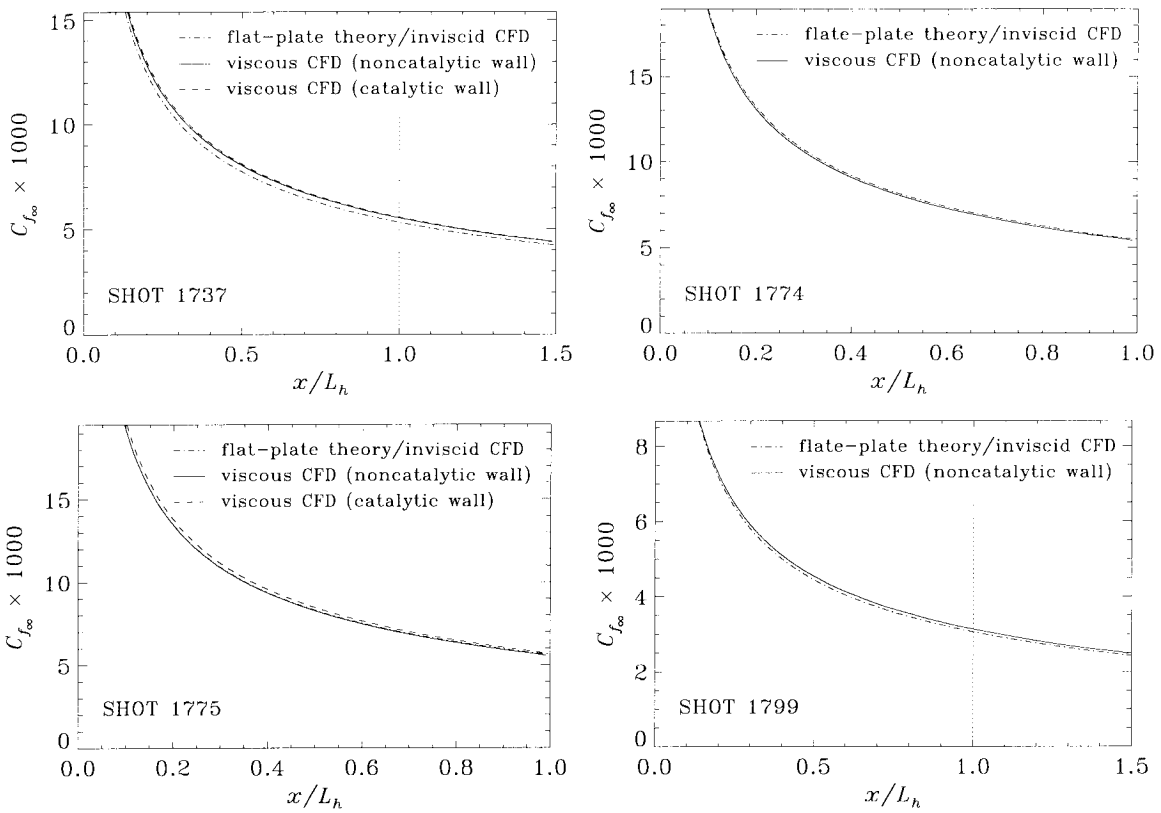

Figure 4.1: Comparisons between skin friction from viscous single wedge computations (solid curve for noncatalytic wall, dashed curve for catalytic wall) and flat-plate perfect-gas theory applied to results from inviscid single wedge computations (dash dot curve); shot 1737 (condition C2, $A_e/A_* = 100$, $\theta_1 = 30°$, $\theta_w = 0°$), shot 1774 (condition B1, $A_e/A_* = 400$, $\theta_1 = 15°$, $\theta_w = 15°$), shot 1775 (condition C2, $A_e/A_* = 400$, $\theta_1 = 15°$, $\theta_w = 15°$), and shot 1799 (condition B2, $A_e/A_* = 100$, $\theta_1 = 30°$, $\theta_w = 0°$). Dotted line is hingeline location.

below in Section 4.1.4. Note that γ in Equation 4.17 is computed according to the local dissociation fraction and vibrational energy (*cf.* Equation 3.30). The comparisons between theory and viscous computational fluid dynamics (CFD) are shown in Figure 4.1, where τ_w has been nondimensionalized by $\frac{1}{2}\rho_\infty u_\infty^2$ instead of $\frac{1}{2}\rho_e u_e^2$ for consistency (only the free-stream properties do not change between viscous and inviscid computations). For high-enthalpy cases, the viscous computational result with a catalytic wall is also shown. It is immediately clear that flat-plate nonreacting theory is adequate for predicting skin friction of a laminar boundary layer under these conditions, provided that the inviscid external flow is known. The difference is at most a few percent for the cases with $\theta_1 = 30°$ (shots 1737 and 1799 in Figure 4.1). Noting that the catalytic result for shot 1775 shows slightly increased wall shear over the noncatalytic result, the underprediction for the high-enthalpy shot 1737 might be caused by neglect of recombination in the frozen boundary-layer theory. Real-gas effects on the skin friction are discussed further in Section 5.2.

Turning now to the wall heat flux, we note that $\partial T/\partial y = (1/c_p)\partial h/\partial y$ and $(\partial h/\partial \eta)_w = h_{T_e} g'(0)$, giving for the Stanton number (*cf.* Equation 4.14)

$$St = \frac{h_{T_e} g'(0)}{\sqrt{2}\, Pr (h_{aw} - h_w)} \sqrt{\frac{C}{Re_x} \frac{\mathrm{d} \ln \xi}{\mathrm{d} \ln x}} = \frac{1}{2} C_f \left[\frac{g'(0)}{Pr\, f''(0)(g_{aw} - g_w)} \right] . \tag{4.19}$$

The factor in brackets is the Reynolds-analogy factor that relates heat flux to skin friction. Solutions to Equations 4.10 and 4.11 for $Pr = 1$ and nonzero $\hat{\beta}$ show that for mild favorable pressure gradients $g'(0)$ has a very weak dependence on $\hat{\beta}$, and with the additional restriction of a highly cooled wall, the Reynolds analogy factor is relatively constant. For flat-plate boundary layers with $Pr \neq 1$, it has been shown (empirically by van Driest (1959) and analytically by Spence (1960)) that a good approximation for cold walls is given by setting the Reynolds-analogy factor to $Pr^{-2/3}$, *i.e.*

$$St \simeq \frac{C_f}{2\, Pr^{2/3}} . \tag{4.20}$$

The usefulness of Equation 4.20 may also be checked using the single-wedge viscous and inviscid computations from Section 3.4. For each grid point along the wall in the inviscid solution, a theoretical value for the heat flux $\dot{q}$ corresponding to nonreacting flat-plate boundary-layer flow is found by substituting Equations 4.18 and 4.20 into Equation 4.14. Results are shown in Figure 4.2. As for Figure 4.1, free-stream conditions are used to nondimensionalize the heat flux, models for transport properties are given in Section 4.1.4, and catalytic-wall results from viscous CFD are shown for high-enthalpy cases. Also shown for the high-enthalpy shots 1737 and 1775 is a flat-plate theory result with h_w in Equation 4.14 evaluated for $\alpha_w = 0$, serving as a first approximation to a reacting-flow boundary layer that is fully recombined at the wall (whether due to a catalytic effect or to gas-phase reactions). This approximation considers the difference in chemical enthalpy across the boundary layer but neglects diffusion (which may increase the heat flux further) and assumes γ and Pr are constant at their edge values when calculating T^*. For either condition on α_w, the vibrational temperature is assumed in equilibrium with the wall temperature when computing h_w.

The flat-plate theory works well for predicting heat flux for the low-enthalpy shots 1774 and 1799 in Figure 4.2. For shot 1775, the noncatalytic CFD result is matched reasonably well by the original theory which assumes $\alpha_w = \alpha_e$. The noncatalytic CFD result for shot 1737, however, indicates that under this higher-density condition, recombination at the wall occurs without the presence of a catalytic effect, and the heat flux is better matched by the $\alpha_w = 0$ approximation. Though they considered only recombining stagnation-point boundary layers and not flat-plate boundary layers, Fay and Riddell (1958) showed that the heat flux is well predicted by this approximation when the Lewis number is close to unity or if the flow is close to equilibrium, because under these conditions the diffusion and conduction mechanisms for energy transport are of similar magnitude. Real-gas effects on heat flux are discussed further in Section 5.2.3. The flat-plate theory introduced here is used in Section 4.1.2 to aid in interpretation of experimental heat flux results in the flap region.

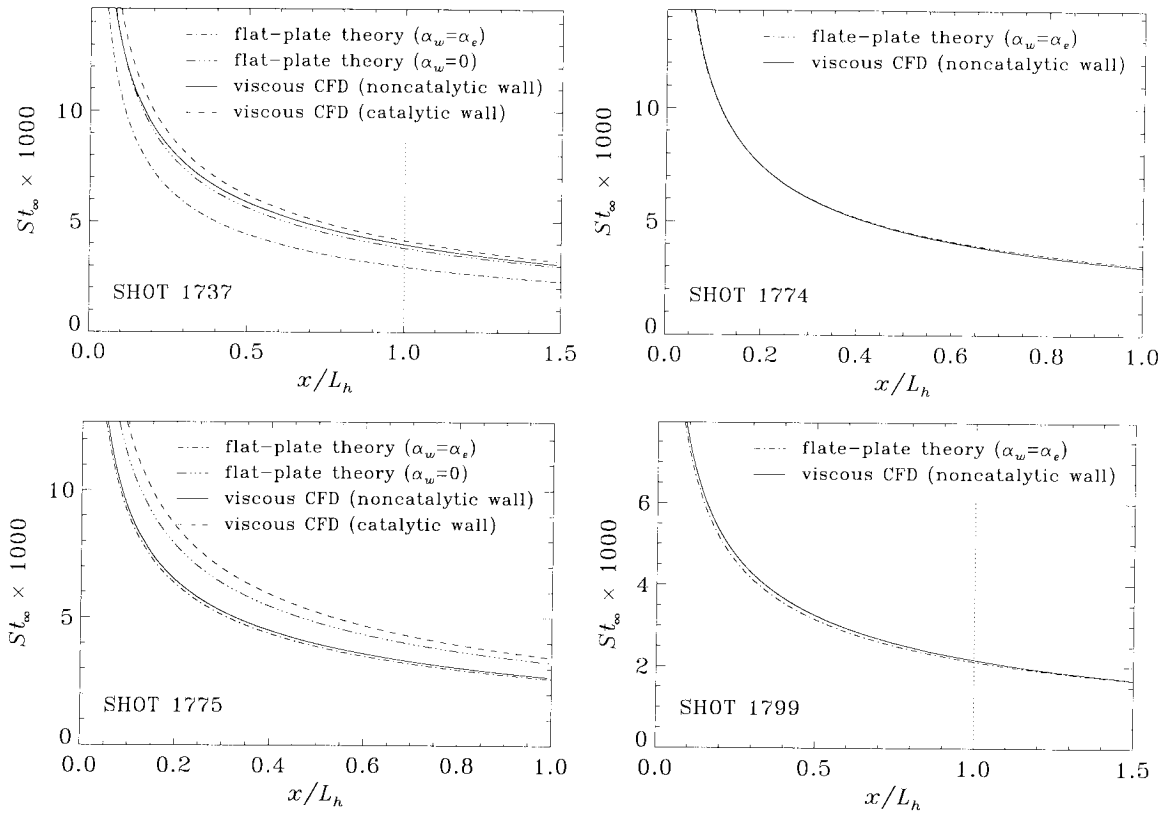

Figure 4.2: Comparisons between heat flux from viscous single wedge computations (solid curve for noncatalytic wall, dashed curve for catalytic wall) and flat-plate perfect-gas theory applied to results from inviscid single wedge computations (dash–dot curve for $\alpha_w = \alpha_e$ assumption, dash–dot–dot–dot curve for $\alpha_w = 0$ assumption); shot 1737 (condition C2, $A_e/A_* = 100$, $\theta_1 = 30°$, $\theta_w = 0°$), shot 1774 (condition B1, $A_e/A_* = 400$, $\theta_1 = 15°$, $\theta_w = 15°$), shot 1775 (condition C2, $A_e/A_* = 400$, $\theta_1 = 15°$, $\theta_w = 15°$), and shot 1799 (condition B2, $A_e/A_* = 100$, $\theta_1 = 30°$, $\theta_w = 0°$). Dotted line is hingeline location, and St_∞ is defined by Equation 2.12. Experimental results for these conditions are shown in Figure 3.13.

4.1.1.4 Boundary-Layer Thickness

For several applications in the present work, it is desirable to have analytical expressions for the boundary-layer thickness and displacement thickness (*e.g.* Sections 3.4.1 and 3.4.2). These can be obtained from the flat-plate boundary-layer theory presented here for nonreacting flows. Following Mallinson *et al.* (1996a), we start with the Crocco integral of the boundary-layer energy equation which relates the temperature and velocity profiles;

$$\frac{T}{T_e} = \frac{T_w}{T_e}(1 - f') + f' + \sqrt{Pr}\frac{\gamma - 1}{2}M_e^2(1 - f')f', \tag{4.21}$$

which is derived strictly for $C = 1$, $Pr = 1$, and c_p =constant, but the recovery factor $\sqrt{Pr}$ has been introduced to the compressibility term to account approximately for $Pr \neq 1$. This is substituted into the definition of boundary-layer thickness obtained by inverting the normal-coordinate

transformation (Equation 4.9),

$$\delta = \frac{\sqrt{2\xi}}{\rho_e u_e} \int_0^{\eta_e} \frac{\rho_e}{\rho} \, \mathrm{d}\eta = x \sqrt{\frac{2C}{Re_x} \frac{\mathrm{d}\ln\xi}{\mathrm{d}\ln x}} \int_0^{\eta_e} \frac{T}{T_e} \, \mathrm{d}\eta \,. \tag{4.22}$$

Since we are interested in the inertial boundary-layer thickness defined as the value of y where $u = 0.99u_e$, the upper integration limit is taken to be $\eta_e = \eta_{99}$ (where $f'(\eta_{99}) = 0.99$) as in Stewartson (1964), though Mallinson *et al.* (1996a) suggest using the thermal thickness $\eta_e = \eta_{99}/\sqrt{Pr}$. Setting $\mathrm{d}\ln\xi/\mathrm{d}\ln x = 1$ for flat-plate flow, evaluating the integrals with $f(\eta)$ given by the Blasius solution, and replacing C by C^* to approximately account for cold walls using the reference temperature, we obtain

$$\frac{\delta}{x} \simeq 1.719 \sqrt{\frac{C^*}{Re_x}} \left[1.866 + \frac{T_w}{T_e} + 0.192\sqrt{Pr}(\gamma - 1)M_e^2 \right] . \tag{4.23}$$

Note that while the derivation allows $C = C^* \neq 1$ in the momentum equation, it relies on setting $C = 1$ in the energy equation; this works because the temperature profile is insensitive to the viscosity law when $Pr \sim 1$ (Stewartson, 1964). Comparison of Equation 4.23 to the exact results of van Driest (1947) for cold walls (with $T_w/T_e = 0.25$, $Pr = 0.75$, and using Sutherland's viscosity law) shows good agreement for $M_e \lesssim 5$, the regime of interest to the present experiments. (Note that the result given by Mallinson *et al.* (1996a) includes an arithmetic error in the coefficient of the compressibility term.)

The displacement thickness δ^* is similarly defined as

$$\delta^* = \int_0^\infty \left(1 - \frac{\rho u}{\rho_e u_e} \right) \mathrm{d}y = x \sqrt{\frac{2C}{Re_x} \frac{\mathrm{d}\ln\xi}{\mathrm{d}\ln x}} \int_0^\infty \left[\frac{T}{T_e} - f' \right] \mathrm{d}\eta \,. \tag{4.24}$$

Again setting $\mathrm{d}\ln\xi/\mathrm{d}\ln x = 1$ and $C = C^*$, substituting Equation 4.21, and using a finite upper integration limit (the thermal thickness $\eta_{99}/\sqrt{Pr}$ works well since the integrand is already nearly zero at η_{99}),

$$\delta^* \simeq 1.721 \sqrt{\frac{C^*}{Re_x}} \left[\frac{T_w}{T_e} + 0.193\sqrt{Pr}(\gamma - 1)M_e^2 \right] . \tag{4.25}$$

As for the skin friction and heat flux results in the previous section, these expressions for δ and δ^* can be evaluated using local edge conditions from an inviscid calculation (including γ given by Equation 3.30), assuming frozen flow with constant species concentrations across the boundary layer, and using the transport models given below in Section 4.1.4. For purposes of setting up numerical grids for viscous computations on a wedge (*cf.* Sections 3.4 and 3.5), the edge conditions are estimated using perfect-gas relations for an oblique shock.

4.1.2 Turbulent Model

In order to investigate the state of the reattached boundary layer in the experiments, a predictive method is required for turbulent as well as laminar boundary layers. A successful model for compressible turbulent boundary layers with cold walls is that due to White and Christoph (1972), given by the following equations:

$$C_f \simeq \frac{1}{F_c} \frac{0.445}{\ln^2 (0.06\, Re_x\, F_{Re})}, \tag{4.26}$$

where

$$F_c = \frac{T_{aw}/Te - 1}{\left(\sin^{-1} A + \sin^{-1} B\right)^2}, \qquad F_{Re} = \frac{1}{\sqrt{F_c}} \frac{\mu_e}{\mu_w} \sqrt{\frac{T_e}{T_w}},$$

$$A = \frac{2a^2 - b}{\sqrt{b^2 + 4a^2}}, \qquad B = \frac{b}{\sqrt{b^2 + 4a^2}}, \tag{4.27}$$

$$a = \sqrt{\frac{\gamma - 1}{2} M_e^2 \frac{T_e}{T_w}}, \qquad b = \frac{T_{aw}}{T_w} - 1,$$

and the adiabatic wall temperature is given by

$$\frac{T_{aw}}{T_e} = 1 + r \frac{\gamma - 1}{2} M_e^2, \tag{4.28}$$

with the recovery factor $r \simeq \sqrt[3]{Pr}$ for a turbulent boundary layer. The Reynolds analogy factor is the same as that for laminar flows, therefore the Stanton number is given by Equation 4.20.

4.1.3 Comparison to Experiment

Transition to turbulence can cause large changes in separation length and reattachment heating depending on its location (*cf.* Sections 1.5.2.1 and 1.5.3). It is thus important to ascertain, if possible, the existence and location of transition in the experiments. Some of the experiments clearly have Reynolds number high enough to cause transition in the separated free-shear layer. Transition may also begin at or even slightly downstream of reattachment, such that much of the flap region is in a transitional regime with heat flux between the expected laminar and turbulent levels. The results in Section 3.5.3 suggest that transition may occur in many of the experiments. Inviscid triple-wedge computational results can be used together with analytical expressions given above for the laminar and turbulent heat flux of a flat-plate boundary layer in order to investigate the state of the reattached boundary layer in experiments.

Recall from Section 3.3.3 that the inviscid triple-wedge computations often underpredict the flap pressure. It is thus of interest to attempt a correction of the computed edge conditions used as input to boundary-layer theory, based on the experimental pressure measurements in the flap region. In Section 3.4.2 it was noted that, given a pressure correction, isentropic relations do not

recover the necessary corrections for temperature and density. A more reasonable method is to base corrections on changes in the oblique shock which processes the gas. Using the perfect-gas shock jump conditions, the relative change in pressure can be related to the relative changes in density and temperature, through the relative change in M_{2n}, the shock-normal Mach number upstream of the reattachment shock. This gives

$$\frac{\Delta\rho}{\rho} = F_\rho \frac{\Delta p}{p} \qquad \text{and} \qquad \frac{\Delta T}{T} = F_T \frac{\Delta p}{p}, \tag{4.29}$$

where F_ρ and F_T are functions of γ_2 and M_{2n}. In the present experiments, $1 < M_{2n} < 3$ and $1.3 < \gamma_2 < 1.4$; over this range, $0.35 < F_\rho < 0.77$ and $0.23 < F_T < 0.65$ in such a way that $F_\rho + F_T = 1$. Since the calculation of heat flux depends on the product $\rho_e T_e$ in the denominator of the Stanton-number definition (Equation 4.14), a reasonable approximation for the correction factors is

$$F_\rho = F_t = \frac{1}{2}. \tag{4.30}$$

The corrections also enter through the definition of T^* (Equation 4.17) and C_f (Equation 4.13) as well as the calculation of viscosity. A spline curve fit is made to the experimental pressure measurements in the flap region to give the corrected pressure, and the above factors are applied to obtain the corrected density and temperature over the same region. No correction is made to the velocity from the computation, and the Mach number is modified using the temperature correction.

Results obtained using laminar boundary-layer theory (Equations 4.14, 4.18 and 4.20) and the turbulent boundary-layer model (Equations 4.14, 4.20, and 4.26) with edge conditions from inviscid triple-wedge computations are shown in Figure 4.3 for four different experiments, including the three investigated by viscous double-wedge computations in Section 3.5.3. Just as for the viscous computational studies described in Chapter 3, the wall temperature is assumed constant at 300 K. Only the laminar theory is given upstream of separation. For the high-enthalpy cases (shots 1741 and 1796), results with and without the $\alpha_w = 0$ approximation are shown. Over the physical extent of the flap pressure measurements, the heat flux is recomputed using corrected edge conditions as discussed above; these are shown as curves through circular symbols denoting the pressure transducer locations. Due to recompression of the boundary layer upon reattachment, use of the leading edge of the first wedge as an origin for the flap boundary layer is inappropriate. It is not clear what choice of origin should give the most accurate results. One possibility is the reattachment location, but this may tend to overestimate the heat flux near reattachment because the stagnation point at reattachment is different from an inviscid stagnation point (*cf.* Figures 2.9 and 2.11). A worse difficulty is the rather large uncertainty in the measured reattachment location. A choice for the origin that gives more consistent results is the hingeline. Other authors, such as Kumar and Stollery (1994), have also used this origin for the reattaching boundary layer.

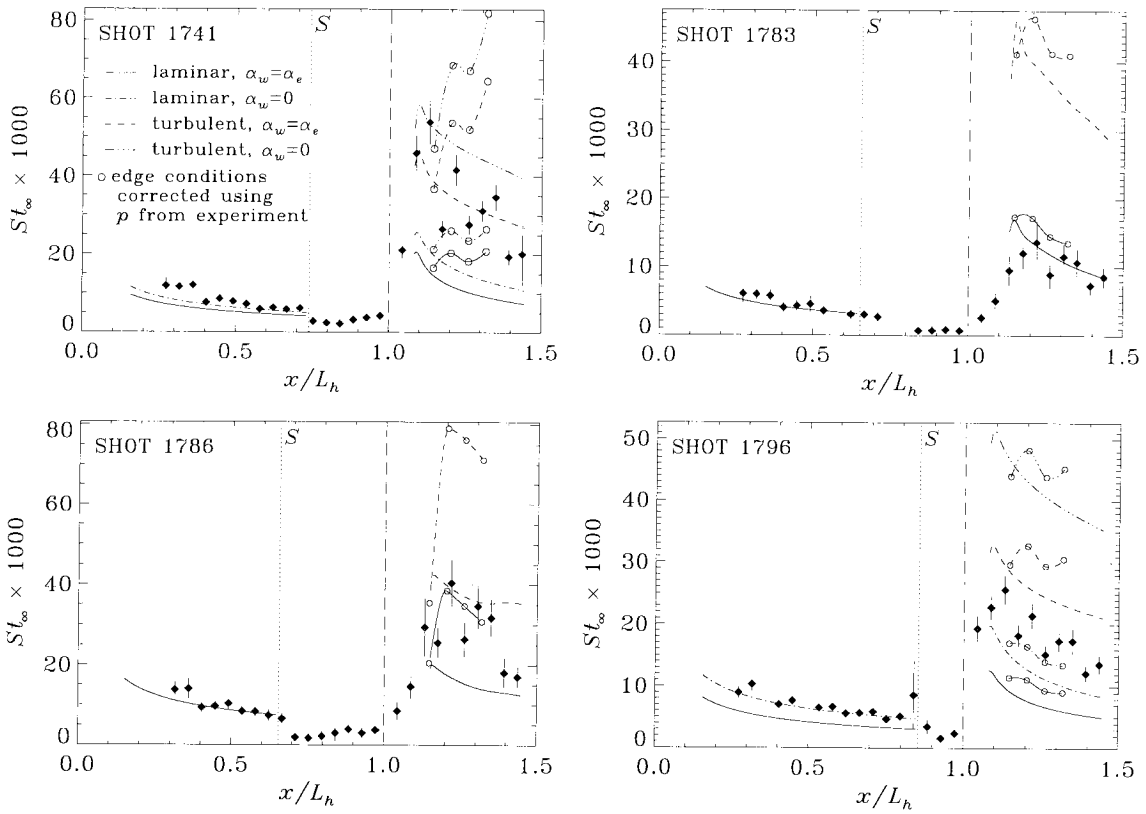

Figure 4.3: Four example comparisons between experimental heat flux and flat-plate boundary-layer theory, including different curves as indicated for laminar and turbulent results, with and without the $\alpha_w = 0$ approximation for high-enthalpy cases, and with and without the experimental pressure correction; shot 1741 (condition C2, $A_e/A_* = 225$, $\theta_1 = 30°$, $\theta_w = 25°$), shot 1783 (condition B1, $A_e/A_* = 225$, $\theta_1 = 15°$, $\theta_w = 20°$), shot 1786 (condition B1, $A_e/A_* = 400$, $\theta_1 = 40°$, $\theta_w = 20°$), and shot 1796 (condition C2, $A_e/A_* = 100$, $\theta_1 = 40°$, $\theta_w = 15°$). ♦ are experimental measurements, vertical dashed line is hingeline location, dotted line is separation location measured from flow visualization, St_∞ is defined by Equation 2.12, and error bars are described in Section 2.5.3. Origin for boundary layer downstream of reattachment is taken at $x = L_h$. Viscous computational results for shots 1741, 1783, and 1796 are shown in Figure 3.15.

For shot 1783 in Figure 4.3, the reattached boundary layer is clearly laminar, consistent with the viscous computational result in Figure 3.15. The results in Figure 3.15 indicated the possibility of transition occurring in shots 1741 and 1796. For shot 1796 in Figure 4.3, the $\alpha_w = 0$ approximation is assumed to be more accurate in the flap region because it represents the experimental data very well upstream of separation; hence the flap heat flux is seen to fall much closer to the laminar than the turbulent prediction. We conclude that reattachment is laminar in shot 1796, or at worst, just beginning transition; the discrepancy seen in the flap region when comparing experimental heat flux to viscous double-wedge computations (*cf.* Section 3.5.3) for this shot must be due to an error in the computation downstream of reattachment, because the heat flux upstream of separation is well matched. Shot 1741 in Figure 4.3 shows measured peak heating consistent with turbulent predictions. Further downstream of reattachment, however, the data actually lie closer to the laminar

result with measured-pressure correction and $\alpha_w = 0$ approximation, making it difficult to determine the boundary-layer state with certainty. The heat flux prediction based on experimental pressure generally shows better agreement with the measured heat flux, but not in every case as can be seen in for shot 1783. The correction can make a large difference in cases where the triple-wedge computation fails to reproduce the flow geometry of a strong shock–shock interaction, as shown for shot 1786 in Figure 4.3. The experimental data indicate jet impingement at $x \simeq 1.2L_h$, which is clearly missing from the uncorrected predictions. Instead of the transitional state suggested by the uncorrected predictions, the reattached boundary layer is assumed to be laminar.

Heat flux predictions such as those in Figure 4.3 are presented in Appendix F for every shot which has a corresponding inviscid triple-wedge computational result. In addition to the other evidence considered in Section 6.1.2, these predictions provide insight to the laminar–transitional–turbulent state of the reattaching boundary layer.

4.1.4 Models for Transport Properties

Throughout the present work, whenever the mixture viscosity or thermal conductivity is needed to evaluate a parameter (the Prandtl number in the expression for reference temperature, the free-stream Reynolds number, *etc.*), the simple models in this section are relied upon rather than the more complex models used in the N–S code (*cf.* Section 3.1.2). The viscosity for each species is found as a function of temperature using the curve fits of Blottner *et al.* (1971),

$$\mu_s = 0.1 \exp\left[(A_s \ln T + B_s) \ln T + C_s\right] , \tag{4.31}$$

where the constants A_s, B_s, and C_s are given in Table 4.1 for N and N_2, which, with T in degrees Kelvin, give μ_s in units of kg/m·s. The translational–rotational thermal conductivity for each species is given by an approximate Eucken relation (Vincenti and Kruger, 1965),

$$k_s = \mu_s \left(\frac{5}{2} c_{v_{tr,s}} + c_{v_{r,s}} \right) . \tag{4.32}$$

For molecular nitrogen, the vibrational thermal conductivity is found using Equation 3.13 and an approximate expression for D_{11} from kinetic theory (Chapman and Cowling, 1939);

$$k_v = \frac{6}{5} \mu_{N_2} (1 - \alpha) c_{v_v} , \tag{4.33}$$

where c_{v_v} is given by Equation 3.14. This is added to the translational–rotational conductivity to obtain the total thermal conductivity for N_2. Then the mixture viscosity and thermal conductivity are calculated from Wilke's mixing rule (Wilke, 1950);

$$\mu = \sum_s \frac{X_s \mu_s}{\phi_s}, \qquad k = \sum_s \frac{X_s k_s}{\phi_s},$$
$$\phi_s = \sum_r X_r \left[1 + \sqrt{\frac{\mu_r}{\mu_s}} \left(\frac{\mathcal{M}_r}{\mathcal{M}_s}\right)^{1/4}\right]^2 \left[8\left(1 + \frac{\mathcal{M}_s}{\mathcal{M}_r}\right)\right]^{-1/2}, \tag{4.34}$$

where X_s is the mole fraction and $\mathcal{M}_s$ the molecular weight of species s. The viscosity of dissociating nitrogen is seen in Figure 4.4 to increase with temperature and with atomic mass fraction α, but is much less sensitive to α at lower temperatures. Prandtl number $Pr = \mu c_p / k$ is formed using the mixture values for μ, c_p, and k. The specific heat at constant pressure, c_p, also includes vibrational heat capacity, *i.e.* $c_p = R + c_v + (1 - \alpha) c_{v_v}$. Under this simplified model, Pr depends only on the dissociation fraction and vibrational energy, not on the temperature.

species	A_s	B_s	C_s
N	0.0115572	0.6031679	-12.4327495
N_2	0.0268142	0.3177838	-11.3155513

Table 4.1: Coefficients in Equation 4.31 for viscosity curve fits of Blottner *et al.* (1971).

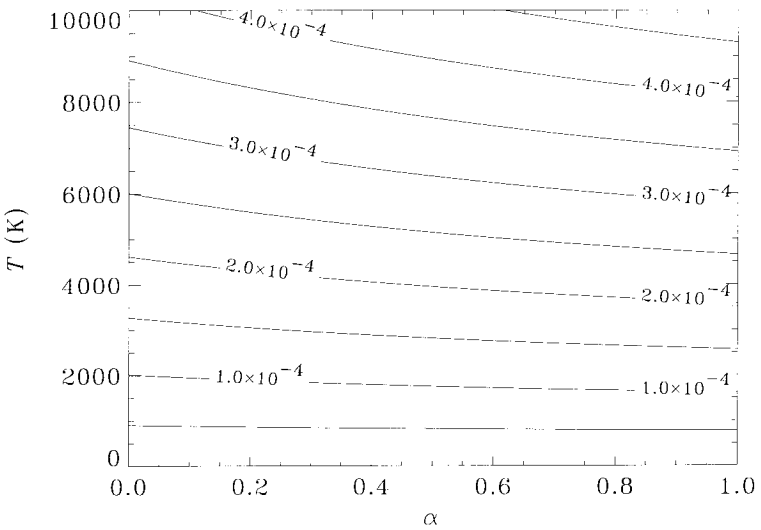

Figure 4.4: Contour plot of viscosity (in kg/m·s) for dissociating N_2 as a function of temperature and atomic mass fraction.

4.2 Analysis of Separation Length

The physical process that controls length of separation is complex (*cf.* Section 1.4). The limitations to varying important flow parameters independently of each other in the T5 experiments, along with the real-gas effects introduced at high enthalpy, make it impossible within the present study to completely verify any of the proposed scaling laws in Section 1.5.2.2 for perfect-gas flows. None

of the previously found empirical scaling laws include the effect of changing T_w/T_e, which varies significantly in the present experiments. It has been suggested by Katzer (1989) that the wall temperature effect might be obtained analytically through the application of triple-deck theory (TDT). The approach taken here is to develop a theoretical scaling law, similar to that of Burggraf (1975), which reproduces at least some of the factors in previously found empirical scaling laws but includes a wall temperature factor appropriate to cold nonadiabatic walls. Then dependencies on the remaining factors can be found empirically from the present experiments; this is done in Section 6.1. The necessary results from triple-deck theory are presented first in Section 4.2.1, followed by their application in Section 4.2.2 to a simple model of separation length to produce the scaling law. Additional triple-deck results of use in the present study are given in Section 4.2.3.

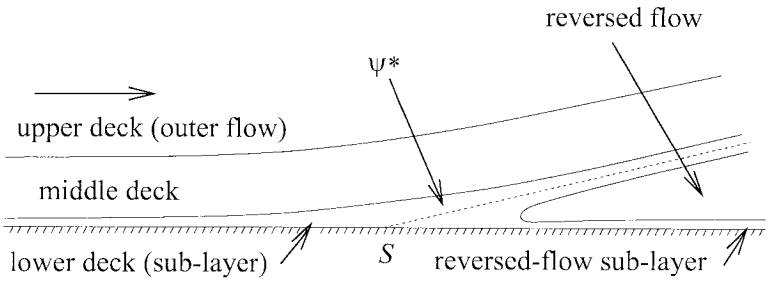

Figure 4.5: Schematic of multi-deck boundary-layer structure at separation.

4.2.1 Triple-Deck Theory

Triple-deck theory is an asymptotic theory for dealing with disturbances to a boundary layer, wherein the flow is divided into three separate decks, shown upstream of separation in Figure 4.5, with different physical processes dominating each deck. For a compressible boundary layer, the lower deck, or sub-layer, is viscous and incompressible, while the middle deck is inviscid and compressible. The upper deck consists of the fluid immediately outside the boundary layer. For supersonic flow and wall-generated disturbances (including free-interaction flow), the upper deck is described by isentropic flow relations. With hypersonic edge flow, compressive waves generated by the sub-layer tend to coalesce into shocks by the edge of the boundary layer, and a different assumption is needed for the upper deck (*e.g.* tangent-wedge theory).

The present analysis uses the classical triple-deck formulation of Stewartson and Williams (1969) for self-induced separation upstream of any externally enforced disturbance. They consider flow near separation as a perturbation to the undisturbed incoming boundary layer. Flow variables are expanded in terms of the small parameter $\epsilon = Re_{x_1}^{-1/8}$ and written as functions of the following scaled coordinates (recall that x_1 refers to the separation point):

$$Y_U = \epsilon^{-3} y \sim O(1), \quad X = \epsilon^{-3}(x - x_1) \sim O(1) \quad \text{in the upper deck,} \tag{4.35}$$

$$Y_M = \epsilon^{-4} y \sim O(1), \quad X = \epsilon^{-3}(x - x_1) \sim O(1) \quad \text{in the middle deck, and} \tag{4.36}$$

$$Y_L = \epsilon^{-5} y \sim O(1), \quad X = \epsilon^{-3}(x - x_1) \sim O(1) \quad \text{in the lower deck.} \tag{4.37}$$

This scaling is not evident *a priori*, but is assumed and found afterwards to produce self-consistent results. The expanded variables are substituted into the Navier–Stokes equations to obtain equations for the expansion coefficients, which are then simplified using scaling arguments and dominant balances. These simplifications show the middle deck to be inviscid and the lower deck to be incompressible and isothermal. The upper deck is described by the Prandtl–Glauert equation for inviscid supersonic (isentropic) flow. Perturbations to conduction and diffusion terms in the energy equation are not considered; in other words, the effect of heat transfer enters the problem only through the definition of the undisturbed boundary layer. In more recent work by Brown *et al.* (1990), a critical wall temperature is identified that governs the applicability of this assumption regarding the energy equation. The conditions of the present experiments are found to be well within the supercritical wall temperature range where classical theory is appropriate.

The boundary conditions between the decks are found by asymptotic matching, which can only be achieved for the scaling given above. The problem reduces to one of solving the equations for the lower deck subject to boundary conditions that are related to the effect of a pressure perturbation on the upper deck. In the triple-deck framework, the free interaction that leads to separation is one between the pressure rise in the outer flow and growth of the incompressible sub-layer; the middle deck transmits information between the upper and lower decks, and is simply displaced by the growth of the lower deck. In order to nondimensionalize the lower-deck equations to a canonical form, Stewartson and Williams (1969) introduced the following scaled variables (denoted with a tilde):

$$\begin{gathered} \tilde{x} = \frac{X}{a} = \frac{x - x_1}{a\epsilon^3}, \quad \tilde{y} = \frac{Y_L}{b} = \frac{y}{b\epsilon^5}, \quad \tilde{p} = \frac{p - p_1}{c\epsilon^2}, \\ \tilde{u} = \frac{bu}{d\epsilon}, \qquad \text{and} \qquad \tilde{v} = \frac{av}{d\epsilon^3}, \end{gathered} \tag{4.38}$$

where the constants a, b, c, and d are functions of the incoming Mach number M_1, the wall conditions, and the skin friction of the undisturbed boundary layer. These are given by

$$\begin{aligned} a &= \left[\frac{M_1^2}{\sqrt{M_1^2 - 1}}\right]^{3/4} \frac{U_0'(0)^{1/4}}{M_0'(0)^{3/2}} \left(\frac{\epsilon^8}{\nu_w}\right)^{1/4}, \quad b = \left[\frac{M_1^2}{\sqrt{M_1^2 - 1}}\right]^{1/4} \frac{\left(\nu_w/\epsilon^8\right)^{1/4}}{U_0'(0)^{1/4}\, M_0'(0)^{1/2}}, \\ c &= \frac{\gamma_1 p_1 M_1 M_0'(0)}{\left(M_1^2 - 1\right)^{1/4} U_0'(0)^{1/2}} \left(\frac{\nu_w}{\epsilon^8}\right)^{1/2}, \qquad d = \frac{M_1^2}{\left(M_1^2 - 1\right)^{1/4}} \frac{U_0'(0)^{1/2}}{M_0'(0)} \left(\frac{\nu_w}{\epsilon^8}\right)^{1/2}, \end{aligned} \tag{4.39}$$

where $\nu = \mu/\rho$ is the kinematic viscosity, $U_0(Y_M)$ and $M_0(Y_M)$ are the velocity and Mach-number profiles of the undisturbed boundary layer, and prime denotes differentiation with respect to Y_M.

Note that $U_0'(0)$ and $M_0'(0)$ are related simply by a_w, the sound speed at wall conditions. In these scaled variables, the lower-deck equations have exactly the same form as the incompressible boundary-layer equations.

It is not, however, the solution of the lower-deck equations that are of interest for the present study. Instead, we are interested in the solution of an asymptotic structure describing the flow well downstream of separation, which relies on the same scaling given above. This structure, presented by Stewartson and Williams (1973) as well as Neiland (1971b), has five decks as shown in Figure 4.5; what was the lower deck upstream of separation becomes a thin incompressible layer in which the dividing streamline ψ^* is embedded, and underneath this there are inviscid and viscous decks corresponding to the reversed flow. For large scaled distance $\tilde{x}$ downstream of separation, a form is found for the flow near ψ^* that asymptotically matches the flow near separation; the leading-order term in the asymptotic series for the scaled velocity is

$$\tilde{u} \sim \tilde{x}^{1/3} F_0'(\tilde{\eta}), \qquad \text{with} \qquad \tilde{\eta} = \frac{\tilde{y} - A(\tilde{x})}{\tilde{x}^{1/3}}. \tag{4.40}$$

Prime denotes differentiation with respect to $\tilde{\eta}$, and the function $A(\tilde{x})$ is linear for large $\tilde{x}$ such that $\tilde{\eta} = 0$ corresponds to the dividing streamline. In the next section, this result from multi-structural boundary-layer theory is applied to a simple model for separation length. The scaling transformations given above in Equations 4.38 and 4.39 are used to relate Equation 4.40 to physical variables. We mention in passing a thorough review of these classical multi-structural boundary-layer techniques by Stewartson (1974).

4.2.2 Scaling of Separation Length

The process controlling separation length is modeled in Section 1.4 as a balance between pressure forces and shear forces acting on the separation bubble. Here we rewrite Equation 1.1 as

$$\int_{x_1}^{x_R} \left(\mu \frac{\partial u}{\partial y} \right)_{\psi^*} \mathrm{d}x = \int_0^{y_R} (p_{\psi^*} - p_2) \, \mathrm{d}y \propto y_R (p_3 - p_2). \tag{4.41}$$

The proportionality introduced on the right-hand side implies that the pressure at reattachment scales with the inviscid flap pressure downstream. This is not expected in general to be true, but for lack of any better theory of the reattachment process, is assumed to hold at least approximately under the conditions of the present work. Then, using the transformations in Equation 4.38, the chain rule for partial derivatives, plus the leading-order asymptotic expression for velocity and the $\tilde{y}$ $\tilde{\eta}$ relationship from Equation 4.40, the integrand on the left-hand side of Equation 4.41 may be written

$$\left. \frac{\partial u}{\partial y} \right|_{\psi^*} \mathrm{d}x \sim \frac{ad}{\epsilon b^2} F_0''(0) \, \mathrm{d}\tilde{x}. \tag{4.42}$$

Similarly, we write $y_R = \epsilon^5 b \tilde{x}^{1/3}$ from the definition of $\tilde{\eta}$. Substituting these into Equation 4.41, taking the viscosity along the dividing streamline to be the same as that at the wall near separation ($\mu_{\psi^*} = \mu_w$), and solving for $\tilde{x}_R$ gives

$$\tilde{x}_R \propto \left[\frac{\epsilon^6 b^3 (p_3 - p_2)}{a\, d\, \mu_w F''(0)}\right]^{3/2} . \tag{4.43}$$

Then $x_R - x_1$ is identified with L_{sep} so that

$$L_{sep} = \epsilon^3 a \tilde{x}_R \propto \epsilon^{12} \left(\frac{b^9}{a}\right)^{1/2} \left[\frac{(p_3 - p_2)}{\mu_w d\, F_0''(0)}\right]^{3/2} . \tag{4.44}$$

Finally, the constants from Equation 4.39 are expanded, giving

$$L_{sep} \propto \frac{(p_3 - p_2)^{3/2}}{\mu_w \rho_w^{1/2} U_0'(0)^2 Re_{x_1}} , \tag{4.45}$$

and with the help of the perfect-gas relation for sound speed,

$$\frac{L_{sep}}{x_1} \propto \frac{1}{\gamma_1^{3/2} M_1^3} \left(\frac{u_e}{x_1 U_0'(0)}\right)^2 \left(\frac{\rho_e}{\rho_w}\right)^{1/2} \left(\frac{\mu_e}{\mu_w}\right) \left(\frac{p_3 - p_2}{p_1}\right)^{3/2} . \tag{4.46}$$

The parameter $F_0''(0)$ has been left out because it is a constant, and the subscript e refers to the boundary-layer edge upstream of separation (*i.e.* the incoming conditions in region 1).

Equation 4.46 is a generalized result valid for any form of the undisturbed boundary-layer profile. It is most important to note the inverse-square dependence on the velocity gradient at the wall of the undisturbed boundary layer, *i.e.* the development of shear stress along the dividing streamline is characterized by the wall shear of the incoming boundary layer. In Section 4.1.1.3 it was shown that the flat-plate compressible Blasius solution for a laminar boundary layer, with reference-temperature modification, gives a reasonable approximation for skin friction under the conditions of the present experiments. Thus we evaluate $U_0'(0)$ from Equations 4.13 and 4.18 as

$$U_0'(0) = \frac{\partial y}{\partial Y_M} \frac{\partial u}{\partial y}\bigg|_w = 0.332 \frac{u_e\, \mu^*\, \rho^*}{x_1\, \mu_w\, \rho_w} \sqrt{\frac{1}{C^*}} . \tag{4.47}$$

Substituting this into Equation 4.46 gives

$$\frac{L_{sep}}{x_1} \propto \frac{\Lambda_1}{\gamma_1^{3/2} M_1^3} \left(\frac{p_3 - p_2}{p_1}\right)^{3/2} , \tag{4.48}$$

where

$$\Lambda = \left(\frac{\mu_w}{\mu^*}\right) \left(\frac{T^*}{T_e}\right) \left(\frac{T_w}{T_e}\right)^{1/2} . \tag{4.49}$$

The dependence on M_1 is exactly as found by experiment in previous studies (*cf.* Section 1.5.2.2), but the dependence on the reattachment pressure rise does not correspond to previous empirical results. The dependence on γ_1 has not been shown in previous work presumably because it does not vary in the perfect-gas flows usually considered. The factor Λ is unique to the present work and essentially describes the effect on skin friction of wall-to-edge temperature ratio for arbitrary viscosity law, the latter accounted for using the reference-temperature concept. For an ideal fluid with $C = 1$, Λ reduces to $(T_w/T_e)^{3/2}$. Interestingly, if we follow the method of Burggraf (1975), who considered not the model in Equation 4.41 but the model of Chapman *et al.* (1958) concerning total pressure (*cf.* Section 1.4), and apply the triple-deck result to the incompressible Bernoulli equation along the dividing streamline, we obtain the same result. This is because, within the triple-deck framework, the dividing streamline resides inside a thin incompressible layer.

Equation 4.48 may be viewed as a decoding, generalization, and extension of the result of Burggraf (1975) for well separated flows. It cannot provide a predictive capability, only a partial scaling for the length of separation. It corresponds to the leading-order term of a theory that is asymptotic for large Re_{x_1}, and hence any dependence on Re_{x_1} must be found by experiment. The correct dependence on the pressure rise at reattachment must also be found empirically. In Section 6.1, the new factor Λ is shown to provide some measure of collapse for data spanning a large range in Λ.

4.2.3 Other Triple-Deck Results

Briefly mentioned here are some additional results from triple-deck theory regarding the plateau region in well separated flow. These are based on the results of Inger (1994a,b), who applied the reference-temperature concept to triple-deck theory for supersonic separation. The flap pressure for incipient separation p_{inc} and the plateau pressure p_2 are assumed to scale in an identical fashion to each other;

$$\frac{p_2 - p_1}{p_1} \propto \frac{p_{\text{inc}} - p_1}{p_1} \sim 1.04\gamma_1 M_1^2 \left(\frac{C^*/Re_{x_1}}{M_1^2 - 1} \right)^{1/4} . \tag{4.50}$$

The constant of proportionality is based on results for scaled plateau pressure $\tilde{p}_2$ from triple-deck computations. The angle of the separation streamline θ_{sep} and the ramp angle for incipient separation θ_{inc} also scale in the same manner, as (the proportionality again coming from calculations)

$$\theta_{sep} \propto \theta_{inc} \sim 0.91 \left[\frac{C^*}{Re_{x_1}} \left(M_1^2 - 1 \right) \right]^{1/4} . \tag{4.51}$$

4.3 Summary

A simplified flat-plate, nonreacting boundary-layer theory based on the reference-temperature concept, when used with edge conditions computed by the methods of Chapter 3 for nonequilibrium

inviscid external flow, was shown to provide reasonable approximations of the skin friction and heat transfer under the experimental conditions, as evidenced by comparisons to experimental data as well as full nonequilibrium viscous computational results. Skin friction estimates are desired for analysis of experimental separation length measurements, and heat flux estimates are useful in determining whether a particular experiment experiences transition to turbulence.

A new scaling for separation length in nonreacting flow, extending previous results to arbitrary viscosity law using the reference-temperature concept, was developed by application of an asymptotic multi-deck theoretical result for flow downstream of separation to the model for separation length presented in Section 1.4. The result partially reproduces previously found empirical scaling laws, but more importantly, offers a theoretical basis for including wall temperature effects in the scaling. In the next chapter, this scaling is used along with the boundary-layer theory mentioned above to develop part of a framework for describing real-gas effects on separation length. It is also used in Chapter 6 to interpret experimental measurements of separation length.

Chapter 5 Analysis of Real-Gas Effects

In Chapter 4, analytical developments for nonreacting flow were presented concerning boundary layers and separation length; in this chapter, these are used along with models for reacting flow to shed light on real-gas effects in shock/boundary-layer interaction. A framework is developed to describe the effects of chemistry on the phenomena of separation length and reattachment heating in a qualitative sense. The central idea behind this framework is a classification scheme which divides mechanisms for real-gas effects into processes that occur external and internal to viscous flow regions such as the boundary layer and separated region. External mechanisms are considered first in Section 5.1, and internal mechanisms second in Section 5.2.

5.1 External Mechanisms

External mechanisms for real-gas effects arise from changes in the external inviscid flow field over a double wedge, with respect to thermochemically frozen flow at the same free-stream conditions, and the effect these changes have on a nonreacting boundary layer, shear layer, and separation bubble. The expressions given in Chapter 4 for separation length and heat transfer with frozen boundary-layer flow can be used to investigate external mechanisms independently of internal mechanisms by considering boundary-layer edge conditions corresponding to frozen and reacting external flow. A simplified model useful for estimating real-gas effects in the external flow is the ideal dissociating gas (IDG) model due to Lighthill (1957). This model and the method by which it is used to compute frozen and equilibrium external flow conditions are described in Section 5.1.1. Then in Section 5.1.2, the IDG model is used to assess external real-gas effects on separation length by considering changes, due to equilibrium flow, in the various parameters of a scaling law for separation length. This scaling law is assembled from the present theoretical result in Section 4.2.2, present empirical results (*cf.* Section 6.1.1), and previous empirical results (*cf.* Section 1.5.2.2). Finally, in Section 5.1.3, the IDG model is applied in a similar manner to a scaling law for reattachment heat flux constructed from the analysis in Section 4.1.1 and previous results given in Section 1.5.3.

5.1.1 Application of the IDG Model

The heart of the IDG model is an approximation concerning the contribution of internal energy modes to the law of mass action for a binary dissociating gas. Specifically, the factor inside square brackets in Equation 3.28 is a weak function of temperature over a wide range, and is taken to be

constant at an average value ρ_d (often called the characteristic density since it has units of kg/m^3). This approximation effectively forces the vibrational energy of the molecular component of the gas to be constant at half of its fully excited value, *i.e.* for nitrogen, $c_{v_v} = \frac{1}{2}R_{N_2}$ and the caloric equation of state becomes

$$h = R_{N_2}\left[(4+\alpha)T + \alpha\theta_d\right] \tag{5.1}$$

(θ_d is the characteristic temperature for dissociation). In practice, this result for the vibrational energy is what most limits the usefulness of the model. The IDG model is of interest here for the relative ease with it produces frozen-flow and equilibrium-flow solutions for the oblique shocks on a double wedge. The nonequilibrium IDG model is used only to find the initial postshock reaction rates; calculation of nonequilibrium flow fields with multiple shocks requires advanced computational techniques such as that already implemented for more detailed thermochemical modeling (*cf.* Section 3.1). The equilibrium and frozen solutions can in many cases indicate the limits of real-gas effects.

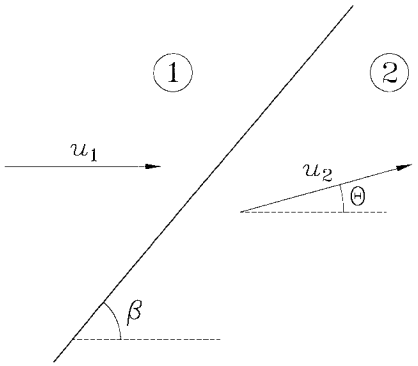

Figure 5.1: Notation for IDG oblique-shock equations.

The IDG model has previously been applied to oblique shocks by Sanderson (1995); rather than repeat the entire analysis, we give only results of direct interest to the present study. First, a nondimensional form of the shock jump equations is obtained by introducing the following parameters after Hornung (1995), written here for nitrogen: the static-to-dynamic pressure ratio

$$P = \frac{p}{\rho u^2} \propto \frac{1}{M^2}, \tag{5.2}$$

the ratio of kinetic energy to dissociation energy

$$K = \frac{u^2}{2R_{N_2}\theta_d}, \tag{5.3}$$

and the ratio of stagnation enthalpy to dissociation energy

$$H_0 = \frac{h_0}{R_{N_2}\theta_d} = K\left[1 + 2P\left(\frac{4+\alpha}{1+\alpha}\right)\right] + \alpha. \tag{5.4}$$

For an oblique shock as shown in Figure 5.1, with shock angle β relative to the upstream flow direction, and upstream and downstream states denoted by 1 and 2 respectively, the normal-shock jump conditions are applied using the shock-normal component of the velocity; thus we need the shock-normal component of the above nondimensional parameters as well,

$$P_{1n} = \frac{P_1}{\sin^2\beta}, \qquad K_{1n} = K_1 \sin^2\beta, \qquad \text{and} \qquad H_{0_{1n}} = fn\,(P_{1n},\, K_{1n})\,. \tag{5.5}$$

Introducing also the notation $\hat{\rho} = \rho_2/\rho_1$, *etc.* for the postshock/preshock ratio, and utilizing the ideal-gas thermal equation of state (*cf.* Equation 3.23) with the IDG caloric equation of state (Equation 5.1), the conservation equations for momentum and energy (*cf.* Equations 3.25 3.26) can be combined to give a single quadratic equation for the density ratio across an oblique shock,

$$(H_{0_{1n}} - \alpha_2)\,\hat{\rho}^2 - 2K_{1n}(1 + P_{1n})\left(\frac{4+\alpha_2}{1+\alpha_2}\right)\hat{\rho} + K_{1n}\left(\frac{7+\alpha_2}{1+\alpha_2}\right) = 0\,. \tag{5.6}$$

Only one of the two solutions corresponds to a shock discontinuity (the other corresponds to relaxation from a nonequilibrium upstream state), given always by the larger of the two roots;

$$\hat{\rho} = \frac{K_{1n}(1+P_{1n})(4+\alpha_2)(1+\sqrt{D})}{(H_{0_{1n}} - \alpha_2)(1+\alpha_2)}, \tag{5.7}$$

$$D = 1 - \frac{(H_{0_{1n}} - \alpha_2)(7+\alpha_2)(1+\alpha_2)}{K_{1n}(4+\alpha_2)^2(1+P_{1n})^2}\,. \tag{5.8}$$

Written this way, it is apparent that a real solution must have

$$H_{0_{1n}} > \alpha_2 \geq \alpha_{min} = fn(\alpha_1,\, K_{1n},\, P_{1n})\,, \tag{5.9}$$

where the determinant $D = 0$ at $\alpha_2 = \alpha_{min}$. For frozen flow, $\alpha_2 = \alpha_1$ and the density ratio reduces to

$$\hat{\rho}_{fr} = \frac{7+\alpha_1}{1+\alpha_1+2P_{1n}(4+\alpha_1)}\,. \tag{5.10}$$

For equilibrium flow, α_2 is given by the solution to Equation 3.28, which for the IDG model using the present oblique-shock notation is

$$\frac{\alpha_2^2}{1-\alpha_2} = \frac{\rho_d}{\rho_1}\exp\left\{\frac{(1+\alpha_2)\hat{\rho}^2}{2K_{1n}\left[1-\hat{\rho}(1+P_{1n})\right]}\right\}. \tag{5.11}$$

For wedge flows, the flow deflection angle θ shown in Figure 5.1 is known but the shock angle β is not; another equation relating θ and β is needed to close the problem. From geometrical considerations and conservation of mass,

$$\tan(\beta - \theta) = \frac{\tan\beta}{\hat{\rho}}\,. \tag{5.12}$$

For a given wedge angle θ and upstream state (α_1, P_1, K_1, and ρ_d/ρ_1), a steady oblique shock solution is found by simultaneously solving Equations 5.7, 5.8, 5.11, and 5.12 for equilibrium flow, or Equations 5.10 and 5.12 for frozen flow (knowledge of ρ_d/ρ_1 is not required for a frozen-flow solution). In general, there are two oblique-shock solutions corresponding to two values of β; only

the weak-shock solution, with the smaller value of β, is physically realistic for a shock attached to the wedge leading edge. (Note that the phrase "weak oblique shock" used elsewhere in this work does not refer to the weak-shock solution in general, but to a weak-shock solution with small $\hat{\rho}$.) There is only one solution at $\theta = \theta_{max}$, the wedge angle for shock detachment. The solution procedure requires numerical iterative methods, with two levels of iteration for the equilibrium case since α_2 is given only implicitly by Equation 5.11. In the present work, we rely on Brent's inverse quadratic interpolation algorithm to find the zero of a function and Brent's inverse parabolic interpolation algorithm to find the minimum of a function; both algorithms are presented by Press *et al.* (1992). For frozen flow, the solution procedure to find β_{fr} and $\hat{\rho}_{fr}$ is as follows:

1. Given α_1, P_1, and K_1, find θ_{max} and the corresponding β_{max} by minimizing $-\theta(\beta)$ using Equation 5.12 with $\hat{\rho}(\beta)$ given explicitly by Equation 5.10 and with β initially bracketed between the Mach angle $\beta_{min} = \sin^{-1}(1/M_1)$ and 90°.

2. If $\theta < \theta_{max}$, then find β_{fr} by zeroing Equation 5.12 with $\hat{\rho}_{fr}$ given explicitly by Equation 5.10 and with initial bracketing $\beta \in (\beta_{min}, \beta_{max})$ to assure convergence on the weak-shock solution.

Note that β_{max} does not refer to the maximum value of β (which is 90°), but to the value of β at the maximum value of θ. The procedure for equilibrium flow, to find β_{eq}, $\hat{\rho}_{eq}$, and α_2, is more complicated:

1. Given α_1, P_1, K_1, and ρ_d/ρ_1, first create a table of equilibrium oblique-shock solutions $\hat{\rho}(\beta)$ and $\alpha_2(\beta)$ by the following method:

   (a) specify values for β by dividing into small equal intervals the range between the Mach angle $\beta_{min} = \sin^{-1}(1/M_1)$ and 90°;

   (b) for each value of β in the table, first find two values of α_2 which bracket the equilibrium solution, starting with $\alpha_2 \in [0, H_{0_{1_n}})$, but in the case that $D(0) < 0$, replacing the lower bound with α_{min} found by zeroing $D(\alpha_2)$ (Equation 5.8);

   (c) with correct bracketing as above, find the equilibrium solution α_2 for each value of β by zeroing Equation 5.11 with $\hat{\rho}$ given explicitly by Equations 5.7 and 5.8;

   (d) if no solution is found for $\beta = \beta_{min}$, then perform a simple iteration to find a new β_{min} for the table, corresponding to the smallest β for which an equilibrium shock solution exists (this occurs only for $\alpha_1 > 0$ and arises from the Chapman–Jouget (C-J) limit for exothermic discontinuities, *i.e.* for $\beta < \beta_{min}$, an equilibrium downstream state with $\alpha_2 < \alpha_1$ cannot be attained by a discontinuous process).

2. Find θ_{max} and β_{max} by minimizing $-\theta$ using Equation 5.12 with $\hat{\rho}(\beta)$ given by spline interpolation of the equilibrium solution table, and with β bracketed by the table limits β_{min} and 90°; obtain θ_{min} directly from Equation 5.12 using the lower limit β_{min}.

3. If $\theta_{min} < \theta < \theta_{max}$, then find β_{eq} by zeroing Equation 5.12 with $\hat{\rho}_{eq}$ given by spline interpolation of the equilibrium solution table.

4. Finally, β_{eq} can be used to find α_2 by spline interpolation of the equilibrium solution table.

Once $\hat{\rho}$, β, and α_2 are found as described above, for either frozen or equilibrium flow, other important parameters can be evaluated explicitly. The speed ratio is found from conservation of mass,

$$\hat{u} = \frac{\sin\beta}{\hat{\rho}\sin(\beta-\theta)}, \tag{5.13}$$

and the temperature ratio is found from the thermal equation of state with pressure eliminated using the momentum equation,

$$\hat{T} = \frac{1}{\hat{\rho}}\left(\frac{1+\alpha_1}{1+\alpha_2}\right)\left[1+\left(1-\frac{1}{\hat{\rho}}\right)\frac{1}{P_{1n}}\right]. \tag{5.14}$$

The pressure ratio is found similarly. Dimensional temperatures are needed for several purposes, including evaluation of the Mach number, viscosity, and reaction rate. The nondimensional parameters P and K do not explicitly contain temperature, but may be substituted into the thermal equation of state to give

$$T = \frac{2PK\theta_d}{1+\alpha}. \tag{5.15}$$

Calculation of the Mach number also requires an expression for the sound speed, which is different for frozen and equilibrium states;

$$a_{fr}^2 = \frac{(4+\alpha)}{3}R_{N_2}(1+\alpha)T, \tag{5.16}$$

$$a_{eq}^2 = \frac{R_{N_2}T\left[\alpha(1-\alpha^2)\left(1+2T/\theta_d\right)+\left(8+3\alpha-\alpha^3\right)\left(T/\theta_d\right)^2\right]}{\alpha(1-\alpha)+3(2-\alpha)\left(T/\theta_d\right)^2}. \tag{5.17}$$

Viscosity is found using the model described in Section 4.1.4. The initial reaction rate immediately downstream of a frozen shock, with shock angle fixed at β_{eq} given by the equilibrium shock solution, provides insight regarding the extent to which the nonequilibrium solution may depart from the frozen or equilibrium solutions. An expression for the local reaction rate due to Freeman (1958) is

$$\frac{\mathrm{d}\alpha}{\mathrm{d}t} = C\rho T^{\eta}\left[(1-\alpha)\exp\left(\frac{-\theta_d}{T}\right)-\frac{\rho}{\rho_d}\alpha^2\right]. \tag{5.18}$$

This is evaluated at the downstream state of a frozen oblique shock with $\beta = \beta_{eq}$ and nondimensionalized using a time scale based on the downstream velocity u_2 from the equilibrium solution and the length of the wedge;

$$\Delta = \frac{L}{u_{2,eq}}\left(\frac{\mathrm{d}\alpha_2}{\mathrm{d}t}\right)_{fr,\,\beta=\beta_{eq}}. \tag{5.19}$$

The IDG Damköhler number Δ defined here is slightly different from the typical definition given for blunt-body flows where the (shock-normal) free-stream velocity is used. Equilibrium flow corresponds to $\Delta \gg 1$ while frozen flow corresponds to $\Delta \ll 1$. For $\Delta \sim 1$, the distance downstream of the shock and parallel to the wedge that is required to achieve equilibrium is of the same order as the length of the wedge itself, and nonequilibrium effects are important. The constants R_{N_2}, ρ_d, θ_d, C, and η used in the IDG model for nitrogen are given in Table 5.1

R_{N_2}	ρ_d	θ_d	C	η
297 J/kg·K	1.3×10^5 kg/m^3	113200 K	2.7×10^{21} m^3·K$^{2.5}$/kg·s	-2.5

Table 5.1: Constants used in the IDG model.

The IDG model for oblique shocks described above may be applied to a double-wedge configuration to obtain inviscid external flow properties. These can be substituted into expressions for separation length and heat flux in nonreacting flow based on the present theoretical results from Chapter 4 and on previous empirical results from Section 1.5. In this manner, the IDG model can show how differences between frozen and equilibrium external flow affect the phenomenon of separation length and reattachment heating, without consideration of changes due to reactions occurring in the viscous regions of the flow. In other words, external mechanisms for real-gas effects are illuminated independently of internal mechanisms.

The geometry considered for IDG model calculations in the present study is shown in Figure 5.2; it is an inviscid double wedge with only two oblique shocks, one from the leading edge and one from the hingeline. This simplification is necessary because it is not possible to predict the separation geometry, which in any case may depend on the internal mechanisms we want to exclude. Any effect due to splitting of the shock between separation and reattachment, such as a pressure overshoot at reattachment, is thus neglected. The notation for external flow regions in separated double-wedge flow (introduced in Figure 1.3), however, is maintained here for consistency. The triple-deck results in Section 4.2.3 are used to provide information on region 2 between separation and reattachment, when it is needed. The IDG model is applied to the two oblique shocks in Figure 5.2 to obtain three different solutions for a specified free-stream condition and specified geometry; one with frozen flow on both wedges, one with equilibrium flow on both wedges, and one with frozen flow on the first wedge and equilibrium flow on the second wedge. The latter solution approximates a case where the first shock does not induce a significant reaction rate,

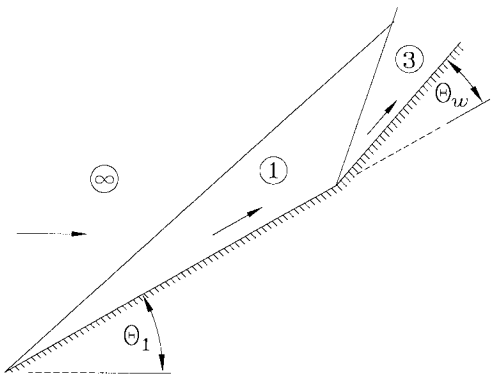

Figure 5.2: Notation for IDG double-wedge calculations.

but increases the density and temperature enough so that the second shock does induce a significant reaction rate. Note that this analysis technique also assumes a uniform free stream. An advantage to using the relatively simple IDG model instead of, for example, the nonequilibrium computational code described in Chapter 3, is the efficiency with which a wide range of parameter space may be explored. Limited results from such a study are presented in the following sections.

5.1.2 Separation Length

The various scaling laws for separation length in nonreacting flow, presented in Sections 1.5 and 4.2.2, are based on local flow conditions outside the boundary layer. Thus external mechanisms for real-gas effects on separation length are found by modifying the local external flow conditions according to reacting-flow calculations such as those obtained by the IDG model described in the previous section. Only relative changes in L_{sep} can be shown, because only the scaling for L_{sep} is known. The particular scaling used here,

$$\frac{L_{sep}}{x_1} \propto \frac{\Lambda_1 \sqrt{Re_{x_1}}}{\gamma_1^{3/2} M_1^3} \left(\frac{p_3 - p_2}{p_1} \right), \tag{5.20}$$

is assembled from several different results. The Λ wall temperature factor and the dependence on γ come from the triple-deck result, Equation 4.48. The Mach-number dependence is that given by both the triple-deck result and previous empirical results. The 3/2-power law theoretical result for dependence on the reattachment pressure ratio, however, is not used; instead, a linear dependence is assumed, consistent with the previous empirical results of Katzer (1989) (*cf.* Equation 1.10) and the present empirical results presented in Section 6.1.1 for supersonic interactions. The Reynolds-number dependence from the empirical results of Needham (1965) (*cf.* Equation 1.5) is also included in Equation 5.20.

Two parametric studies are considered, one with varying stagnation enthalpy H_{0_∞}, presented in Section 5.1.2.1, the other with varying incidence angle θ_1, presented in Section 5.1.2.2. General results for external real-gas effects on separation length are summarized, and compared qualitatively to previous results in the literature, in Section 5.1.2.3.

5.1.2.1 Variation with H_{0_∞}

In Figures 5.3–5.5 are presented IDG results for a double-wedge geometry of $\theta_1 = 30°$ and $\theta_w = 15°$ over a large range in nondimensional stagnation enthalpy H_{0_∞} obtained by varying K_∞ while keeping P_∞ and ρ_d/ρ_∞ fixed. Two sets of values are considered for the latter parameters, based on experimental condition C2 with $A_e/A_* = 100$ and $A_e/A_* = 400$ as shown in Table 5.2. Though these two cases for fixed P_∞ and ρ_d/ρ_∞ are denoted in Figures 5.3–5.5 by the corresponding value of A_e/A_*, it is important to note that the relationship to A_e/A_* holds only for a particular value of

K_∞; in a real shock tunnel flow, K_∞ cannot be varied independently of P_∞ without also changing A_e/A_*. The classification by A_e/A_* is intended to represent the highest and lowest free-stream density (an important parameter in reacting flow) attainable in the high-enthalpy experiments. Two cases are also considered for the free-stream dissociation; the partially dissociated condition produced by T5 ($\alpha_\infty = 0.11$), and a nondissociated condition ($\alpha_\infty = 0$) that corresponds to free flight at the same P_∞, K_∞, and ρ_d/ρ_∞ as the experiment. Results are generally plotted as the ratio of the equilibrium-flow solution to the frozen-flow solution. All of the parameters in Equation 5.20 are considered independently before combining them to show real-gas effects on separation length.

condition	A_e/A_*	P_∞	K_∞	H_{0_∞}	ρ_d/ρ_∞	α_∞
C2	100	0.034	0.48	0.71	1.2×10^7	0.11
C2	400	0.017	0.51	0.70	3.2×10^7	0.11

Table 5.2: Approximate values of the nondimensional free-stream parameters for condition C2 at two values of A_e/A_*.

Parameters which depend only on the solution for the first wedge (Re_{x_1}, M_1, and Λ_1) are considered in Figure 5.3. The Reynolds number (written Re_1 since the length scale is arbitrary when considering only ratios) is shown in Figure 5.3a to increase over the frozen-flow value as stagnation enthalpy is increased, its behavior dominated by the lower temperature (and hence lower viscosity) as well as the higher density found downstream of an equilibrium dissociation shock. At constant α_∞, this increase is somewhat larger for the higher-density free-stream condition ($A_e/A_* = 100$) due to a larger equilibrium value of α_1; similarly, at constant A_e/A_*, the increase is larger for the nondissociated free-stream condition. The equilibrium-to-frozen ratio of Re_1 is less than unity for $\alpha_\infty > 0$ at moderate enthalpy where the equilibrium solution is recombined with respect to the free stream, *i.e.* $\alpha_1 < \alpha_\infty$. These recombination branches of the solution terminate at a minimum value of H_{0_∞} due to the phenomenon mentioned in Section 5.1.1, whereby there is a lower limit on the shock angle for recombination shocks described as exothermic discontinuities. The limit is found at the Chapman–Jouget (C–J) condition; when the upstream shock-normal velocity u_{1n} reaches the C J velocity u_{CJ}, the equilibrium downstream shock-normal velocity u_{2n} becomes sonic. Decreasing u_{1n} below u_{CJ}, *i.e.* by decreasing β below β_{min} for a fixed upstream state, results in a flow that can only be described by a dispersed wave. The C–J condition also gives a minimum flow deflection angle θ_{min} corresponding to β_{min}. The curves for $\alpha_\infty = 0.11$ in Figure 5.3 terminate where θ_{min} becomes greater than 30°. The behavior of M_1 (Figure 5.3b) and Λ_1 (Figure 5.3c) at high enthalpy is also dominated by the lower postshock temperature found for equilibrium dissociating flow. Recall that Λ_1 depends on both the temperature and the Mach number (*cf.* Equations 4.17 and 4.49), thus it shows a stronger increase than M_1. As for Re_1, recombination at moderate enthalpy has the opposite effect.

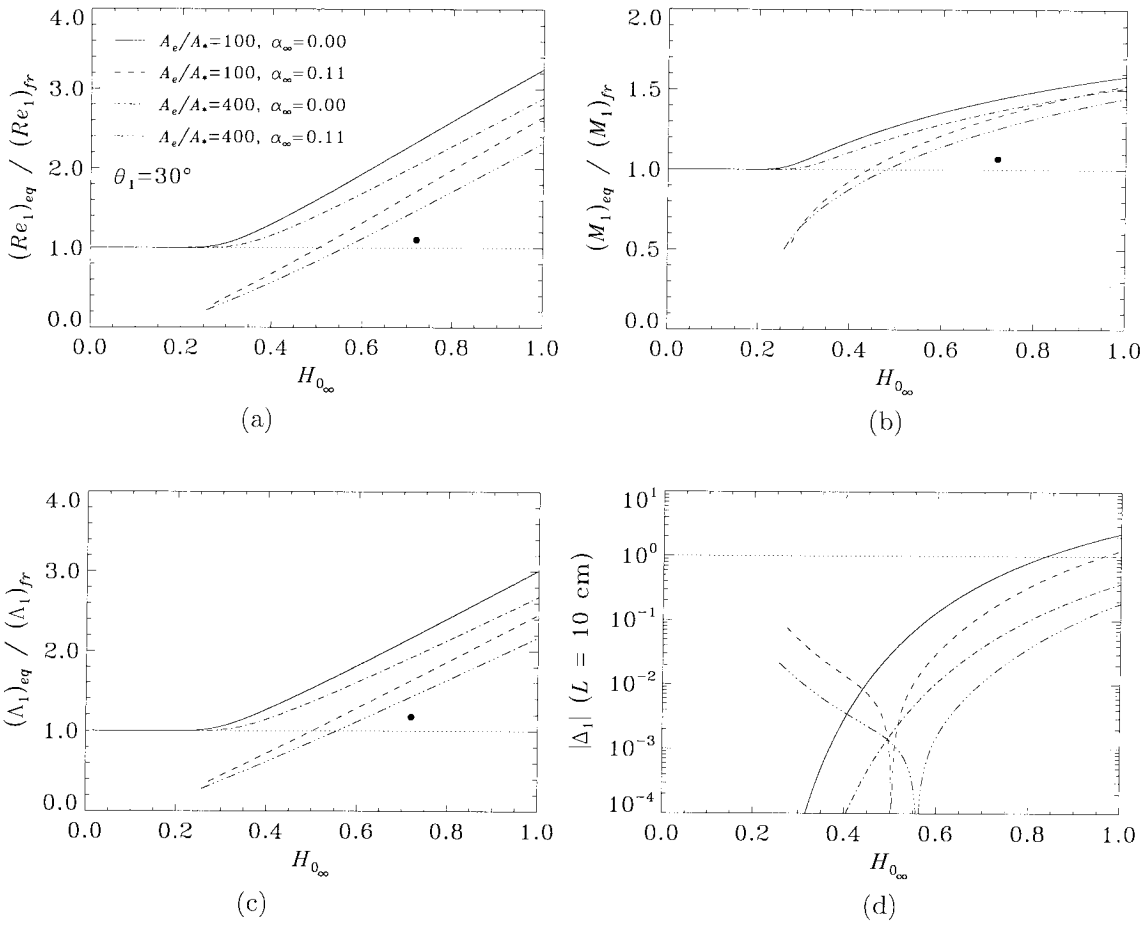

Figure 5.3: IDG results for the first wedge plotted against H_{0_∞} with $\theta_1 = 30°$, P_∞ and ρ_d/ρ_∞ fixed according to condition C2 at $A_e/A_* = 100$ and 400, and free-stream dissociation varied independently as indicated; (a) equilibrium-to-frozen ratio of Re_1; (b) equilibrium-to-frozen ratio of M_1; (c) equilibrium-to-frozen ratio of Λ_1; (d) $|\Delta_1|$. Curves for $\alpha_\infty = 0.11$ exhibit a minimum in H_{0_∞} at the C–J condition due to recombination. The • represents inviscid double-wedge computational results for shot 1747 (C2, $A_e/A_* = 225$, $\theta_1 = 30°$, $\theta_w = 15°$). The cusp-like feature in $|\Delta_1|$ for curves with $\alpha_\infty = 0.11$ marks the transition from recombination at moderate H_{0_∞} to dissociation at high H_{0_∞}.

In order to gauge the importance of these effects under typical experimental conditions, the external double-wedge flow was recomputed for one case using the full thermochemical nonequilibrium code instead of the IDG model. These inviscid double-wedge computations for frozen and nonequilibrium flow were set up in a similar manner to that described for inviscid triple-wedge computations in Section 3.3, with the grid initialized according to the free-stream computation for shot 1747 (condition C2, $A_e/A_* = 225$, $\theta_1 = 30°$, $\theta_w = 15°$). Results, generated by taking flow properties at the wall just upstream of the hingeline, are represented by a single point in each of Figures 5.3a–c. If equilibrium flow existed on the first wedge in the experiment, then this point might be expected to fall between the IDG results for $A_e/A_* = 100$ and $A_e/A_* = 400$, barring any large discrepancies from other approximations inherent to the IDG model such as a uniform free stream or simplified

modeling of internal energy. Instead, a nonequilibrium flow on the first wedge is indicated, closer to the frozen-flow solution than to the equilibrium-flow solution. In fact, inspection of the computed nonequilibrium results shows only marginal dissociation occurring on the first wedge, with $\alpha_1 - \alpha_\infty = 0.005$. This small amount of dissociation with respect to the upstream state is not entirely insignificant because of the relatively large amount of energy required to dissociate each molecule.

Another way to gauge the appropriateness of frozen or equilibrium IDG solutions is to look at the Damköhler parameter Δ defined by Equation 5.19; this is done for flow on the first wedge in Figure 5.3d, using $L_h = 10$ cm for a length scale. The absolute value of Δ_1 is used in order to show both dissociation and recombination on the same log plot. The cusp-like features in the curves for $\alpha_\infty = 0.11$ mark the transition, where Δ_1 changes sign, from recombination at moderate enthalpy to dissociation at high enthalpy. At $H_{0_\infty} \simeq 0.7$ corresponding to experimental condition C2, the results for $\alpha_\infty = 0.11$ indicate $\Delta_1 \lesssim 0.1$, suggesting at most only moderate departure from the frozen solution. Interestingly, the recombination branches show nonnegligible Δ_1 near the C J points, though recombination shocks are generally not found in shock tunnel flows due to limited size of the test models and to very small reaction rates behind the weak oblique shocks for which the equilibrium downstream state may be recombined with respect to the free stream.

In Figure 5.4 are shown results for the reattachment pressure ratio $(p_3 - p_2)/p_1$, where p_2 is computed from the first-wedge solution using Equation 4.50. For frozen flow on the first wedge and equilibrium flow on the second wedge (Figure 5.4a), the pressure ratio decreases at high enthalpy relative to fully frozen flow because dissociation on the second wedge lowers the pressure there. The pressure ratio increases very quickly on the branches corresponding to a recombination shock on the second wedge. For equilibrium flow on both wedges (Figure 5.4c), the behavior is complicated by the changes in p_1. Initially, the drop in p_3 dominates, but as enthalpy is increased, the drop in p_1 dominates. (p_2 behaves in a similar fashion to θ_{sep}, which is shown in Section 5.1.3 to vary very little with H_{0_∞}.) Where recombination occurs on the first wedge for $\alpha_\infty = 0.11$, p_1 actually increases, producing an even larger drop in $(p_3 - p_2)/p_1$. For either of the above solutions, frozen–equilibrium or equilibrium–equilibrium, the plots of Δ_3 in Figures 5.4b and 5.4d (this time using the length of the second wedge) indicate only moderate departure from frozen-flow conditions on the second wedge. The nonequilibrium computational result falls very close to the frozen–frozen IDG solution, but so does the equilibrium–equilibrium IDG solution with $\alpha_\infty = 0.11$ near the same value of H_{0_∞} in Figure 5.4c, and the nonequilibrium result was already shown in Figure 5.3 to give nonfrozen flow on the first wedge. It just so happens for this condition that the nonequilibrium effects on pressure in regions 1 and 3 nearly cancel each other in the ratio $(p_3 - p_2)/p_1$.

Finally, the effect of increasing H_{0_∞} on separation length is presented in Figure 5.5 under the assumed scaling law given by Equation 5.20. The frozen equilibrium solutions in Figure 5.5a are

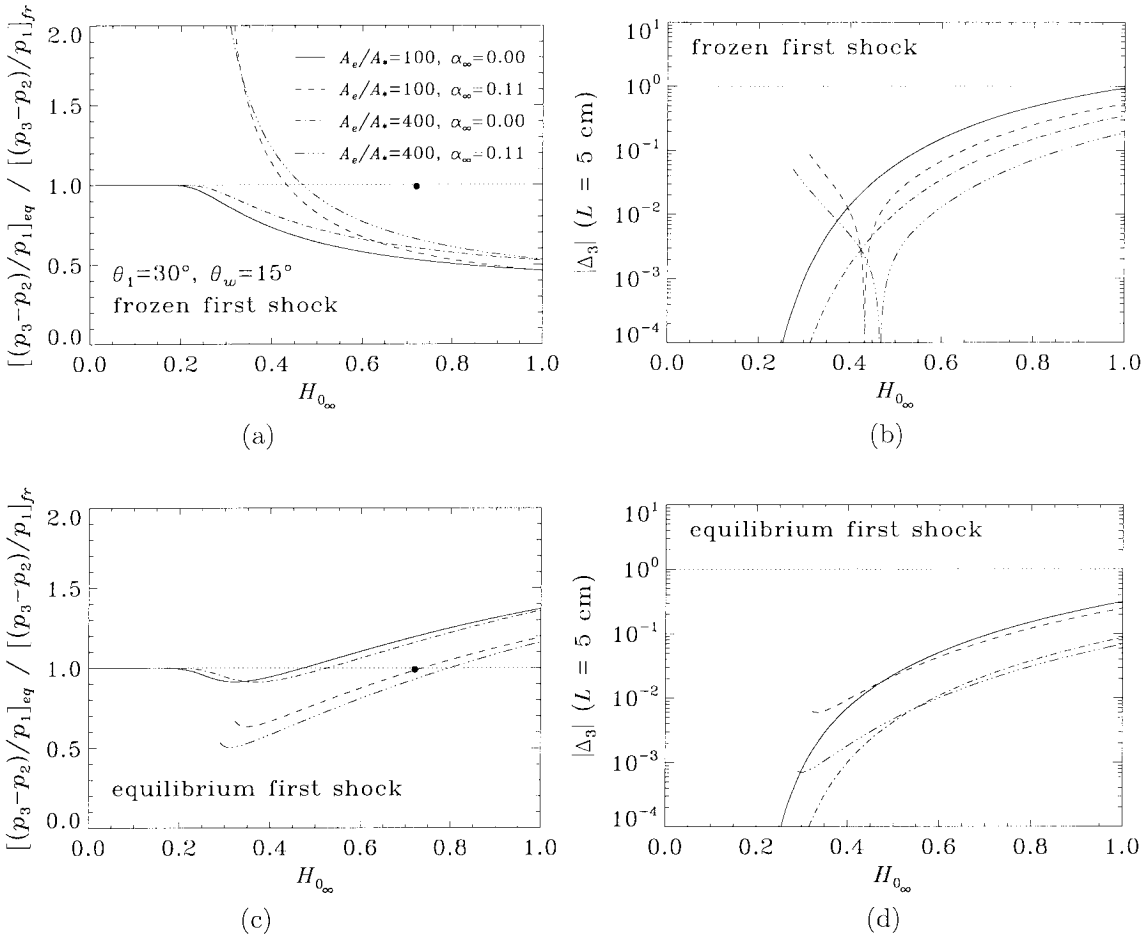

Figure 5.4: IDG results for the second wedge plotted against H_{0_∞} with $\theta_1 = 30°$, $\theta_w = 15°$, and other conditions fixed as described in Figure 5.3; (a) equilibrium-to-frozen ratio of $(p_3 - p_2)/p_1$ with frozen flow on first wedge; (b) $|\Delta_3|$ with frozen flow on first wedge; (c) equilibrium-to-frozen ratio of $(p_3 - p_2)/p_1$ with equilibrium flow on first wedge; (d) $|\Delta_3|$ with equilibrium flow on first wedge. The •, the minimum in H_{0_∞} for $\alpha_\infty = 0.11$, and the cusp-like feature in $|\Delta_3|$ are described in Figure 5.3.

identical to those shown for $(p_3 - p_2)/p_1$ in Figure 5.4a because the only changes in L_{sep} in this case stem from changes in p_3. The equilibrium–equilibrium results in Figure 5.5b also follow the same trend as found for $(p_3 - p_2)/p_1$ in Figure 5.4c, but with a wider range in H_{0_∞} where $(L_{sep})_{eq} < (L_{sep})_{fr}$ due to the increased Mach number in region 1, and a stronger increase at high enthalpy due to the increase in Λ_1 and Re_1. For nonequilibrium flow in general, real-gas effects on L_{sep} due to external mechanisms might fall anywhere between the frozen–equilibrium and equilibrium–equilibrium IDG solutions, *i.e.* they may cause an increase or a decrease in L_{sep}. The nonequilibrium computational result shows that under the experimental conditions of shot 1747, external real-gas effects on L_{sep} are negligible despite nonfrozen flow. Though the equilibrium IDG solutions clearly do not correspond to flow in T5 for the geometry investigated ($\theta_1 = 30°$, $\theta_w = 15°$), the same trends observed in Figures 5.3 5.5 are expected to hold for higher-incidence configurations or higher-density free-stream conditions where the double-wedge flow is closer to chemical equilibrium.

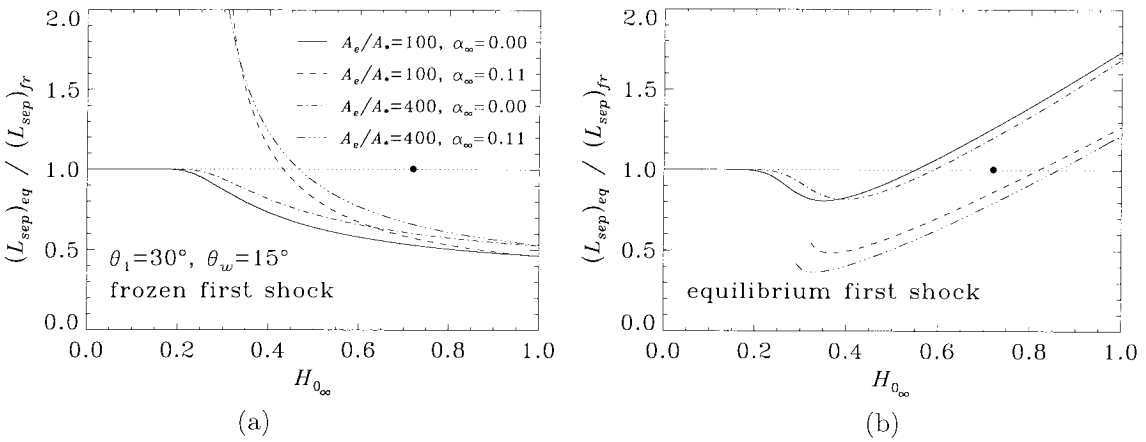

Figure 5.5: IDG results for L_{sep} plotted against H_{0_∞} with $\theta_1 = 30°$, $\theta_w = 15°$, and other conditions fixed as described in Figure 5.3; (a) equilibrium-to-frozen ratio of L_{sep} with frozen flow on first wedge; (b) equilibrium-to-frozen ratio of L_{sep} with equilibrium flow on first wedge. The •, and the minimum in H_{0_∞} for $\alpha_\infty = 0.11$, are described in Figure 5.3.

5.1.2.2 Variation with θ_1

A second set of IDG results is presented in Figures 5.6–5.9 for fixed stagnation enthalpy and varying incidence angle $0° < \theta_1 < 45°$. The flap deflection angle is also fixed at $\theta_w = 15°$. These solutions extend to the higher incidence angles tested in T5, where nonequilibrium effects become more pronounced. With normalization by free-stream or frozen flat-plate ($\theta_1 = 0°$) values instead of the frozen-flow result at the same incidence angle, these solutions provide information on how increasing incidence affects the various flow parameters for either frozen or equilibrium flow. The free stream is fixed according to experimental condition C2 with $A_e/A_* = 100$, and again, two values are considered for α_∞. Two nonequilibrium computational results are included in the plots, obtained from inviscid triple-wedge computations of shot 1776 (condition C2, $A_e/A_* = 100$, $\theta_1 = 15°$, $\theta_w = 15°$) and shot 1796 (condition C2, $A_e/A_* = 100$, $\theta_1 = 40°$, $\theta_w = 15°$); data for regions 1 and 3 are taken upstream of separation and downstream of reattachment respectively. In order to nondimensionalize the nonequilibrium data in a manner consistent with the IDG results, an inviscid double-wedge computation was performed on a flat-plate configuration ($\theta_1 = 0°$, $\theta_w = 15°$) using the free stream computed for shot 1776.

Solutions on the first wedge are given in Figure 5.6. The Reynolds number (Figure 5.6a) shows a maximum with respect to θ_1; both density and temperature increase with incidence, the former dominating at low incidence and the latter dominating at high incidence. At very high incidence, the decrease in velocity also plays a role. Compared to frozen flow, this maximum for equilibrium flow is larger in magnitude and occurs at much higher incidence; the equilibrium-to-frozen ratio, however, continues to increase with θ_1 beyond the maximum in Re_1. The frozen solutions terminate at a maximum θ_1 corresponding to the maximum wedge angle for an attached shock (for equilibrium

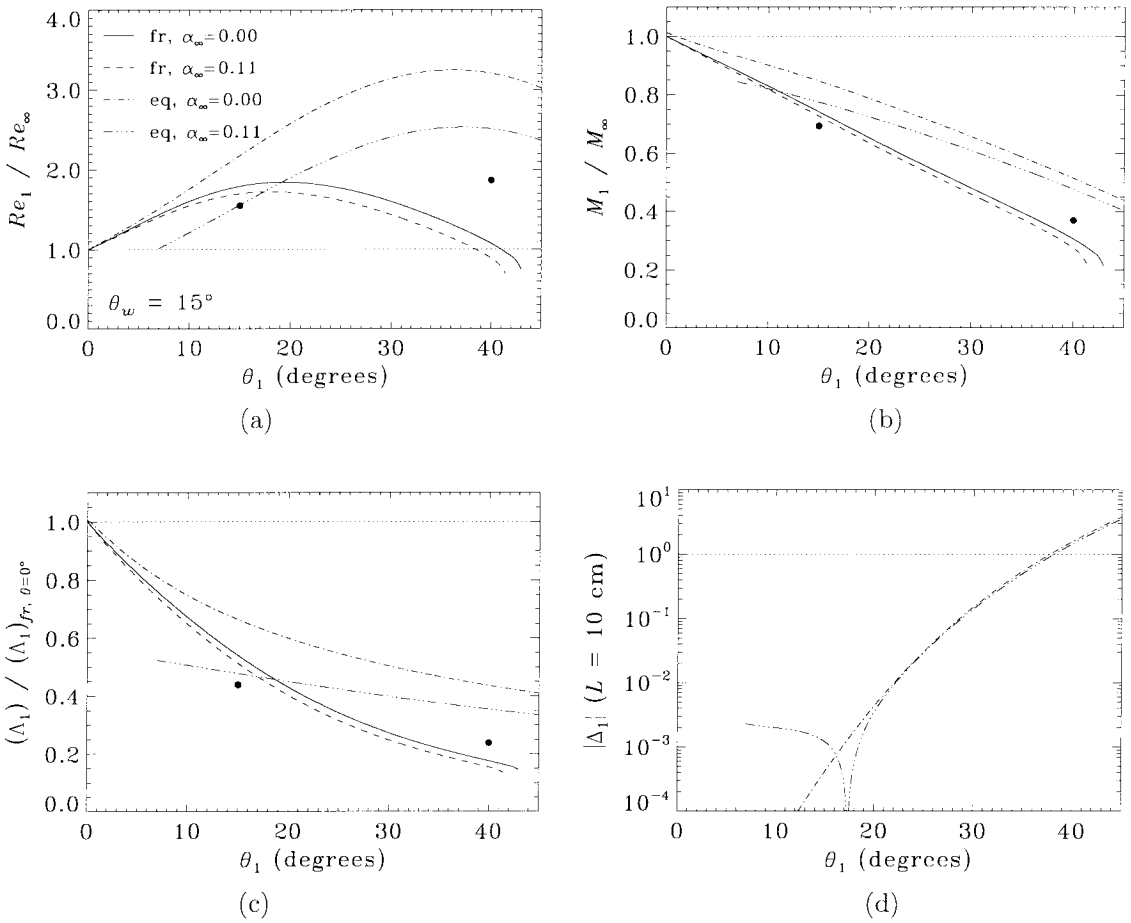

Figure 5.6: IDG results for the first wedge plotted against θ_1 with $\theta_w = 15°$, K_∞, P_∞, and ρ_d/ρ_∞ fixed according to condition C2 at $A_e/A_* = 100$, and free-stream dissociation varied independently as indicated; (a) ratio of Re across shock; (b) ratio of M_1 across shock; (c) ratio of Λ_1 to frozen flat-plate solution; (d) $|\Delta_1|$. Equilibrium curve for $\alpha_\infty = 0.11$ has a minimum in θ_1 at the C–J condition due to recombination. Frozen curves have a maximum in θ_1 at the detachment condition. The • symbols represent inviscid triple-wedge computational results for shots 1776 ($\theta_1 = 15°$) and 1796 ($\theta_1 = 40°$) at condition C2, $A_e/A_* = 100$, and $\theta_w = 15°$. The cusp-like feature in $|\Delta_1|$ for curves with $\alpha_\infty = 0.11$ marks the transition from recombination at low θ_1 to dissociation at high θ_1.

flow, the maximum wedge angle occurs beyond the range of the plot). The equilibrium solution with $\alpha_\infty = 0.11$ terminates at the C-J condition where $\theta_1 = \theta_{min}$, as discussed in the previous section. The decrease in M_1 and Λ_1 with incidence, seen in Figures 5.6b–c, is expected from the increase in temperature with incidence. Note that the equilibrium solutions for M_1 and Λ_1 with $\alpha_\infty = 0.11$ do not meet the frozen solutions at $\theta_1 = 0°$ because the $\alpha_\infty = 0.11$ free-stream condition is not in equilibrium. The plot of Δ_1 in Figure 5.6d indicates a high degree of nonequilibrium at $\theta_1 = 40°$, with an order of magnitude increase in Δ_1 over the $\theta_1 = 30°$ configuration considered previously. For $\theta_1 = 15°$, the flow is essentially frozen, and the nonequilibrium computational result should fall closest to the frozen-flow IDG solution with $\alpha_\infty = 0.11$; in fact it falls closer to the equilibrium-flow IDG solution on the plots for Re_1 and Λ_1. Though the nonequilibrium computation does show

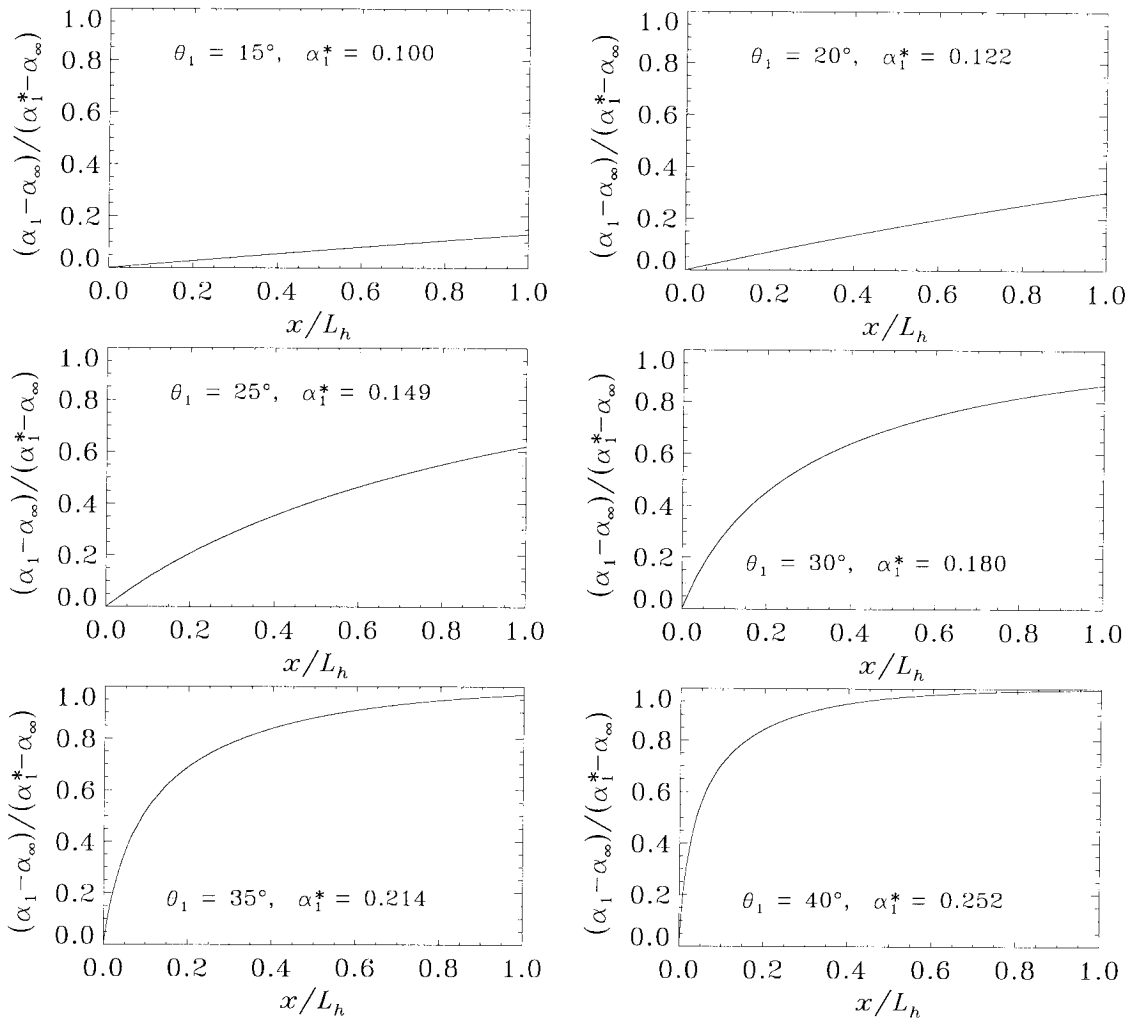

Figure 5.7: Nonequilibrium IDG results for α_1 at various θ_1 with $\alpha_\infty = 0.11$, and other conditions fixed as described in Figure 5.6. α_1^* is the equilibrium value for a given θ_1, and x is distance from the shock along the equilibrium streamline direction (*i.e.* parallel to the wedge).

a very small amount of recombination ($\alpha_\infty - \alpha_1 < 0.001$), the discrepancy is more likely due to inconsistencies with the IDG model. For $\theta_1 = 40°$, the nonequilibrium result falls well in between the frozen and equilibrium IDG results.

Before continuing with the second-wedge solutions, it is of interest to take a small digression here to look at nonequilibrium IDG solutions on the first wedge for various θ_1. The purpose of this exercise is to lend physical meaning to the interpretation of Δ, *i.e.* to understand what the various values taken by $\Delta_1 = 1$ actually mean in terms of the amount of dissociation occurring on the first wedge. Consider a streamline which passes through the oblique shock close to the wall but well outside the boundary layer. The nonequilibrium IDG result is found by integrating the rate expression, Equation 5.18, along this streamline starting from frozen-flow postshock conditions, using the local velocity to convert from time to distance. This streamline is generally curved for nonequilibrium

flow, since only the shock-normal velocity component changes as the reaction proceeds. For the present purpose, however, a reasonable estimate of how the reaction proceeds along the wedge is made by taking the shock angle and the streamline direction from the equilibrium solution. The integration is performed with α_1 as the independent variable; the fixed step size in α_1 assures that the integration can be stopped arbitrarily close to the equilibrium condition α_1^* without overshooting.

The results in Figure 5.7 for nonequilibrium dissociation fraction are shown in terms of the normalized parameter $(\alpha_1 - \alpha_\infty)/(\alpha_1^* - \alpha_\infty)$, which goes from 0 at the frozen condition to 1 at the equilibrium condition, plotted against x/L_h, nondimensional distance from the shock in a direction parallel to the wedge. Six different angles θ_1 are considered, and the equilibrium dissociation fraction α_1^* is given for each one (the frozen value is given by $\alpha_\infty = 0.11$). Though the flow is clearly in nonequilibrium even down to $\theta_1 = 20°$, the actual amount of dissociation that occurs by the time the gas has reached the end of the first wedge at $x = L_h$ only begins to have significance at $\theta_1 = 30°$, and does not become appreciable until $\theta_1 \geq 35°$. (Note that the value of $\alpha_1 - \alpha_\infty$ found here for $A_e/A_* = 100$ is considerably higher than that found previously at $\theta_1 = 30°$ for $A_e/A_* = 225$ in the nonequilibrium computation for shot 1747.) The case at $\theta_1 = 15°$ shows a small degree of recombination, as was also noted for the full nonequilibrium computation of shot 1776.

IDG solutions for the second wedge as a function of θ_1 are shown in Figure 5.8. The pressure ratio (Figure 5.8a) is normalized by the frozen-flow solution for $\theta_1 = 0°$, and for each value of α_∞, three solutions are presented corresponding to frozen–frozen, frozen–equilibrium, and equilibrium equilibrium. Again, p_2 is computed using Equation 4.50. With increasing incidence, the leading-

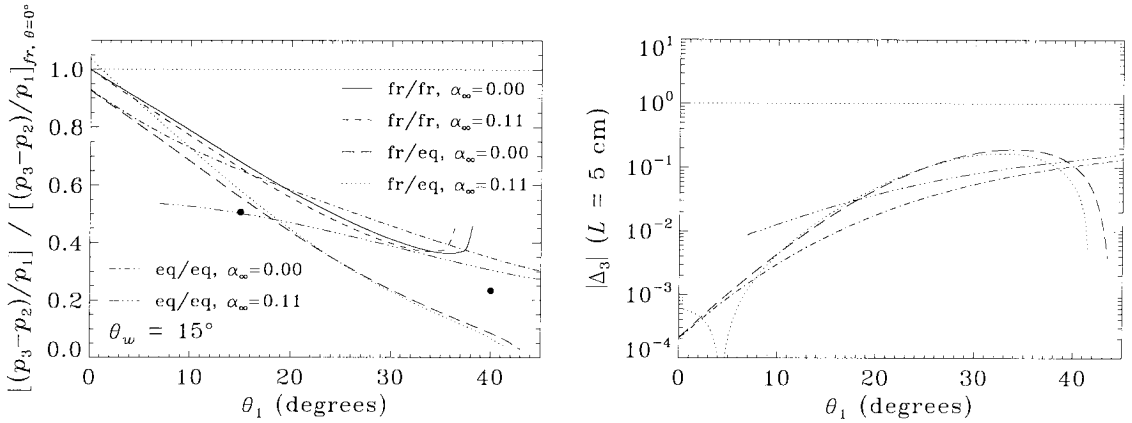

Figure 5.8: IDG results for the second wedge plotted against θ_1 with $\theta_w = 15°$, and other conditions fixed as described in Figure 5.6; (a) ratio of $(p_3 - p_2)/p_1$ to frozen flat-plate solution; (b) $|\Delta_3|$. Each plot shows three sets of solutions; frozen flow on both wedges (fr/fr), frozen flow on first wedge with equilibrium flow on second wedge (fr/eq), and equilibrium flow on both wedges (eq/eq). Each solution set has two different curves for different free-stream dissociation levels as indicated. The • symbols, the minimums and maximums in θ_1, and the cusp-like feature in $|\Delta_3|$ are described in Figure 5.6.

edge shock grows stronger while the hingeline shock grows weaker, thus giving rise to a large decline seen for the reattachment pressure ratio. Aside from the recombination branch, the equilibrium equilibrium solutions are not greatly different from the frozen–frozen solutions; equilibrium dissociation causes lower pressures in regions 1 and 3 but does not strongly affect the ratio between the two. The frozen–equilibrium solutions, however, show a larger decrease in $(p_3 - p_2)/p_1$ with incidence. Note that the frozen–frozen solutions terminate at a value θ_{max} for which the shock on the second wedge becomes detached, while the frozen–equilibrium solutions terminate where the first-wedge shock becomes detached. Though the nonequilibrium solution at $\theta_1 = 15°$ should be close to the frozen–frozen IDG solution, the fact that it falls closer to the equilibrium equilibrium solution with $\alpha_\infty = 0.11$ is at least partially explained by the axial gradient in free-stream properties which is excluded from the IDG computations, *i.e.* the difference in p_3 between nonequilibrium and IDG results is larger at the $\theta_1 = 0°$ condition used to normalize the pressure ratio. A similar discrepancy should apply to the nonequilibrium result at $\theta_1 = 40°$, suggesting that this flow is most consistent with the equilibrium–equilibrium IDG solution. It is not possible to gauge the departure from frozen flow because a frozen-flow solution does not exist for $\theta_1 = 40°$. The nondimensional reaction rate parameter Δ_3 is shown in Figure 5.8b.

The variation of L_{sep} with θ_1 shown in Figure 5.9 for frozen–frozen and frozen- equilibrium solutions is generally nonmonotonic due to competition between decreasing Λ_1 and $(p_3 - p_2)/p_1$ on the one hand, and increasing Re_1 plus decreasing M_1 on the other hand. For the equilibrium–equilibrium solutions, L_{sep} increases continuously with θ_1, passing the flat-plate frozen value $(L_{sep})_{fr,\,\theta=0°}$ at an intermediate incidence angle. Only the frozen–equilibrium solutions are significantly different from the frozen–frozen solutions at high enthalpy. We have already seen, however, that the equilibrium–equilibrium solutions are a better approximation to the fully nonequilibrium flow typically found in T5 at high incidence. Whether external mechanisms for real-gas effects cause a larger or smaller L_{sep} with respect to frozen flow depends on the degree of free-stream dissociation as well as the incidence angle. The nonequilibrium computational results with $\alpha_\infty = 0.11$ suggest that external mechanisms should act to decrease L_{sep} in the experiments. At $\theta_1 = 40°$, the decrease

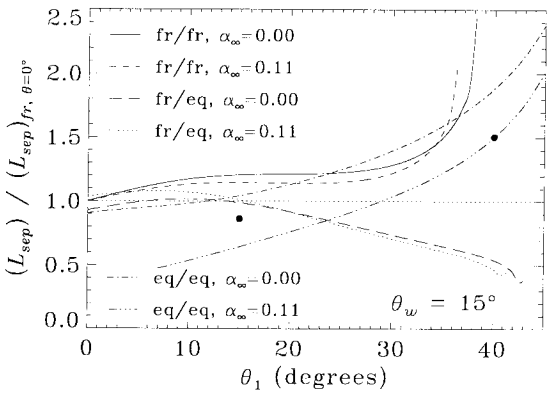

Figure 5.9: IDG results for the ratio of L_{sep} to frozen flat-plate solution, plotted against θ_1 with $\theta_w = 15°$, and other conditions fixed as described in Figure 5.6. The legend abbreviations are described in Figure 5.8. The • symbols, and the minimums and maximums in θ_1, are described in Figure 5.6.

is dominated by dissociation effects on M_1, though a direct comparison to frozen flow is not possible. At $\theta_1 = 15°$, slight recombination may cause some decrease in L_{sep} due to higher p_1, lower Re_1, and lower Λ_1, but the effect should be smaller than that seen in Figure 5.9 for the reason discussed above.

5.1.2.3 Summary of External Effects on Separation Length

Though obviously a very complex phenomenon, real-gas effects on L_{sep} due to external mechanisms may be summarized overall as follows: for low θ_1 and high θ_w where flow in region 1 is essentially frozen but flow in region 3 is not, L_{sep} decreases at high enthalpy due to a lower pressure in region 3; for high θ_1 and moderate θ_w with nonequilibrium or equilibrium flow in both regions 1 and 3, L_{sep} tends to increase at high enthalpy when $\alpha_\infty = 0$ but can decrease when $\alpha_\infty > 0$. A limited number of comparisons between nonequilibrium flow and frozen flow computed with the N-S code described in Chapter 3 show that external mechanisms are only important in the experiments at very high incidence ($\theta_1 > 30°$) where they cause L_{sep} to decrease due to free-stream dissociation; there is also some evidence for a marginal effect due to recombination at low incidence ($\theta_1 = 15°$). Unfortunately, the experimental measurements of physical separation length cannot be used to verify external mechanisms, because (1) external mechanisms cannot be separated from unknown internal mechanisms which also exist in the experiments, (2) shots with frozen and reacting flows have different free-stream conditions and thus cannot be directly compared with each other as done in the IDG study, and (3) the conditions at very high incidence often do not admit a frozen-flow solution. In addition, it should be noted that any effects due to external mechanisms in the experiments depend on free-stream dissociation which does not exist for free flight. The experimental measurements are used in Chapter 6 to study internal mechanisms by assuming that external mechanisms can be scaled out of the measurements using a scaling law similar to Equation 5.20. The frozen IDG model is applied to experimental results in Section 6.1.3 to look at the combined effects of external and internal mechanisms.

With this framework for describing external real-gas effects, an attempt can be made to explain some of the results from previous authors discussed in Section 1.5.4.1. In particular, the decrease in L_{sep} compared to frozen flow is observed for equilibrium compression-corner flow analyzed by Anders and Edwards (1968), for equilibrium compression-corner flow ($\theta_1 = 0°$) computed by Grasso and Leone (1992), and for nonequilibrium shock-impingement flow computed by Furumoto *et al.* (1997). In each of these cases, there is no dissociation upstream of separation, so the only external mechanism available is the affect of dissociation on the reattachment pressure. This does not necessarily mean, however, that internal mechanisms are negligible, only that they either act in the same direction or are weaker than the external mechanism. The decrease in L_{sep} found by Brenner *et al.* (1993) and Oswald *et al.* (1995) for equilibrium hyperboloid–flare flow, with nondissociated free stream,

is not so easily explained by external mechanisms. Though an axisymmetric configuration, the hyperboloid–flare has flow-deflection angles similar to the geometry considered in the present IDG study for varying H_{0_∞} ($\theta_1 = 30°$, $\theta_w = 15°$). The free-flight condition used by Brenner *et al.* (1993) has a free-stream density two orders of magnitude lower than found in T5. The equilibrium IDG solutions in Figure 5.5 show that as A_e/A_* increases (*i.e.* as ρ_∞ decreases), the point at which $(L_{sep})_{eq} = (L_{sep})_{fr}$ moves to higher enthalpy. This could explain by external mechanisms the decrease in L_{sep} for equilibrium hyperboloid–flare flows at low-density free-stream conditions, if in fact external mechanisms dominate internal mechanisms for these flows. Similar reasoning may explain the decrease in L_{sep} observed experimentally by Krek *et al.* (1996) for hyperboloid–flare flows. The shock-impingement flows studied by Ballaro and Anderson (1991) and Grumet *et al.* (1994) can be considered equivalent to the case of a compression corner with $\theta_1 = 0°$ and $\alpha_\infty > 0$. Their results do not appear to be consistent with the external mechanisms described here, except perhaps the high-pressure case computed by Grumet *et al.* (1994). This one case indicates recombination occurring downstream of reattachment, which could increase p_3 and contribute to the observed increase in L_{sep}. Internal mechanisms may be very important in these flows.

5.1.3 Reattachment Heat Flux

External mechanisms for real-gas effects on the heat flux at reattachment can be investigated by using the IDG model for equilibrium and frozen flow on a double wedge together with the laminar boundary-layer theory embodied in Equations 4.14, 4.18, and 4.20. The resulting expression for peak reattachment heating is

$$\dot{q}_{pk} = 0.332 \frac{\rho_3 u_3 c_{p_3} (T_{aw_3} - T_w)}{Pr^{2/3}} \sqrt{\frac{C^*}{Re_{L_{pk}}}}, \tag{5.21}$$

where the adiabatic wall temperature depends on T_3 as well as M_3. The Reynolds number is evaluated for a length scale L_{pk}, defined by Equation 1.14, that describes the growth length for a reattaching boundary layer. To compute L_{pk}, Equation 4.51 is used to obtain θ_{sep} and δ_s is assumed to be approximately equal to the boundary-layer thickness δ_1 at the end of the first wedge, calculated using Equation 4.23. The wall enthalpy is evaluated assuming an entirely frozen boundary layer with $\alpha_w = \alpha_e$, and constant c_{v_v} according to the IDG model. In this way effects due to external mechanisms can be shown independently of internal mechanisms. The results are again divided into studies for varying H_{0_∞} (Section 5.1.3.1) and varying θ_1 (Section 5.1.3.2), with a summary provided in Section 5.1.3.3.

5.1.3.1 Variation with H_{0_∞}

We first consider the IDG solutions for varying H_{0_∞} in Figures 5.10 and 5.11. The only parameters determining $\dot{q}_{pk}$ that depend on the first-wedge solution but not the second-wedge solution are θ_{sep} and δ_1, which are used to define the growth length L_{pk} for the boundary layer in region 3. IDG solutions for these two parameters are shown in Figure 5.10. The equilibrium boundary-layer thickness (Figure 5.10a) decreases at high enthalpy relative to the frozen solution; the behavior is clearly dominated by the increased Reynolds number seen in Figure 5.3a, since the trends in M_1 and T_1 would tend to increase δ_1. The equilibrium recombination branches of the solutions with $\alpha_\infty > 0$ show the opposite effect on δ_1, as expected. As observed for the other parameters investigated in region 1, the nonequilibrium computational result indicates only a slight departure from the frozen-flow solution. The separation angle (Figure 5.10b) changes very little when going from frozen flow to equilibrium flow because it is such a weak function of Reynolds number and Mach number (*cf.* Equation 4.51).

The frozen–equilibrium and equilibrium–equilibrium solutions for peak heating are presented in Figure 5.11. The decrease in δ_1 for equilibrium flow contributes to the increase seen in the equilibrium–equilibrium solutions for $\dot{q}_{pk}$ (Figure 5.11b) at high enthalpy as opposed to the decrease seen in the frozen–equilibrium solutions (Figure 5.11a). It is not immediately obvious that there should be any other differences between the two sets of solutions since the other parameters controlling $\dot{q}_{pk}$ all come from the equilibrium IDG solution in region 3. Compared to frozen–frozen flow, either set of equilibrium solutions should give lower T_3 and higher Re_3, which might be expected to cause a decrease in $\dot{q}_{pk}$ at high enthalpy. Careful examination of the solutions produced by the double-wedge IDG model reveals that there is only one significant difference between the two sets

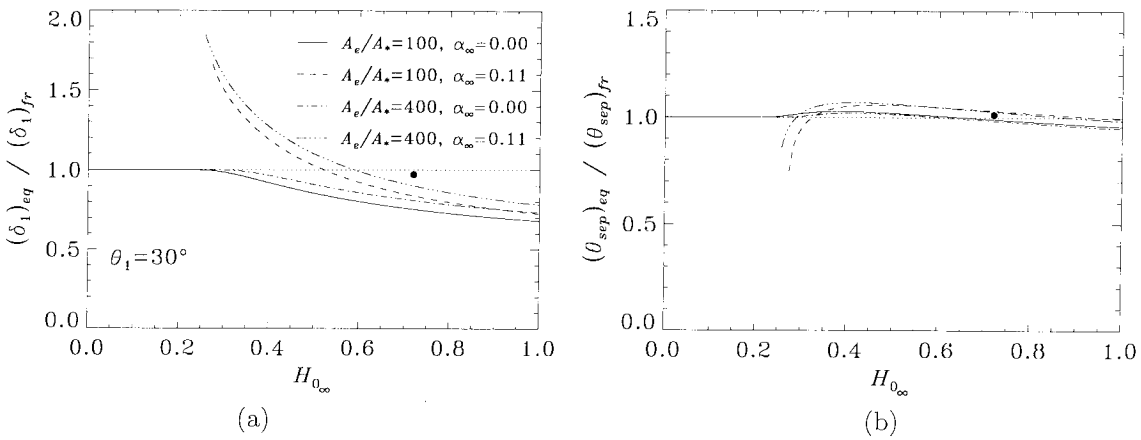

Figure 5.10: IDG results for δ_1 and θ_{sep} plotted against H_{0_∞} with $\theta_1 = 30°$, and other conditions fixed as described for Figure 5.3; (a) equilibrium-to-frozen ratio of δ_1 with frozen flow on first wedge; (b) equilibrium-to-frozen ratio of θ_{sep} with equilibrium flow on first wedge. The •, and the minimum in H_{0_∞} for $\alpha_\infty = 0.11$, are described in Figure 5.3.

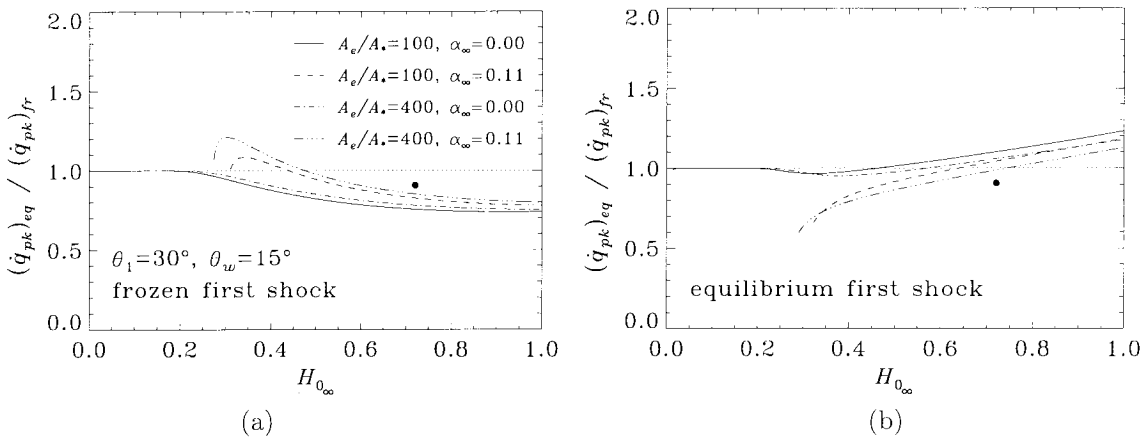

Figure 5.11: IDG results for $\dot{q}_{pk}$ plotted against H_{0_∞} with $\theta_1 = 30°$, $\theta_w = 15°$, and other conditions fixed as described for Figure 5.3; (a) equilibrium-to-frozen ratio of $\dot{q}_{pk}$ with frozen flow on first wedge; (b) equilibrium-to-frozen ratio of $\dot{q}_{pk}$ with equilibrium flow on first wedge. The •, and the minimum in H_{0_∞} for $\alpha_\infty = 0.11$, are described in Figure 5.3.

of solutions at $H_{0_\infty} \simeq 0.7$; the density in region 3 is approximately 20% higher for the equilibrium equilibrium solution than for the frozen–equilibrium solution. Since $\dot{q}_{pk}$ has a direct dependence on ρ_3 (apart from Re_3), this relatively mild effect may also be contributing to the difference in behavior between the two sets of solutions. In either case, whether $\dot{q}_{pk}$ increases or decreases with enthalpy, it does not stray far from the frozen–frozen solution. The nonequilibrium computational result falls in between the frozen–equilibrium and equilibrium–equilibrium IDG results for $\alpha_\infty = 0.11$, suggesting that the small amount of dissociation occurring for nonequilibrium flow in region 3 ($\alpha_3 - \alpha_\infty = 0.02$) causes a slight decrease in the heat flux due to external mechanisms for real-gas effects. (The effect on L_{sep} was negligible because the change in pressure is much smaller than the change in temperature.)

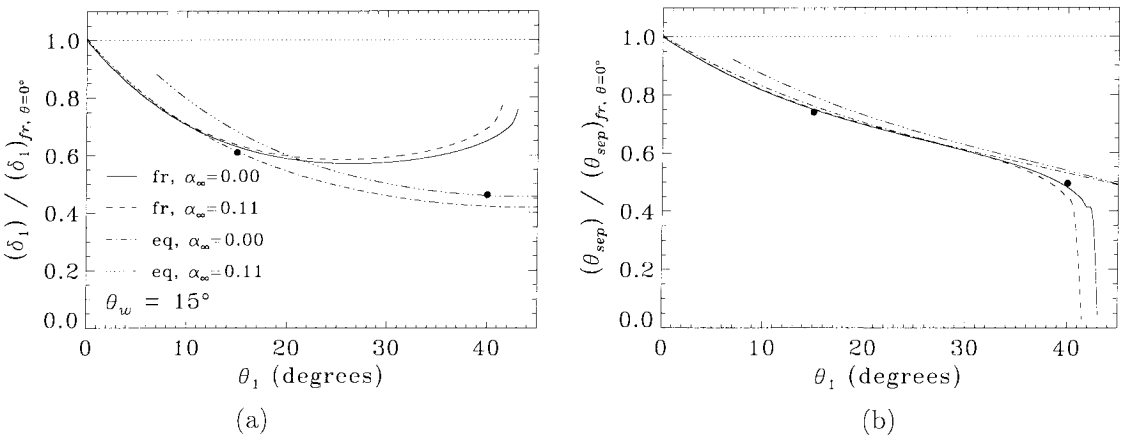

Figure 5.12: IDG results for δ_1 and θ_{sep} plotted against θ_1 with conditions fixed as described for Figure 5.6; (a) ratio of δ_1 to frozen flat-plate solution; (b) ratio of θ_{sep} to frozen flat-plate solution. The • symbols, and the minimums and maximums in θ_1, are described in Figure 5.6.

5.1.3.2 Variation with θ_1

The IDG solutions for varying incidence are shown in Figures 5.12–5.13. Both δ_1 (Figure 5.12a) and θ_{sep} (Figure 5.12b) are seen to drop with increasing incidence, with the only significant difference between frozen and equilibrium flows occurring for δ_1 at high incidence. Regarding the plot of δ_1, the nonequilibrium computational results fall very close to the frozen IDG solution at $\theta_1 = 15°$ and to the equilibrium IDG solution at $\theta_1 = 40°$, in contrast to results for other parameters in region 1 (*cf.* Figure 5.6). It may be simply fortuitous that the nonequilibrium effects on Re_1, M_1, and T_w/T_1, at the particular condition represented by the $\theta_1 = 40°$ case, happen to balance each other in the expression for δ_1 in such a way as to produce the same result given by equilibrium flow. IDG solutions for the peak heating (Figure 5.13) show a strong nonmonotonic behavior with increasing incidence, a maximum in $\dot{q}_{pk}$ occurring inthe range $\theta_1 = 20$–$30°$. That $\dot{q}_{pk}$ should increase with incidence is expected due to increasing temperature and density in region 3 as well as decreasing L_{pk}. Close inspection of the IDG results shows that ρ_3 and L_{pk} tend to level off above moderate θ_1, where the velocity in region 3 starts to decrease rather strongly with θ_1. Thus the behavior of $\dot{q}_{pk}$ with θ_1 at high incidence appears to be dominated by u_3. Compared to the frozen–frozen solutions, the peak heating for equilibrium solutions is generally lower; the only exception consists of the equilibrium–equilibrium solutions at very high incidence. The nonequilibrium computational results at $\theta_1 = 15°$ and $\theta_1 = 40°$ in this case fall close to the frozen–frozen and equilibrium–equilibrium solutions, respectively.

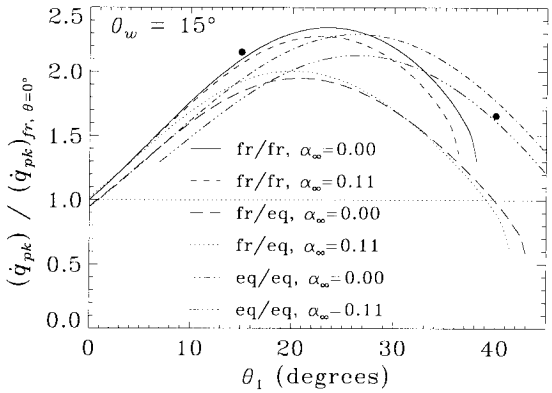

Figure 5.13: IDG results for the ratio of $\dot{q}_{pk}$ to frozen flat-plate solution, plotted against θ_1 with $\theta_w = 15°$, and other conditions fixed as described for Figure 5.6. The legend abbreviations are described in Figure 5.8. The • symbols, and the minimums and maximums in θ_1, are described in Figure 5.6.

5.1.3.3 Summary of External Effects on Peak Heating

To summarize, external mechanisms for real-gas effects may cause either an increase or decrease in the reattachment heat flux at high enthalpy, though in either case the change is relatively mild (only up to 20%). An increase only occurs at high enthalpy and high incidence, for which there is significant dissociation upstream of separation. The nonequilibrium computations using the N S

code suggest that, for the high-enthalpy experimental condition, external mechanisms on $\dot{q}_{pk}$ are not very important. A slight decrease in $\dot{q}_{pk}$ compared to frozen flow appears possible at $\theta_1 = 30°$. At $\theta_1 = 40°$, the equilibrium–equilibrium IDG solution appears to be a good approximation to nonequilibrium effects on $\dot{q}_{pk}$, as was also found for separation length in Figure 5.9. Consideration of the experimental heat flux results is deferred until Chapter 6.

As discussed in Section 1.5.4.2, nearly all computational results from previous authors indicate an increase in peak heating due to real-gas effects. Only the two studies of equilibrium flow on a hyperboloid flare consider configurations which might, according to the IDG model results, be expected to show an increased heat flux due to external mechanisms. One of these (Brenner *et al.*, 1993), however, shows the increase in $\dot{q}_{pk}$ exists only for a catalytic wall condition, and not for a non-catalytic condition. Thus external mechanisms appear in many cases to be unimportant compared to internal mechanisms for real-gas effects on peak heating. The computations by Furumoto *et al.* (1997) for a shock-impingement flow with undissociated free stream ($\theta_1 = 0°$, $\alpha_1 = 0$) do show lower $\dot{q}_{pk}$ for nonequilibrium flow compared to frozen flow, consistent with the IDG results for external mechanisms; but they also show dissociation occurring near the wall downstream of separation and reattachment, and the results of Grasso and Leone (1992) for the analogous compression-corner flow indicate the opposite trend, suggesting that external mechanisms are unimportant in these flows as well.

5.2 Internal Mechanisms

Internal mechanisms for real-gas effects encompass any changes in viscous regions of the flow on a double wedge, with respect to a frozen boundary layer having the same external flow conditions. The definition of viscous regions includes everything that is not part of the external flow; the boundary layer, free-shear layer, and recirculating fluid inside the separation bubble. The boundary layer upstream of separation may affect separation length through changes in the undisturbed wall shear stress, according to the scaling for separation length in Equation 4.46. Thermochemical nonequilibrium processes in the shear layer and separated region are also expected to affect L_{sep}, but these mechanisms cannot be included in the present theoretical results for separation length scaling. Real-gas effects in the reattached boundary layer cannot change L_{sep}, but can play a significant role in determining the peak reattachment heating. The transformed boundary-layer equations for reacting flow presented in Section 4.1.1.1 offer some insight to how internal mechanisms may arise in a boundary layer. For the boundary layer upstream of separation, a more quantitative analysis is performed using the N S code described in Chapter 3 to compute boundary layers in thermochemical nonequilibrium under external conditions similar to those found in region 1 of the experimental double-wedge flows. Internal mechanisms arising in the separated region can only be

considered qualitatively in the present study. The scope of the computational boundary-layer study is described in Section 5.2.1. Then the computational results are used to study internal mechanisms for real-gas effects on separation length in Section 5.2.2 and on reattachment heating in Section 5.2.3.

5.2.1 Computational Boundary-Layer Study

The N–S code used to study laminar nonequilibrium boundary layers is described in Section 3.1, and the method used to set up the numerical grid and initialize it is discussed in Section 3.6. As shown in Figure 5.14, the computations are restricted to flat-plate boundary layers with free-stream conditions based on inviscid triple-wedge computational results at station 1, just upstream of separation. Twelve different free-stream conditions are considered, corresponding to extremes of h_0, A_e/A_*, and θ_1 encompassed by the experiments. In this manner, approximate nonequilibrium boundary-layer solutions are obtained over a range of experimental conditions with less computational effort than is required for viscous wedge flow. The twelve cases are detailed in Table 5.3, including the experimental conditions to which they roughly correspond. Each case has three designations F, N, and C referring to computations for frozen flow, nonequilibrium flow with a noncatalytic wall condition, and nonequilibrium flow with a catalytic wall condition, respectively. For the two high-enthalpy cases at $\theta_1 = 40°$ (cases 1 and 2) the free-stream conditions based on inviscid wedge computations describe a nonequilibrium flow state that is significantly departed from a frozen or equilibrium flow state, *i.e.* the dissociation fraction in the flow external to the boundary-layer increases with distance from the leading edge. At $x = 5$ cm, where information is gathered from the boundary-layer computations, this results in a nonnegligible difference between the edge conditions for frozen flow and reacting flow. An approximate correction is made by using a different set of free-stream conditions for the frozen-flow calculations, taken from the edge conditions at $x = 5$ cm computed for the same case in nonequilibrium flow; these modified conditions are shown separately in Table 5.3.

Cases 9–12 in Table 5.3 encompass a range of conditions with $\theta_1 = 0°$, a configuration for which separation length measurements were not made (for reasons given in Section 2.4.4) and heat flux measurements suffered from poor signal-to-noise ratio (*cf.* Section 2.5.3). These cases are included

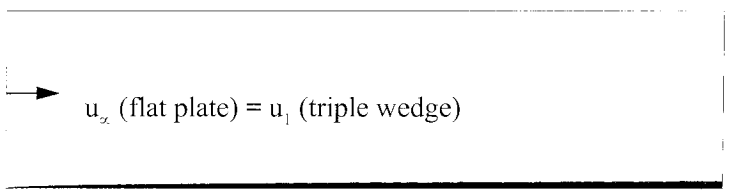

Figure 5.14: Sketch of domain for nonequilibrium boundary-layer computations.

case no.	ρ_∞ kg/m^3	u_∞ m/s	T_∞ K	T_{v_∞} K	α_∞	M_∞	Re_∞ $L = 5$ cm	T5 cond.	A_e/A_*	θ_1
1N/C	0.015	3000	7200	7400	0.21	1.61	1.24×10^4	C2	400	40°
1F	0.01506	3023	6921	6967	0.2198	1.65	1.30×10^4			
2N/C	0.055	2900	6700	6700	0.23	1.60	4.65×10^4	C2	100	40°
2F	0.05524	2906	6600	6603	0.2333	1.61	4.73×10^4			
3	0.015	1700	3600	3300	0.0002	1.45	1.28×10^4	B1	400	40°
4	0.025	1700	3600	3300	0.0005	1.45	2.14×10^4	B1	225	40°
5	0.008	5600	3000	4200	0.12	4.88	2.50×10^4	C2	400	15°
6	0.022	5300	4400	4300	0.11	3.84	4.88×10^4	C2	100	15°
7	0.009	3300	940	3300	0.0005	5.49	3.94×10^4	B1	400	15°
8	0.015	3200	1000	3100	0.0005	5.16	6.10×10^4	B1	225	15°
9	0.02	3000	250	2000	0.0	9.64	1.88×10^5	A2	400	0°
10	0.03	2500	320	2200	0.0	7.11	2.02×10^5	A3	100	0°
11	0.005	3400	450	3100	0.0005	8.18	3.68×10^4	B1	225	0°
12	0.009	5700	2600	4000	0.11	5.36	3.20×10^4	C2	100	0°

Table 5.3: Description of cases encompassed by the computational boundary-layer study.

in the boundary-layer study because only for $\theta_1 = 0°$ can moderate hypersonic Mach number be attained in external flow region 1, and only in the hypersonic regime can interesting effects arise due to large Eckert number. The Eckert number is defined by $E = u_e^2/(h_e - h_w)$, and when it is large, the temperature profile is determined more by viscous dissipation than by conduction or diffusion, causing a maximum temperature in the boundary layer that is higher than the edge temperature.

An immediate result of the nonequilibrium computations is that under many conditions attainable for flow of nitrogen on a double wedge in T5, the boundary layer is close to a chemically frozen flow state. A noticeable difference between the frozen-flow and nonequilibrium/noncatalytic solutions is found in only five of the cases studied; profiles of dissociation fraction α are shown for four of these in Figure 5.15. Case 12 is not shown but looks very similar to case 5. These profiles are extracted at $x = 5$ cm, as are all computational boundary-layer data presented in this chapter. The normal coordinate is nondimensionalized by the inertial boundary-layer thickness δ, taken as the location of the first grid point for which $u > 0.99u_e$; the edge conditions themselves are taken where the temperature profile changes by less than 0.01% (since the thermal thickness is larger than the inertial thickness for $Pr < 1$). Points corresponding to cell centers in the computational grid are shown on the catalytic-wall solutions to indicate the degree of grid refinement relative to the profile shape.

For a noncatalytic wall, it is clear from Figure 5.15 and Table 5.3 that α_w depends strongly on the free-stream density, though also on the free-stream temperature and dissociation. Cases 1 and 6 have the closest values of ρ_∞ and similar values for α_w, with the lower ρ_∞ in case 1 compensated for by a higher T_∞. Note that the noncatalytic profiles of mass fraction do have zero gradient at

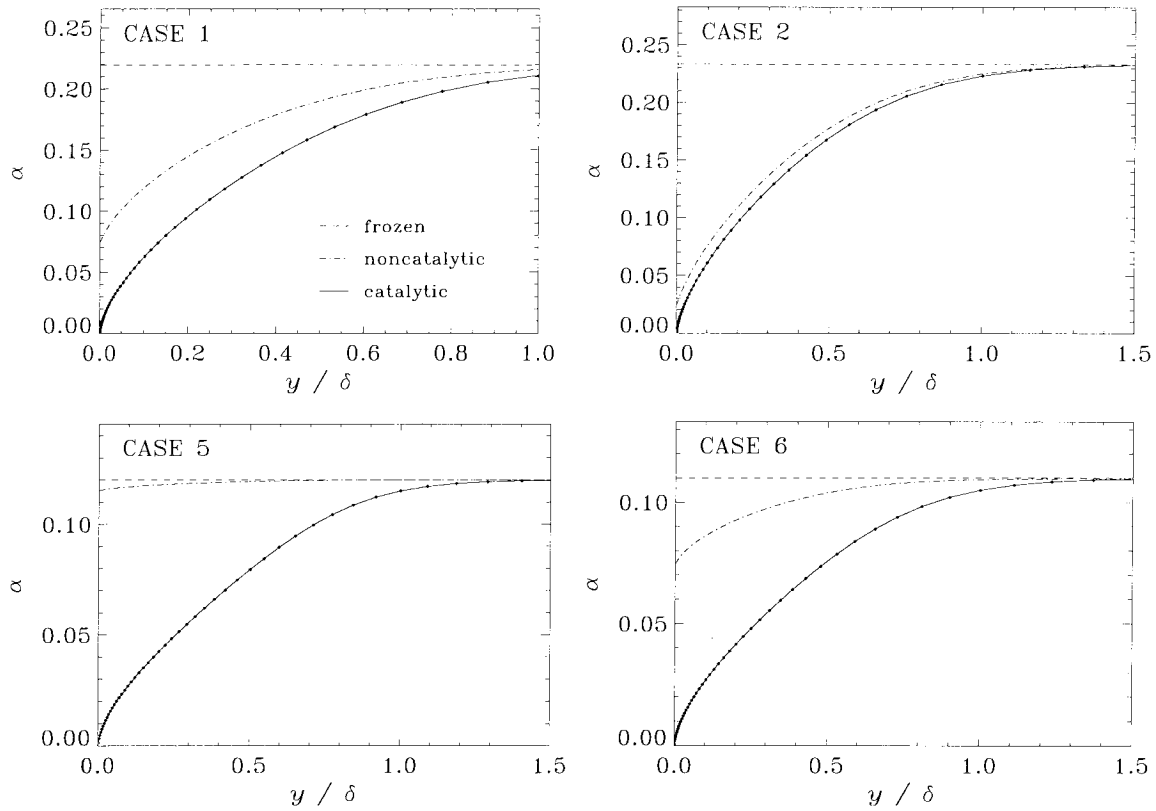

Figure 5.15: Selected computational boundary-layer results for α. Dashed curve is frozen-flow result, dash–dot curve is nonequilibrium result for a noncatalytic wall, and solid curve is nonequilibrium result for a catalytic wall; this convention is maintained for all boundary-layer profile plots throughout Section 5.2. Points on the curves for catalytic-wall results indicate cell centers from computational grid. Cases are described in Table 5.3.

the wall, though it is not evident on the physical scale used in Figure 5.15. Though not shown here, the noncatalytic results also indicate a significant variation in α_w with streamwise coordinate, starting close to the free-stream value at the leading edge and recombining along the length of the plate. Full recombination is forced in the catalytic-wall computations, but the the effect on other flow properties is only significant if the edge condition is partially dissociated in the first place, *i.e.* for cases 1–2, 5–6, and 12.

Boundary-layer profiles of temperature are given in Figure 5.16 to show the magnitude of temperature increase in the boundary layer, due to viscous dissipation, that is possible under the present shock tunnel conditions. The largest increase is found for case 9 which has the highest Mach number, but dissociation with respect to the edge composition remains negligible because the edge temperature is already so low. Cases 7–8 and 10–11 all have $T_{max} > T_e$, where, as indicated for case 11 relative to case 9 in Figure 5.16, T_{max} decreases with decreasing M_∞. At high enthalpy and low incidence (cases 5–6 and 12; the latter is not shown but looks very similar to case 5), a mild increase in temperature is seen. The high-enthalpy cases generally show T_{max} slightly higher for catalytic-

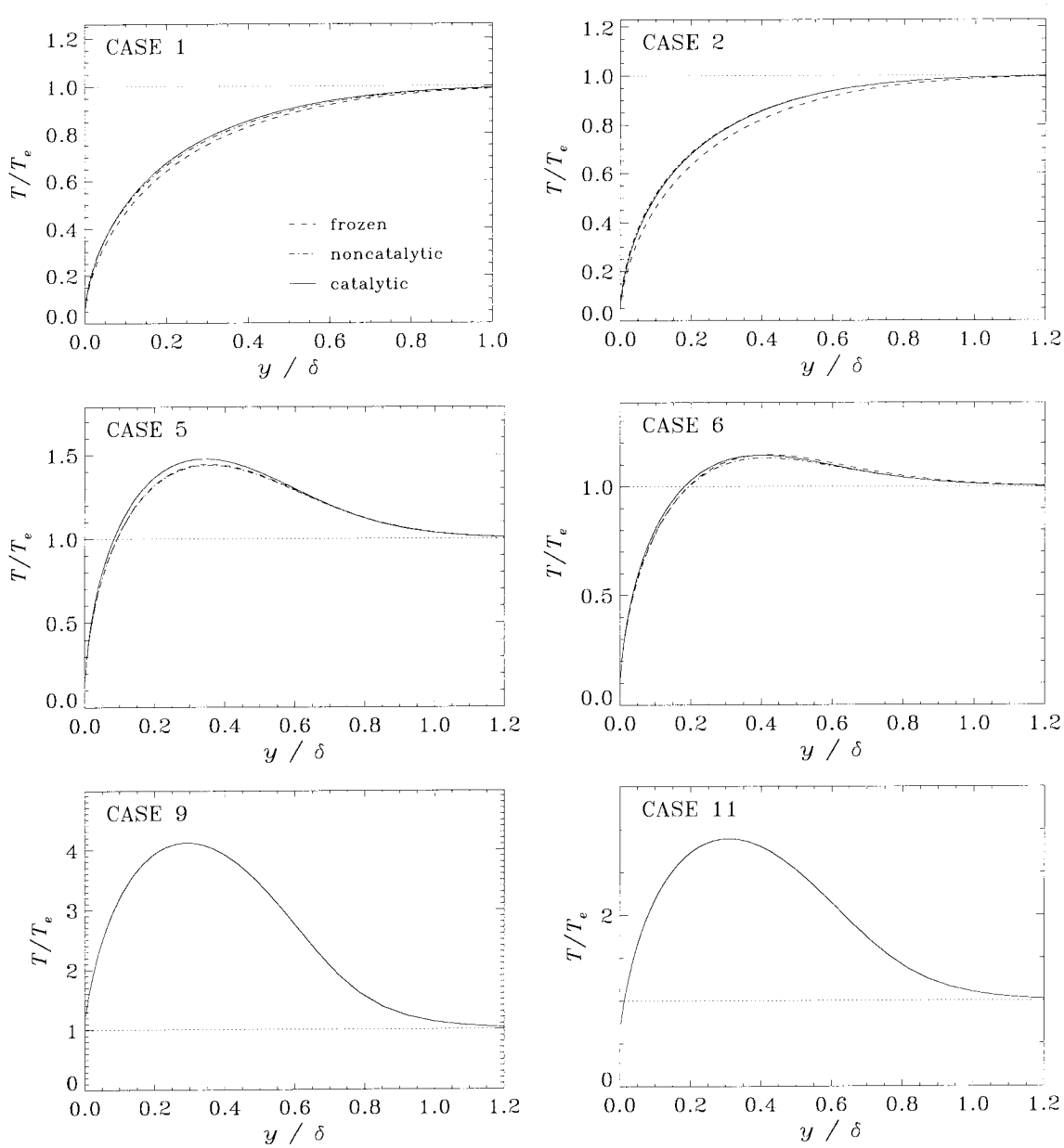

Figure 5.16: Selected computational boundary-layer results for T/T_e. Cases are described in Table 5.3.

wall reacting flow than for frozen flow, as expected for the exothermic recombination process shown by the mass fraction profiles. There are regions in cases 5 and 6, however, where the opposite trend occurs. At high incidence, for cases 1–4 where $M_\infty < 2$, no temperature increase is found, *i.e.* $T_{max} = T_e$ (only cases 1–2 are shown in Figure 5.16). Further results from the computational boundary-layer study are presented as they are needed in the following sections.

5.2.2 Separation Length

Internal mechanisms for real-gas effects on separation length are conveniently divided into those which arise in the boundary layer upstream of separation, and those which arise in the region downstream of separation. In terms of the theoretical scaling for separation length developed in Section 4.2.2, the only internal mechanism arising upstream of separation is a change in the undisturbed boundary-layer profile due to reactions. In particular, separation length depends on the wall shear stress, In Section 5.2.2.1 the effect of recombination on the wall shear stress is investigated using the computational boundary-layer results. Mechanisms arising downstream of separation cannot be studied in terms of the present scaling law, but are considered qualitatively in Section 5.2.2.2 using the viscous double-wedge computations described in Section 3.5.

5.2.2.1 Upstream Boundary Layer

According to the theoretical scaling developed in Section 4.2.2, L_{sep} depends on the wall shear stress of the undisturbed boundary layer. Thus changes in L_{sep} may arise due to real-gas effects on the upstream velocity profile which determines the wall shear stress. From the general boundary-layer equations for a reacting flow, Equations 4.4–4.6, it is apparent that the velocity profile, determined by the momentum equation, is affected only indirectly by changes in the composition of the gas due to reactions. In fact, for a flat plate, the right-hand side of Equation 4.5 is zero, and the self-similar solution for the velocity profile $f'(\eta)$ is coupled to chemistry only by real-gas effects on the Chapman-Rubesin parameter, $C(\eta) = \rho\mu/\rho_e\mu_e$. Changes in the C-profile are directly linked to real-gas effects on the enthalpy profile, as well as the dependence of viscosity on gas composition. If the Schmidt number $Sc = \mu/\rho D_{12}$ were large compared to C, then the direct coupling between C and the mass fraction profile in the mass-diffusion terms of Equations 4.4 and 4.6 would be very weak. This is generally not true, as indicated by the profiles of Sc and C in Figure 5.17 taken from computational results for case 1 of the boundary-layer study. The variation in Sc over all the cases investigated is not large ($1.7 < Sc < 2.7$). The velocity profile in physical coordinates is also affected by changes in the similarity transformation for η due to changes in the density profile, *i.e.* $y \propto \int(\rho_e \mathrm{d}\eta/\rho)$ from Equation 4.2.

The goal in this section is not only to quantify real-gas effects on the skin friction, but also to understand in detail the physical mechanisms which cause the behavior observed by computation. The phenomena are very complex and thus we further subdivide the discussion in this section. First the degree of nonequilibrium is investigated and quantified by a new nondimensional rate parameter. Then results for the effect of recombination on skin friction are presented and found to be inadequately described by previous analyses. The present computational results are then examined in detail to elucidate mechanisms for real-gas effects in recombining boundary layers.

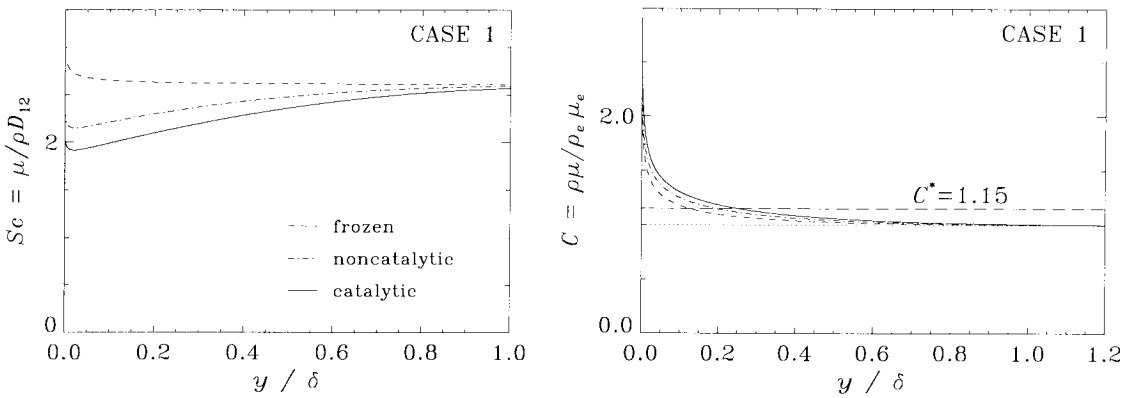

Figure 5.17: Computational boundary-layer results for Sc and C, at the high-enthalpy condition of case 1 described in Table 5.3. Also shown in is C^*, the value of C evaluated at the reference temperature based on edge conditions.

Finally, the computational results are also compared to frozen-flow predictions using the analytical results from Section 4.1.1.

Reaction-Rate Parameter for Nonequilibrium Boundary Layers: Before presenting the computational results for wall shear stress, it is desired to develop an appropriate nondimensional reaction-rate parameter that may illuminate trends in the nonequilibrium behavior. The local dimensional reaction rate $\mathrm{d}\alpha/\mathrm{d}t$, formed from local values of the net mass production rate of N per unit volume w_N and density ρ computed by the N–S code, is shown in Figure 5.18 for the high-enthalpy cases 1–2 and 5–6. The absolute value of w_N is used to show both dissociation ($w_\mathrm{N} > 0$) and recombination ($w_\mathrm{N} < 0$) in the same log scale. Note that w_N/ρ varies by at least an order of magnitude between the boundary-layer edge and the wall. This is one reason we rely on the N–S code to obtain reasonably accurate predictions of the real-gas effects, instead of the self-similar boundary-layer equations; even if the streamwise gradients are small so that local similarity applies, the third similarity condition in Equation 4.7 is seriously violated by the strong variation of w_N/ρ with η. In fact, w_N/ρ can even change sign in the boundary layer, as seen in Figure 5.18 for the high-incidence cases 1 and 2, where the edge condition experiences nonequilibrium dissociation. The low-incidence cases 5 and 6 have weak nonequilibrium recombination outside the boundary layer, as noted in Section 5.1.2 in connection with the inviscid computational result for shot 1776.

Where $\mathrm{d}\alpha/\mathrm{d}t$ is small, the gas is close to its local equilibrium composition; in Figure 5.18 this appears to occur at the dissociation–recombination transition in cases 1 and 2, and throughout much of the boundary layer in cases 5 and 6. At the wall, however, only the catalytic-wall results show local equilibrium, where it has actually been enforced by setting $\alpha_w = 0$, the equilibrium composition at the wall temperature. For a noncatalytic wall, the imposed boundary condition $(\partial\alpha/\partial y)_w = 0$ causes the composition at the wall to be determined by conditions slightly away from the wall, where the velocity may be high enough to maintain a nonequilibrium state. In fact,

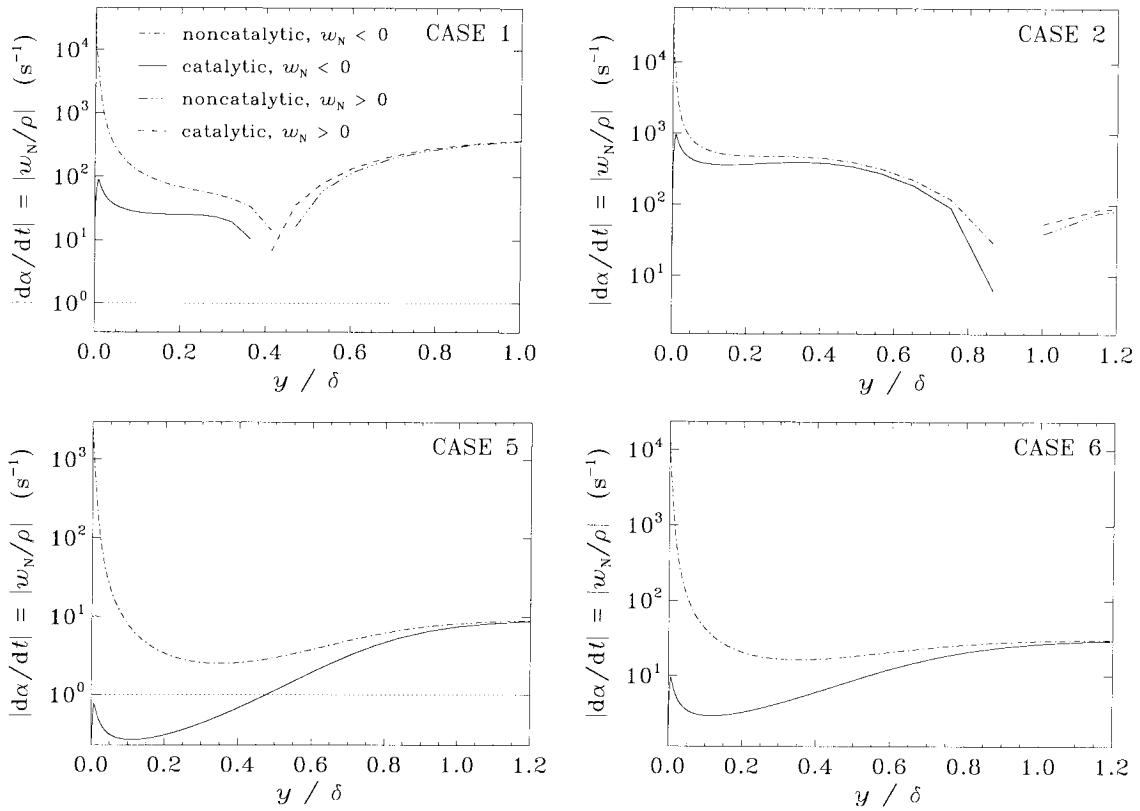

Figure 5.18: Selected computational boundary-layer results for the local reaction rate $|d\alpha/dt| = |w_N/\rho|$. The break in curves for cases 1 and 2 occurs at transition between net dissociation ($w_N > 0$) and recombination ($w_N < 0$). Cases are described in Table 5.3.

close to the wall, there are two velocities which need to be considered in determining the degree of nonequilibrium; the streamwise velocity u which may convect the gas downstream at a rate comparable to the recombination rate, and the normal-direction diffusion velocity v_N which may move atoms towards the wall at a rate comparable to the recombination rate. Close examination of the computational results shows that v_N is only comparable to u very close to the wall, and only dominates u in the catalytic-wall results. The latter observation may explain the narrow peak in recombination rate observed near a catalytic wall for all cases in Figure 5.18, *i.e.* the high diffusion velocity causes a higher degree of nonequilibrium.

It is difficult to define a global Damköhler parameter for reacting boundary-layer flows because there are several phenomena of importance; convection, diffusion, and wall boundary condition. One might nondimensionalize the reaction rate by a time scale based on either the streamwise velocity and distance from the leading edge, or the normal diffusion velocity and boundary-layer thickness. But since both of these velocities vary significantly through the boundary layer, it is not clear what values best characterize the time scales for convection and diffusion. Fay and Riddell (1958) introduced a rate parameter for nonequilibrium gas-phase recombination in stagnation-point boundary layers; Inger (1964, 1995a,b) and Inger and Elder (1991) presented in addition Damköhler parameters to

characterize nonequilibrium wall recombination for an arbitrarily catalytic wall in stagnation-point boundary layers and nonequilibrium dissociation in flat-plate boundary layers. Recombination-dominated flat-plate boundary layers, however, have not been considered. After trying several formulations, the following simplified gas-phase Damköhler parameter, similar to one given by Rae (1963), was found to best correlate the present computational results for nonequilibrium effects on the wall shear stress:

$$\Gamma = \frac{x}{u_e}\left(\frac{\mathrm{d}\alpha}{\mathrm{d}t}\right)_{w,\,\alpha=\alpha_e}, \tag{5.22}$$

where the reaction rate is evaluated at the wall temperature and density but the free-stream composition, and x/u_e is used to characterize the streamwise flow time. This gives an indication of the initial reaction rate, relative to the external flow rate, when the free-stream gas is brought instantaneously to the wall condition at the leading edge of the boundary layer. In this way Γ is analogous to the parameter Δ given in Section 5.1.1 for inviscid flow, which concerns the initial reaction rate immediately downstream of a chemically frozen shock wave. Because the recombining gas in the boundary layer is flowing at a much smaller velocity than u_e, $\Gamma \sim 1$ does not correspond to strong nonequilibrium as $\Delta \sim 1$ does for inviscid flow; $\Gamma \to 0$ and $\Gamma \to \infty$ do, however, correspond to frozen and equilibrium flow respectively. The convention $\Gamma < 0$ for recombination is maintained for consistency with Δ. This boundary-layer Damköhler parameter Γ is only useful for noncatalytic walls, because for catalytic walls, α_w is forced immediately to its equilibrium value even at the leading edge.

Computational Results for Skin Friction: The effect of recombination on wall shear stress is presented in Figure 5.19 by plotting the ratio of reacting-to-frozen results for C_f, the local skin friction coefficient defined by Equation 4.13, against $-\Gamma$, the gas-phase recombination Damköhler number defined by Equation 5.22. Perhaps the most important (and immediately obvious) result is that under the present conditions, recombination in the boundary layer has only a minor effect on the wall shear stress, causing not more than a 5% increase. The increase found here for the high-incidence cases 1 and 2 may even overestimate the effect under experimental wedge-flow conditions where α_e actually increases continuously from the leading edge to reach the value at station 1 used for the boundary-layer computation free stream. For catalytic-wall cases, the increase in wall shear depends only on α_e, which is $\simeq 0.22$ for cases 1–2 and $\simeq 0.11$ for cases 5–6 and 12; the catalytic-wall cases at smaller Γ have negligible dissociation to begin with. For a noncatalytic wall, the reacting-to-frozen wall-shear ratio gradually increases with increasing $-\Gamma$ for the range $-\Gamma \gtrsim 100$. The low-enthalpy high-incidence cases 3 and 4 show a very slight ($< 1\%$) decrease in wall shear for reacting flow compared to frozen flow despite negligible recombination (except at the wall, which should cause the opposite effect); the only observable difference which might explain this behavior is that the edge conditions in the reacting-flow computations for these cases are slightly changed from

those in the frozen-flow computations due to vibrational nonequilibrium, *i.e.* the discrepancy may disappear if the frozen-flow free stream for cases 3 and 4 is modified as it was done for cases 1 and 2. Cases 9 and 10 have extremely small Γ and are not shown in Figure 5.19. Since L_{sep} is inversely proportional to the square of the wall shear according to the general scaling in Equation 4.46, the present results suggest that when there is significant dissociation in the external flow, recombination in the boundary layer causes a slight decrease in separation length.

The above result that skin friction increases with recombination is not consistent with the suggestion of Mallinson *et al.* (1996b, 1997b) that boundary-layer thickness δ and displacement thickness δ^* should increase for a recombination-dominated boundary layer (and hence increase L_{sep} according to the various scalings which show a direct proportionality between L_{sep} and δ or δ^*, *cf.* Equations 1.7 - 1.12) based on their analysis of real-gas effects in boundary layers (Mallinson, 1994; Mallinson *et al.*, 1997b). This analysis considers the chemical energy released or absorbed along a streamline in the boundary layer, and the effect this has on the temperature and density profiles which determine boundary-layer thickness in the physical plane. The endothermic process of dissociation is found to increase the density and hence decrease the thickness by the dilatational mechanism mentioned earlier; the opposite is assumed to occur for gas-phase recombination. The relationship between boundary-layer thickness and the wall shear used to scale L_{sep} in the present study appears to be straightforward; at constant Reynolds number, increasing the thickness stretches out the velocity profile in the physical normal coordinate, resulting in a lower shear stress at the wall. The computational results in Figure 5.19 for the reacting-to-frozen ratio of δ, however, show instead a decrease in δ due to recombination, and only for the highest values of α_e found in cases 1 and 2 despite the recombination occurring in cases 5–6 and 12. There is also no difference between the catalytic and noncatalytic results. Interestingly, the decrease is less for the higher-density case 2 than for case 1.

A completely different analysis of reacting boundary-layer flow was undertaken by Ikawa (1979),

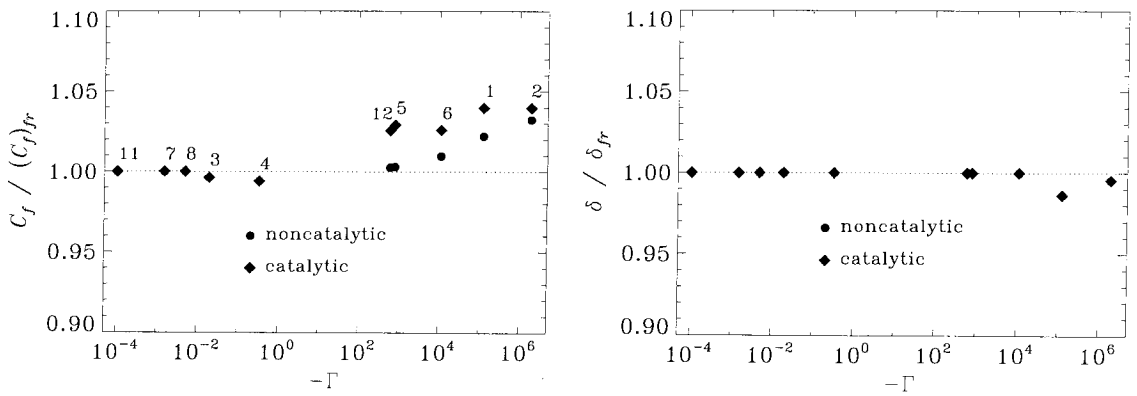

Figure 5.19: Comparison between frozen and reacting computational boundary-layer results for C_f and δ, plotted against the nondimensional reaction-rate parameter Γ given by Equation 5.22. ◆ are catalytic-wall results, • are noncatalytic-wall results, and the numbered cases are described in Table 5.3.

who extended Klineberg's momentum integral method to include the species conservation equation and considered a fully dissociated edge condition and fully recombined wall condition (*cf.* Sections 1.5.1.1 and 1.5.4.1). He assumes that diffusion dominates over nonequilibrium chemistry, *i.e.* that $w_N \simeq 0$ and the last term in Equation 4.4 can be neglected, and finds a large decrease in δ^* for reacting flow compared to frozen flow as well as a decrease in L_{sep}. (Strangely, he also shows negligible increase in C_f upstream of separation but a large increase at reattachment with respect to frozen flow.) This result is consistent with the idea that diffusion of high-speed atoms towards the wall and low-speed molecules away from the wall acts to make the velocity profile fuller and the thickness smaller, and taken together with the analysis of Mallinson *et al.* (1997b) described above (which entirely neglects diffusion and considers instead the energy released by recombination), suggests that diffusion and recombination have compensating effects on the boundary-layer thickness and wall shear, with diffusion dominating the present results which show decreased thickness and increased wall shear for recombination.

In fact, the problem is more complicated than implied by either of these approximate methods. For example, in the analysis of Mallinson *et al.* (1997b), the difference between equilibrium flow and frozen flow inside the boundary layer is given by an exchange between chemical energy and thermal energy at constant pressure, constant enthalpy, and constant specific heat; thus for recombination with respect to frozen dissociated flow, the temperature increases and the density decreases. Inside a boundary layer experiencing strong recombination, however, the specific heat cannot be approximated as a constant, and energy released by recombination can be carried away by conduction or diffusion due to the presence of gradients in temperature and mass fraction. Conduction can be particularly important very close to a cold wall, where the temperature is constrained. It is not immediately obvious what effect recombination has in general on the temperature and density in a boundary layer, or how these effects translate into changes in shear stress. A deeper understanding of the physics involved is desired in order to extrapolate the present results for recombining cold-wall boundary layers to other situations such as dissociation-dominated boundary layers, hot walls, and flow in the separated shear layer downstream of separation.

Detailed Examination of Boundary-Layer Recombination: We use the present computational boundary-layer results to look first at the effect of recombination in the main part of the boundary layer away from the wall. Figures 5.20–5.22 present boundary-layer profiles from the reacting-flow solutions normalized by the frozen-flow solution profiles, and plotted against physical distance from the wall normalized be the frozen-flow boundary-layer thickness. This makes clear what changes occur due to chemistry. Cases 2 and 6 are shown because they exhibit different behavior (these cases are described in Table 5.3; see also Figure 5.15 for mass-fraction profiles and Figure 5.16 for edge-normalized temperature profiles). In Figure 5.20, the temperature is seen to

increase for case 2 but decrease over a large part of the boundary layer for case 6. Under the assumptions used in the analysis by Mallinson *et al.* (1997b), recombination is expected to cause a temperature rise by the conversion of potential chemical energy into thermal energy. The magnitude of temperature increase for a given degree of recombination depends on how the specific heat changes with recombination; in fact, c_p decreases with respect to frozen boundary-layer flow according to

$$\frac{c_p}{c_{p,\,fr}} = \frac{3\alpha + 7}{3\alpha_e + 7}\,. \tag{5.23}$$

This effect may be important in the lower region of the boundary layer for case 2, where $\alpha_e - \alpha$ is largest.

In order for the temperature to decrease with recombination, the assumption of constant local enthalpy used by Mallinson *et al.* (1997b) must be violated. From the boundary-layer equation for conservation of energy (Equation 4.6), it is apparent that if $Le \neq 1$, the effect of chemistry on the temperature depends on the species and enthalpy gradients, in particular, $\partial h/\partial y$, $\partial \alpha/\partial y$, and $\partial^2 \alpha/\partial y^2$. In addition, the conduction term depends on the second derivative of enthalpy. An obvious difference in this regard between cases 2 and 6 can be seen in the edge-normalized temperature profiles (Figure 5.16); only case 6 has a region where $\partial T/\partial y < 0$, which coincides with

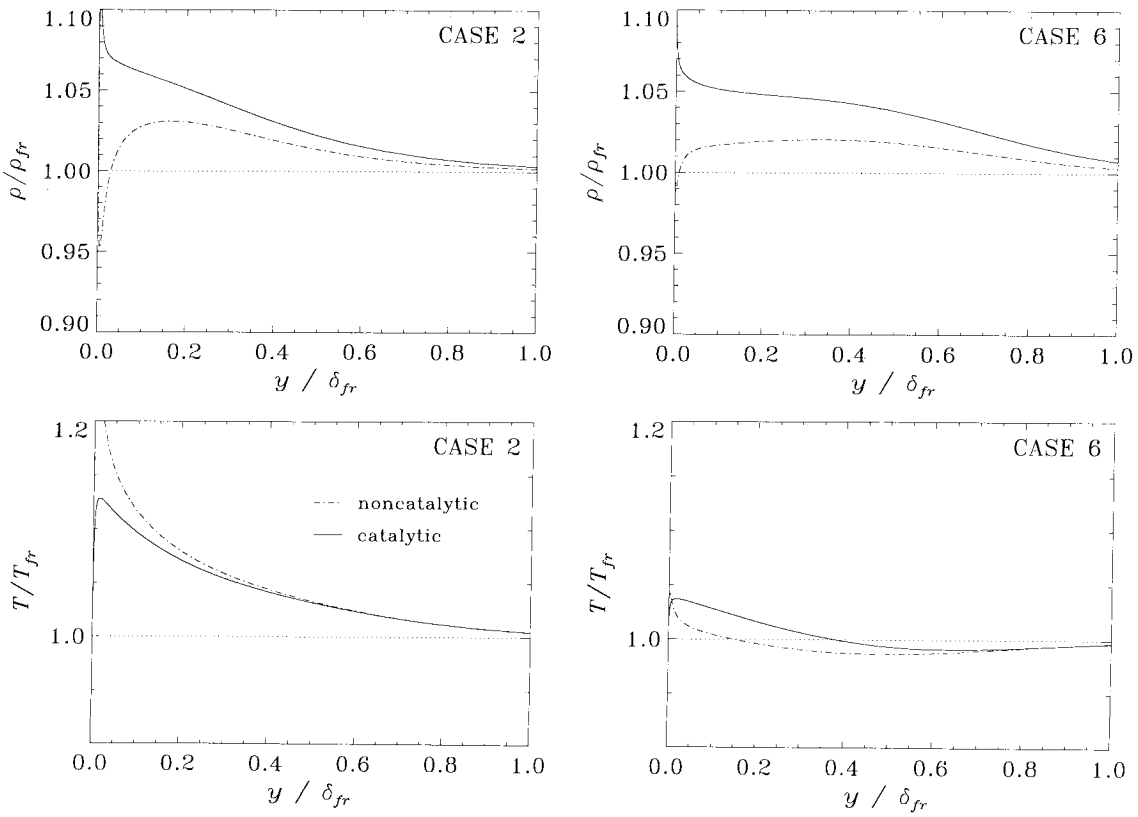

Figure 5.20: Boundary-layer profiles of reacting-to-frozen ratios of T and ρ taken from computational boundary-layer results for cases 2 and 6 described in Table 5.3.

the region of temperature decrease, at least for the catalytic solution, seen in Figure 5.20. The outer part of the boundary layer in case 6 is also the only region where $\partial^2 T/\partial y^2 > 0$; for case 5 in Figure 5.16, it appears that $T/T_{fr} < 1$ only where $\partial^2 T/\partial y^2 > 0$. The temperature decrease in the noncatalytic solution for case 6 extends down to $y \simeq 0.2\delta_{fr}$ where $T = T_e$ and all derivatives are of the same sign as in case 2, suggesting that the relative magnitudes of the derivatives are as important as their relative signs. Though they do not change sign, the mass-fraction derivatives are smaller for case 6 due to less dissociation at the boundary-layer edge. While it can be shown by expanding the conduction and diffusion terms in Equation 4.6 that the sign and magnitude of the various derivatives are important in determining the sign and magnitude these terms overall, it is not clear exactly what trends should be expected for the effect of recombination on the local temperature. In addition, a nonequilibrium boundary layer may have streamwise derivatives of temperature and species concentration, particularly near a noncatalytic cold wall, which contribute to the energy balance (*cf.* Equation 3.4). The result for case 6 suggests that having $\partial\alpha/\partial y$ and $\partial T/\partial y$ of opposite sign, $\partial^2 T/\partial y^2 > 0$, or $\partial\alpha/\partial y$ small relative to $\partial T/\partial y$ may cause a change in the energy balance that results in decreased temperature with recombination.

The effect a change in temperature due to reactions has on the density is simply given by the thermal equation of state. When this is written as in Equation 3.23, it is quite evident that the direction of change depends strongly on the degree of recombination;

$$\frac{\rho}{\rho_{fr}} = \frac{T_{fr}}{T}\left(\frac{1+\alpha_e}{1+\alpha}\right), \tag{5.24}$$

since the pressure remains essentially constant across the boundary layer. Thus whether density increases or decreases with recombination depends on a balance between the change in α and the change in T. The former can be significant in the lower region of a recombining boundary layer, and clearly dominates the effect on density for case 2 in Figure 5.20. The density increases for case 6 as well, controlled by the decrease in temperature where the change in α is relatively small.

It was mentioned at the beginning of this section that real-gas effects on the velocity profile may arise from changes in the Chapman-Rubesin parameter C and changes in the physical scale related to changes in the density profile. The density was seen in Figure 5.20 to increase with recombination over much of the boundary layer. The effect of recombination on C and u is shown in Figure 5.21, causing an increase in C but different results for u in each case. The effect of changes in C on the velocity profile may be seen by considering the approximate boundary-layer formulation wherein C is taken to be constant and is moved into the similarity transformation. From Equation 4.9, this gives $y \propto \sqrt{C}$, *i.e.* increasing C reduces the fullness of the velocity profile by enlarging the physical coordinate. Since we also have $y \propto \int(\rho_e d\eta/\rho)$, increasing the density has the opposite effect. The change in velocity for case 2 in Figure 5.21 is dominated by the change in C which is larger than

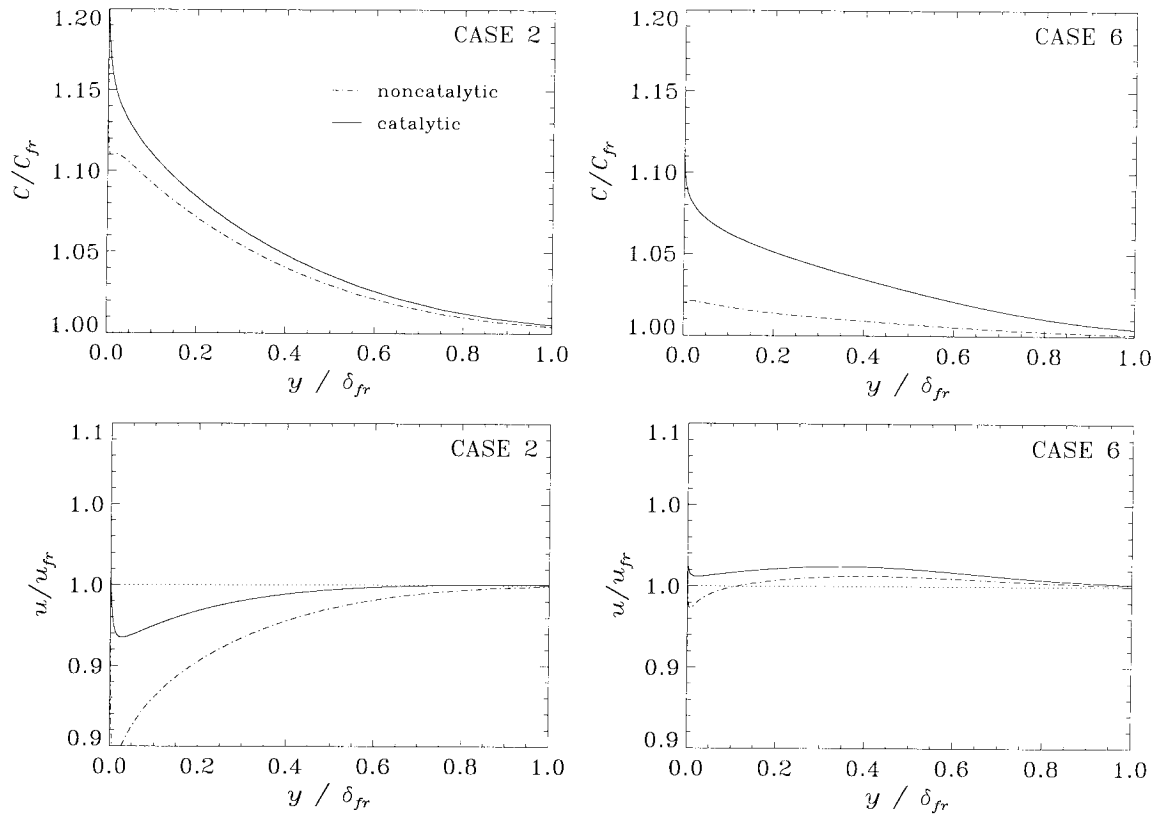

Figure 5.21: Boundary-layer profiles of reacting-to-frozen ratios of C and u taken from computational boundary-layer results for cases 2 and 6 described in Table 5.3.

for case 6. The change in velocity for case 6 is dominated over much of the boundary layer by the increase in density (*cf.* Figure 5.20), particularly because it is the integral of the density that is important, and the profile of ρ/ρ_{fr} is fuller than in case 2.

Ultimately we are interested in the shear stress, which depends on the velocity gradient and the viscosity; all three are shown in Figure 5.22 for cases 2 and 6. The reacting-to-frozen ratios of $\partial u/\partial y$ and τ are indeterminate at the boundary-layer edge where they both become zero. The behavior in this region depends on small numerical errors and has no physical significance; the ratios are plotted this way to quantify the local relative changes due to recombination inside the boundary layer. It was shown in Section 4.1.4 that the viscosity of dissociating nitrogen increases with temperature and atomic mass fraction, but is most sensitive to the temperature; hence the similarity between profiles of μ/μ_{fr} in Figure 5.22 and T/T_{fr} in Figure 5.20. Results for the reacting-to-frozen ratio of $\partial u/\partial y$ are consistent with the results for u/u_{fr} in Figure 5.21. The uniform decrease in fullness of the velocity profile for case 2 decreases the gradient in the lower part of the boundary layer and increases it in the outer part of the boundary layer; *vice versa* for case 6 (except near the wall). The shear stress is seen to increase across the boundary layer for case 2, dominated by the increased viscosity in the lower region. For case 6, τ follows the behavior of $\partial u/\partial y$, the decrease in viscosity

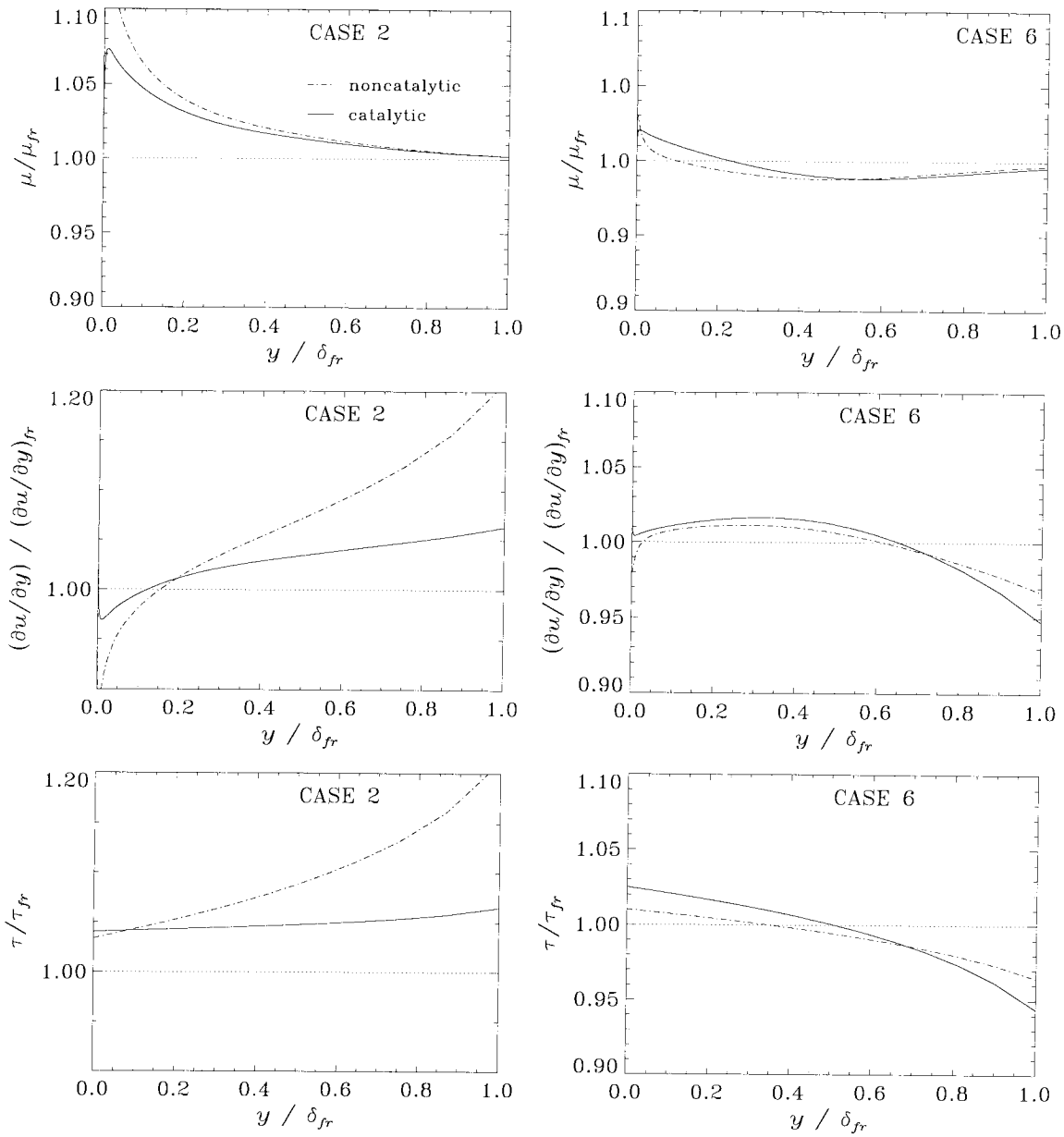

Figure 5.22: Boundary-layer profiles of reacting-to-frozen ratios of μ, $\partial u/\partial y$, and τ taken from computational boundary-layer results for cases 2 and 6 described in Table 5.3. The curves for $\partial u/\partial y$ and τ have no significance near $y = \delta_{fr}$ where the ratios are indeterminate.

causing only a shift in the point $\tau = \tau_{fr}$ to lower y/δ_{fr}.

The effect of recombination on the shear stress in the middle part of the boundary layer is of interest for the discussion in the next section concerning the behavior of τ in the separated shear layer. The skin friction of the incoming boundary layer, however, depends on what happens near the wall, which is difficult to discern in Figures 5.20–5.22. Near-wall ($y \leq 0.1\delta_{fr}$) profiles of reacting-to-frozen ratios of various parameters are presented in Figure 5.23 using a log coordinate. Only case 2 is shown because case 6 has similar, though less prodigious, behavior in this region. The curves

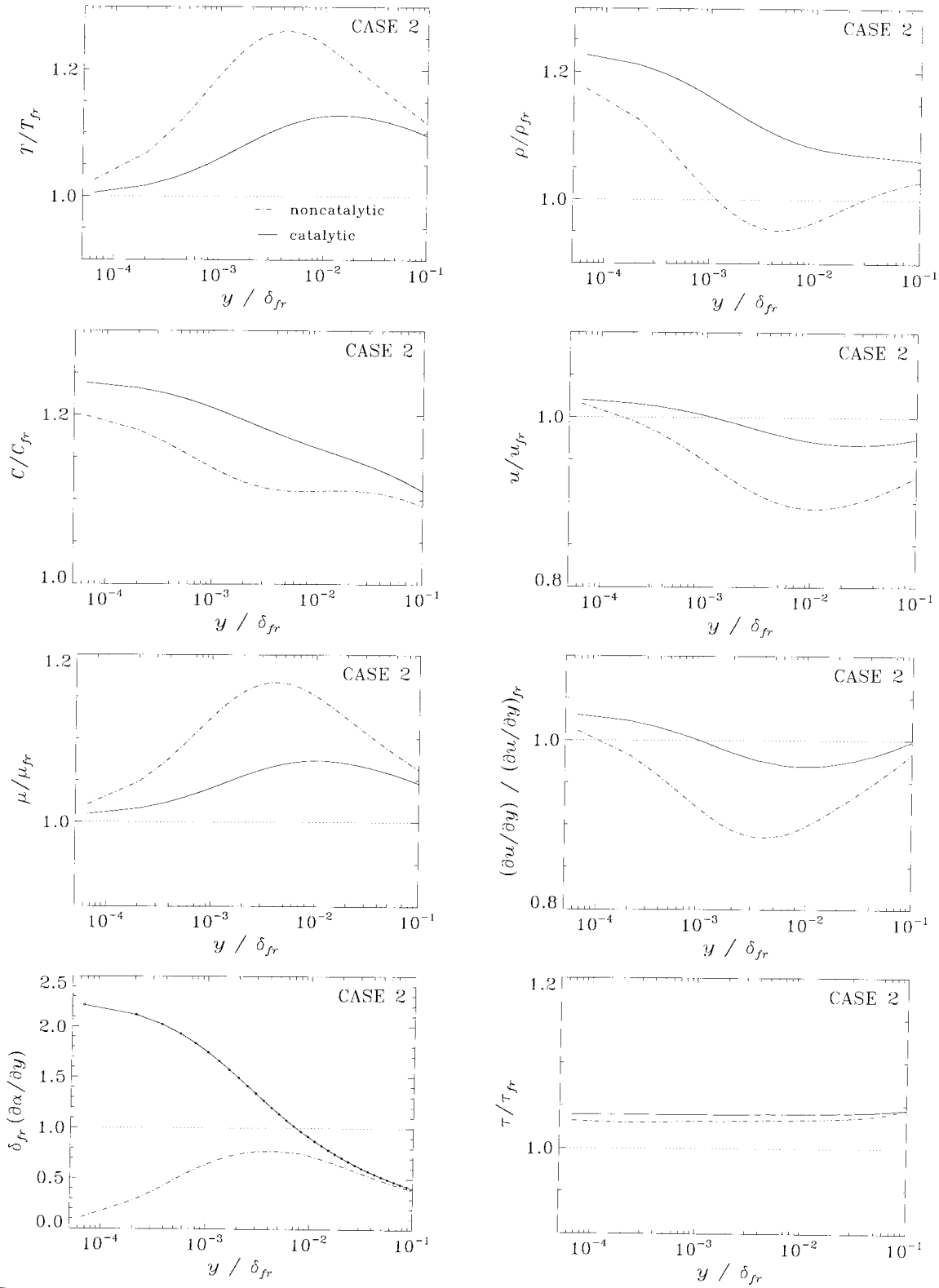

Figure 5.23: Near-wall ($y \leq 0.1\delta_{fr}$) boundary-layer profiles of reacting-to-frozen solution ratios for computational case 2 described in Table 5.3. Points on catalytic-wall curve for $\delta_{fr}(\partial\alpha/\partial y)$ indicate cell centers from computational grid.

end at the center of the computational cell adjacent to the wall, and points corresponding to the other cell centers are shown on the catalytic-wall solution for mass-fraction gradient. To correctly compute derivatives, it was necessary to add a datum on the wall and to avoid the use of curve fits for data-smoothing (all results in Figures 5.20–5.23 involving derivatives were computed from a shape-preserving cubic-spline interpolant).

The effect of recombination on the temperature becomes quite significant in the region near, but slightly away from, the wall. For a noncatalytic wall condition, the increase is twice that found for a catalytic wall. Since α is not much different in this region between the two cases (*cf.* Figure 5.15), the difference in temperature increase cannot be attributed to the effect of recombination on c_p given by Equation 5.23. Instead, we look for differences in the temperature and mass fraction gradients which as indicated earlier, may play an important role in determining the magnitude and direction of temperature change due to recombination. The gradient of α, nondimensionalized in Figure 5.23 by using the frozen-flow boundary-layer thickness, is seen to behave quite differently near the wall, as expected, for catalytic and noncatalytic boundary conditions. Note that in the noncatalytic solution, the location where $\partial^2\alpha/\partial y^2$ changes sign coincides with the location of maximum temperature. This suggests that the curvature of the mass-fraction profile is determining the degree to which temperature increases from recombination. The temperature rise for the noncatalytic wall is large enough to dominate the decrease in α (*cf.* Equation 5.24) and produce a region where $\rho/\rho_{fr} < 1$. Very close to the cold wall, however, the temperature is constrained and the density increases due to the decrease in α, while the chemical energy released by recombination is conducted to the wall by the large gradient in temperature. The increase in density very close to the wall dominates the effect of recombination on velocity and velocity gradient; for the noncatalytic wall $u/u_{fr} > 1$ and $\partial u/\partial y > 1$ at the wall-adjacent computational cell despite the large value of C/C_{fr} and the region of decreased density a slight distance away from the wall. Because the viscosity increases due to an increase in temperature over the same region where $\partial u/\partial y < 1$, the shear stress turns out to be nearly constant across the inner part of the boundary layer.

Summary of Internal Mechanisms Arising Upstream of Separation: Under the conditions of the present study, skin friction is found to increase at high enthalpy with respect to a frozen-flow boundary layer with the same edge conditions (*cf.* Figure 5.19), hence causing a decrease separation length. The effect is too small to be detected using the present experimental techniques. The increase in skin friction is due entirely to the dilatational effect of increased density at the wall which occurs for recombination under the condition of constrained temperature at the wall. The change in α also dominates the effect of recombination on density throughout much of the boundary layer, leading to the decrease in boundary-layer thickness seen in Figure 5.19. This decrease is less for case 2 than case 1, probably because the near-wall temperature increase and corresponding density decrease is

greater for case 2 and the integral quantity δ is sensitive to changes near the wall where the density is highest. According to the above mechanism, flows with no free-stream dissociation and a catalytic wall but with dissociation occurring inside the boundary layer should not experience an increase in skin friction due to real-gas effects, because $\alpha_w = 0$ regardless of whether the flow is frozen or reacting. For flows with an isothermal wall hot enough to cause dissociation, the skin friction may decrease over frozen flow due to increased α at constrained T_w. For an adiabatic wall, however, T_w is not constrained, and C_f may depend on how the flow behaves a short distance from the wall. The present results for increased skin friction at a cold wall cannot necessarily be extrapolated to flight conditions, for which the wall temperature is typically much greater.

Aside from the work of Ikawa (1979) mentioned previously, the present author knows of no other literature giving computed results for a recombination-dominated flat-plate boundary layer. Of those authors considering dissociation-dominated flat-plate boundary layers (Blottner, 1964; Inger, 1964, 1995a,b; Moore, 1952; Rae, 1963), only Moore (1952) looked at the effect of reactions on skin friction, finding an increase for very high wall enthalpy. Debestrian and Anderson (1993) and Ott and Anderson (1993) compared skin friction computed for dissociating boundary layers to predictions using the reference temperature, but not to frozen-flow results. It should also be noted that Blottner (1964) found a decreased boundary-layer thickness due to dissociation over a catalytic wall, consistent with the analysis of Mallinson *et al.* (1997b).

Comparison Between Computation and Theory: The computational boundary-layer results may also be used to study the error involved in approximating C_f and δ by applying the reference-temperature concept under the assumptions of local similarity, flat-plate flow, and chemically frozen flow. These are the assumptions used to obtain the scaling for separation length in Equation 4.48. Comparisons between the computational result (labeled CFD) and the result from this simple theory for C_f (Equation 4.18) and δ (Equation 4.23) using edge conditions taken from the computations are shown in Figure 5.24 as a function of M_e. The corresponding case number for each datum can be found by referencing M_∞ in Table 5.3.

As expected from the results in Figure 5.19, the theory-to-computation ratio of C_f is smaller for reacting flow than for frozen flow in those cases where significant recombination occurs. Even for frozen flow, however, the error remains small only at moderate Mach number; the theory overpredicting C_f by more than 5% at $M_e \simeq 5$ and 15% at $M_e \gtrsim 7$. The prediction for δ is within $\pm 10\%$ at low Mach number, but falls off almost linearly with increasing Mach number, underpredicting the computational result by 50% at $M_e \simeq 9$. The main difference between low- and high-Mach-number cases is the degree of viscous interaction. This causes an increased favorable pressure gradient which acts to increase skin friction and decrease thickness according to self-similar boundary-layer theory (*e.g.* Cohen and Reshotko, 1956 or Rogers, 1992). In Figure 5.24, however, the opposite holds true;

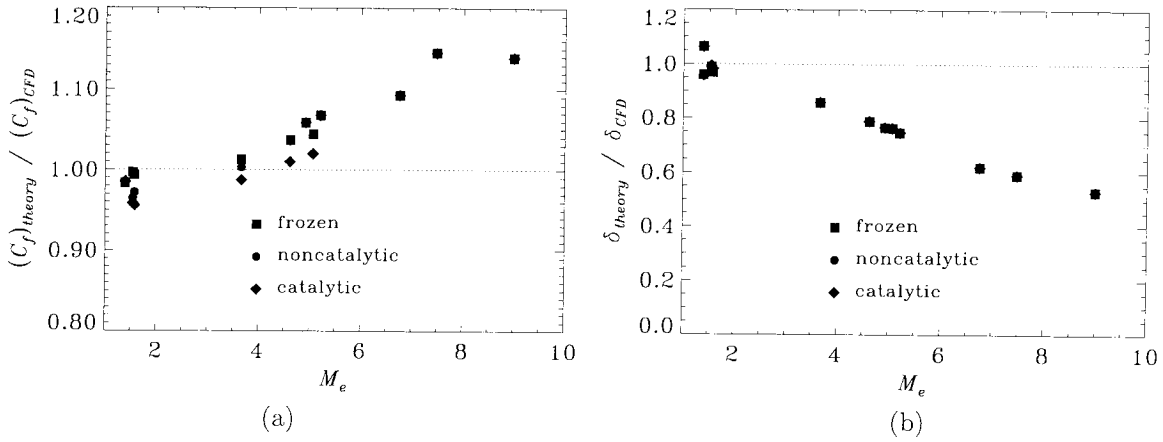

Figure 5.24: Comparison between frozen-flow flat-plate theory and computational boundary-layer results for (a) C_f and (b) δ, plotted against M_e, which can be used to reference cases in Table 5.3. ■ are frozen-flow results, ♦ are catalytic-wall results, and • are noncatalytic-wall results.

C_f is lower than predicted and δ is higher than predicted. The only other candidates for error sources are the reference-temperature formulation, which Dorrance (1962) suggests is less valid at high Mach number for cold isothermal walls, or the viscosity model. The viscosity computed by the method in Section 4.1.4 is compared in Figure 5.25 with the viscosity output by the N–S code, which has been computed by the more advanced model mentioned in Section 3.1.2, using the computational boundary-layer result for case 9 which has the highest Mach number ($M_e \simeq 9$). The simpler model does give a higher value for the viscosity, but not enough to account for the difference seen in Figure 5.24 for case 9. In the present experiments for which separation length was measured, $M_1 \lesssim 5$ and the reference-temperature method provides an adequate approximation for the wall shear stress, as was also indicated by the comparisons in Section 4.1.1.3.

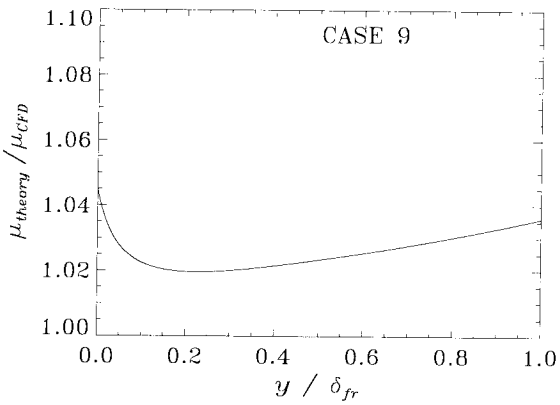

Figure 5.25: Comparison between viscosity models for computational boundary-layer case 9 in Table 5.3. μ_{theory} is the simplified model given in Section 4.1.4, μ_{CFD} is the advanced model used in the N–S code.

5.2.2.2 Separated Shear Layer

We now turn our attention to internal mechanisms for real-gas effects on separation length which arise downstream of separation. These cannot be included in the present scaling for separation length which relies on an asymptotic multi-deck structure, developed for perfect-gas flow, to describe flow

about the dividing streamline. Such a structure would need to be developed that includes the energy and species equations for reacting flow. Several authors have included the energy equation in triple-deck theory for flow at separation (Brown *et al.*, 1990; Kerimbekov *et al.*, 1994; Rizzetta, 1979), and Inger (1997) also generalized this theory for nonequilibrium flow with an arbitrarily catalytic wall. It may be possible to extend these more complete theories to the region downstream of separation in a manner similar to that used by Stewartson and Williams (1973), but such an undertaking is beyond the scope of the present work. Instead, we consider the problem only qualitatively, using the viscous double-wedge computations (*cf.* Section 3.5) as an aid to interpretation. A separated flow region was computed for the high-enthalpy experimental conditions corresponding to shots 1741 and 1796. Unfortunately, they could not be recomputed with frozen chemistry because either the reattachment shock or leading-edge shock is detached for frozen flow on these configurations. The nonequilibrium computations are still useful, in and of themselves, for obtaining information on how reactions proceed downstream of separation.

Figure 5.26a shows how a profile of flow properties through the shear layer is extracted from the viscous double-wedge computation of shot 1796. In Figure 5.26b, the Mach number and dissociation fraction along this extraction line are plotted against normal distance from the wall nondimensionalized by the distance y_{ψ^*} to the dividing streamline. The flow at ψ^* is in the high subsonic regime, and reversed flow occurs for $y < 0.5y_{\psi^*}$. Recombination occurs in the shear layer above ψ^*, but α and T remain constant over much of the separation bubble before falling to a low value at the noncatalytic wall. Note that the temperature inside the recirculating region is still more than half its value outside the shear layer, and does not equilibrate with the wall temperature. The dissociation fraction along the wall and along the dividing streamline (approximated in the computational results by taking a streamline very close to the wall upstream of separation) are shown in Figure 5.27 for both shots 1741 and 1796. Upstream of separation, α_w falls from the free-stream value due to nonequilibrium gas-phase recombination in the boundary layer near the noncatalytic wall. This recombination is stronger for shot 1796 due to higher density. Downstream of separation, α_w drops precipitously to a low value and then increases very slightly; this may correspond to a reverse-flow boundary layer with weak nonequilibrium departure from equilibrium conditions, being fed by the more highly dissociated gas near the wall at reattachment. The gas that has recombined near the wall upstream of separation is seen to begin dissociating as soon as it leaves the wall and follows the dividing streamline, which becomes insulated from the wall by the recirculating region and thus rises in temperature. The degree of dissociation attained is higher for shot 1796 because it has higher α in region 2 outside the shear layer. At reattachment, the dissociated gas near ψ^* is brought back close to the wall, resulting at least initially in a significantly higher mass-fraction gradient at the wall downstream of reattachment than existed in the boundary layer upstream of separation.

For flows with dissociation in the free stream, or occurring downstream of the leading-edge shock,

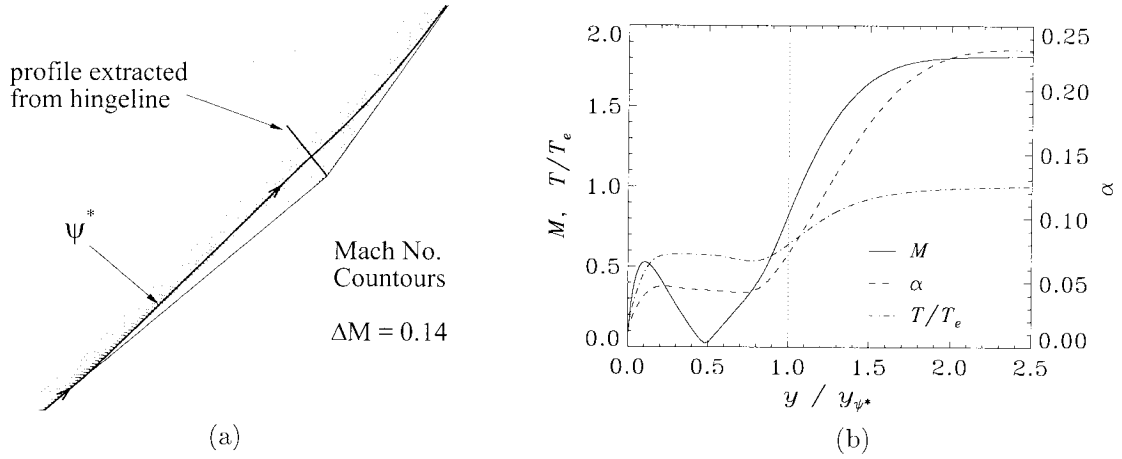

Figure 5.26: Viscous double-wedge computational results in the separation region for shot 1796 (condition C2, $A_e/A_* = 100$, $\theta_1 = 40°$, $\theta_w = 15°$); (a) Mach number contours, dividing streamline ψ^*, and line from which shear-layer profile is extracted; (b) profiles of M (solid curve), α (dashed curve), and T/T_e (dash–dot curve) through the separated shear layer ($T_e = 6940$ K).

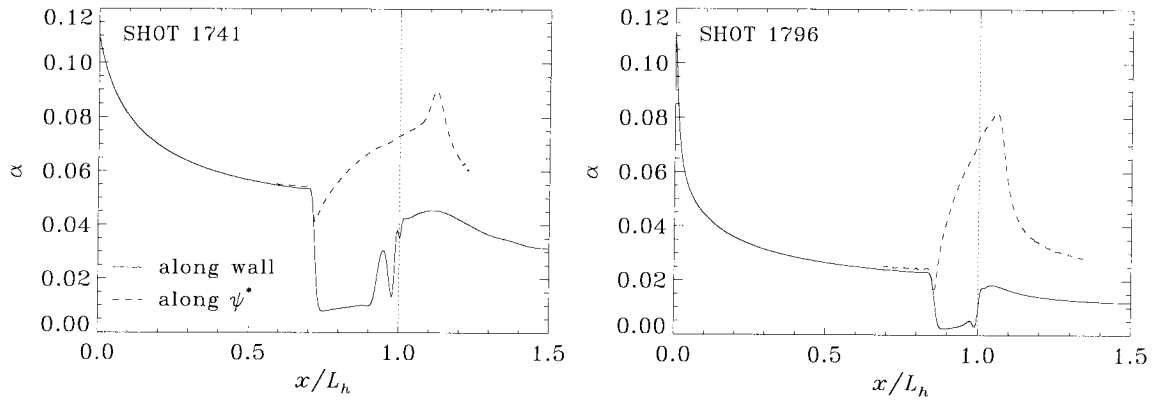

Figure 5.27: Viscous double-wedge computational results for α near the wall (solid curve) and along the dividing streamline ψ^* (dashed curve); shot 1741 (condition C2, $A_e/A_* = 225$, $\theta_1 = 30°$, $\theta_w = 25°$) and shot 1796 (condition C2, $A_e/A_* = 100$, $\theta_1 = 40°$, $\theta_w = 15°$). The distance along the streamline is projected on the wall in a direction perpendicular to the first wedge surface.

recombination in the recirculating region may cause a change in L_{sep} with respect to frozen flow which has constant mass fraction everywhere. The mass-fraction gradients are seen in Figure 5.26b to be very small over much of the recirculating region, which, as suggested by the near-wall noncatalytic boundary-layer result in Figure 5.23, may result in a temperature rise due to recombination high enough to dominate the change in density, giving a lower density and hence a larger separation bubble. The present model for separation length described by Equation 4.41, however, considers only the shear stress along the dividing streamline, and the boundary-layer results of the previous section also show that changes in shear stress due to recombination are not necessarily related in a direct manner to the dilatational effect of changes in density, but depend as well on changes in the viscosity and the density–viscosity product C. In any case, the mechanism which increases the

wall shear stress in a recombining boundary layer was found to arise from an extreme thermal wall condition that does not exist for the dividing streamline in a shear layer. Thus the shear stress τ_{ψ^*} at the dividing streamline ψ^* might be expected to follow the same trends as found in the previous section for the outer part of the boundary layer where the temperature and mass-fraction gradients are smaller. Based on the results in Figures 5.20–5.22, τ_{ψ^*} should increase due to recombination, except for one particular situation. A decrease in τ_{ψ^*} can only occur if $\mu/\mu_{fr} < 1$, which requires that $T/T_{fr} < 1$, and if the resulting velocity increase (due to increased density) is greater below ψ^* than above ψ^* so that $(\partial u/\partial y)_{\psi^*}$ decreases. In other words, the behavior must mimic that found in Figures 5.20–5.22 for the outer part of the boundary layer in case 6.

Because the experimental results for separation length in the present study, discussed in Chapter 6, indicate an increased separation length due to internal mechanisms for real-gas effects (and hence a decreased τ_{ψ^*}), it is desirable to consider whether or not the situation described above could indeed occur for a recombination-dominated separation zone. In the previous section, it was suggested that the temperature decrease in the outer part of the boundary layer for case 6 is linked to the fact that, unlike in the lower part of the boundary layer (or the entire boundary layer in case 2), $\partial T/\partial y < 0$ and $\partial^2 T/\partial y^2 > 0$. In fact, it can be noted from the temperature profile in Figure 5.26b that $\partial^2 T/\partial y^2 > 0$ near ψ^* in the shear layer, though $\partial T/\partial y > 0$. Another important difference can be seen in the mass-fraction profile; whereas $\partial^2 \alpha/\partial y^2 < 0$ throughout the outer part of a recombining boundary layer, $\partial^2 \alpha/\partial y^2 > 0$ near ψ^* in the recombining shear layer. This latter condition was found in the previous section to coincide with a large temperature increase near a noncatalytic wall for boundary-layer case 2. The situation in that case, however, is different in terms of the other derivatives, *i.e.* $\partial^2 T/\partial y^2 < 0$ near the wall. The flow near ψ^* also has significant streamwise derivatives in mass fraction and temperature, and as evident in Figure 5.27, these are not only larger than the streamwise derivatives near the wall upstream of separation, but of opposite sign as well. A possible consequence of the particular combination of temperature and mass-fraction gradients found near ψ^* is that the energy balance (*cf.* Equation 4.6 or 3.4) results in a decrease in temperature, and hence viscosity, due to recombination. Since the second derivatives of T and y change sign again a short distance above ψ^*, the resulting increase in velocity may be greater below ψ^*, giving a decrease in τ_{ψ^*}. As seen in Figure 5.22 for boundary-layer case 6, however, a decrease in τ does not require a decrease in $\partial u/\partial y$ if the viscosity also decreases. The present computations cannot be used to verify the effect of recombination on temperature or shear stress along the dividing streamline. We can only speculate that the present experimental results in Section 6.1, as well as some previous results discussed in the next section, may be explained by a decrease in temperature and shear stress with recombination, due to the gradients acting on the energy balance.

The laminar shear layer in compressible flow has been studied by a number of authors, but not in the context of a dissociating or recombining gas. Crane (1957) discussed the effects of the

change in scale between incompressible and compressible flow; as elaborated upon in the previous section for boundary layers, real-gas effects on the change in scale are more complicated. Mills (1968) showed that for a zero-velocity low-speed side with lower temperature than the high-speed side (which has some semblance to the present free-shear flow), decreasing the temperature ratio across the layer has the effect of slightly decreasing the maximum shear stress and moving the location of maximum shear stress (which he found lies within the low-speed side) closer to ψ^*. Denison and Baum (1963) included the effect of finite initial thickness in self-similar solutions for the separated shear layer downstream of a backward-facing step; finite initial thickness is even more important for boundary-layer separation upstream of a wedge, where the shear layer may still be in the nearfield at reattachment. Their solutions indicate that the maximum shear occurs outside the dividing streamline and increases with distance downstream of separation. Most interesting, however, is their result that a hot recirculating region gives a significantly longer separation length than a cold recirculating region; recombination inside the recirculating region with respect to the external flow (as seen in Figure 5.26b) may cause the same effect with respect to frozen flow. An excellent review of previous analysis of shear layers is given by Kennedy and Gatski (1994).

5.2.2.3 Summary of Internal Effects on L_{sep}

Internal mechanisms for real-gas effects on separation length are very complex. Under the present experimental conditions of partially dissociated external flow and a cold wall, internal mechanisms can only arise from recombination in the boundary layer or the separated region. Recombination at the wall is shown to increase the skin friction of the boundary layer upstream of separation which should act to decrease separation length, but only by a slight amount and only at the highest-density conditions for a noncatalytic wall. Recombination in the recirculating region and the shear layer is speculated to cause an increase in separation length, but this cannot be proven using computations undertaken in the present study. It is not clear whether conditions without free-stream dissociation but with significant dissociation in the boundary layer and shear layer should exhibit the opposite effects on separation length.

Many of the previous computational results for shock/boundary-layer interaction in reacting flow (*cf.* Section 1.5.4.1) show increased skin friction downstream of reattachment compared to frozen flow (Ballaro and Anderson, 1991; Furumoto *et al.*, 1997; Grasso and Leone, 1992; Grumet *et al.*, 1994), regardless of free-stream dissociation, whether dissociation occurs in the outer part of the boundary layer, whether the wall is catalytic or noncatalytic, or whether the wall temperature is the same as the free-stream temperature or lower. With the present results indicating increased skin friction as well, this suggests that reactions in the boundary layer act to increase the wall shear stress under any situation, except perhaps for a very hot wall as noted previously. The decrease in separation length for reacting flow observed by Furumoto *et al.* (1997) and Grasso and Leone (1992)

may be partially due to dissociation occurring in the separation region, though the behavior can be explained by external mechanisms. Grumet *et al.* (1994) found a large increase in L_{sep} when strong recombination occurs in the separation region, consistent with the idea proposed in the previous section. They also showed a slight decrease in L_{sep} at the low-pressure condition for a catalytic wall compared to a noncatalytic wall, consistent with the present boundary-layer computational results showing higher skin friction for a catalytic wall when the reaction rate is not high. The case computed by Ballaro and Anderson (1991), however, also has recombination occurring in the separation region, but shows a slight decrease in L_{sep} for reacting flow. The difference between the work of Ballaro and Anderson (1991) and Grumet *et al.* (1994) is that Grumet *et al.* consider much higher pressures and densities. Recombination might also be expected to occur in the separated region in hyperboloid-flare flow studied by Brenner *et al.* (1993); they show a decrease in L_{sep} as well, but in this case the behavior may be dominated by external mechanisms because the frozen flow remains undissociated behind the leading-edge shock.

It is very important to note that the internal mechanisms discussed here describe changes in L_{sep} with respect to frozen flow with the same local external conditions, not frozen flow with the same free-stream conditions; this distinction can be important for double-wedge flows. Thus it is not clear from the present analysis what is the combined effect of internal and external mechanisms for real-gas effects on separation length.

5.2.3 Reattachment Heat Flux

It was noted in Section 5.1.3.3 that internal mechanisms for real-gas effects on reattachment heating appear from existing results in the literature to dominate external mechanisms. In terms of the expression for peak heating given by Equation 5.21, the only direct effect of reactions in the boundary or shear layer upstream of reattachment is to change the thickness of the reattaching shear layer and thus the growth length for peak heating. Chemistry effects on the boundary-layer thickness upstream of separation were shown in Figure 5.19 to be quite small under the present experimental conditions. Of course, reactions upstream of reattachment also indirectly affect the peak heating downstream of reattachment; for example, dissociation occurring along the dividing streamline (*cf.* Figure 5.27) causes a drastic change in the atomic mass-fraction profile at reattachment, making it much fuller than it would be on a flat plate with the same edge conditions.

From Equation 4.6 it is evident that direct coupling between the mass-fraction profile and the enthalpy profile, which determines wall heat flux, exists for $Le \neq 1$. If $Le = 1$, the two are coupled only indirectly through the effects of reactions on the Chapman–Rubesin parameter. As shown in Figure 5.28, the Lewis number is not only significantly different from unity, it also varies across the boundary layer. For completeness, a profile of Prandtl number for the same case is also given in Figure 5.28. Computational boundary-layer results for the effects of recombination on total heat flux

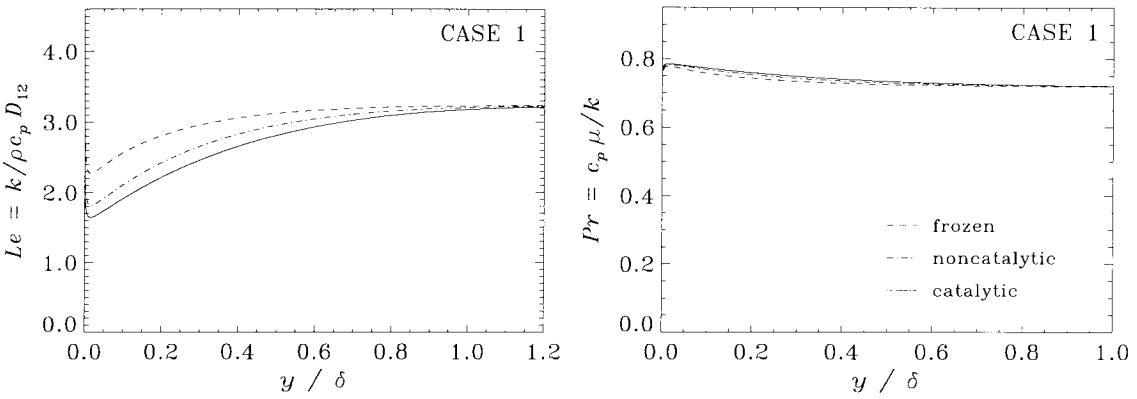

Figure 5.28: Computational boundary-layer results for Le and Pr at the high-enthalpy condition of case 1 described in Table 5.3.

to the wall $\dot{q}$ are plotted in Figure 5.29 against the Damköhler parameter Γ defined by Equation 5.22. Clearly, real-gas effects on heat flux can be quite significant compared to real-gas effects on skin friction (*cf.* Figure 5.19); $\dot{q}$ increases by almost a factor of two over frozen flow for the high-enthalpy, high-incidence case 2. The increase appears to depend primarily on the amount of recombination at the wall, as indicated by the decreasing difference between catalytic and noncatalytic results as $-\Gamma$ increases; α_w for a noncatalytic wall approaches α_w for a catalytic wall as $-\Gamma$ increases. For smaller values of $-\Gamma$, dissociation at the edge of the boundary layer is negligible to begin with, and thus all reacting-flow computations give the same result as frozen-flow computations. Note that these computations were undertaken for edge conditions derived from the flow upstream of separation on a double wedge in T5; increased density and dissociation in region 3 downstream of reattachment may cause even larger differences in reattachment heat flux between reacting and frozen flow.

A mechanism commonly cited to explain increased heat flux for a catalytic wall when there is dissociation present, either external or internal to the boundary layer, is the diffusion of atoms to the wall where they recombine, releasing their chemical energy to the wall. It can be seen most clearly from Equation 3.4 that mass diffusion does indeed create an additional heat flux term when there are significant differences in enthalpy between the different species; $\sum_s \rho_s h_s v_{s_j}$ is a diffusion heat flux analogous to the translational–rotational heat flux $\dot{q}_j$ and vibrational heat flux $\dot{q}_{v_j}$, and proportional to the mass fraction gradients instead of the temperature gradient. At a catalytic wall, the diffusion velocities are of opposite sign ($v_{\mathrm{N}_2} > 0$ and $v_{\mathrm{N}} < 0$), but $\rho_{\mathrm{N}} = 0$ and thus the summation reduces to

$$\dot{q}_{diff,\,catalytic} \;=\; \rho_w h_w v_{\mathrm{N}_2,\,w} \;=\; \rho_w h_w D_{12} \left(\frac{\partial \alpha}{\partial y} \right)_w . \tag{5.25}$$

The second equality shows a simplification from applying Fick's Law; in the present computational results, v_s is given by Equation 3.11. The proportionality between diffusion heat flux and wall gradient of mass fraction, together with the result in Figure 5.27, suggests that the diffusional contribution to wall heat flux downstream of reattachment can be quite large for a catalytic wall.

Though the viscous double-wedge computations in Figure 5.27 are for a noncatalytic wall, the result that gas near the dividing streamline dissociates downstream of separation should not depend on wall catalyticity. Upon reattachment, this dissociated gas is brought quickly back to the wall, inducing a mass-fraction gradient close to the wall of much higher magnitude than found upstream of separation. This mechanism for increased heating depends only on changes in the wall gradient of mass fraction with respect to frozen flow, and thus may be expected also to occur for a dissociating boundary layer with $\alpha_e = 0$ and catalytic wall.

While the above mechanism explains increased heat transfer for a catalytic wall, it is shown in Figure 5.29 that the heat transfer to a noncatalytic wall increases over frozen flow to the same degree as a catalytic wall when the gas is close to fully recombined at the wall. By definition, the mass-fraction gradient is zero at a noncatalytic wall, and thus there must be a different mechanism for increased heat flux to a noncatalytic wall. This mechanism is apparent from the discussion in Section 5.2.2.1 regarding the role of temperature and species gradients in determining recombination effects on the local thermal state. As shown in Figure 5.23, the temperature rise near the wall due to recombination is significantly higher for a noncatalytic wall than for a catalytic wall. Compared to frozen flow, reacting flow with a catalytic wall shows increased wall heat transfer due to both the presence of diffusion heat flux and a slight increase in the conduction heat flux, while reacting flow with a noncatalytic wall shows increased wall heat transfer, if recombination occurs near the wall, due to a large increase in the conduction heat flux.

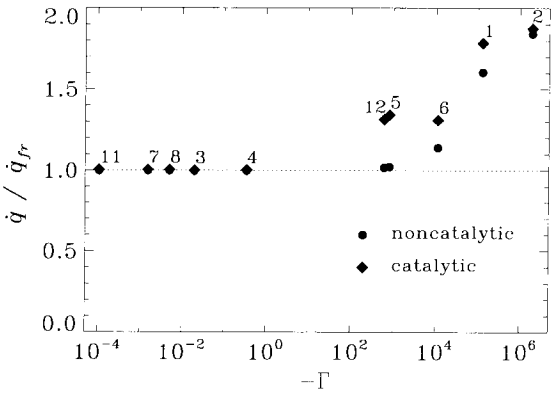

Figure 5.29: Comparison between frozen and reacting computational boundary-layer results for $\dot{q}$, plotted against the nondimensional reaction-rate parameter Γ given by Equation 5.22. ♦ and • are catalytic-wall and noncatalytic-wall results respectively, and the numbers refer to cases described in Table 5.3.

As mentioned in Section 5.2.2.1, results in the literature for recombination-dominated flat-plate boundary layers are practically nonexistent. Using a momentum-integral technique, Ikawa (1979) showed large increases in $\dot{q}$ both upstream of separation and downstream of reattachment due to diffusion at a catalytic wall. East *et al.* (1980) presented experimental heat-transfer results from the T3 shock tunnel for flat-plate flow at 0° and 12° incidence using air, which includes the possibility of endothermic reactions in the boundary layer. The high-enthalpy measurements were consistent with predictions for a nearly frozen flow with noncatalytic wall at 0° incidence, but lower than predicted at 12° incidence.

Recombination-dominated stagnation-point boundary layers have been considered more extensively; a small sample of the work includes Lees (1956), Fay and Riddell (1958), and Inger and Elder (1991). Lees (1956) looked at the two limiting cases of a fully catalytic wall with no reactions ($w_s = 0$) and equilibrium flow in which there is no diffusion at the wall, and showed that the maximum difference in $\dot{q}$ between these two cases goes as $Le^{-2/3}$; if $Le = 1$, then $\dot{q}$ is the same in both cases, independent of the mechanism for energy transfer. Fay and Riddell (1958) extended the analysis to finite-rate gas-phase recombination and $Le \neq 1$, showing a phenomenon very similar to that seen in Figure 5.29 for the present nonequilibrium flat-plate computations. While the catalytic-wall heat transfer remains almost constant for a given α_e, the fraction of it due to conduction depends on the recombination rate parameter; $\dot{q}$ consists entirely of conduction for equilibrium but includes both conduction and diffusion as the boundary layer freezes. The heat transfer for a noncatalytic wall follows a trend similar to the conduction part of the catalytic-wall heat transfer, but falls off at a much lower value of the overall reaction-rate parameter due to the build-up of a blanket of atoms at the wall which keeps the reaction rate locally high. (The latter effect can clearly be seen in Figure 5.18 for the present noncatalytic solutions.) This result is consistent with the explanation above for the behavior of case 2 in Figure 5.29. Inger and Elder (1991) considered as well the dependence of heat transfer on a surface reaction-rate parameter describing the degree of catalyticity. For stagnation-point flow, the boundary-layer equations are made self-similar by the approximation $M_e \simeq 0$, which is certainly not the case near reattachment in double-wedge flow. It seems, however, that mechanisms for real-gas effects in a boundary layer with dissociated edge conditions and a cold wall are the same for flat-plate flows or stagnation flows.

Equilibrium–dissociating flat-plate boundary layers were considered by Moore (1952) who found that chemistry effects on heat transfer appear only when the wall temperature is high enough to cause dissociation there, in which case the sign of the change in $\dot{q}$ depends on the Mach number. For nonequilibrium, dissociation-dominated flat-plate boundary layers, Rae (1963) showed that the heat flux for a noncatalytic wall falls below that for a catalytic wall with distance downstream of the leading edge; Blottner (1964) indicated that the catalytic-wall heat flux is no different from the frozen-flow heat flux because dissociation lowers the conduction heat flux (due to lower maximum temperature in the boundary-layer) and raises the diffusion heat flux simultaneously. Similar results were found by Inger (1964, 1995a).

To summarize internal mechanisms for real-gas effects on reattachment heating, it is clear that if dissociation occurs either external or internal to the boundary layer, and either the wall is catalytic or the reaction rates near the wall are high, then the heat flux for reacting flow increases over that found for frozen flow. Additional mechanisms for increasing the peak heating in reacting flow are dissociation of gas along the dividing streamline which is brought close to the wall at reattachment, and a possible reduction in the growth length of the reattaching boundary layer due to reduced

upstream boundary-layer thickness. The only conditions which might produce a lower heat flux for reacting flow are those of a very hot catalytic wall or moderately hot noncatalytic wall, and no dissociation external to the boundary layer but dissociation occurring inside the boundary layer. As discussed in Section 1.5.4.2, only the computational study of Furumoto *et al.* (1997) shows a decrease in $\dot{q}_{pk}$ for reacting flow. This result also shows dissociation of oxygen occurring along the wall downstream of separation and reattachment, although the wall is isothermal at only 1200 K. Though not stated, the wall boundary condition in this study is noncatalytic (G. H. Furumoto, priv. comm.).

As was done in the previous section for skin friction, the computational boundary-layer results may be compared to the prediction methods presented in Section 4.1.1.3. The comparisons are shown in Figure 5.30a for the frozen-flow assumption where $\alpha_w = \alpha_e$ is assumed in evaluating the Stanton number in Equation 4.14, and in Figure 5.30b for the catalytic-wall/equilibrium-flow approximation where $\alpha_w = 0$ is assumed in Equation 4.14. As expected, the first assumption grossly underpredicts $\dot{q}$ for reacting flow when $\alpha_w < \alpha_e$, while the second assumption grossly overpredicts $\dot{q}$ for frozen flow when $\alpha_e > 0$ and for a noncatalytic wall when the reaction-rate parameter is small. The $\alpha_w = 0$ approximation still underpredicts the heat flux both for a catalytic wall and for a noncatalytic wall close to equilibrium, suggesting that there is no connection between this approximation and the division of heat flux into parts due to conduction and diffusion. Considering the frozen-flow results in Figure 5.30a, the same general trend is found, of increasing overprediction with increasing Mach number, as for the skin friction in Figure 5.24a because the predicted skin friction is used in the Reynolds analogy (Equation 4.20) to predict heat flux.

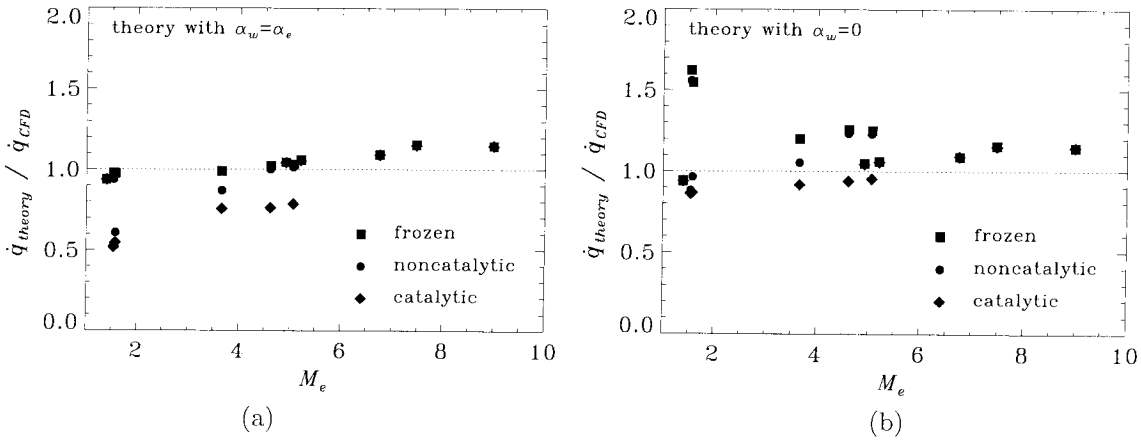

Figure 5.30: Comparison between computational boundary-layer results and frozen-flow flat-plate theory for $\dot{q}$ with h_w in Equation 4.14 evaluated assuming either (a) $\alpha_w = \alpha_e$ or (b) $\alpha_w = 0$, and plotted against M_e, which can be used to reference cases in Table 5.3. ■ are frozen-flow results, ♦ are catalytic-wall results, and • are noncatalytic-wall results.

5.3 Summary

Real-gas effects on separation length and reattachment heating consist of many complex phenomena that cannot be described in a single statement. In this chapter, a classification was introduced to separate these physical phenomena into mechanisms arising external and internal to viscous regions of the flow such as the boundary layer and separation zone, with internal mechanisms further subdivided into those arising upstream and downstream of separation. Analysis of the external and internal flow using various computational models gave some quantitative results bearing on the conditions of the present experimental work, and much qualitative insight into the various mechanisms. The mechanisms, and their effects on separation length and reattachment heating in nonequilibrium double-wedge flow with respect to a frozen flow with either the same free-stream conditions (when describing external mechanisms) or same external flow conditions (when describing internal mechanisms), are outlined in the following list:

- External mechanisms due to reactions in the external inviscid flow

  1. Effects on separation length

     (a) For low θ_1 and high θ_w, dissociation downstream of the reattachment shock lowers p_3 and decreases L_{sep}; this mechanism is not important in the present experiments.

     (b) For high θ_1, dissociation downstream of the leading-edge shock increases Re_1, M_1, and Λ_1, but the effect on $(p_3 - p_2)/p_1$ depends on α_∞, and L_{sep} may increase or decrease; results indicate that the only effect arising in the present experiments is a decrease in L_{sep} at the highest incidence.

     (c) Under conditions where $\alpha_1 < \alpha_\infty$ (recombination shock), separation length decreases with recombination downstream of the leading-edge shock but increases with recombination downstream of the reattachment shock.

  2. Effects on reattachment heating

     (a) For low θ_1 and high θ_w, dissociation downstream of the reattachment shock causes a slight decrease in $\dot{q}_{pk}$ due to lower T_3 and higher Re_3; this mechanism may exist in the present experiments because T_3 is sensitive to dissociation.

     (b) For high θ_1, dissociation downstream of the leading-edge shock results in smaller δ for a reacting boundary layer (shortening the reattachment length scale) and a stronger increase in ρ_3, both of which can lead to a slight increase in $\dot{q}_{pk}$; the highest-incidence experiments are in this regime.

- Internal mechanisms due to reactions in the boundary layer, shear layer, or separation bubble

  1. Effects on separation length

(a) For $\alpha_1 > 0$, recombination at a cold wall (due either to catalyticity or high reaction rates) increases C_{f,x_1} and decreases L_{sep}; in the present experiments this effect does not cause more than a 5% change in C_{f,x_1}.

(b) It is speculated that for $\alpha_1 > 0$ and a cold wall, recombination in the separation region may cause a decrease in τ_{ψ^*} and hence an increase in L_{sep}; this mechanism cannot be verified using the present computations.

2. Effects on reattachment heating

(a) For $\alpha_3 > 0$, or a dissociating boundary layer with catalytic wall, recombination at a cold wall (due either to catalyticity or high reaction rates) increases $\dot{q}_{pk}$; in the present experiments, this mechanism can cause at least a twofold increase in $\dot{q}_{pk}$ at high incidence.

(b) For $\alpha_1 > 0$ and recombination occurring at a cold wall, δ may decrease (shortening the reattachment length scale) and cause a further slight increase in $\dot{q}_{pk}$; this mechanism is unimportant in the present experiments.

This framework for describing real-gas effects provides some insight when applied to previously published results for separated, high-enthalpy corner flows or shock-impingement flows, but in general it is difficult to separate external and internal mechanisms using the limited data reported. In the next chapter, the present experimental results for separation length and reattachment heating are examined in light of the knowledge gained in the present chapter.

Chapter 6 Experimental Results

The experimental data on separation length and reattachment heating in high-enthalpy double-wedge flows, obtained by the methods in Chapter 2, are now presented with the aid of computational and theoretical results from Chapters 3 and 4. Interpretation of the data benefits from the framework developed in Chapter 5 to describe real-gas effects on these phenomena. Separation length is considered in Section 6.1 and reattachment heating in Section 6.2.

6.1 Separation Length

From the review in Section 1.5.2, it was clear that the length of separation due to shock/boundary-layer interaction depends in a nonsimple manner on the local flow conditions at separation and on the strength of the pressure rise causing the separation to occur. The raw experimental data on separation length, measured as described in Section 2.4.4, is useless without additional knowledge of the local flow conditions; the motivation for undertaking the computations described in Sections 3.2 and 3.3 was to obtain estimates for local properties in the external flow field under conditions of a nonuniform free-stream flow and thermochemical nonequilibrium. The existing scaling laws for separation length (*cf.* Section 1.5.2.2) do not include the effect of wall temperature, an important parameter in the present experiments; this was the motivation for the development presented in Section 4.2 of a new scaling law based on results from triple-deck theory. In Section 6.1.1, the new scaling is applied to experimental data on separation length to show the importance of the new scaling parameter Λ_1 and to determine the dependence on reattachment pressure ratio. Then in Section 6.1.2, the behavior of separation length with Reynolds number is considered. Finally, in Section 6.1.3, experimentally observed real-gas effects on separation length are discussed.

6.1.1 Application of Triple-Deck Scaling Result

This section is divided into several parts. First, in Section 6.1.1.1, the scaling law is used to show a linear dependence of separation length on the reattachment pressure ratio, consistent with previous results in the literature for supersonic interactions. Then in Section 6.1.1.2, the new scaling parameter for the effects of wall temperature is shown quantitatively to result in better collapse of the experimental data while at the same time segregating the high- and low-enthalpy data (the latter is discussed further in Section 6.1.3). In Section 6.1.1.3, experimental data on separation angle are compared to a result from triple-deck theory.

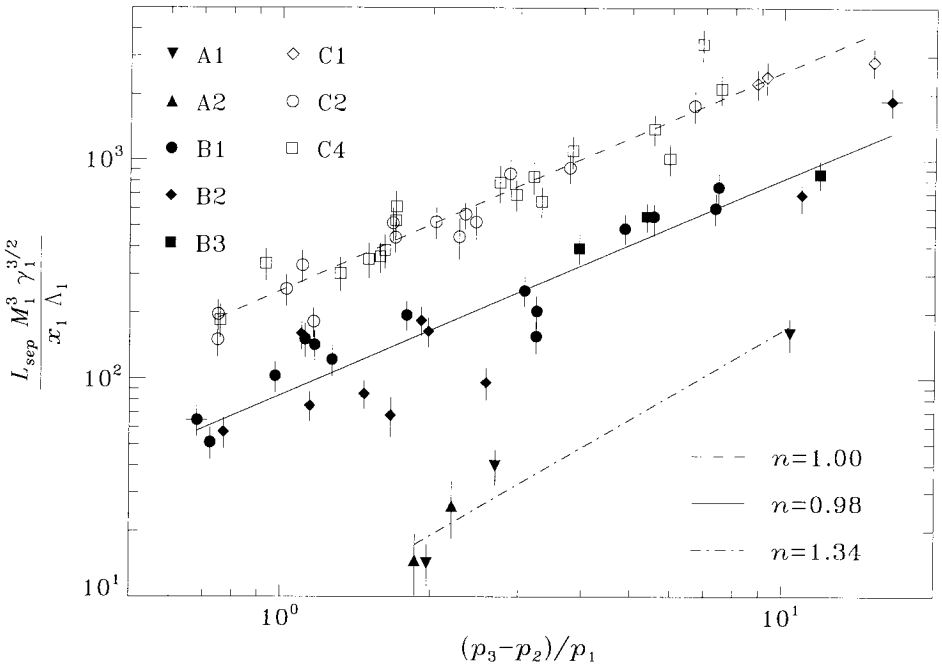

Figure 6.1: Experimental L_{sep} data correlated against $(p_3 - p_2)/p_1$ from computations. Different symbols represent the different shock tunnel conditions described in Table 2.1, as indicated by the legend. Error bars include measurement uncertainty in L_{sep} and uncertainty in the computed parameters due to uncertainty in reservoir conditions; horizontal error bars are given only for the two experiments with the largest and smallest values of $(p_3 - p_2)/p_1$. Lines represent fits to select sets of conditions (dash dot for A1–2, solid for B1–3, dashed for C1–4), and n is the slope of each line in log–log coordinates.

6.1.1.1 Dependence on Reattachment Pressure Ratio

Consider first the scaling given in Equation 4.48, which assumes a flat-plate nonreacting boundary layer approximately described using the reference-temperature method. The exponent on the pressure ratio factor does not match previous experimental or computational results which suggest either a linear dependence (*cf.* Equation 1.10) or a quadratic dependence (*cf.* Equation 1.5). For the present experiments, this exponent is found by empirical correlation of the separation length, scaled by the other parameters in Equation 4.48, against the pressure ratio factor; this correlation is shown in Figure 6.1 using log–log coordinates. The only parameter measured directly from experiment is L_{sep}/x_1. All other parameters in Figure 6.1 are obtained from the inviscid triple-wedge computations, with the viscosities in Λ_1 evaluated using the model in Section 4.1.4. When plotted this way, the data do not collapse to a single line; there is clearly some additional dependence not accounted for, such as Reynolds-number or real-gas effects. When the data are divided into subsets based on stagnation enthalpy, however, straight lines fit to each subset in log–log coordinates indicate an average dependence on the pressure ratio factor that is extremely close to linear. The scarcity of data at conditions A1–2 prevents a useful fit in this range, the slope of the line being controlled

heavily by a single datum. (Note that the sets for conditions C1 and C4 include a couple shots which were significantly departed from nominal operating conditions and labeled as C0 in Appendix D.)

Though experimental pressure measurements appear to have large uncertainty and unknown reliability (*cf.* Section 2.6.3), it was noted in Section 3.3.3 that the computed pressure has a tendency to underpredict the measured pressure in the flap region. The question arises as to what effect the use of experimental pressure data, instead of computational pressure data, has on the correlation presented in Figure 6.1. Only $p_3 = p_R$ can be obtained consistently from the experiments by the method mentioned in Section 2.6.3, thus p_1 must still come from the inviscid triple-wedge computations. The plateau pressure p_2 can be estimated from the triple-deck result in Equation 4.50 using computational results for region 1. In Figure 6.2, the values of $(p_3 - p_2)/p_1$ thus obtained are used to correlate separation length data as in Figure 6.1. The values from Figure 6.1 based entirely on computational results are also shown, with dotted lines connecting the two sets of results. For most, but not all, of the shots, use of the experimental reattachment pressure shifts the data to higher pressure ratio $(p_3 - p_2)/p_1$. The difference varies from shot to shot with no apparent trend. Use of $p_3 = p_R$ from experiment increases the relative scatter of the data, but has virtually no effect on the slope obtained from linear fits in log–log coordinates, *i.e.* the average dependence on pressure ratio is still very close to linear. This suggests that external flow conditions obtained from the present computational results are indeed appropriate for studying the behavior of separation length. The computed results for $(p_3 - p_2)/p_1$ are used exclusively for the other plots in this chapter.

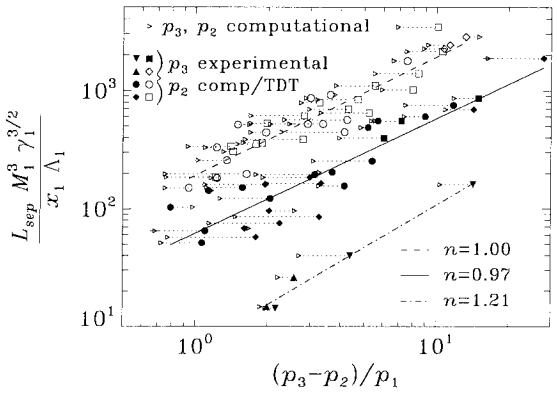

Figure 6.2: Comparison between use of computational and experimental data for p_3 in correlation of L_{sep} against pressure ratio; large symbols defined in Figure 6.1 represent use of experimental p_3 with p_2 found from computed p_1 and Equation 4.50, small ▷ represent use of computational p_3 and p_2, and dotted lines connect corresponding pairs of data. The linear fits, giving slope n in log–log coordinates, include only data based on experimental p_3.

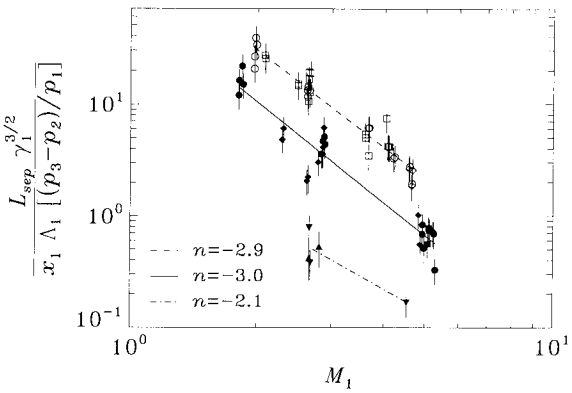

Figure 6.3: Correlation of experimental L_{sep} against M_1 from computations; symbols, error bars, lines, and n are described in Figure 6.1.

A linear dependence on the pressure ratio has previously been found for supersonic interactions (Katzer, 1989) and for transitional or turbulent interactions (Kumar, 1995). The experimental data presented here for a double wedge with $\theta_1 \geq 15°$ is shown in Figure 6.3 to encompass only $1 < M_1 \lesssim 5$ and not extend into the hypersonic regime. As mentioned in Section 1.5.2.2, previous results in the literature indicate a linear dependence on the pressure ratio for supersonic interactions and a quadratic dependence for hypersonic interactions, but not exclusively; Needham (1965) found a quadratic dependence on pressure ratio for the data of Hakkinen *et al.* (1959) at $M_1 = 2$. A difference in power-law behavior might be explained by a change in the reattachment process from an essentially isentropic process in supersonic interactions to a nonisentropic process in hypersonic interactions, for which the reattachment shock forms closer to the wall; in the latter case, a loss in total pressure at reattachment requires a longer separation length to overcome the same rise in pressure. Experiments were performed with $\theta_1 = 0°$ in order to verify this hypothesis, but reliable measurements of separation length could not be obtained from them (*cf.* Section 2.4.4), and difficulties arise in any case with application of the inviscid computational technique to this configuration. Also shown in Figure 6.3 is the cubic dependence on Mach number recovered when L_{sep} is scaled by Λ_1 and $(p_3 - p_2)/p_1$.

6.1.1.2 Importance of Wall Temperature Parameter Λ

The scatter in Figures 6.1 and 6.3 is relatively large, in fact larger than the error bars, which include measurement uncertainty in L_{sep} and the reservoir conditions but none of the other uncertainties due to approximations involved in the computations (*cf.* Section 3.3.3) or in the derivation of Λ_1 from flat-plate boundary-layer theory using the reference temperature. If Λ_1 is removed from the scaling, however, the relative scatter becomes worse, as shown in Figure 6.4b. The value of Λ_1 is seen in Figure 6.4a to vary by more than an order of magnitude over the experimental conditions. There is a tendency for high-enthalpy experiments to have low Λ_1 and low-enthalpy experiments to have high Λ_1, with some overlap in between. Thus it is not surprising to see that when Λ_1 is removed from the scaling for L_{sep} used in Figure 6.1, the high-enthalpy and low-enthalpy data which were segregated now fall mostly in the same region. It is merely coincidence that the curve fits in Figure 6.4b without Λ_1 give an exponent for the pressure ratio factor that is close to the triple-deck result of 3/2; because Λ_1 tends to be smaller at high incidence where $(p_3 - p_2)/p_1$ is also smaller, removing Λ_1 from the correlation results in a steeper rise than found in Figure 6.1.

The apparent increase in relative scatter for each subset of data when Λ_1 is removed from the scaling can be quantified using statistical analysis of the relative root-square deviations,

$$d = \sqrt{\left(\frac{\mathcal{L} - \mathcal{L}_{fit}}{\mathcal{L}_{fit}}\right)^2}, \tag{6.1}$$

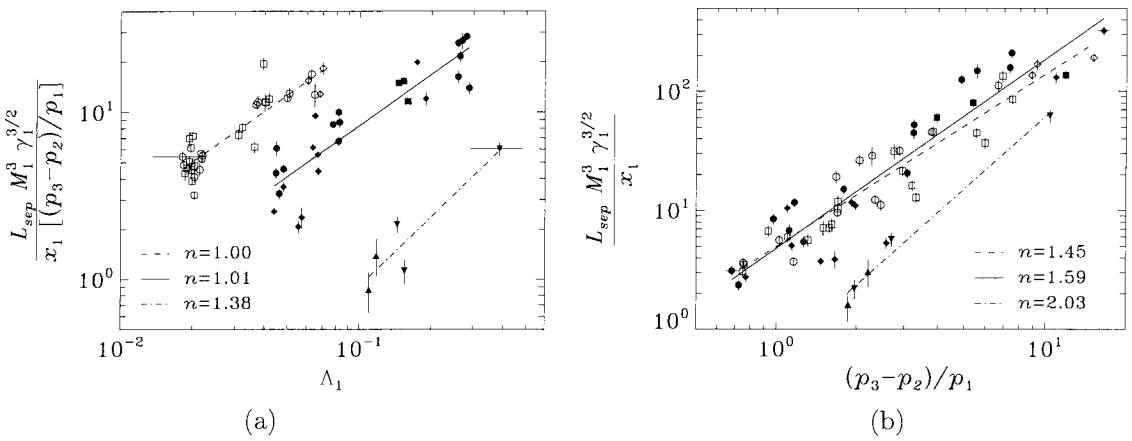

Figure 6.4: Effect of Λ_1 on correlation of experimental L_{sep}; (a) correlation of scaled L_{sep} against Λ_1, (b) repeat of the pressure correlation in Figure 6.1 with Λ_1 removed from the L_{sep} scaling. Symbols, error bars, lines, and n are described in Figure 6.1.

	with Λ_1		without Λ_1				
condition	$\bar{d}$	σ	$\bar{d}$	σ	ν	$\lvert t\rvert$	P
B1–3	0.293	0.288	0.533	0.631	36.4	1.80	0.081
C1–4	0.157	0.155	0.318	0.248	55.2	3.21	0.002

Table 6.1: Statistical analysis of scatter in L_{sep} correlations; the scatter is quantified by the mean $\bar{d}$ and standard deviation σ of the relative deviations d defined by Equation 6.1, and P is the two-sided probability, based on a test statistic using Student's t-distribution, that the increase in $\bar{d}$ when Λ_1 is removed has no statistical significance.

where $\mathcal{L}$ are data for the ordinate of scaled separation length in Figures 6.1 or 6.4b, and $\mathcal{L}_{fit}$ are values for the ordinate predicted by the curve fits. In Table 6.1 are given the mean $\bar{d}$ and standard deviation σ for each set of relative deviations; low-enthalpy and high-enthalpy conditions, with and without inclusion of Λ_1 in the scaling. The mean deviation from each curve fit is clearly smaller when Λ_1 is included in the scaling. The statistical significance of the difference in $\bar{d}$ can be determined by a statistical test of the null hypothesis that both sets of deviations have the same population mean. For unknown population standard deviations and unequal sample standard deviations, the appropriate test statistic relies on Student's two-sided t-distribution parameterized by the degrees of freedom ν (Dieter, 1991);

$$t = \frac{\bar{d}_1 - \bar{d}_2}{\sqrt{\sigma_1^2/N_1 + \sigma_2^2/N_2}}, \tag{6.2}$$

$$\nu = \frac{1}{k^2/\nu_1 + (1-k)^2/\nu_2}, \qquad k = \frac{\sigma_1^2/N_1}{\sigma_1^2/N_1 + \sigma_2^2/N_2}, \tag{6.3}$$

where subscripts 1 and 2 are deviation data with and without Λ_1 in the scaling, σ are the known sample standard deviations, $N_1 = N_2 = N$ is the sample size, and $\nu_1 = \nu_2 = N - 1$ is the number of degrees of freedom. For a specific ν given by Equation 6.3, the area under the two-sided t-distribution

for $|t|$ greater than the value given by Equation 6.2 is the probability P that the null hypothesis is true. In other words, $1 - P$ is the confidence level that the difference in scatter with and without Λ_1 in the scaling is statistically significant. From the results in Table 6.1, the confidence that the reduction in scatter (when Λ_1 is employed) is statistically significant is approximately 92% for the low-enthalpy data and $> 99\%$ for the high-enthalpy data.

In Section 4.2.2 it was pointed out that Λ_1 reduces to $(T_w/T_1)^{3/2}$ for an ideal (Chapman) fluid with $\mu \propto T$. To see if the reference-temperature approximation used in Λ_1 provides any improved accuracy for the present data over the simpler assumption of an ideal fluid, correlations are given in Figure 6.5 using T_w/T_1 instead of Λ_1. A power law with exponent 7/5, instead of 3/2, is suggested by the curve fits in Figure 6.5a; this deviation gives the departure from ideal-fluid conditions. Scaling L_{sep} by $(T_w/T_1)^{3/2}$ instead of Λ as in Figure 6.5b results in a large shift upwards of the data but only small changes in their positions relative to each other, compared to Figure 6.1. While use of the reference-temperature approximation for arbitrary viscosity law in the scaling for wall temperature effects on separation length does not improve the scatter of the present data, it is expected in general to provide improved accuracy over the simpler model with $\mu \propto T$.

Review of the analysis in Section 4.2.2 reveals an assumption worthy of further comment; the assumption that the viscosity on the dividing streamline, μ_{ψ^*}, equals the viscosity at the wall upstream of separation, μ_w, does not appear to accurately reflect the situation in a real flow where $\mu_{\psi^*} = \mu_w$ at separation and then increases significantly along ψ^* as the temperature increases. The assumption is, however, self-consistent within the framework of the asymptotic theory used to obtain the present scaling for Λ_1 in Equation 4.49. Substituting a viscosity more representative of μ_{ψ^*}, such as the viscosity μ_2^* at the reference temperature based on the edge conditions of the shear layer, into Equations 4.43–4.46 to arrive at a different formulation of Λ_1 only accentuates the difference

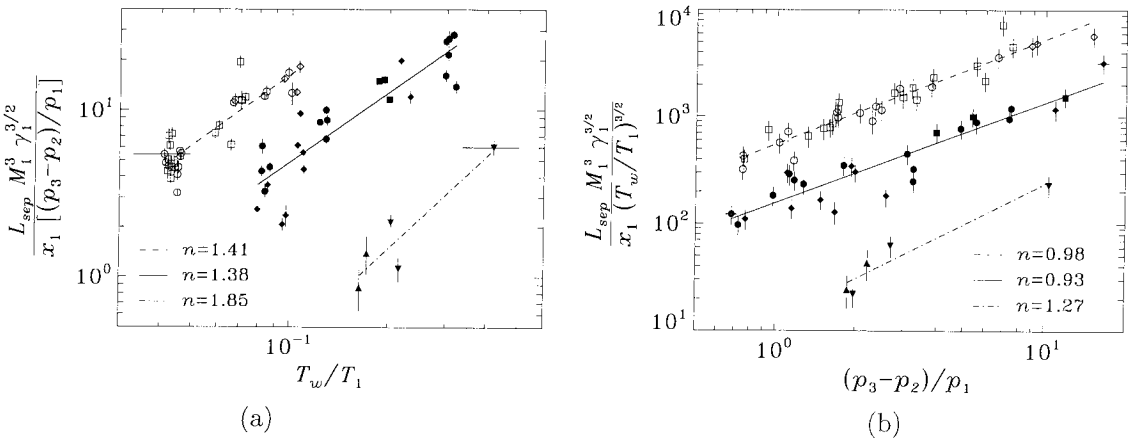

Figure 6.5: Correlation of experimental L_{sep} using T_w/T_1 instead of Λ_1; (a) correlation of scaled L_{sep} against T_w/T_1, (b) repeat of the pressure correlation in Figure 6.1 with Λ_1 replaced by $(T_w/T_1)^{3/2}$. Symbols, error bars, lines, and n are described in Figure 6.1.

in Λ_1 between high- and low-enthalpy conditions, and gives a power-law relationship $L_{sep} \propto \Lambda_1^{4/5}$ inconsistent with the theory.

Previous empirical correlations in the literature do not encompass the range of wall-to-edge temperature ratios existing in the present experiments. Because its use recovers the linear dependence on pressure ratio found in previous results for supersonic interactions, the new factor Λ_1 introduced in the present work appears to at least approximately account for wall temperature effects on separation length. The fact that Λ_1 also appears to segregate the high- and low-enthalpy data from each other is discussed further in Section 6.1.3. The factor $\gamma^{3/2}$ does vary in the present experiments, but only a small amount.

6.1.1.3 Separation Angle

Since experimental measurements of θ_{sep} are available, it is of some interest to see how well these are correlated by the triple-deck result in Equation 4.51, which predicts a weak dependence on Reynolds number and Mach number. The data are plotted in Figure 6.6, where it is seen that the constant of proportionality in Equation 4.51 gives a line that passes near the middle of the experimental results. This plot also emphasizes, however, the large scatter and uncertainty in measurements of θ_{sep}. This uncertainty may be partially responsible for the discrepancies between computed and experimental flap pressures (*cf.* Section 3.3.3). The uncertainty in experimental measurement of L_{sep}, obtained by measuring L_u and θ_{sep}, is dominated by the uncertainty in measured L_u, not in measured θ_{sep}.

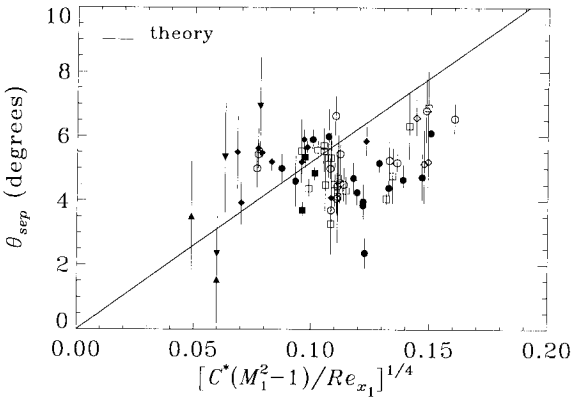

Figure 6.6: Correlation of experimental θ_{sep} against triple-deck theory result given by Equation 4.51 (solid line). The parameters in the abscissa are obtained from computations. Symbols and error bars are described in Figure 6.1.

6.1.2 Reynolds-number effects

Thus far we have not considered the Reynolds number as a parameter, which may be a source for the segregation seen in Figure 6.1. Separation length scaled by all the other parameters, using the linear pressure ratio dependence found for the present experiments instead of the 3/2-power law suggested by the triple-deck scaling, is plotted against Re_{x_1} in Figure 6.7. This plot looks in some ways very similar to one presented by Needham and Stollery (1966a,b) which correlates several authors' results

against Reynolds number and shows a precipitous drop in scaled separation length due to transition occurring upstream of reattachment (as expected by the physical argument in Section 1.4). A sharp decrease is seen in Figure 6.7 to occur in the range $1 \times 10^5 < Re_{x_1} < 4 \times 10^5$, which is significantly lower than the range $1 \times 10^6 < Re_{x_1} < 4 \times 10^6$ found by Needham and Stollery. There are several clues, however, indicating that transition is also causing the decrease in scaled separation length observed for the present experiments. One is that the present data exhibit the same behavior with respect to flap deflection angle as was found by Needham and Stollery, namely that transition occurs at a smaller Re_{x_1} as θ_w is increased while the conditions in region 1 are kept constant. This result is simply explained by the increase in L_{sep} with increasing θ_w; the location of transition in a free-shear layer depends on distance from its origin at separation. Some of the interferograms presented in Appendix F also show what appear to be instabilities or turbulent structures in the boundary layer downstream of reattachment (particularly noteworthy examples are shots 1294–1298).

The most reliable indicator of transition, however, is comparison of measured heat flux in the reattachment region with predictions based on laminar and turbulent models, as described in Section 4.1.3. This comparison was made for every shot in Figure 6.7, as shown on the Stanton-number plots in Appendix F. For shots with significant dissociation in the external flow, the laminar and turbulent predictions were also computed under the wall recombination approximation described in

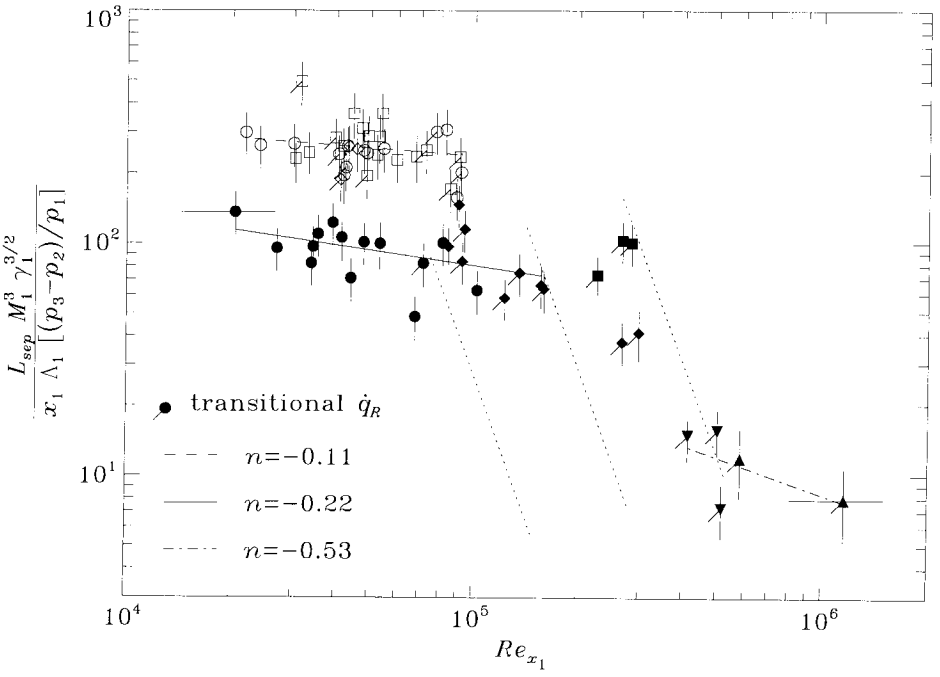

Figure 6.7: Correlation of experimental L_{sep} against Re_{x_1} from computations. Symbols, error bars, lines, and n are described in Figure 6.1. Flagged symbols indicated suspected transitional interactions, which are excluded from the fits for conditions B1–3 and C1–4. Dotted lines are a visual aid to show possible transitional paths.

Section 4.1.1.3 by setting $\alpha_w = 0$ when evaluating $\dot{q}$ from the Stanton-number definition. For all shots, further predictions were obtained by correcting the computed conditions in region 3 to account for the experimental pressure measurements as also described in Section 4.1.3. Any shot showing heat flux measurements that fall above the laminar predictions by more than about about 25% of the difference between laminar and turbulent predictions was assumed to be transitional, and the corresponding data in Figure 6.7 are flagged as indicated. In making the determination, the $\alpha_w = 0$ approximation was used if it provided a better prediction of the measured heat flux upstream of separation. If both laminar results underpredicted the heat flux upstream of separation, then they were assumed to underpredict the heat flux downstream of reattachment as well. The pressure-corrected predictions were preferred over those based entirely on computational results. In some cases the measured reattachment heat flux is obscured by the effects of a strong shock–shock interaction, such that an otherwise laminar reattachment appears to be transitional; these shots were not considered transitional. Care must also be exercised interpreting cases with strong shock–shock interactions for which the computational result is commonly nonconverged in much of region 3 (*cf.* Section 3.3.2). Based on the results of this comparison, it is clear in Figure 6.7 that the experiments at moderate to high Reynolds number suffered transition upstream of reattachment, causing the observed drop in separation length. A few transitional cases are also observed at lower Reynolds number for the high-enthalpy conditions, perhaps due to transition occurring downstream of reattachment where it does not influence L_{sep}. The transitional high-enthalpy datum for condition C4 which falls far above the others is shot 1320, which had an unusually large separated region. The experiment at the highest Re_{x_1} is shot 1757, which appears in Appendix F to be transitional upstream of separation.

The large difference in transition Reynolds number between the present results and those of Needham and Stollery (1966a,b) was thought to be possibly due to a difference in the characteristic boundary-layer temperature, as given by the reference temperature. While $T^*/T_1 < 1$ for most of the present experiments, the experiments of Needham (1965) were in the hypersonic regime where the Eckert number is large and $T^*/T_1 > 1$. It was shown by Adam (1997) that boundary-layer transition is well correlated by a Reynolds number $Re^*_{x_1}$ evaluated at the reference conditions; transition in the boundary layer on a cone was found to occur at approximately the same $Re^*_{x_1}$ for both flight experiments and shock tunnel experiments, though the values of Re_{x_1} at transition were different by more than an order of magnitude. While evaluation of $Re^*_{x_1}$ does show $Re^*_{x_1} > Re_{x_1}$ for the present experiments and $Re^*_{x_1} < Re_{x_1}$ for the experiments of Needham (1965), this accounts for only a small part of the difference in transition Reynolds number between the two studies. Though the disturbance levels in the different experimental facilities may be quite different, a more likely explanation for the discrepancy is the stabilizing effect of a higher Mach number in Needham's experiments. Larson and Keating (1960) studied transition of a separated shear layer over a cavity on an axisymmetric (ogive–cylinder) body, and found a marked increase in transition Reynolds

number with increasing Mach number, as did Chapman *et al.* (1958) for two-dimensional separation at steps and corners. Compilations of data on compressible shear-layer transition by Birch and Keyes (1972) and by King *et al.* (1991) show the same trend.

The Reynolds number of interest, here denoted $Re_{L_{sep}}$, is one based on distance from the origin of the shear layer and local external conditions. For the present experiments, this is evaluated at the conditions in region 2 taken from inviscid computations, using the experimental measurements for L_{sep}. Scaled separation length is plotted against $Re_{L_{sep}}$ in Figure 6.8, showing transition to occur for a number of shots in the range $2 \times 10^4 < Re_{L_{sep}} < 2 \times 10^5$, corresponding to $2 < M_1 < 5$. Both Birch and Keyes (1972) and King *et al.* (1991) indicated transition Reynolds numbers on the order of 10^5 but varying by at least a factor of four over this range in Mach number. Larson and Keating (1960) showed in addition that the transition Reynolds number can decrease well below 10^5 with decreasing T_w/T_{aw}, and also decreases with decreasing unit Reynolds number. Even the low-enthalpy conditions in the present experiments have T_w/T_{aw} an order of magnitude lower than investigated by Larson and Keating (1960), suggesting that the temperature ratio is an important factor in producing the small transition Reynolds numbers seen in Figure 6.8. The wall temperature effect also explains the somewhat earlier transition observed for high-enthalpy conditions. The present experiments have much smaller M_1 and T_w/T_{aw} than the experiments of Needham (1965), thus resulting in transition Reynolds numbers an order of magnitude smaller. The unknown acoustic disturbance levels are probably not a factor; the experiments of King *et al.* (1991) with laminar and turbulent nozzle wall boundary layers showed virtually no effect of the noise environment on transition of a separated shear layer over a two-dimensional cavity. They also found disturbances being convected upstream through the separation region, presumably originating from reattachment, and postulated that these disturbances dominate the transition process. Such disturbances can also be seen in the present heat flux measurements (*cf.* Figure 2.23a), but no attempt has been made to correlate them. In a computational study, Gathmann *et al.* (1993) showed that acoustic wall modes are not important for transition, lending further credence to the idea that disturbances from reattachment are driving transition.

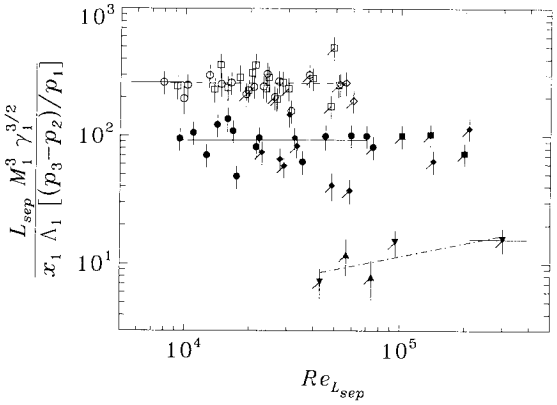

Figure 6.8: Correlation of experimental L_{sep} against $Re_{L_{sep}}$ from computations; see Figure 6.7 for a description of symbols, *etc.*

Correlation of the present experiments against Re_{x_1} as shown in Figure 6.7 does not recover the square-root dependence on Reynolds number for laminar interactions found by Needham (1965).

In fact, even with the known transitional cases disregarded, the line fits show on average a slight decrease in scaled L_{sep} with increasing Re_{x_1}. One possible contribution to the difference in behavior is the dependence on T_w/T_1 accounted for in the present study by use of Λ_1; the data of Needham at $M_1 = 9.7$ are fit very well by the square-root dependence in Equation 1.5 but also have T_w/T_1 increasing with Re_{x_1}. Removing Λ_1 from the scaling in Figure 6.7, however, results only in much-increased scatter. The present laminar interaction data cover a limited range in Re_{x_1} and have a high degree of scatter, thus making it very difficult to obtain an empirical correlation with Re_{x_1} to any reasonable accuracy. Unfortunately, as pointed out in Section 1.5.2.2, the functional dependence of L_{sep} on Reynolds number has not been well established even for perfect-gas flows. An important observation from Figure 6.7 is that the dependence on Re_{x_1} is not significantly different between high- and low-enthalpy experiments with laminar interactions, *i.e.* a Reynolds-number effect cannot account for the shift in high-enthalpy data above the low-enthalpy data seen in all of Figures 6.1–6.3, 6.4b, and 6.5–6.8.

6.1.3 Real-Gas Effects

This leads us to a central topic of the present work; real-gas effects on separation length. We propose that the shift in high-enthalpy data is due to an internal mechanism for real-gas effects. The upward shift is likely due to either an increase in the measured separation length that is not accounted for in the scaling, or an overprediction of the parameter group $M_1^3\gamma^{3/2}/\Lambda_1$ due to phenomena not accounted for in the external-flow computations. It is very important to note that the scaling of separation length by local flow parameters found by computation of the nonequilibrium external flow already includes external mechanisms for real-gas effects; any differences between low- and high-enthalpy cases due to reactions occurring in the external inviscid flow have been scaled out of the data presented in this Sections 6.1.1 and 6.1.2. As discussed in Section 5.1.2.3, the present experiments in T5 are not useful for verification of external mechanisms in any case. To be sure that the observed shift is in fact due to real-gas effects, other possible causes must be eliminated; this is done below in the Section 6.1.3.1. Then in Section 6.1.3.2, the observed discrepancy between high- and low-enthalpy data is attributed to an internal mechanism arising downstream of separation, and previous results are discussed in light of this. Finally, in Section 6.1.3.3, the data are reconsidered in terms of scaling parameters evaluated for frozen external flow in order to investigate the combined effects of external and internal mechanisms.

6.1.3.1 Elimination of Other Causes for the Observed Discrepancy

The discrepancy between low-enthalpy conditions A1–2 and other data in Figure 6.1 is clearly due to the effects of transition to turbulence as Reynolds number increases, as shown in Figure 6.7. Transition cannot, however, explain the difference between high- and low-enthalpy results because

this difference exists as well in the low-Re range, where there are a significant number of data clearly showing fully laminar interactions for both high- and low-enthalpy experiments. The difference also cannot be accounted for by any reasonable systematic error in the methods used to predict the external flow parameters; the largest uncertainty in the values of these parameters arises from uncertainty in the reservoir conditions, the effect of which is already included in the error bars shown in each figure. Other sources for error in the computations have been considered in Chapter 3 and were shown to be no greater than that due to uncertainty in the reservoir conditions.

Some of the flow-quality issues addressed in Section 2.7 may be of concern. There is no reason to believe that the effects of three-dimensional flow discussed in Section 2.7.5 should have a significant dependence on stagnation enthalpy. While the flow was shown by two different estimation procedures to be fully established well before the time at which separation-length data were obtained, the margin for error is smaller at high-enthalpy. If steady separated flow has not been established, however, the resulting measurement of L_{sep} would be smaller, not larger. The only flow-quality issue which may be of importance is contamination of the test-section flow by helium from the driver section of the shock tunnel. In Section 2.7.2.2, results from driver-gas detection studies in T5 at $h_0 \simeq 20$ MJ/kg were applied to the present test conditions at higher enthalpy to show that only condition C4 is likely to harbor significant contamination. It is possible, but unlikely, that the results at $h_0 \simeq 20$ MJ/kg cannot be extrapolated to higher enthalpy; verification requires further detection experiments under the present conditions at $h_0 \geq 24$ MJ/kg. Condition C1, however, has the same stagnation enthalpy (though a higher stagnation pressure) as examined by Sudani *et al.* (1998), yet is well correlated with the other high-enthalpy conditions in Figure 6.1. This indicates two possibilities; either the degree of contamination in condition C4 is not significant, or contamination has only a weak effect on separation length.

A simple analysis was performed to gauge the magnitude of contamination effects on the parameter grouping used to scale separation length in Figure 6.1. This consisted of a perfect-gas nozzle expansion followed by a perfect-gas wedge flow, using a gas composition with various mass fractions of helium (0.0, 0.1, 0.25, and 0.5) and setting the mass fractions of N and N_2 to keep the same degree of dissociation as found in the free stream for condition C2. This procedure neglects any effect of the helium diluent on the nitrogen recombination rate which may produce a different frozen composition in the free stream. Although perfect-gas nozzle flow is clearly a poor assumption for predicting free-stream conditions, it should provide a useful estimate bounding relative changes in the flow conditions due to changes in the ratio of specific heats γ as the fraction of helium in the gas is increased. As helium is added, γ increases from 1.43 for the 10% dissociated free stream with no helium to 1.52 at 50% contamination. The effects this has on the nozzle free stream and on the wedge flow tend to compensate each other; for a fixed free stream, the shock angle on the wedge increases with γ, but M_∞ also increases with γ, driving the shock angle back down. Due to these competing

effects, changes due to contamination do not exhibit a monotonic behavior with wedge angle θ_1. At low θ_1, T_1 decreases with increasing contamination but M_1 remains essentially unchanged. At high θ_1, T_1 actually increases slightly with contamination, and the effect on M_1 becomes more important. Taking Λ_1 to be approximately $(T_w/T_1)^{3/2}$, the largest overall relative change in the parameter grouping $M_1^3\gamma_1^{3/2}(T_1/T_w)^{3/2}$ due to contamination was found to be on the order of a 15% reduction. This means that L_{sep} measured in contaminated flow but scaled by parameters computed under the assumption of helium-free flow would result in an erroneous upward shift of the data in Figure 6.1. While the direction is consistent with the observed shift, the magnitude of the error is far too small to account for the difference, which is approximately a factor of two increase in scaled separation length for high-enthalpy cases compared to low-enthalpy cases. A full nonequilibrium computation of the nozzle and wedge flows including helium is required to verify that chemistry effects (*e.g.* changes in the reaction rates due to helium dilution) do not significantly alter the present conclusion. The flow history may also be important in determining the effects of contamination on separation length; if the separated flow is well established when helium arrives, then most of the helium flows past the separation zone without entering the recirculating region. Evidence for an increase in L_{sep} at late time, long after the expected time of driver-gas contamination, can be seen in Figure 2.23b.

The results in Figures 6.1 and 6.4 might be construed as suggesting the discrepancy between low- and high-enthalpy data is due entirely to scaling of L_{sep} by the parameter Λ_1. We assert instead that the new scaling parameter actually serves to elucidate real-gas effects on separation length. It has already been pointed out that while the introduction of Λ_1 in Figure 6.1 results in a shift of the high-enthalpy data away from the low-enthalpy data, it also results in significantly reduced scatter among each set of data independently of the other. It has been shown qualitatively by numerous previous investigations in perfect-gas flows that L_{sep} increases with increasing T_w/T_1 (*cf.* Section 1.5.2.1). The new parameter Λ_1 quantifies this effect by linking T_w/T_1 to the skin friction of the incoming boundary layer using the reference-temperature method and the scaling from triple-deck theory, producing a dependence on T_w/T_1 consistent with previous qualitative results. The large range in T_w/T_1 evident in Figure 6.5a suggests that any dependence of L_{sep} on T_w/T_1 is important in the present experiments. This dependence is at least approximately scaled out with normalization by Λ_1, leaving only internal mechanisms for real-gas effects as the likely cause for the discrepancy between low- and high-enthalpy data in Figure 6.1.

6.1.3.2 Internal Mechanism Causing the Observed Discrepancy

By the above arguments, all potential sources, other than real-gas effects, for the observed shift in high-enthalpy data have been eliminated. The question now arises as to what internal mechanism in particular is responsible for the increase in scaled separation length measured for high-enthalpy flows. The correlation of high-enthalpy data in Figure 6.1 includes experiments at both high and low

incidence angles as well as large and small nozzle area ratios. The main thing they have in common that differentiates them from the low-enthalpy conditions B1–3 is the presence of partial dissociation in the free stream, suggesting that recombination is responsible for the observed difference. It was shown using nonequilibrium computations of boundary layers in Section 5.2.2 that under the present experimental conditions, dissociation in the boundary layer is entirely negligible and changes in the skin friction of the undisturbed boundary layer upstream of separation due to recombination are relatively unimportant, inducing no more than a 5% increase in C_f. The generalized scaling for L_{sep} in Equation 4.46 indicates an inverse-square dependence on the wall shear, so that the corresponding relative decrease in L_{sep} may be larger than 5%. The effect is too small to account for the observed difference and acts in the wrong direction.

The internal mechanism causing the difference must, by elimination, be a mechanism arising in the region downstream of separation. In Section 5.2.2 it was speculated that differences in the species and temperature gradients between flow near the dividing streamline in a shear layer and flow near the cold wall in the boundary layer may lead to a large decrease in τ_{ψ^*} while τ_w increases slightly with recombination. This would result in a larger separation length for recombination-dominated flows with respect to frozen flow. Such a mechanism could explain the effect observed in the present experiments. The ratio of high- to low-enthalpy scaled separation length seen in Figure 6.1 is approximately a constant factor three over a wide range of pressures; for the high enthalpy experiments, the computed pressure in region 2 external to the shear layer (*cf.* Appendix E) ranges from $\simeq$ 15 kPa at high A_e/A_* and $\theta_1 = 15°$ to $\simeq$ 170kPa at low A_e/A_* and $\theta_1 = 40°$. This suggests that nonequilibrium effects which depend on the reaction rate are not important, since it was shown in Section 5.2 that the cases with $\theta_1 = 15°$ and high A_e/A_* have nearly frozen boundary layers. On the other hand, no computations in the present study have been performed for the flow downstream of separation under these conditions. It is possible that nonequilibrium effects are important in the region downstream of separation even when they are not important in the boundary layer upstream of separation, due to the presence of slow recirculation close to a cold wall. The constancy of the ratio of high- to low-enthalpy L_{sep} also suggests that the magnitude of the effect does not depend strongly on the degree of dissociation at separation, since the high-enthalpy results in Figure 6.1 include high-incidence cases with $0.11 < \alpha_1 < 0.25$.

The mechanism described above may explain the computational results of Grumet *et al.* (1994) for shock-impingement flows with $\alpha_1 > 0$. At a low-pressure condition where only a small amount of recombination occurs in the free-shear layer, they found a slight decrease in L_{sep} for a catalytic wall which may be attributable to the increase in C_f upstream of separation. At a high-pressure condition with p_1 of the same order as in the present experiments, they found a large increase in L_{sep}, suggesting that an internal mechanism in the free-shear layer causes a decrease in τ_{ψ^*} much stronger than the increase in τ_w upstream of separation.

While such computational results are expected to include the relevant physics, it is also important to consider previous experimental results on high-enthalpy shock/boundary-layer interaction to see if they exhibit the same behavior. Several experimental studies were discussed in Section 1.5.4.1, but the information on local external flow conditions necessary for application of the new scaling law was available to the present author only for the compression-corner experiments of Mallinson (1994). External mechanisms are negligible for these experiments, but the high-enthalpy cases do have free-stream dissociation of oxygen which may recombine in the separated region and cause a change in separation length. The information supplied by S. G. Mallinson (priv. comm.) for eight experiments at three different operating conditions of T3 included free-stream conditions, the local conditions p_1, γ_1, M_1, Re_{x_1}, and C^* (different from the free stream due to viscous interaction at high Mach number on a flat plate), the wall temperature, and the distance L_u between the corner and the location of separation observed from flow visualization. The local temperature T_1 was found by assuming $(T_1 - T_\infty)/T_\infty \simeq 0.3(p_1 - p_\infty)/p_\infty$ based on the correction method discussed in Section 4.1.3 applied to very weak shock waves, and the viscosities in Λ_1 were calculated using the model in Section 4.1.4. The reattachment pressure p_3 was taken from measurements presented in graphical form (Mallinson, 1994), and p_2 was calculated using Equation 4.50. Although the present scaling was developed to describe the behavior of L_{sep}, the behavior of L_u is expected to be qualitatively similar.

In Figure 6.9a, Mallinson's data for L_u is plotted in the same form as used in Figure 6.1 for the present data. Interestingly, the dependence on pressure ratio is closer to a linear one than the quadratic one expected for hypersonic interactions based on previous work in perfect-gas flows (*cf.* Section 6.1.1). This may be due in part to the use of L_u instead of L_{sep} since $\partial L_{sep}/\partial L_u > 1$. The shock tunnel conditions B, D, and G for T3 are listed in order of decreasing stagnation en-

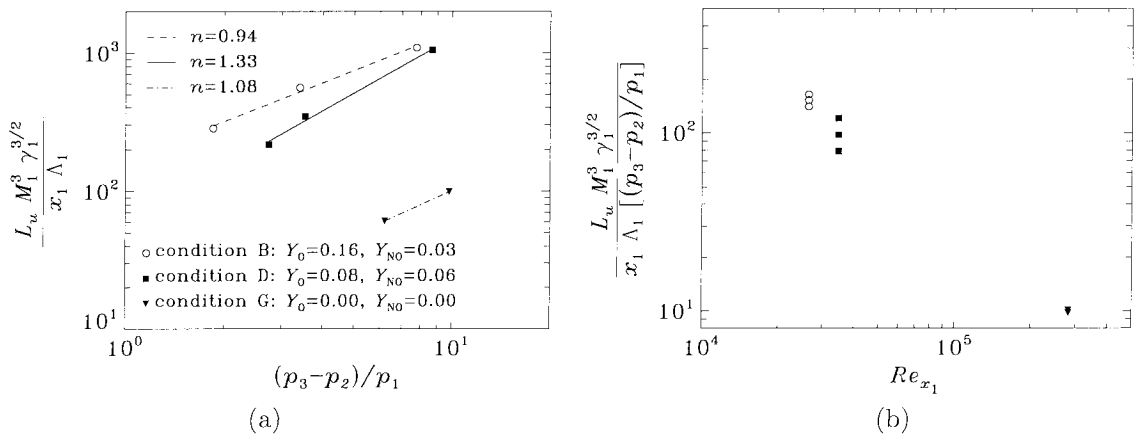

Figure 6.9: Correlations of L_u data from experimental study of Mallinson (1994); (a) against pressure ratio, (b) against Reynolds number. Conditions B, D, and G in T3 have the indicated free-stream mass fractions of O and NO. Lines are linear fits in log–log coordinates giving slope n.

thalpy. The experiments used air, resulting in free-stream composition which includes dissociated oxygen and some nitric oxide as indicated, but negligible dissociation of nitrogen. The plot against Reynolds number (assuming a linear dependence on pressure) in Figure 6.9b suggests that the difference between condition G and the other conditions might be a Reynolds-number effect. The same magnitude of reduction in scaled separation length, however, was found in the present experiments at somewhat higher Re_{x_1}. The increase in separation length with increasing free-stream dissociation might be explained by recombination in the shear layer. Unfortunately, the very limited number of data makes it difficult to verify that the same trend is occurring for the T3 experiments as found for the present experiments in Figure 6.1, particularly when the uncertainty and scatter are considered as well.

6.1.3.3 Combined Effect of Internal and External Mechanisms

As mentioned previously in Section 5.1.2.3, external mechanisms cannot be separated from internal mechanisms. We may, however, consider the net effect of internal and external mechanisms by evaluating the scaling parameters for a thermochemically frozen external flow. This is done in Figure 6.10 by use of the frozen-flow IDG model presented in Section 5.1.1. The model assumes a uniform free stream with properties taken from the nozzle centerline at the double-wedge leading edge, and is further limited by the approximation that gives constant vibrational excitation. Thus the separation length scaled in this manner cannot be directly compared to the separation length scaled by parameters from the nonequilibrium computations; only relative differences within the results from each scaling provide additional information. Furthermore, some of the high-incidence, high-enthalpy conditions do not admit a frozen-flow solution with attached shocks, although these are the conditions most likely to show external mechanisms for real-gas effects. These conditions have the lowest values of $(p_3 - p_2)/p_1$, and it can be seen by comparing Figure 6.1 to Figure 6.10 that some data in this regime are missing from the latter. The comparison also shows very little difference in the positions of data relative to each other. Only two experiments at high incidence under condition C4 (□) show a noticeable difference, with scaled separation length smaller than the corresponding experiments at lower-enthalpy condition C2 (○) when L_{sep} is scaled by frozen-flow parameters. This is consistent with the result in Section 5.1.2.3 that dis-

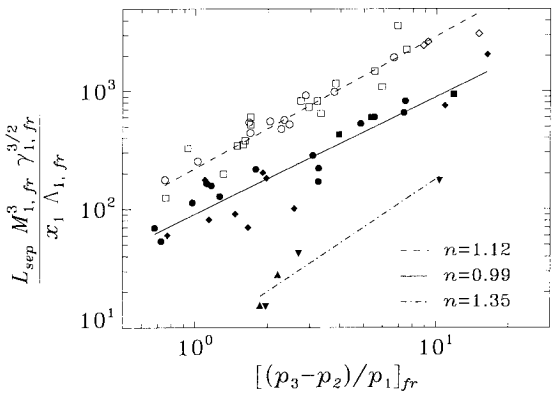

Figure 6.10: Correlation of experimental L_{sep} using parameters from IDG frozen flow; see Figure 6.1 for a description of symbols, *etc.*

sociation in region 1 relative to the free stream causes a decrease in L_{sep} if $\alpha_\infty > 0$. The decrease in this regime relative to the low-incidence regime causes a slightly steeper slope for the high-enthalpy curve fit seen in Figure 6.10 compared to Figure 6.1. It is important to note, however, that the decrease is found not by experimental observation but by substituting different models (frozen and reacting) for the external flow, and that the decrease is no larger than the existing scatter among high-enthalpy data.

It is thus evident from Figure 6.10 that the increased separation length for high-enthalpy data, attributed to an internal mechanism for real-gas effects, holds also with respect to frozen external flow at the same free-stream conditions, because external mechanisms are unimportant for most of the present experiments. Only very high-incidence, high-enthalpy conditions indicate significant external mechanisms, and these act to reduce the increase due to internal mechanisms. The internal mechanism elucidated by the scaling in Figure 6.10 thus appears to depend largely on the free-stream dissociation level.

6.2 Reattachment Heat Flux

The experimental heat flux measurements described in Section 2.5 may be used together with local external-flow parameters from the inviscid triple-wedge computations described in Section 3.3 to see if the various correlations from previous work in perfect gas flows, presented in Section 1.5.3, produce any interesting results for the present experiments. The maximum measured heat flux $\dot{q}_{pk}$ from each experiment was not useful due to very large scatter and the obscuring phenomenon of strong shock–shock interaction. Only the averaged heat flux measurement $\dot{q}_R$ from downstream of reattachment (*cf.* Section 2.5.3) is used in this section. The experimental data are applied to two of the previous correlations from Section 1.5.3; the results of Simeonides *et al.* (1994) are considered in Section 6.2.1, and the results of Bushnell and Weinstein (1968) are considered in Section 6.2.2.

6.2.1 Correlation using results of Simeonides et al

Because it successfully correlated a wide range of data from perfect-gas flows, the result presented by Simeonides *et al.* (1994) appears the most promising. In particular, they give a plot of the scaled heat flux $(\dot{q}_{pk}/\dot{q}_{fp})(p_{fp}u_{fp}/p_{pk}u_{pk})^n(L_{pk}/x_{pk})^{1-n}$, with n given by Equation 1.18, against the Reynolds number $Re^*_{x_{pk}}$ evaluated in region 3 at reference conditions, in which laminar interaction data are found to be independent of $Re^*_{x_{pk}}$ within $\pm 20\%$, while transitional and turbulent data correlate within $\pm 20\%$ of a power-law in $Re^*_{x_{pk}}$. No such behavior, however, can be discerned from the present experimental data, the scatter being much too large. In Figure 6.11 we do not consider $Re^*_{x_{pk}}$ at all, but instead look at the scaling used by Simeonides *et al.* (1994) to nondimensionalize the peak heating. While Simeonides *et al.* reference the measured heat flux to a value predicted

for a flat plate at the same distance x_{pk} from the leading edge as reattachment, here the measured heat flux $\dot{q}_R$ from the reattachment region is referenced to the measured heat flux $\dot{q}_1$ upstream of separation. This scales out internal mechanisms for real-gas effects on heat transfer to the extent that they induce the same magnitude change in $\dot{q}$ relative to a frozen boundary layer for both regions 1 and 3. The growth length L_{pk} for the reattaching boundary layer is estimated, after Bushnell and Weinstein (1968), using Equation 1.14 with the thickness δ_s at reattachment taken to be the sum of the upstream boundary-layer thickness and the additional growth of a zero-initial-thickness shear layer over the distance L_{sep}, *i.e.*

$$\delta_s = \delta_{x_1} + \delta_{L_{sep},\,2}\,, \tag{6.4}$$

where δ is estimated from Equation 4.23 using computed external flow properties for region 1 or 2 as appropriate. Other parameters in Figure 6.11 are taken directly from the inviscid triple-wedge computations. Note that external mechanisms for real-gas effects are also scaled out by use of local external flow solutions from nonequilibrium computation. Experiments suspected of having transitional interactions according to the criterion discussed in Section 6.1.2 are flagged and used for separate curve fits from the laminar interaction data. The error bars are based on the experimental uncertainty (described in Section 2.5.3) for the largest single heat flux measurement $\dot{q}_{pk}$ from the ramp, even when this measurement was not included in the averaging to obtain $\dot{q}_R$.

As shown in Figure 6.11, a curve fit to all of the data, including those suspected of being transitional, reproduces the square-root dependence found by Simeonides *et al.* (1994). The scatter about this curve fit, however, is on the order of $\pm 50\%$, greatly exceeding the scatter in perfect-gas data presented by Simeonides *et al.* When the present data are divided into subsets based upon high or low enthalpy and laminar or transitional interactions, only the line fit to high-enthalpy laminar data shows a similar slope to the line fit to all data. Worse yet, the fits to transitional data indicate a power law weaker than a square root, not stronger as given by the result of Simeonides *et al.* (*cf.* Equation 1.18). One contribution to the scatter may be the estimation for L_{pk}; it was shown in Section 5.2.2.1 that Equation 4.23 underpredicts the boundary-layer thickness by 20% at $M_1 \simeq 5$, and L_{pk} also depends on the measured angle θ_{sep} which was shown in Section 6.1.1 to have large uncertainty. This source of error cannot on its own account for $\pm 50\%$ scatter. Though $\dot{q}_R$ was averaged from heat flux measurements which appeared to be upstream of any influence due to a strong shock–shock interaction, there remains some question concerning the consistency of these measurements because in some cases the influence approached close to reattachment. Removing all data seen from the interferograms in Appendix F to have a strong shock–shock interaction, however, has no effect on the scatter. There is also no discernible trend for differences between results with and without a strong shock–shock interaction. Other sources for scatter are the uncertainty in effective thermal properties which appear to differ from thermocouple to thermocouple, and the possible

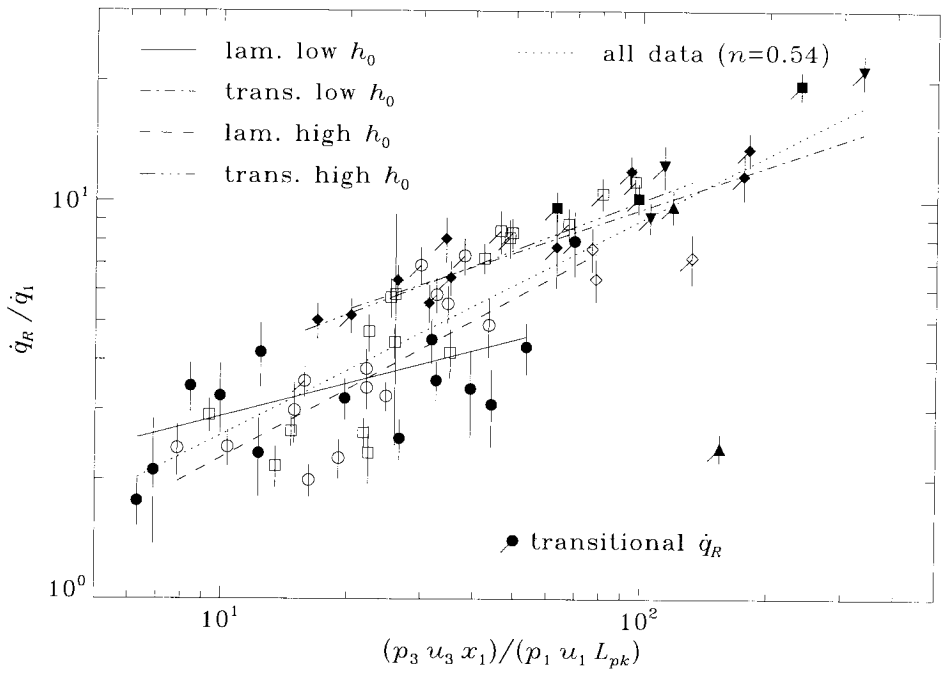

Figure 6.11: Experimental data for the ratio of reattachment heat flux $\dot{q}_R$ to heat flux $\dot{q}_1$ measured just upstream of separation, plotted against the parameter grouping suggested by Simeonides *et al.* (1994). Symbols denote different reservoir conditions as given in Figure 6.1. Flagged symbols indicate experiments suspected of having a transitional interaction. Error bars are given by the measurement uncertainty in $\dot{q}_{pk}$. Lines are fits to various subsets of the data as indicated, giving slope n in log–log coordinates.

presence of vortical structures in the boundary layer downstream of reattachment (*cf.* Section 2.5.3). Possibly the most important cause of scatter in the data is the prediction method for external flow conditions at reattachment, *i.e.* the inviscid triple-wedge computations. Various sources of error in this method were discussed in Section 3.3.3, and it was shown in Section 4.1.3 that modifying the edge conditions in region 3 according to the experimentally measured pressure gives a heat-flux prediction that is usually closer to experiment. The correction method is not used in Figure 6.11 because it does not work consistently for all shots.

If the reattachment heat flux data are normalized by a reference value predicted by nonreacting boundary-layer theory, then it may be possible to discern internal mechanisms for real-gas effects. This is done in Figure 6.12 using a correlation otherwise similar to that used in Figure 6.11. The length x_{ref} is equal to L_h plus the distance from the corner to reattachment, and is used with local flow parameters in region 3 from the nonequilibrium computations to calculate $\dot{q}_{ref}$ from Equations 4.14 and 4.20. For Figure 6.12a, the wall enthalpy in Equation 4.14 is computed using $\alpha_w = \alpha_e$, while for Figure 6.12b, it is computed using $\alpha_w = 0$. The latter approximation is applied only to the high-enthalpy shots with $\theta_1 > 15°$, under the assumption that a noncatalytic wall better represents the experiment and gives at most a moderate degree of recombination for $\theta_1 = 15°$ (see

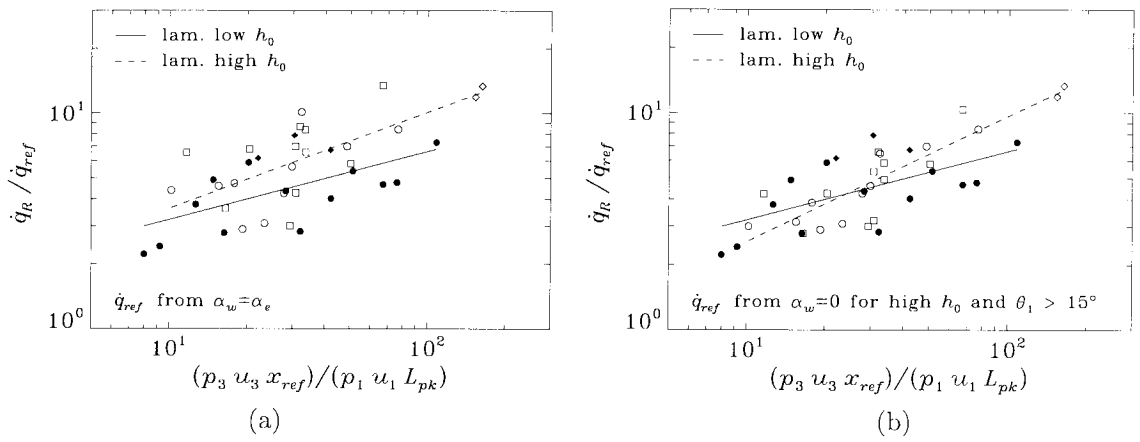

Figure 6.12: Ratio of reattachment heat flux measurements to theoretical flat-plate reference values assuming (a) $\alpha_w = \alpha_e$ for all shots, or (b) $\alpha_w = 0$ for high-enthalpy shots with $\theta_1 > 15°$ and $\alpha_w = \alpha_e$ for remaining shots, plotted against parameter grouping suggested by Simeonides *et al.* (1994). Shots suspected of having transitional interactions are not shown. Symbols are described in Figure 6.1. Lines are fits to high- and low-enthalpy data as indicated.

Section 5.2.1, as well as the comparisons between experiment and prediction for high-enthalpy low-incidence shots in Appendix F). Only the laminar interaction data are presented. On average, the high-enthalpy data fall slightly higher than the low-enthalpy data in Figure 6.12a, which may be explained by the increase in $\dot{q}_R$, due to recombination, over that expected for a frozen boundary layer (*cf.* Section 5.2.3). The scatter, however, is much larger than the average difference between the two sets of data. On the other hand, use of the $\alpha_w = 0$ approximation in Figure 6.12b, shown in Sections 4.1.1.3 and 4.1.3 to provide a reasonable estimate for the effect of recombination in the boundary layer, reduces the scatter somewhat and brings the curve fits to low- and high-enthalpy data into better positional agreement (though worse agreement in terms of the slope). In short, the present data do show that reattachment heat flux increases due to recombination, but do not yield any useful information concerning the magnitude of this increase.

6.2.2 Correlation using results of Bushnell and Weinstein

Bushnell and Weinstein (1968) found that laminar reattachment heating data in perfect-gas flows from a number of authors was well correlated by Equation 1.15, though the total number of experiments included was far fewer than used by Simeonides *et al.* (1994). This correlation essentially states that the Stanton number at reattachment depends on the Reynolds number evaluated at the wall conditions, instead of the edge conditions as in Equation 4.20, because the peak heating at reattachment depends on the growth of a sub-layer downstream of the stagnant reattachment point. The present data, again using the averaged measurements $\dot{q}_R$, are plotted in Figure 6.13 to see how well they fit Equation 1.15. Again, since the low-incidence high-enthalpy shots have nonequilibrium boundary layers closer to frozen flow than to equilibrium flow, they are excluded from the $\alpha_w = 0$

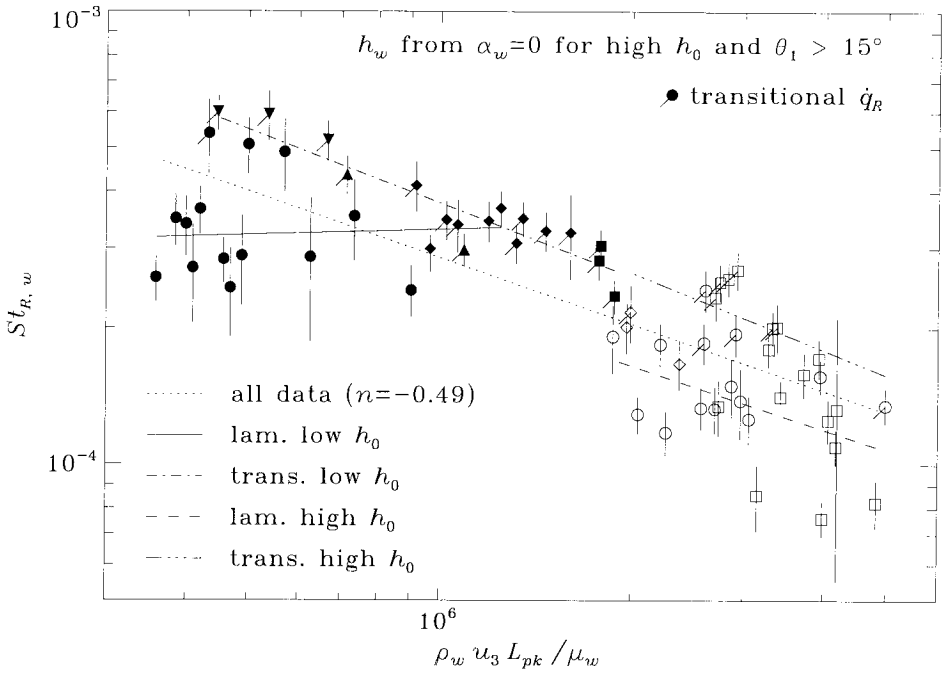

Figure 6.13: Reattachment heat flux data $\dot{q}_R$ correlated according to the result of Bushnell and Weinstein (1968) given in Equation 1.15, using $\alpha_w = 0$ when evaluating ρ_w and h_w in St_w for high-enthalpy experiments with $\theta_1 \geq 15°$. See Figure 6.11 for description of symbols, flags, error bars, lines, and n.

approximation for the effect of recombination. The $\alpha_w = 0$ approximation is also used to find ρ_w and μ_w, though the effect on viscosity is minimal. The length scale L_{pk} is calculated as described previously for Figure 6.11. A curve fit to all of the data in Figure 6.13 gives an inverse square-root dependence as found by Bushnell and Weinstein (1968) for laminar interactions. The same dependence is found when fitting curves to various subsets of the data, except for the low-enthalpy laminar interactions. These are on average independent of $\rho_w u_3 L_{pk}/\mu_w$, but have very large scatter. The data suspected of transitional interactions have the least scatter, across low- and high-enthalpy conditions. Transitional data are not expected to adhere to the result in Equation 1.15 for fully turbulent interactions, but they clearly show higher heat flux than

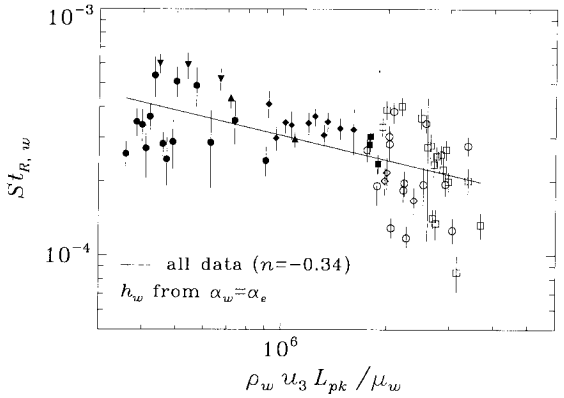

Figure 6.14: Reattachment heat flux data $\dot{q}_R$ correlated according to the result of Bushnell and Weinstein (1968) given in Equation 1.15, using $\alpha_w = \alpha_e$ for all shots when evaluating St_w. See Figure 6.11 for description of symbols, flags, error bars, lines, and n.

expected for purely laminar interactions.

The importance of approximately including internal mechanisms for real-gas effects by setting $\alpha_w = 0$ where appropriate is evident from Figure 6.14, in which the data are replotted without this approximation. The high-enthalpy high-incidence data shifts to the left and upward due to smaller values of ρ_w and $h_e - h_w$, and also shows increased scatter. A curve fit to all the data now gives an exponent n for Equation 1.15 which is significantly smaller than -1/2. Possible reasons for the large scatter in Figures 6.13 and 6.14 were discussed earlier in connection with Figure 6.11. As done for separation length in Section 6.1.3, the combined effect of internal and external mechanisms could be studied by using frozen-flow solutions to evaluate the scaling parameters. The present data, however, offer no useful information in this regard because the scatter is large and, as discussed in Section 5.1.3, the effects of external mechanisms are relatively small. The striking difference between laminar low-enthalpy data and laminar high-enthalpy data seen in Figure 6.13 is also evident in Figures 6.11 and 6.12. It is not clear why the low-enthalpy laminar-interaction data should behave diffferently.

6.3 Summary

The present experimental data on separation length and reattachment heating in double-wedge flows in T5 have been investigated using various correlations, including the new scaling law for separation length developed in Chapter 4. In particular, the new parameter Λ_1 in Equation 4.48, which approximately accounts for wall temperature effects on the skin friction, was shown to provide a better collapse of the experimental L_{sep} data while at the same time illuminating a difference between low- and high-enthalpy data. External mechanisms for real-gas effects were scaled out by the use of local external flow parameters found from the inviscid nonequilibrium computations discussed in Chapter 3, and other possible causes for the observed discrepancy between high- and low-enthalpy data were considered and eliminated, leaving us with the conclusion that the result is due to an internal mechanism for real-gas effects. The mechanism increases L_{sep} at high enthalpy, which is not consistent with the effects of recombination occurring upstream of separation, but is speculated to be consistent with a mechanism due to recombination occurring downstream of separation, as discussed in Chapter 5. The magnitude of the increase is, on average, a factor of three in scaled separation length.

The reattachment heat flux data was found on average to reproduce the behavior given by previous correlations in the literature, but with much larger scatter. This scatter prohibits investigation of external mechanisms for real-gas effects, but the existence of an internal mechanism, whereby recombination in the boundary layer increases the wall heating, is shown by comparison of experimental heat flux to heat flux predicted using approximate methods for frozen and equilibrium recombining boundary layers.

Chapter 7 Conclusions

The following list itemizes the most important goals accomplished in the present study.

- Experiments were performed in the T5 Hypervelocity Shock Tunnel to investigate the interaction between a shock and a boundary layer at the upstream-facing corner on a double wedge under conditions of high-enthalpy flow in nitrogen test gas. Separation length was measured using flow visualization and heat flux distributions were measured using surface thermocouples.

- The local flow properties near separation and reattachment could not be measured and were instead estimated for each experiment by use of an advanced computational code to predict the inviscid external flow over the experimentally measured separated-flow geometry, under conditions of thermochemical nonequilibrium and nonuniform free stream.

- The scaling originally introduced by Burggraf (1975) was decoded, generalized, and extended to include arbitrary viscosity law by the application of results from multi-deck asymptotic boundary-layer theory to a simple model regarding the balance of forces on the separation bubble, using the reference-temperature method to account approximately for wall temperature effects on the skin friction. A new parameter Λ_1 gives the functional dependence of separation length on wall-to-edge temperature ratio.

- A framework for describing real-gas effects on separation length and reattachment heating was introduced which classifies mechanisms into those arising in the external inviscid flow and in the internal viscous flow, the latter divided further into mechanisms arising in the boundary layer upstream of separation or in the shear layer and recirculating region downstream of separation. External mechanisms were investigated by application of the ideal dissociating gas model to the new scaling law. Internal mechanisms were further subdivided into those arising upstream and downstream of separation, and the former were investigated by application of a thermochemical nonequilibrium Navier–Stokes code to flat-plate boundary layers. The framework provides a context in which previous, present, and future results for real-gas effects on separated flow may be discussed.

- The experimental data on separation length and reattachment heating were investigated by use of various correlations in the literature as well as the new scaling law developed in the present study. For separation length, a linear dependence on the reattachment pressure ratio was found, in accordance with previous results for supersonic interactions in perfect-gas flow. A Reynolds-number effect due to transition moving upstream of reattachment was found for

some of the low-enthalpy experiments. The Reynolds-number dependence of previous perfect-gas results for laminar interactions, however, could not be reproduced. A significant increase in scaled separation length was observed for high-enthalpy laminar-interaction data with respect to low-enthalpy laminar-interaction data, and attributed to recombination occurring in the separated shear layer. Reattachment heat flux was found to agree roughly with previous scaling results, but excessive scatter prevented verification of real-gas effects aside from the qualitative result that heat flux increases when recombination occurs in the boundary layer.

Specific conclusions regarding internal and external mechanisms for real-gas effects from computational analysis and experimental observation are listed in Sections 7.1 and 7.2 on separation length and reattachment heating respectively. It is important to note that while external mechanisms induce changes with respect to a thermochemically frozen flow at the same free-stream conditions, internal mechanisms are considered in terms of the changes they induce relative to a frozen flow with the same local external flow conditions. The practical relevance of the present results is discussed in Section 7.3, and recommendations for future work are presented last in Section 7.4.

7.1 Separation Length

7.1.1 External Mechanisms

Analysis

- If dissociation occurs downstream of the reattachment shock but not in the region downstream of the leading-edge shock, then the reattachment pressure decreases with respect to frozen flow and causes a decrease in separation length, by as much as 50% for equilibrium flow at high enthalpy. This mechanism may in general be important at low incidence and high flap deflection, but not under the conditions of the present experiments where the reaction rate downstream of reattachment remains small for such configurations.

- If dissociation occurs downstream of the leading-edge shock, then the local Reynolds number, Mach number, and wall-to-edge temperature ratio at separation all increase with respect to frozen flow, but these have competing effects on the separation length. In addition, whether the reattachment pressure increases or decreases depends on the free-stream dissociation level. Thus the separation length may in general either increase or decrease, but appears to be affected under conditions of the present high-enthalpy experiments only at very high incidence, where a slight decrease is expected.

- Under conditions where recombination or other exothermic processes occur instead of dissociation, reactions downstream of the reattachment shock decrease separation length while

reactions downstream of the leading-edge shock increase separation length.

Experiments

- External mechanisms could not be studied independently from internal mechanisms using the present experiments. Furthermore, the scaling for separation length used to investigate experimental results depends on local external flow conditions, which were computed for the present experiments to account for nonuniform, nonequilibrium flow. The combined effects of internal and external mechanisms were considered by computing the local external conditions for frozen flow, which showed that external mechanisms were important only for the very high-incidence cases and acted to decrease separation length.

7.1.2 Internal Mechanisms

Analysis

- If the local external flow is dissociated, either due to reactions occurring downstream of the leading-edge shock or to dissociation in the free stream, recombination near a cold wall in the boundary layer can increase the skin friction upstream of separation (relative to frozen flow with the same external dissociation level) and decrease separation length. For a noncatalytic wall, the magnitude of the change depends on the degree of nonequilibrium near the wall. This mechanism has a relatively small effect (less than 5% increase in skin friction) under the present experimental conditions which include up to 25% dissociation in the local external flow at separation.

- Recombination occurring in the separated shear layer and recirculating region with respect to a dissociated external flow condition is expected to have an effect on the shear stress along the dividing streamline. The existence, let alone the direction and magnitude, of this mechanism could not be verified using the present computational analysis, but it was speculated that the shear stress along the dividing streamline may decrease relative to frozen flow, the difference in behavior from the wall shear upstream of separation being attributed to differences in the gradients of temperature and species concentration.

- Other conditions, such as a dissociating boundary layer with no dissociation in the external flow or an adiabatic wall, were not considered in detail.

Experiments

- Scaled properly by local parameters computed for nonuniform, nonequilibrium flow, the experimental measurements showed an increase in separation length, approximately by a factor of

three, for high-enthalpy experiments relative to low-enthalpy experiments. The increase could only be recognized when the new parameter Λ_1 was included in the scaling to account for wall temperature effects on a nonreacting, separating boundary layer. The increase could not be explained by driver-gas contamination and was attributed to an internal mechanism due to recombination occurring downstream of separation, the effects of which cannot be included in the present scaling law.

7.2 Reattachment Heat Flux

7.2.1 External Mechanisms

Analysis

- If dissociation occurs downstream of the reattachment shock but not in the region downstream of the leading-edge shock, then the temperature decreases downstream of reattachment and reduces the heat flux relative to frozen flow. This mechanism may in general occur at low incidence and high flap deflection, but induces a change no larger than 20% even for equilibrium high-enthalpy flows. For these configurations in the present experiments, this mechanism may cause a weak effect because temperature is sensitive to nonequilibrium dissociation (unlike the pressure which determines the effect on separation length).

- If dissociation occurs downstream of the leading-edge shock, the boundary-layer thickness is reduced relative to frozen flow and the density downstream of reattachment increases beyond that for dissociation occurring only downstream of reattachment. These both lead to slightly increased heat flux at high enthalpy and high incidence, but can result in a slight decrease at moderate enthalpy if the free stream is partially dissociated. Under the conditions of the present experiments at high incidence, this mechanism produces a slightly increased heat flux.

Experiments

- External mechanisms could not be studied independently from internal mechanisms using the present experiments because correlations for heat flux depend on local external flow conditions, which were computed for the present experiments to account for nonuniform, nonequilibrium flow. In any case, the external mechanisms are expected to produce only small effects which would be obscured by the large scatter in experimental heat flux data.

7.2.2 Internal Mechanisms

Analysis

- If the local external flow at reattachment is dissociated, either due to reactions occurring downstream of the reattachment shock or to dissociation in the free stream, recombination near a cold wall in the boundary layer can increase the heat flux relative to frozen flow regardless of whether the wall is catalytic or noncatalytic, though for a noncatalytic wall the degree of recombination depends on the degree of nonequilibrium in the flow near the wall. This mechanism can cause up to a factor of two increase in heat flux under the conditions of the present high-incidence experiments which include up to 25% dissociation in the local external flow.

- If the local external flow upstream of separation is dissociated, either due to reactions occurring downstream of the leading-edge shock or to dissociation in the free stream, recombination in the boundary layer can reduce the boundary-layer thickness and increase the peak heating at reattachment by shortening the length scale for growth of the sub-layer at reattachment. This mechanism produces only a very small effect under the conditions of the present high-incidence experiments.

- If the local external flow both upstream and downstream of separation is dissociated, and recombination occurs at the wall upstream of separation, then subsequent dissociation along the dividing streamline results in an increased mass-fraction gradient at the wall near reattachment, which may also contribute to increased heat flux.

Experiments

- An increased heat flux was observed in the experiments by comparison to predictions for a frozen boundary layer under the same external flow conditions. The magnitude of the increase, however, could not be gleaned from experimental data due to the large scatter. When the effect of recombination was approximately accounted for in the predictive method by considering the enthalpy difference between external conditions and a fully recombined state at the wall, the experimental measurements better matched existing correlations for reattachment heating in perfect-gas flows.

7.3 Relevance of Present Results

Though the exact mechanism responsible for the present experimental observation of increased separation length at high enthalpy has not been determined with certainty, much progress has been made

in understanding the physics of real-gas effects on separation in general. The framework introduced in the present work to describe mechanisms for real-gas effects, and the limited parametric studies presented to quantify these effects, should prove useful in future investigations of shock/boundary-layer interaction. The ideas developed here may be applied to separated flows found in many different situations, including external flow on control surfaces of a reentry vehicle, internal flow in a high-speed propulsion system, or flow on a test article in a ground-testing facility. It is important to emphasize that real-gas effects were investigated in the present work under free-stream conditions obtainable in the T5 Hypervelocity Shock Tunnel, and that these conditions do not exactly duplicate flight conditions for reentry vehicles. In particular, the shock tunnel experiments at high enthalpy have partial free-stream dissociation, and have a wall temperature much lower than typically found in flight even for a vehicle with surface cooling. Furthermore, the main real-gas effect observed in the present experiments, of increased separation length at high enthalpy, appears to arise from the combined presence of free-stream dissociation and recombination near a cold wall. It is not entirely clear from the present study how this observation relates, for example, to a flight condition with dissociation downstream of the leading shock but no dissociation in the free stream.

7.4 Recommendations for Future Work

Though much has been accomplished in the present study to elucidate the effects of dissociation and recombination on the phenomenon of shock/boundary-layer interaction, further research in this area is required to extend the present work to regimes not yet considered in depth, and to provide supporting evidence confirming (or disproving) the present results. The following ideas are listed approximately in order of decreasing importance by this author's opinion.

- A mechanism for the experimentally observed increase in separation length at high enthalpy shock tunnel conditions has been proposed, but consistency with the Navier–Stokes equations for flow in thermochemical nonequilibrium could not be proven with the computations undertaken in the present study. Computations of a laminar free shear layer under both frozen-flow and nonequilibrium-flow conditions are required to shed light on how the shear stress on the dividing streamline changes with recombination, and why it does.

- A very limited number of experiments were performed with carbon dioxide test gas, but these were not analyzed in the present study due to time constraints. A nonequilibrium computational code for carbon dioxide is required in order to repeat the methods used for nitrogen flows in the present study. Because carbon dioxide is more easily dissociated than nitrogen, real-gas effects on separation length may be stronger than found for nitrogen. In addition, interesting but unexplained phenomena were found by Adam (1997) for heat transfer in carbon dioxide

flows. All of the data necessary to analyze the carbon dioxide experiments by the methods of the present work are presented in Appendix G.

- The present study did not include experiments at moderate enthalpy which may give nonnegligible dissociation in the flap region while the flow upstream of separation remains at a very low dissociation level. Additional experiments under such a flow condition may be useful to verify external mechanisms for real-gas effects on separation length.

- The present experiments included configurations at zero incidence to obtain high interaction Mach numbers, but these presented difficulties for measuring separation length or heat flux. An experimental study in perfect-gas flow spanning a large range in local interaction Mach number, from supersonic to hypersonic, could be performed by using a double wedge of variable incidence in several different supersonic and hypersonic flow facilities. If the separation length could be measured using a consistent method over the entire Mach number range, then this data could be used to verify the apparent change in the functional dependence of separation length on reattachment pressure ratio, found in previous results, as the Mach number increases from the supersonic to the hypersonic regime.

- The transition Reynolds number for the free-shear layer between separation and reattachment is much lower for the present experiments than has been found for previous experiments in hypersonic perfect-gas flows. There is evidence in the literature that the difference may be due to Mach-number and wall temperature effects, but further work is needed to verify and quantify these phenomena.

- It is clear from critical review of the existing literature that the state-of-the-art in computational techniques cannot consistently predict viscous separation even for nonreacting flow. An exhaustive investigation is needed of grid-convergence issues for these types of computations. It is apparent from the present work that there is difficulty also in predicting the external inviscid flow downstream of reattachment on double-wedge configurations. Though many possibilities were advanced for the cause of this difficulty, additional work is needed to quantify the improvement in accuracy when these are eliminated.

- Further work is required to prove beyond any doubt that driver-gas contamination is not a factor in the present results. A series of driver-gas detection experiments should be performed in T5 under the present high-enthalpy experimental conditions because they are outside the range previously investigated for driver-gas contamination. In addition, a computational code similar to the one used in the present study could be set up to include helium as a third species and used to investigate the effect of contamination on double-wedge flow.

- The test model used in the present experiments was prepared for the installation of thermocouple instrumentation densely packed in the spanwise direction, both upstream of separation and downstream of reattachment. Thus this model could be used to study spanwise variations in heat flux due to three-dimensional instabilities in the concave flow at reattachment, to confirm their existence under particular flow conditions in T5. Especially important is the magnitude of the possible uncertainty that results from taking measurements along a single streamwise array of thermocouples as was done in the present study.

References

ADAM P.H. (1997) *Enthalpy Effects on Hypervelocity Boundary Layers.* Ph.D. thesis, California Institute of Technology.

ANDERS J.B. (1970) Wedge-induced laminar-boundary-layer separation on a flat plate in low-density, hypervelocity flow. NASA TN D-5791.

ANDERS J.B. and EDWARDS C.L.W. (1968) A real-gas study of low-density wedge-induced laminar separation on a highly cooled blunt flat plate at M_∞=12. NASA TN D-4320.

ANDERSON J.D. (1989) *Hypersonic and High Temperature Gas Dynamics.* McGraw-Hill.

ASTM (1993) *Manual on the Use of Thermocouples in Temperature Measurement*, 4th edition.

BALL K.O.W. (1971) Flap span effects on boundary-layer separation. *AIAA Journal*, 9(10):2080–2081.

BALL K.O.W. and KORKEGI R.H. (1968) An investigation of the effect of suction on hypersonic laminar boundary-layer separation. *AIAA Journal*, 6(2):239 243.

BALLARO C.A. and ANDERSON JR. J.D. (1991) Shock strength effects on separated flows in non-equilibrium chemically reacting air shock wave/boundary layer interaction. AIAA Paper 91-0250. (29th Aerospace Sciences Meeting, Jan 7-10, Reno, NV, USA).

BARTLETT E.P., KENDALL R.M., and RINDAL R.A. (1968) An analysis of the coupled chemically reacting boundary layer and charing ablator. Part IV: A unified approximation for mixture transport properties for multicomponent boundary layer applications. NASA CR-1063.

BÉLANGER J. (1990) Description and use of a computer program for unsteady one-dimensional calculations of shock tunnel processes. GALCIT FM 90-3.

BÉLANGER J. (1993) *Studies of Mixing and Combustion in Hypervelocity Flows with Hot Hydrogen Injection.* Ph.D. thesis, California Institute of Technology.

BEVINGTON P.R. (1969) *Data Reduction and Error Analysis for the Physical Sciences.* McGraw-Hill.

BIRCH S.F. and KEYES J.W. (1972) Transition in compressible free shear layers. *Journal of Spacecraft and Rockets*, 9(8):623–624.

BLOTTNER F.G. (1964) Chemical nonequilibrium boundary layer. *AIAA Journal*, 2(2):232 240.

BLOTTNER F.G., JOHNSON M., and ELLIS M. (1971) Chemically reacting viscous flow program for multi-component gas mixtures. Sandia National Laboratories SC-RR-70-754.

BLOY A.W. and GEORGEFF M.P. (1974) The hypersonic laminar boundary layer near sharp compression and expansion corners. *Journal of Fluid Mechanics*, 63(3):431–447.

BRENNER G., GERHOLD T., HANNEMANN K., and RUES D. (1993) Numerical simulation of shock/shock and shock-wave/boundary-layer interactions in hypersonic flows. *Computers and Fluids*, 22:427–439.

BRENNER G. and PRINZ U. (1992) Numerical simulation of chemical and thermal nonequilibrium flows after compression shocks. AIAA Paper 92-2879. (27th Thermophysics Conference, Jul 6-8, Nashville, TN, USA).

BROWN S.N., CHENG H.K., and LEE C.J. (1990) Inviscid-viscous interaction on triple-deck scales in a hypersonic flow with strong wall cooling. *Journal of Fluid Mechanics*, 220:309–337.

BROWN S.N. and STEWARTSON K. (1975) A non-uniqueness of the hypersonic boundary layer. *Quarterly Journal of Mechanics and Applied Mathematics*, 28(1):75 90.

BROWN S.N., STEWARTSON K., and WILLIAMS P.G. (1975) Hypersonic self-induced separation. *The Physics of Fluids*, 18(6):633–639.

BRÜCK S. and HANNEMANN K. (1997) The effect of nozzle-flow disturbances on shock wave/boundary layer interaction. In *Proceedings of the 21st International Symposium on Shock Waves*. Fyshwick, Australia: Panther Publishing and Printing. (Jul 20–25, Great Keppel, Australia).

BURGGRAF O.R. (1975) Asymptotic theory of separation and reattachment of a laminar boundary layer on a compression ramp. In *Flow Separation*. AGARD CP-168.

BURGGRAF O.R., RIZZETTA D., WERLE M.J., and VATSA V.N. (1979) Effect of Reynolds number on laminar separation of a supersonic stream. *AIAA Journal*, 17(4):336–343.

BUSHNELL D.M. and WEINSTEIN L.M. (1968) Correlation of peak heating for reattachment of separated flows. *Journal of Spacecraft and Rockets*, 5(9):1111 1112.

CANDLER G. (1988) *The Computation of Weakly Ionized Hypersonic Flows in Thermo-Chemical Nonequilibrium*. Ph.D. thesis, Stanford University.

CHANETZ B. and COËT M.C. (1993) Shock wave boundary layer interaction analyzed in the R5Ch laminar hypersonic wind tunnel. *La Recherche Aérospatiale*, 5:43–56. (English edition).

CHAPMAN D.R. (1950) Laminar mixing of a compressible fluid. NACA R 958.

CHAPMAN D.R. and KORST H.H. (1957) Theory for base pressures in transonic and supersonic flow. *Journal of Applied Mechanics*, 24:484–485. (correspondence).

CHAPMAN D.R., KUEHN D.M., and LARSON H.K. (1958) Investigation of separated flows in supersonic and subsonic streams with emphasis on the effect of transition. NACA R 1356.

CHAPMAN S. and COWLING T.G. (1939) *The Mathematical Theory of Non-Uniform Gases*. Cambridge University Press.

CHENG H.K. (1993) Perspectives on hypersonic viscous flow research. *Annual Review of Fluid Mechanics*, 25:455–484.

CHUE R.S.M. and ITOH K. (1996) Influence of reflected-shock/boundary-layer interaction on driver-gas contamination in high-enthalpy shock tunnels. In *Proceedings of the 20th International Symposium on Shock Waves*. Singapore: World Scientific. (Jul 1995, Pasadena, CA, USA).

COËT M. and CHANETZ B. (1993) Experiments on shock wave/boundary layer interaction in hypersonic flow. *La Recherche Aérospatiale*, 1:61–74. (English edition).

COËT M. and CHANETZ B. (1994) Sur les effets thermiques dans les interactions onde de choc/couche limite en écoulement hypersonique. *La Recherche Aérospatiale*, 4:251–268.

COHEN C.B. and RESHOTKO E. (1956) Similar solutions for the compressible laminar boundary layer with heat transfer and pressure gradient. NACA R 1293.

COLEMAN G.T. and STOLLERY J.L. (1972) Heat transfer from hypersonic turbulent flow at a wedge compression corner. *Journal of Fluid Mechanics*, 56(4):741–752.

CRANE K.C.A. and STALKER R.J. (1977) Mass-spectrometric analysis of hypersonic flows. *Journal of Physics D: Applied Physics*, 10:679–695.

CRANE L.J. (1957) The laminar and turbulent mixing of jets of compressible fluid. Part II: The mixing of two semi-infinite streams. *Journal of Fluid Mechanics*, 3:81–92.

CROCCO L. and LEES L. (1952) A mixing theory for the interaction between dissipative flows and nearly isentropic streams. *Journal of the Aeronautical Sciences*, 19(10):649–676.

CURLE N. (1961) The effects of heat transfer on laminar-boundary-layer separation in supersonic flow. *The Aeronautical Quarterly*, 12:309–336.

DAVIES L. and BERNSTEIN L. (1969) Heat transfer and transition to turbulence in the shock-induced boundary layer on a semi-infinite flat pate. *Journal of Fluid Mechanics*, 36. part 1.

DAVIES L. and WILSON J.L. (1969) Influence of reflected shock and boundary-layer interaction on shock-tube flows. *The Physics of Fluids*, 12(5, Supplement I):37–43.

DAVIS J. (1996) Further tests on the HALIS axisymmetric configuration in the T5 hypervelocity shock tunnel. GALCIT FM 96-2.

DEBESTRIAN D.J. and ANDERSON JR. J.D. (1993) Reference temperature method and Reynolds analogy for chemically reacting nonequilibrium flowfields. *Journal of Thermophysics*, 8(1):190–192.

DENISON M.R. and BAUM E. (1963) Compressible free shear layer with finite initial thickness. *AIAA Journal*, 1(2):342–349.

DIETER G.E. (1991) *Engineering Design: A Materials and Processing Approach*. McGraw-Hill, 2nd edition.

DORRANCE W.H. (1962) *Viscous Hypersonic Flow*. McGraw-Hill.

DUMITRESCU L.Z., BURTSCHELL Y., and ZEITOUN D. (1996) Throat design for hypersonic nozzles. In *Proceedings of the 20th International Symposium on Shock Waves*. Singapore: World Scientific. (Jul 1995, Pasadena, CA, USA).

EAST R.A., STALKER R.J., and BAIRD J.P. (1980) Measurements of heat transfer to a flat plate in a dissociated high-enthalpy laminar air flow. *Journal of Fluid Mechanics*, 97(4):673–699.

ECKERT E.R.G. (1955) Engineering relations for friction and heat transfer to surfaces in high velocity flow. *Journal of Aeronautical Sciences*, 22(8):585–587.

EDNEY B. (1968) Anomalous heat transfer and pressure distributions on blunt bodies at hypersonic speeds in the presence of an impinging shock. Flygtekniska Försöksanstalten (Aeronautical Research Institute of Sweden) Report 115.

EITELBERG G. and KASTELL D. (1997) Heat transfer in the wake of a planetary probe, measured on a sting. In *Proceedings of the 21st International Symposium on Shock Waves*. Fyshwick, Australia: Panther Publishing and Printing. (Jul 20–25, Great Keppel, Australia).

ELFSTROM G.M. (1972) Turbulent hypersonic flow at a wedge-compression corner. *Journal of Fluid Mechanics*, 53(1):113–127.

FAY J.A. and RIDDELL F.R. (1958) Theory of stagnation point heat transfer in dissociated air. *Journal of the Aeronautical Sciences*, 25(2):73 -85.

FAY J.F. and SAMBAMURTHI J. (1992) Laminar hypersonic flow over a compression corner using the HANA code. AIAA Paper 92-2896. (27th Thermophysics Conference, Jul 6-8, Nashville, TN, USA).

FERGUSON H. and SCHAEFER J.W. (1962) Heat transfer and pressure distribution on cone-cylinder-flare configuration with boundary-layer separation. NASA TN D-1436.

FREEMAN N.C. (1958) Non-equilibrium flow of an ideal dissociating gas. *Journal of Fluid Mechanics*, 4:407–425.

FURUMOTO G.H., ZHONG X., and SKIBA J.C. (1997) Numerical studies of real-gas effects on two-dimensional hypersonic shock-wave/boundary-layer interaction. *Physics of Fluids*, 9(1):191–210.

GADD G.E., HOLDER D.W., and REGAN J.D. (1954) An experimental investigation of the interaction between shock waves and boundary layers. *Proceedings of the Royal Society of London A*, 226:227–253.

GAI S.L., REYNOLDS N.T., ROSS C., and BAIRD J.P. (1989) Measurements of heat transfer in separated high-enthalpy dissociated laminar hypersonic flow behind a step. *Journal of Fluid Mechanics*, 199:541 561.

GATHMANN R.J., SI-AMEUR M., and MATHEY F. (1993) Numerical simulations of three-dimensional natural transition in the compressible confined shear layer. *Physics of Fluids A*, 5(11):2946–2968.

GEORGEFF M.P. (1974) Momentum integral method for viscous-inviscid interactions with arbitrary wall cooling. *AIAA Journal*, 12(10):1393–1400.

GINOUX J.J. (1965) Streamwise vortices in laminar flow. In *Recent Developments in Boundary Layer Research, Part I*, pp. 395–422. AGARDograph no. 97.

GLICK H.S. (1962) Modified Crocco-Lees mixing theory for supersonic separated and reattaching flows. *Journal of the Aeronautical Sciences*, 29(10):1238–1249.

GRASSO F. and LEONE G. (1992) Chemistry effects in shock wave boundary layer interaction problems. In *Proceedings of the IUTAM Symposium on Aerothermochemsitry of Spacecraft and Associated Hypersonic Flows*. Paris: Jouve. (Sep 1–4, Marseille, France).

GRASSO F., LEONE G., and DELERY J.M. (1994) Validation procedure for the analysis of shock-wave/boundary-layer interaction problems. *AIAA Journal*, 32(9):1820–1827.

GRASSO F. and MARINI M. (1996) Analysis of hypersonic shock-wave laminar boundary-layer interaction phenomena. *Computers & Fluids*, 25(6):561–581.

GRIFFITH B.J., MAUS J.R., and BEST J.T. (1983) Explanation of the hypersonic longitudinal stability problem – lessons learned. In *Shuttle Performance: Lessons Learned, Part 1*. NASA CP-2283. (Mar 8–10, Hampton, VA, USA).

GRUMET A., ANDERSON JR. J.D., and LEWIS M.J. (1994) Numerical study of the effects of wall catalysis on shock wave/boundary-layer interaction. *Journal of Thermophysics and Heat Transfer*, 8(1):40–47.

GUPTA R.G., YOS J.M., THOMPSON R.A., and LEE K. (1990) A review of reaction rates and thermodynamic and transport properties for an 11-species air model for chemical and thermal nonequilibrium calculations to 30000 K. NASA RP-1232.

HAKKINEN R.J., GREBER I., TRILLING L., and ABARBANEL S.S. (1959) The interaction of an oblique shock wave with a laminar boundary layer. NASA MEMO 2-18-59W.

HANKEY W.L. and HOLDEN M.S. (1975) Two-dimensional shock wave-boundary layer interactions in high speed flows. AGARD AG-203.

HANNEMANN K., KREK R., and EITELBERG G. (1996) Latest calibration results of the HEG contoured nozzle. In *Proceedings of the 20th International Symposium on Shock Waves*. Singapore: World Scientific. (Jul 1995, Pasadena, CA, USA).

HARVEY W.D. (1968) Experimental investigation of laminar-flow separation on a flat plate induced by deflected trailing-edge flap at Mach 19. NASA TN D-4671.

HAYAKAWA K. and SQUIRE L.C. (1982) The effect of the upstream boundary-layer state on the shock interaction at a compression corner. *Journal of Fluid Mechanics*, 122:369–394.

HAYES W.D. and PROBSTEIN R.F. (1959) *Hypersonic Flow Theory*. Academic Press.

HENCKELS A., KREINS A.F., and MAURER F. (1993) Experimental investigations of hypersonic shock-boundary layer interaction. *Zeitschrift für Flugwissenschaften und Weltraumforschung*, 17:116 124.

HOLDEN M. (1978) A study of flow separation in regions of shock wave-boundary layer interaction in hypersonic flow. AIAA Paper 78-1169. (11th Fluid and Plasma Dynamics Conference, Jul 10-12, Seattle, WA, USA).

HOLDEN M.S. (1966) Experimental studies of separated flows at hypersonic speeds. Part II: Two-dimensional wedge separated flow studies. *AIAA Journal*, 4(5):790–799.

HOLDEN M.S. (1971a) Boundary-layer displacement and leading-edge bluntness effects on attached and separated laminar boundary layers in a compression corner. Part II: Experimental study. *AIAA Journal*, 9(1):84–93.

HOLDEN M.S. (1971b) Establishment time of laminar separated flows. *AIAA Journal*, 9(11):2296–2298.

HOLDEN M.S. (1972) Shock wave-turbulent boundary layer interaction in hypersonic flow. AIAA Paper 72-74. (10th Aerospace Sciences Meeting, Jan 17-19, San Diego, CA, USA).

HOLDEN M.S. and MOSELLE J.R. (1968) Theoretical and experimental studies of the shock wave-boundary layer interaction on compression surfaces in hypersonic flow. Aerospace Research Laboratories, USAF-OAR ARL-70-0002.

HOLLIS B.R. (1995) User's manual for the one-dimensional hypersonic experimental aerothermodynamic (1DHEAT) data reduction code. NASA CR-4691.

HORNUNG H. (1992) Performance data of the new free-piston shock tunnel at GALCIT. AIAA Paper 92-3943. (17th Aerospace Ground Testing Conference, Jul 6–8, Nashville, TN, USA).

HORNUNG H. and BÉLANGER J. (1990) Role and techniques of ground testing for simulation of flows up to orbital speed. AIAA Paper 90-1377. (16th Aerodynamic Ground Testing Conference, Jun 18–20, Seattle, WA, USA).

HORNUNG H., STURTEVANT B., BÉLANGER J., SANDERSON S., and BROUILLETTE M. (1991) Performance data of the new free-piston shock tunnel T5 at GALCIT. In *Proceedings of the 18th International Symposium on Shock Waves*. Springer-Verlag. (Jul 1991, Sendai, Japan).

HORNUNG H.G. (1995) Ae234 class notes (hypersonic aerodynamics). California Institute of Technology.

HUNG C.M. and MACCORMACK R.W. (1976) Numerical solutions of supersonic and hypersonic laminar compression corner flows. *AIAA Journal*, 14(4):475–481.

HUNG F.T. and BARNETT D.O. (1973) Shock-wave/boundary-layer interference heating analysis. AIAA Paper 73-237. (11th Aerospace Sciences Meeting, Jan 10-12, Washington, D.C., USA).

HUNTER JR. L.G. and REEVES B.L. (1971) Results of a strong interaction, wake-like model of supersonic separated and reattaching turbulent flows. *AIAA Journal*, 9(4):703–712.

IGARASHI S., HONDA M., and ONODERA K. (1988) Analysis of interactions between shock waves and laminar boundary layers with heat transfer. *Acta Mechanica*, 73:221–230.

IKAWA H. (1977) A re-entry control effectiveness methodology for the space shuttle orbiter. *Journal of Spacecraft and Rockets*, 14(11):669–675.

IKAWA H. (1979) Real gas laminar boundary layer separation methodology as applied to orbiter control surface effectiveness prediction. AIAA Paper 79-0212. (17th Aerospace Sciences Meeting, Jan 15-17, New Orleans, LA, USA).

ILLINGWORTH C.R. (1949) Steady flow in the laminar boundary layer of a gas. *Proceedings of the Royal Society of London A*, 199:533–558.

INGER G.R. (1964) Highly nonequilibrium boundary-layer flows of a multicomponent dissociated gas mixture. *International Journal of Heat and Mass Transfer*, 7:1151–1174.

INGER G.R. (1994a) Scaling of incipient separation in high speed laminar flows. *Aeronautical Journal*, 98:178–181.

INGER G.R. (1994b) Scaling of incipient separation in supersonic/transonic speed laminar flows. *AIAA Journal*, 33(1):227–231.

INGER G.R. (1995a) Non-equilibrium boundary layer effects on the aerodynamic heating of hypersonic vehicles. *Acta Astronautica*, 36(4):205–216.

INGER G.R. (1995b) Nonequilibrium boundary-layer effects on the aerodynamic heating of hypersonic waverider vehicles. *Journal of Thermophysics and Heat Transfer*, 9(4):595–604.

INGER G.R. (1996) A theory of local heat transfer in shock/laminar boundary layer interactions. AIAA Paper 96-2003. (27th Fluid Dynamics Conference, Jun 17–20, New Orleans, LA, USA).

INGER G.R. (1997) Shock/boundary layer interaction effects on heating in nonequilibrium-dissociated flow along arbitrarily-catalytic surfaces. In *Proceedings of the 21st International Symposium on Shock Waves*. Fyshwick, Australia: Panther Publishing and Printing. (Jul 20–25, Great Keppel, Australia).

INGER G.R. and ELDER J. (1991) Recombination-dominated nonequilibrium heat transfer to arbitrarily catalytic hypersonic vehicles. *Journal of Thermophysics*, 5(4):449–455.

JESSEN C., VETTER M., and GRÖNIG H. (1993) Experimental studies in the Aachen hypersonic shock tunnel. *Zeitschrift für Flugwissenschaften und Weltraumforschung*, 17:73–81.

JOHNSON C.B. (1968) Pressure and flow-field study at Mach number 8 of flow separation on a flat plate with deflected trailing-edge flap. NASA TN D-4308.

KATZER E. (1989) On the lengthscales of laminar shock/boundary-layer interaction. *Journal of Fluid Mechanics*, 206:477–496.

KENDALL D.N., DIXON W.P., and SCHULTE E.H. (1967) Semiconductor surface thermocouples for determining heat-transfer rates. *IEEE Transactions on Aerospace and Electronic Systems*, AES-3(4):596–603.

KENNEDY C.A. and GATSKI T.B. (1994) Self-similar supersonic variable-density shear layers in binary systems. *Physics of Fluids*, 6(2):662–673.

KERIMBEKOV R.M., RUBAN A.I., and WALKER J.D.A. (1994) Hypersonic boundary-layer separation on a cold wall. *Journal of Fluid Mechanics*, 274:163–195.

KING R.A., CREEL T. R. J., and BUSHNELL D.M. (1991) Experimental transition investigation of a free-shear layer above a cavity at Mach 3.5. *Journal of Propulsion and Power*, 7(4):626–634.

KLINEBERG J.M. and LEES L. (1969) Theory of laminar viscous-inviscid interactions in supersonic flow. *AIAA Journal*, 7(12):2211–2221.

KORDULLA W., RIEDELBAUCH S., BRENNER G., and PRINZ U. (1992) Hypersonic viscous flow simulations. *Fluid Dynamics Research*, 10:451–468.

KORNILOV V.I. (1997) Correlation of the separation length in shock wave/channel boundary layer interaction. *Experiments in Fluids*, 23(6):489–497.

KORST H.H. (1956) A theory for base pressures in transonic and supersonic flow. *Journal of Applied Mechanics*, 23:593–600.

KREK R., BECK W., and EITELBERG G. (1996) Hyperboloid flare experiments in the HEG. In *Proceedings of the 20th International Symposium on Shock Waves*. Singapore: World Scientific. (Jul 1995, Pasadena, CA, USA).

KUMAR D. (1995) *Hypersonic Control Effectiveness*. Ph.D. thesis, Cranfield University.

KUMAR D. and STOLLERY J.L. (1994) Hypersonic control flap effectiveness. ICAS 94-4.4.3. (19th ICAS Congress).

KUMAR D. and STOLLERY J.L. (1996) The effects of shear layer transition and leading edge bluntness on control flap effectiveness. In *Proceedings of the 20th International Symposium on Shock Waves*. Singapore: World Scientific. (Jul 1995, Pasadena, CA, USA).

LARSON H.K. and KEATING JR S.J. (1960) Transition Reynolds numbers of separated flows at supersonic speeds. NASA TN-D-349.

LEE J.Y. and LEWIS M.J. (1993) Numerical study of the flow establishment time in hypersonic shock tunnels. *Journal of Spacecraft and Rockets*, 30(2):152–163.

LEES L. (1956) Laminar heat transfer over blunt-nosed bodies at hypersonic flight speeds. *Jet Propulsion*, 26(4):259–269.

LEES L. and REEVES B.L. (1964) Supersonic separated and reattaching laminar flows: I. general theory and application to adiabatic boundary-layer/shock-wave interactions. *AIAA Journal*, 2(11):1907–1920.

LEWIS J.E., KUBOTA T., and LEES L. (1968) Experimental investigation of supersonic laminar, two-dimensional boundary-layer separation in a compression corner with and without cooling. *AIAA Journal*, 6(1):7–14.

LEYLAND P. (1996) Shock-wave/boundary layer interactions at hypersonic speed by an implicit Navier-Stokes solver. *Computational Fluid Dynamics*, 6:71–87.

LI T. and NAGAMATSU H.T. (1955) Similar solutions of compressible boundary-layer equations. *Journal of the Aeronautical Sciences*, 22:607–616.

LIGHTHILL M.J. (1953) On boundary layers and upstream influence. II. Supersonic flows without separation. *Proceedings of the Royal Society of London A*, 217:478–507.

LIGHTHILL M.J. (1957) Dynamics of a dissociating gas. Part I. *Journal of Fluid Mechanics*, 2:1–32.

MACCORMACK R.W. and CANDLER G.V. (1989) The solution of the Navier-Stokes equations using Gauss-Seidel line relaxation. *Computers and Fluids*, 17(1):135–150.

MALLINSON S.G. (1994) *Shock Wave/Boundary Layer Interaction at a Compression Corner*. Ph.D. thesis, The University of New South Whales.

MALLINSON S.G., GAI S.L., and MUDFORD N.R. (1995) High enthalpy, hypersonic compression corner flow. AIAA Paper 95-0155. (33rd Aerospace Sciences Meeting and Exhibit, Jan 9-12, Reno, NV, USA).

MALLINSON S.G., GAI S.L., and MUDFORD N.R. (1996a) The boundary layer on a flat plate in hypervelocity flow. *Aeronautical Journal*, 100(994):135–141.

MALLINSON S.G., GAI S.L., and MUDFORD N.R. (1996b) Upstream influence and peak heating in hypervelocity shock wave/boundary-layer interaction. *Journal of Propulsion and Power*, 12(5):984–990.

MALLINSON S.G., GAI S.L., and MUDFORD N.R. (1997a) Establishment of steady separated flow over a compression-corner in a free-piston shock tunnel. *Shock Waves*, 7:249–253.

MALLINSON S.G., GAI S.L., and MUDFORD N.R. (1997b) The interaction of a shock wave with a laminar boundary layer at a compression corner in high-enthalpy flows including real gas effects. *Journal of Fluid Mechanics*, 342:1–35.

MARK H. (1958) The interaction of a reflected shock wave with the boundary layer in a shock tube. NACA TM-1418.

MAUS J.R., GRIFFITH B.J., and SZEMA K.Y. (1984) Hypersonic Mach number and real gas effects on space shuttle orbiter aerodynamics. *Journal of Spacecraft and Rockets*, 21(2):136 141.

MCDONALD H. (1964) Turbulent shear layer re-attachment with special emphasis on the base pressure problem. *The Aeronautical Quarterly*, 15:247–280.

MCDONALD H. (1965) A study of the turbulent separated-flow region occurring at a compression corner in supersonic flow. *Journal of Fluid Mechanics*, 22:481–505.

MCINTOSH M.K. (1979) A computer program for the numerical calculation of equilibrium and perfect gas conditions in shock tunnels. Australian Defence Scientific Service Technical Note CPD 169.

MILLER D.S., HIJMAN R., and CHILDS M.E. (1964) Mach 8 to 22 studies of flow separations due to deflected control surfaces. *AIAA Journal*, 2(2):312–321.

MILLIKAN R.C. and WHITE D.R. (1963) Systematics of vibrational relaxation. *Journal of Chemical Physics*, 39:3209–3213.

MILLS R.D. (1968) Numerical and experimental investigations of the shear layer between two parallel streams. *Journal of Fluid Mechanics*, 33:591–616.

MOORE L.L. (1952) A solution of the laminar boundary-layer equations for a compressible fluid with variable properties, including dissociation. *Journal of the Aeronautical Sciences*, 19(8):505–518.

NASH J.F. (1963) An analysis of two-dimensional base flow including the effect of the approaching boundary layer. Aeronautical Research Council R&M No. 3344.

NEEDHAM D.A. (1965) *Laminar Separation in Hypersonic Flow*. Ph.D. thesis, University of London.

NEEDHAM D.A. and STOLLERY J.L. (1966a) Boundary layer separation in hypersonic flow. AIAA Paper 66-455. (4th Aerospace Sciences Meeting, Jun 27-29, Los Angeles, CA, USA).

NEEDHAM D.A. and STOLLERY J.L. (1966b) Hypersonic studies of incipient separation and separated flows. In *Separated Flows, Part I*. AGARD CP-4.

NEILAND V.Y. (1971a) The asymptotic theory of the interaction of a supersonic flow with a boundary layer. *Fluid Dynamics*, 4:41–47. (English translation of *Izvestiya Akademii Nauk SSSR, Mekhanika Zhidkosti i Gaza*).

NEILAND V.Y. (1971b) Flow behind the boundary layer separation point in a supersonic stream. *Fluid Dynamics*, 3:19–25. (English translation of *Izvestiya Akademii Nauk SSSR, Mekhanika Zhidkosti i Gaza*).

NIELSEN J.N., GOODWIN F.K., and KUHN G.D. (1970) Review of the method of integral relations applied to viscous interaction problems including separation. In *Viscous Interaction Phenomena in Supersonic and Hypersonic Flow*. University of Dayton Press. (May 7–8, 1969, Wright-Patterson Air Force Base, OH, USA).

OLEJNICZAK J. (1997) *Computational and Experimental Study of Nonequilibrium Chemistry in Hypersonic Flows*. Ph.D. thesis, University of Minnesota.

OLEJNICZAK J. and CANDLER G.V. (1996) Numerical study of shock interactions on double-wedge geometries. AIAA Paper 96-0041. (34th Aerospace Sciences Meeting, Jan 15–18, Reno, NV, USA).

OLEJNICZAK J., WRIGHT M.J., and CANDLER G.V. (1997) Numerical study of inviscid shock interactions on double-wedge geometries. *Journal of Fluid Mechanics*, 352:1–25.

OSWALD J., DEMARGNE A., and BOUSQET J. (1995) Hypersonic laminar computations of separated flows with account of real gas effects. AIAA Paper 95-2271. (26th Fluid Dynamics Conference, Jun 19-22, San Diego, CA, USA).

OTT J.D. and ANDERSON JR. J.D. (1993) Effects of nonequilibrium chemistry on the reference temperature method and Reynolds analogy. *Journal of Thermophysics*, 8(2):381–384.

PARK C. (1988a) Assessment of a two-temperature model for dissociating and weakly ionizing nitrogen. *Journal of Thermophysics and Heat Transfer*, 2(1):8–16.

PARK C. (1988b) Two-temperature interpretation of of dissociation rate data for N_2 and O_2. AIAA Paper 88-0458.

POWER G.D. and BARBER T.J. (1988) Analysis of complex hypersonic flows with strong viscous/inviscid interaction. *AIAA Journal*, 26(7):832–840.

PRESS W.H., TEUKOLSKY S.A., VETTERLING W.T., and FLANNERY B.P. (1992) *Numerical Recipes in FORTRAN: The Art of Scientific Computing*. Cambridge University Press, 2nd edition.

RAE W.J. (1963) A solution for the nonequilibrium flat-plate boundary layer. *AIAA Journal*, 1(10):2279–2288.

RAMAKRISHNAN R., THORNTON E.A., and WIETING A.R. (1991) Adaptive finite element analysis of hypersonic laminar flows for aerothermal load predictions. *Journal of Thermophysics*, 5(3):308-317.

RAYNER J.P. (1973) *Boundary Layer Separation and Thermal Choking*. Ph.D. thesis, Australian National University.

REIN M. (1989) SURF: a program for calculating inviscid supersonic reacting flows in nozzles. GALCIT FM 89-1.

REIN M. (1991) Partial chemical equilibrium: Theory and implementation in the program surf. GALCIT FM 91-1.

RIZZETTA D. and MACH K. (1989) Comparative numerical study of hypersonic compression ramp flows. AIAA Paper 89-1877. (20th Fluid Dynamics Conference, Jun 12-14, Buffalo, NY, USA).

RIZZETTA D.P. (1979) Asymptotic solutions of the energy equation for viscous supersonic flow past corners. *The Physics of Fluids*, 22(2):218–223.

RIZZETTA D.P., BURGGRAF O.R., and JENSON R. (1978) Triple-deck solutions for viscous supersonic and hypersonic flow past corners. *Journal of Fluid Mechanics*, 89(3):535–552.

ROGERS D.F. (1992) *Laminar Flow Analysis*. Cambridge University Press.

ROSHKO A. (1995) Free shear layers, base pressure and bluff-body drag. In *Symposium on Developments in Fluid Dynamics and Aerospace Engineering*. Bangalore: Interline. (Dec 9–10, 1993, Bangalore, India).

ROSHKO A. and THOMKE G.J. (1970) Supersonic, turbulent boundary-layer interaction with a compression corner at very high Reynolds number. In *Viscous Interaction Phenomena in Supersonic and Hypersonic Flow*. University of Dayton Press. (May 7–8, 1969, Wright-Patterson Air Force Base, OH, USA).

ROSHKO A. and THOMKE G.J. (1976) Flare-induced interaction lengths in supersonic, turbulent boundary layers. *AIAA Journal*, 14(7):873–879.

ROUSSET B. (1995) *Calibration and Study of the Contoured Nozzle of the T5 Free-Piston Hypervelocity Shock Tunnel*. Engineer's degree thesis, California Institute of Technology.

RUDY D.H., THOMAS J.L., KUMAR A., and GNOFFO P.A. (1989) Computation of laminar hypersonic compression-corner flows. *AIAA Journal*, 29(7):1108–1113.

SANDERSON S.R. (1995) *Shock Wave Interaction in Hypervelocity Flow*. Ph.D. thesis, California Institute of Technology.

SCHULTZ D.L. and JONES T.V. (1973) Heat-transfer measurements in short-duration hypersonic facilities. AGARD AG-165.

SETTLES G.S. and BOGDONOFF S.M. (1982) Scaling of two- and three- dimensional shock/turbulent boundary-layer interactions at compression corners. *AIAA Journal*, 20(6):782–789.

SETTLES G.S., FITZPATRICK T.J., and BOGDONOFF S.M. (1979) Detailed study of attached and separated compression corner flowfields in high Reynolds number supersonic flow. *AIAA Journal*, 17(6):579–585.

SIMEONIDES G. and HAASE W. (1995) Experimental and computational investigations of hypersonic flow about compression ramps. *Journal of Fluid Mechanics*, 283:17 -42.

SIMEONIDES G., HAASE W., and MANN M. (1994) Experimental, analytical, and computational methods applied to hypersonic compression ramp flows. *AIAA J*, 32(2):301–310.

SMITH F.T. (1988) A reversed-flow singularity in interacting boundary layers. *Proceedings of the Royal Society of London A*, 420:21–52.

SMITH F.T. and FARID KHORRAMI A. (1991) The interactive breakdown in supersonic ramp flow. *Journal of Fluid Mechanics*, 224:197–215.

SPENCE D.A. (1960) A note on the recovery and Reynolds-analogy factors in laminar flat-plate flow. *Journal of the Aerospace Sciences*, 27:878–879.

STACEY C.H.B. and SIMMONS J.M. (1992) Measurement of shock-wave/boundary-layer interaction in a free-piston shock tunnel. *AIAA Journal*, 30(8):2095–2098.

STALKER R.J. (1967) A study of the free-piston shock tunnel. *AIAA Journal*, 5(12):2160-2165.

STEWARTSON K. (1964) *The Theory of Laminar Boundary Layers in Compressible Fluids*. Oxford University Press.

STEWARTSON K. (1974) Multistructured boundary layers on flat plates and related bodies. *Advances in Applied Mechanics*, 14:145–239.

STEWARTSON K. and WILLIAMS P.G. (1969) Self-induced separation. *Proceedings of the Royal Society of London A*, 312:181–206.

STEWARTSON K. and WILLIAMS P.G. (1973) On self-induced separation II. *Mathematika*, 20:98–108.

SUDANI N. and HORNUNG H.G. (1997) Detection and reduction of driver gas contamination in a high-enthalpy shock tunnel. In *Proceedings of the 21st International Symposium on Shock Waves*. Fyshwick, Australia: Panther Publishing and Printing. (Jul 20–25, Great Keppel, Australia).

SUDANI N. and HORNUNG H.G. (1998) Gasdynamical detectors of driver gas contamination in a high-enthalpy shock tunnel. *AIAA Journal*, 36(3):313–319.

SUDANI N., VALIFERDOWSI B., and HORNUNG H.G. (1998) Test time increase by delaying driver gas contamination for reflected shock tunnels. AIAA Paper 98-2771. (20th Advanced Measurement and Ground Testing Technology Conference, Jun 15–18, Albuquerque, NM, USA).

SUNDQVIST B. (1992) Thermal diffusivity and thermal conductivity of chromel, alumel, and constantan in the range 100–450 K. *Journal of Applied Physics*, 72(2):539–545.

SYCHEV V.V. (1982) Asymptotic theory of separation flows. *Fluid Dynamics*, 17(2):179–188. (English translation of *Izvestiya Akademii Nauk SSSR, Mekhanika Zhidkosti i Gaza*).

THOMAS J.L. (1992) An implicit multigrid scheme for hypersonic strong-interaction flowfields. *Communications in Applied Numerical Methods*, 8:683–693.

TODISCO A. and REEVES B.L. (1970) Turbulent boundary layer separation and reattachment at supersonic and hypersonic speeds. In *Viscous Interaction Phenomena in Supersonic and Hypersonic Flow*. University of Dayton Press. (May 7–8, 1969, Wright-Patterson Air Force Base, OH, USA).

VAN DRIEST E.R. (1947) Investigation of laminar boundary layer in compressible fluids using the Crocco method. NACA TN 2597.

VAN DRIEST E.R. (1959) Convective heat transfer in gases. In *Turbulent Flows and Heat-Transfer* (editor C.C. Lin), volume 5 of *High Speed Aerodynamics and Jet Propulsion*. Princeton University Press.

VINCENTI W.G. and KRUGER C.H. (1965) *Introduction to Physical Gas Dynamics*. Krieger Publishing.

WEILMUENSTER K.J., GNOFFO P.A., and GREENE F.A. (1994) Navier–Stokes simulations of orbiter aerodynamic characteristics including pitch trim and bodyflap. *Journal of Spacecraft and Rockets*, 31(3):355–366.

WERLE M.J. and VATSA V.N. (1974) New method for supersonic boundary-layer separations. *AIAA Journal*, 12(11):1491–1497.

WHITE F.M. (1991) *Viscous Fluid Flow*. McGraw-Hill, 2nd edition.

WHITE F.M. and CHRISTOPH G.H. (1972) A simple theory for the two-dimensional compressible turbulent boundary layer. *Journal of Basic Engineering*, 94:636–642.

WILKE C.R. (1950) A viscosity equation for gas mixtures. *Journal of Chemical Physics*, 18(4):517–519.

WOODS W.C., ARRINGTON J.P., and HAMILTON II H.H. (1983) A review of preflight estimates of real-gas effects on space shuttle aerodynamic characteristics. In *Shuttle Performance: Lessons Learned, Part 1*. NASA CP-2283. (Mar 8–10, Langley, VA, USA).

Appendix A Drawings of Test Model

In Figure A.1 is pictured a three-dimensional view of the assembled test model, including new support hardware which was created for the present study. On the following pages are reproduced a few of the original engineering drawings used to build this model. There are three sub-assemblies;

1. front plate enclosure,
2. rear flap enclosure, and
3. support structure.

Assembly drawings are given for each sub-assembly, but detailed, dimensioned drawings are only given for the three parts which are wetted by the test flow of interest;

1. leading edge,
2. front instrument plate, and
3. rear instrument plate.

The drawings have been scaled to 75% of their original size, and any written scale is affected accordingly. All dimensions are in inches.

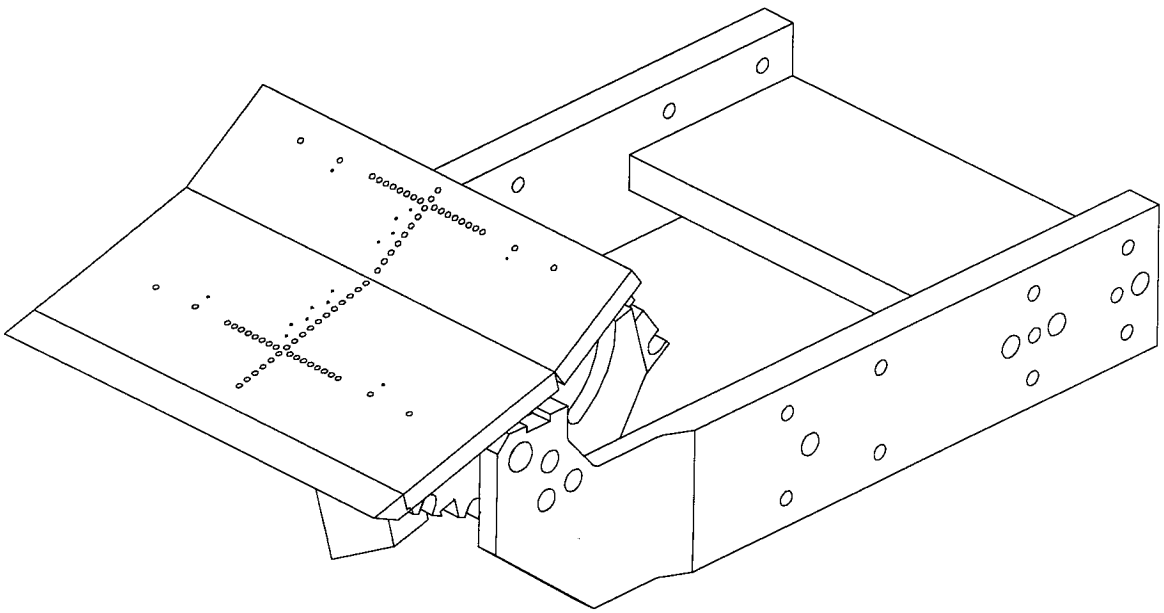

Figure A.1: Assembly drawing of test model with new support structure.

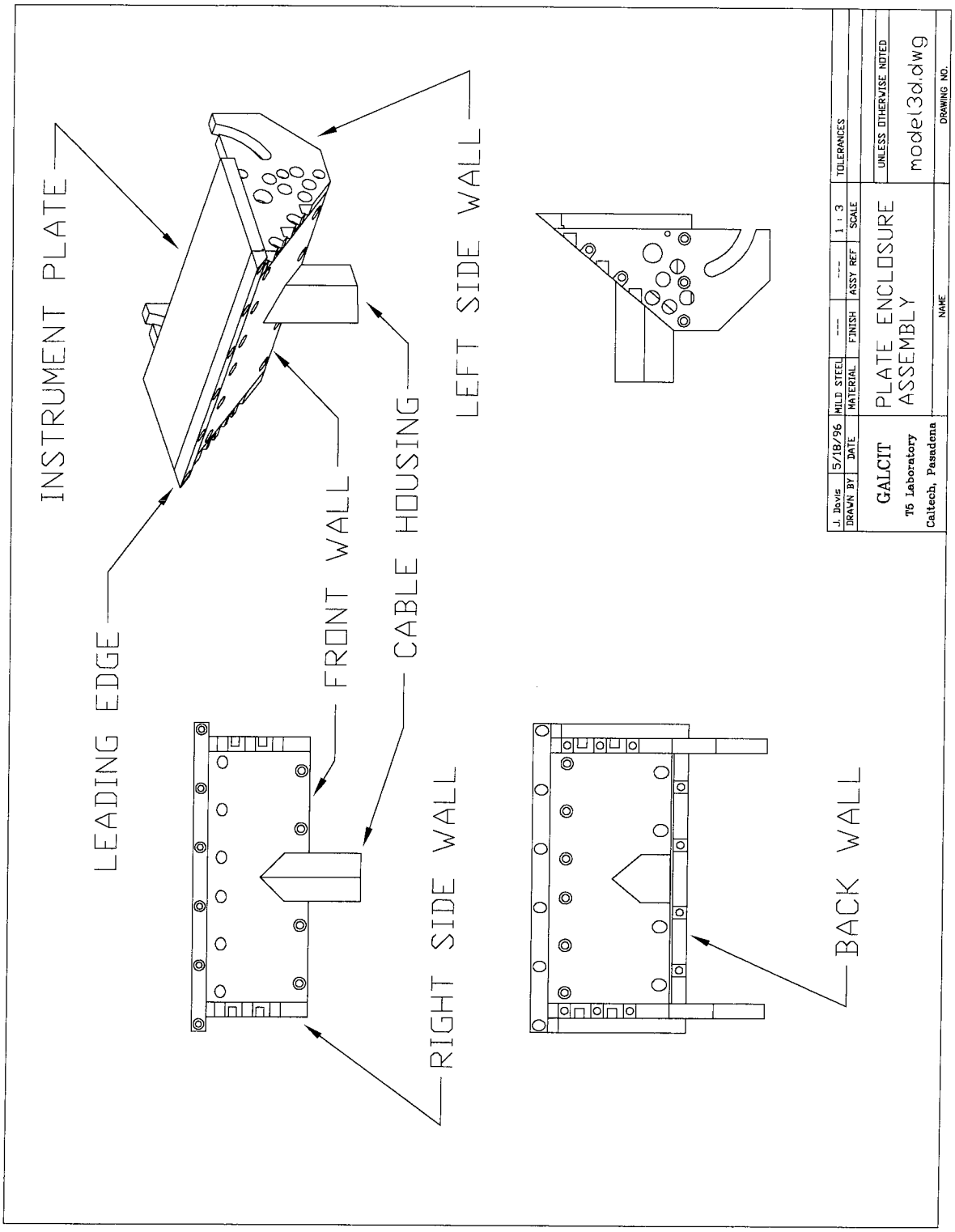
INSTRUMENT PLATE
LEADING EDGE
FRONT WALL
CABLE HOUSING
LEFT SIDE WALL
RIGHT SIDE WALL
BACK WALL
J. Davis
DRAWN BY
5/18/96
DATE
MILD STEEL
MATERIAL

FINISH

ASSY REF
1 : 3
SCALE
TOLERANCES
UNLESS OTHERWISE NOTED
GALCIT
76 Laboratory
Caltech, Pasadena
PLATE ENCLOSURE ASSEMBLY
model3d.dwg
NAME
DRAWING NO.

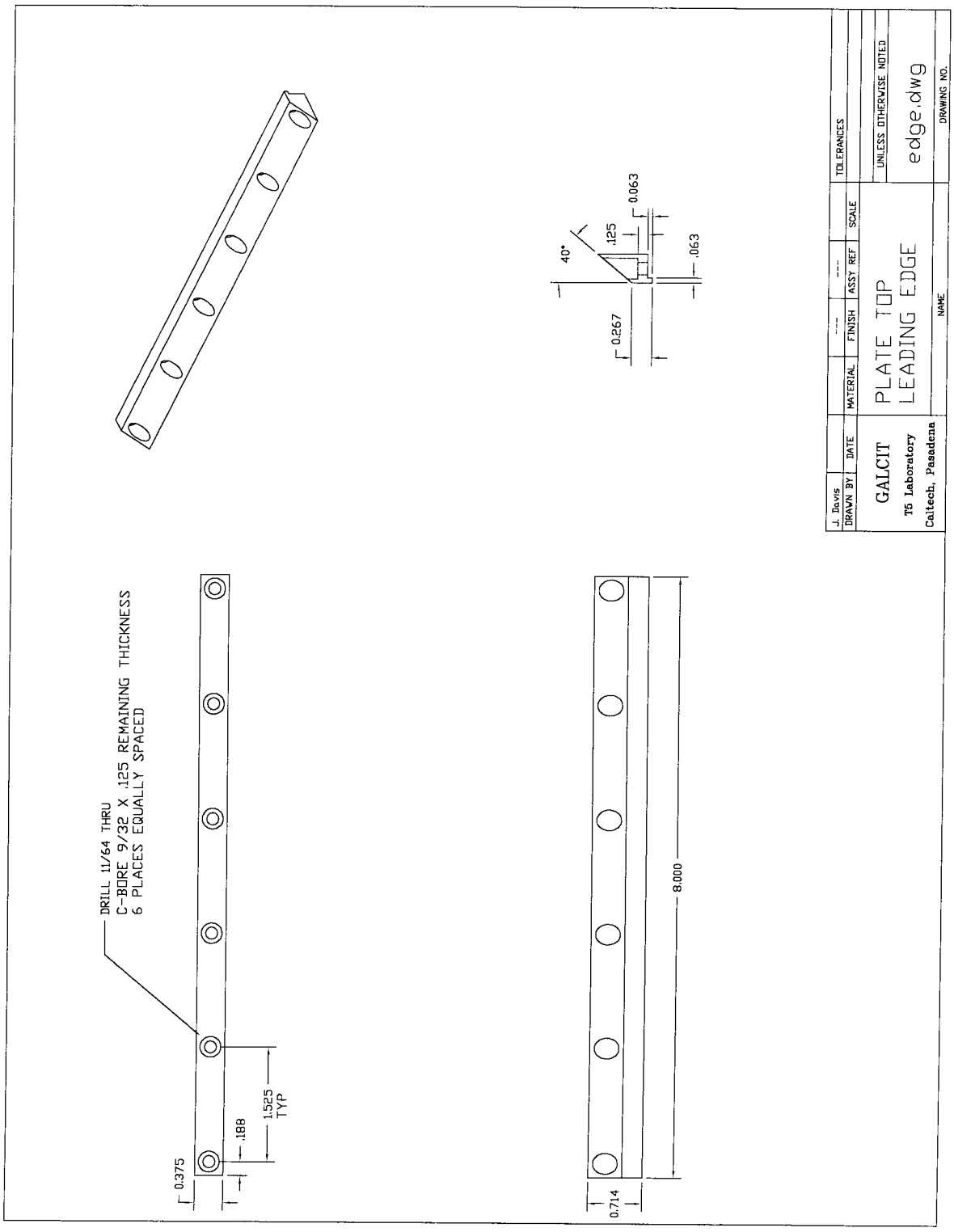
DRILL 11/64 THRU
C-BORE 9/32 X .125 REMAINING THICKNESS
6 PLACES EQUALLY SPACED
0.375
.188
1.525
TYP
0.714
8.000
40°
.125
0.063
0.267
.063
J. Davis
DRAWN BY
DATE
MATERIAL
FINISH
ASSY REF
SCALE
TOLERANCES
UNLESS OTHERWISE NOTED
GALCIT
T5 Laboratory
Caltech, Pasadena
PLATE TOP
LEADING EDGE
NAME
edge.dwg
DRAWING NO.

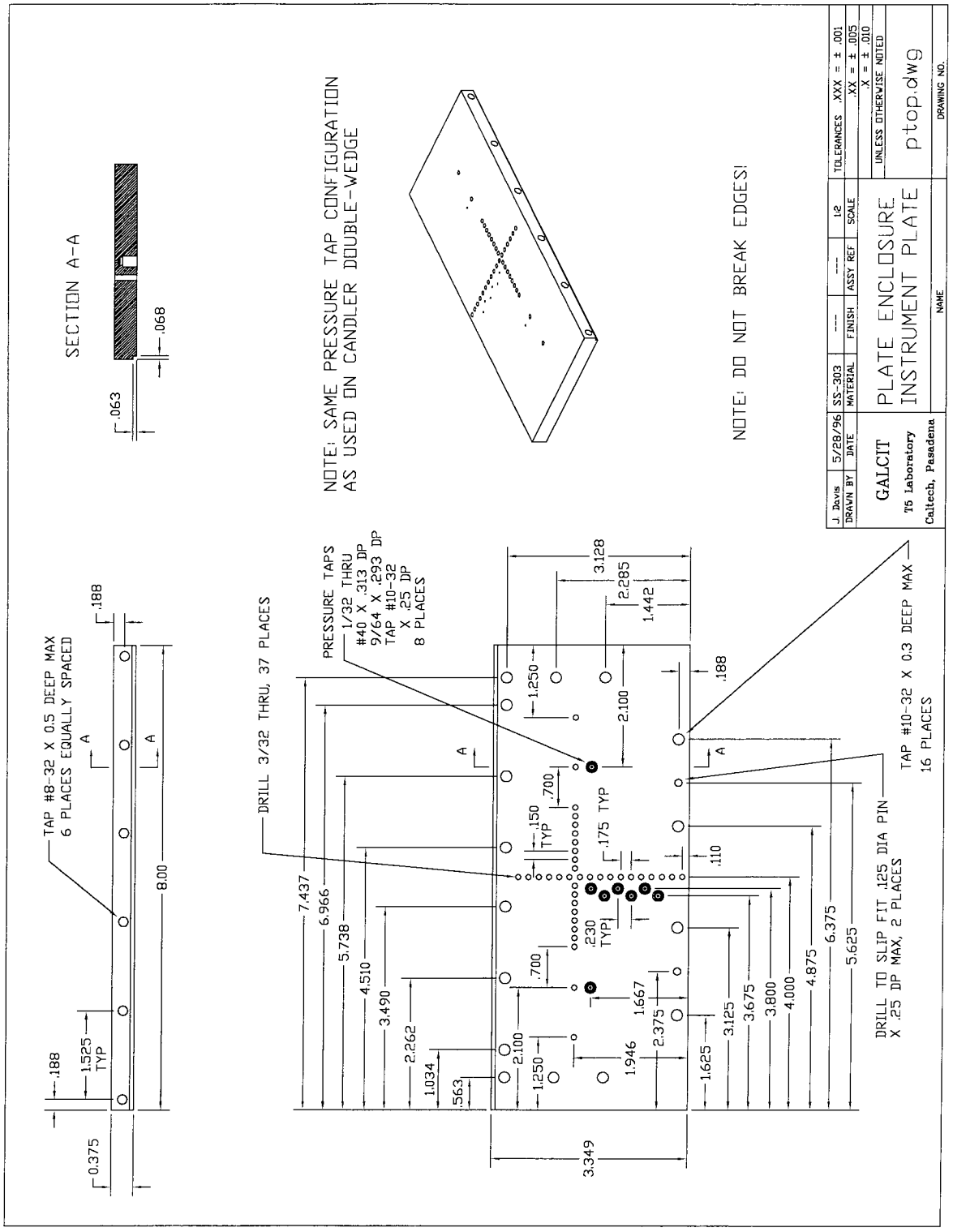
SECTION A-A
.063
.068
NOTE: SAME PRESSURE TAP CONFIGURATION
AS USED ON CANDLER DOUBLE-WEDGE
NOTE: DO NOT BREAK EDGES!
TAP #8-32 X 0.5 DEEP MAX
6 PLACES EQUALLY SPACED
.188
1.525
TYP
0.375
8.00
DRILL 3/32 THRU, 37 PLACES
PRESSURE TAPS
1/32 THRU
#40 X .313 DP
9/64 X .293 DP
TAP #10-32
X .25 DP
8 PLACES
7.437
6.966
5.738
4.510
3.490
2.262
1.034
.563
2.100
1.250
.700
.150
TYP
.175 TYP
.230
TYP
1.946
1.667
2.375
1.625
3.125
3.675
3.800
4.000
4.875
6.375
5.625
3.349
3.128
2.285
1.442
1.250
2.100
.188
.110
DRILL TO SLIP FIT .125 DIA PIN
X .25 DP MAX, 2 PLACES
TAP #10-32 X 0.3 DEEP MAX
16 PLACES
J Davis
DRAWN BY
5/28/96
DATE
SS-303
MATERIAL

FINISH

ASSY REF
12
SCALE
TOLERANCES .XXX = ± .001
.XX = ± .005
.X = ± .010
UNLESS OTHERWISE NOTED
GALCIT
T5 Laboratory
Caltech, Pasadena
PLATE ENCLOSURE
INSTRUMENT PLATE
NAME
ptop.dwg
DRAWING NO.

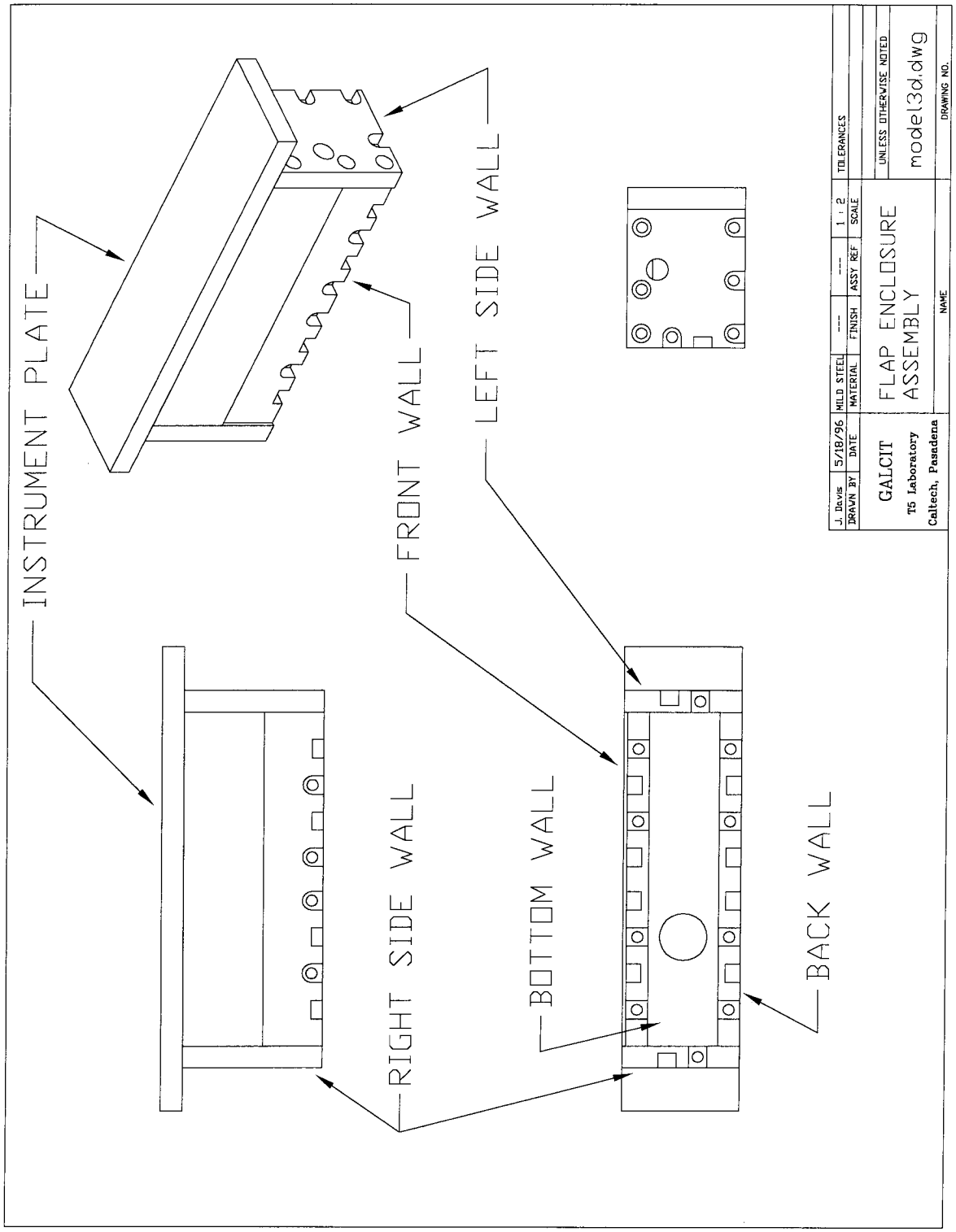
INSTRUMENT PLATE
FRONT WALL
LEFT SIDE WALL
RIGHT SIDE WALL
BOTTOM WALL
BACK WALL
J. Davis
DRAWN BY
5/18/96
DATE
MILD STEEL
MATERIAL

FINISH

ASSY REF
1 : 2
SCALE
TOLERANCES
UNLESS OTHERWISE NOTED
GALCIT
T5 Laboratory
Caltech, Pasadena
FLAP ENCLOSURE ASSEMBLY
NAME
model3d.dwg
DRAWING NO.

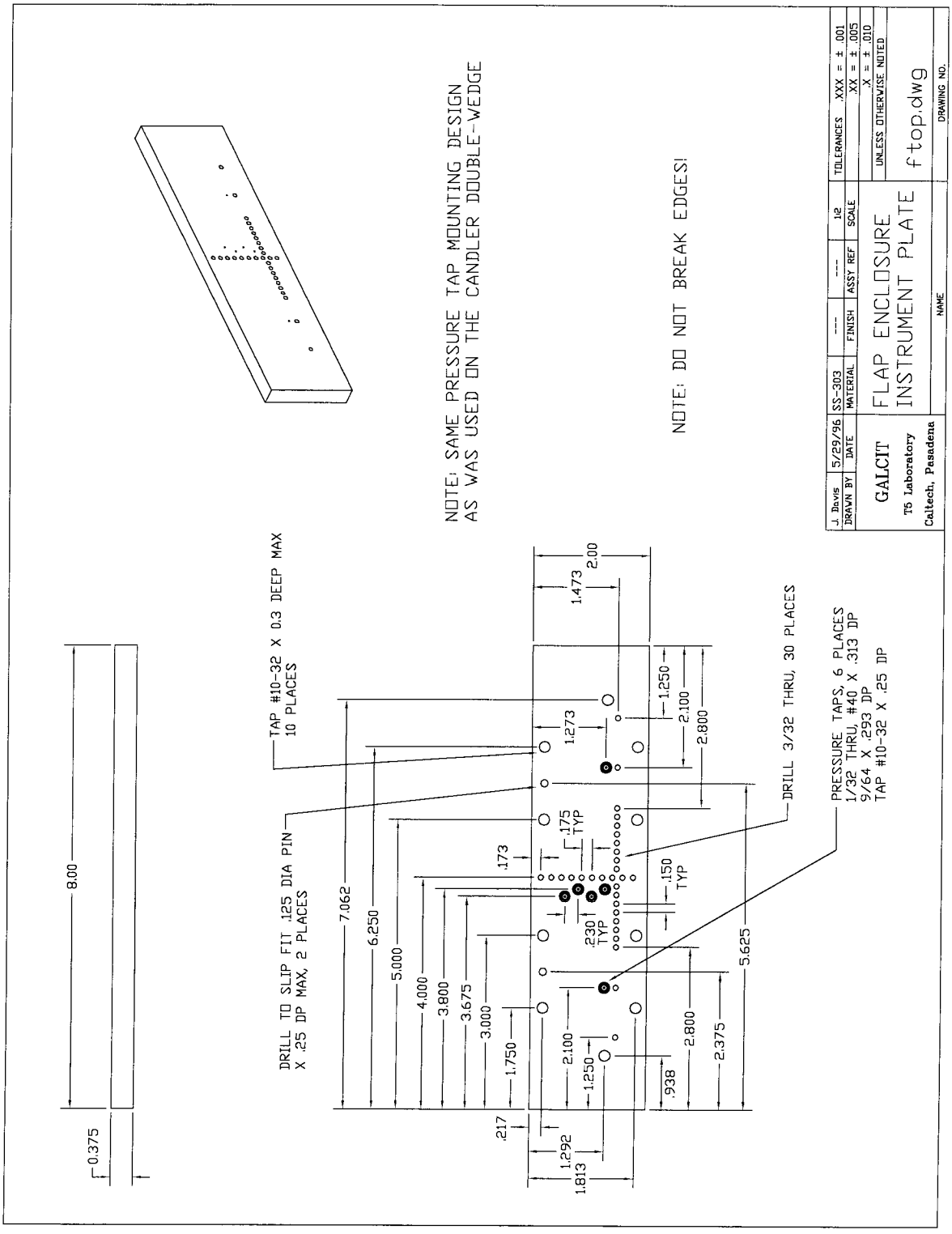
NOTE: SAME PRESSURE TAP MOUNTING DESIGN
AS WAS USED ON THE CANDLER DOUBLE-WEDGE
NOTE: DO NOT BREAK EDGES!
TAP #10-32 X 0.3 DEEP MAX
10 PLACES
DRILL TO SLIP FIT .125 DIA PIN
X .25 DP MAX, 2 PLACES
DRILL 3/32 THRU, 30 PLACES
PRESSURE TAPS, 6 PLACES
1/32 THRU, #40 X .313 DP
9/64 X .293 DP
TAP #10-32 X .25 DP
8.00
0.375
7.062
6.250
5.000
4.000
3.800
3.675
3.000
1.750
2.100
1.250
.938
2.800
2.375
5.625
.217
1.292
1.813
.173
.175 TYP
.230 TYP
.150 TYP
1.273
1.473
2.00
1.250
2.100
2.800
J. Davis
DRAWN BY
5/29/96
DATE
SS-303
MATERIAL

FINISH

ASSY REF
12
SCALE
TOLERANCES
.XXX = ± .001
.XX = ± .005
.X = ± .010
UNLESS OTHERWISE NOTED
GALCIT
T5 Laboratory
Caltech, Pasadena
FLAP ENCLOSURE
INSTRUMENT PLATE
NAME
ftop.dwg
DRAWING NO.

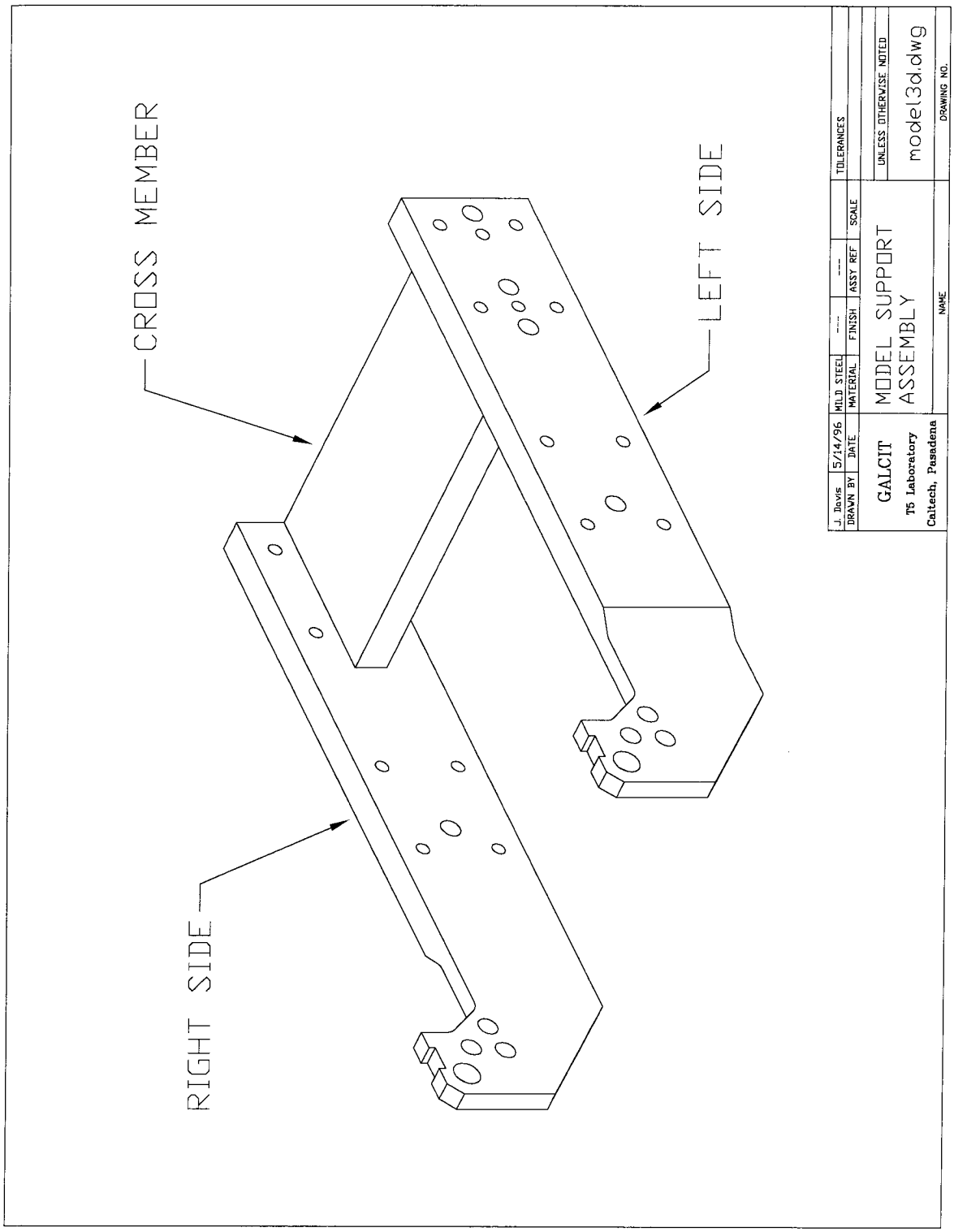
CROSS MEMBER
LEFT SIDE
RIGHT SIDE
J. Davis
DRAWN BY
5/14/96
DATE
MILD STEEL
MATERIAL

FINISH

ASSY REF
SCALE
TOLERANCES
UNLESS OTHERWISE NOTED
GALCIT
T5 Laboratory
Caltech, Pasadena
MODEL SUPPORT
ASSEMBLY
NAME
model3d.dwg
DRAWING NO.

Appendix B Heat Flux Instrumentation

The thermocouple instrumentation and methods to deduce heat flux from thermocouple signals were discussed in Section 2.5. Further details, of particular interest to experimenters using high-enthalpy shock tunnels, are provided in this appendix; methods to deconvolve heat flux from temperature signals are discussed in Section B.1, microscopy results regarding the thermoelectric junction are presented in Section B.2, and issues regarding the thermal properties are dealt with in Section B.3.

B.1 Methods to Deconvolve Heat Flux

The thermocouples measure a rise in temperature over time at the surface of the test model in T5. In order to deduce heat flux from this signal, it is assumed that the problem of heat conduction near the surface of the test model is well approximated by the theory of one-dimensional heat conduction in a semi-infinite body, as given by Equations 2.4–2.6. The approximation of a semi-infinite body is valid as long as the instrument plate is thicker than the thermal penetration depth during the test time of interest. This depth is typically no more than 0.5 mm for T5 flows. The approximation of one-dimensional heat conduction is assumed to be reasonable, despite multiple materials in and around the thermocouple with differing thermal properties. The properties do not vary widely between the different materials, and an accurate result is presumably obtainable by considering average thermal properties. Thermal properties are discussed further in Section B.3.

An analytical solution to Equations 2.4–2.6 requires that the thermal properties remain constant with temperature, *i.e.* that Equation 2.4 is linear. Schultz and Jones (1973) used Laplace transforms to obtain the following solution for the heat flux at the surface as a function of the temperature at the surface:

$$\dot{q}(t) = \sqrt{\frac{\rho c k}{\pi}} \int_0^t \frac{\mathrm{d}T(\tau)}{\mathrm{d}\tau} \frac{\mathrm{d}\tau}{\sqrt{t-\tau}} \qquad \text{or} \qquad \dot{q}_n = \sqrt{\frac{\rho c k}{\pi}} \sum_{i=1}^{n} \frac{T_i - T_{i-1}}{\sqrt{t_n - t_i} + \sqrt{t_n - t_{i-1}}}, \tag{B.1}$$

where the second expression gives the discretized form which may be applied to a digitally acquired temperature time history with $n+1$ samples to find the heat flux $\dot{q}_n$ at each time. Equation B.1 is referred to as the direct method for computing heat flux from a time-resolved temperature signal. A slightly different method due originally to Kendall *et al.* (1967), referred to as the indirect method, is obtained by first integrating the temperature rise to find the total heat accumulated,

$$Q(t) = \sqrt{\frac{\rho c k}{\pi}} \int_0^t \frac{T(\tau)\mathrm{d}\tau}{\sqrt{t-\tau}} \qquad \text{or} \qquad Q_n = \sqrt{\frac{\rho c k}{\pi}} \sum_{i=1}^{n} \frac{T(t_i) - T(t_{i-1})}{\sqrt{t_n - t_i} + \sqrt{t_n - t_{i-1}}} (t_n - t_{n-1}) , \quad \text{(B.2)}$$

then differentiating to find the heat flux,

$$\dot{q}(t) = \frac{\mathrm{d}Q(t)}{dt} \qquad \text{or} \qquad \dot{q}_n = \frac{2Q_{n+8} + Q_{n+4} - Q_{n-4} - 2Q_{n-8}}{40\,\Delta t} . \quad \text{(B.3)}$$

Again, the second expression gives a discretized version suitable for use with digital signals. The indirect method has been most popular with shock tunnel experimenters because it tends to remove noise from the signal by the integration in Equation B.2 and the wide differencing scheme in Equation B.3. Approximate and empirical means of including the effects of variable thermal properties have been considered by a number of authors (see, for example, the review by Hollis, 1995), but these require either that only the thermal conductivity k varies while the thermal diffusivity $\alpha = k/\rho c$ remains relatively constant (which is a poor approximation for the materials in a type E thermocouple), or empirically derived correction factors (which have not been found for the materials in a type E thermocouple).

A method introduced to T5 by Sanderson (1995) is the spectral method for deconvolving heat flux. The equations are given in Section 2.5.2 and not repeated here. The potential advantages of this method over the direct or indirect methods described above are several; the effect of a finite junction thickness on the gauge response can be included, the filtering of noise in the original signal can be specified more exactly, and the computational effort is much reduced. For these reasons, the spectral method was preferred for the present study. The only disadvantage is that the application of spectral deconvolution to a finite nonperiodic time series of temperature using the fast Fourier transform technique can introduce acausal anomalies. Press *et al.* (1992) indicate that such anomalies can be entirely avoided by padding all time series to twice their original length with zeros, so that the deconvolved signal is not corrupted by wrap-around of the response function under the periodic assumption. It was found in the present study, however, that the spectral deconvolution process applied to thermocouple measurements gives corrupted results even with zero-padding to twice the original length of the time series. The effect is shown in Figure B.1a, in which the spectral method has been applied to an artificial time history, the latter obtained by direct numerical integration of Equation 2.7 for a specified heat flux corresponding to a step function (also shown in Figure B.1a). The sample rate and data length are the same as used in actual T5 experiments, and only the first few milliseconds are shown because this is the time of interest in the experiments. The spectral method, with 2× zero-padding, is seen to give a heat flux that is up to 20% too low, both before and after the initial rise in temperature. This error is somewhat smaller if the heat flux falls off quickly after the initial rise, as it typically does in high-enthalpy experiments.

In Figure B.1b, the spectral method is again applied to the same problem, but with padding of

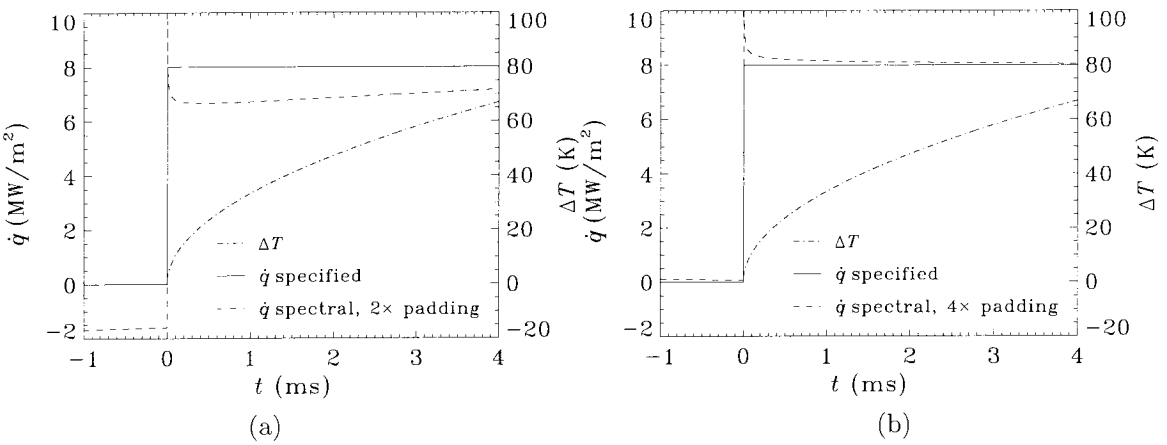

Figure B.1: Effect of increasing the amount of zero-padding in the spectral deconvolution method, from (a) two times the original record length to (b) four times the original record length. Solid curve is specified heat flux history, dash–dot curve is corresponding theoretical temperature history, and dashed curve is the result of spectral deconvolution applied to the temperature history.

all time series to four times their original length; this drastically reduces the error but still shows some acausal effect. Further increasing the padding to eight times the original length gives very little improvement, thus 4× padding is used in the present study. (Only padding to 2×, 4×, 8×, *etc.* is used because, for best efficiency of the fast Fourier transform algorithm, the data length must be a power of two.) The cause for this effect is not entirely clear, but may be due to the use of a response function that is discontinuous on both ends. The thermocouple response function $g(x,t)$ given by Equation 2.8 does not go to zero by the end of the time series. Repeating the exercise in Figure B.1 with an arbitrary response function which does go to zero before the end of the time series shows a very accurate result with 2× padding.

The solution of Equations 2.4 2.6 can also be obtained using a finite-volume numerical technique. The principle advantage of this method is the ease with which variable thermal properties can be included; given a curve fit or model for the various properties, they can be evaluated for each cell in the numerical grid at each time step. The technique has been implemented by Hollis (1995), and is used in Section B.3 to find an appropriate temperature at which to evaluate thermal properties in the various constant-property methods.

B.2 Junction Depth

The depth, or thickness, of the thermoelectric junction at the surface of the thermocouple determines the response time of the thermocouple, and may be included in the spectral deconvolution technique for deducing heat flux. A junction of finite depth results in an EMF that depends on the average temperature across the junction, not the temperature at the surface. As mentioned in Section 2.5.1, the present thermocouple design due to Sanderson (1995) incorporates a taper between the inner and

outer electrodes in order to minimize the junction depth. Sanderson (1995) estimated the depth, from the taper ratio and assumed surface roughness, to be approximately 1.5 μm, but apparently used a depth of 5.0 μm when processing his experimental data. In order to verify the real junction depth, several thermocouples used in the present study were subsequently removed from the double-wedge model and examined by microscopic techniques. Preparation of the samples involves embedding a thermocouple in a plastic resin and polishing away both materials to expose a cross-section through the surface of the thermocouple. Micrographs from one such cross-section are presented in Figure B.2, showing the junction at two locations on the thermocouple removed from port TC11. It is not clear that there is any contact between the two thermoelement materials at the two locations seen here, suggesting that only intermittent contact occurs around the circular surface junction. If there is contact in Figure B.2b, the corresponding junction depth is very thin, perhaps no more than 1 μm. This is the value used in the present study, which gives heat flux results that are no more than a fraction of a percent different from those obtained by assuming zero junction depth (note, however, that Equation 2.7 is not properly defined for $x = 0$).

A perhaps more important observation from Figure B.2 is that there exists a significant volume of epoxy insulation just below the junction. The one-dimensional heat-conduction analysis used to deduce the heat flux assumes that the junction sits on a semi-infinite substrate of thermal properties given by averaging the properties of the two thermoelement materials. This is clearly not the case. If the epoxy is a perfect insulator with respect to the metallic materials, then the short time scale for lateral conduction in this small region (10–20 μm wide) should result in little deviation from the behavior expected for a junction which sits on a wholly metallic substrate. This author found no published information regarding the thermal properties of epoxy resins. It is possible that differences in the junction geometry from thermocouple to thermocouple contribute significantly to the scatter

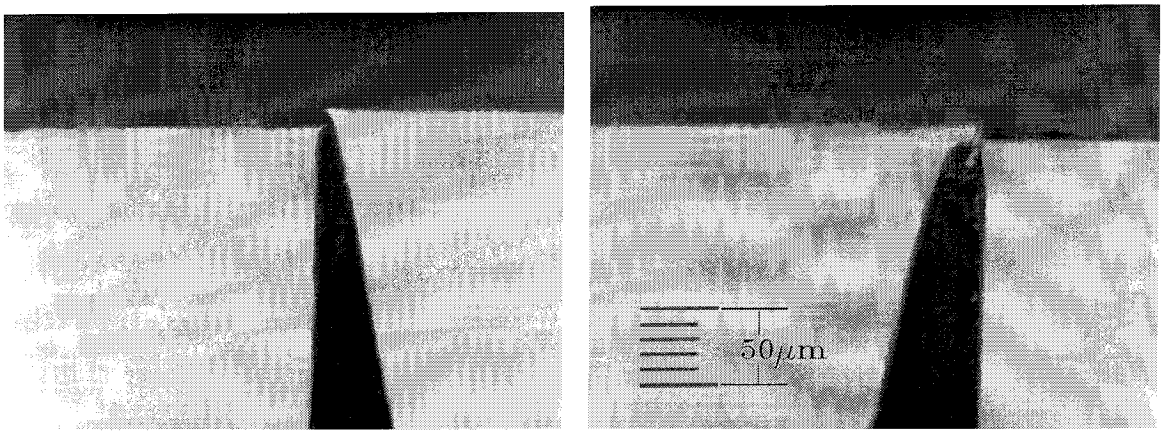

(a) (b)

Figure B.2: Micrographs of cross-section through surface of TC11 showing geometry of the thermoelectric junction at two locations.

in heat flux measurements seen, for example, in Figure 3.13. Micrographs of other thermocouples (not shown) indicate that this geometry is not consistent with regard to the apparent volume of epoxy immediately adjacent to the surface junction, as might be suspected since the thermocouples are assembled by hand.

	constantan	chromel
ρ (kg/m^3)	8900	8670
α (m^2/s)	6.38×10^{-6}	4.60×10^{-6}
k (W/m·K)	22.7	17.3

Table B.1: Thermal property data from Sundqvist (1992) for constantan and chromel at 300 K.

B.3 Thermal Properties

The thermal properties of constantan (45% copper, 55% nickel) and chromel (10% chromium, 90% nickel) used in type E thermocouples have, surprisingly, been very little investigated in the temperature regime of interest to measurements in shock tunnel flows. Sundqvist (1992) presents experimental data for the thermal diffusivity of both materials up to 450 K, but uses theoretical calculations to obtain the specific heat capacity. The calculations match the sparse previous data on specific heat capacity of chromel above room temperature, and existing data on specific heat capacity of constantan at room temperature and below. Experimental data on the specific heat capacity of constantan above room temperature do not exist in the literature. In the present study, we rely solely on the data given by Sundqvist (1992), for which the values at a temperature of 300 K are given in Table B.1.

The variation of thermal properties with temperature found by Sundqvist (1992) are shown graphically in Figure B.3 in terms of the square root of the thermal product, $\sqrt{\rho ck}$. For a given temperature rise, the heat flux is proportional to this factor. Using thermal properties evaluated at room temperature can result in an underestimation of the actual heat flux if the total temperature rise during the test time of interest is significant. In the present study, $\Delta T < 100$ K even under the highest heat loading; for blunt-body flows at high-enthalpy, high-pressure shock tunnel conditions, however, $\Delta T > 200$ is common. Sanderson (1995) used thermal properties at 373 K to reduce the resulting error, but for the present study, a more

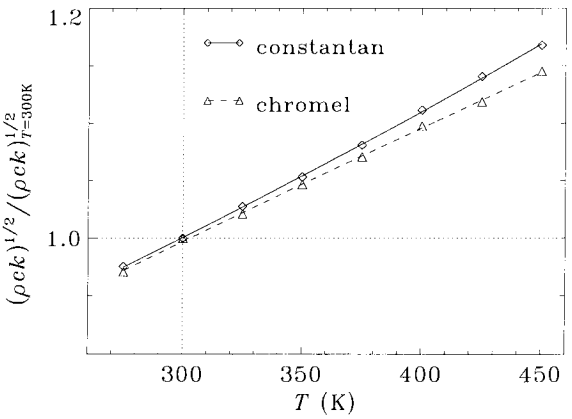

Figure B.3: Variation of thermal product $\sqrt{\rho ck}$ with temperature for constantan (◊ with solid curve) and chromel (△ with dashed curve), from data of Sundqvist (1992). Curves are parabolic fits used to evaluate properties in the present study.

accurate method was desired. In Figure B.4, results from the finite-volume method using variable properties are compared to results from the indirect method using constant properties evaluated at various temperatures. Both methods are applied to an artificial temperature history given by the (numerically integrated) exact solution for constant properties and a step function in heat flux. The indirect method is used here because the small acausal anomaly of the spectral method can obscure the comparison. The finite-volume solution uses 600 grid cells distributed uniformly over 1 mm depth; increasing the spatial resolution can be shown to reduce the magnitude of the overshoot at $t = 0$, but not its temporal extent which depends on the sampling rate of the temperature data.

The heat flux deconvolved using variable thermal properties is seen in Figure B.4 to rise slowly with time due to the increasing thermal product $\sqrt{\rho ck}$ at the surface (since the artificial temperature history was derived for a constant heat flux with constant properties). The constant-property solutions consider properties evaluated at the initial temperature, the final temperature reached at the test time of interest ($t = 2.5$ ms), and an intermediate temperature found by averaging the temperature history between the initial temperature rise and the test time of interest. Use of the latter temperature to evaluate properties in the constant-property solution most accurately reproduces the heat flux level of the variable-property solution at the test time of interest. Thus for reduction of heat flux data in the present experiments, the properties are taken as constant but evaluated separately for each thermocouple signal using the average temperature between the initial rise and the time t_{las} of flow visualization.

Calibration of the thermocouples was not performed for the present experiments. The technique described by Jessen *et al.* (1993), whereby the surface of a coaxial thermocouple is exposed very quickly to a hot liquid reservoir of known temperature and known thermal properties, could be used to calibrate the effective $\sqrt{\rho ck}$ of each thermocouple. If T_i is the initial temperature of the thermocouple and T_s is the measured temperature rise at the surface junction, then the heat-conduction equation for two semi-infinite bodies brought into instantaneous contact gives

$$\frac{(\sqrt{\rho ck})_{\mathrm{TC}}}{(\sqrt{\rho ck})_{liquid}} = \frac{T_{liquid} - T_s}{T_s - T_i}. \tag{B.4}$$

The method is sensitive to uncertainty in the measured temperatures because $\sqrt{\rho ck}$ for liquids is significantly smaller than for solids. This is one reason oils are often used instead of water. Extreme care must also be taken to make sure the surface junction is aligned to the liquid surface and submerges only a very short distance in a very quick time in order to eliminate any effects due to fluid motion. This is another reason oil is often preferred, because it has high viscosity.

Two thermocouples of the design used in the present study were calibrated by Jan Martinez-Schramm at the DLR using this method. The apparatus he designed uses an electrical actuator to submerge the thermocouple surface in a very quick motion (J. Martinez-Schramm, priv.

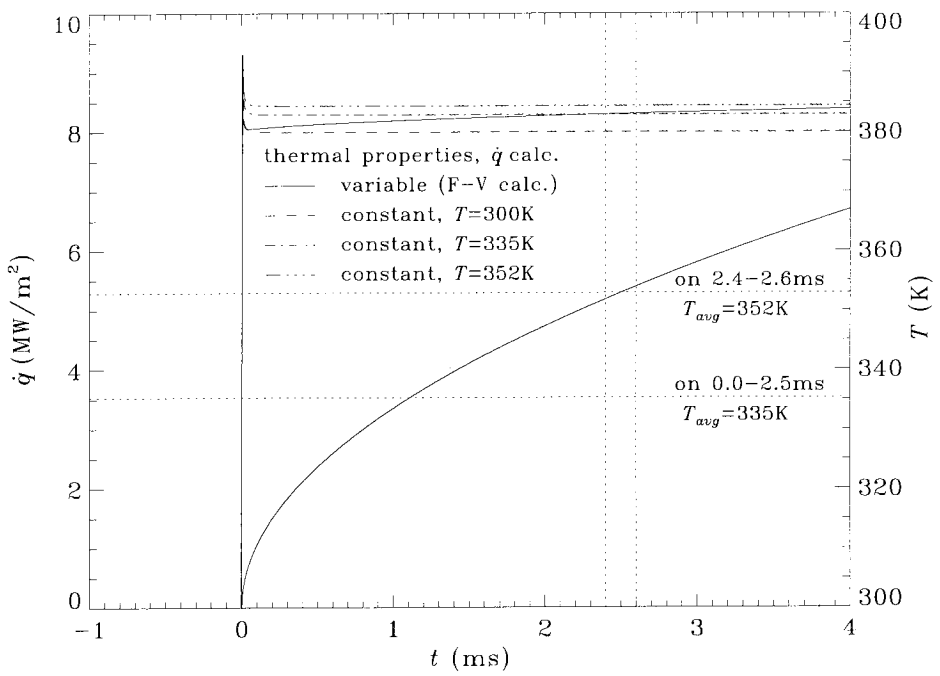

Figure B.4: Comparison between finite-volume calculation with variable thermal properties (upper solid curve) and constant-property results using the indirect deconvolution method at various temperatures (dashed curve for initial temperature, dash–dot–dot dot curve for final temperature at time of interest during test, and dash–dot curve for average temperature between 0 and 2.5 ms). The lower solid curve is temperature history. Horizontal dotted lines indicate various temperature levels and vertical dotted lines indicate the time of interest.

comm.). The values he found by calibration in 70°C water for $\sqrt{\rho ck}$ of these thermocouples were 9257 J/m·K·s$^{1/2}$ ±1.5% and 8950 J/m·K·s$^{1/2}$ ±1.6%, where the uncertainty includes only random error based on statistical analysis of a large number of measurements using the same apparatus. Assuming the surface temperature after submersion was approximately 30°C, the average of constantan and chromel data from Sundqvist (1992) gives 8642 J/m·K·s$^{1/2}$ ±5.4%, where the uncertainty is based on that suggested by Sundqvist for his data. The calibrated values are within 4% of each other, typical of the thermocouple-to-thermocouple variation found by Martinez-Schramm for calibrations of commercial coaxial thermocouples. The calibrated value can also be more than 7% higher than the published data of Sundqvist, which is why the ±8% uncertainty in $\sqrt{\rho ck}$ applied to the present experimental data was considered appropriate. If the presence of epoxy insulator adjacent to the surface junction is important, it might be expected to lower the effective $\sqrt{\rho ck}$ of the gauge due to the lower density and conductivity, suggesting that this is not the primary reason for the observed differences. To draw any further conclusions would require calibration of more than two thermocouples.

Appendix C Pressure Instrumentation

The piezo-electric pressure transducers used in the present study (PCB model no. 105B12) have a sensitivity on the order of 5 mV/psi, which is in fact much smaller than required to measure typical pressures on the double-wedge model, and one reason for the poor signal-to-noise ratio found for low incidence configurations of the test model. Though original factory calibrations were available, the sensitivities of these devices can change over time with use and with contamination by the sooty particles prevalent in T5. After the second experimental campaign, the pressure transducers were calibrated using a simple apparatus. This consists of a vessel holding pressurized nitrogen and a fast electrical valve to apply the pressure in a sudden fashion to the transducer being calibrated. An analog pressure gauge of high accuracy is used to measure the pressure in the vessel, the reading being taken after the valve has been opened. The transducers are mounted in a manner similar to that described for the double-wedge model (*cf.* Section 2.6.1), with a layer of silicone sealant over the gauge head and silicone sealant packed into the mounting threads.

An example of a calibration voltage signal is shown in Figure C.1 for transducer serial number 4323. The oscillation of approximately 1.3 ms period corresponds to the time it takes acoustic waves to travel to one end of the vessel and back. The decline in voltage at late time is due to the discharge

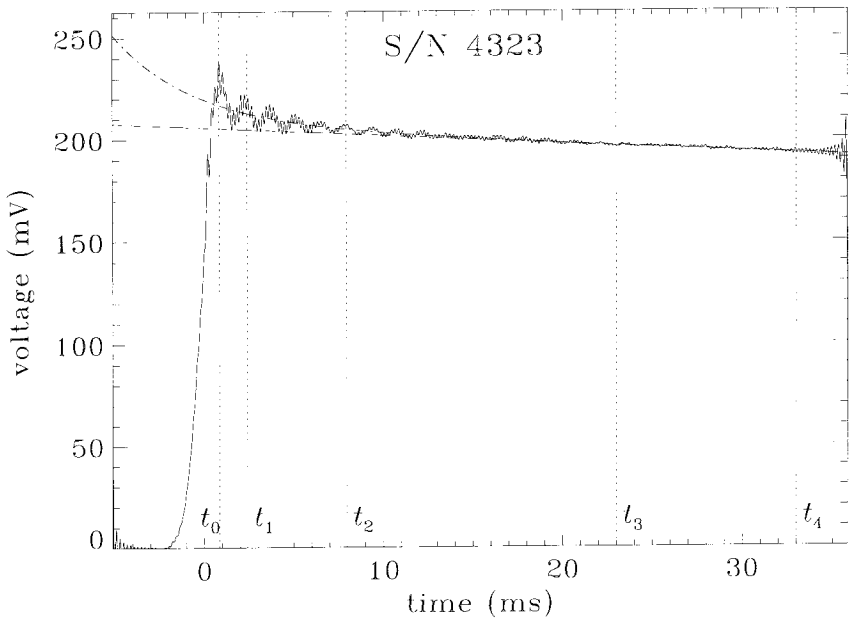

Figure C.1: Example of calibration signal from pressure transducer, processed with 5 kHz low-pass cutoff filter. Dashed line is exponential curve fit to points at t_3 and t_4, and dash–dot line is an additional exponential curve fit to average voltages at points t_1 and t_2. Time t_0 corresponds to the maximum signal.

time constant of the transducer, which is on the order of 1–2 s. The faster drop at early time is presumably due to a gas-dynamic phenomenon germane to the apparatus and does not correspond to the final pressure. The dashed line is an exponential curve fit to the voltage levels measured at times t_3 and t_4; the voltage at which this curve intersects $t = t_0$ is taken as the voltage corresponding to the measured pressure in the vessel after the gas settles. Time t_0 corresponds to the time of peak pressure. The dash-dot line is an exponential curve fit to the remaining voltage above the dashed line, using values at t_1 and t_2 found by averaging over one oscillation period. Calibration using the lower curve better matches the original factory calibrations. The sensitivities obtained in this manner are listed in Table C.1 for the transducers used in the present experiments, along with their installation locations on the test model (*cf.* Figure 2.4). The uncertainties are based on the deviation of the present calibrations from original factory calibrations. (The random error due to repeatability was much smaller.)

serial number	sensitivity (mV/MPa)	shots 1278–1785	shots 1786–1799
4324	621 ±4	P1	P10
4307	804 ±9	P2	P2
4320	744 ±26	P3	P3
4319	603 ±29	P4	P4
4322	656 ±22	P5	P5
4316	761 ±42	P6	P6
4318	679 ±4	P7	P7
4323	604 ±7	P8	P8
4325	840 ±9	P9	P9
4313	812 ±15	P10	P1
4314	708 ±2	P11	P11
4317	827 ±32	P12	P12
4315	692 ±15	P13	P13
4321	776 ±22	P14	P14

Table C.1: Pressure transducer sensitivities and arrangement.

Appendix D Experimental Data Tables

The tables in this appendix present experimentally obtained information and data for each shot. These are sorted in Table D.1 first by nominal operating condition, then by increasing A_e/A_*, then by decreasing θ_1, then by decreasing θ_w. All other tables throughout the appendices are sorted by shot number; to reference any information that is not in Table D.1 by the test condition and double-wedge configuration, first look up the condition in Table D.1 to find the corresponding shot number. Conversely, too find a particular shot number in Table D.1, first look up the condition by referring to Tables D.2 or D.3. The conditions A0, B0, and C0 consist of experiments for which the reservoir conditions deviated significantly from the nominal conditions of A1–2, B1–3, and C1–4.

Table D.1 gives reservoir conditions and other basic information concerning each experiment, TLR refers to the interface-tailoring condition of the shock tube deduced from nozzle-reservoir pressure time histories;

UT undertailored,

SU slightly undertailored,

T tailored,

SO slightly overtailored,

OT overtailored,

and the column VIS indicates whether or not separation length was measured using flow visualization. Only the shots marked "Y" were subjected to full analysis using inviscid triple-wedge computations and were part of the data presented in Chapter 6. The distances x_{le} and y_{le} give the position of the model relative to the nozzle, as shown in Figure 2.3, and the time t_{las} is the time at which flow visualization was performed, with respect to the time of shock reflection in the nozzle reservoir.

Table D.2 gives experimental measurements taken from flow visualization, and D.3 gives experimental measurements taken from heat flux and pressure instrumentation. θ_{sep}, L_u, and L_{sep} are defined in Figure 1.3, and β_1 is the angle of the leading shock with respect to horizontal. $\dot{q}_{pk}$ is the highest single heat flux measurement from the flap region, $\dot{q}_R$ and $\dot{q}_1$ are averaged heat flux measurements from downstream of reattachment and upstream of separation respectively, and p_R is an averaged pressure measurement from downstream of reattachment. The column TRN in Table D.3 indicates which shots were suspected of having transitional interactions (*cf.* Section 6.1.2).

Table D.1: Reservoir conditions, geometry, *etc.* for every shot, sorted by condition.

cond.	A_e/A_*	θ_1	θ_w	h_0	p_0	TLR	x_{le}	y_{le}	t_{las}	shot	VIS
				MJ/kg	MPa		cm	cm	ms	no.	
A0	100	30°	0°	2.19	1.67	O	6.0	1.2	1.75	1730	
			0°	4.18	6.50	O	7.1	1.2	1.75	1731	
			0°	4.75	7.40	O	7.1	1.2	1.79	1727	
		0°	30°	4.65	15.8	SO	3.7	1.2	1.50	1307	
A0	400	30°	0°	4.27	4.45	O	4.1	1.2	1.54	1725	
A1	100	30°	25°	3.98	11.0	T	4.7	1.1	1.70	1752	Y
			20°	3.78	12.0	SO	4.8	1.1	1.70	1754	Y
		15°	40°	4.14	12.0	T	4.4	1.2	1.50	1312	
			30°	4.08	12.3	T	4.3	1.2	1.50	1308	
			30°	4.08	11.7	T	4.4	1.2	1.50	1311	Y
		0°	20°	3.67	10.9	SO	4.9	0.6	1.70	1759	
			10°	3.50	11.5	SO	5.0	0.6	1.70	1761	
A2	100	30°	20°	4.83	37.9	SO	6.5	1.1	1.60	1758	
			20°	4.85	37.6	SO	6.4	1.1	1.60	1757	Y
A2	225	30°	20°	4.94	39.6	T	7.0	1.1	1.70	1755	
A2	400	0°	20°	4.95	39.0	T	6.9	0.6	1.60	1760	
			10°	4.97	39.6	T	6.5	0.6	1.60	1762	
A3	100	30°	25°	4.49	41.5	T	7.4	1.1	1.70	1751	
			15°	4.35	40.5	T	7.6	1.1	1.70	1748	
B0	400	30°	30°	8.23	22.1	SO	4.6	1.2	1.25	1287	
			20°	9.24	18.5	SO	4.3	1.2	1.25	1286	
			20°	9.94	18.0	SO	4.5	1.2	1.25	1282	
B1	100	30°	0°	6.14	4.48	T	6.7	1.2	1.50	1729	
			0°	7.19	6.20	SO	4.8	1.1	1.50	1798	
		0°	10°	7.29	6.02	SO	2.8	0.6	1.70	1770	

Table D.1: (continued)

cond.	A_e/A_*	θ_1	θ_w	h_0	p_0	TLR	x_{le}	y_{le}	t_{las}	shot	VIS
				MJ/kg	MPa		cm	cm	ms	no.	
B1	225	40°	20°	6.95	6.41	SO	3.3	0.5	1.70	1787	Y
			15°	6.77	6.55	SO	3.3	0.5	1.70	1793	Y
		15°	25°	6.60	6.12	SO	2.8	0.6	1.70	1781	Y
			20°	6.71	6.30	SO	2.6	0.6	1.70	1783	Y
			15°	6.81	6.55	T	3.2	0.6	1.70	1778	Y
		0°	10°	6.87	6.12	T	3.1	0.6	1.70	1764	
B1	400	40°	20°	7.03	6.58	T	3.3	0.5	1.70	1786	Y
			15°	6.68	6.60	SO	3.5	0.5	1.70	1792	Y
		30°	25°	6.95	6.27	SO	2.8	1.1	1.50	1742	Y
			20°	7.33	6.75	T	3.0	1.1	1.70	1743	Y
			15°	7.09	6.52	SO	2.8	1.1	1.70	1746	Y
			10°	7.08	6.47	SO	2.7	1.1	1.70	1745	Y
		15°	25°	7.02	6.68	SO	2.2	0.6	1.70	1779	Y
			20°	7.32	6.87	T	2.7	0.6	1.70	1782	Y
			15°	7.05	6.22	SO	1.5	0.6	1.70	1774	Y
B2	100	30°	25°	8.34	18.8	SO	5.3	1.1	1.50	1750	Y
			20°	8.19	19.3	SO	5.2	1.1	1.50	1753	Y
			15°	8.41	19.5	SO	5.6	1.1	1.50	1749	
			0°	8.47	20.6	T	7.8	1.1	1.50	1799	
B2	225	35°	20°	8.71	20.7	SO	5.1	1.2	1.25	1290	Y
			15°	8.13	20.1	SO	4.4	1.2	1.25	1291	Y
		30°	15°	7.82	18.1	SO	6.3	1.2	1.25	1300	Y
		15°	40°	8.67	19.8	SO	5.0	1.2	1.25	1315	Y
			30°	8.22	19.8	SO	4.8	1.2	1.25	1316	Y
B2	400	30°	30°	7.97	18.4	SO	4.6	1.2	1.25	1299	

Table D.1: (continued)

cond.	A_e/A_*	θ_1	θ_w	h_0	p_0	TLR	x_{le}	y_{le}	t_{las}	shot	VIS
				MJ/kg	MPa		cm	cm	ms	no.	
			30°	8.36	22.3	SO	4.7	1.2	1.25	1289	
			20°	8.01	20.6	SO	4.4	1.2	1.25	1285	Y
			20°	8.38	19.8	SO	4.6	1.2	1.25	1305	Y
			20°	9.00	22.5	SO	4.6	1.2	1.25	1284	
			15°	8.27	19.9	SO	4.6	1.2	1.25	1302	Y
B3	400	15°	30°	10.1	55.2	SO	7.0	1.2	1.25	1296	Y
			20°	11.0	59.3	SO	7.1	1.2	1.25	1295	Y
			15°	10.7	57.5	SO	7.3	1.2	1.25	1322	Y
C0	100	30°	20°	26.4	13.8	T	2.9	1.1	0.85	1736	Y
			20°	29.5	13.6	T	3.4	1.1	0.85	1735	Y
			0°	21.3	14.2	U	7.4	1.2	0.85	1732	
			0°	24.1	14.5	SU	3.1	1.1	0.85	1737	
			0°	29.5	13.6	T	7.6	1.2	0.89	1733	
			0°	30.5	13.9	SO	7.6	-1.0	0.89	1734	
		15°	30°	24.0	20.2	SU	5.4	1.2	0.85	1297	Y
			5°	21.9	47.2	SU	7.8	1.2	0.85	1323	
		0°	15°	26.6	15.1	SO	4.1	0.6	0.95	1768	
C0	225	30°	5°	23.5	19.0	SO	4.7	1.2	0.90	1278	
			5°	27.1	20.2	SO	4.7	1.2	0.80	1279	
C0	400	15°	30°	22.1	29.6	SU	5.0	1.2	0.85	1309	Y
C1	400	15°	40°	19.9	28.1	SU	5.3	1.2	0.85	1314	Y
			40°	20.5	27.2	SU	5.3	1.2	0.85	1313	
			30°	19.7	26.4	T	5.4	1.2	0.85	1310	Y
C2	100	40°	20°	24.2	16.2	SU	4.3	0.5	0.85	1790	Y
			15°	24.1	15.9	SU	4.2	0.5	0.85	1796	Y

Table D.1: (continued)

cond.	A_e/A_*	θ_1	θ_w	h_0	p_0	TLR	x_{le}	y_{le}	t_{las}	shot	VIS
				MJ/kg	MPa		cm	cm	ms	no.	
		15°	20°	24.3	16.7	T	3.8	0.6	0.85	1785	Y
			15°	24.4	15.9	SU	3.7	0.6	0.85	1776	Y
		0°	15°	23.1	15.6	SU	4.0	0.6	0.85	1766	
			10°	24.2	16.4	SU	4.1	0.6	0.85	1772	
C2	225	30°	25°	23.4	16.9	SU	3.2	1.1	0.84	1741	Y
			25°	23.9	18.1	SU	4.1	1.1	0.85	1740	Y
			20°	23.8	17.3	SU	3.7	1.1	0.85	1744	Y
			15°	23.8	17.5	SU	4.3	1.1	0.85	1747	Y
		15°	20°	24.7	17.2	SU	3.8	0.6	0.85	1784	Y
			15°	24.6	16.9	SU	3.5	0.6	0.85	1777	Y
C2	400	40°	20°	24.8	17.4	SU	4.4	0.5	0.85	1788	Y
			15°	24.7	17.1	SU	4.3	0.5	0.85	1795	Y
		15°	25°	24.3	17.0	SU	4.0	0.6	0.85	1780	Y
			15°	24.1	17.0	SU	3.8	0.6	0.85	1775	Y
		0°	10°	23.1	16.9	SU	4.2	0.6	0.85	1765	
C3	100	15°	5°	23.9	46.2	T	7.7	1.2	0.85	1324	
C4	100	15°	30°	26.9	21.2	T	5.1	1.2	0.85	1298	Y
			20°	28.1	23.2	T	5.2	1.2	0.85	1294	Y
C4	225	30°	30°	26.7	24.0	SO	5.2	1.2	0.85	1288	Y
			30°	28.5	23.4	SO	5.0	1.2	0.85	1306	Y
			20°	28.4	22.7	SO	5.1	1.2	0.85	1304	Y
			20°	28.6	23.7	T	5.0	1.2	0.80	1283	Y
			20°	28.7	24.2	T	5.3	1.2	0.80	1281	
			20°	29.7	22.9	SO	4.9	1.2	0.80	1280	Y
			15°	28.1	23.3	SO	5.9	1.2	0.85	1303	Y

Table D.1: (continued)

cond.	A_e/A_*	θ_1	θ_w	h_0	p_0	TLR	x_{le}	y_{le}	t_{las}	shot	VIS
				MJ/kg	MPa		cm	cm	ms	no.	
		15°	30°	28.8	22.8	SO	5.1	1.2	0.85	1317	Y
			30°	29.6	22.4	SO	5.1	1.2	0.85	1320	Y
			20°	28.4	22.5	SO	5.1	1.2	0.85	1319	Y
			20°	30.1	22.7	SO	5.2	1.2	0.85	1318	
			15°	29.4	23.8	SO	5.2	1.2	0.85	1321	Y
C4	400	40°	20°	28.8	25.3	SO	5.2	1.2	0.85	1293	Y
			15°	27.4	24.0	SO	5.3	1.2	0.85	1292	Y

Table D.2: Flow visualization measurements, sorted by shot number.

shot no.	θ_{sep}	L_u cm	L_{sep} cm	β_1	cond.	A_e/A_*	θ_1	θ_w
1280	$4.51° \pm 0.68°$	2.45 ± 0.22	3.13 ± 0.31	39.4°	C4	225	30°	20°
1283	$4.49° \pm 0.80°$	1.70 ± 0.14	2.20 ± 0.22	38.0°	C4	225	30°	20°
1285	$5.20° \pm 0.36°$	1.97 ± 0.05	2.63 ± 0.09	38.7°	B2	400	30°	20°
1288	$5.33° \pm 0.62°$	2.79 ± 0.13	3.35 ± 0.18	39.3°	C4	225	30°	30°
1290	$5.48° \pm 0.14°$	1.37 ± 0.01	1.86 ± 0.02	45.0°	B2	225	35°	20°
1291	$5.62° \pm 0.62°$	0.84 ± 0.05	1.39 ± 0.09	44.6°	B2	225	35°	15°
1292	$5.57° \pm 0.29°$	1.35 ± 0.12	2.13 ± 0.19	49.9°	C4	400	40°	15°
1293	$5.71° \pm 0.55°$	2.21 ± 0.20	3.04 ± 0.29	49.3°	C4	400	40°	20°
1294	$3.28° \pm 0.57°$	2.04 ± 0.12	2.43 ± 0.17	23.7°	C4	100	15°	20°
1295	$5.35° \pm 0.33°$	2.37 ± 0.04	3.21 ± 0.09	21.7°	B3	400	15°	20°
1296	$4.85° \pm 0.21°$	3.84 ± 0.06	4.52 ± 0.08	22.0°	B3	400	15°	30°
1297	$4.13° \pm 1.45°$	3.04 ± 0.18	3.49 ± 0.27	23.8°	C0	100	15°	30°
1298	$4.31° \pm 0.43°$	3.56 ± 0.22	4.12 ± 0.26	23.2°	C4	100	15°	30°
1300	$5.20° \pm 0.28°$	0.96 ± 0.04	1.45 ± 0.07	39.4°	B2	225	30°	15°
1302	$5.90° \pm 0.30°$	1.58 ± 0.05	2.56 ± 0.12	38.5°	B2	400	30°	15°
1303	$5.54° \pm 0.64°$	1.26 ± 0.05	2.02 ± 0.17	39.7°	C4	225	30°	15°
1304	$5.33° \pm 0.79°$	2.15 ± 0.06	2.88 ± 0.17	39.4°	C4	225	30°	20°
1305	$5.66° \pm 0.18°$	2.00 ± 0.05	2.77 ± 0.08	39.0°	B2	400	30°	20°
1306	$4.70° \pm 1.33°$	3.31 ± 0.22	3.89 ± 0.32	38.4°	C4	225	30°	30°
1309	$6.58° \pm 0.56°$	4.34 ± 0.18	5.46 ± 0.26	22.1°	C0	400	15°	30°
1310	$5.15° \pm 1.22°$	4.89 ± 0.34	5.82 ± 0.48	21.6°	C1	400	15°	30°
1311	$6.93° \pm 1.53°$	2.65 ± 0.18	3.38 ± 0.31	21.6°	A1	100	15°	30°
1314	$5.21° \pm 0.81°$	5.40 ± 0.16	6.08 ± 0.22	21.7°	C1	400	15°	40°
1315	$5.85° \pm 0.45°$	6.40 ± 0.23	7.33 ± 0.28	22.0°	B2	225	15°	40°
1316	$4.09° \pm 1.76°$	4.08 ± 0.23	4.67 ± 0.40	21.3°	B2	225	15°	30°

Table D.2: (continued)

shot no.	θ_{sep}	L_u cm	L_{sep} cm	β_1	cond.	A_e/A_*	θ_1	θ_w
1317	$6.32° \pm 1.04°$	4.03 ± 0.14	5.00 ± 0.27	23.0°	C4	225	15°	30°
1319	$4.77° \pm 0.86°$	2.51 ± 0.16	3.25 ± 0.27	22.2°	C4	225	15°	20°
1320	$6.89° \pm 1.14°$	5.13 ± 0.35	6.51 ± 0.53	22.1°	C4	225	15°	30°
1321	$4.06° \pm 0.17°$	1.87 ± 0.23	2.45 ± 0.30	22.2°	C4	225	15°	15°
1322	$3.71° \pm 0.26°$	1.97 ± 0.09	2.52 ± 0.13	21.2°	B3	400	15°	15°
1735	$4.38° \pm 0.31°$	1.87 ± 0.09	2.38 ± 0.12	41.5°	C0	100	30°	20°
1736	$5.54° \pm 0.99°$	1.80 ± 0.16	2.47 ± 0.28	40.5°	C0	100	30°	20°
1740	$4.45° \pm 0.89°$	2.54 ± 0.19	3.06 ± 0.26	39.3°	C2	225	30°	25°
1741	$5.45° \pm 0.29°$	2.64 ± 0.07	3.35 ± 0.10	38.6°	C2	225	30°	25°
1742	$2.37° \pm 0.47°$	3.62 ± 0.17	3.99 ± 0.21	38.1°	B1	400	30°	25°
1743	$3.86° \pm 0.35°$	2.62 ± 0.07	3.30 ± 0.12	37.7°	B1	400	30°	20°
1744	$4.07° \pm 0.45°$	2.18 ± 0.05	2.73 ± 0.10	38.0°	C2	225	30°	20°
1745	$4.70° \pm 0.49°$	1.37 ± 0.05	2.10 ± 0.14	39.0°	B1	400	30°	10°
1746	$4.26° \pm 0.39°$	1.94 ± 0.07	2.72 ± 0.14	39.1°	B1	400	30°	15°
1747	$3.71° \pm 0.48°$	1.29 ± 0.07	1.74 ± 0.12	37.5°	C2	225	30°	15°
1750	$3.93° \pm 0.68°$	1.47 ± 0.11	1.74 ± 0.14	39.3°	B2	100	30°	25°
1752	$5.34° \pm 1.72°$	1.42 ± 0.09	1.79 ± 0.20	39.8°	A1	100	30°	25°
1753	$5.50° \pm 1.13°$	0.96 ± 0.12	1.32 ± 0.19	38.9°	B2	100	30°	20°
1754	$2.34° \pm 1.18°$	0.65 ± 0.10	0.73 ± 0.12	40.2°	A1	100	30°	20°
1756	$1.55° \pm 1.36°$	0.80 ± 0.20	0.87 ± 0.22	38.5°	A2	225	30°	20°
1757	$3.52° \pm 1.73°$	0.46 ± 0.12	0.56 ± 0.15	40.1°	A2	100	30°	20°
1774	$4.65° \pm 0.46°$	1.27 ± 0.09	1.83 ± 0.15	21.7°	B1	400	15°	15°
1775	$6.80° \pm 0.99°$	0.94 ± 0.09	1.71 ± 0.27	22.1°	C2	400	15°	15°
1776	$4.55° \pm 0.62°$	1.49 ± 0.11	2.15 ± 0.20	23.8°	C2	100	15°	15°
1777	$5.25° \pm 0.60°$	1.28 ± 0.05	1.99 ± 0.15	23.0°	C2	225	15°	15°

Table D.2: (continued)

shot no.	θ_{sep}	L_u cm	L_{sep} cm	β_1	cond.	A_e/A_*	θ_1	θ_w
1778	$3.97° \pm 0.55°$	1.81 ± 0.12	2.41 ± 0.19	22.1°	B1	225	15°	15°
1779	$6.10° \pm 0.08°$	4.38 ± 0.21	5.72 ± 0.27	22.0°	B1	400	15°	25°
1780	$6.55° \pm 0.47°$	3.62 ± 0.24	4.83 ± 0.34	22.2°	C2	400	15°	25°
1781	$4.40° \pm 0.25°$	4.31 ± 0.32	5.19 ± 0.39	22.0°	B1	225	15°	25°
1782	$4.73° \pm 0.72°$	3.53 ± 0.36	4.58 ± 0.52	21.8°	B1	400	15°	20°
1783	$5.17° \pm 0.28°$	3.50 ± 0.17	4.68 ± 0.24	21.6°	B1	225	15°	20°
1784	$5.18° \pm 0.27°$	2.32 ± 0.09	3.10 ± 0.13	23.1°	C2	225	15°	20°
1785	$4.50° \pm 0.53°$	2.49 ± 0.08	3.21 ± 0.15	23.8°	C2	100	15°	20°
1786	$5.99° \pm 0.86°$	3.48 ± 0.27	4.91 ± 0.49	52.2°	B1	400	40°	20°
1787	$4.61° \pm 0.79°$	3.30 ± 0.16	4.25 ± 0.29	51.6°	B1	225	40°	20°
1788	$6.64° \pm 0.61°$	2.51 ± 0.14	3.71 ± 0.27	50.0°	C2	400	40°	20°
1790	$5.44° \pm 0.37°$	1.85 ± 0.07	2.52 ± 0.11	50.4°	C2	100	40°	20°
1792	$5.90° \pm 0.30°$	1.71 ± 0.07	2.79 ± 0.15	51.5°	B1	400	40°	15°
1793	$5.00° \pm 0.44°$	1.56 ± 0.10	2.32 ± 0.17	51.4°	B1	225	40°	15°
1795	$5.00° \pm 0.31°$	1.65 ± 0.08	2.46 ± 0.14	49.2°	C2	400	40°	15°
1796	$5.00° \pm 0.59°$	1.46 ± 0.07	2.18 ± 0.17	51.0°	C2	100	40°	15°

Table D.3: Heat flux and pressure measurements, sorted by shot number.

shot no.	$\dot{q}_{pk}$ MW/m^2	$\dot{q}_R$ MW/m^2	$\dot{q}_l$ MW/m^2	p_R kPa	TRN	cond.	A_e/A_*	θ_l	θ_w
1280	16.07 ± 1.43	16.07	6.14	235.1		C4	225	30°	20°
1283	35.79 ± 4.06	32.24	5.61	237.0		C4	225	30°	20°
1285	8.39 ± 1.08	7.22	0.90	115.2	Y	B2	400	30°	20°
1288	93.16 ± 8.09	54.95	6.59	388.9	Y	C4	225	30°	30°
1290	15.81 ± 1.61	10.22	1.58	254.0	Y	B2	225	35°	20°
1291	8.37 ± 0.85	7.64	1.48	165.0	Y	B2	225	35°	15°
1292	20.58 ± 2.00	17.84	6.13	129.8		C4	400	40°	15°
1293	33.10 ± 2.90	19.96	7.55	151.9		C4	400	40°	20°
1294	47.09 ± 5.81	39.63	4.70	279.3	Y	C4	100	15°	20°
1295	17.49 ± 1.55	15.05	1.48	191.7	Y	B3	400	15°	20°
1296	35.38 ± 2.96	29.35	1.50	345.5	Y	B3	400	15°	30°
1297	60.27 ± 5.19	54.99	4.90	395.3	Y	C0	100	15°	30°
1298	69.93 ± 6.61	61.45	5.87	447.7	Y	C4	100	15°	30°
1300	8.16 ± 0.75	7.24	1.14	133.4		B2	225	30°	15°
1302	5.35 ± 0.56	4.76	0.95	78.3		B2	400	30°	15°
1303	15.65 ± 1.87	12.93	5.98	152.9		C4	225	30°	15°
1304	28.00 ± 3.13	25.20	5.35	185.6		C4	225	30°	20°
1305	6.05 ± 0.67	5.34	0.96	103.3		B2	400	30°	20°
1306	58.02 ± 5.09	50.42	7.00	352.0		C4	225	30°	30°
1309	30.04 ± 3.79	19.55	3.06	170.5		C0	400	15°	30°
1310	24.01 ± 3.06	18.77	2.46	158.1		C1	400	15°	30°
1311	10.09 ± 1.03	9.53	0.45	284.2	Y	A1	100	15°	30°
1314	42.17 ± 6.13	28.30	3.91	195.1	Y	C1	400	15°	40°
1315	31.16 ± 4.15	19.30	1.67	416.3	Y	B2	225	15°	40°
1316	15.03 ± 1.48	13.80	1.02	212.6	Y	B2	225	15°	30°

Table D.3: (continued)

shot no.	$\dot{q}_{pk}$ MW/m^2	$\dot{q}_R$ MW/m^2	$\dot{q}_1$ MW/m^2	p_R kPa	TRN	cond.	A_e/A_*	θ_1	θ_w
1317	43.66 ± 4.08	39.47	4.49	244.6	Y	C4	225	15°	30°
1319	20.19 ± 2.87	13.78	3.30	137.9		C4	225	15°	20°
1320	40.82 ± 4.53	35.11	4.33	237.3	Y	C4	225	15°	30°
1321	9.66 ± 1.61	7.58	3.25	99.0		C4	225	15°	15°
1322	14.77 ± 1.41	12.69	1.32	159.4	Y	B3	400	15°	15°
1735	37.63 ± 21.99	34.38	5.88	245.7		C0	100	30°	20°
1736	38.95 ± 3.52	25.15	5.68	241.8		C0	100	30°	20°
1740	37.39 ± 3.82	27.62	4.73	213.9	Y	C2	225	30°	25°
1741	42.45 ± 4.53	33.15	4.79	240.0	Y	C2	225	30°	25°
1742	3.29 ± 0.43	2.18	0.48	64.3		B1	400	30°	25°
1743	2.24 ± 0.27	1.81	0.56	40.9		B1	400	30°	20°
1744	21.61 ± 2.56	15.67	4.13	143.8		C2	225	30°	20°
1745	1.09 ± 0.15	0.84	0.48	18.8		B1	400	30°	10°
1746	1.41 ± 0.32	1.08	0.46	22.1		B1	400	30°	15°
1747	15.90 ± 2.82	13.13	4.40	115.6		C2	225	30°	15°
1750	31.04 ± 2.79	23.74	2.00	286.6	Y	B2	100	30°	25°
1752	11.61 ± 1.45	8.10	0.66	289.4	Y	A1	100	30°	25°
1753	21.29 ± 4.53	18.52	2.41	252.7	Y	B2	100	30°	20°
1754	7.78 ± 0.70	6.61	0.72	185.8	Y	A1	100	30°	20°
1756	12.34 ± 1.23	11.33	1.16	299.8	Y	A2	225	30°	20°
1757	16.37 ± 1.37	15.17	6.31	539.0	Y	A2	100	30°	20°
1774	0.79 ± 0.09	0.66	0.26	15.0		B1	400	15°	15°
1775	4.39 ± 0.41	3.75	1.88	46.4		C2	400	15°	15°
1776	14.96 ± 1.81	11.48	3.37	101.7		C2	100	15°	15°
1777	6.41 ± 0.73	5.56	2.46	66.5		C2	225	15°	15°

Table D.3: (continued)

shot no.	$\dot{q}_{pk}$ MW/m^2	$\dot{q}_R$ MW/m^2	$\dot{q}_1$ MW/m^2	p_R kPa	TRN	cond.	A_e/A_*	θ_1	θ_w
1778	1.50 $\pm$ 0.17	1.21	0.34	25.1		B1	225	15°	15°
1779	2.11 $\pm$ 0.32	1.73	0.40	38.5		B1	400	15°	25°
1780	12.85 $\pm$ 2.21	10.98	2.24	77.0		C2	400	15°	25°
1781	4.70 $\pm$ 0.88	3.82	0.48	49.1	Y	B1	225	15°	25°
1782	1.40 $\pm$ 0.34	1.18	0.35	21.6		B1	400	15°	20°
1783	1.63 $\pm$ 0.36	1.38	0.45	32.4		B1	225	15°	20°
1784	14.29 $\pm$ 1.57	12.83	2.32	79.7		C2	225	15°	20°
1785	28.54 $\pm$ 3.05	25.12	3.44	162.5	Y	C2	100	15°	20°
1786	3.18 $\pm$ 0.45	2.16	0.63	43.2		B1	400	40°	20°
1787	5.56 $\pm$ 1.02	3.38	0.81	82.5		B1	225	40°	20°
1788	13.73 $\pm$ 1.47	9.95	4.12	101.8		C2	400	40°	20°
1790	43.32 $\pm$ 3.68	38.02	11.72	337.6		C2	100	40°	20°
1792	1.26 $\pm$ 0.44	1.01	0.48	34.6		B1	400	40°	15°
1793	2.50 $\pm$ 0.51	2.11	0.65	57.5		B1	225	40°	15°
1795	11.81 $\pm$ 1.77	9.49	3.96	113.9		C2	400	40°	15°
1796	33.83 $\pm$ 3.03	28.38	8.02	292.4	Y	C2	100	40°	15°

Appendix E Computational Data Tables

The tables in this appendix present detailed results of the computations undertaken for each experiment, sorted by shot number. From the nozzle-flow computations described in Section 3.2, Table E.1 gives the flow properties in the free stream on the nozzle centerline at the same axial location as the leading edge of the double-wedge test model. From the inviscid triple-wedge computations described in Section 3.3, Tables E.2–E.3 give external flow properties in regions 1–3 at particular stations chosen as described in Section 3.3.4. The viscosities used in forming Reynolds number for Tables E.1 and E.2 were computed using the model in Section 4.1.4.

Table E.1: Computed free-stream conditions, sorted by shot number.

shot no.	M_∞	Re_∞ $L = 10$ cm	α_∞	ρ_∞ kg/m^3	T_∞ K	T_{v_∞} K	p_∞ kPa	u_∞ m/s	cond.	A_e/A_*
1278	6.36	6.19×10^4	0.1020	0.0065	1767	4067	6.68	5784	C0	225
1279	6.20	5.67×10^4	0.1390	0.0061	1982	4162	7.27	6098	C0	225
1280	6.07	5.73×10^4	0.1620	0.0065	2179	4204	8.37	6331	C4	225
1281	6.06	6.14×10^4	0.1480	0.0069	2171	4167	9.00	6269	C4	225
1282	8.45	1.04×10^5	0.0054	0.0068	574	3286	1.76	4142	B0	400
1283	6.07	6.12×10^4	0.1470	0.0069	2154	4168	8.83	6251	C4	225
1284	8.66	1.35×10^5	0.0023	0.0085	505	3101	2.06	3970	B2	400
1285	8.79	1.41×10^5	0.0011	0.0086	439	2996	1.85	3751	B2	400
1286	8.55	1.15×10^5	0.0035	0.0073	527	3190	2.75	4007	B0	400
1287	8.76	1.47×10^5	0.0012	0.0090	453	3003	2.00	3803	B0	400
1288	6.13	6.50×10^4	0.1260	0.0072	2064	4111	8.67	6102	C4	225
1289	8.75	1.46×10^5	0.0014	0.0089	461	3016	2.00	3829	B2	400
1290	7.68	1.73×10^5	0.0019	0.0126	613	2987	3.43	3880	B2	225
1291	7.74	1.92×10^5	0.0013	0.0137	565	2918	3.28	3751	B2	225
1292	7.14	4.96×10^4	0.1410	0.0044	1555	4246	5.69	6225	C4	400

Table E.1: (continued)

shot	M_∞	Re_∞	α_∞	ρ_∞	T_∞	T_{v_∞}	p_∞	u_∞	cond.	A_e/A_*
		$L = 10$ cm		kg/m^3	K	K	kPa	m/s		
1293	7.07	4.94×10^4	0.1540	0.0045	1629	4273	6.03	6354	C4	400
1294	4.88	8.01×10^4	0.1350	0.0124	3175	4125	16.1	6058	C4	100
1295	8.34	2.75×10^5	0.0019	0.0188	670	2988	6.06	4400	B3	400
1296	8.39	2.80×10^5	0.0014	0.0187	609	2920	5.15	4225	B3	400
1297	5.06	8.27×10^4	0.0976	0.0120	2742	3967	13.1	5715	C0	100
1298	4.94	7.73×10^4	0.1270	0.0117	3022	4084	14.6	5960	C4	100
1299	8.81	1.28×10^5	0.0011	0.0077	433	3026	1.64	3735	B2	400
1300	7.84	1.86×10^5	0.0010	0.0130	524	2885	2.96	3659	B2	225
1302	8.76	1.32×10^5	0.0014	0.0081	454	3044	1.79	3808	B2	400
1303	6.12	5.75×10^4	0.1420	0.0064	2101	4155	8.47	6206	C4	225
1304	6.11	5.62×10^4	0.1480	0.0063	2112	4171	8.35	6227	C4	225
1305	8.75	1.30×10^5	0.0016	0.0080	461	3061	1.77	3830	B2	400
1306	6.09	5.74×10^4	0.1470	0.0064	2139	4168	8.64	6242	C4	225
1307	6.75	4.63×10^5	0.0000	0.0362	412	2298	7.25	2798	A0	100
1308	6.84	4.22×10^5	0.0000	0.0319	353	2256	5.31	2616	A1	100
1309	7.21	7.07×10^4	0.0749	0.0063	1426	4010	3.76	5796	C0	400
1310	7.41	7.06×10^4	0.0570	0.0060	1256	3929	3.28	5535	C1	400
1311	6.84	3.98×10^5	0.0000	0.0301	352	2269	4.97	2615	A1	100
1312	6.84	4.02×10^5	0.0000	0.0304	357	2273	5.23	2633	A1	100
1313	7.34	6.85×10^4	0.0630	0.0059	1309	3960	3.42	5621	C1	400
1314	7.37	7.24×10^4	0.0567	0.0062	1286	3922	3.52	5567	C1	400
1315	7.69	1.75×10^5	0.0020	0.0127	608	2995	3.29	3867	B2	225
1316	7.74	1.85×10^5	0.0014	0.0132	570	2934	3.23	3769	B2	225
1317	6.10	5.56×10^4	0.1530	0.0062	2137	4183	8.40	6266	C4	225
1318	6.07	5.35×10^4	0.1660	0.0060	2181	4214	8.39	6354	C4	225

Table E.1: (continued)

shot	M_∞	Re_∞	α_∞	ρ_∞	T_∞	T_{v_∞}	p_∞	u_∞	cond.	A_e/A_*
		$L = 10$ cm		kg/m^3	K	K	kPa	m/s		
1319	6.12	5.59×10^4	0.1480	0.0062	2105	4173	8.27	6223	C4	225
1320	6.09	5.39×10^4	0.1610	0.0060	2152	4204	8.27	6311	C4	225
1321	6.06	5.65×10^4	0.1560	0.0064	2188	4187	8.82	6314	C4	225
1322	8.39	2.76×10^5	0.0017	0.0185	643	2964	5.35	4340	B3	400
1323	4.95	1.81×10^5	0.0465	0.0278	2956	3730	31.4	5641	C0	100
1324	4.85	1.61×10^5	0.0628	0.0257	3204	3877	31.8	5814	C3	100
1725	10.70	8.60×10^4	0.0000	0.0038	151	1717	0.33	2693	A0	400
1727	6.87	2.08×10^5	0.0000	0.0160	405	2529	3.11	2818	A0	100
1729	6.77	9.56×10^4	0.0003	0.0078	537	2957	2.70	3193	B1	100
1730	7.28	1.11×10^5	0.0000	0.0074	188	1398	0.46	2036	A0	100
1731	7.81	2.43×10^5	0.0000	0.0155	270	1978	1.42	2614	A0	100
1732	5.35	6.88×10^4	0.0848	0.0091	2256	3912	8.42	5438	C0	100
1733	5.13	4.78×10^4	0.1830	0.0067	2764	4193	7.74	6091	C0	100
1734	5.10	4.93×10^4	0.1940	0.0070	2833	4230	8.63	6171	C0	100
1735	5.04	5.17×10^4	0.1830	0.0074	2841	4214	9.17	6075	C0	100
1736	5.09	5.78×10^4	0.1440	0.0082	2691	4110	9.28	5844	C0	100
1737	5.14	6.51×10^4	0.1140	0.0091	2554	4019	9.73	5662	C0	100
1740	6.35	5.90×10^4	0.1100	0.0061	1773	4094	6.43	5812	C2	225
1741	6.39	5.76×10^4	0.1070	0.0059	1724	4093	6.06	5756	C2	225
1742	8.91	6.21×10^4	0.0004	0.0036	362	3191	0.65	3450	B1	400
1743	8.87	5.68×10^4	0.0008	0.0033	385	3271	0.64	3543	B1	400
1744	6.37	5.75×10^4	0.1100	0.0060	1748	4098	6.17	5791	C2	225
1745	8.89	5.69×10^4	0.0005	0.0033	369	3242	0.61	3479	B1	400
1746	8.89	5.71×10^4	0.0005	0.0033	370	3242	0.62	3484	B1	400
1747	6.38	5.76×10^4	0.1100	0.0060	1749	4097	6.18	5798	C2	225

Table E.1: (continued)

shot	M_∞	Re_∞	α_∞	ρ_∞	T_∞	T_{v_∞}	p_∞	u_∞	cond.	A_e/A_*
		$L = 10$ cm		kg/m^3	K	K	kPa	m/s		
1748	6.83	1.21×10^6	0.0000	0.0925	384	2021	16.8	2724	A3	100
1749	6.43	2.61×10^5	0.0014	0.0238	818	2829	9.50	3756	B2	100
1750	6.43	2.57×10^5	0.0014	0.0234	811	2834	9.92	3743	B2	100
1751	6.80	1.18×10^6	0.0000	0.0914	399	2041	17.3	2768	A3	100
1752	6.86	3.85×10^5	0.0000	0.0289	340	2263	5.64	2580	A1	100
1753	6.44	2.69×10^5	0.0012	0.0244	793	2803	11.4	3708	B2	100
1754	6.88	4.46×10^5	0.0000	0.0331	322	2198	5.40	2517	A1	100
1755	8.09	6.57×10^5	0.0000	0.0414	318	2220	6.49	2940	A2	225
1756	8.10	6.56×10^5	0.0000	0.0413	318	2220	6.37	2940	A2	225
1757	6.74	9.93×10^5	0.0000	0.0784	437	2123	16.3	2874	A2	100
1758	6.75	1.01×10^6	0.0000	0.0798	435	2117	16.1	2867	A2	100
1759	7.03	4.31×10^5	0.0000	0.0310	296	2126	2.95	2465	A1	100
1760	9.17	4.57×10^5	0.0000	0.0247	252	2298	3.15	2962	A2	400
1761	7.30	5.02×10^5	0.0000	0.0342	261	1909	3.30	2403	A1	100
1762	9.15	4.63×10^5	0.0000	0.0251	253	2297	3.24	2966	A2	400
1764	7.91	7.74×10^4	0.0007	0.0052	447	3115	1.09	3406	B1	225
1765	7.45	4.31×10^4	0.1100	0.0036	1273	4194	2.15	5775	C2	400
1766	5.16	7.05×10^4	0.1000	0.0098	2524	3972	9.50	5600	C2	100
1770	6.57	1.10×10^5	0.0014	0.0095	664	3044	3.86	3459	B1	100
1772	5.10	7.04×10^4	0.1100	0.0100	2644	4003	10.7	5701	C2	100
1774	8.86	5.55×10^4	0.0005	0.0033	370	3252	0.60	3469	B1	400
1775	7.41	4.33×10^4	0.1220	0.0036	1315	4231	2.17	5872	C2	400
1776	5.10	6.84×10^4	0.1140	0.0097	2642	4016	10.4	5709	C2	100
1777	6.35	5.45×10^4	0.1220	0.0057	1783	4134	5.14	5864	C2	225
1778	7.91	8.46×10^4	0.0005	0.0057	443	3077	1.10	3392	B1	225

Table E.1: (continued)

shot	M_∞	Re_∞	α_∞	ρ_∞	T_∞	T_{v_∞}	p_∞	u_∞	cond.	A_e/A_*
		$L = 10$ cm		kg/m^3	K	K	kPa	m/s		
1779	8.88	5.95×10^4	0.0004	0.0035	368	3220	0.64	3466	B1	400
1780	7.41	4.29×10^4	0.1240	0.0036	1319	4237	2.09	5890	C2	400
1781	7.93	8.24×10^4	0.0004	0.0055	428	3065	1.01	3339	B1	225
1782	8.86	5.81×10^4	0.0007	0.0034	385	3261	0.65	3539	B1	400
1783	7.91	8.21×10^4	0.0004	0.0055	437	3074	1.06	3367	B1	225
1784	6.34	5.51×10^4	0.1220	0.0057	1794	4134	5.29	5876	C2	225
1785	5.09	7.18×10^4	0.1090	0.0103	2661	4001	11.3	5703	C2	100
1786	8.91	5.80×10^4	0.0004	0.0034	365	3226	0.62	3467	B1	400
1787	7.91	8.07×10^4	0.0007	0.0055	453	3112	1.08	3428	B1	225
1788	7.39	4.29×10^4	0.1280	0.0036	1339	4246	2.09	5934	C2	400
1790	5.11	7.00×10^4	0.1090	0.0099	2623	4000	10.8	5690	C2	100
1792	8.95	6.15×10^4	0.0002	0.0035	344	3161	0.61	3381	B1	400
1793	7.92	8.44×10^4	0.0005	0.0057	440	3071	1.10	3384	B1	225
1795	7.40	4.08×10^4	0.1280	0.0034	1330	4247	2.06	5921	C2	400
1796	5.12	6.89×10^4	0.1100	0.0098	2612	4004	10.2	5687	C2	100
1798	6.63	1.11×10^5	0.0012	0.0095	648	3016	2.92	3437	B1	100
1799	6.47	2.67×10^5	0.0013	0.0243	817	2821	8.18	3777	B2	100

Table E.2: Computed conditions in region 1, sorted by shot number.

shot no.	M_1	Re_{x_1}	α_1	ρ_1 kg/m^3	T_1 K	T_{v_1} K	p_1 kPa	u_1 m/s	cond.	A_e/A_*	θ_1
1280	2.65	4.47×10^4	0.1928	0.0220	7082	7200	55.2	5065	C4	225	30°
1283	2.66	5.23×10^4	0.1757	0.0231	6985	7090	56.3	5005	C4	225	30°
1285	2.85	9.24×10^4	0.0011	0.0300	2747	2984	24.5	3052	B2	400	30°
1288	2.64	4.89×10^4	0.1436	0.0246	6982	7082	58.4	4880	C4	225	30°
1290	2.29	1.23×10^5	0.0019	0.0500	3774	3516	56.1	2870	B2	225	35°
1291	2.30	1.38×10^5	0.0013	0.0517	3518	3266	54.1	2788	B2	225	35°
1292	2.08	3.32×10^4	0.2601	0.0192	7060	7161	50.7	4108	C4	400	40°
1293	2.09	3.04×10^4	0.2861	0.0200	7128	7232	54.4	4195	C4	400	40°
1294	3.60	9.07×10^4	0.1343	0.0277	5111	5019	47.7	5669	C4	100	15°
1295	5.09	2.67×10^5	0.0019	0.0452	1613	2985	21.7	4174	B3	400	15°
1296	5.07	2.26×10^5	0.0014	0.0467	1498	2919	20.8	4003	B3	400	15°
1297	3.67	8.51×10^4	0.0971	0.0279	4561	4331	41.5	5346	C0	100	15°
1298	3.60	7.25×10^4	0.1267	0.0270	4971	4739	44.8	5567	C4	100	15°
1300	2.79	1.56×10^5	0.0010	0.0461	2730	2876	37.4	2973	B2	225	30°
1302	2.87	9.01×10^4	0.0014	0.0280	2810	3034	23.4	3106	B2	400	30°
1303	2.67	5.40×10^4	0.1665	0.0225	6935	7039	54.1	4980	C4	225	30°
1304	2.64	4.74×10^4	0.1723	0.0223	7024	7135	54.4	4982	C4	225	30°
1305	2.86	8.42×10^4	0.0016	0.0277	2857	3051	23.5	3120	B2	400	30°
1306	2.63	4.18×10^4	0.1716	0.0232	7108	7227	57.4	4986	C4	225	30°
1309	4.58	4.58×10^4	0.0748	0.0134	3150	3982	13.5	5473	C0	400	15°
1310	4.66	4.33×10^4	0.0569	0.0134	2827	3912	11.9	5228	C1	400	15°
1311	4.53	5.03×10^5	0.0000	0.0852	715	2269	18.1	2469	A1	100	15°
1314	4.64	4.11×10^4	0.0567	0.0142	2886	3905	12.9	5257	C1	400	15°
1315	4.82	9.39×10^4	0.0020	0.0340	1383	2994	14.0	3656	B2	225	15°
1316	4.86	1.59×10^5	0.0014	0.0346	1292	2934	13.3	3567	B2	225	15°

Table E.2: (continued)

shot no.	M_1	Re_{x_1}	α_1	ρ_1 kg/m^3	T_1 K	T_{v_1} K	p_1 kPa	u_1 m/s	cond.	A_e/A_*	θ_1
1317	4.07	3.96×10^4	0.1524	0.0136	4238	4204	19.8	5889	C4	225	15°
1319	4.11	4.94×10^4	0.1472	0.0133	4134	4182	18.8	5858	C4	225	15°
1320	4.04	3.15×10^4	0.1606	0.0134	4303	4227	19.8	5927	C4	225	15°
1321	4.09	5.31×10^4	0.1557	0.0134	4259	4233	19.6	5946	C4	225	15°
1322	5.12	2.80×10^5	0.0017	0.0446	1553	2962	20.6	4119	B3	400	15°
1735	2.50	5.97×10^4	0.2313	0.0298	6907	6986	75.1	4808	C0	100	30°
1736	2.49	6.79×10^4	0.1764	0.0323	6816	6891	76.8	4634	C0	100	30°
1740	2.63	4.25×10^4	0.1140	0.0203	6618	6698	44.5	4654	C2	225	30°
1741	2.62	4.06×10^4	0.1106	0.0196	6530	6601	42.2	4610	C2	225	30°
1742	2.84	3.39×10^4	0.0004	0.0134	2339	3185	9.3	2799	B1	400	30°
1743	2.86	3.54×10^4	0.0008	0.0122	2445	3262	8.8	2883	B1	400	30°
1744	2.63	4.30×10^4	0.1141	0.0196	6554	6636	42.4	4645	C2	225	30°
1745	2.89	4.15×10^4	0.0005	0.0119	2326	3233	8.3	2841	B1	400	30°
1746	2.88	3.90×10^4	0.0005	0.0121	2342	3234	8.4	2842	B1	400	30°
1747	2.66	4.79×10^4	0.1142	0.0194	6496	6585	41.6	4670	C2	225	30°
1750	2.62	2.67×10^5	0.0014	0.0925	3165	3007	87.0	3010	B2	100	30°
1752	2.66	4.14×10^5	0.0000	0.1177	1471	2259	51.4	2079	A1	100	30°
1753	2.64	2.98×10^5	0.0012	0.0962	3087	2954	88.2	2989	B2	100	30°
1754	2.68	5.18×10^5	0.0000	0.1330	1388	2195	54.8	2033	A1	100	30°
1756	2.81	5.84×10^5	0.0000	0.1521	1740	2210	78.6	2391	A2	225	30°
1757	2.66	1.16×10^6	0.0000	0.3115	1833	2106	169.5	2320	A2	100	30°
1774	5.28	6.77×10^4	0.0005	0.0088	937	3252	2.4	3297	B1	400	15°
1775	4.65	4.19×10^4	0.1217	0.0076	2987	4198	7.6	5558	C2	400	15°
1776	3.68	8.28×10^4	0.1130	0.0224	4447	4294	32.9	5346	C2	100	15°
1777	4.23	5.47×10^4	0.1212	0.0119	3572	4083	14.1	5528	C2	225	15°

Table E.2: (continued)

shot no.	M_1	Re_{x_1}	α_1	ρ_1 kg/m^3	T_1 K	T_{v_1} K	p_1 kPa	u_1 m/s	cond.	A_e/A_*	θ_1
1778	4.97	1.02×10^5	0.0005	0.0152	1008	3077	4.6	3217	B1	225	15°
1779	5.22	4.81×10^4	0.0004	0.0098	955	3220	2.8	3288	B1	400	15°
1780	4.59	3.01×10^4	0.1240	0.0079	3056	4213	8.0	5563	C2	400	15°
1781	4.92	7.14×10^4	0.0004	0.0153	991	3065	4.5	3161	B1	225	15°
1782	5.24	5.35×10^4	0.0007	0.0095	988	3261	2.8	3360	B1	400	15°
1783	4.93	8.13×10^4	0.0004	0.0153	1006	3074	4.6	3188	B1	225	15°
1784	4.20	4.89×10^4	0.1215	0.0122	3620	4089	14.7	5533	C2	225	15°
1785	3.66	7.75×10^4	0.1089	0.0239	4495	4293	35.4	5334	C2	100	15°
1786	1.84	2.04×10^4	0.0004	0.0138	3664	3308	15.0	2268	B1	400	40°
1787	1.81	3.43×10^4	0.0007	0.0228	3673	3294	24.9	2236	B1	225	40°
1788	1.97	2.19×10^4	0.2084	0.0150	7306	7452	39.4	3868	C2	400	40°
1790	1.96	8.89×10^4	0.2305	0.0560	6660	6691	136.1	3714	C2	100	40°
1792	1.85	2.70×10^4	0.0002	0.0140	3469	3224	14.4	2220	B1	400	40°
1793	1.80	4.41×10^4	0.0005	0.0233	3582	3261	24.8	2201	B1	225	40°
1795	1.99	2.40×10^4	0.2083	0.0147	7232	7368	38.2	3869	C2	400	40°
1796	1.97	9.15×10^4	0.2307	0.0550	6659	6685	133.7	3716	C2	100	40°

Table E.3: Computed conditions in region 2, sorted by shot number.

shot no.	M_2	α_2	ρ_2 kg/m^3	T_2 K	T_{v_2} K	p_2 kPa	u_2 m/s	cond.	A_e/A_*	θ_1	θ_{sep}
1280	2.54	0.2060	0.0267	7234	7350	69.3	4938	C4	225	30°	4.51°
1283	2.52	0.1839	0.0283	7287	7375	72.4	4873	C4	225	30°	4.49°
1285	2.63	0.0011	0.0371	3033	2987	33.5	2959	B2	400	30°	5.20°
1288	2.51	0.1573	0.0311	7167	7275	76.6	4737	C4	225	30°	5.33°
1290	2.11	0.0019	0.0616	4082	3665	74.7	2748	B2	225	35°	5.48°
1291	2.10	0.0013	0.0642	3847	3351	73.4	2660	B2	225	35°	5.62°
1292	1.94	0.2698	0.0238	7356	7458	66.1	3931	C4	400	40°	5.57°
1293	1.98	0.3009	0.0248	7252	7367	69.5	4035	C4	400	40°	5.71°
1294	3.42	0.1340	0.0329	5498	5274	60.9	5589	C4	100	15°	3.28°
1295	4.55	0.0019	0.0661	1949	2982	38.3	4097	B3	400	15°	5.35°
1296	4.62	0.0014	0.0651	1751	2916	33.9	3943	B3	400	15°	4.85°
1297	3.45	0.0968	0.0346	4976	4670	56.0	5254	C0	100	15°	4.13°
1298	3.39	0.1263	0.0334	5401	5249	60.2	5470	C4	100	15°	4.31°
1300	2.56	0.0010	0.0579	3030	2882	52.1	2872	B2	225	30°	5.20°
1302	2.61	0.0014	0.0358	3159	3040	33.6	2993	B2	400	30°	5.90°
1303	2.48	0.1756	0.0290	7372	7456	74.5	4805	C4	225	30°	5.54°
1304	2.50	0.1853	0.0282	7276	7392	72.2	4828	C4	225	30°	5.33°
1305	2.62	0.0016	0.0350	3185	3059	33.2	3014	B2	400	30°	5.66°
1306	2.54	0.1878	0.0284	7156	7269	71.6	4864	C4	225	30°	4.70°
1309	4.02	0.0747	0.0196	3893	3979	24.3	5340	C0	400	15°	6.58°
1310	4.24	0.0568	0.0178	3306	3881	18.4	5140	C1	400	15°	5.15°
1311	3.97	0.0000	0.1336	882	2269	35.0	2404	A1	100	15°	6.93°
1314	4.25	0.0566	0.0184	3337	3873	19.3	5174	C1	400	15°	5.21°
1315	4.42	0.0020	0.0431	1595	2991	20.5	3601	B2	225	15°	5.85°
1316	4.51	0.0014	0.0445	1464	2933	19.4	3520	B2	225	15°	4.09°

Table E.3: (continued)

shot no.	M_2	α_2	ρ_2 kg/m^3	T_2 K	T_{v_2} K	p_2 kPa	u_2 m/s	cond.	A_e/A_*	θ_1	θ_{sep}
1317	3.64	0.1520	0.0192	5017	4615	32.9	5740	C4	225	15°	6.32°
1319	3.76	0.1470	0.0175	4755	4315	28.4	5745	C4	225	15°	4.77°
1320	3.64	0.1601	0.0185	5051	4827	32.1	5778	C4	225	15°	6.89°
1321	3.78	0.1555	0.0171	4808	4332	28.2	5848	C4	225	15°	4.06°
1322	4.74	0.0017	0.0584	1769	2960	30.7	4069	B3	400	15°	3.71°
1735	2.38	0.2409	0.0358	7133	7219	94.2	4679	C0	100	30°	4.38°
1736	2.34	0.1878	0.0409	7106	7194	102.6	4469	C0	100	30°	5.54°
1740	2.49	0.1184	0.0243	6938	6998	56.0	4534	C2	225	30°	4.45°
1741	2.45	0.1157	0.0244	6938	7005	56.1	4459	C2	225	30°	5.45°
1742	2.77	0.0004	0.0142	2415	3180	10.2	2771	B1	400	30°	2.37°
1743	2.71	0.0008	0.0140	2616	3257	10.9	2823	B1	400	30°	3.86°
1744	2.50	0.1173	0.0230	6883	6917	52.5	4532	C2	225	30°	4.07°
1745	2.68	0.0005	0.0145	2556	3230	11.0	2760	B1	400	30°	4.70°
1746	2.70	0.0005	0.0143	2539	3230	10.8	2772	B1	400	30°	4.26°
1747	2.52	0.1159	0.0226	6880	6823	51.5	4556	C2	225	30°	3.71°
1750	2.47	0.0014	0.1085	3382	3065	109.0	2933	B2	100	30°	3.93°
1752	2.44	0.0000	0.1467	1626	2257	70.8	2006	A1	100	30°	5.34°
1753	2.41	0.0012	0.1213	3412	3017	123.0	2875	B2	100	30°	5.50°
1754	2.56	0.0000	0.1496	1461	2195	64.9	1997	A1	100	30°	2.34°
1756	2.74	0.0000	0.1630	1795	2209	86.9	2367	A2	225	30°	1.55°
1757	2.49	0.0000	0.3735	1983	2105	219.9	2257	A2	100	30°	3.52°
1774	4.75	0.0005	0.0125	1120	3252	4.2	3244	B1	400	15°	4.65°
1775	3.97	0.1216	0.0120	3859	4190	15.4	5400	C2	400	15°	6.80°
1776	3.40	0.1129	0.0288	4989	4496	47.4	5236	C2	100	15°	4.55°
1777	3.80	0.1212	0.0164	4239	4095	23.1	5406	C2	225	15°	5.25°

Table E.3: (continued)

shot no.	M_2	α_2	ρ_2 kg/m^3	T_2 K	T_{v_2} K	p_2 kPa	u_2 m/s	cond.	A_e/A_*	θ_1	θ_{sep}
1778	4.58	0.0005	0.0200	1155	3077	6.9	3172	B1	225	15°	3.97°
1779	4.66	0.0004	0.0139	1158	3220	4.8	3230	B1	400	15°	6.10°
1780	4.01	0.1239	0.0115	3824	4187	14.7	5426	C2	400	15°	6.55°
1781	4.54	0.0004	0.0199	1135	3065	6.7	3117	B1	225	15°	4.40°
1782	4.75	0.0007	0.0129	1165	3261	4.5	3309	B1	400	15°	4.73°
1783	4.46	0.0004	0.0212	1190	3074	7.5	3133	B1	225	15°	5.17°
1784	3.80	0.1213	0.0165	4251	4111	23.3	5418	C2	225	15°	5.18°
1785	3.42	0.1086	0.0302	4971	4596	49.4	5232	C2	100	15°	4.50°
1786	1.68	0.0004	0.0159	3909	3447	18.4	2137	B1	400	40°	5.99°
1787	1.69	0.0007	0.0254	3844	3451	29.0	2134	B1	225	40°	4.61°
1788	1.86	0.2305	0.0191	7301	7441	50.8	3673	C2	400	40°	6.64°
1790	1.84	0.2399	0.0683	6873	6908	172.8	3548	C2	100	40°	5.44°
1792	1.67	0.0002	0.0166	3743	3279	18.5	2083	B1	400	40°	5.90°
1793	1.66	0.0005	0.0270	3808	3340	30.5	2084	B1	225	40°	5.00°
1795	1.87	0.2197	0.0177	7402	7518	47.3	3709	C2	400	40°	5.00°
1796	1.85	0.2381	0.0659	6880	6920	166.7	3567	C2	100	40°	5.00°

Table E.4: Computed conditions in region 3, sorted by shot number.

shot no.	M_3	α_3	ρ_3 kg/m^3	T_3 K	T_{v_3} K	p_3 kPa	u_3 m/s	cond.	A_e/A_*	θ_1	θ_w
1280	2.06	0.2564	0.0542	8072	8480	163.0	4342	C4	225	30°	20°
1283	2.08	0.2295	0.0556	8050	8455	163.2	4325	C4	225	30°	20°
1285	2.02	0.0011	0.0687	4008	3112	81.8	2607	B2	400	30°	20°
1288	1.80	0.2675	0.0936	7673	7945	270.2	3716	C4	225	30°	30°
1290	1.63	0.0019	0.1072	4929	4381	157.1	2339	B2	225	35°	20°
1291	1.81	0.0013	0.0888	4357	3595	115.0	2433	B2	225	35°	15°
1292	1.67	0.2858	0.0343	7979	8121	104.4	3558	C4	400	40°	15°
1293	1.55	0.3359	0.0440	8081	8360	140.9	3399	C4	400	40°	20°
1294	2.54	0.1466	0.0763	7772	7907	201.8	4962	C4	100	15°	20°
1295	3.26	0.0019	0.1612	3229	2997	154.8	3781	B3	400	15°	20°
1296	2.70	0.0014	0.2498	3770	3281	279.9	3376	B3	400	15°	30°
1297	2.19	0.1404	0.1174	7623	7850	302.8	4217	C0	100	15°	30°
1298	2.22	0.1938	0.1137	7660	7910	308.6	4428	C4	100	15°	30°
1300	2.15	0.0010	0.0876	3644	2950	94.9	2647	B2	225	30°	15°
1302	2.22	0.0014	0.0529	3775	3081	59.3	2779	B2	400	30°	15°
1303	2.19	0.1931	0.0437	8075	8258	125.0	4480	C4	225	30°	15°
1304	2.05	0.2326	0.0559	8039	8438	164.5	4262	C4	225	30°	20°
1305	2.02	0.0016	0.0631	4170	3209	78.2	2663	B2	400	30°	20°
1306	1.78	0.3064	0.0847	7773	8076	255.3	3769	C4	225	30°	30°
1309	2.45	0.0766	0.0615	7320	7042	143.7	4462	C0	400	15°	30°
1310	2.48	0.0571	0.0609	6719	6184	128.3	4285	C1	400	15°	30°
1311	2.49	0.0000	0.4522	1656	2266	222.3	2067	A1	100	15°	30°
1314	2.07	0.0837	0.0891	7419	7749	212.5	3824	C1	400	15°	40°
1315	1.87	0.0020	0.1854	4519	3966	249.1	2561	B2	225	15°	40°
1316	2.45	0.0014	0.1621	3404	2996	164.0	2921	B2	225	15°	30°

Table E.4: (continued)

shot no.	M_3	α_3	ρ_3 kg/m^3	T_3 K	T_{v_3} K	p_3 kPa	u_3 m/s	cond.	A_e/A_*	θ_1	θ_w
1317	2.32	0.1927	0.0641	7994	8320	181.4	4723	C4	225	15°	30°
1319	2.72	0.1476	0.0401	7343	6481	100.2	5167	C4	225	15°	20°
1320	2.31	0.1948	0.0579	8233	8591	169.0	4763	C4	225	15°	30°
1321	2.89	0.1556	0.0341	7007	5786	82.0	5390	C4	225	15°	15°
1322	3.52	0.0017	0.1337	2817	2958	112.0	3813	B3	400	15°	15°
1735	1.94	0.2957	0.0714	7750	8021	212.8	4082	C0	100	30°	20°
1736	1.93	0.2298	0.0769	7750	8038	217.6	3935	C0	100	30°	20°
1740	1.81	0.1810	0.0584	8075	8456	165.3	3665	C2	225	30°	25°
1741	1.81	0.1669	0.0551	8113	8482	154.9	3662	C2	225	30°	25°
1742	1.82	0.0004	0.0352	3715	3215	38.8	2267	B1	400	30°	25°
1743	2.07	0.0008	0.0257	3501	3263	26.7	2501	B1	400	30°	20°
1744	1.95	0.1451	0.0445	8206	8469	124.2	3909	C2	225	30°	20°
1745	2.29	0.0005	0.0211	3046	3228	19.1	2580	B1	400	30°	10°
1746	2.24	0.0005	0.0222	3126	3229	20.6	2558	B1	400	30°	15°
1747	2.14	0.1247	0.0355	7951	7920	94.1	4178	C2	225	30°	15°
1750	1.69	0.0014	0.2418	4642	4301	333.6	2349	B2	100	30°	25°
1752	1.69	0.0000	0.3069	2296	2259	209.2	1646	A1	100	30°	25°
1753	1.89	0.0012	0.2136	4245	3604	269.5	2517	B2	100	30°	20°
1754	1.88	0.0000	0.2899	2006	2193	172.6	1714	A1	100	30°	20°
1756	1.92	0.0000	0.3350	2617	2234	260.2	2003	A2	225	30°	20°
1757	1.87	0.0000	0.6866	2626	2183	535.3	1951	A2	100	30°	20°
1774	3.72	0.0005	0.0246	1652	3252	12.1	3081	B1	400	15°	15°
1775	3.33	0.1216	0.0195	5024	4252	32.6	5170	C2	400	15°	15°
1776	2.84	0.1128	0.0489	6338	5387	102.4	4928	C2	100	15°	15°
1777	3.14	0.1211	0.0279	5589	4369	51.9	5133	C2	225	15°	15°

Table E.4: (continued)

shot no.	M_3	α_3	ρ_3 kg/m^3	T_3 K	T_{v_3} K	p_3 kPa	u_3 m/s	cond.	A_e/A_*	θ_1	θ_w
1778	3.50	0.0005	0.0416	1755	3077	21.7	2985	B1	225	15°	15°
1779	3.02	0.0004	0.0389	2206	3218	25.5	2895	B1	400	15°	25°
1780	2.62	0.1239	0.0299	6838	5545	68.1	4755	C2	400	15°	25°
1781	2.79	0.0004	0.0585	2297	3062	39.9	2728	B1	225	15°	25°
1782	3.28	0.0007	0.0326	2060	3260	19.9	3035	B1	400	15°	20°
1783	3.17	0.0004	0.0504	1986	3073	29.7	2877	B1	225	15°	20°
1784	2.78	0.1213	0.0361	6542	5320	78.6	4915	C2	225	15°	20°
1785	2.57	0.1099	0.0648	7071	6783	151.0	4695	C2	100	15°	20°
1786	1.19	0.0004	0.0251	4717	3638	35.2	1670	B1	400	40°	20°
1787	1.13	0.0007	0.0430	4740	3792	60.6	1585	B1	225	40°	20°
1788	1.47	0.2529	0.0311	8147	8333	94.3	3099	C2	400	40°	20°
1790	1.44	0.2734	0.1177	7444	7552	331.0	2949	C2	100	40°	20°
1792	1.36	0.0002	0.0225	4239	3341	28.3	1811	B1	400	40°	15°
1793	1.32	0.0005	0.0376	4340	3479	48.5	1778	B1	225	40°	15°
1795	1.58	0.2337	0.0256	8108	8185	76.0	3302	C2	400	40°	15°
1796	1.58	0.2544	0.0966	7415	7534	266.7	3182	C2	100	40°	15°

Appendix F Experimental Flow Visualization, Heat Flux, and Pressure Measurements

Each of the following pages contains data from a single experiment in T5, the pages being ordered by shot number. A flow visualization photograph is displayed at the top of the page if one is available in digitized format. The interferograms and shadowgraphs reconstructed from holograms are all printed to the same scale, but the full-field shadowgraphs are printed to a different scale. Experimental heat flux and pressure distributions, both spanwise and streamwise, are presented at the bottom of the page. The heat flux data is nondimensionalized according to Equation 2.12 and the pressure data is nondimensionalized according to Equation 2.14. Dimensional heat flux and pressure are shown for shots which lack a corresponding nozzle-flow computation to obtain free-stream parameters. The different symbols on spanwise distribution plots are defined in Figure 2.26 and repeated here;

- ♦ data from first wedge upstream of corner,
- ▲ data from second wedge downstream of corner.

The shots for which separation length was measured include additional information on the streamwise distribution plots; the measured location of separation is indicated by a vertical dotted line, the inviscid triple-wedge solution is shown on the pressure distribution plot, and various predictions using flat-plate boundary-layer theory with external conditions from inviscid triple-wedge computations are shown on the heat-flux distribution plot. These are described in Figure 4.3 and repeated here;

- ——— laminar prediction with $\alpha_w = \alpha_e$,
- – · – · · laminar prediction with $\alpha_w = 0$,
- – – – – turbulent prediction with $\alpha_w = \alpha_e$,
- — · · · — turbulent prediction with $\alpha_w = 0$,
- ○ predictions corrected using experimental pressure measurements.

no photograph

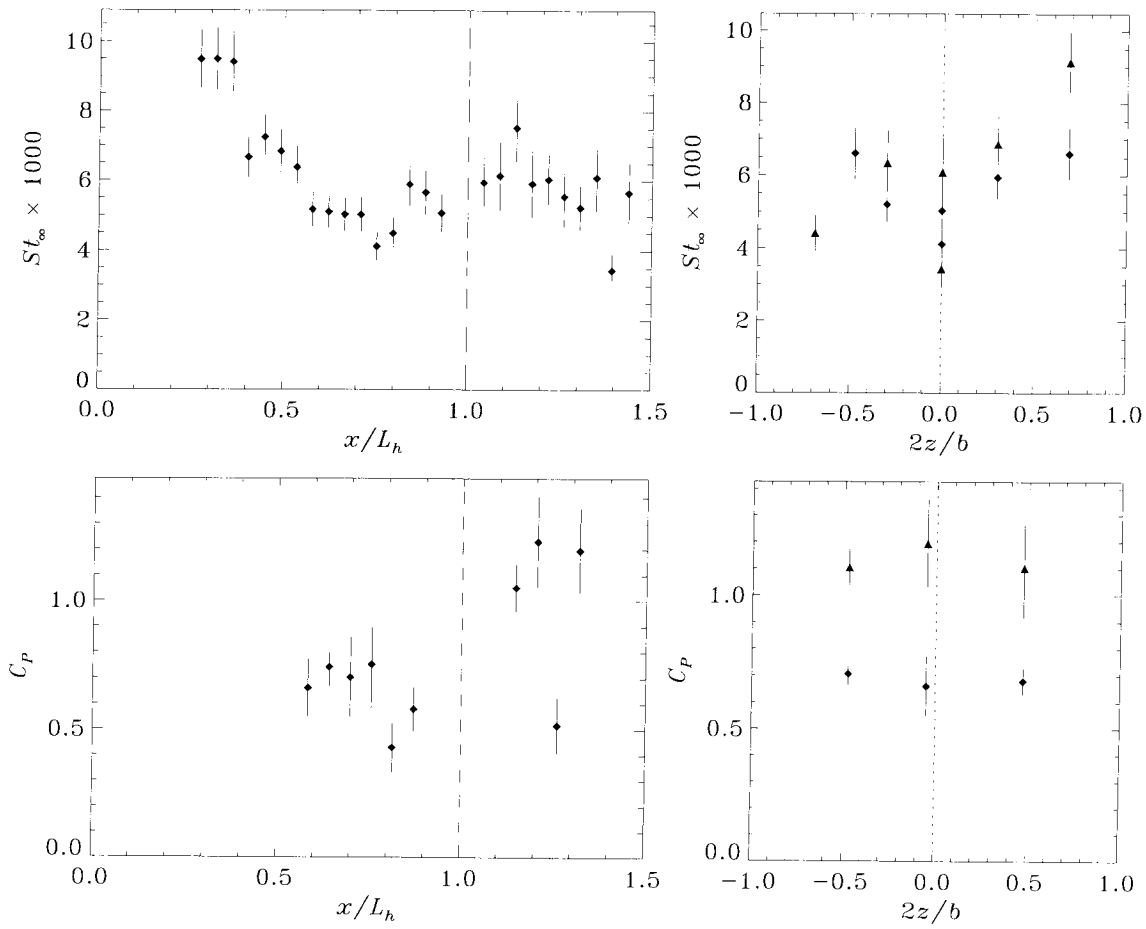

Shot 1278 (condition C0, $A_e/A_* = 225$, $\theta_1 = 30°$, $\theta_w = 5°$)

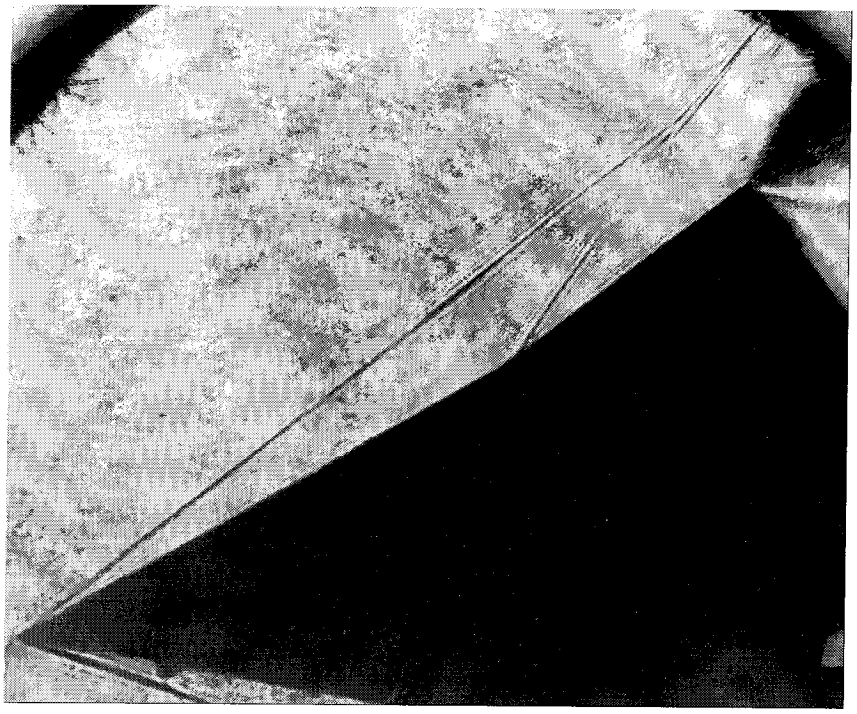

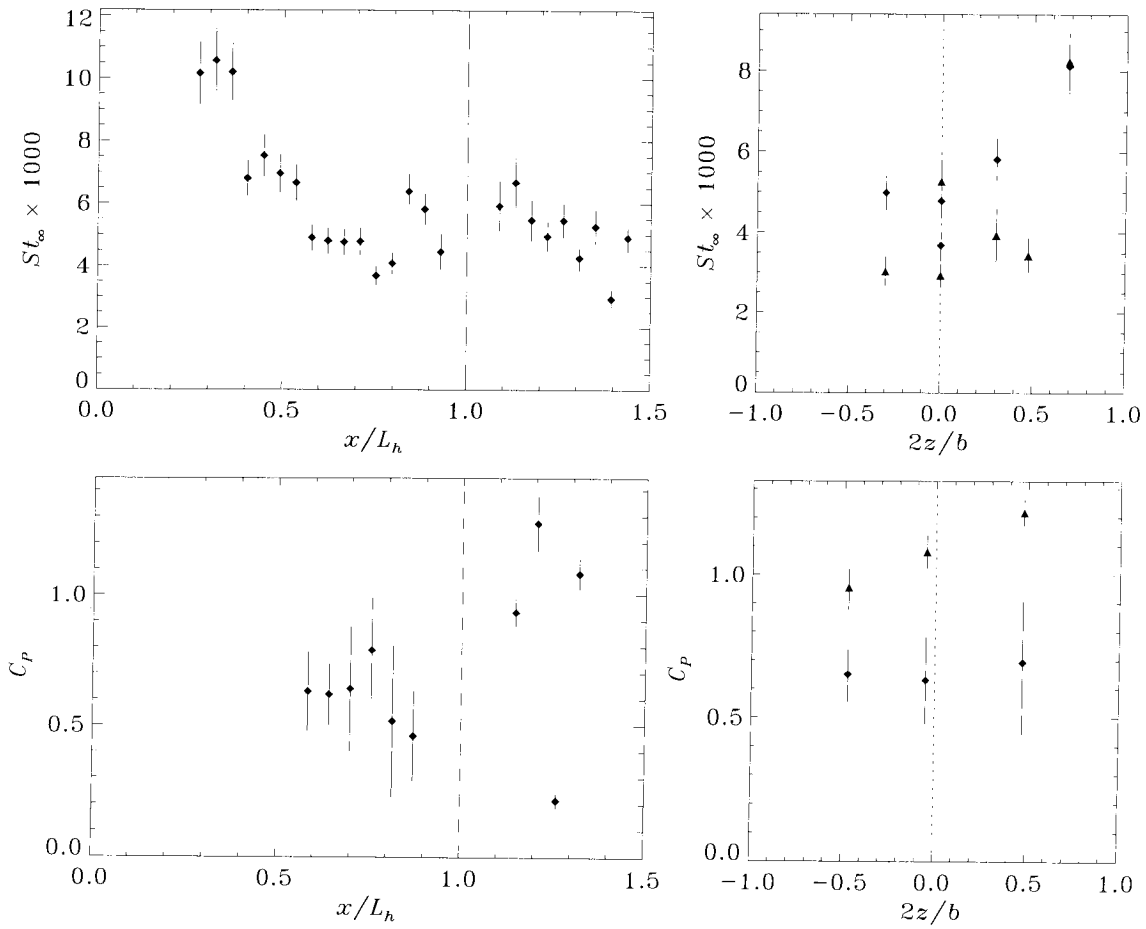

Shot 1279 (condition C0, $A_e/A_* = 225$, $\theta_1 = 30°$, $\theta_w = 5°$)

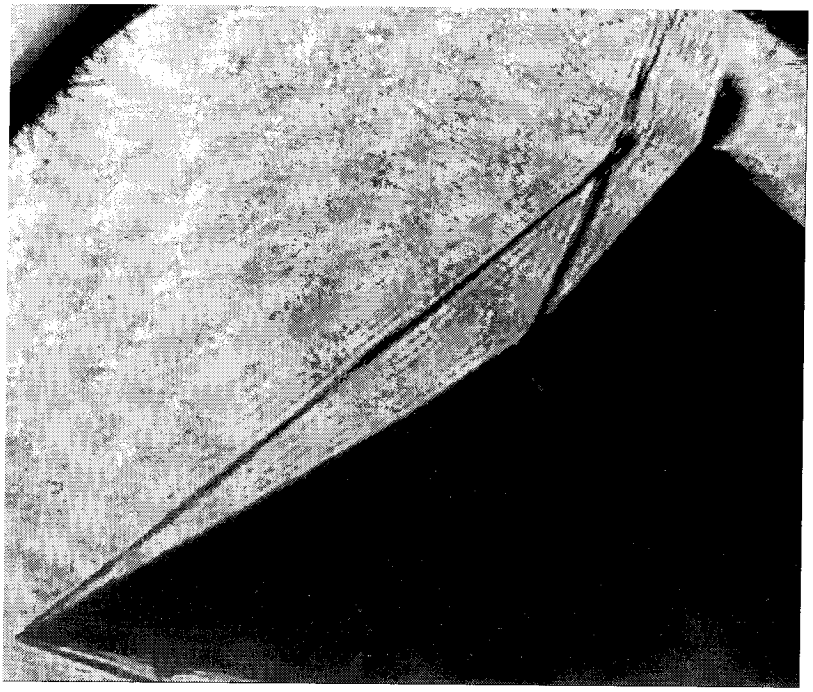

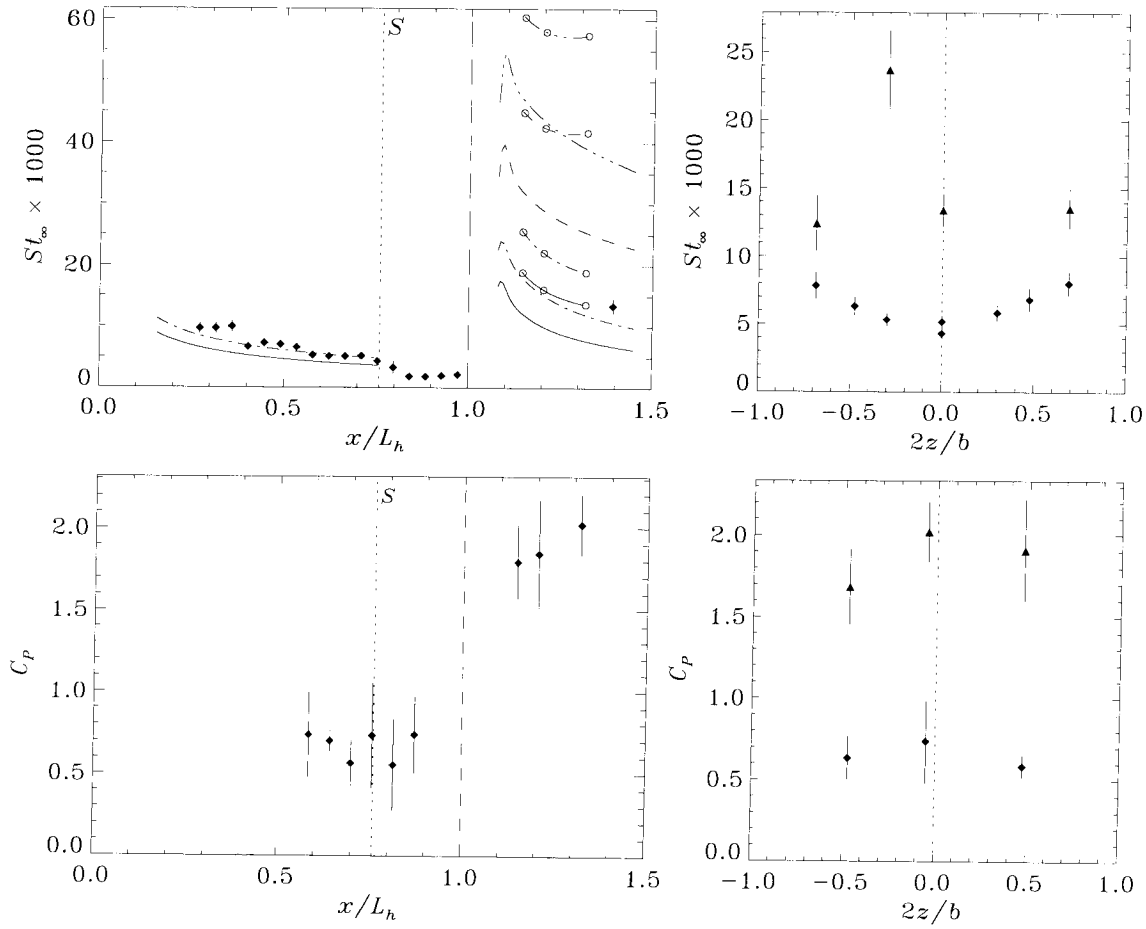

Shot 1280 (condition C4, $A_c/A_* = 225$, $\theta_1 = 30°$, $\theta_w = 20°$)

no photograph

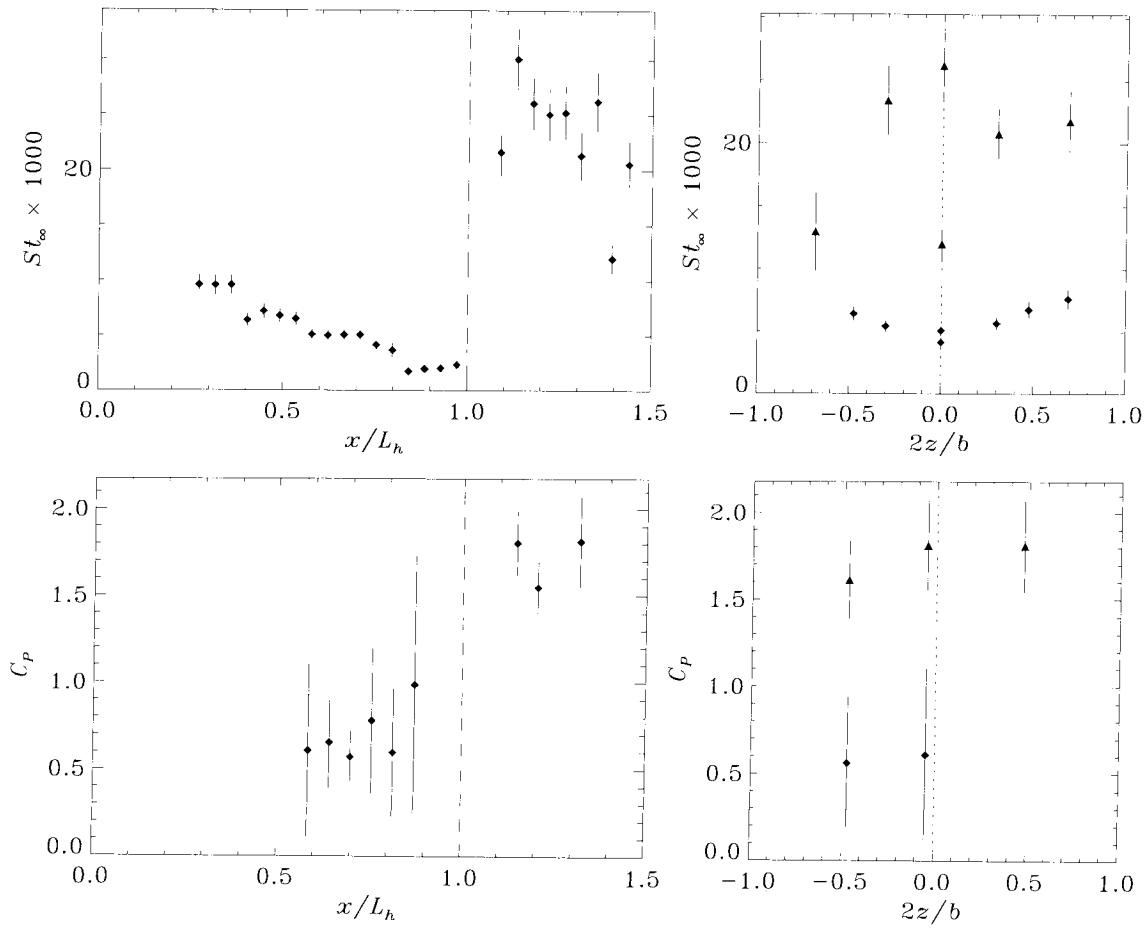

Shot 1281 (condition C4, $A_e/A_* = 225$, $\theta_1 = 30°$, $\theta_w = 20°$)

no photograph

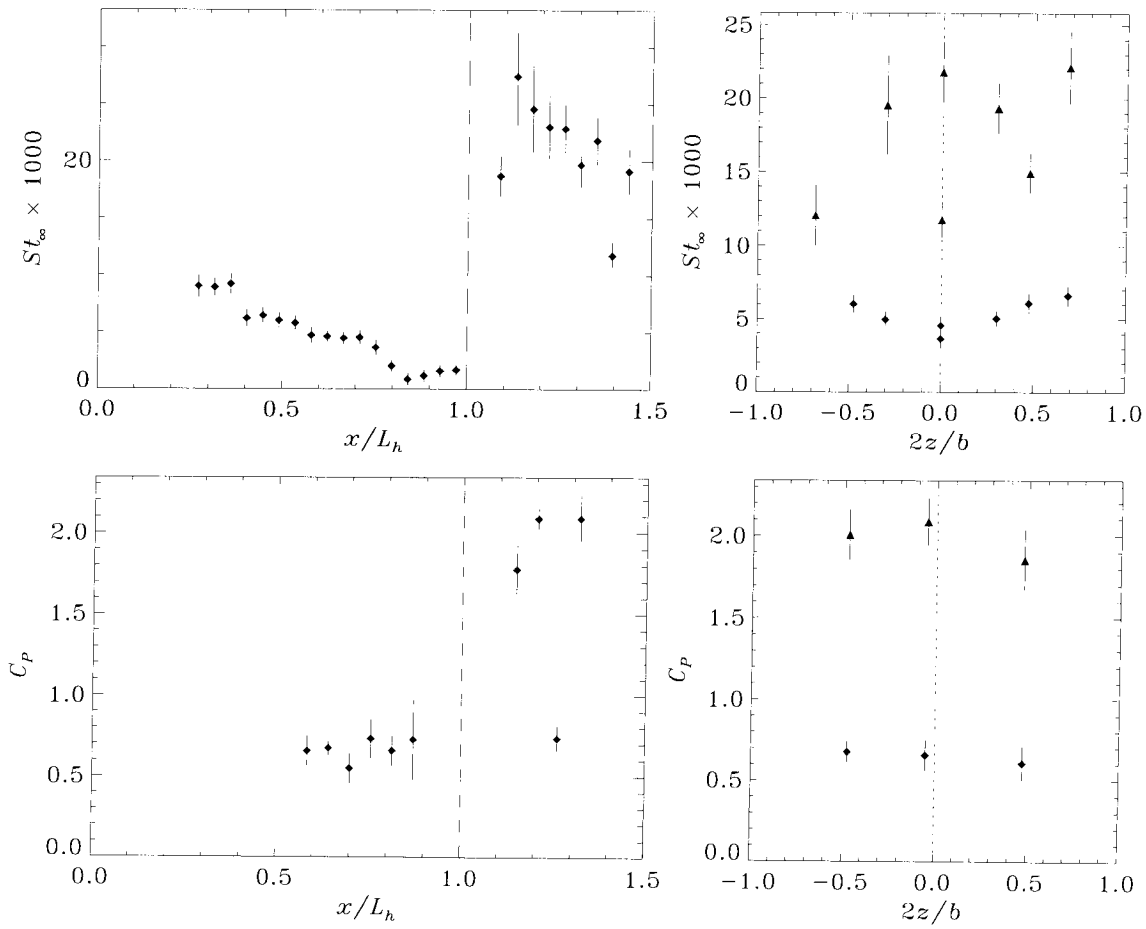

Shot 1282 (condition B0, $A_e/A_* = 400$, $\theta_1 = 30°$, $\theta_w = 20°$)

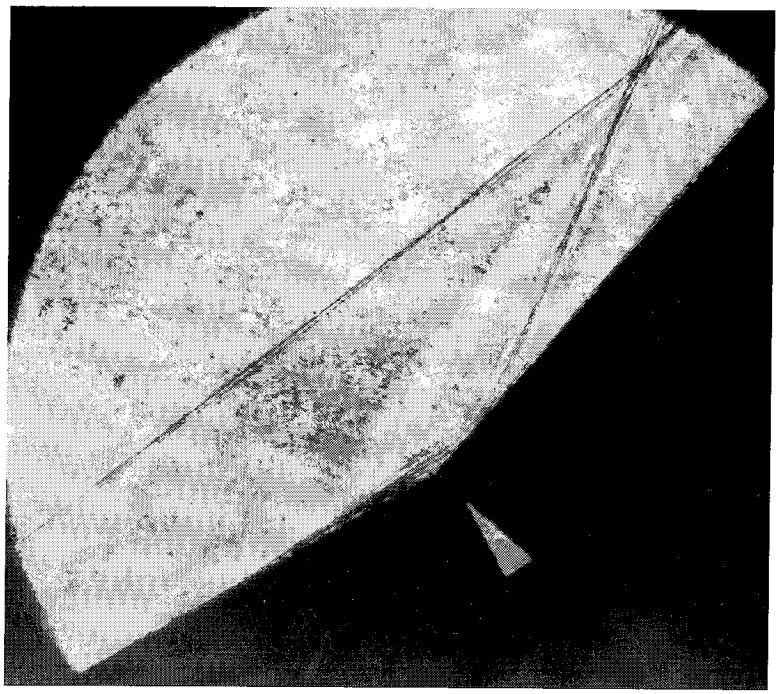

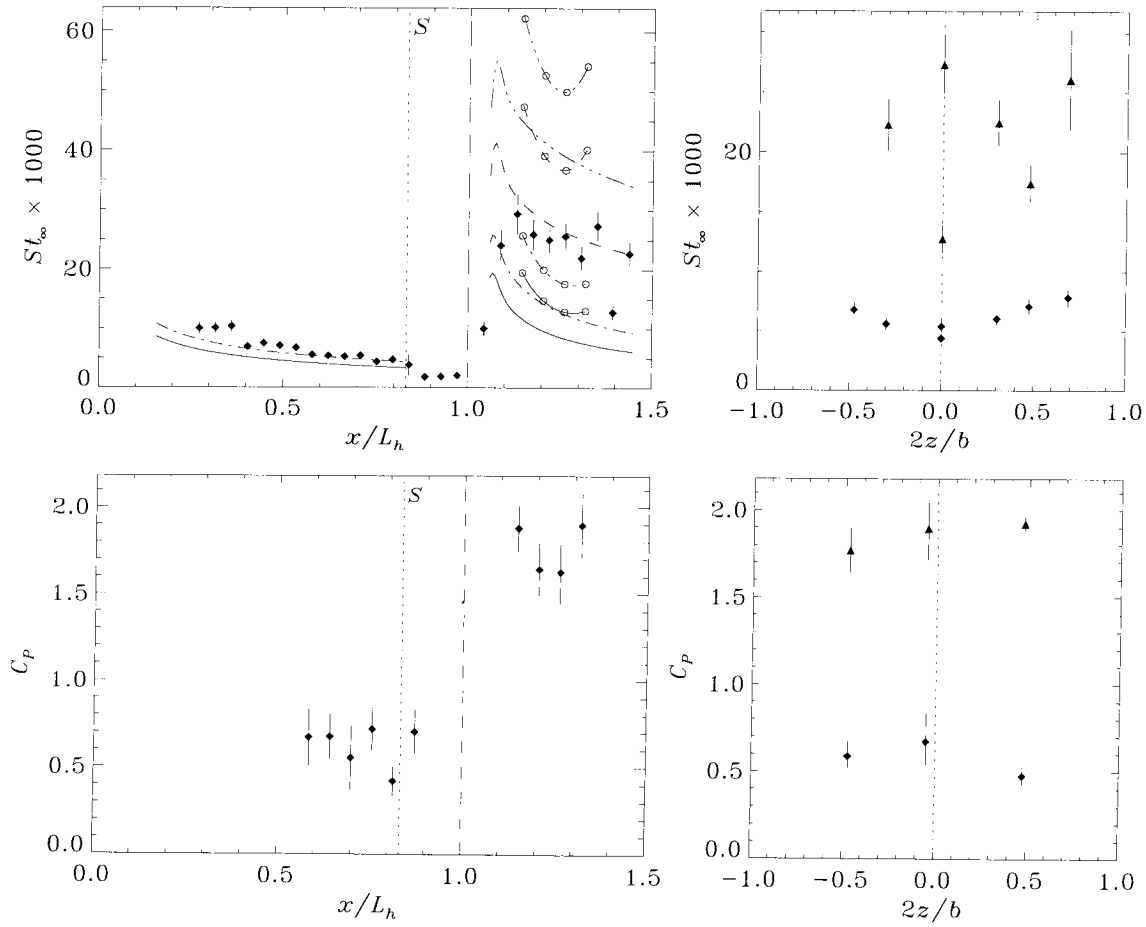

Shot 1283 (condition C4, $A_e/A_* = 225$, $\theta_1 = 30°$, $\theta_w = 20°$)

no photograph

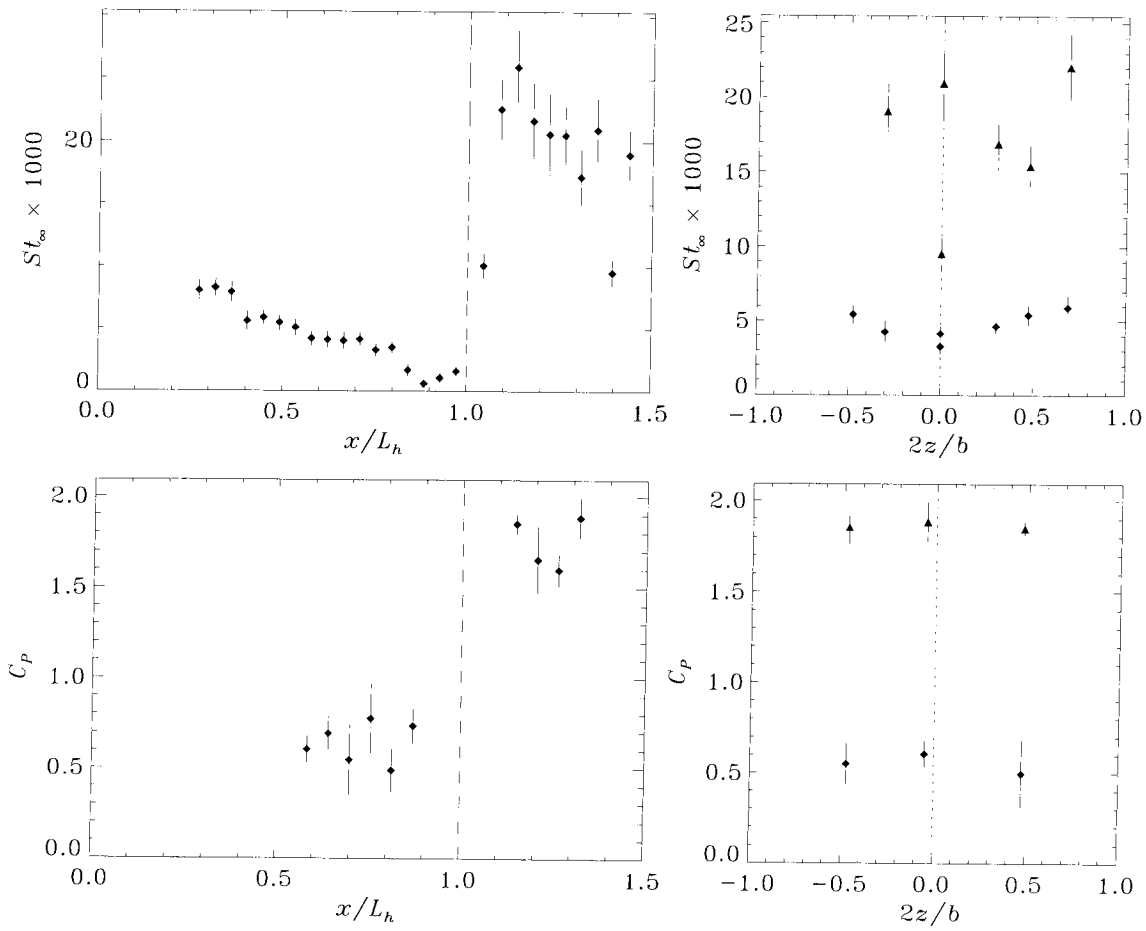

Shot 1284 (condition B2, $A_e/A_* = 400$, $\theta_1 = 30°$, $\theta_w = 20°$)

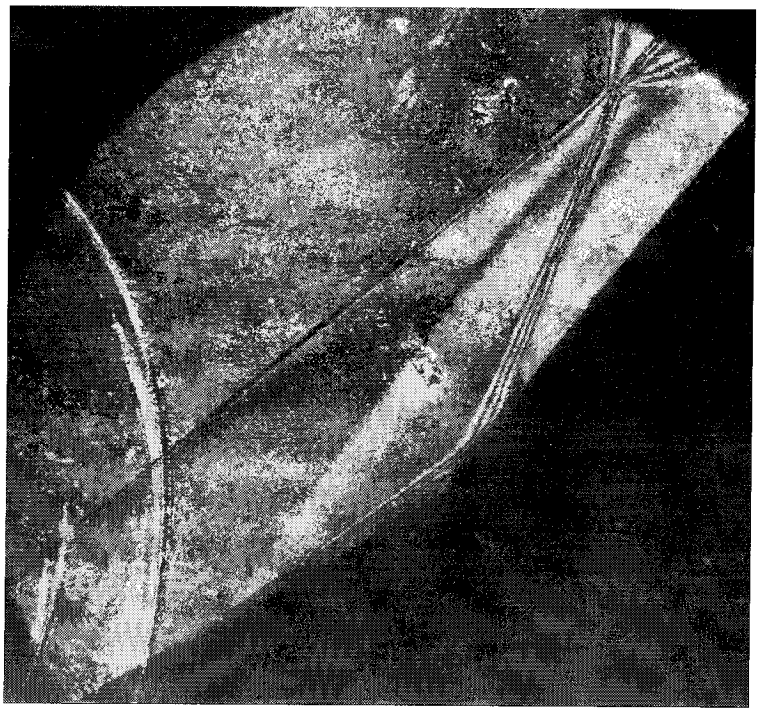

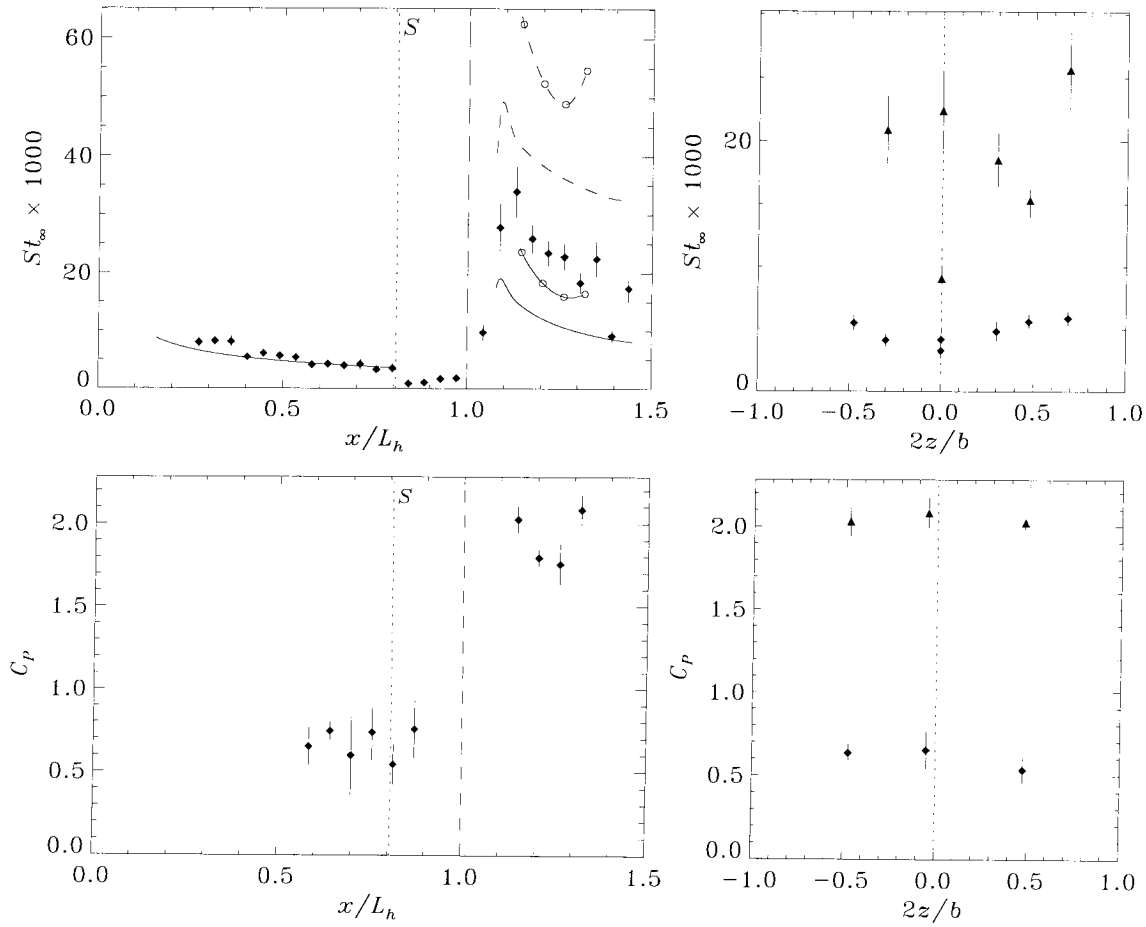

Shot 1285 (condition B2, $A_e/A_* = 400$, $\theta_1 = 30°$, $\theta_w = 20°$)

no photograph

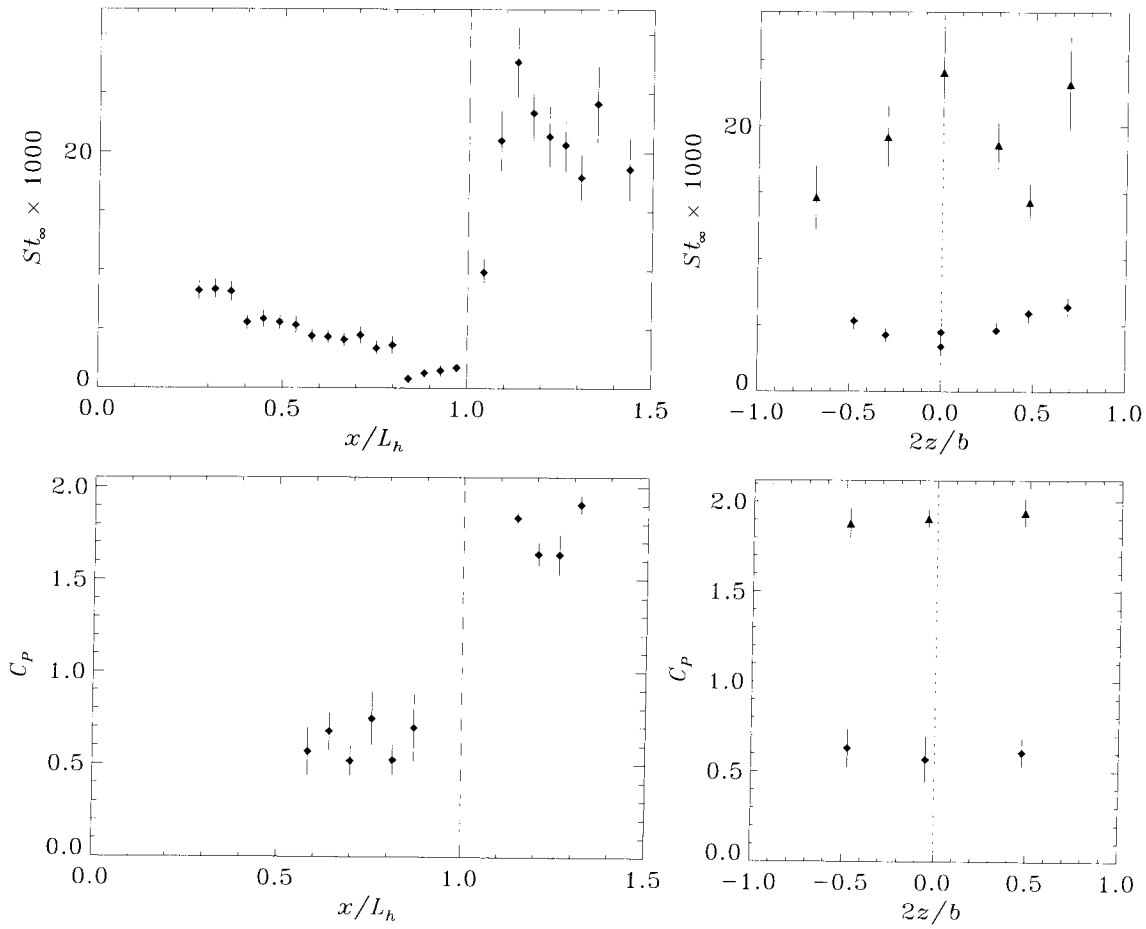

Shot 1286 (condition B0, $A_e/A_* = 400$, $\theta_1 = 30°$, $\theta_w = 20°$)

no photograph

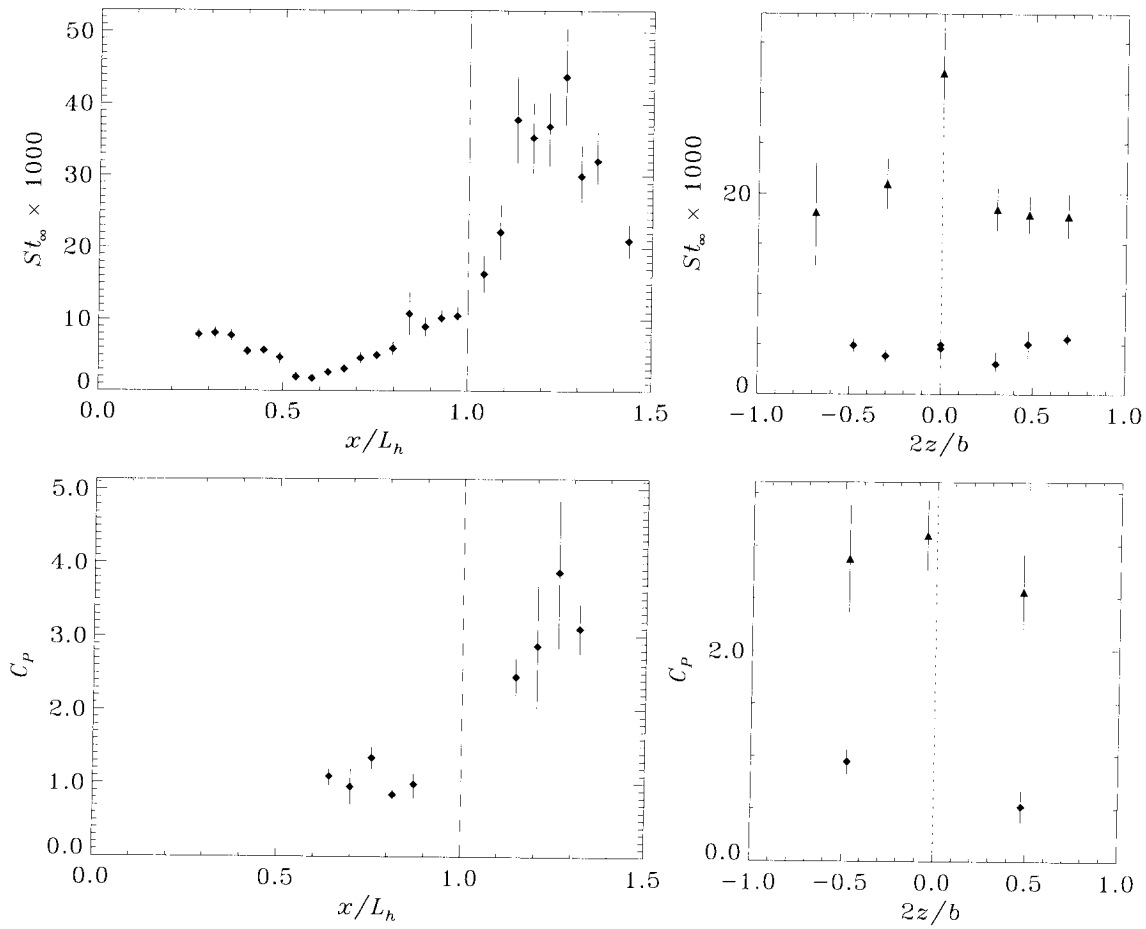

Shot 1287 (condition B0, $A_e/A_* = 400$, $\theta_1 = 30°$, $\theta_w = 30°$)

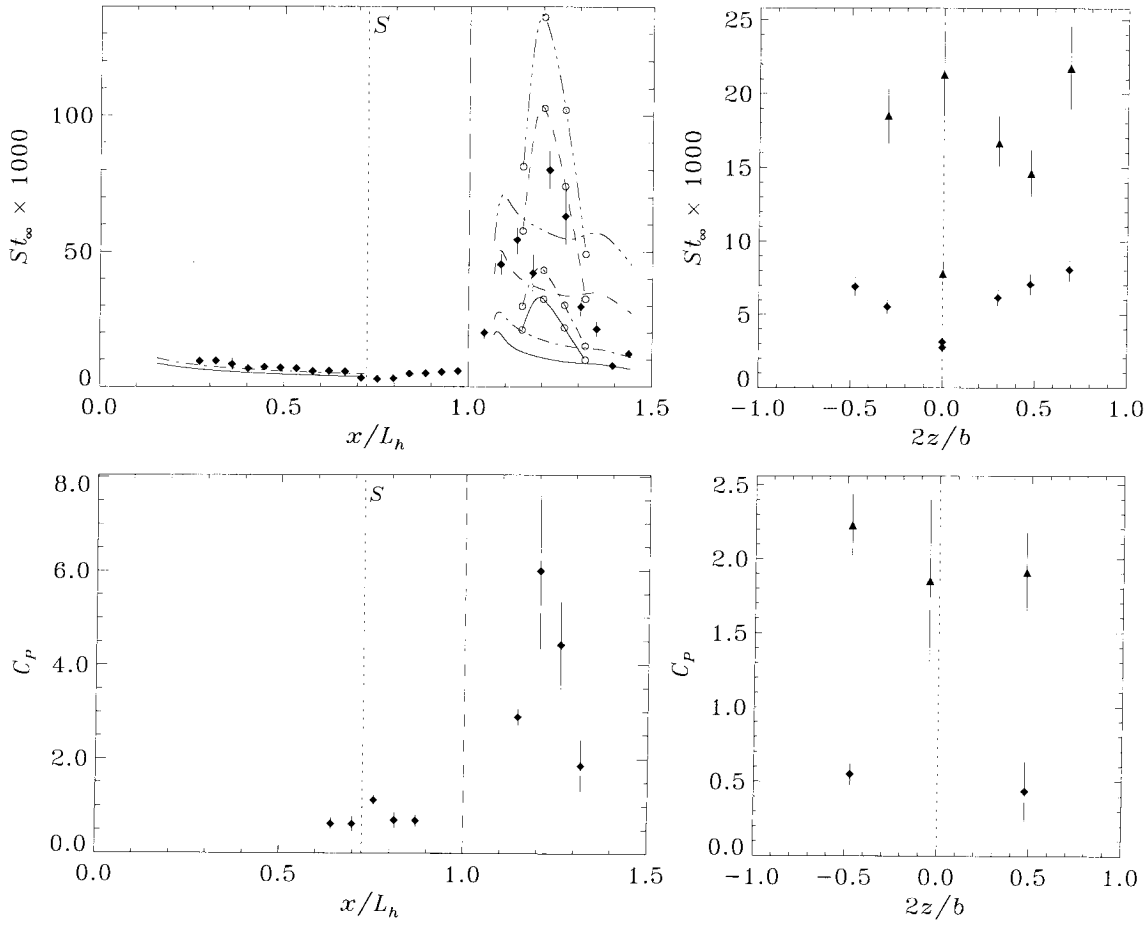

Shot 1288 (condition C4, $A_e/A_* = 225$, $\theta_1 = 30°$, $\theta_w = 30°$)

no photograph

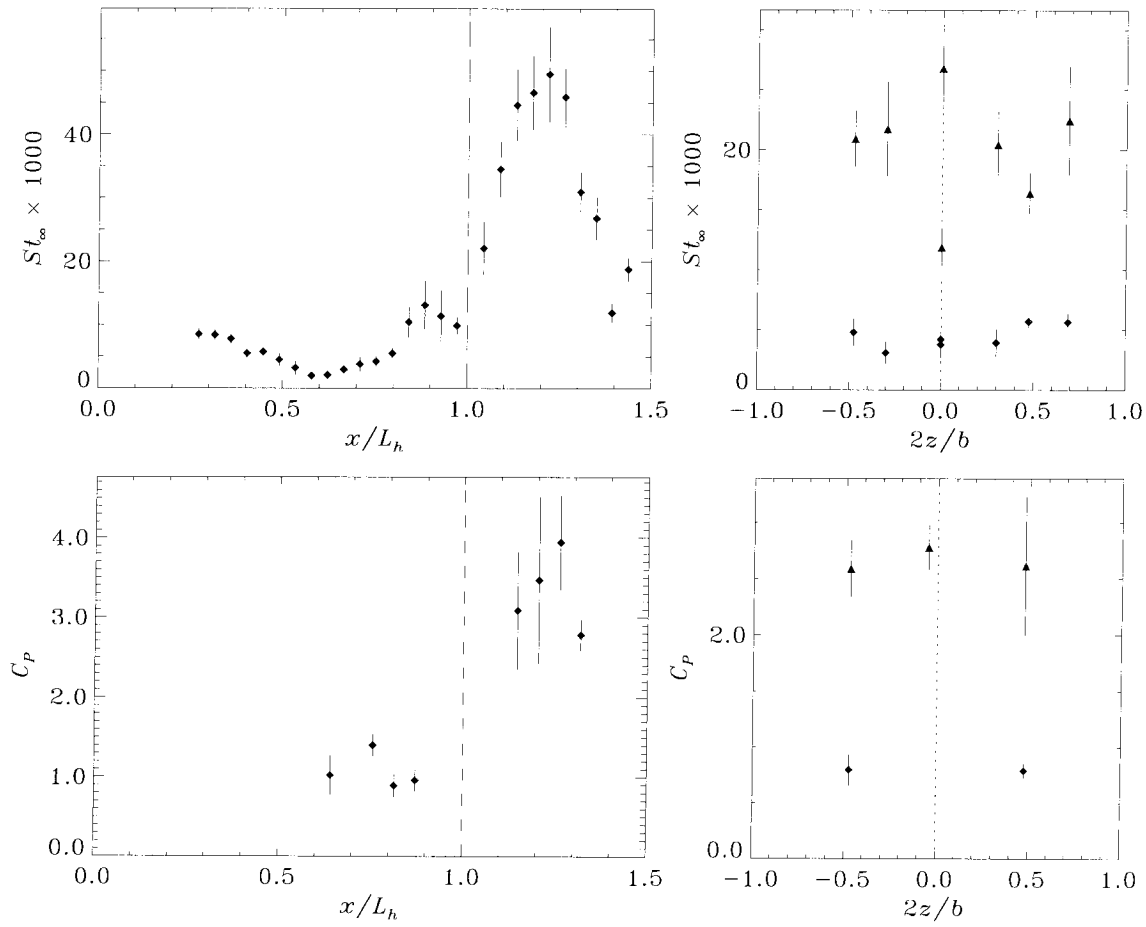

Shot 1289 (condition B2, $A_e/A_* = 400$, $\theta_1 = 30°$, $\theta_w = 30°$)

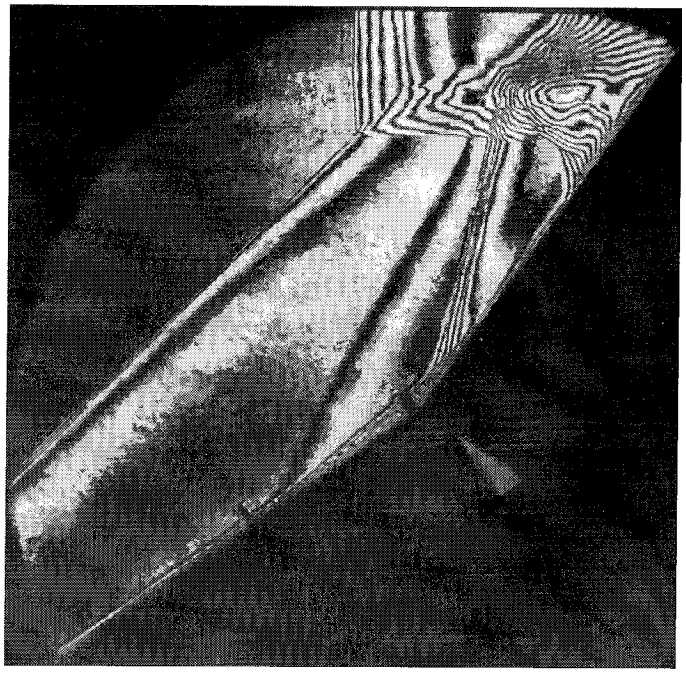

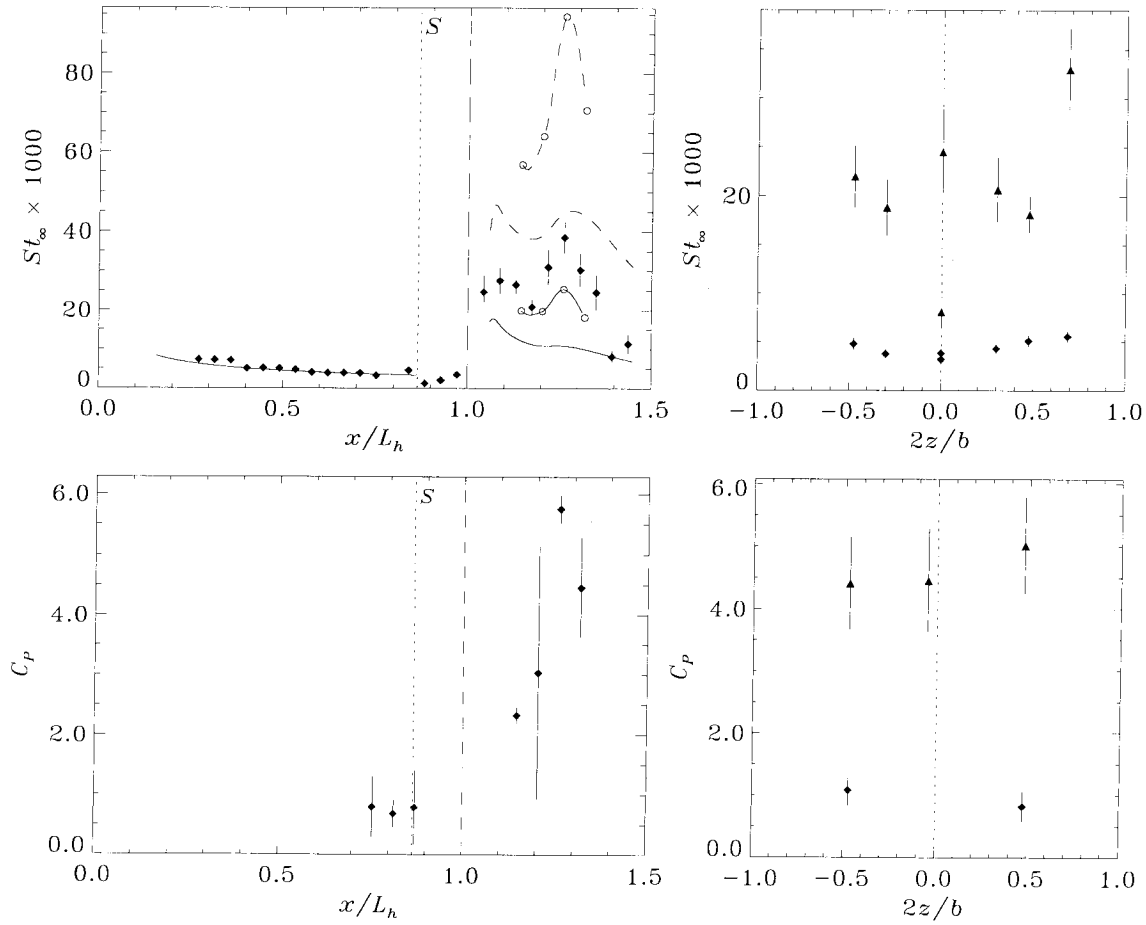

Shot 1290 (condition B2, $A_e/A_* = 225$, $\theta_1 = 35°$, $\theta_w = 20°$)

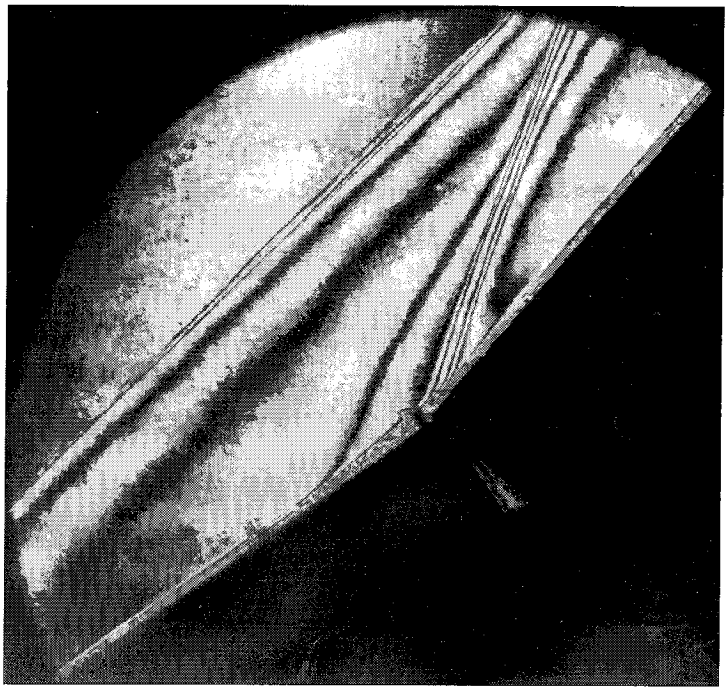

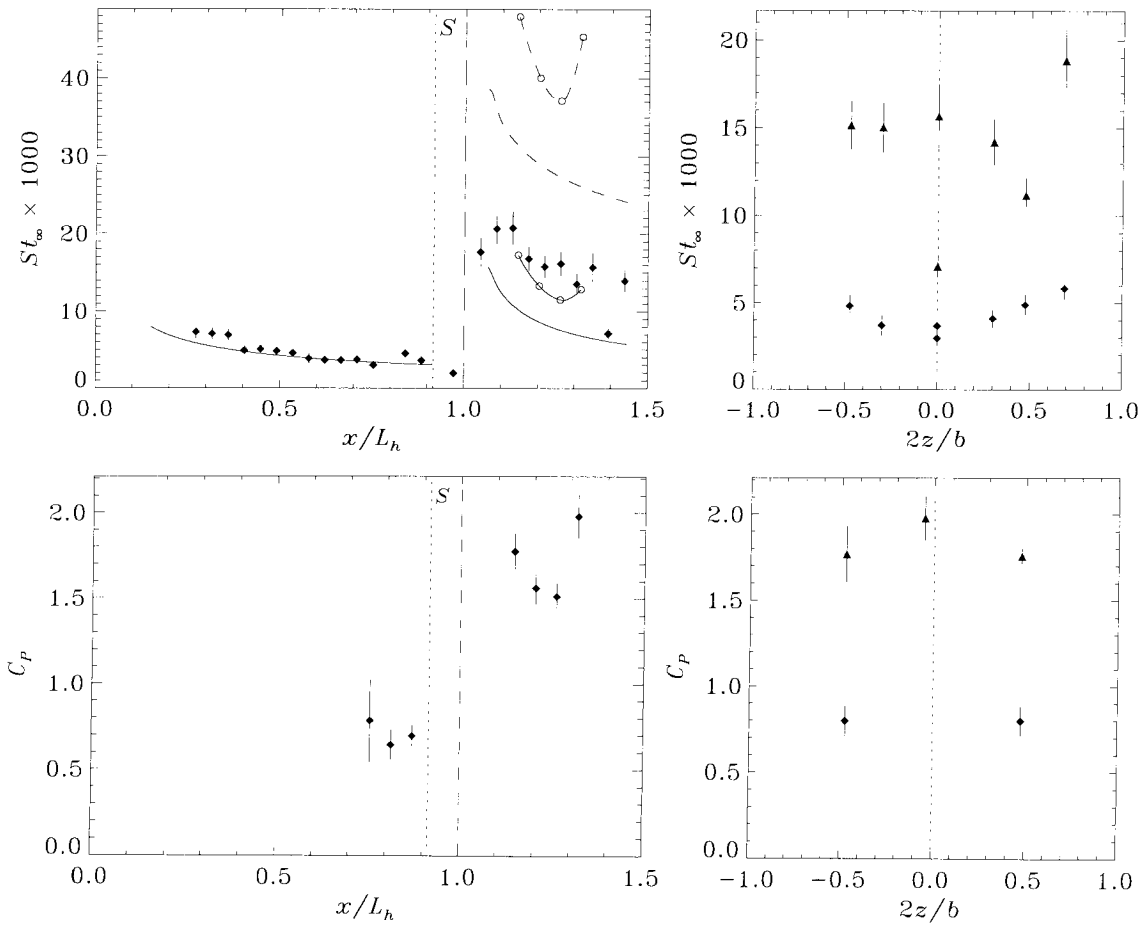

Shot 1291 (condition B2, $A_c/A_* = 225$, $\theta_1 = 35°$, $\theta_w = 15°$)

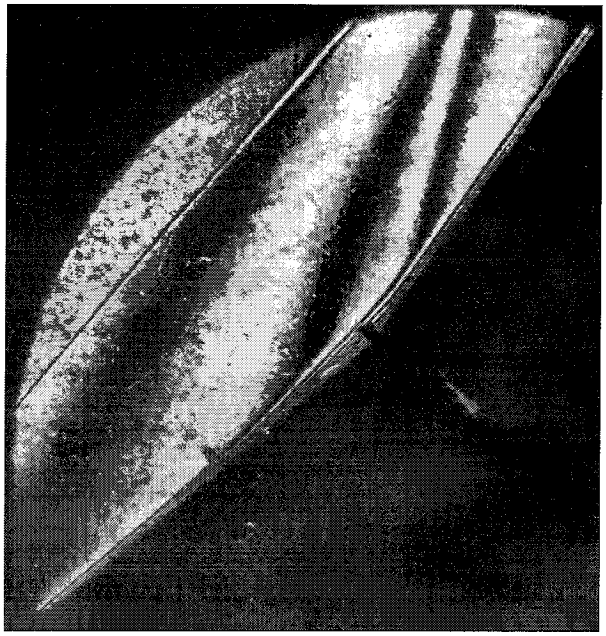

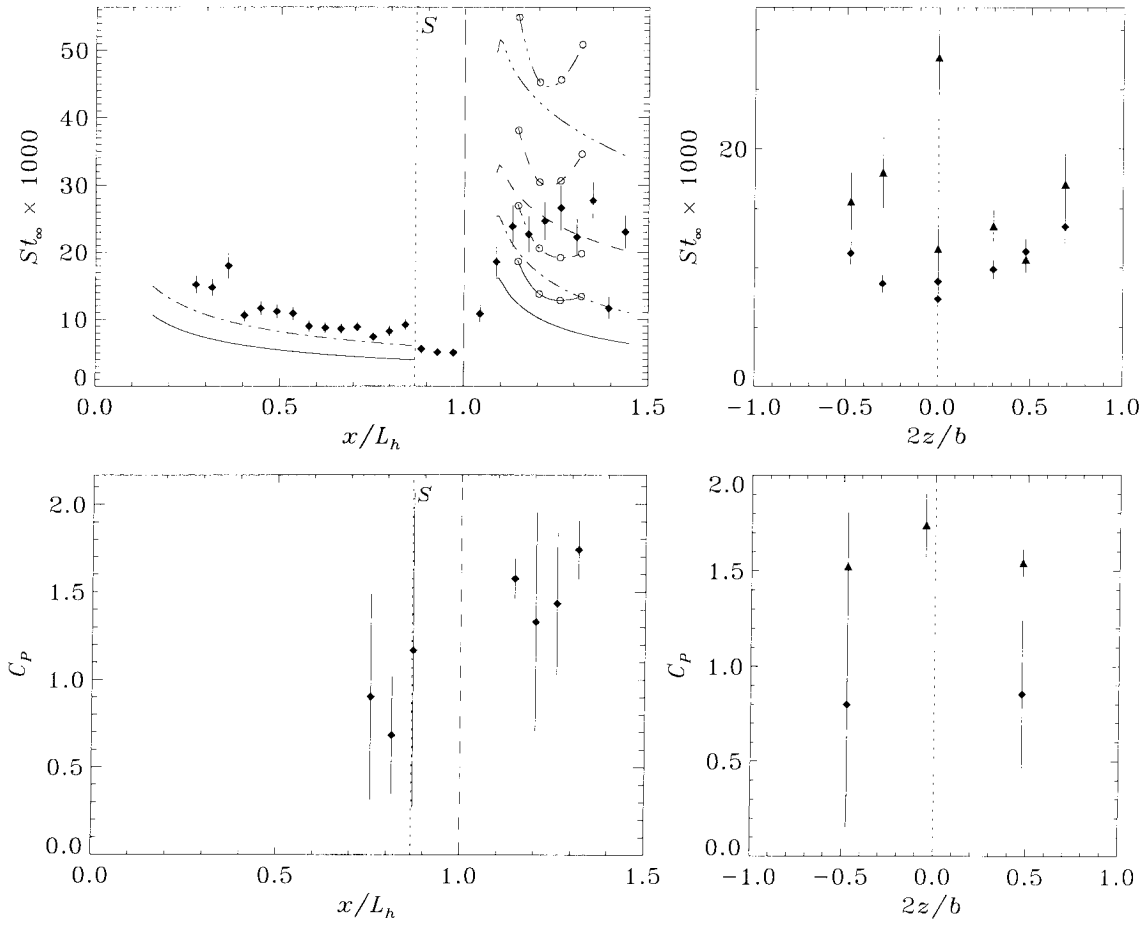

Shot 1292 (condition C4, $A_e/A_* = 400$, $\theta_1 = 40°$, $\theta_w = 15°$)

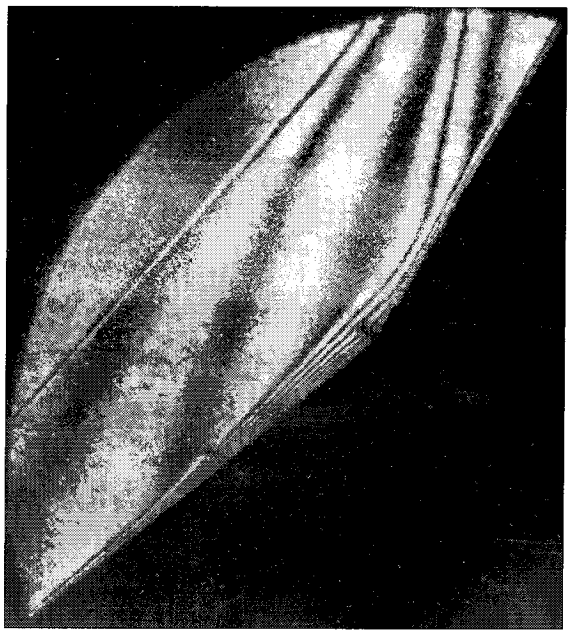

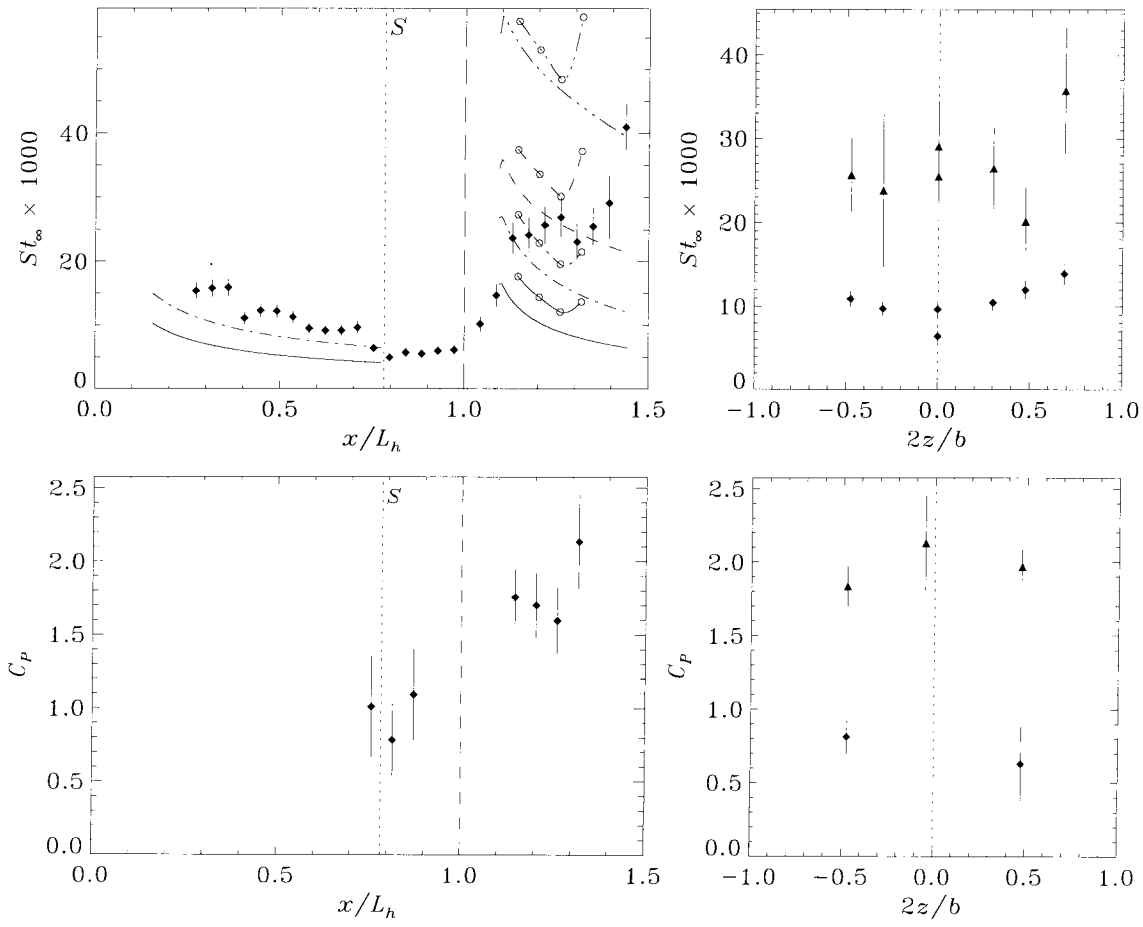

Shot 1293 (condition C4, $A_e/A_* = 400$, $\theta_1 = 40°$, $\theta_w = 20°$)

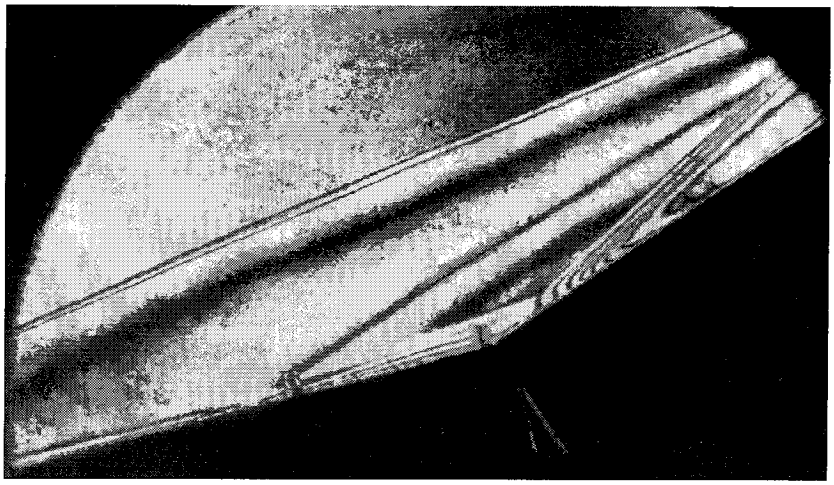

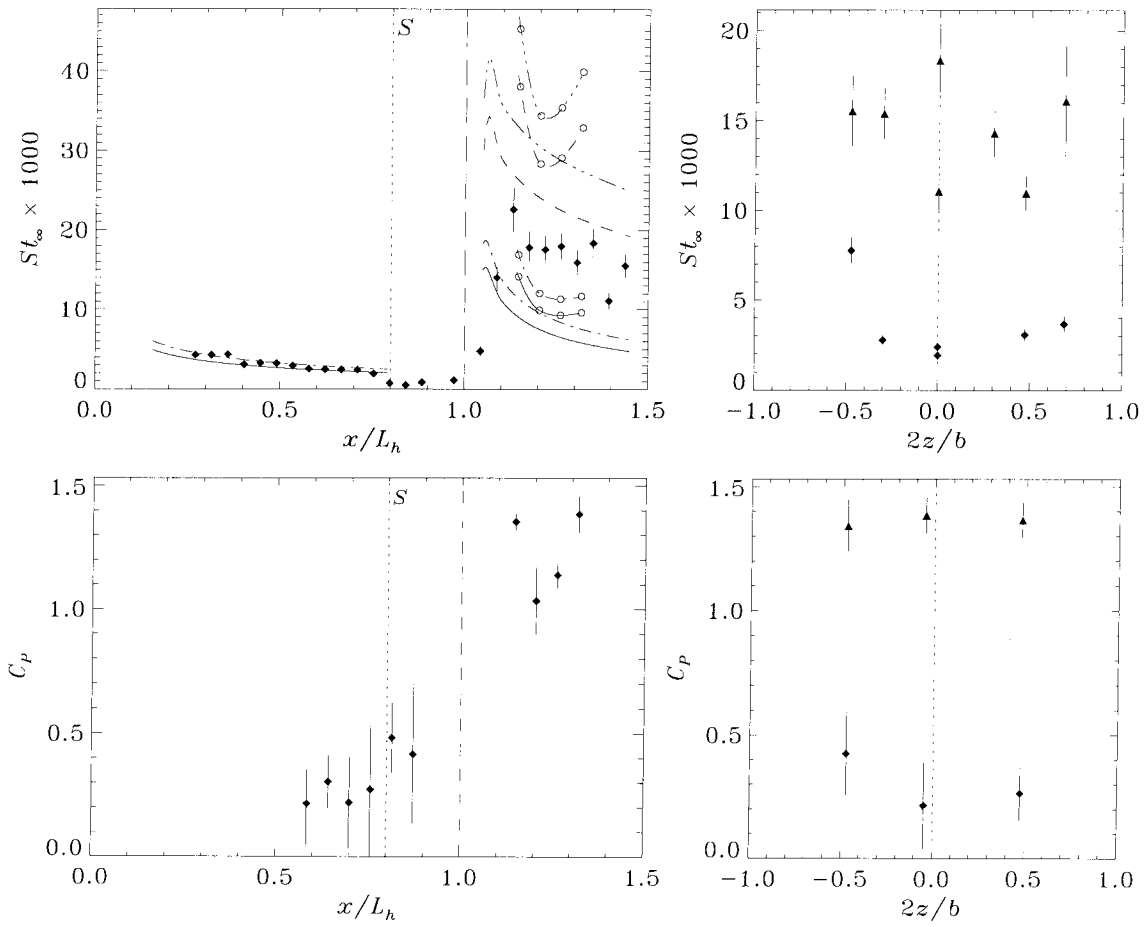

Shot 1294 (condition C4, $A_e/A_* = 100$, $\theta_1 = 15°$, $\theta_w = 20°$)

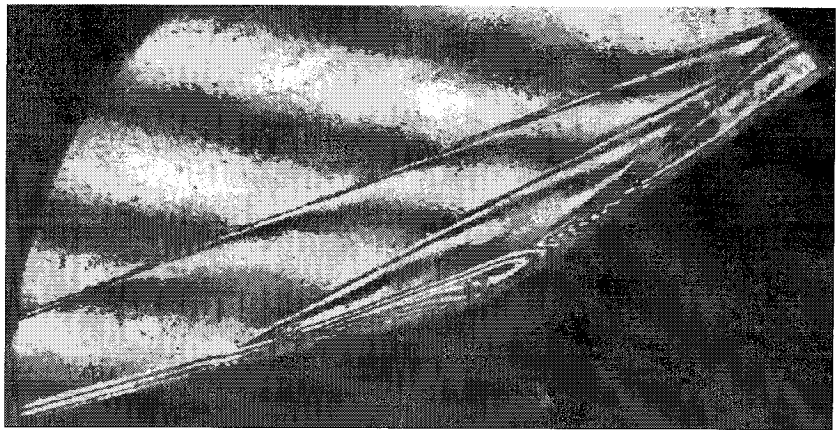

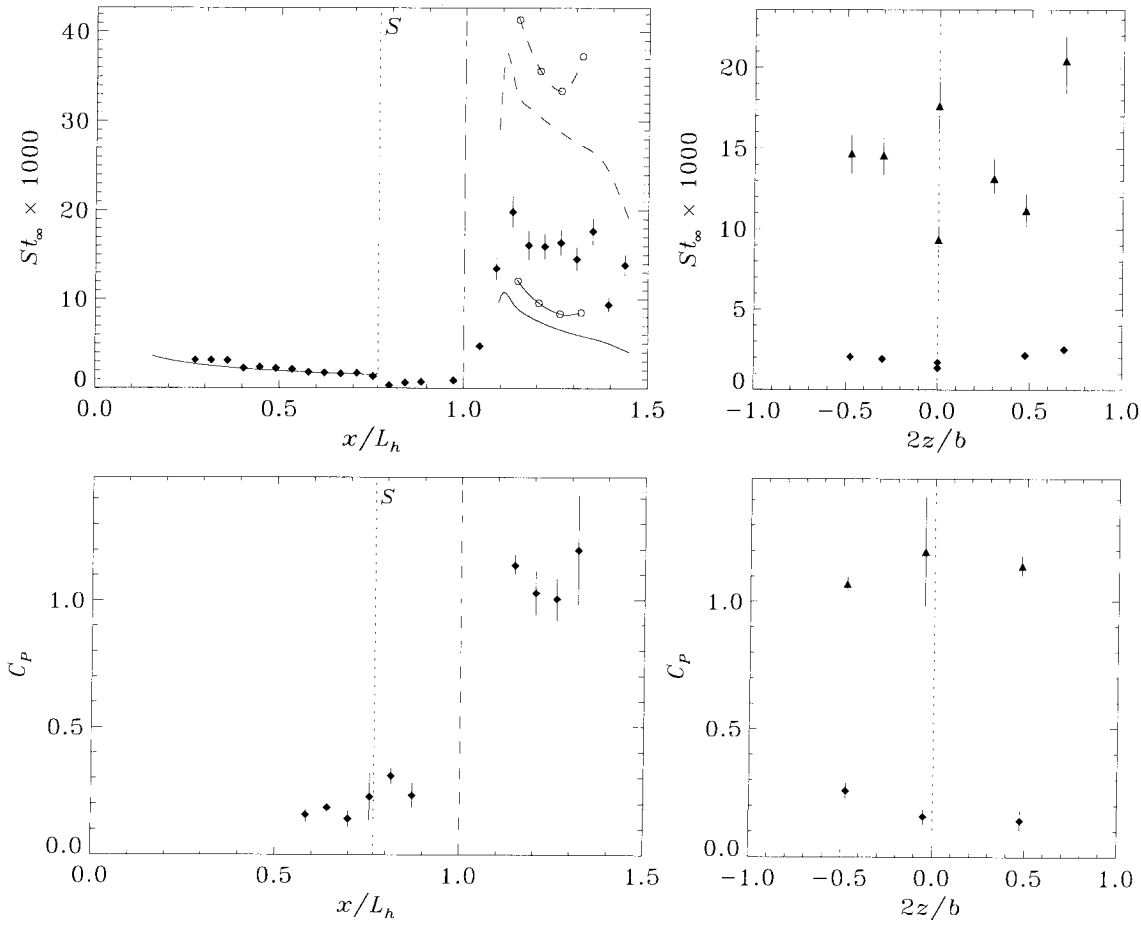

Shot 1295 (condition B3, $A_e/A_* = 400$, $\theta_1 = 15°$, $\theta_w = 20°$)

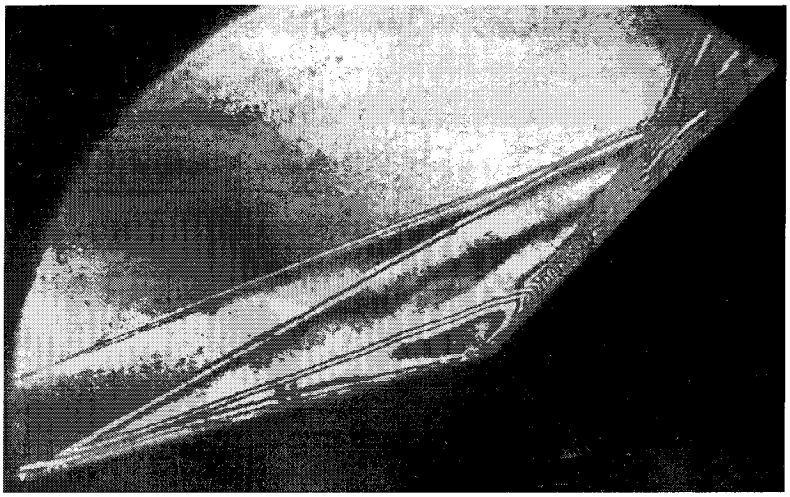

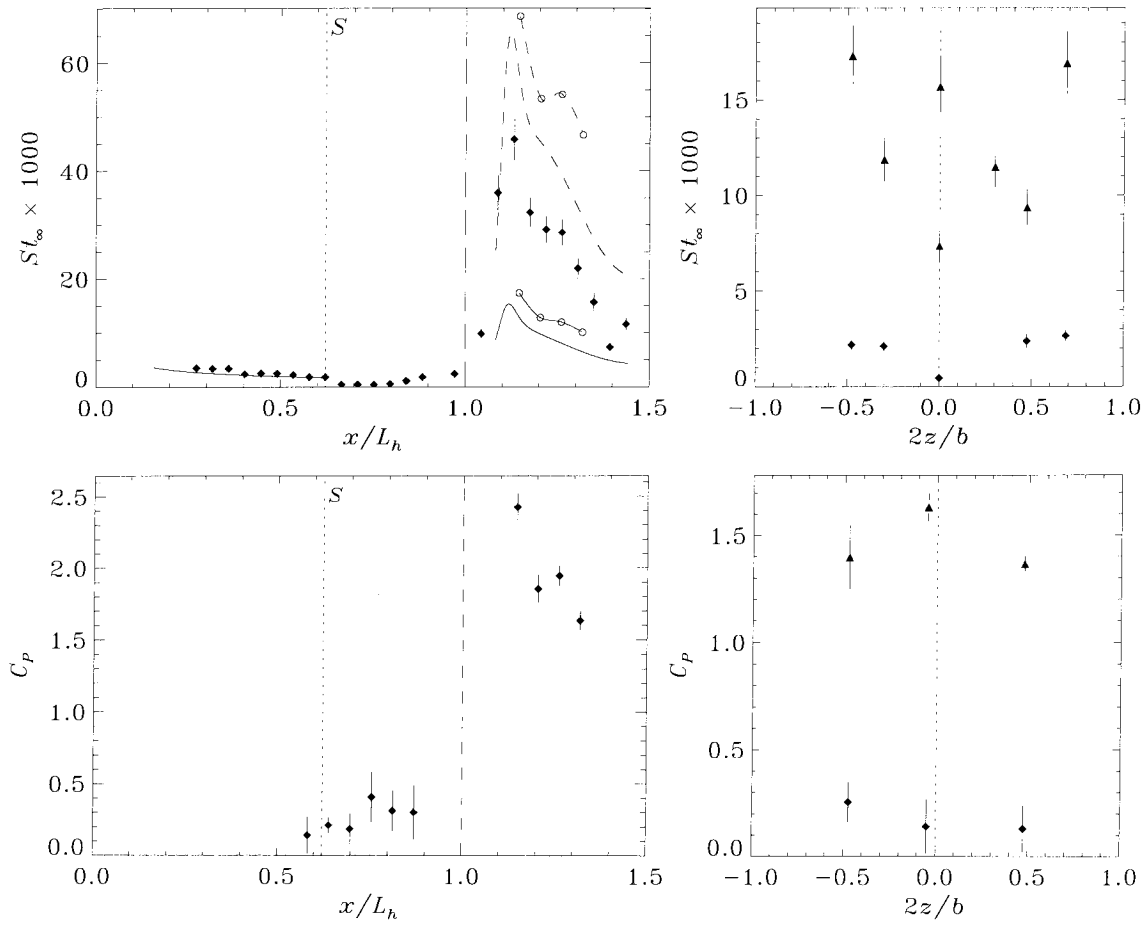

Shot 1296 (condition B3, $A_e/A_* = 400$, $\theta_1 = 15°$, $\theta_w = 30°$)

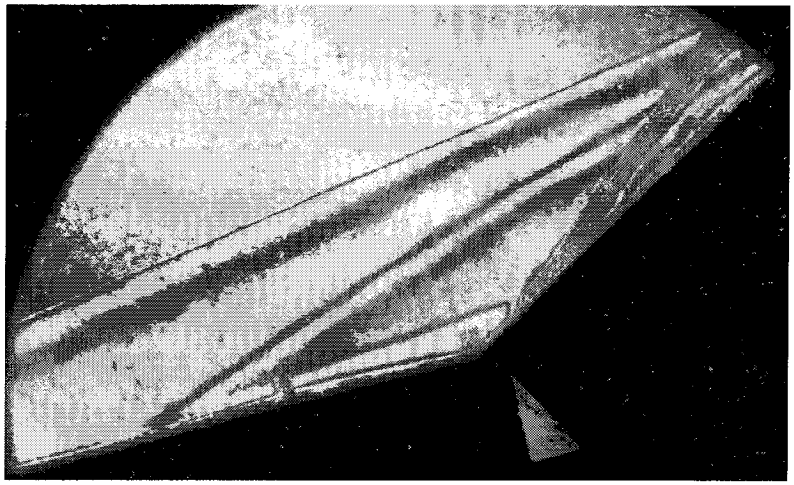

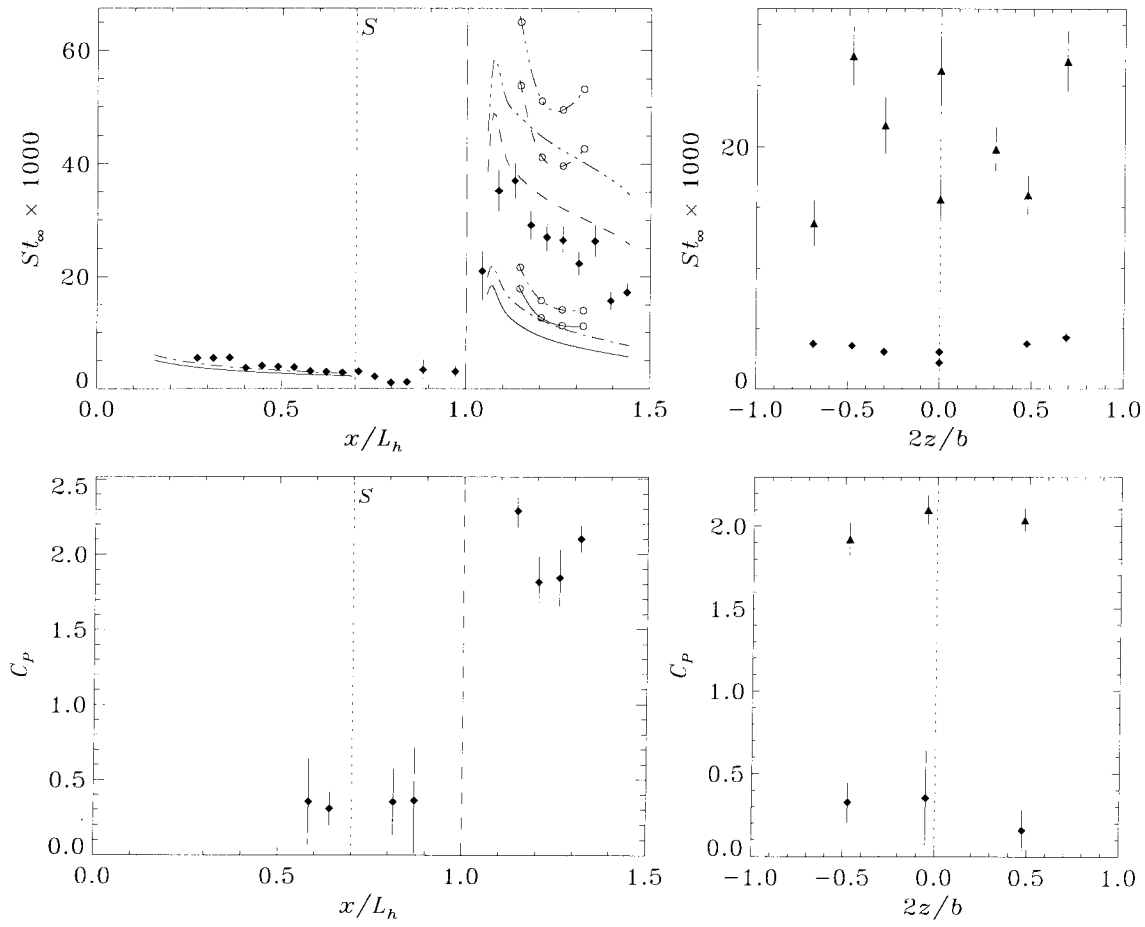

Shot 1297 (condition C0, $A_e/A_* = 100$, $\theta_1 = 15°$, $\theta_w = 30°$)

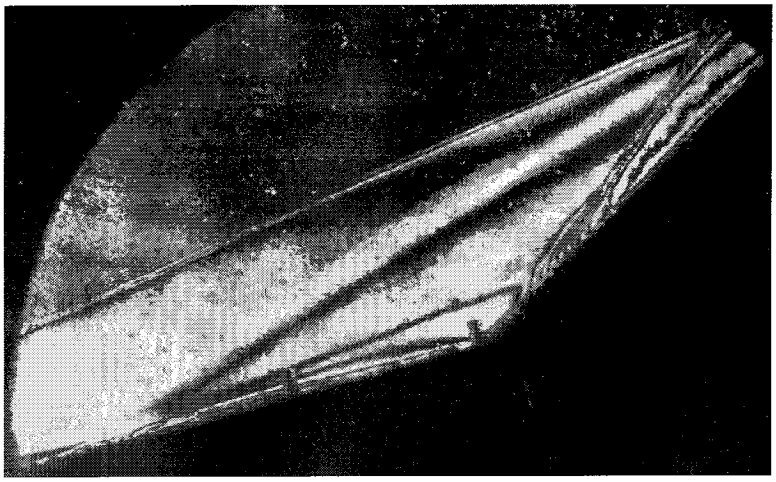

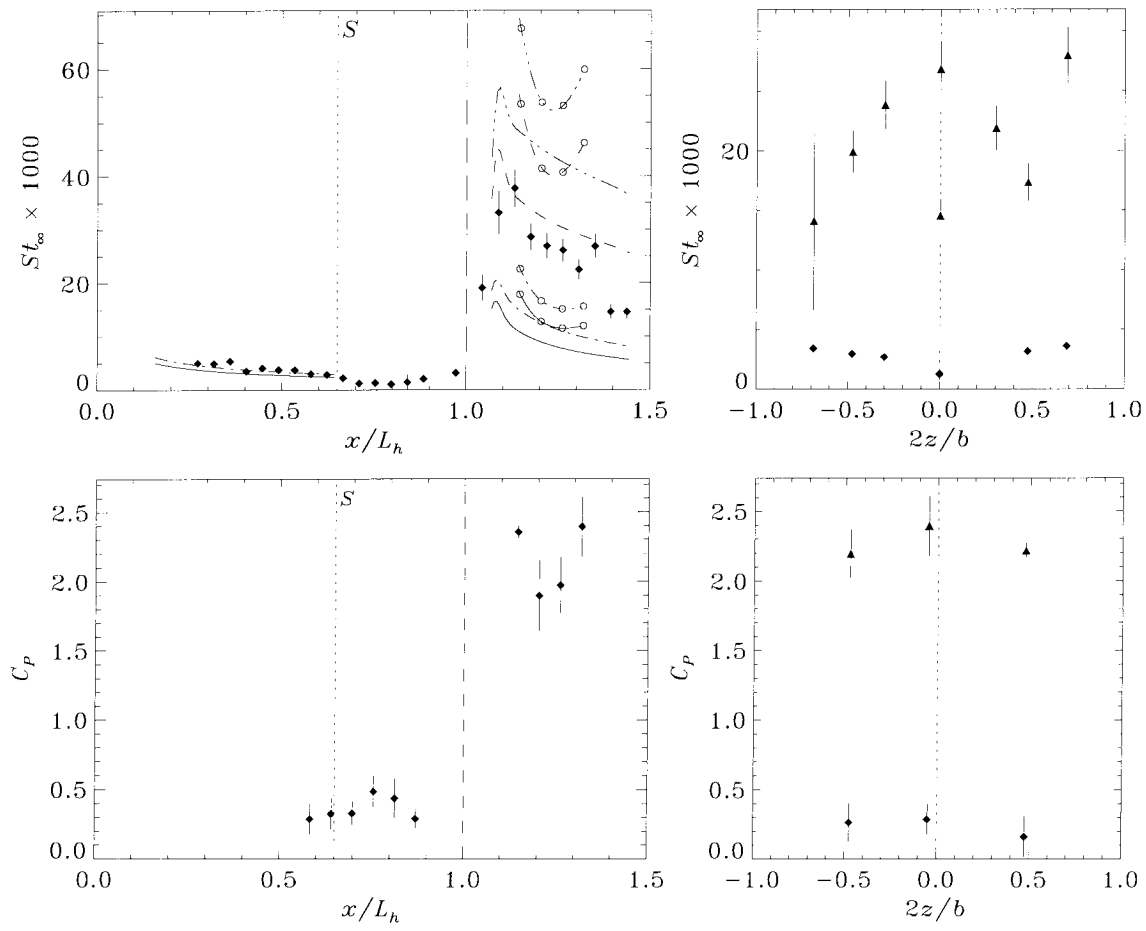

Shot 1298 (condition C4, $A_e/A_* = 100$, $\theta_1 = 15°$, $\theta_w = 30°$)

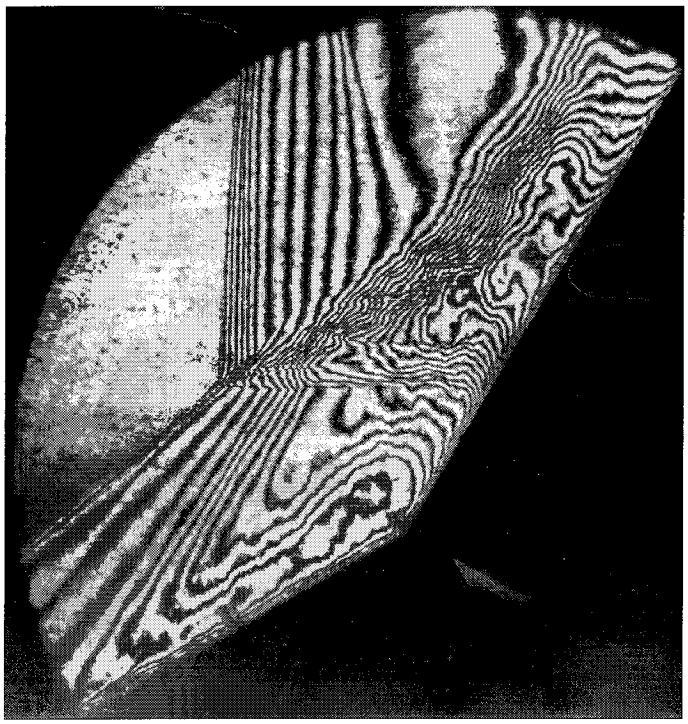

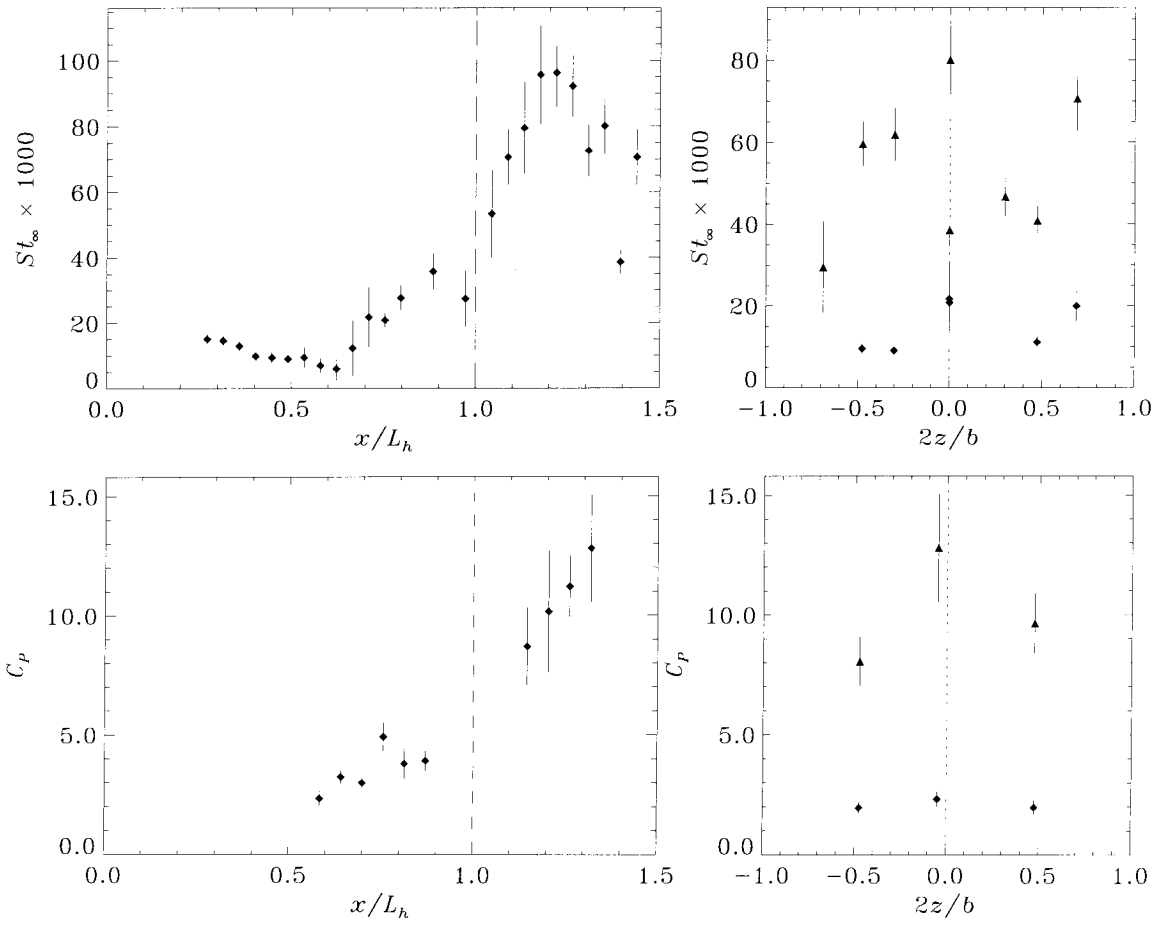

Shot 1299 (condition B2, $A_e/A_* = 400$, $\theta_1 = 30°$, $\theta_w = 30°$)

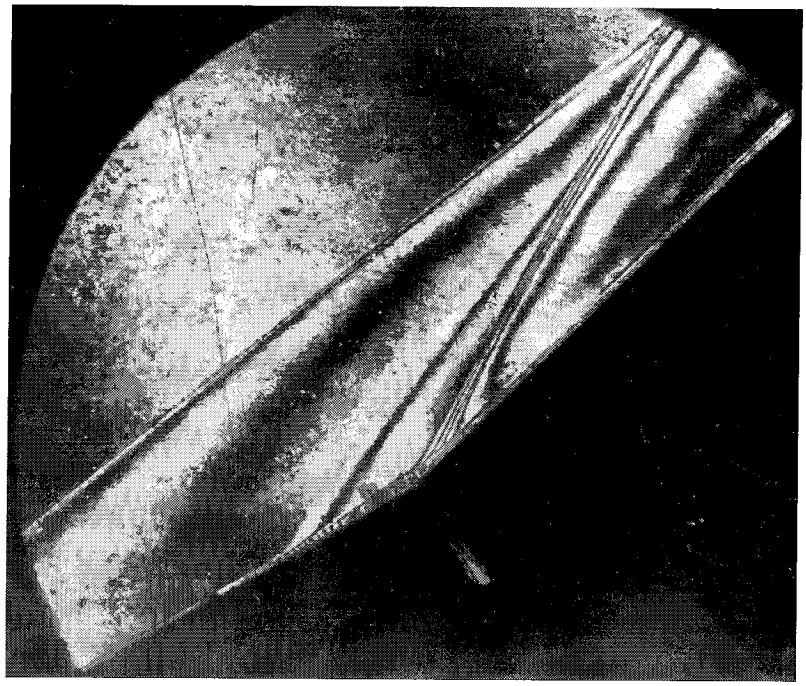

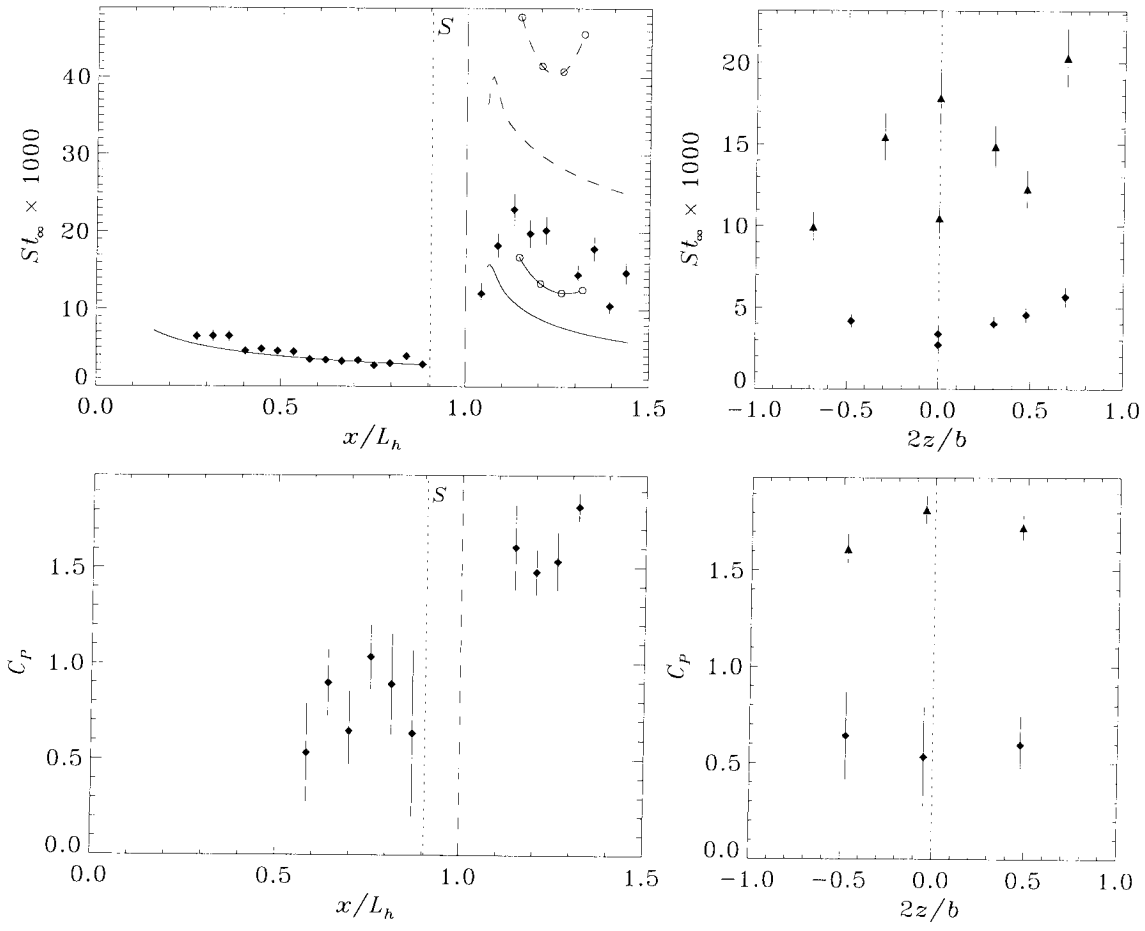

Shot 1300 (condition B2, $A_e/A_* = 225$, $\theta_1 = 30°$, $\theta_w = 15°$)

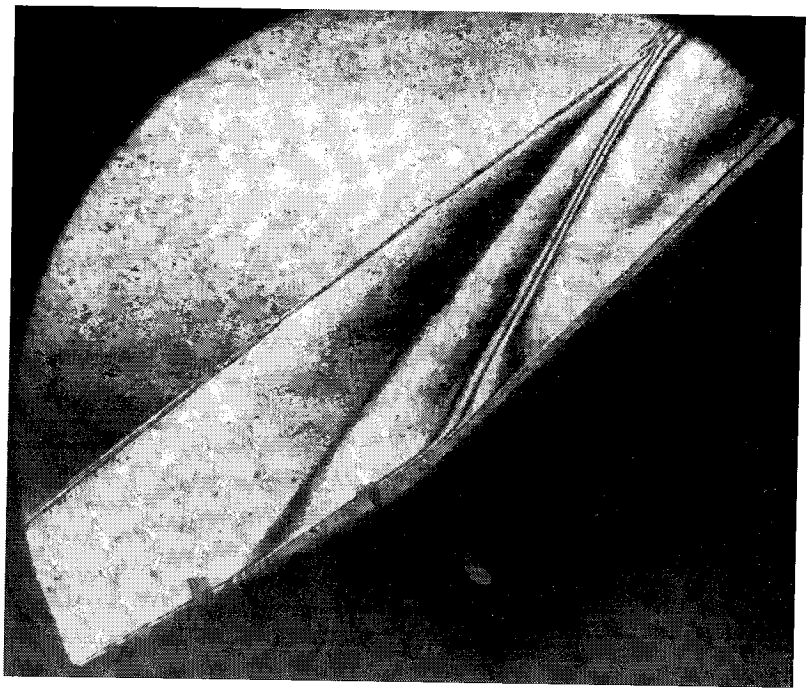

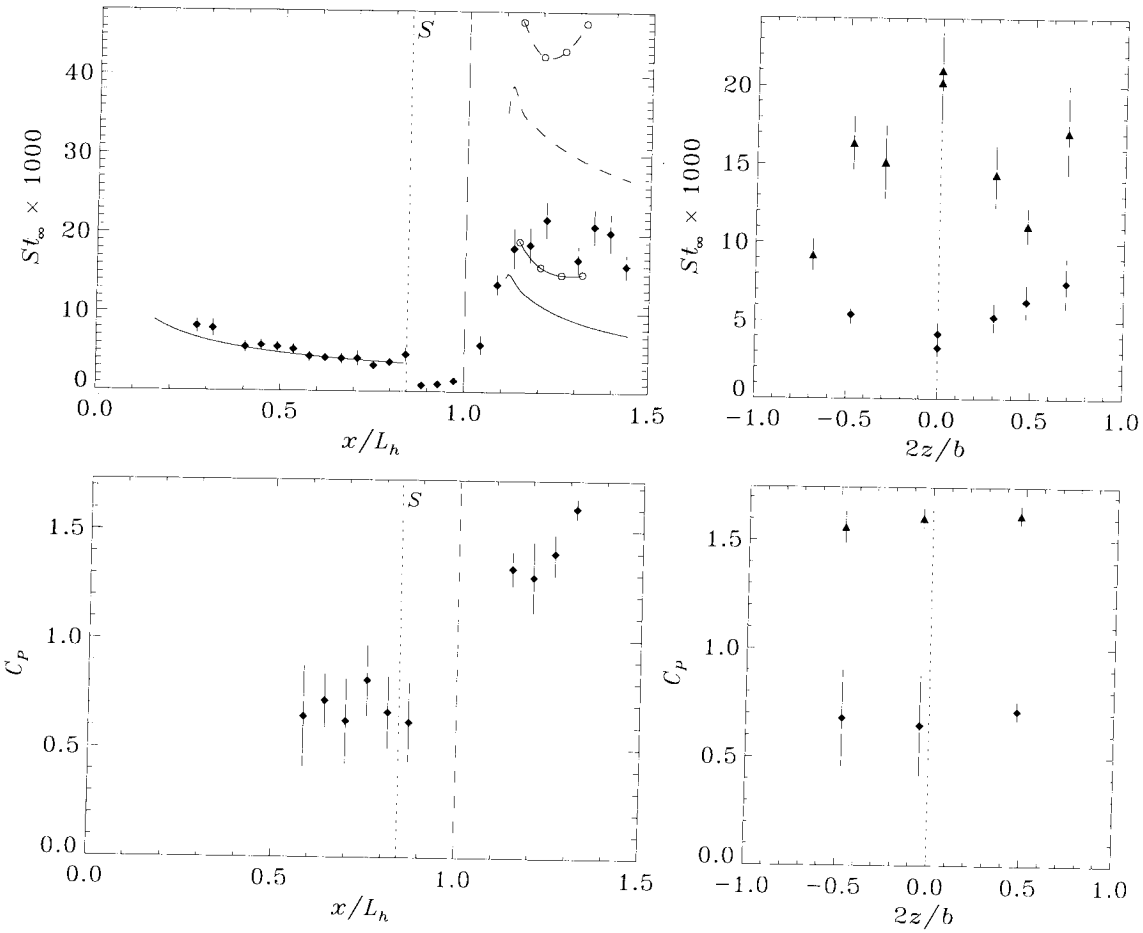

Shot 1302 (condition B2, $A_e/A_* = 400$, $\theta_1 = 30°$, $\theta_w = 15°$)

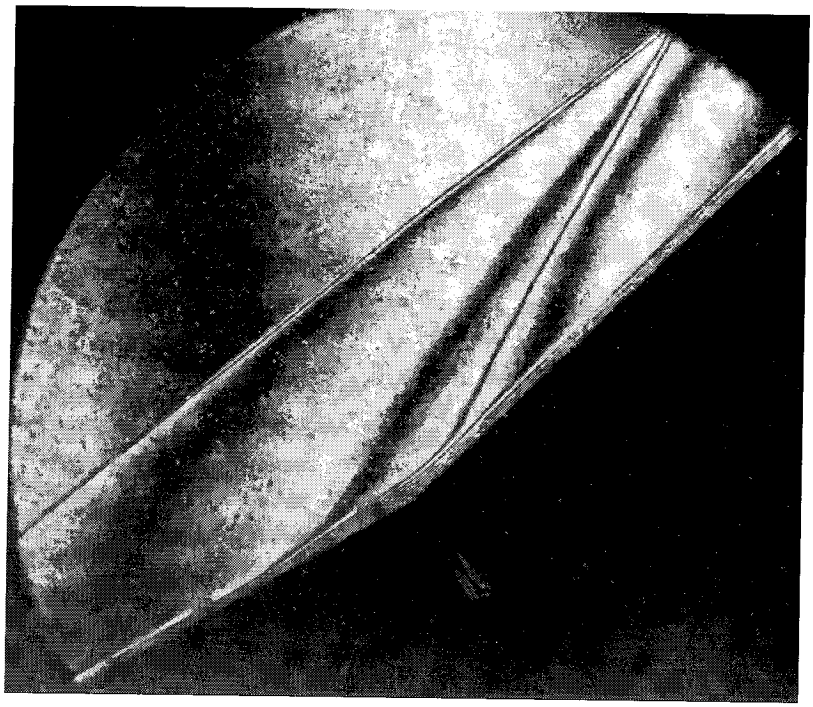

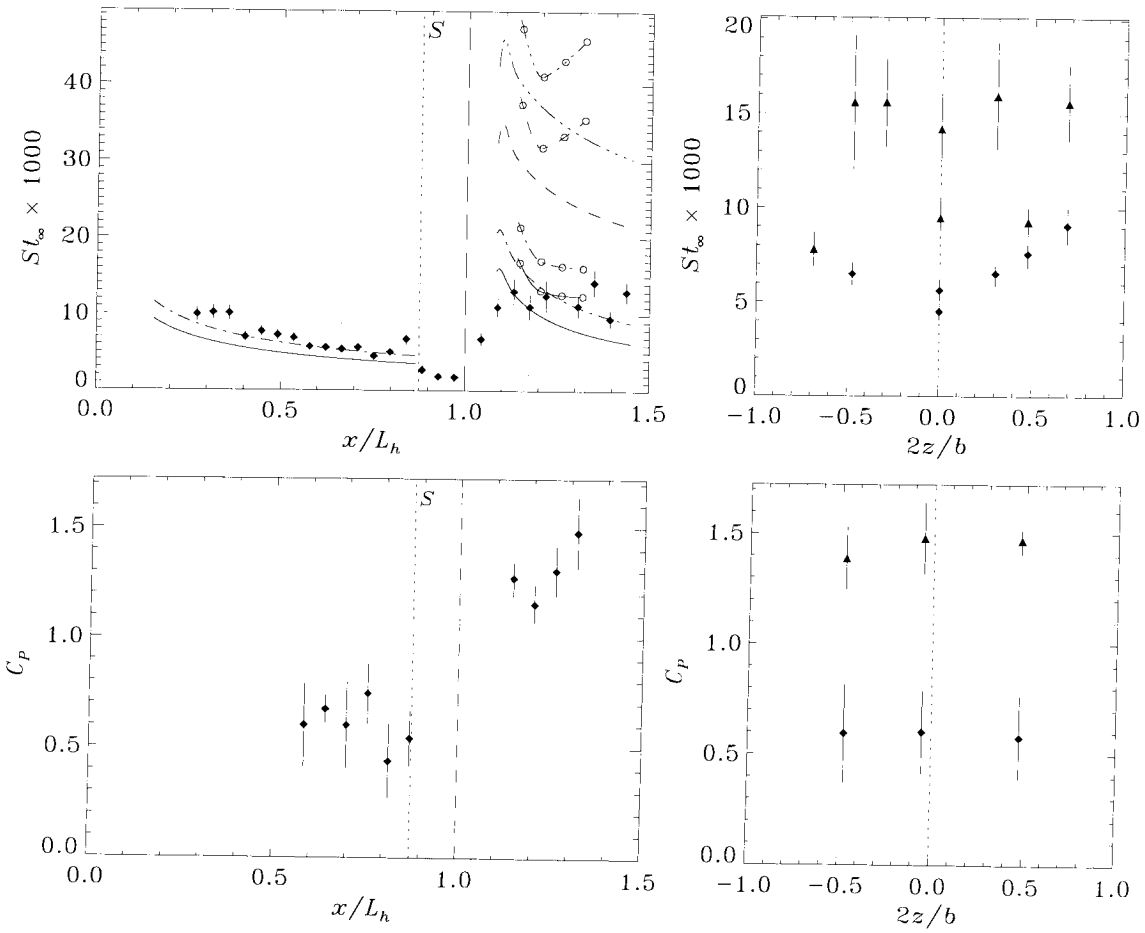

Shot 1303 (condition C4, $A_e/A_* = 225$, $\theta_1 = 30°$, $\theta_w = 15°$)

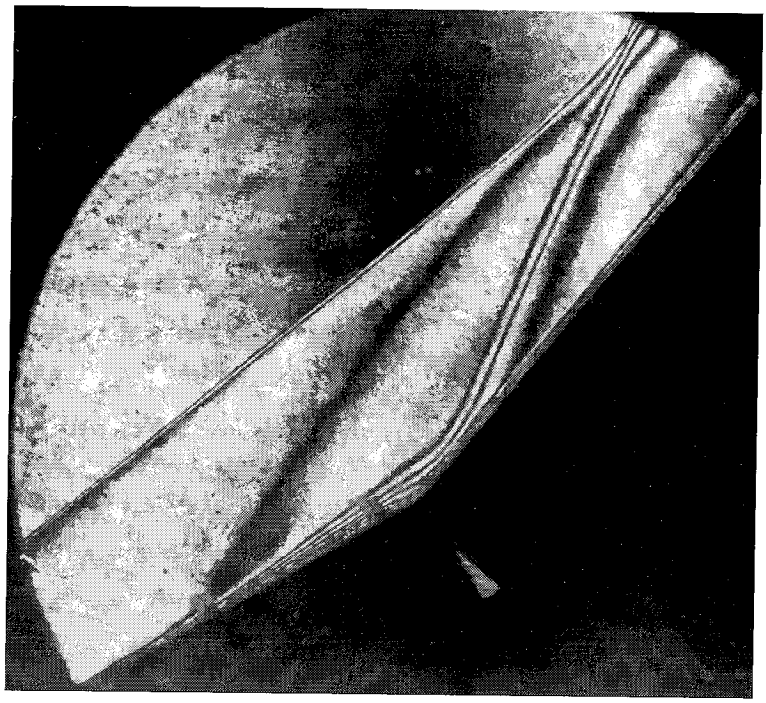

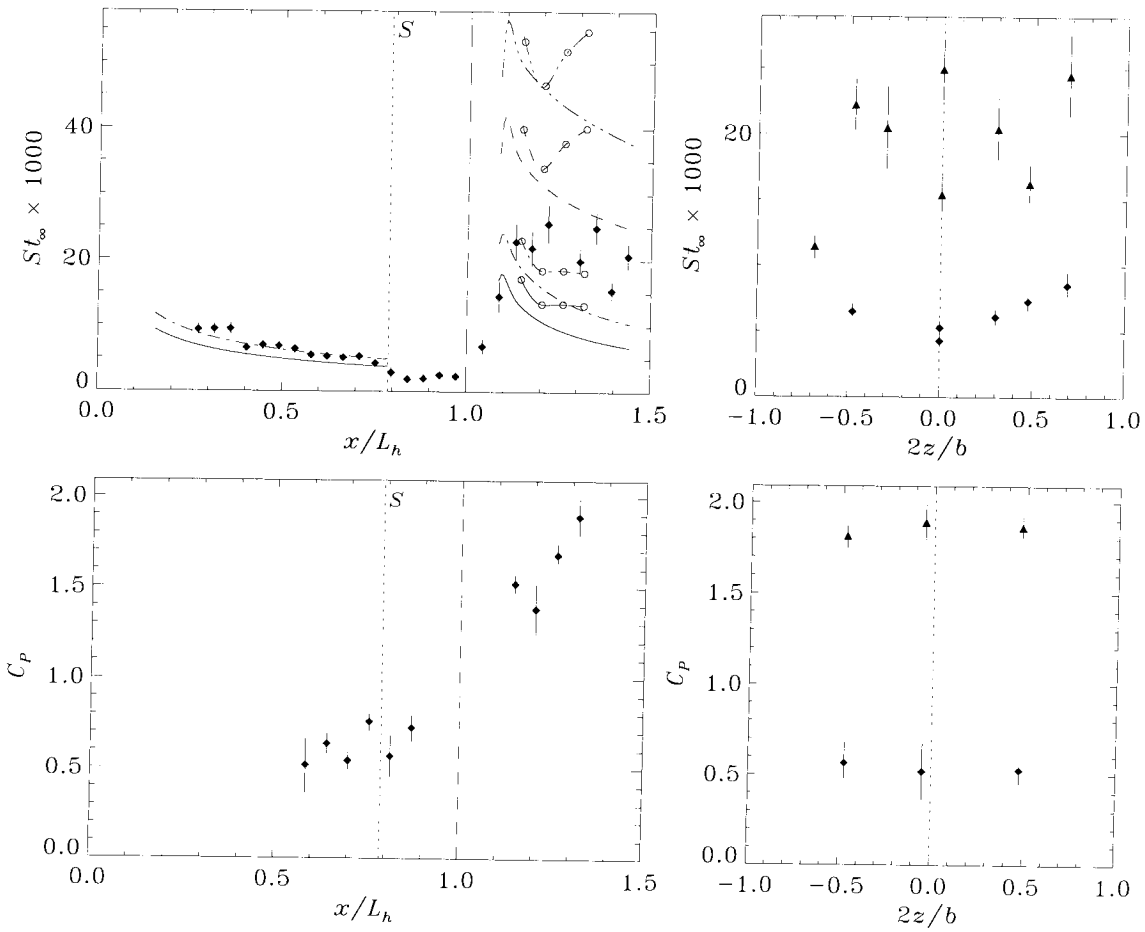

Shot 1304 (condition C4, $A_e/A_* = 225$, $\theta_1 = 30°$, $\theta_w = 20°$)

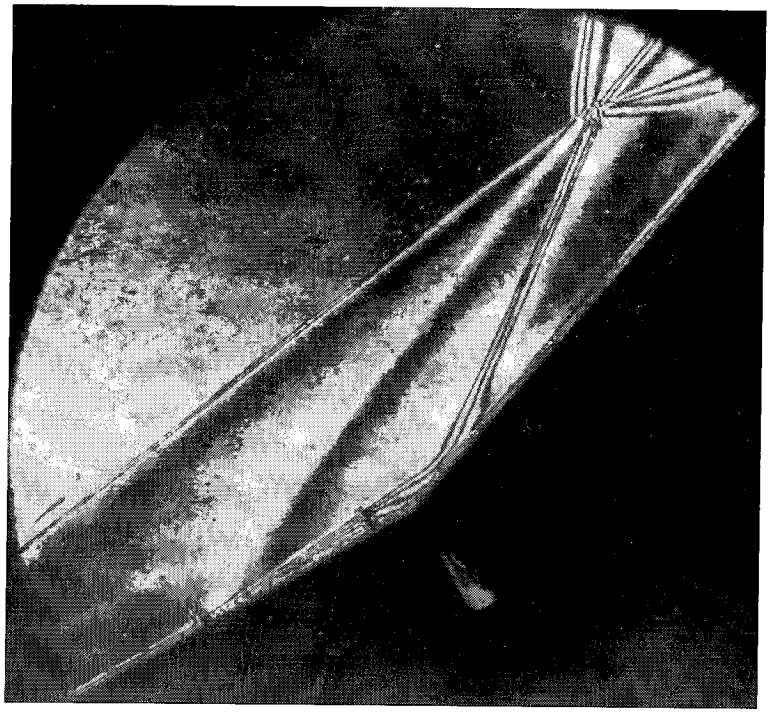

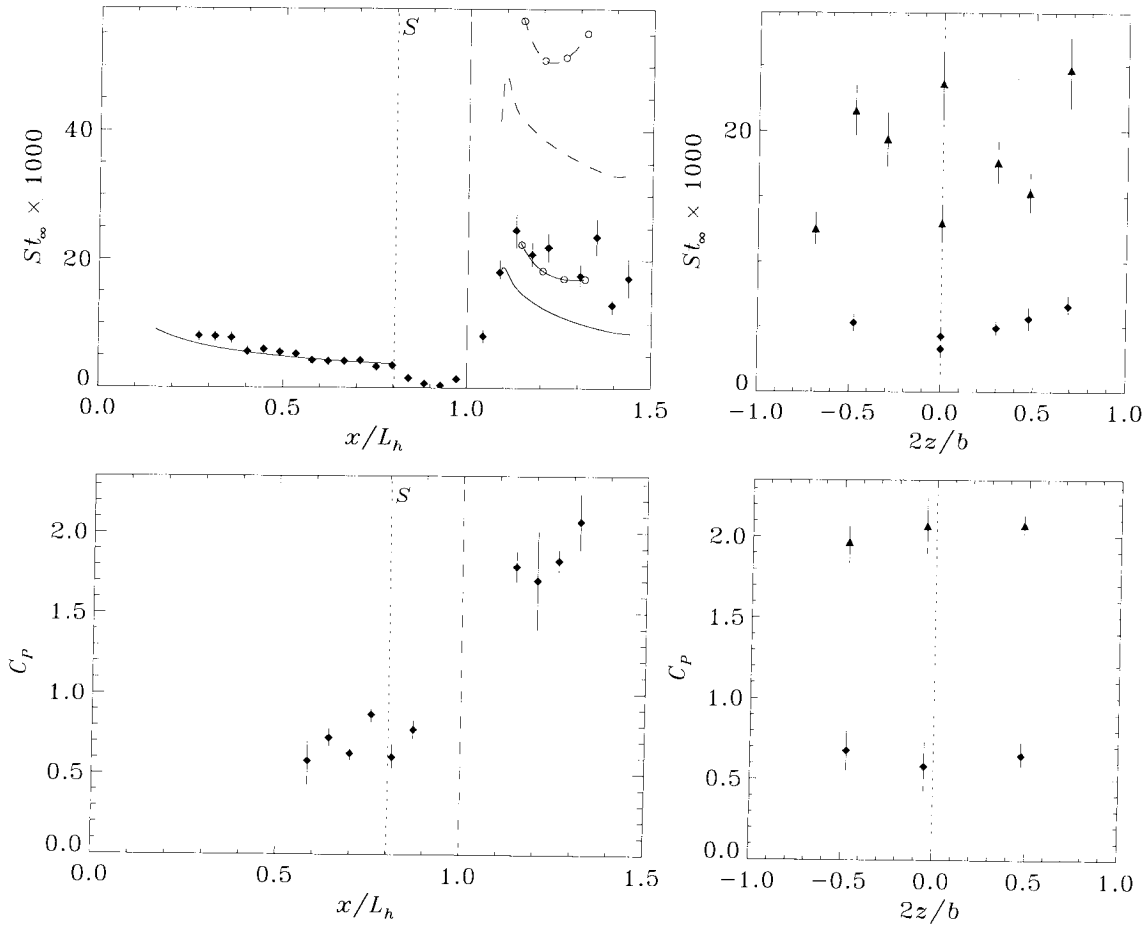

Shot 1305 (condition B2, $A_e/A_* = 400$, $\theta_1 = 30°$, $\theta_w = 20°$)

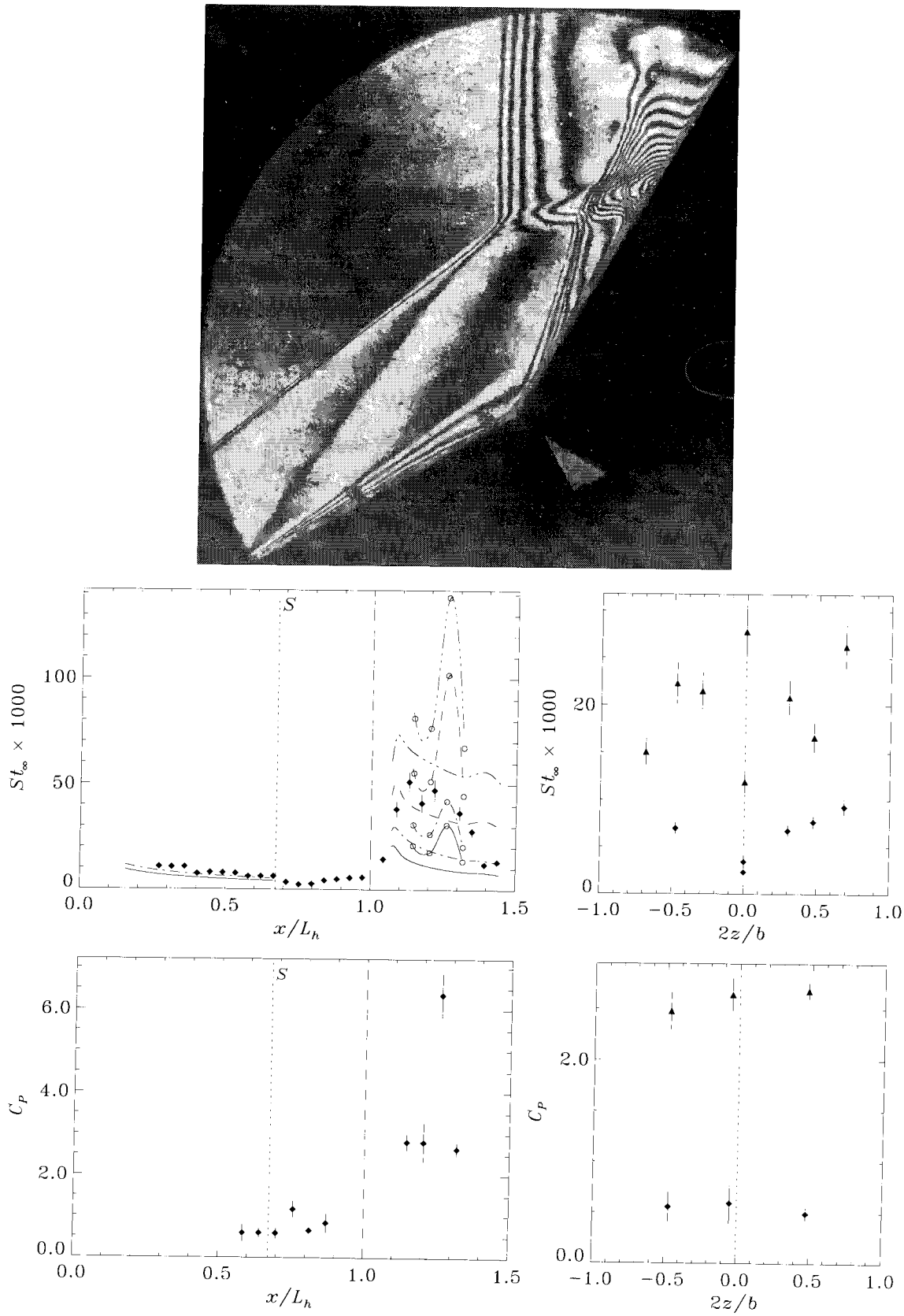

Shot 1306 (condition C4, $A_c/A_* = 225$, $\theta_1 = 30°$, $\theta_w = 30°$)

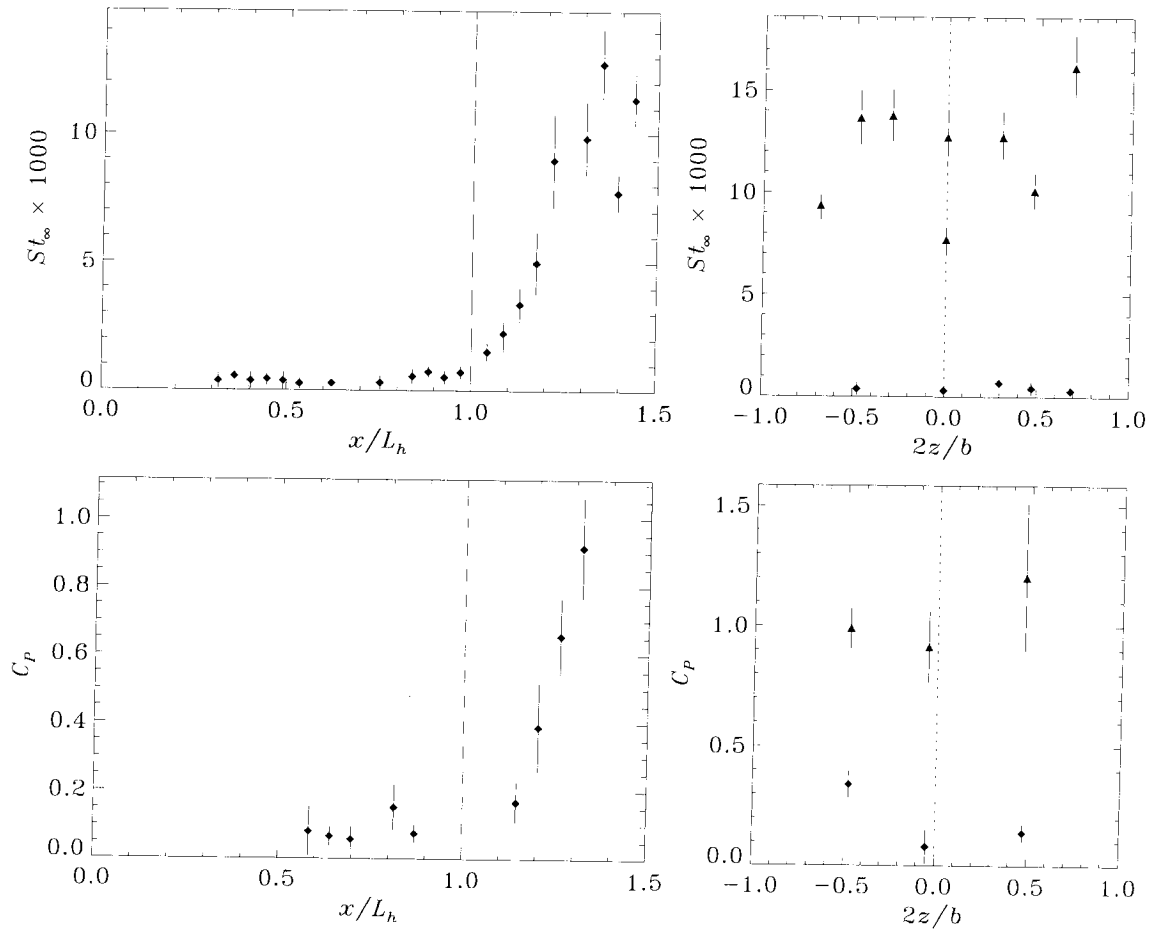

Shot 1307 (condition A0, $A_e/A_* = 100$, $\theta_1 = 0°$, $\theta_w = 30°$)

no photograph

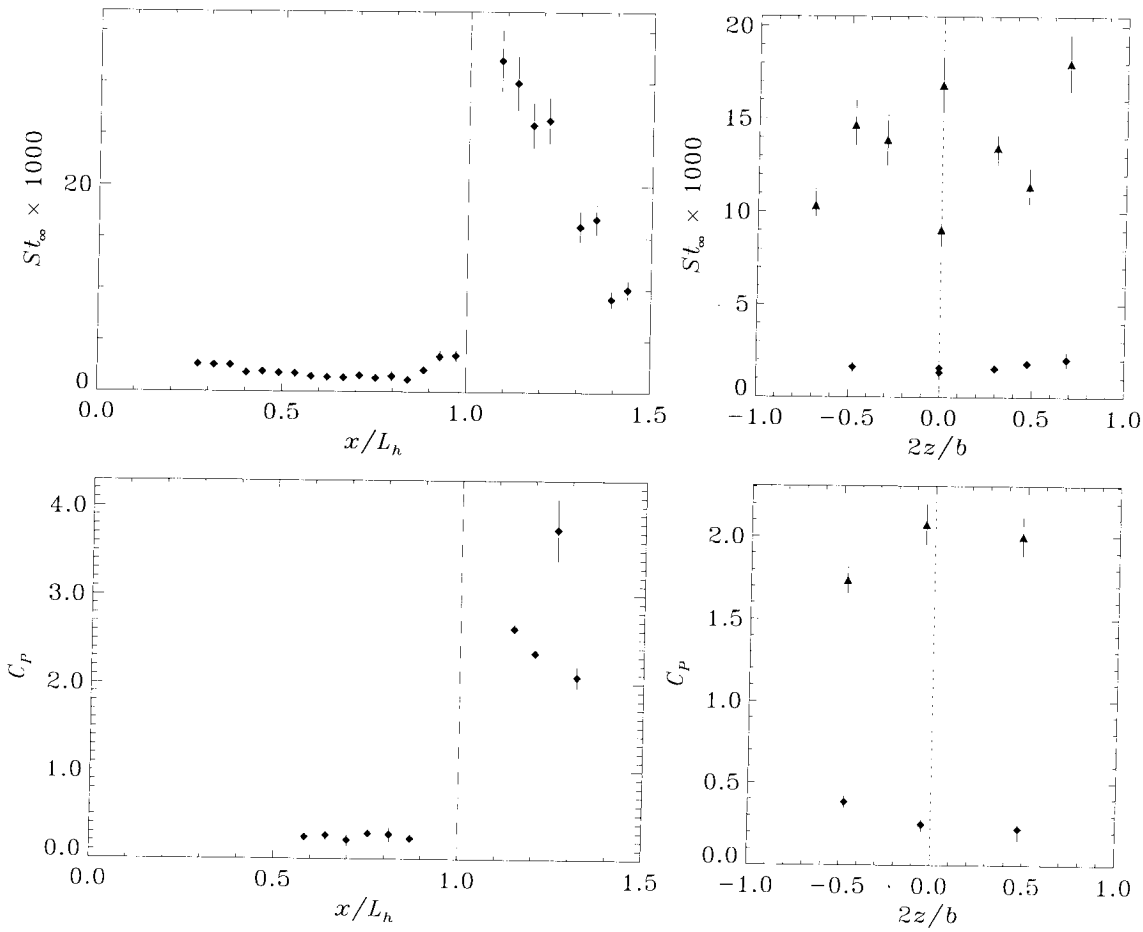

Shot 1308 (condition A1, $A_e/A_* = 100$, $\theta_1 = 15°$, $\theta_w = 30°$)

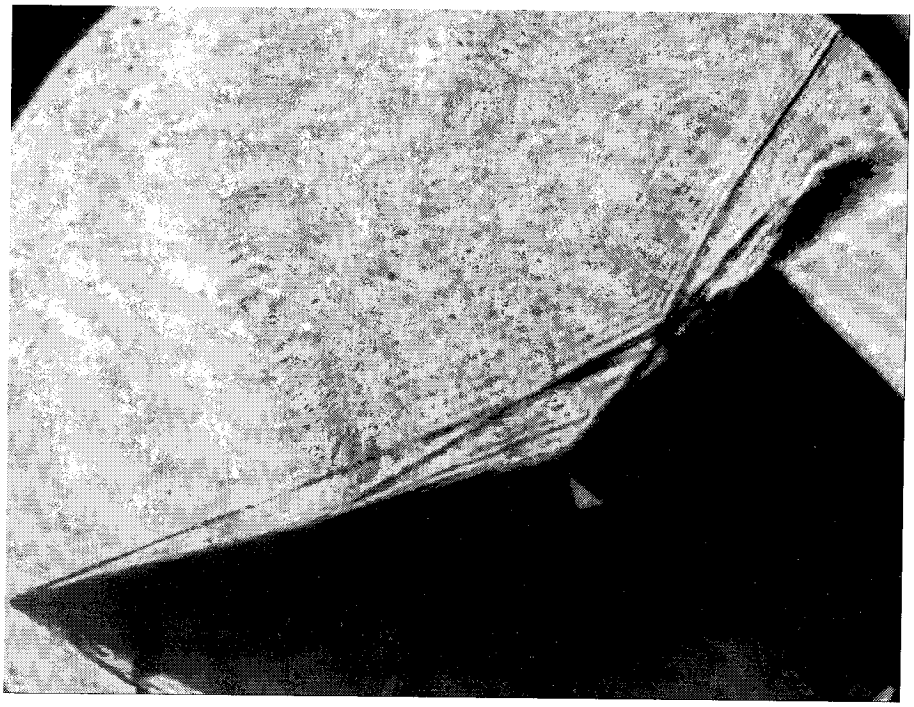

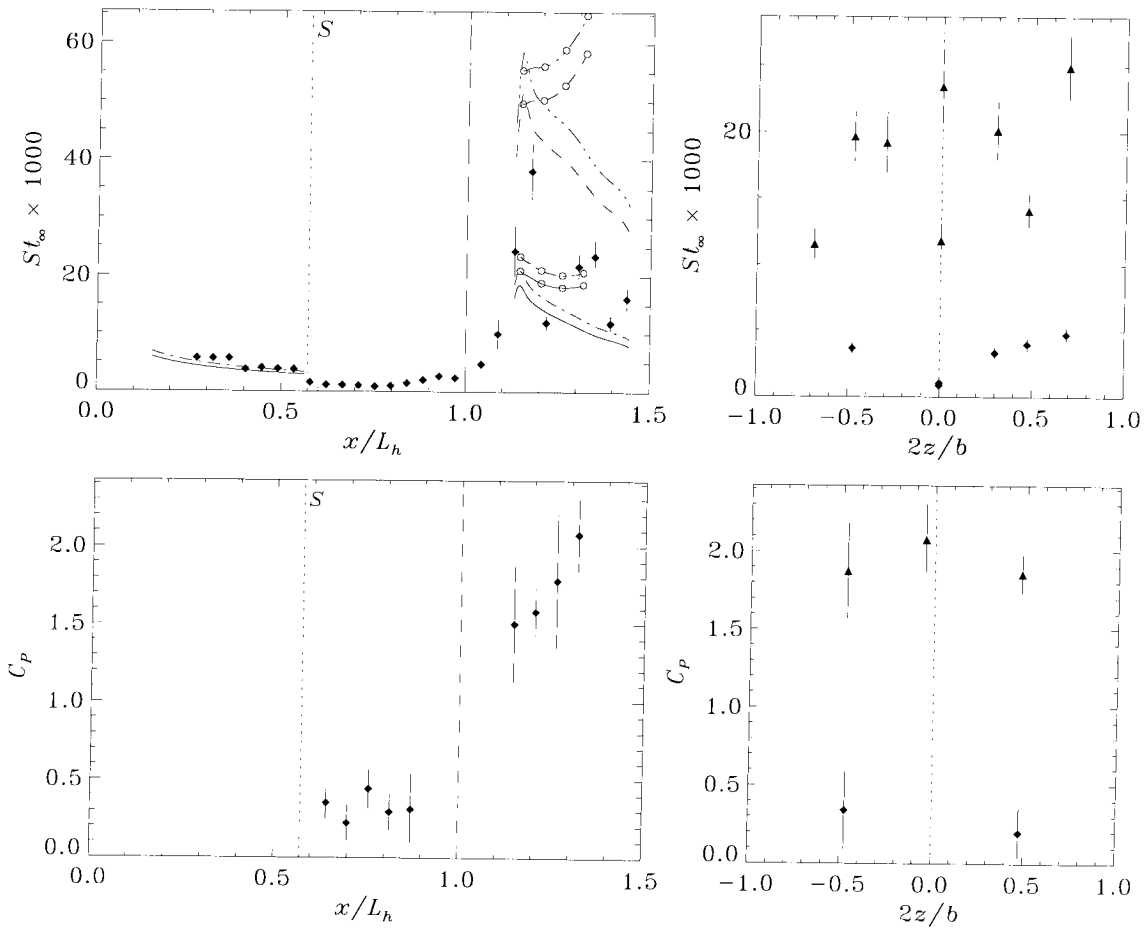

Shot 1309 (condition C0, $A_c/A_* = 400$, $\theta_1 = 15°$, $\theta_w = 30°$)

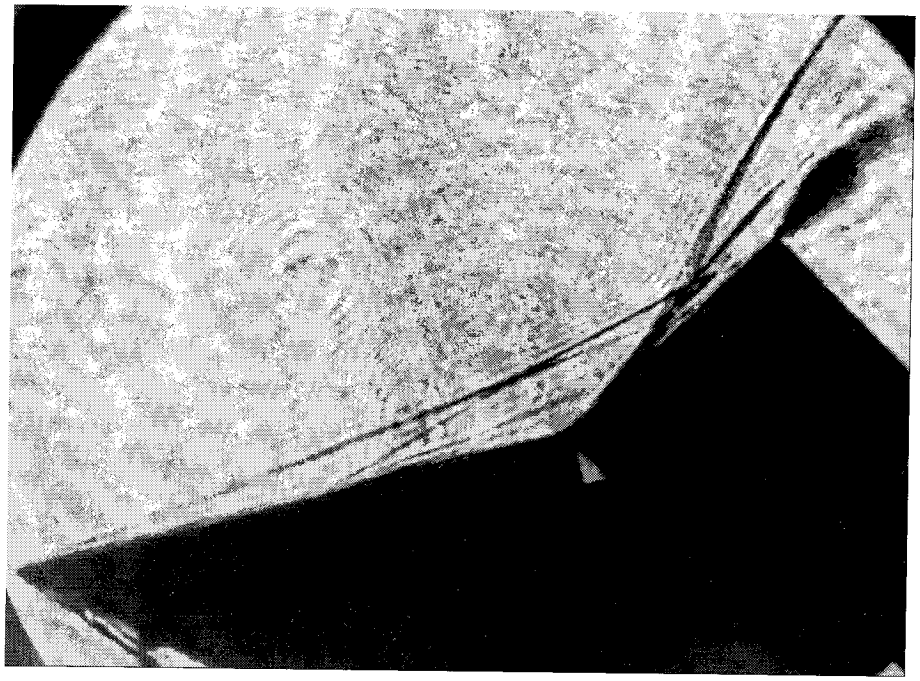

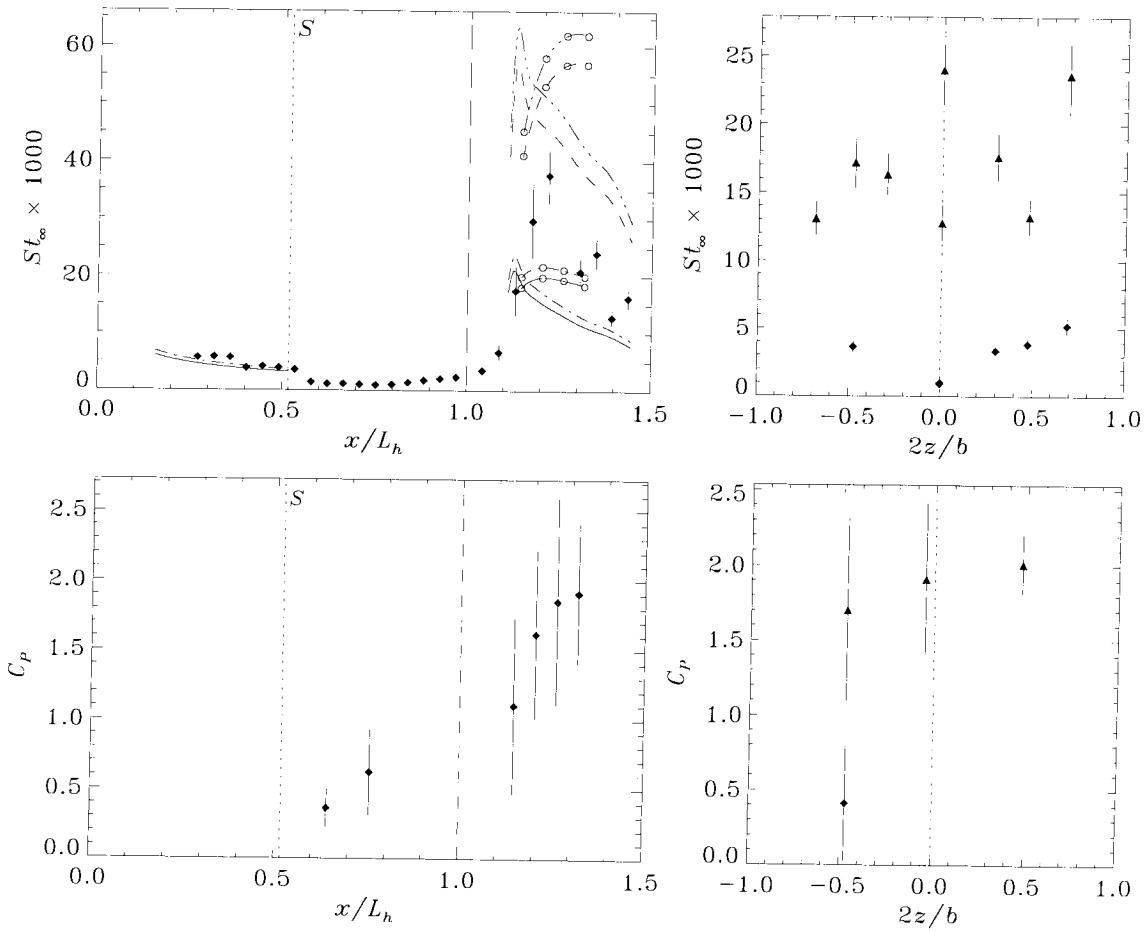

Shot 1310 (condition C1, $A_e/A_* = 400$, $\theta_1 = 15°$, $\theta_w = 30°$)

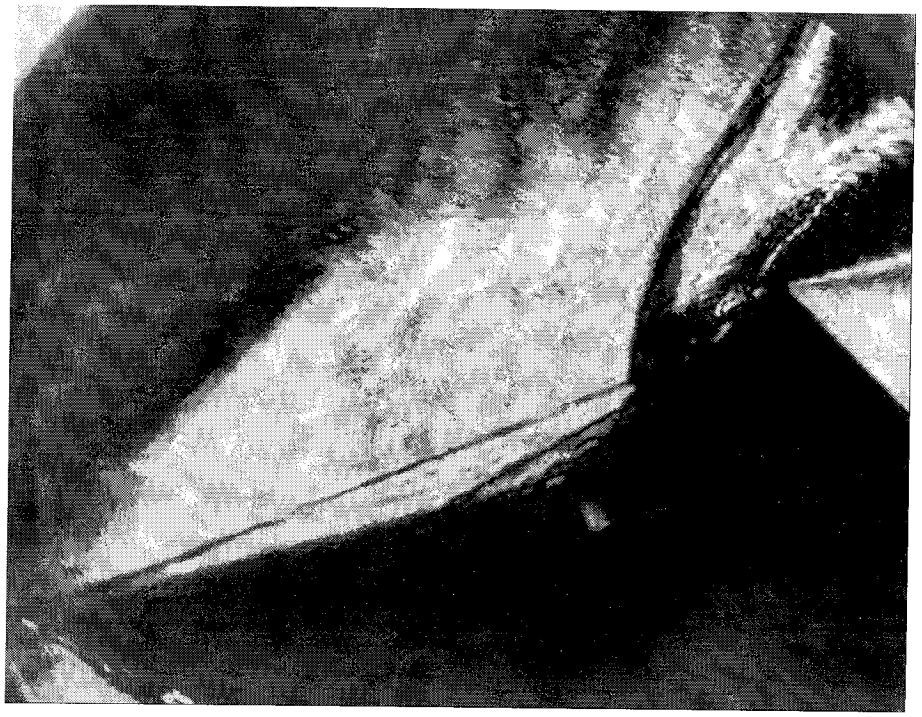

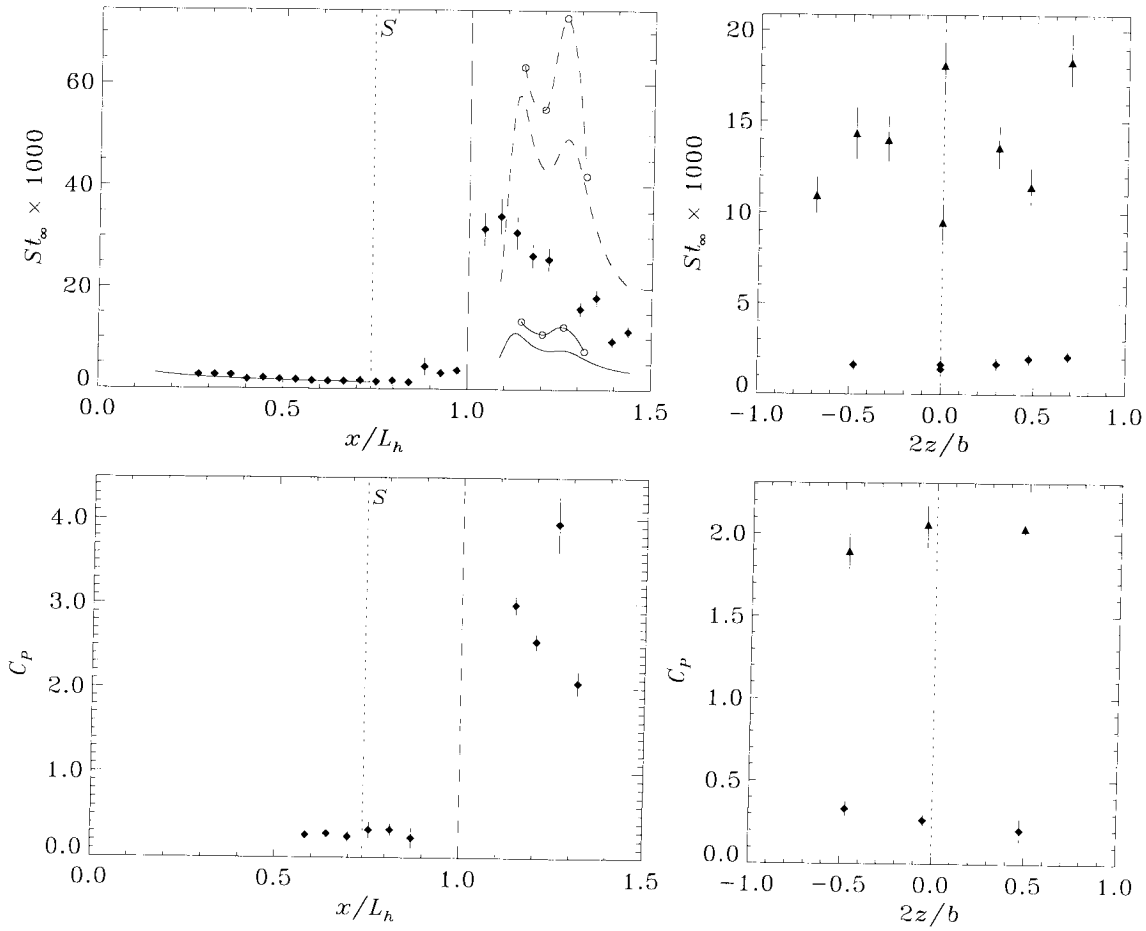

Shot 1311 (condition A1, $A_e/A_* = 100$, $\theta_1 = 15°$, $\theta_w = 30°$)

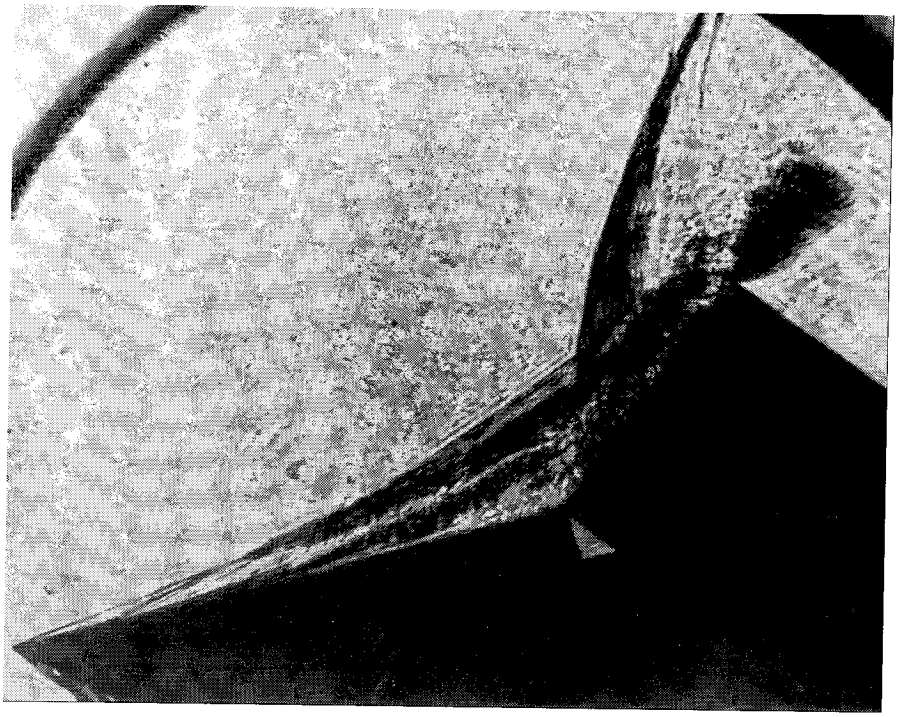

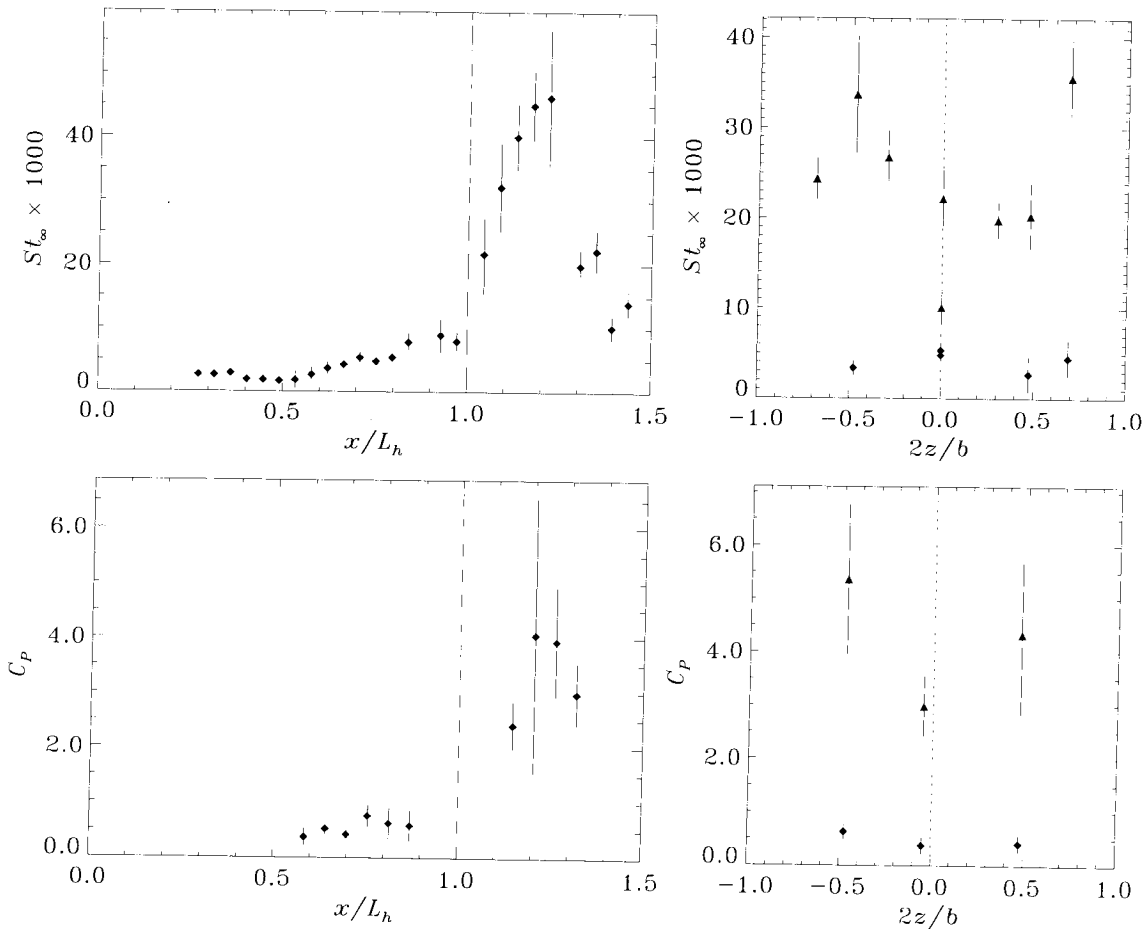

Shot 1312 (condition A1, $A_e/A_* = 100$, $\theta_1 = 15°$, $\theta_w = 40°$)

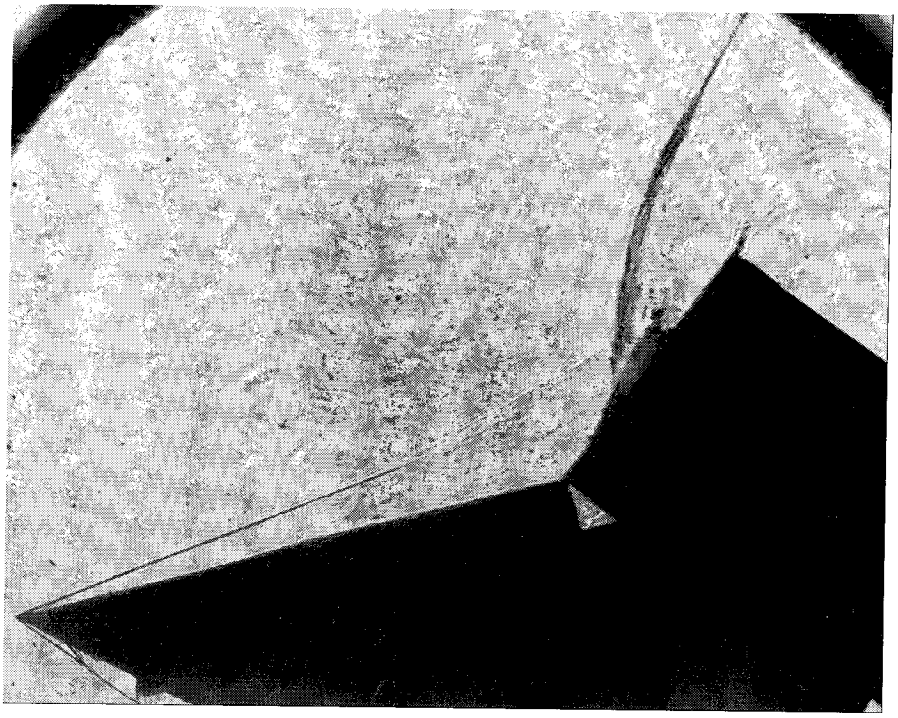

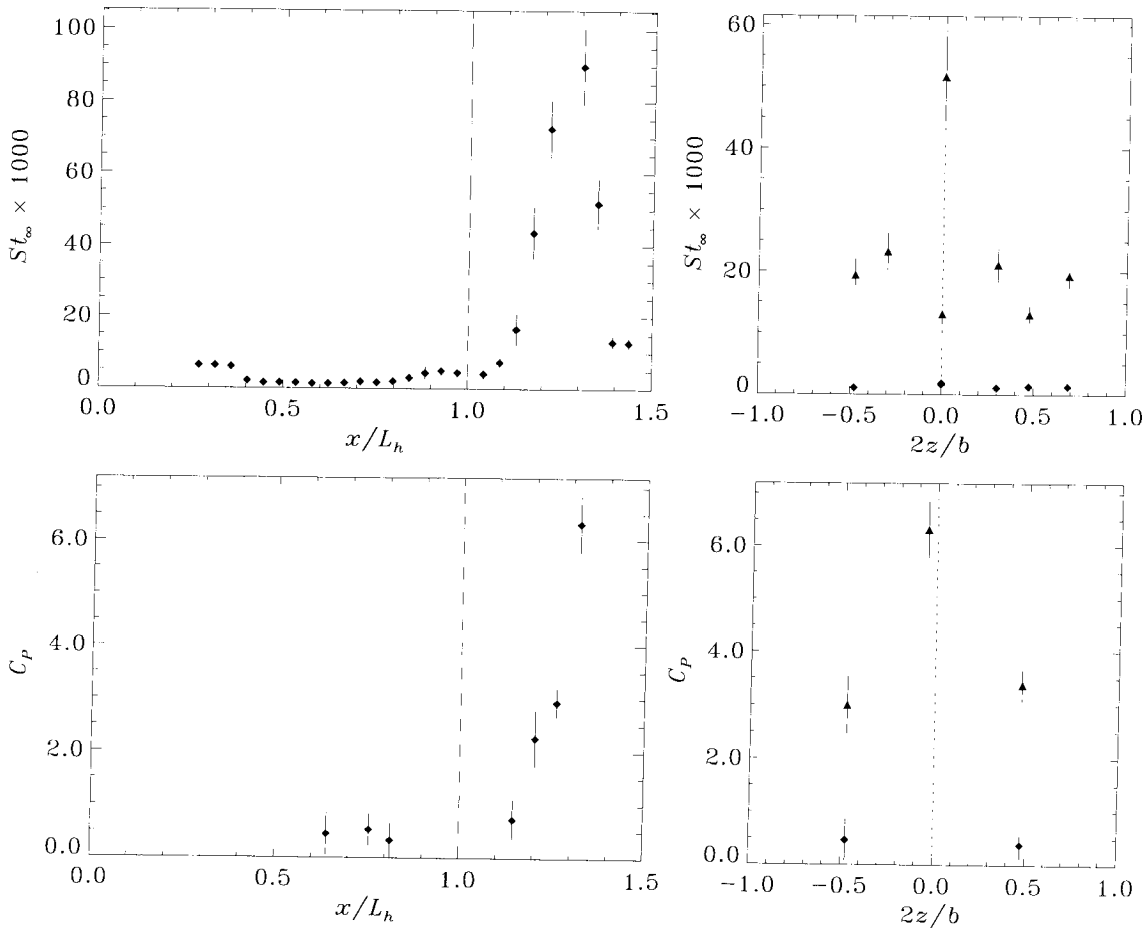

Shot 1313 (condition C1, $A_e/A_* = 400$, $\theta_1 = 15°$, $\theta_w = 40°$)

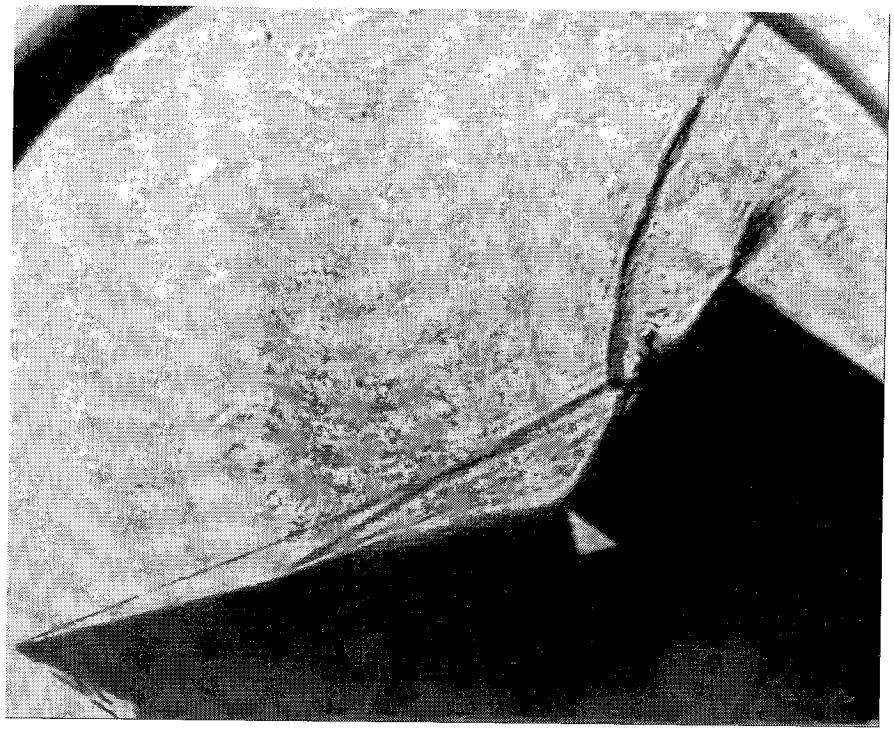

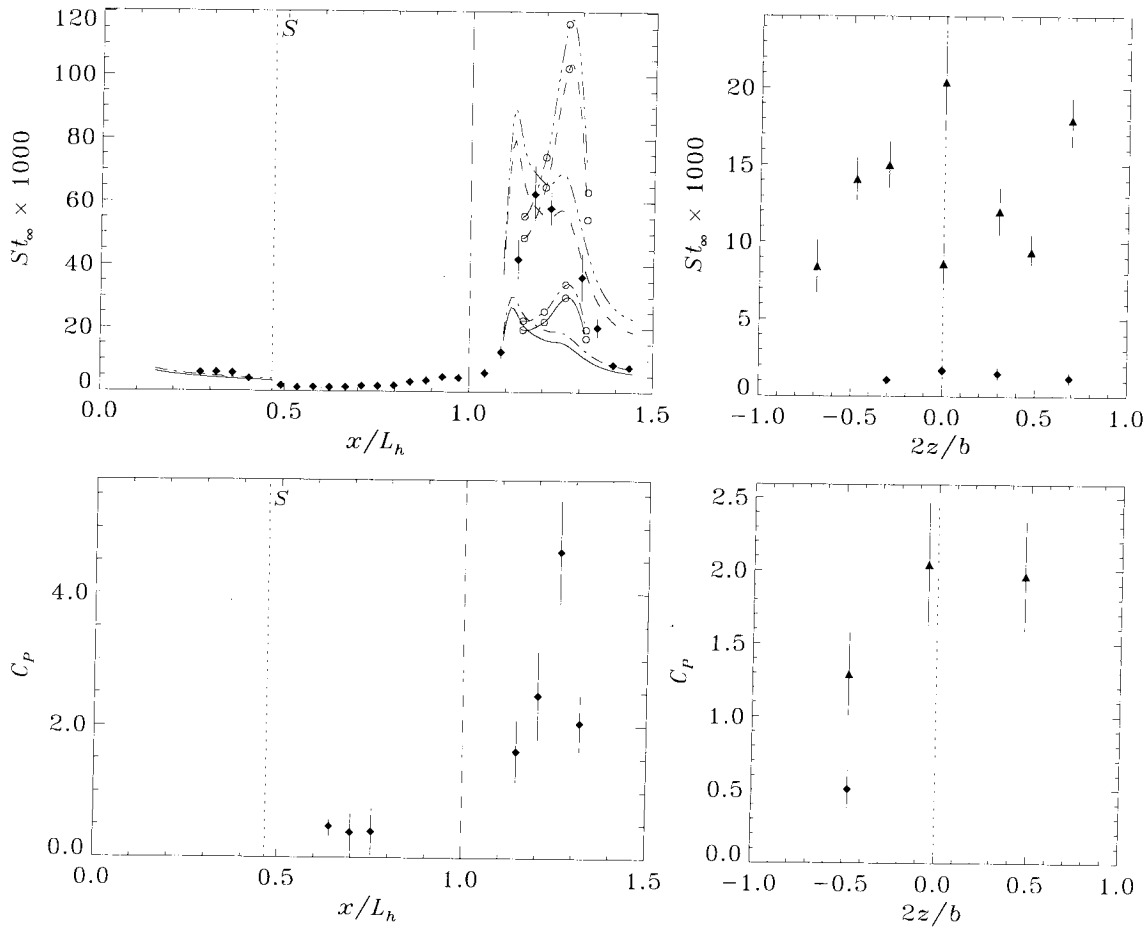

Shot 1314 (condition C1, $A_e/A_* = 400$, $\theta_1 = 15°$, $\theta_w = 40°$)

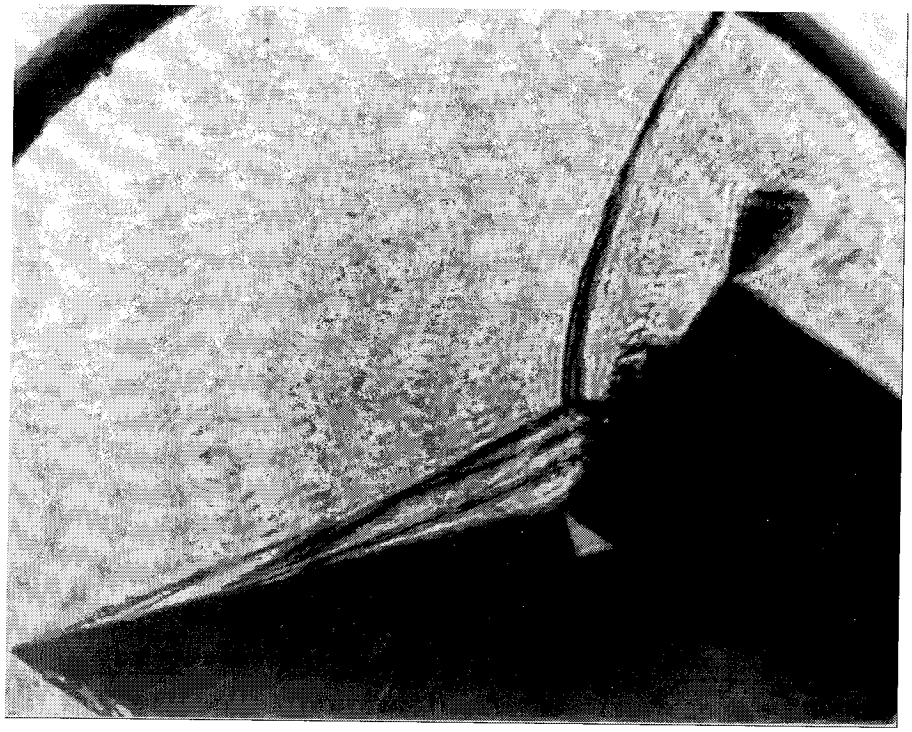

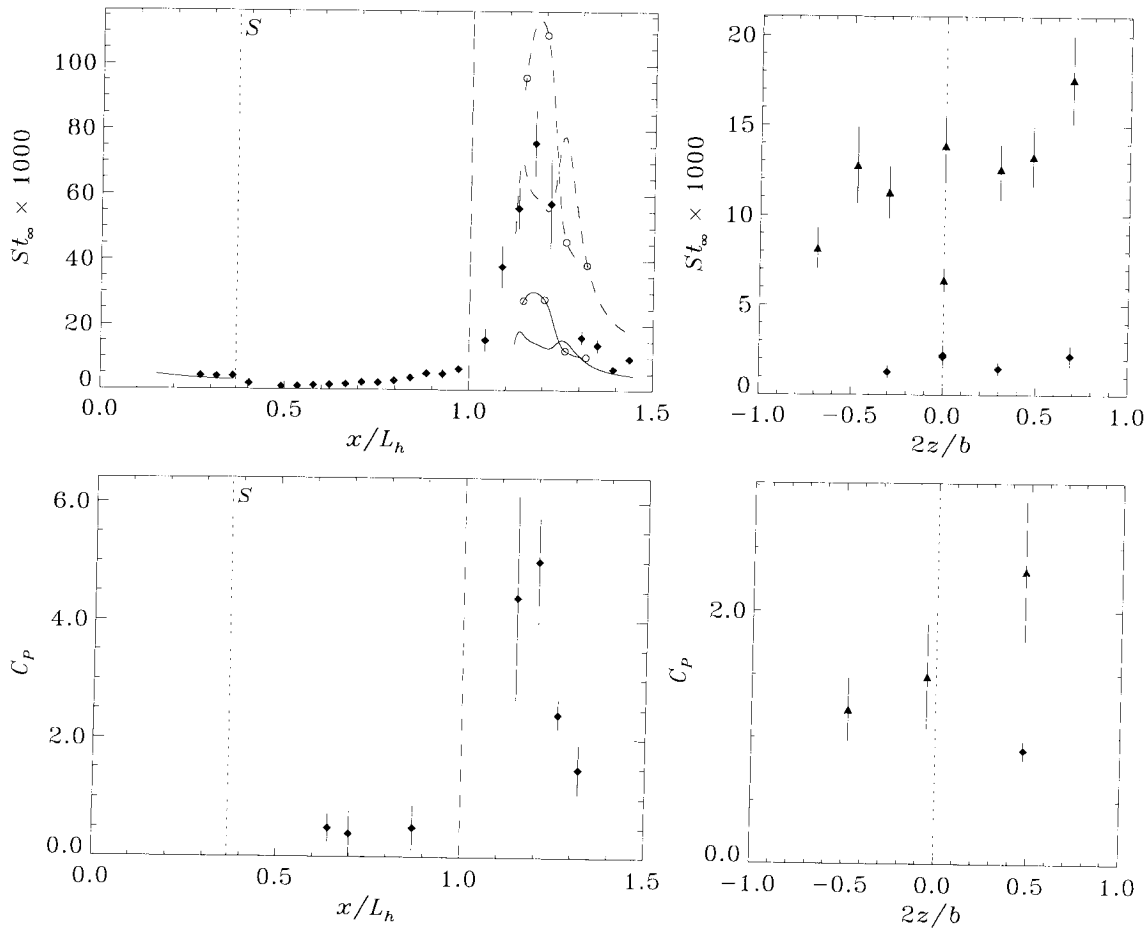

Shot 1315 (condition B2, $A_e/A_* = 225$, $\theta_1 = 15°$, $\theta_w = 40°$)

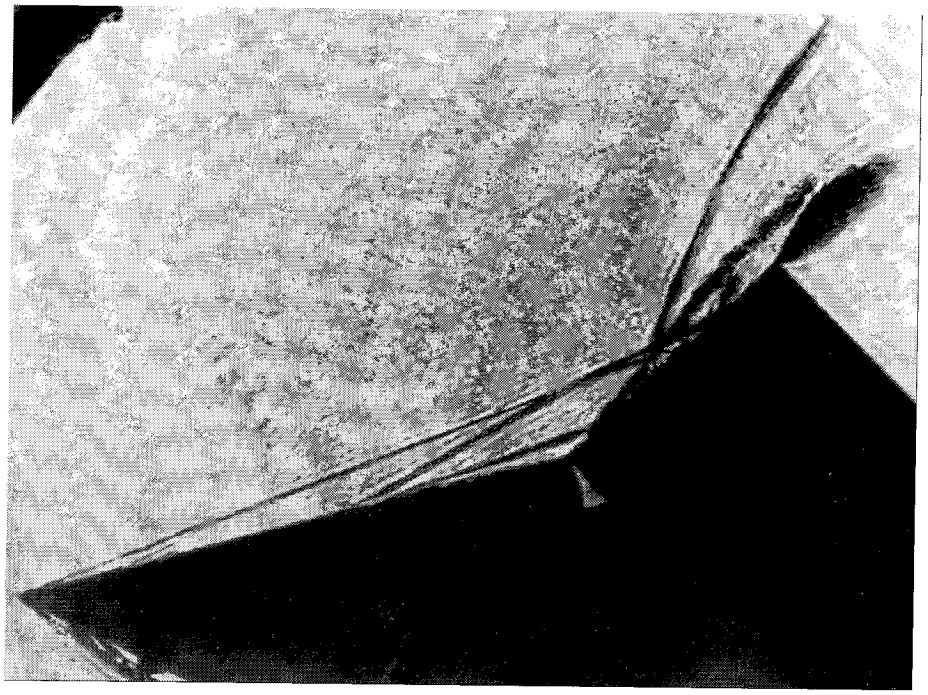

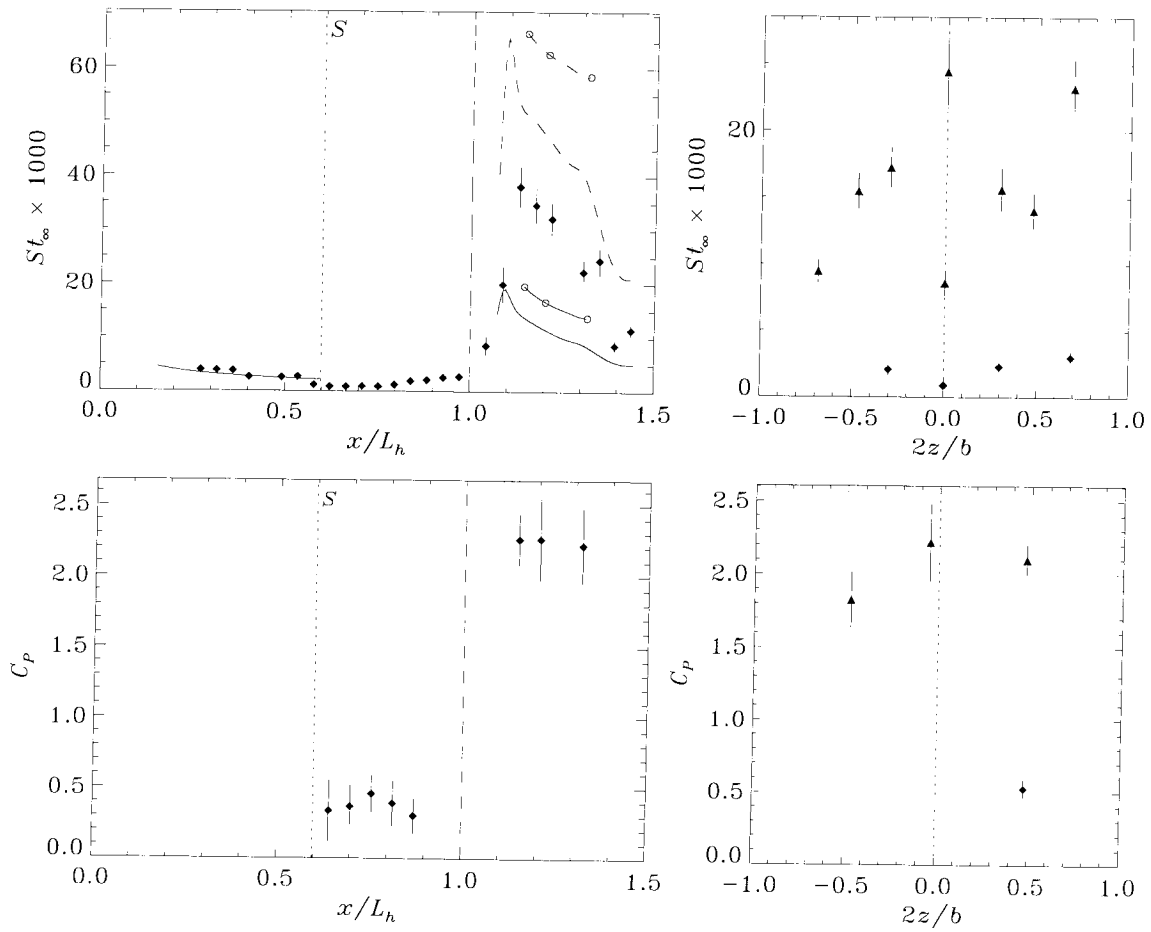

Shot 1316 (condition B2, $A_e/A_* = 225$, $\theta_1 = 15°$, $\theta_w = 30°$)

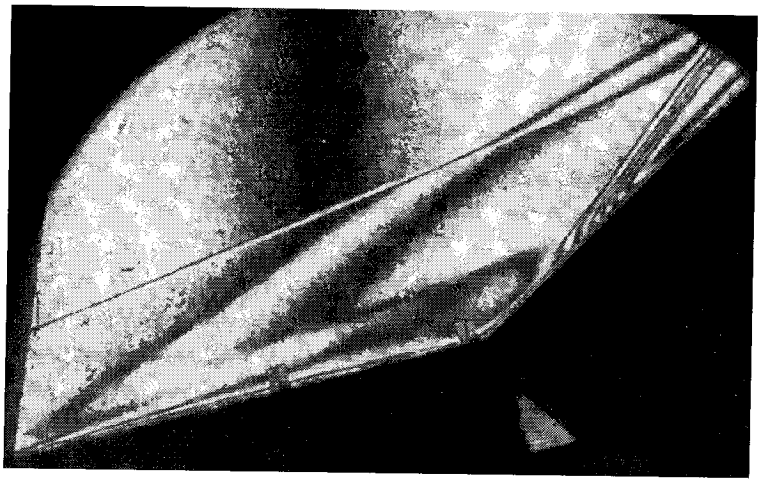

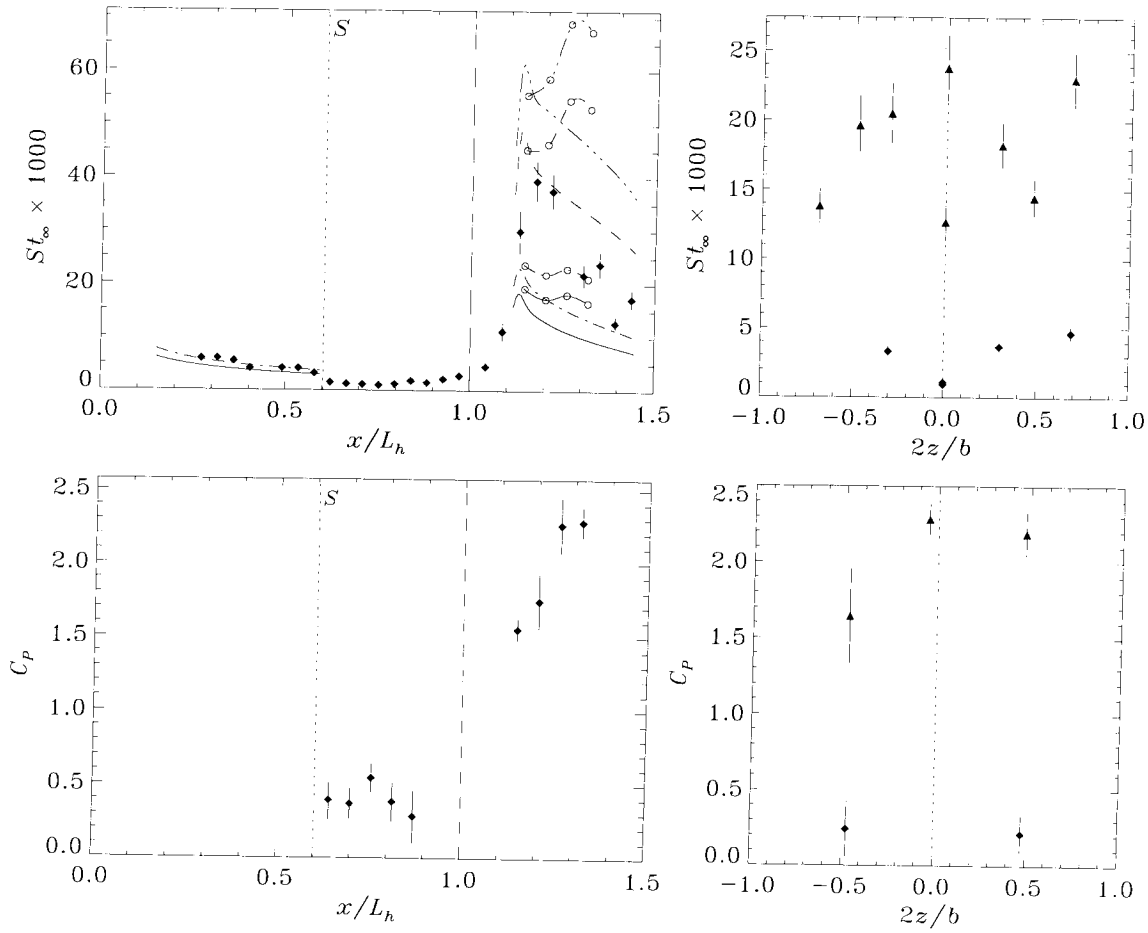

Shot 1317 (condition C4, $A_e/A_* = 225$, $\theta_1 = 15°$, $\theta_w = 30°$)

no photograph

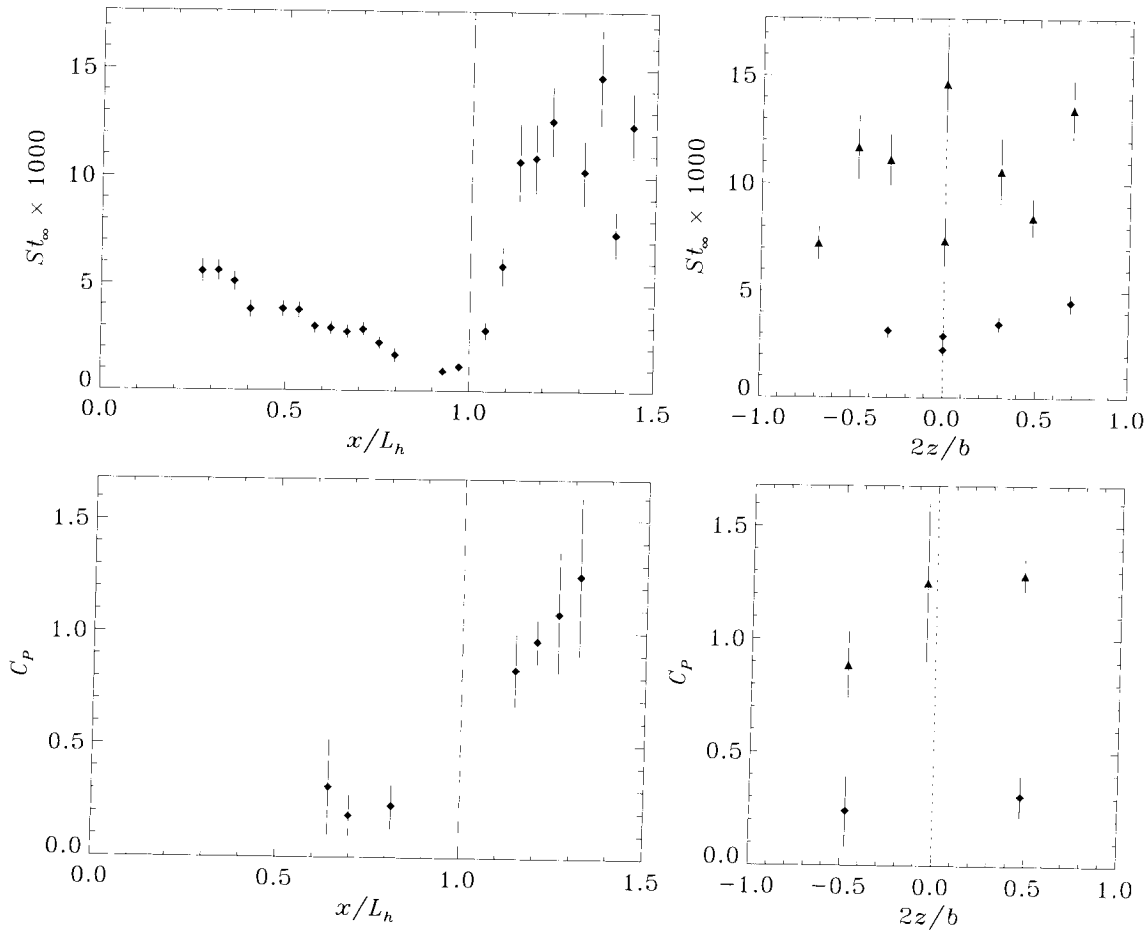

Shot 1318 (condition C4, $A_c/A_* = 225$, $\theta_1 = 15°$, $\theta_w = 20°$)

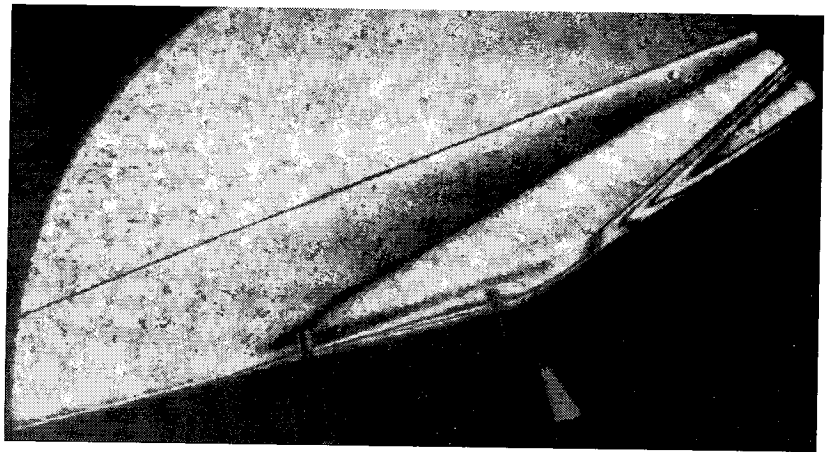

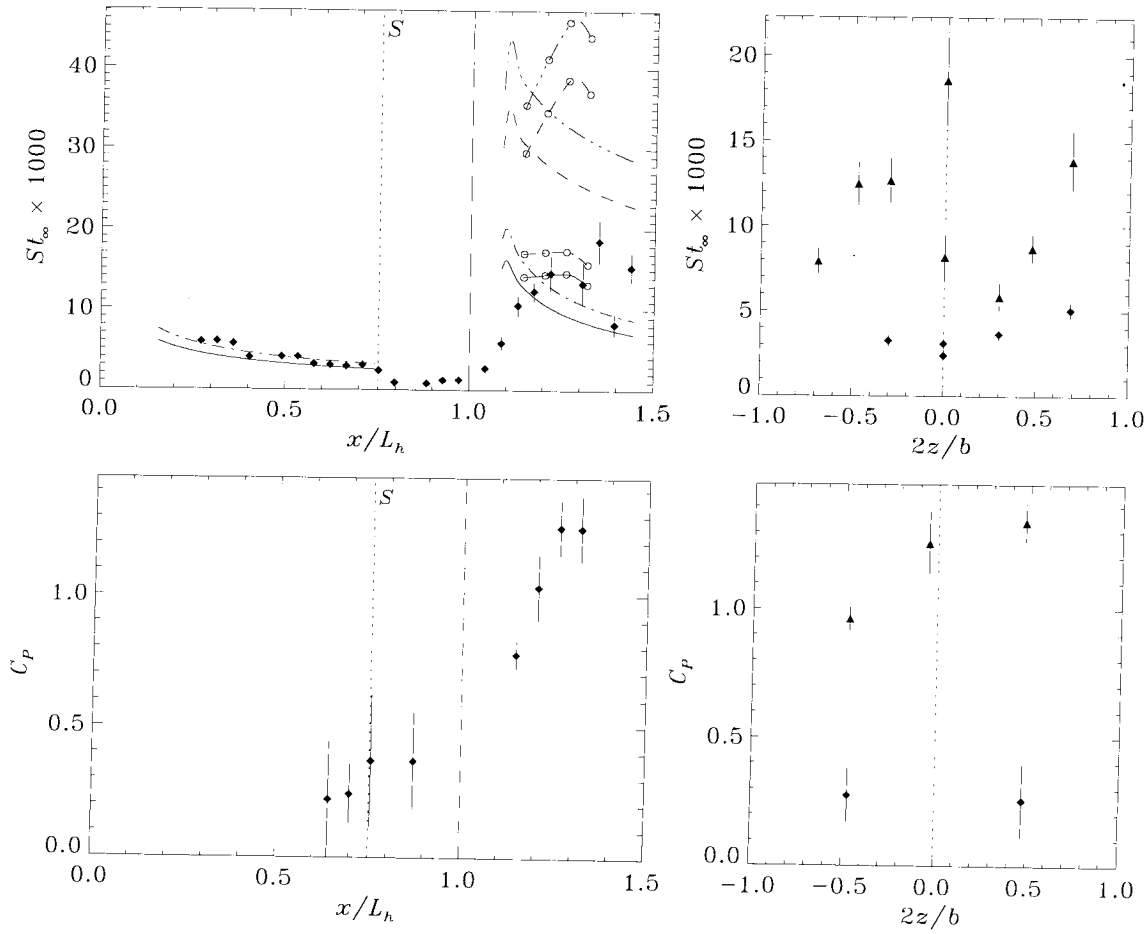

Shot 1319 (condition C4, $A_e/A_* = 225$, $\theta_1 = 15°$, $\theta_w = 20°$)

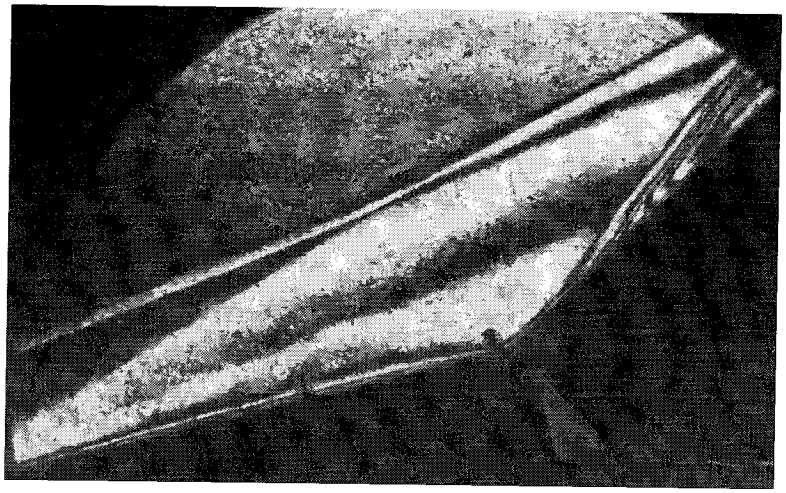

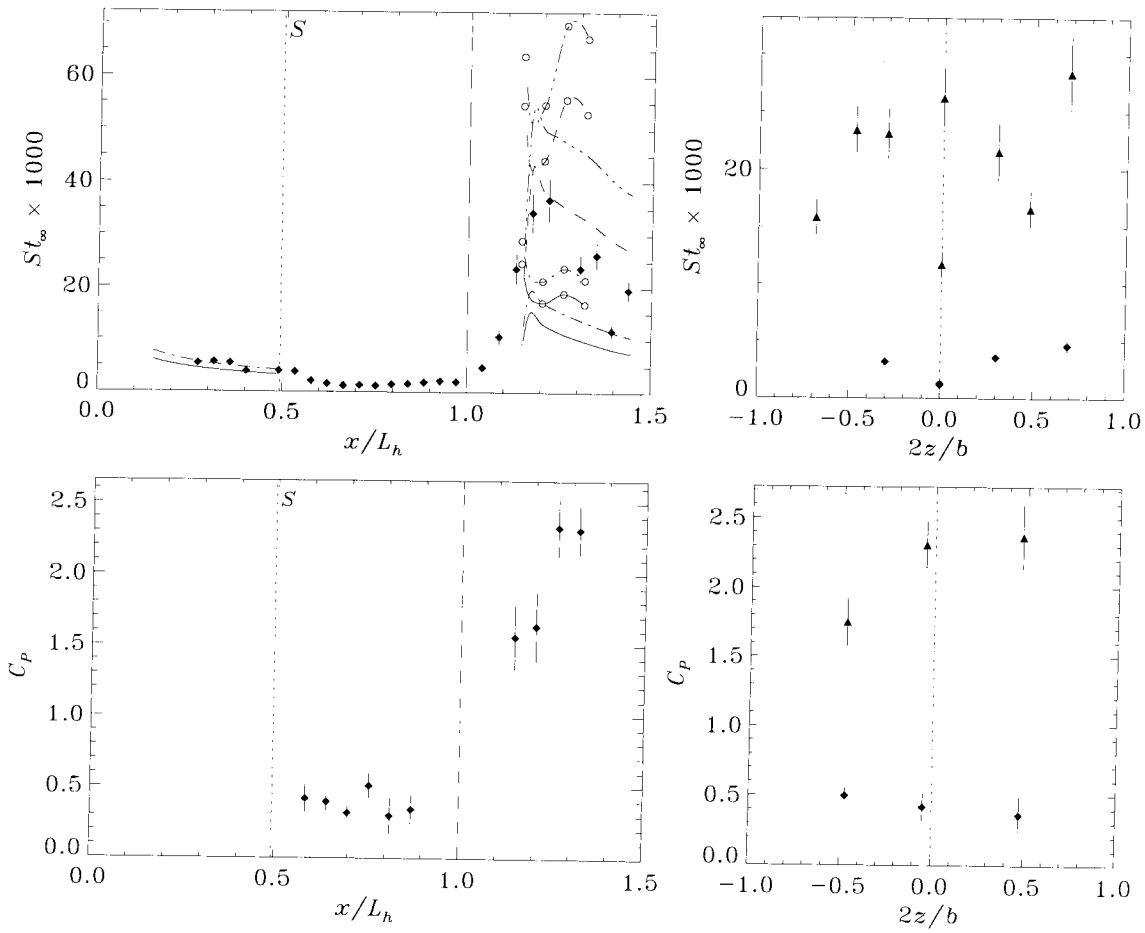

Shot 1320 (condition C4, $A_e/A_* = 225$, $\theta_1 = 15°$, $\theta_w = 30°$)

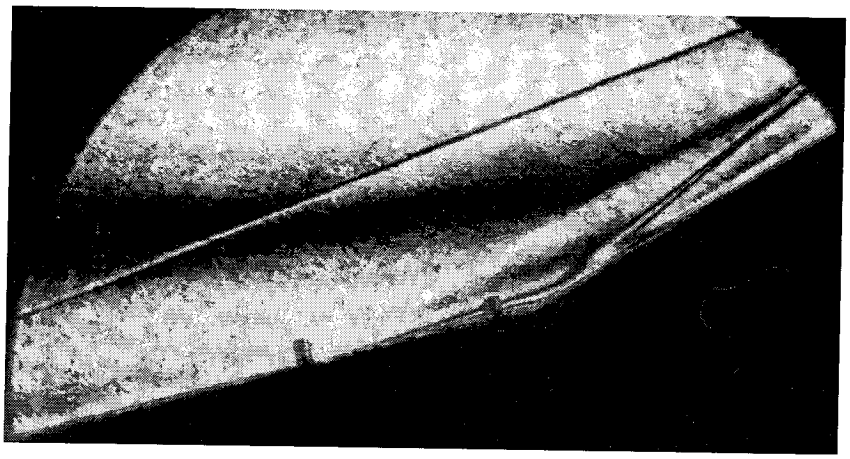

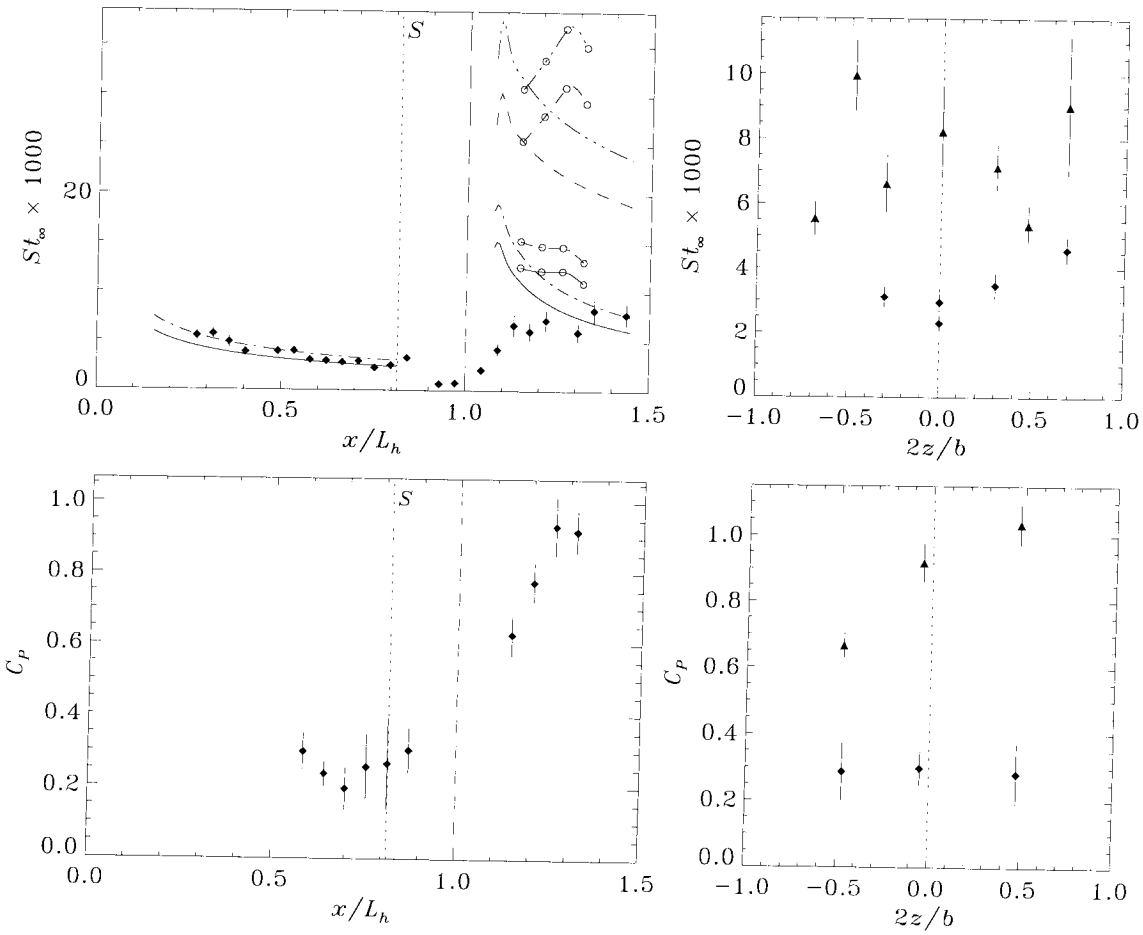

Shot 1321 (condition C4, $A_e/A_* = 225$, $\theta_1 = 15°$, $\theta_w = 15°$)

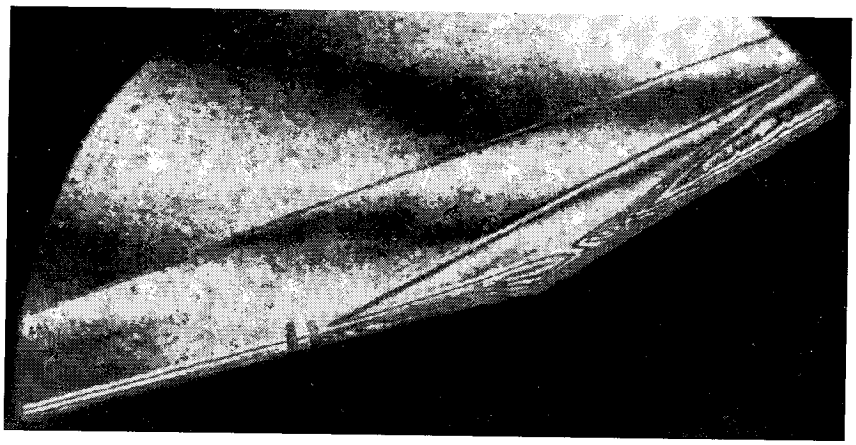

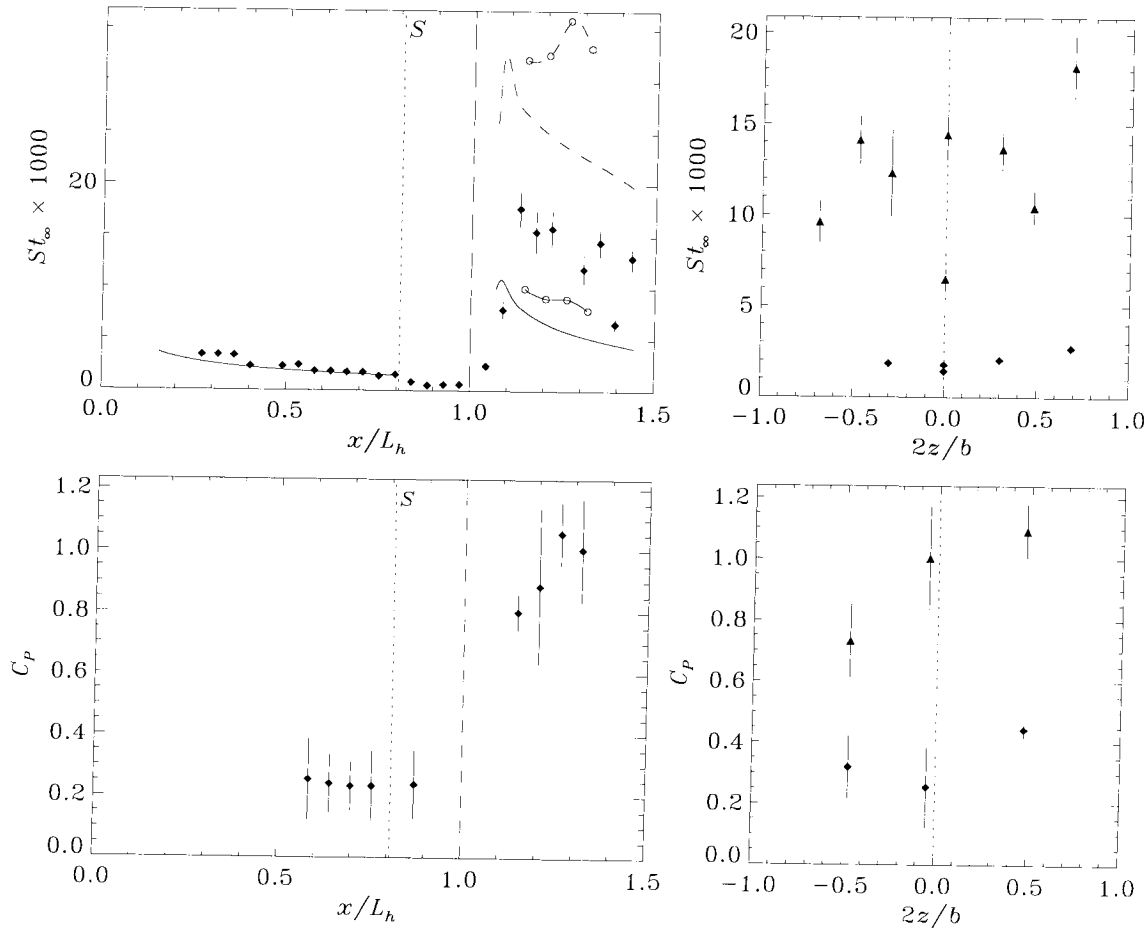

Shot 1322 (condition B3, $A_e/A_* = 400$, $\theta_1 = 15°$, $\theta_w = 15°$)

no photograph

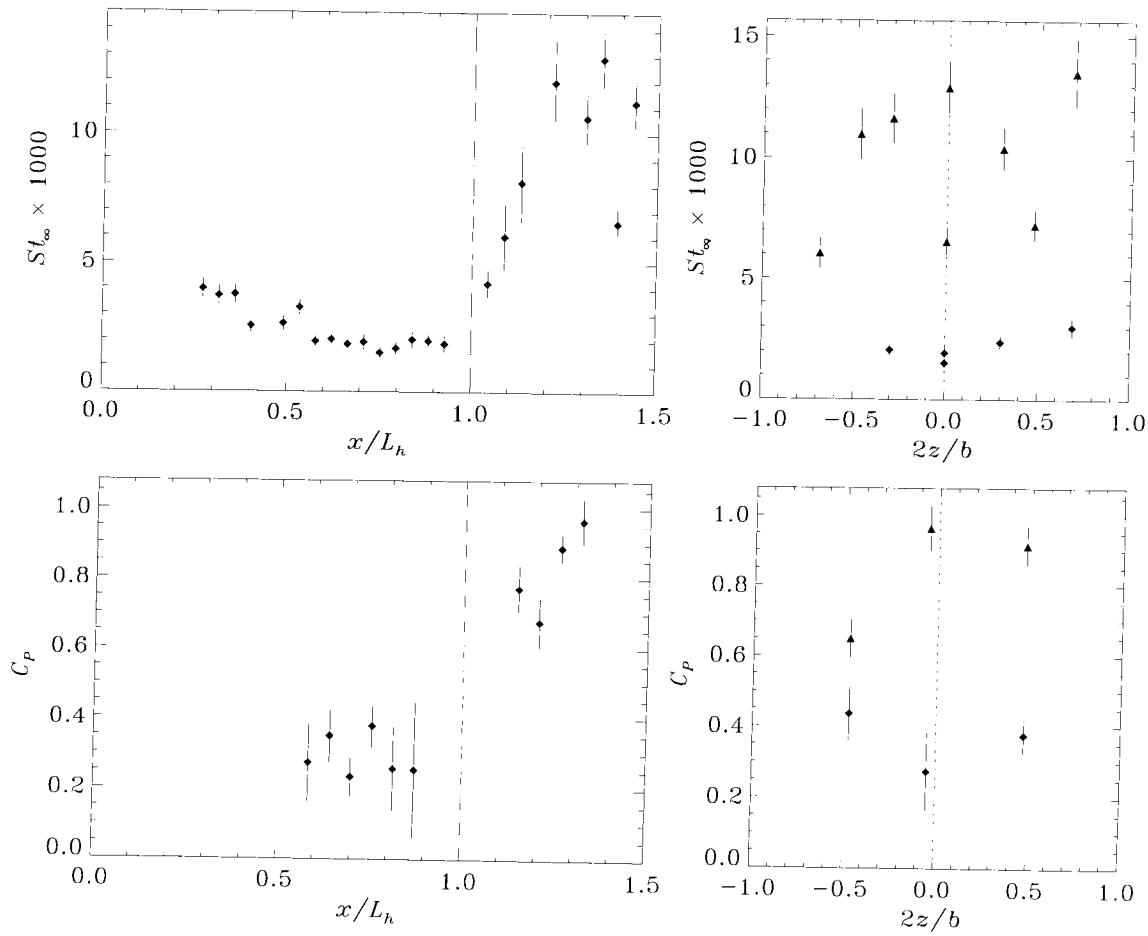

Shot 1323 (condition C0, $A_e/A_* = 100$, $\theta_1 = 15°$, $\theta_w = 5°$)

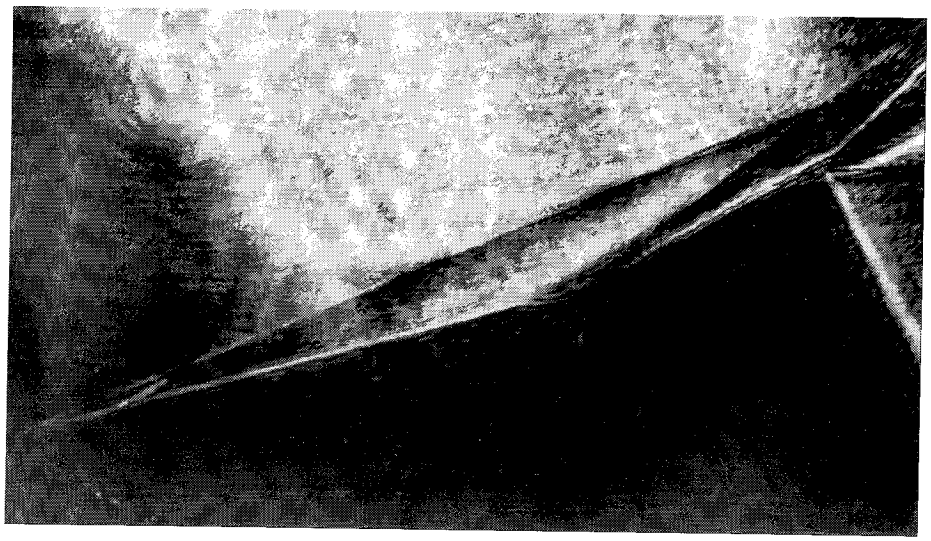

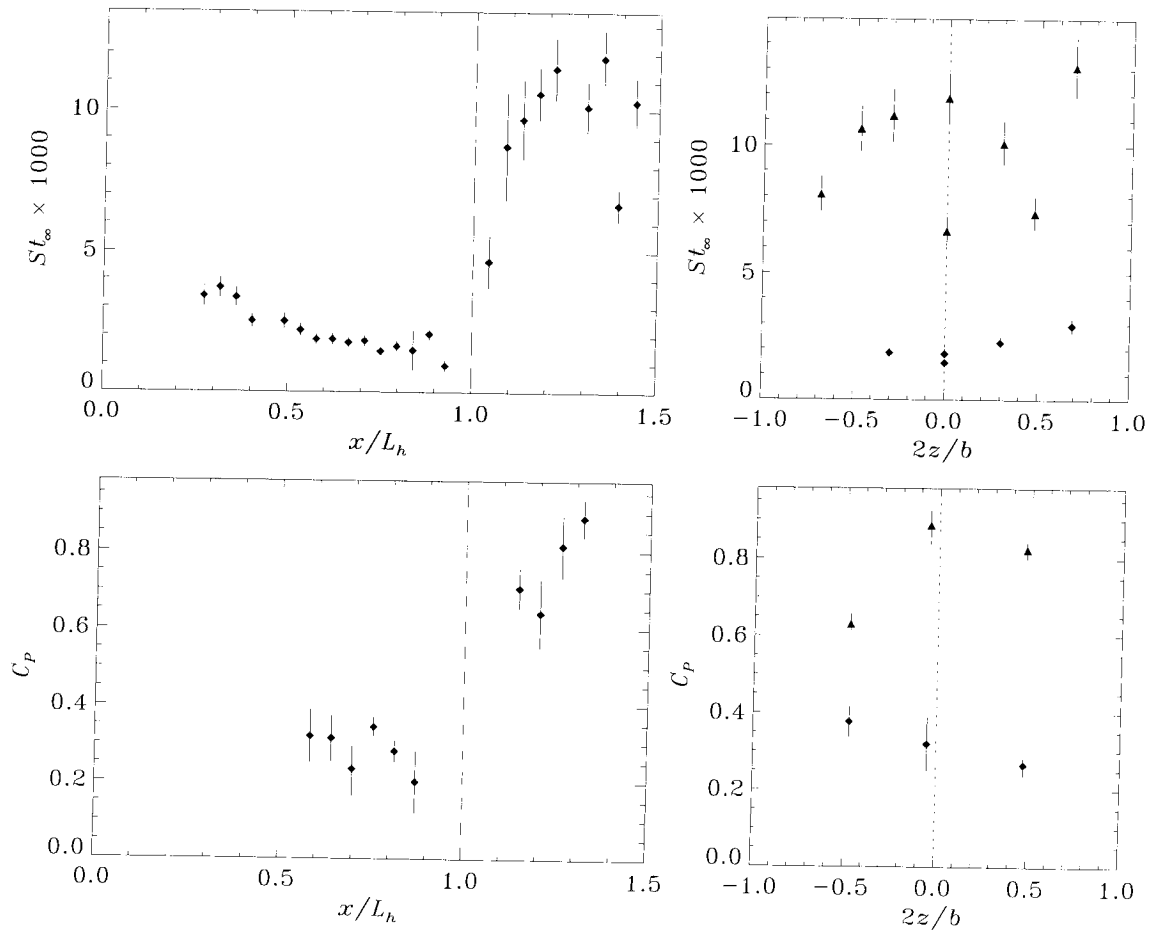

Shot 1324 (condition C3, $A_e/A_* = 100$, $\theta_1 = 15°$, $\theta_w = 5°$)

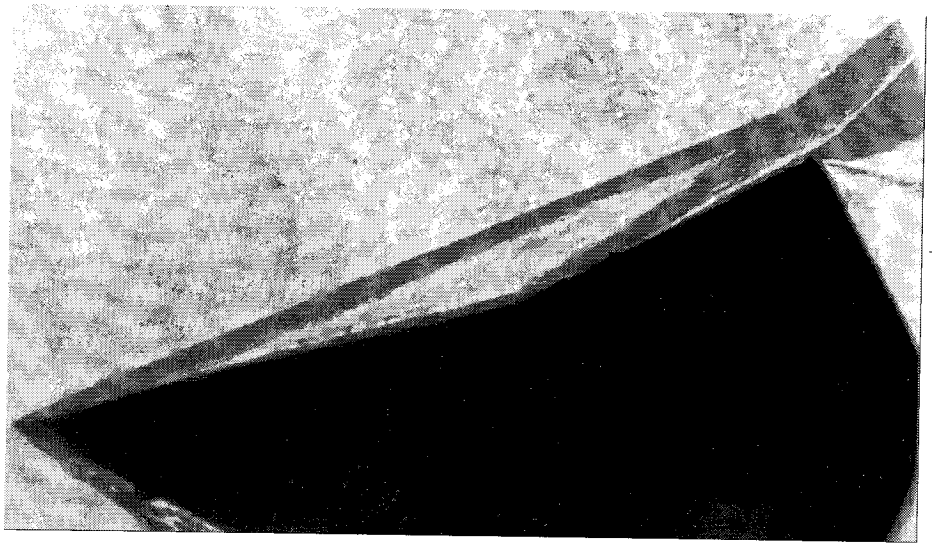

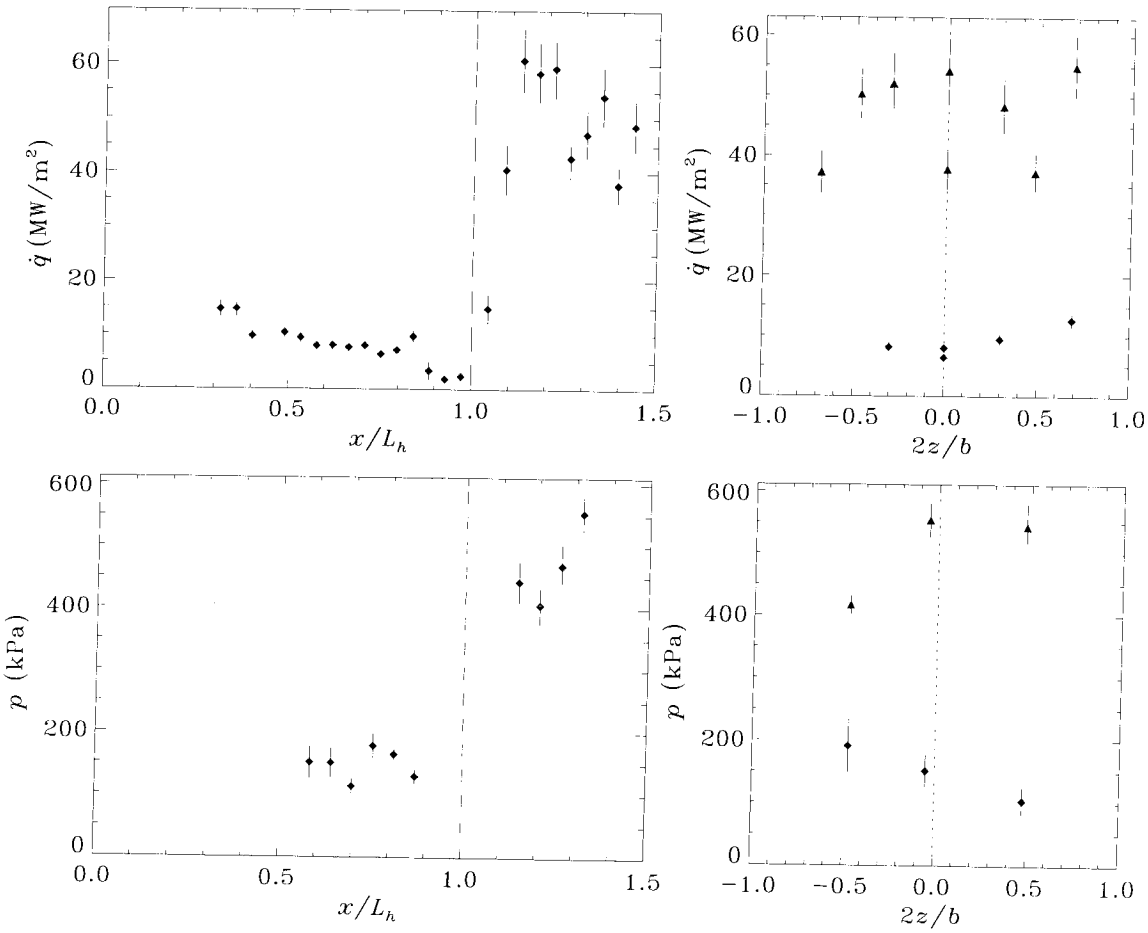

Shot 1325 (condition C3, $A_e/A_* = 110$, $\theta_1 = 15°$, $\theta_w = 5°$)

no photograph

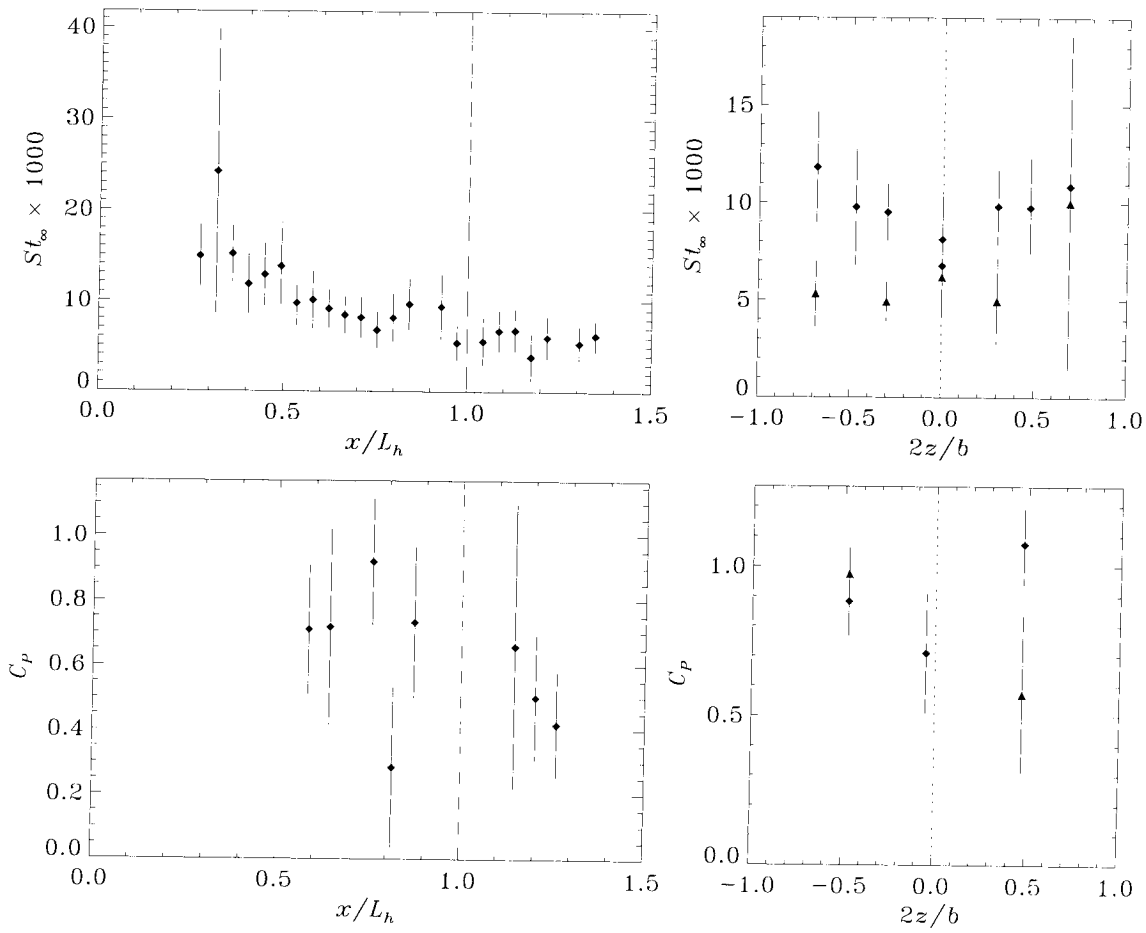

Shot 1725 (condition A0, $A_e/A_* = 400$, $\theta_1 = 30°$, $\theta_w = 0°$)

no photograph

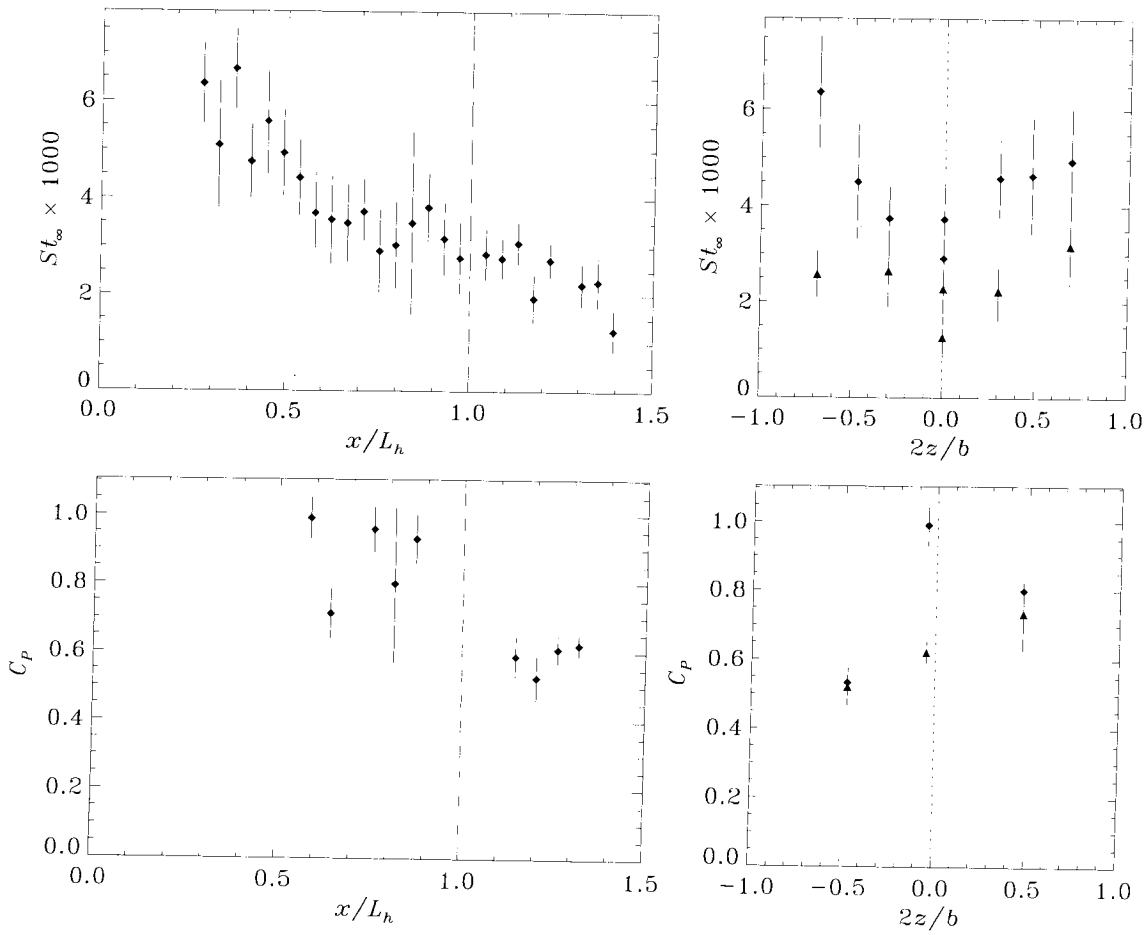

Shot 1727 (condition A0, $A_e/A_* = 100$, $\theta_1 = 30°$, $\theta_w = 0°$)

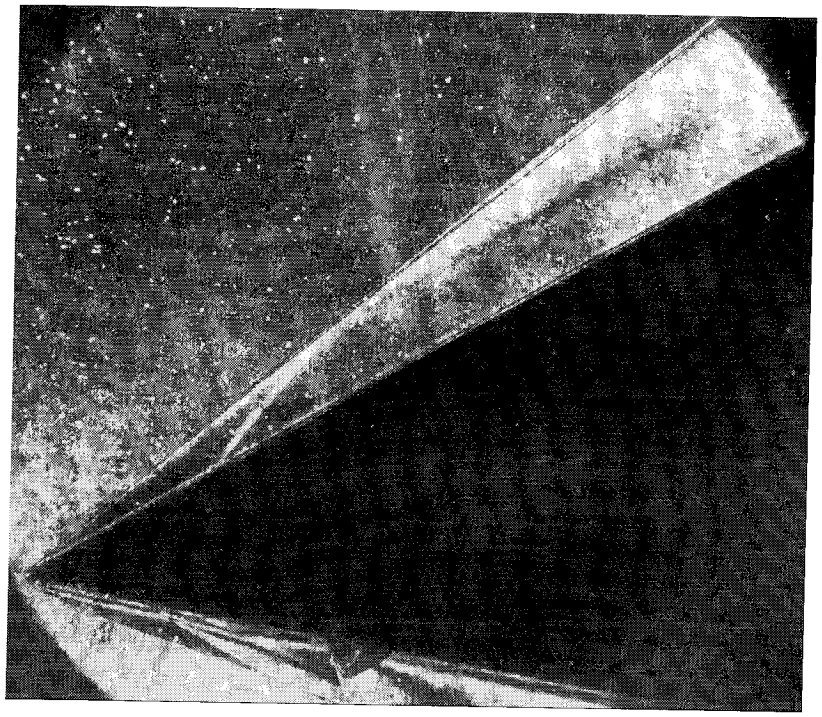

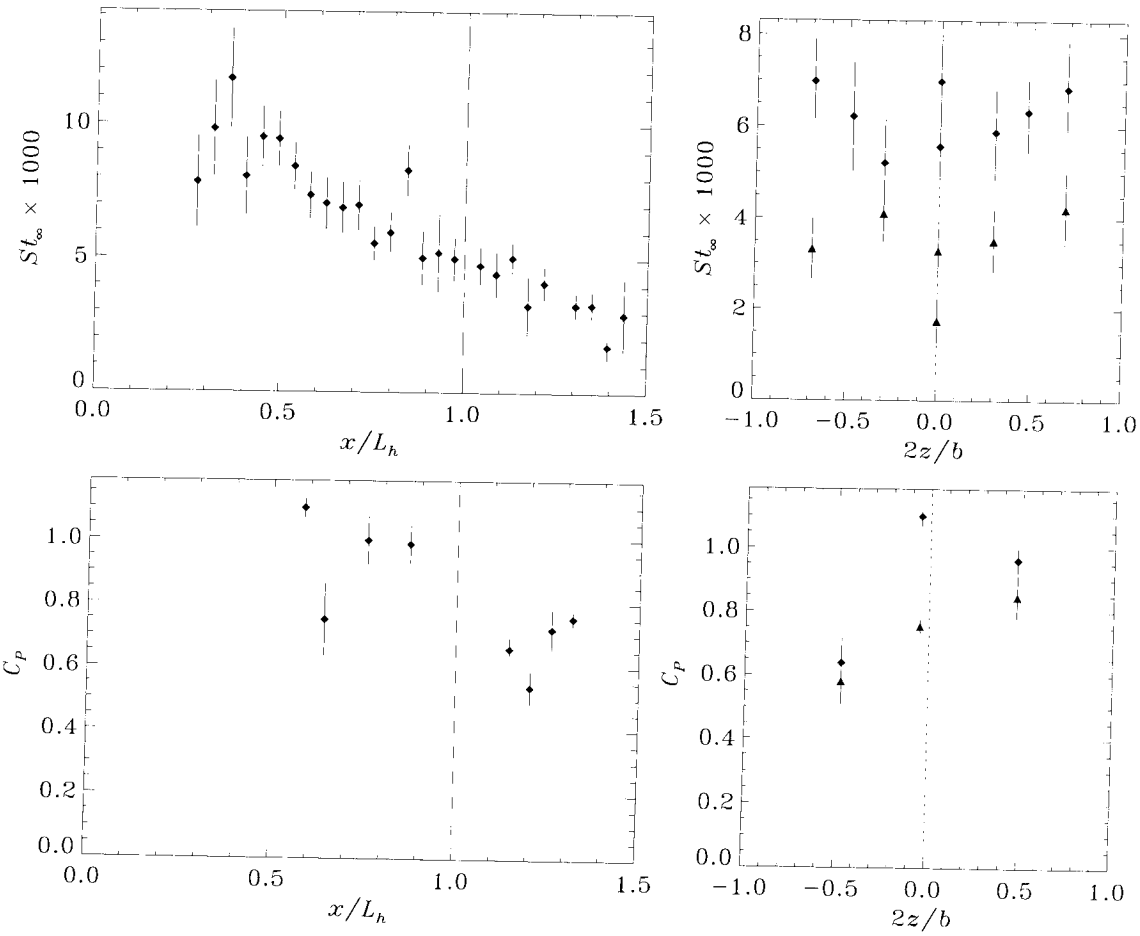

Shot 1729 (condition B1, $A_e/A_* = 100$, $\theta_1 = 30°$, $\theta_w = 0°$)

no photograph

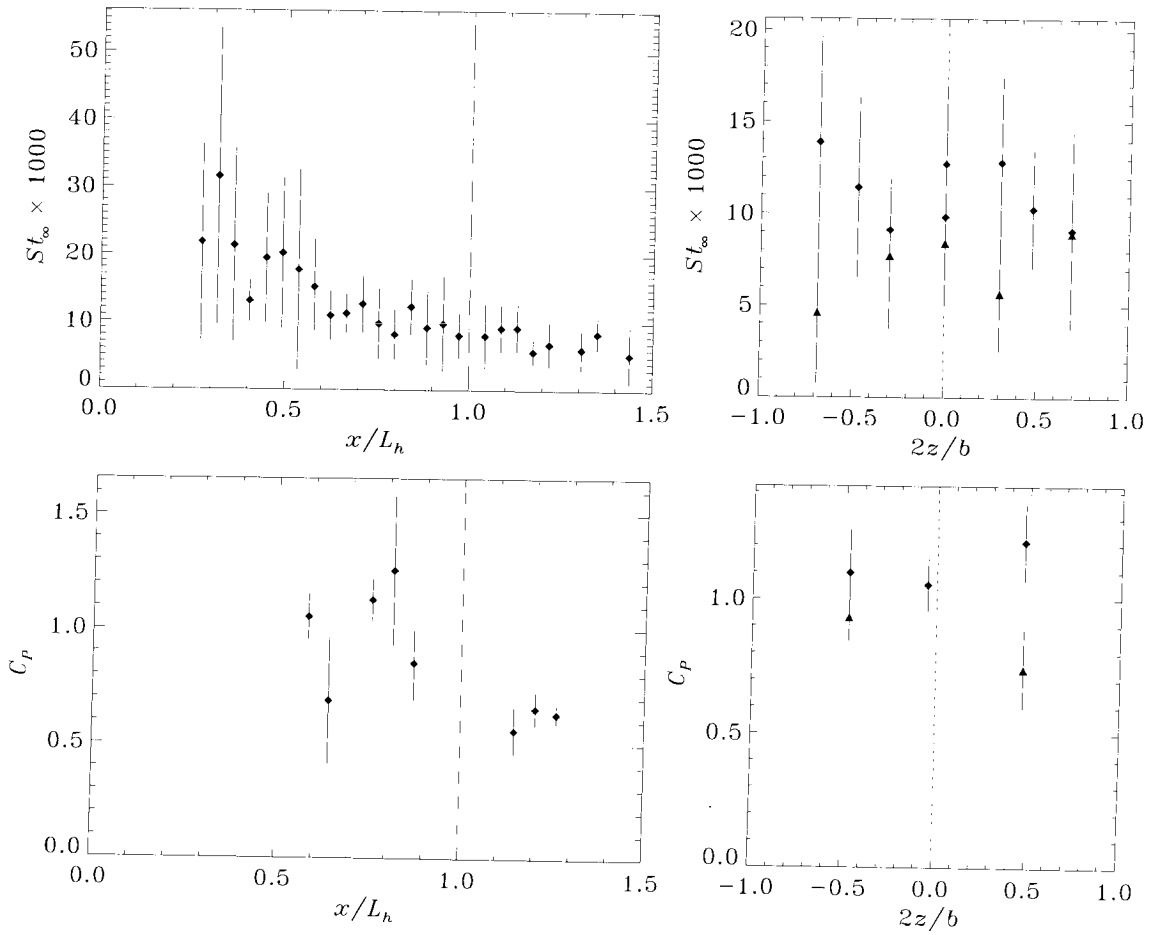

Shot 1730 (condition A0, $A_e/A_* = 100$, $\theta_1 = 30°$, $\theta_w = 0°$)

no photograph

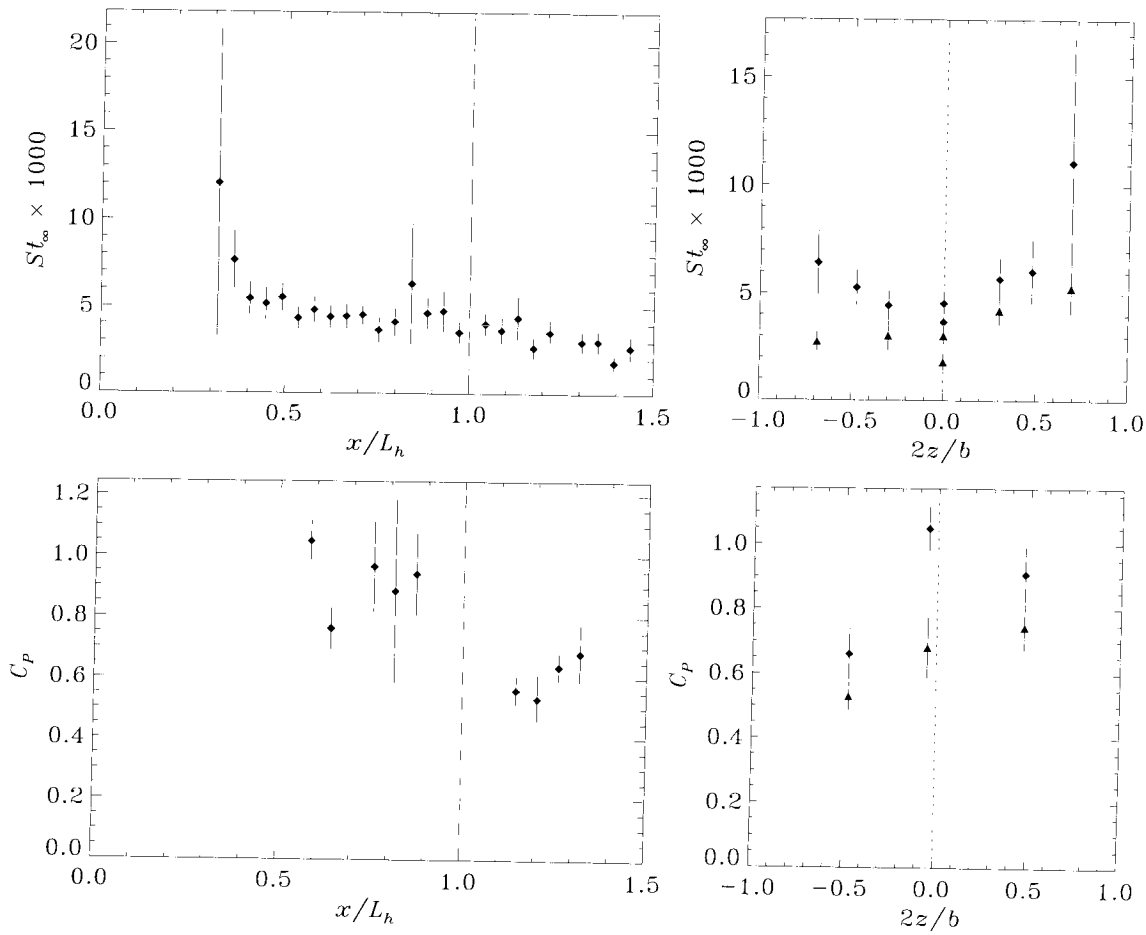

Shot 1731 (condition A0, $A_e/A_* = 100$, $\theta_1 = 30°$, $\theta_w = 0°$)

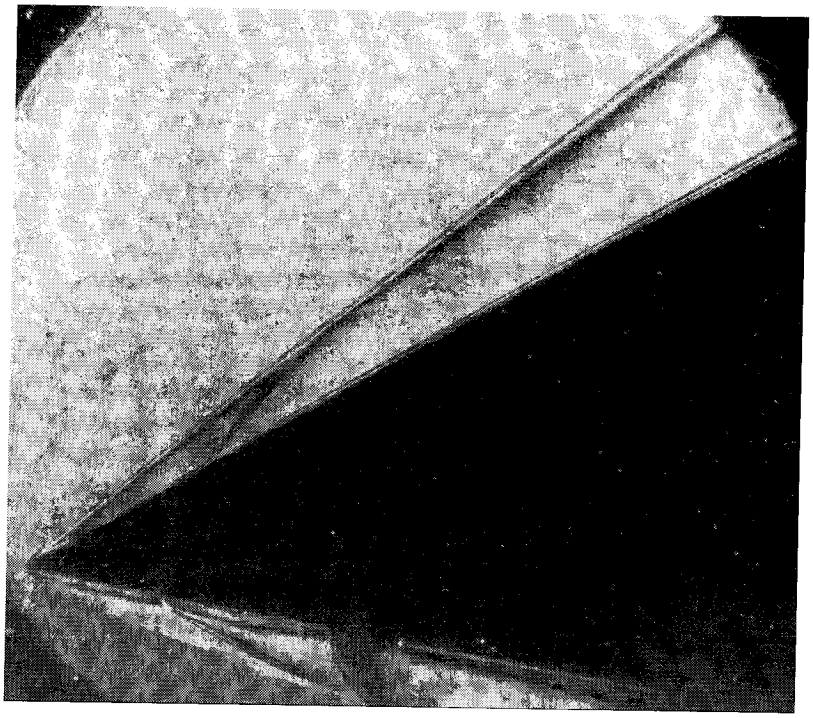

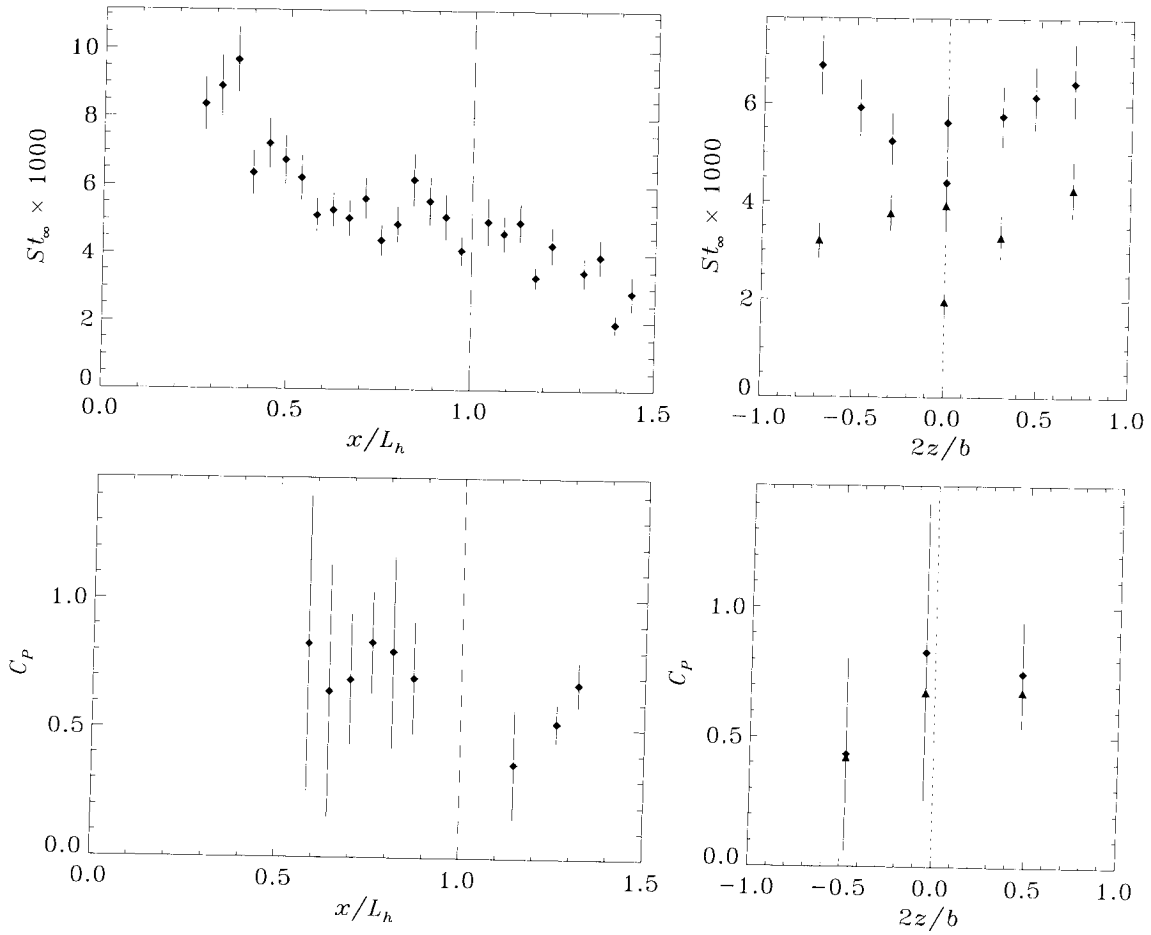

Shot 1732 (condition C0, $A_e/A_* = 100$, $\theta_1 = 30°$, $\theta_w = 0°$)

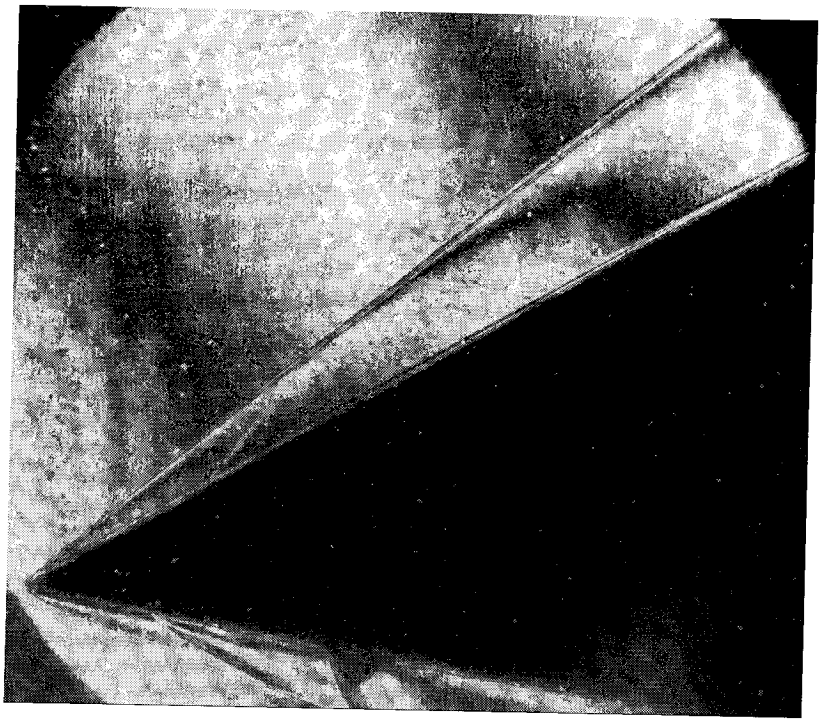

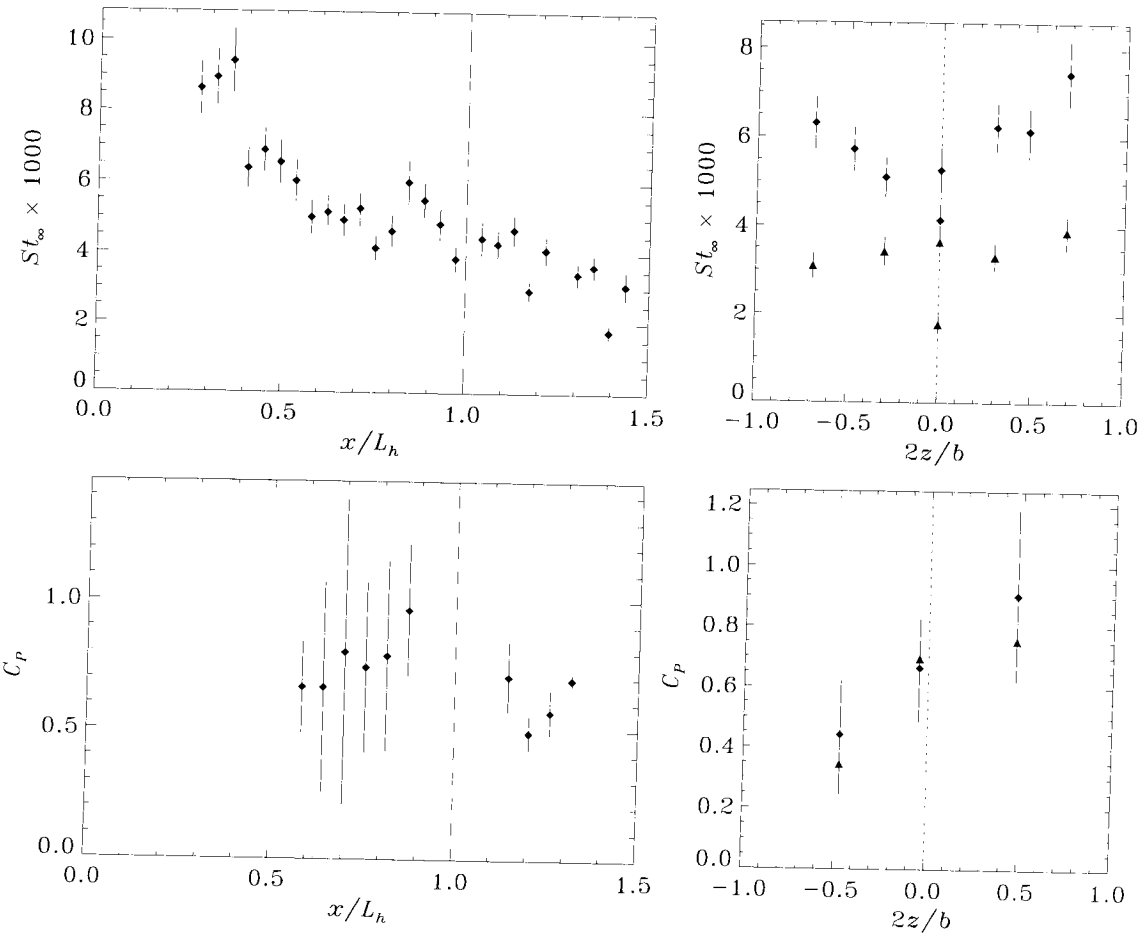

Shot 1733 (condition C0, $A_e/A_* = 100$, $\theta_1 = 30°$, $\theta_w = 0°$)

no photograph

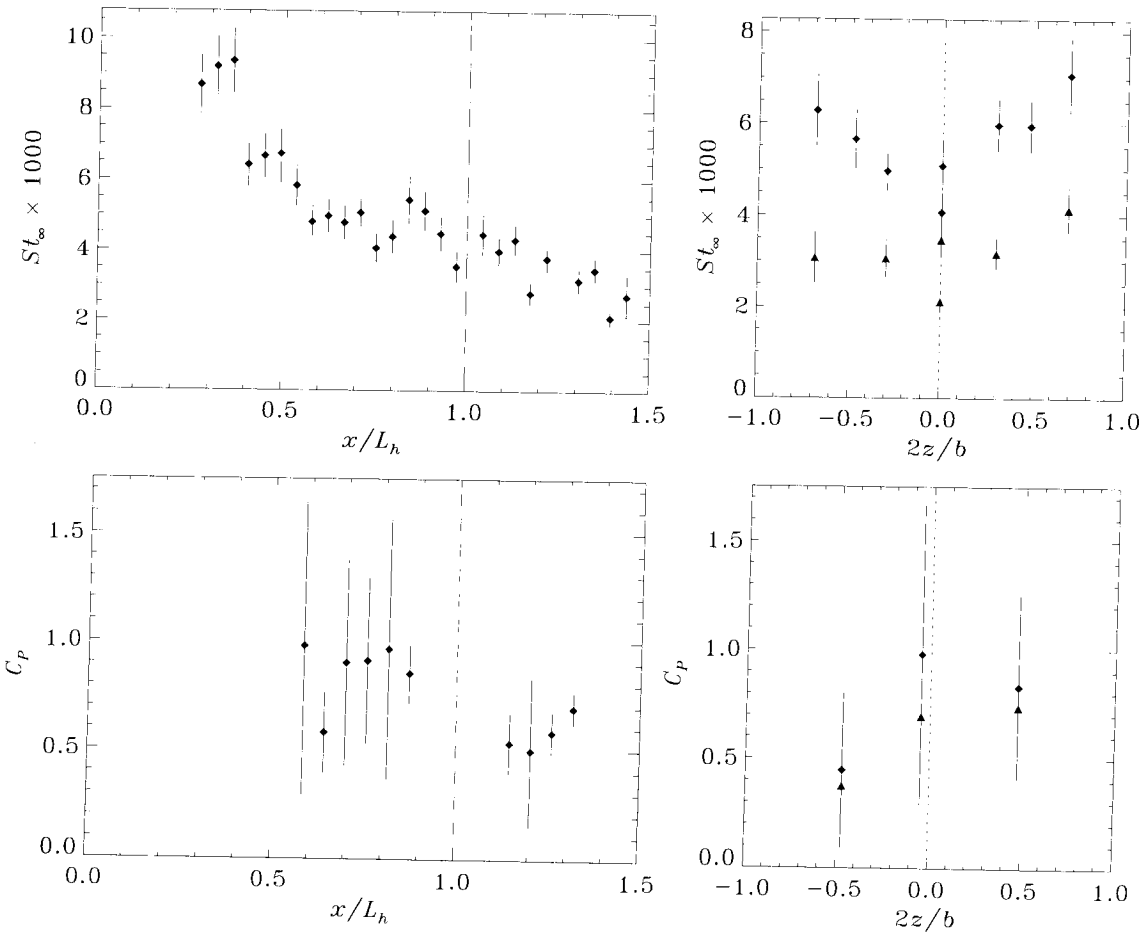

Shot 1734 (condition C0, $A_e/A_* = 100$, $\theta_1 = 30°$, $\theta_w = 0°$)

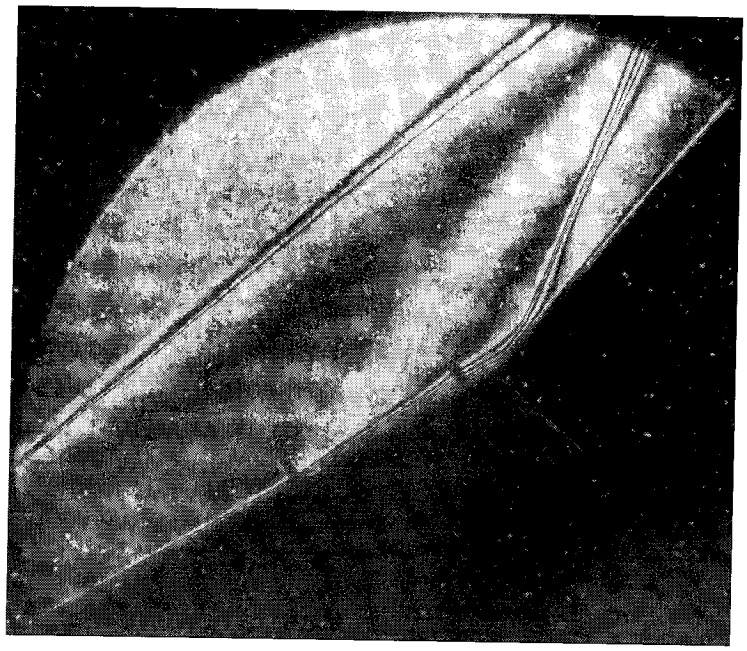

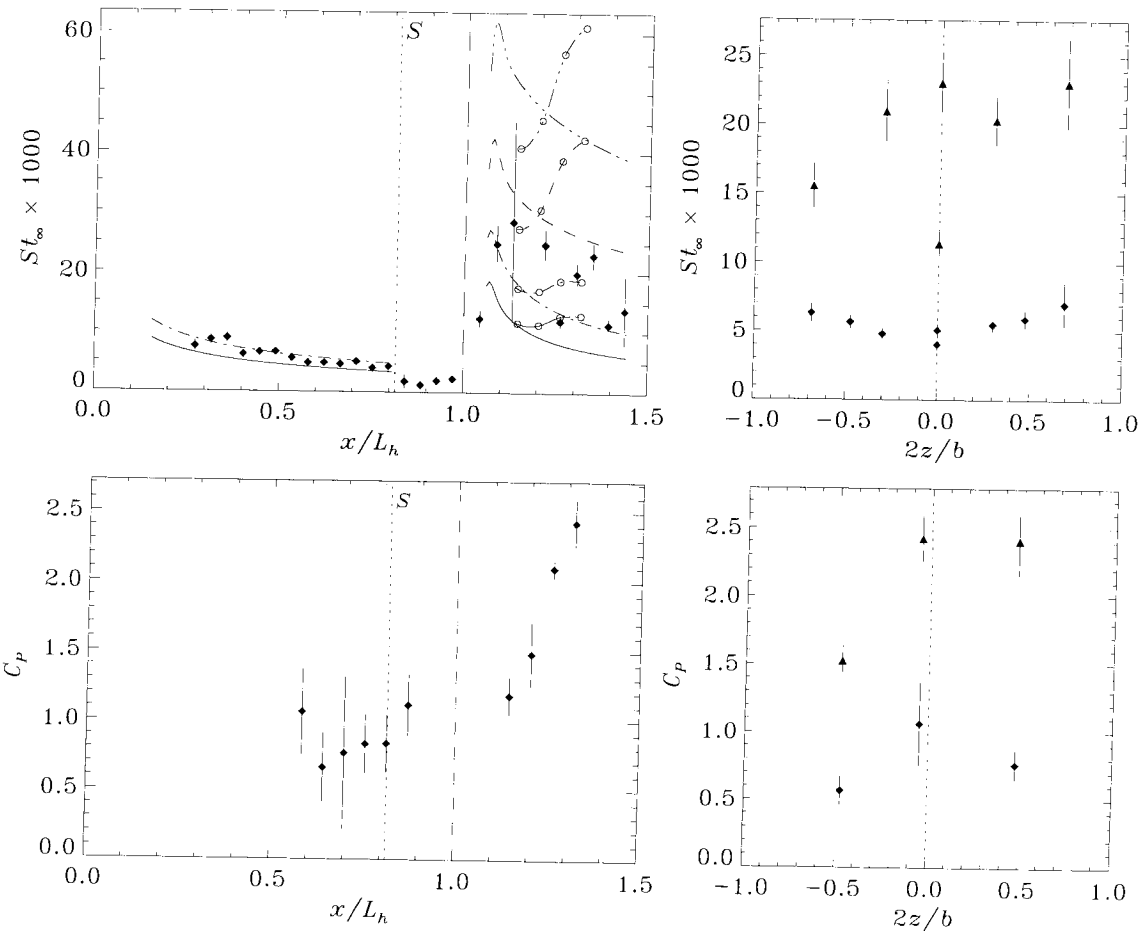

Shot 1735 (condition C0, $A_e/A_* = 100$, $\theta_1 = 30°$, $\theta_w = 20°$)

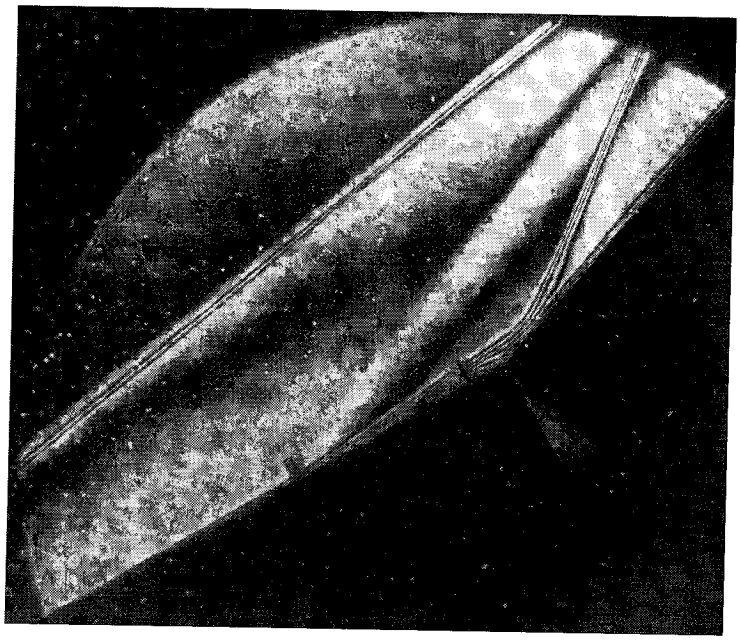

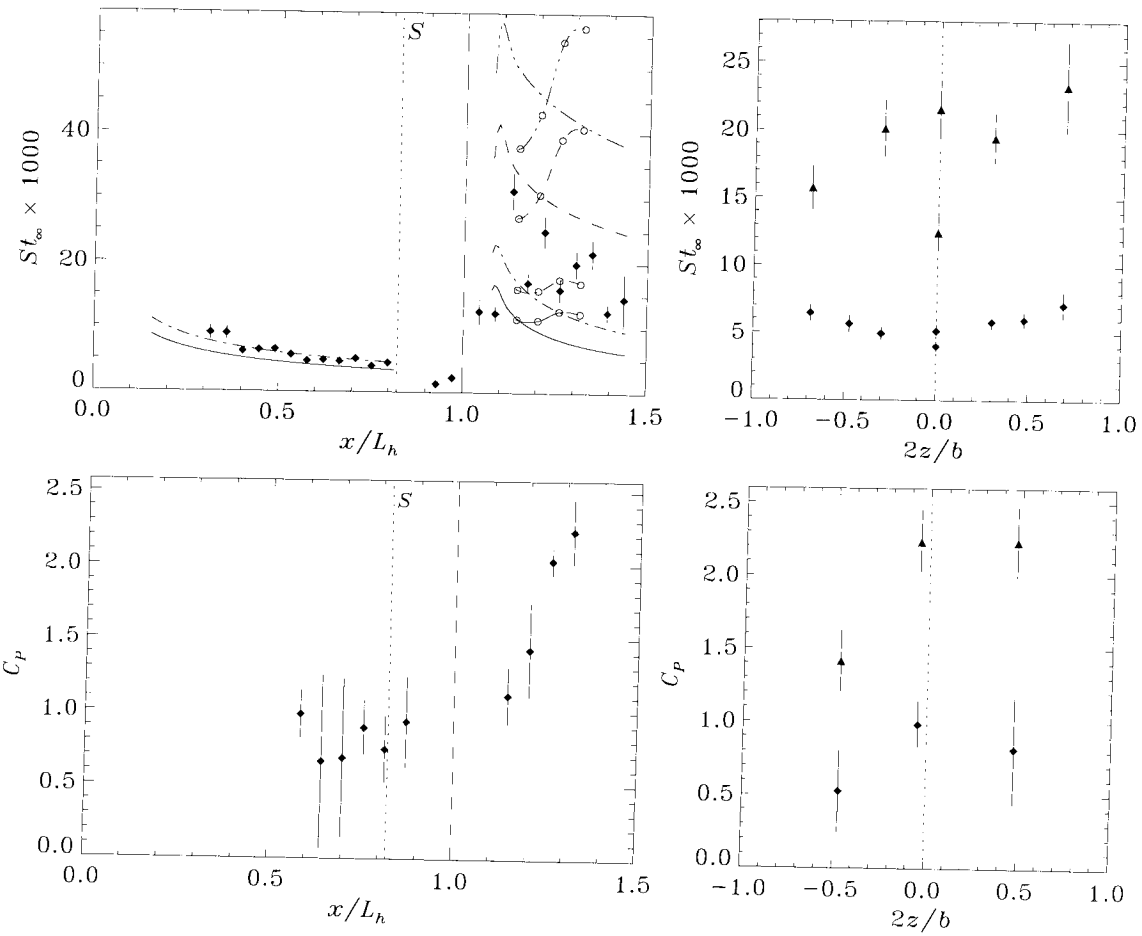

Shot 1736 (condition C0, $A_e/A_* = 100$, $\theta_1 = 30°$, $\theta_w = 20°$)

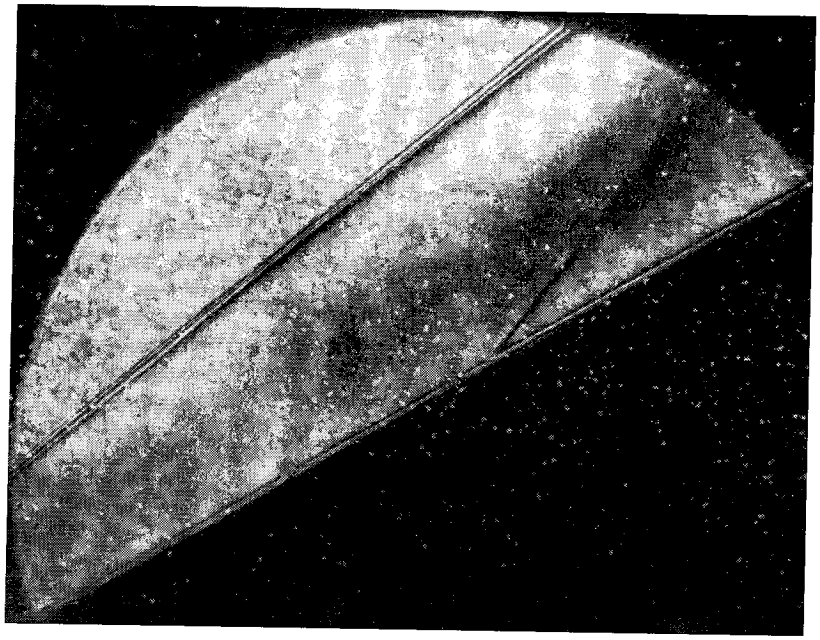

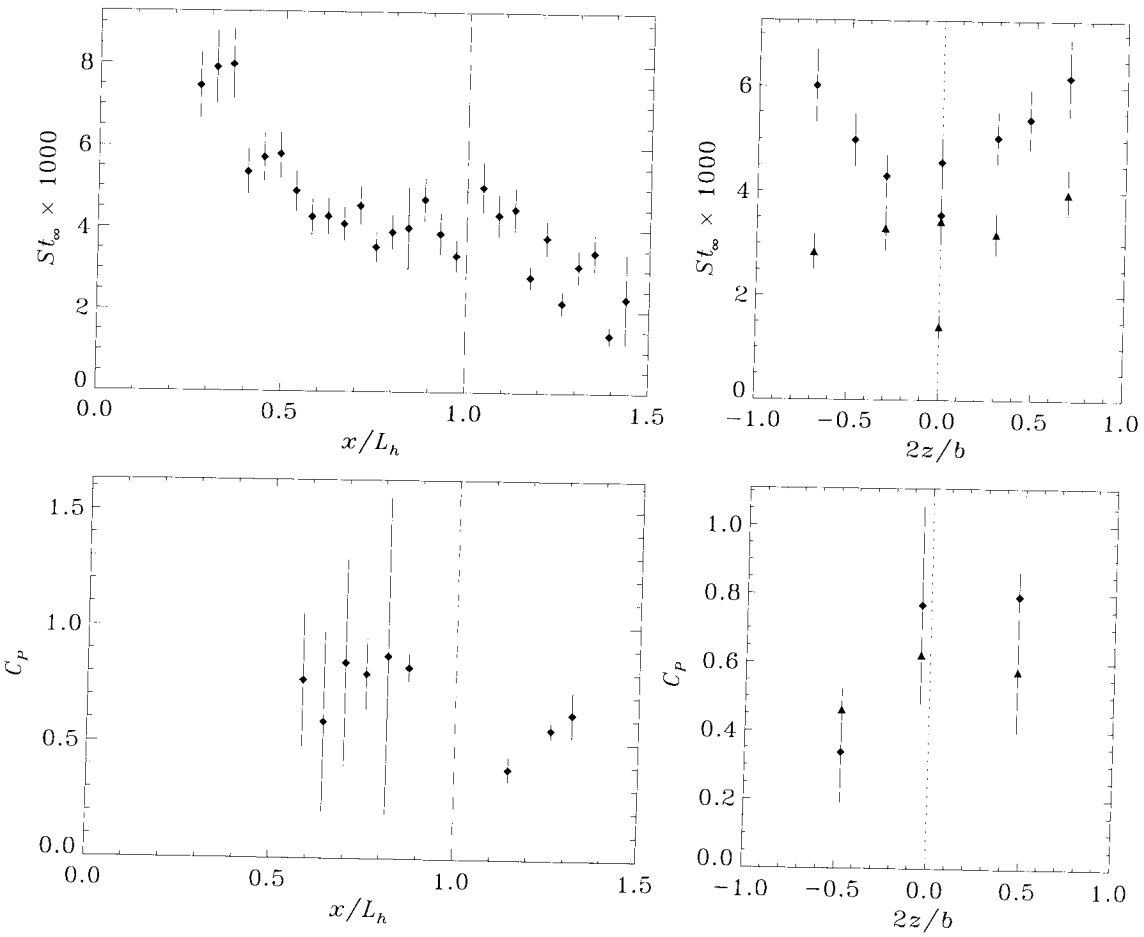

Shot 1737 (condition C0, $A_e/A_* = 100$, $\theta_1 = 30°$, $\theta_w = 0°$)

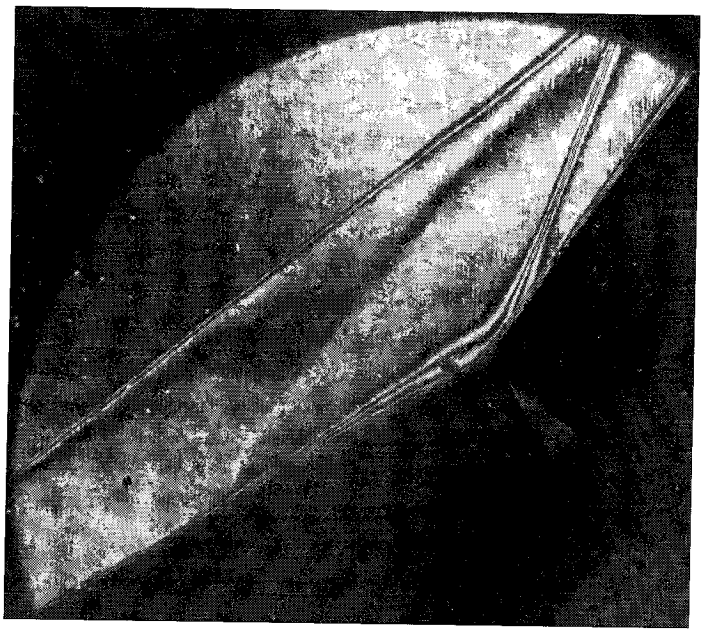

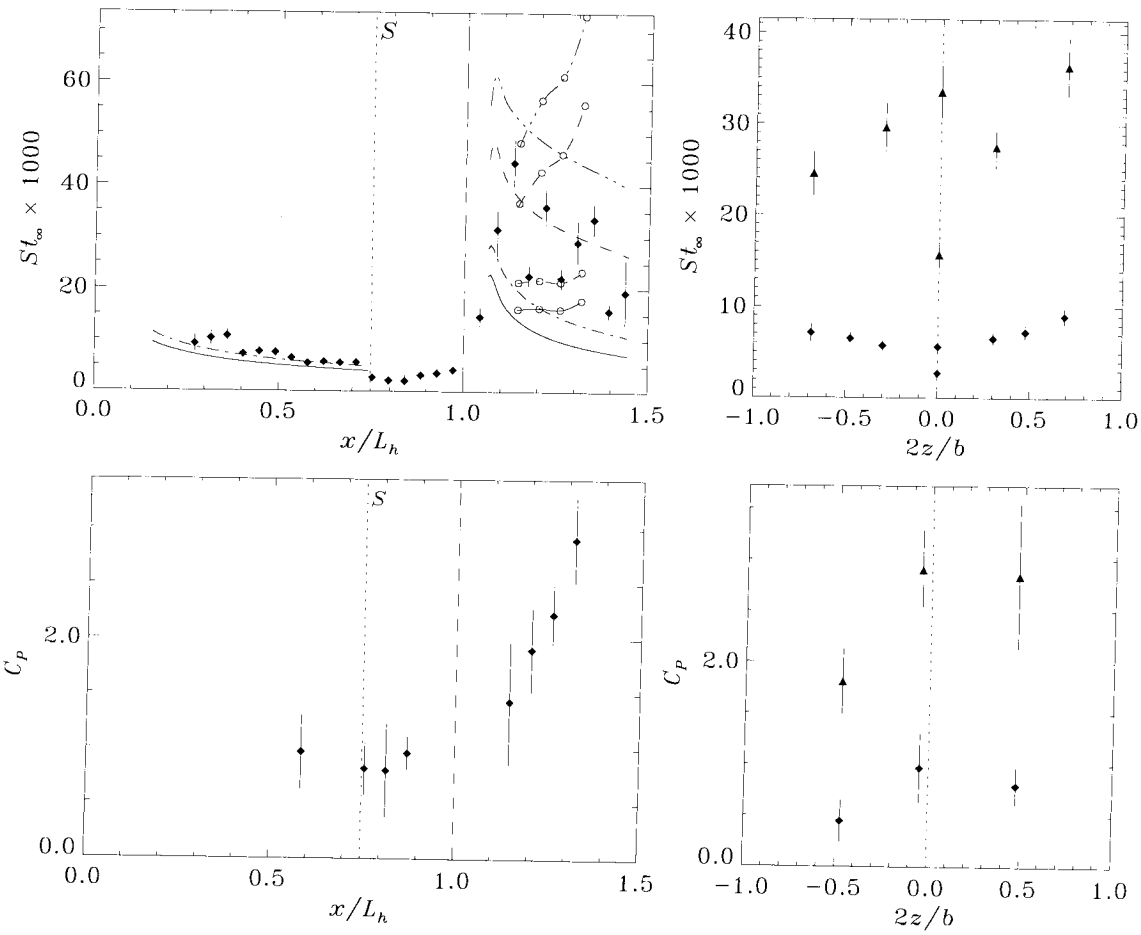

Shot 1740 (condition C2, $A_e/A_* = 225$, $\theta_1 = 30°$, $\theta_w = 25°$)

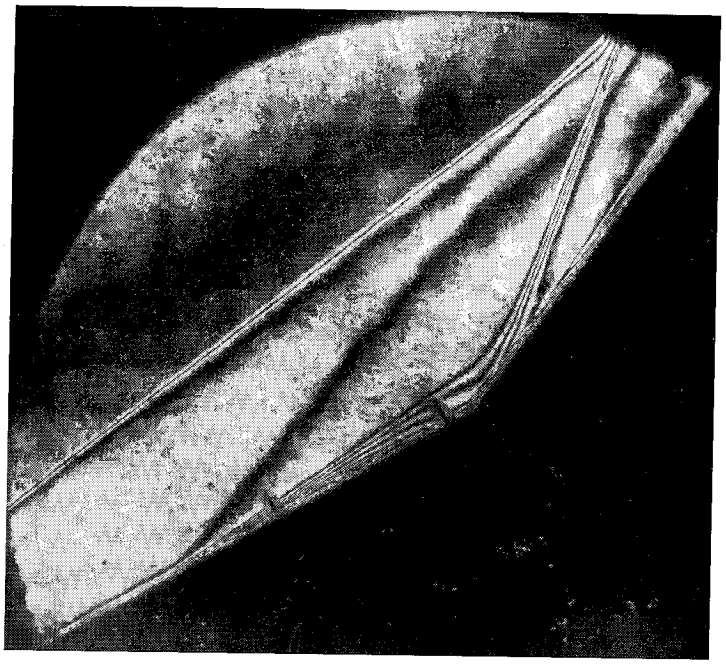

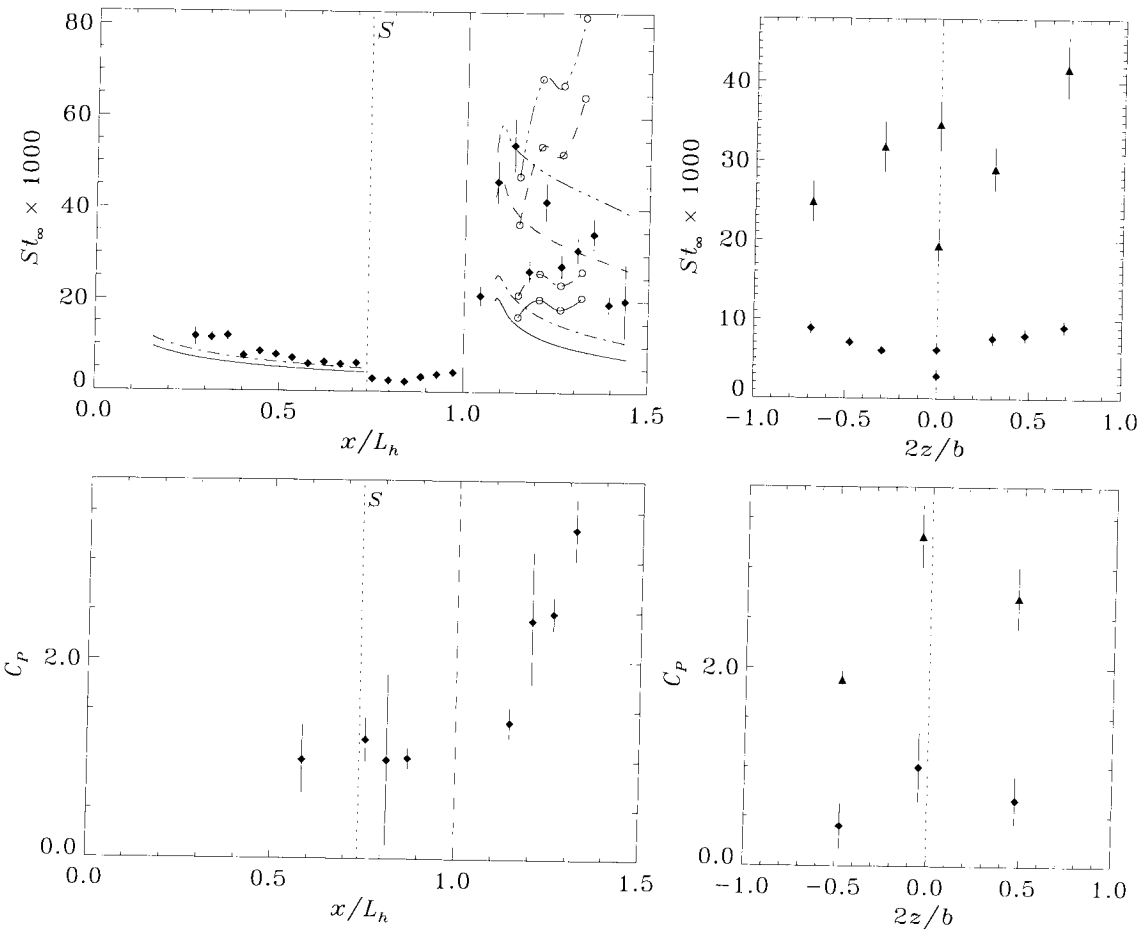

Shot 1741 (condition C2, $A_e/A_* = 225$, $\theta_1 = 30°$, $\theta_w = 25°$)

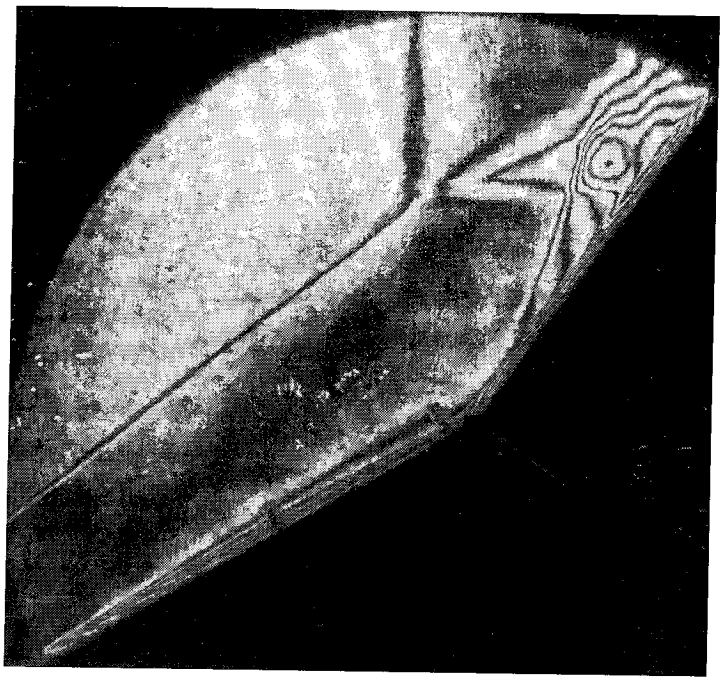

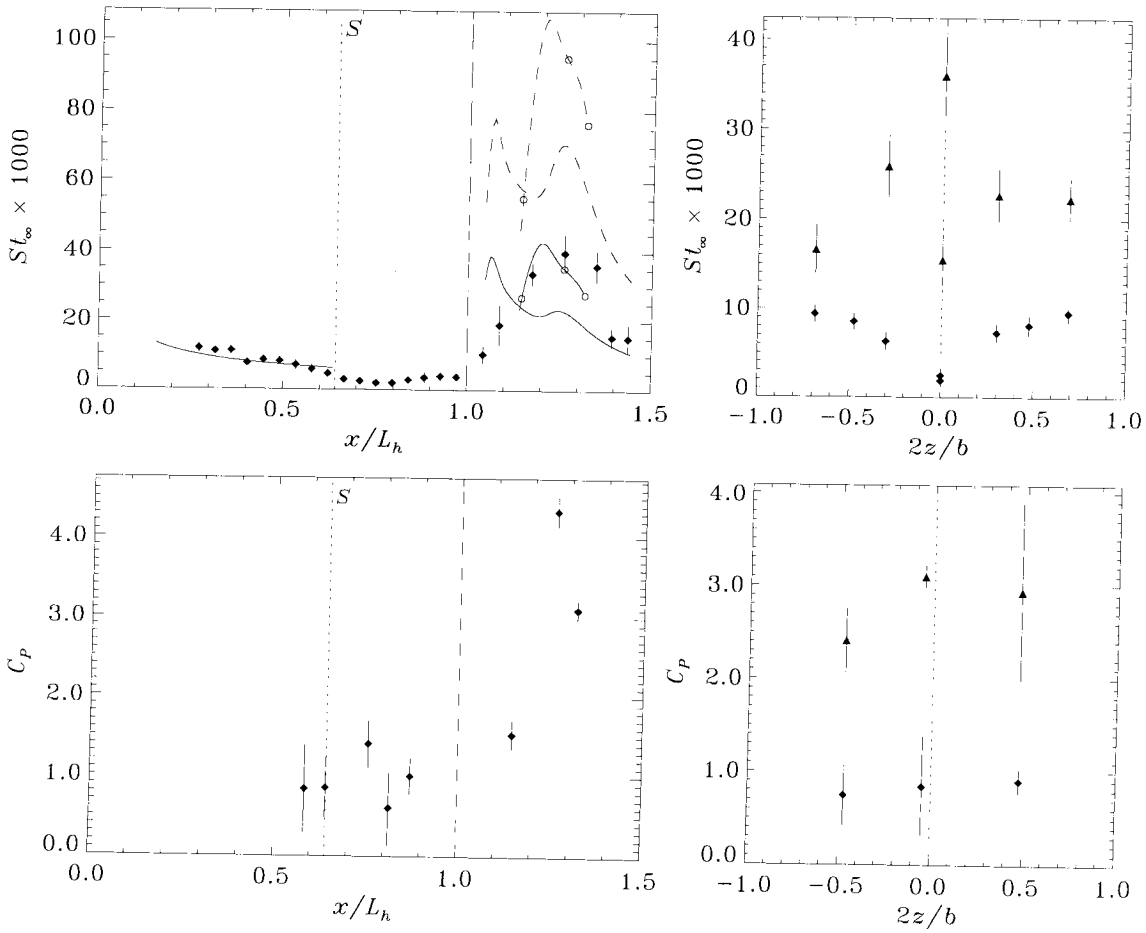

Shot 1742 (condition B1, $A_e/A_* = 400$, $\theta_1 = 30°$, $\theta_w = 25°$)

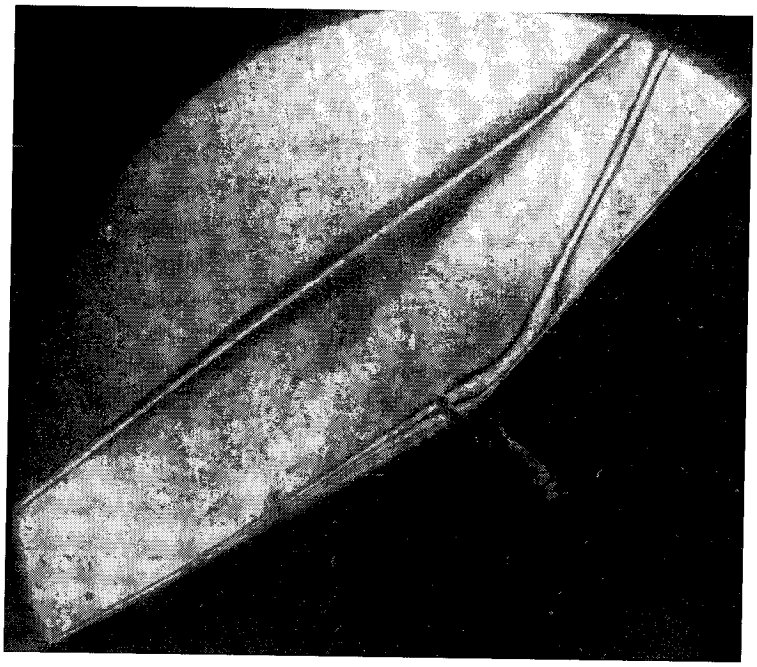

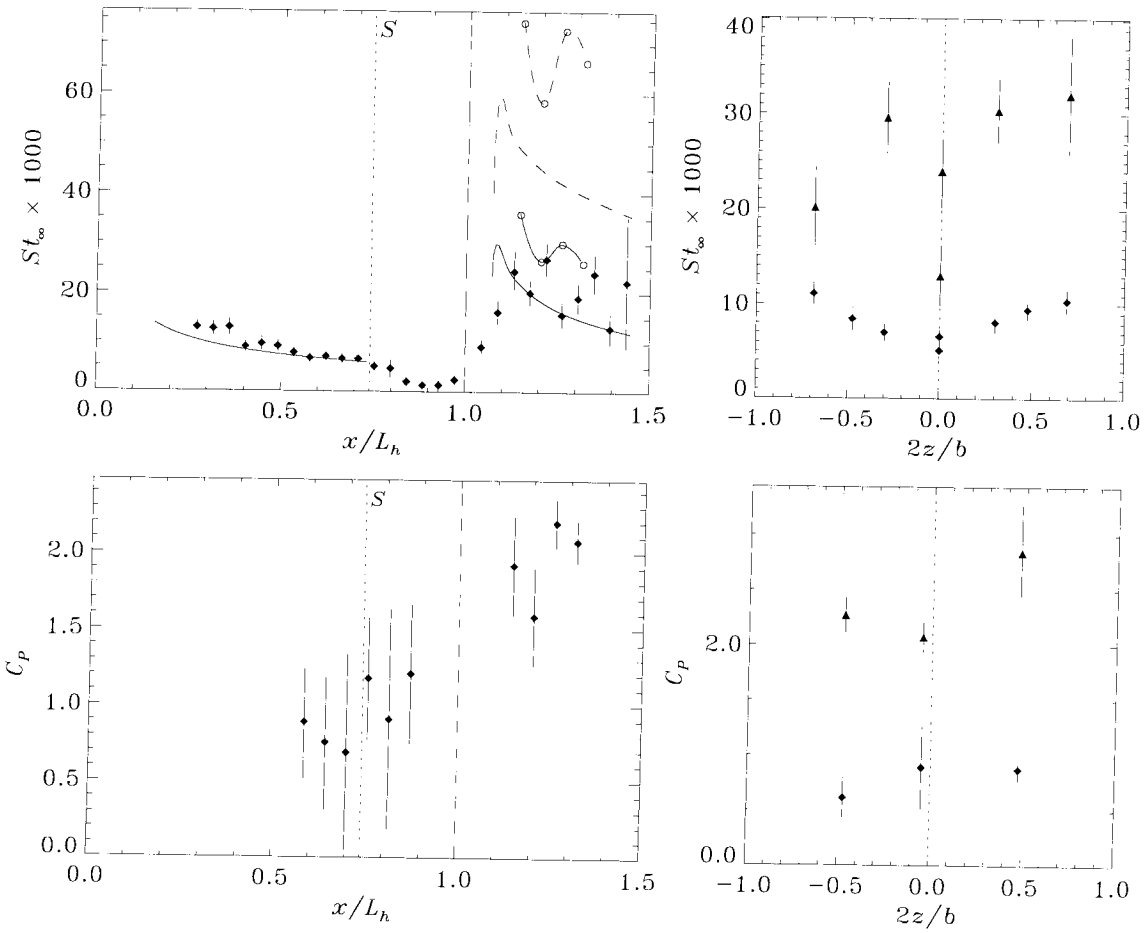

Shot 1743 (condition B1, $A_e/A_* = 400$, $\theta_1 = 30°$, $\theta_w = 20°$)

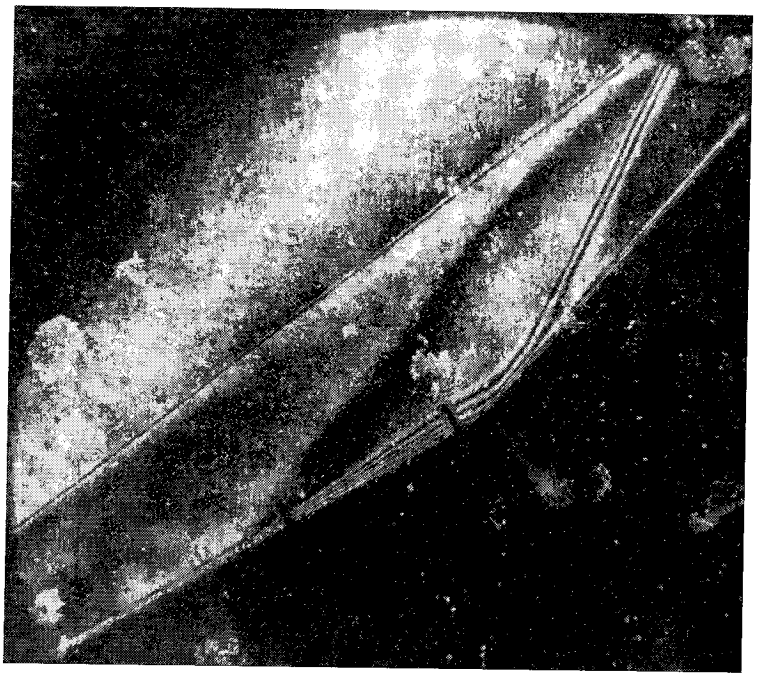

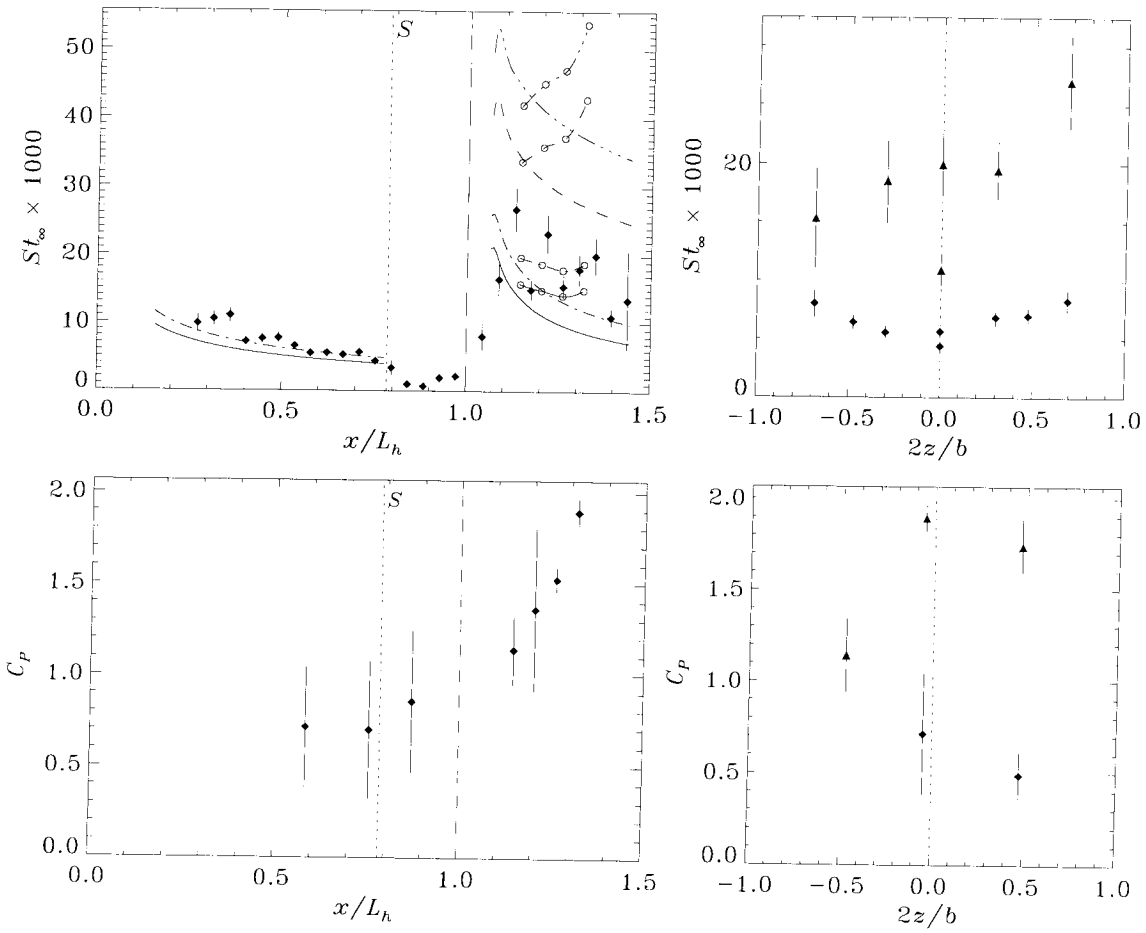

Shot 1744 (condition C2, $A_c/A_* = 225$, $\theta_1 = 30°$, $\theta_w = 20°$)

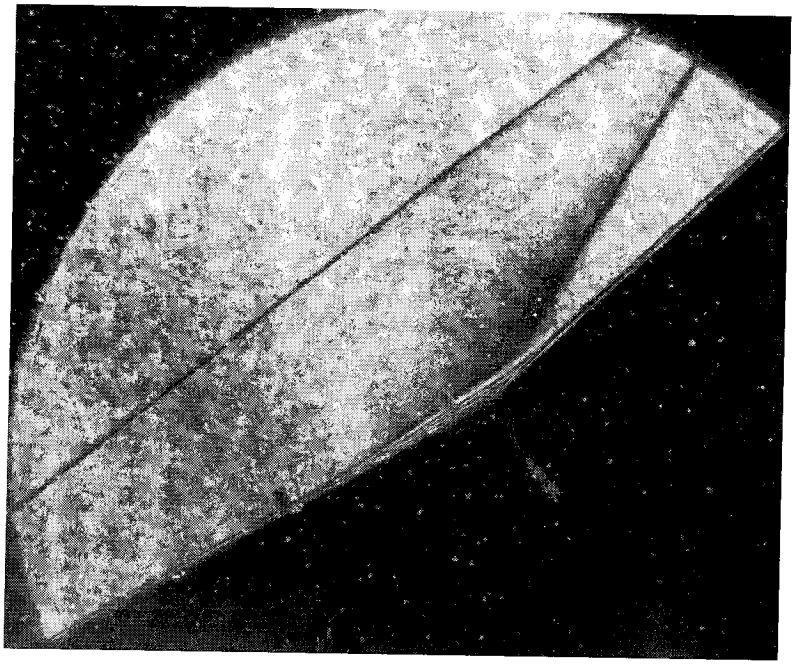

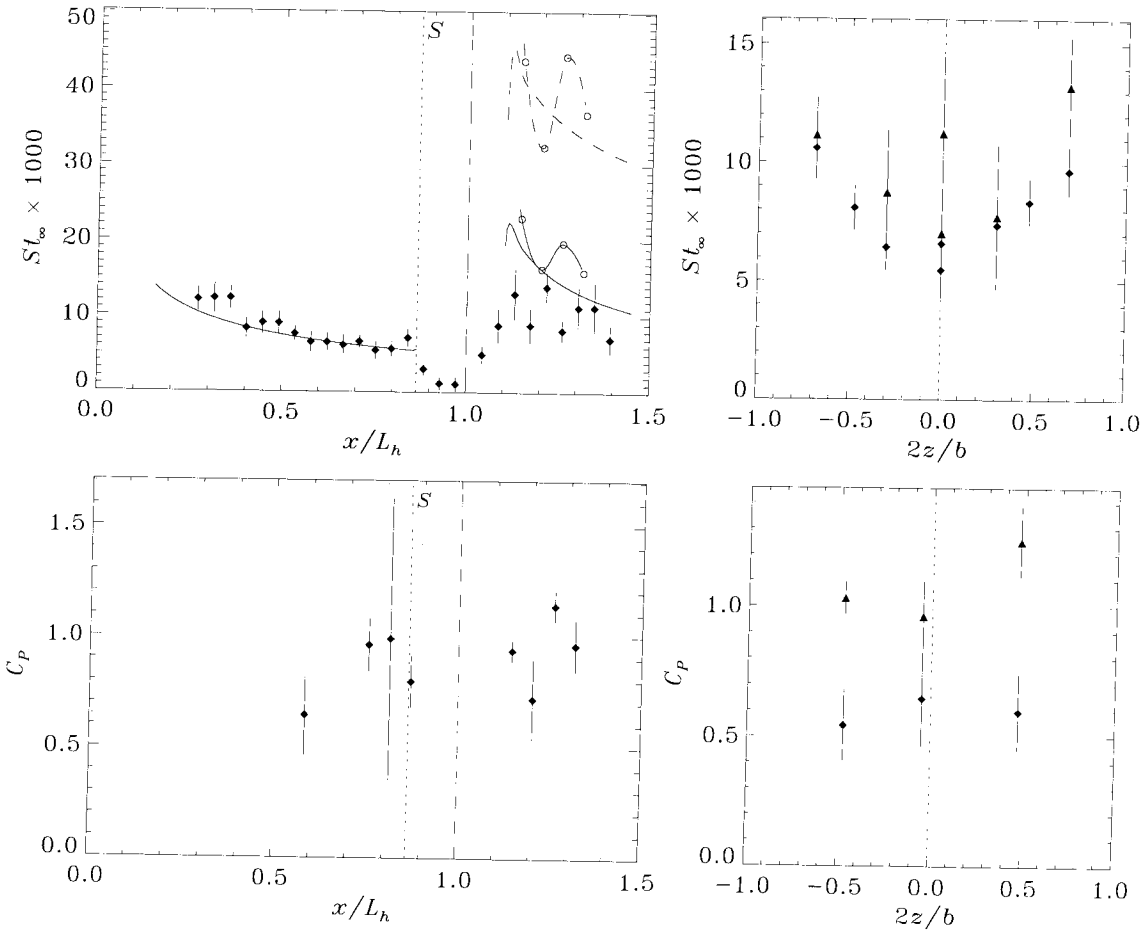

Shot 1745 (condition B1, $A_e/A_* = 400$, $\theta_1 = 30°$, $\theta_w = 10°$)

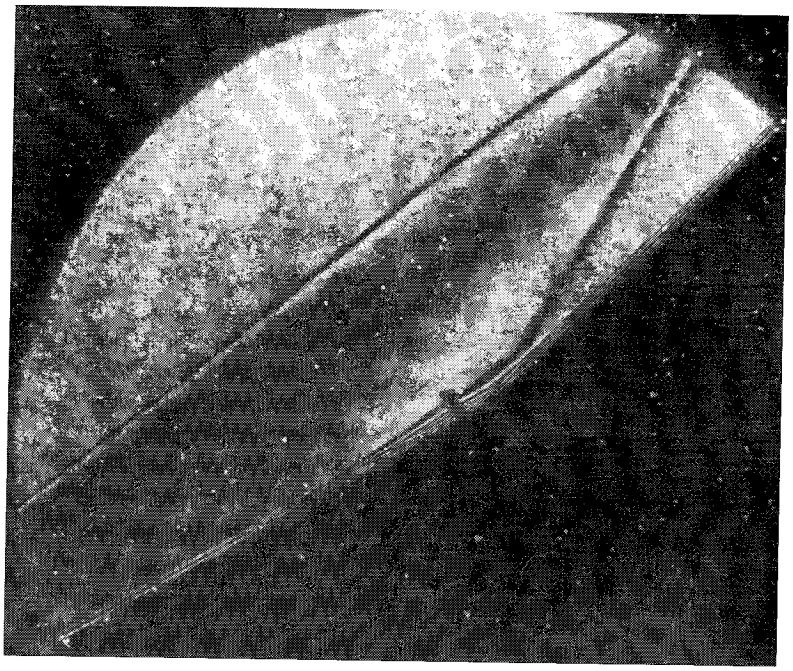

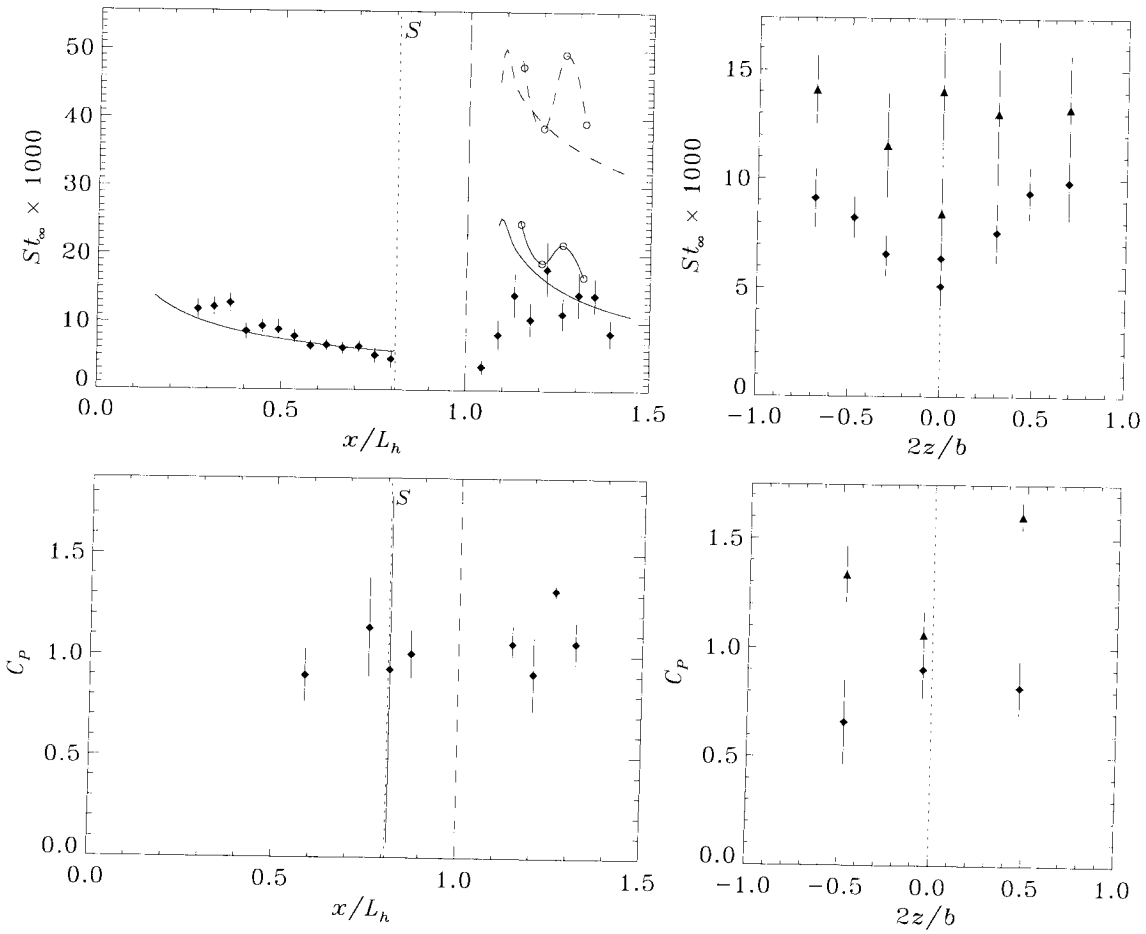

Shot 1746 (condition B1, $A_e/A_* = 400$, $\theta_1 = 30°$, $\theta_w = 15°$)

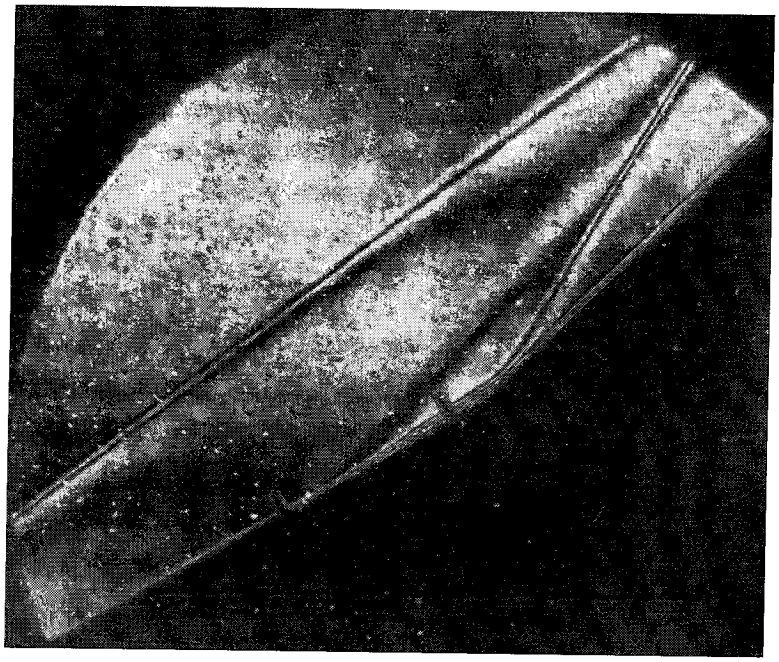

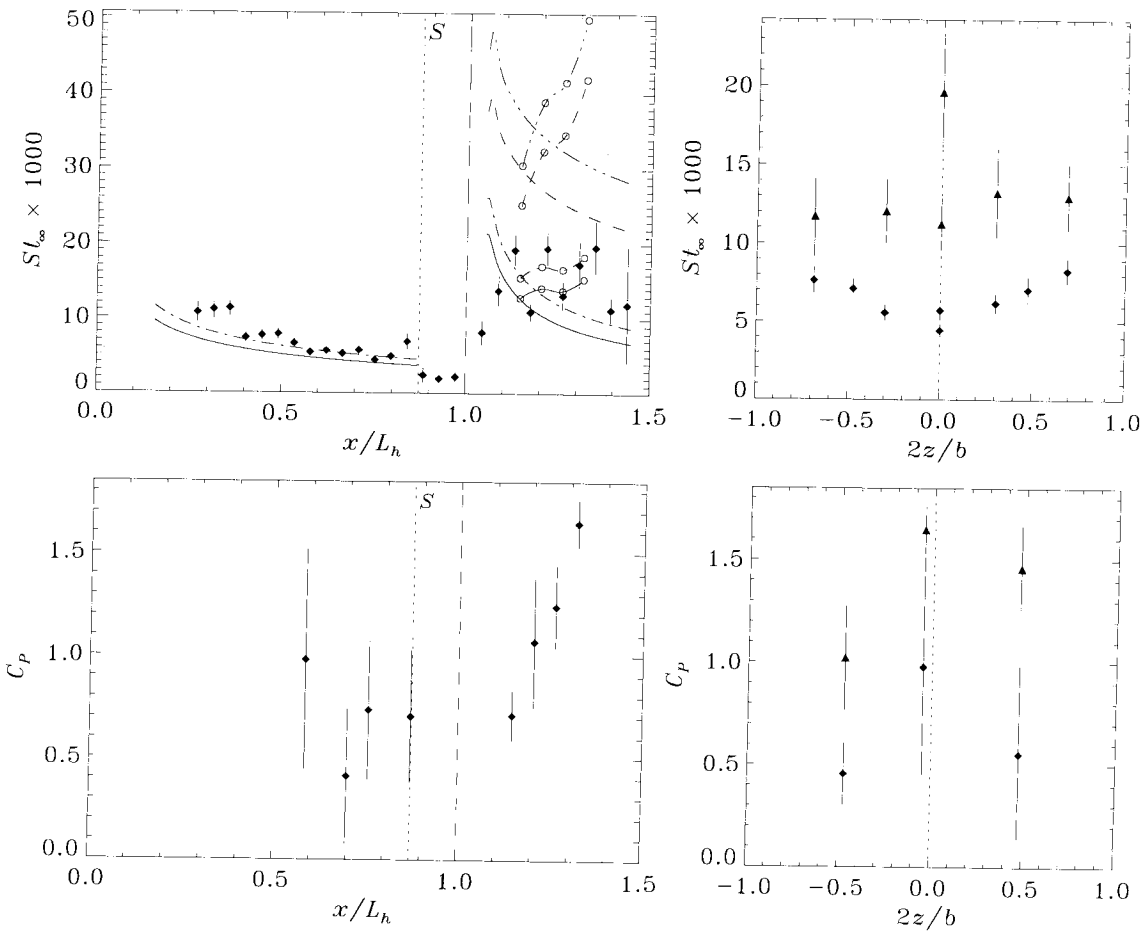

Shot 1747 (condition C2, $A_e/A_* = 225$, $\theta_1 = 30°$, $\theta_w = 15°$)

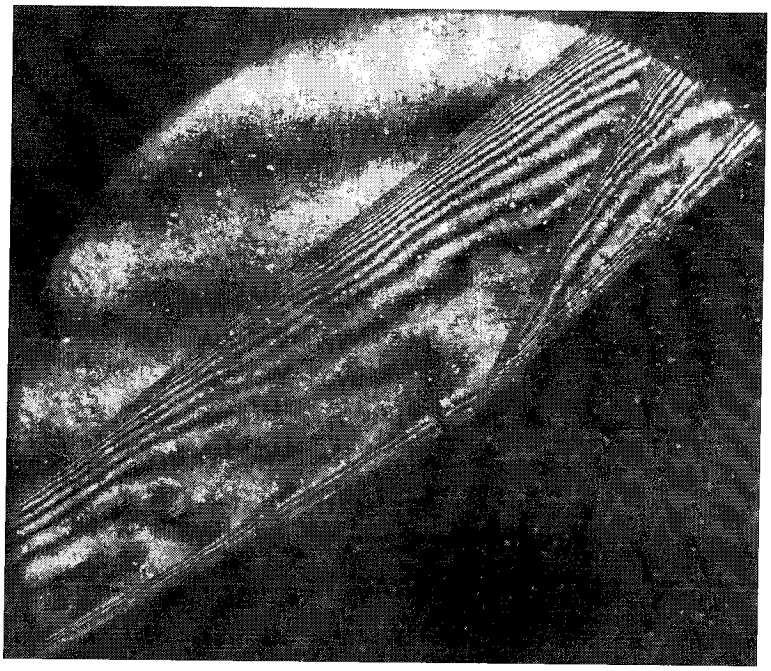

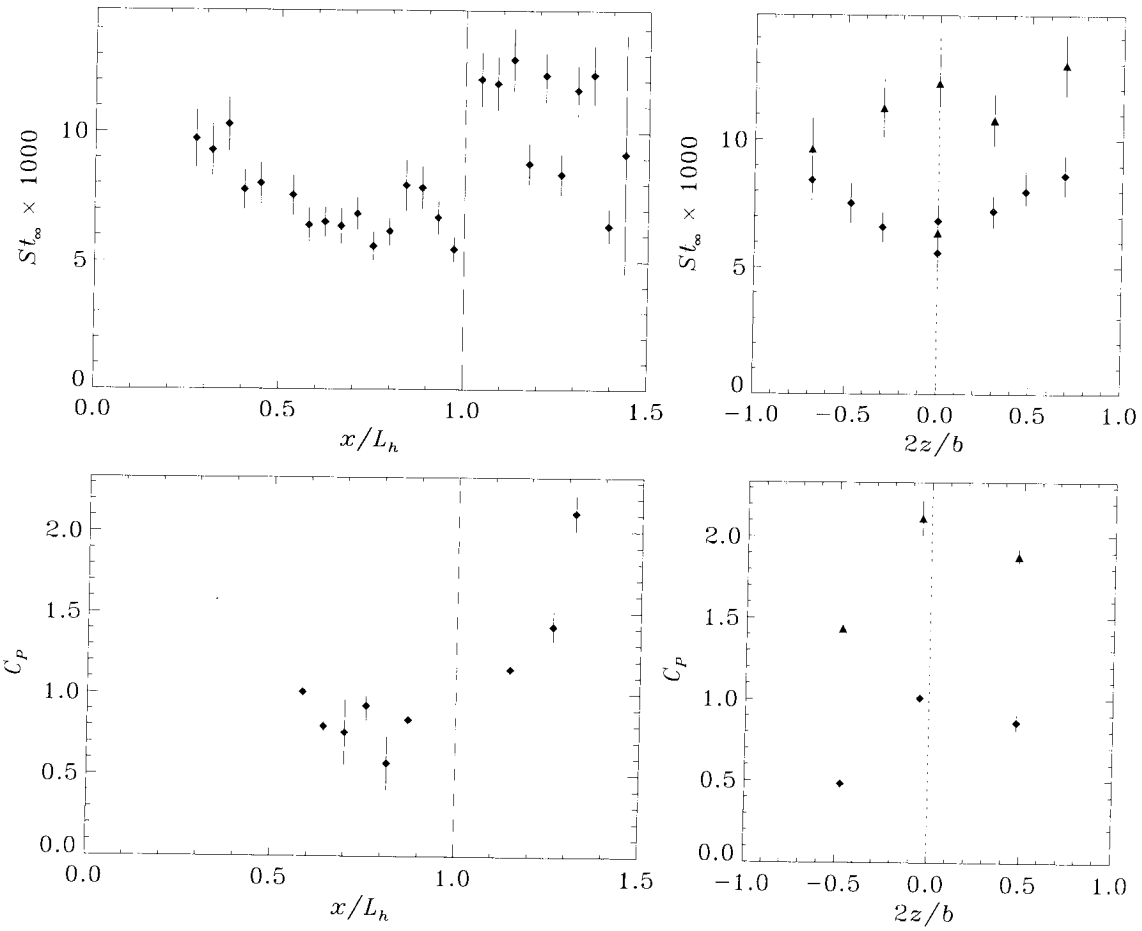

Shot 1748 (condition A3, $A_e/A_* = 100$, $\theta_1 = 30°$, $\theta_w = 15°$)

no photograph

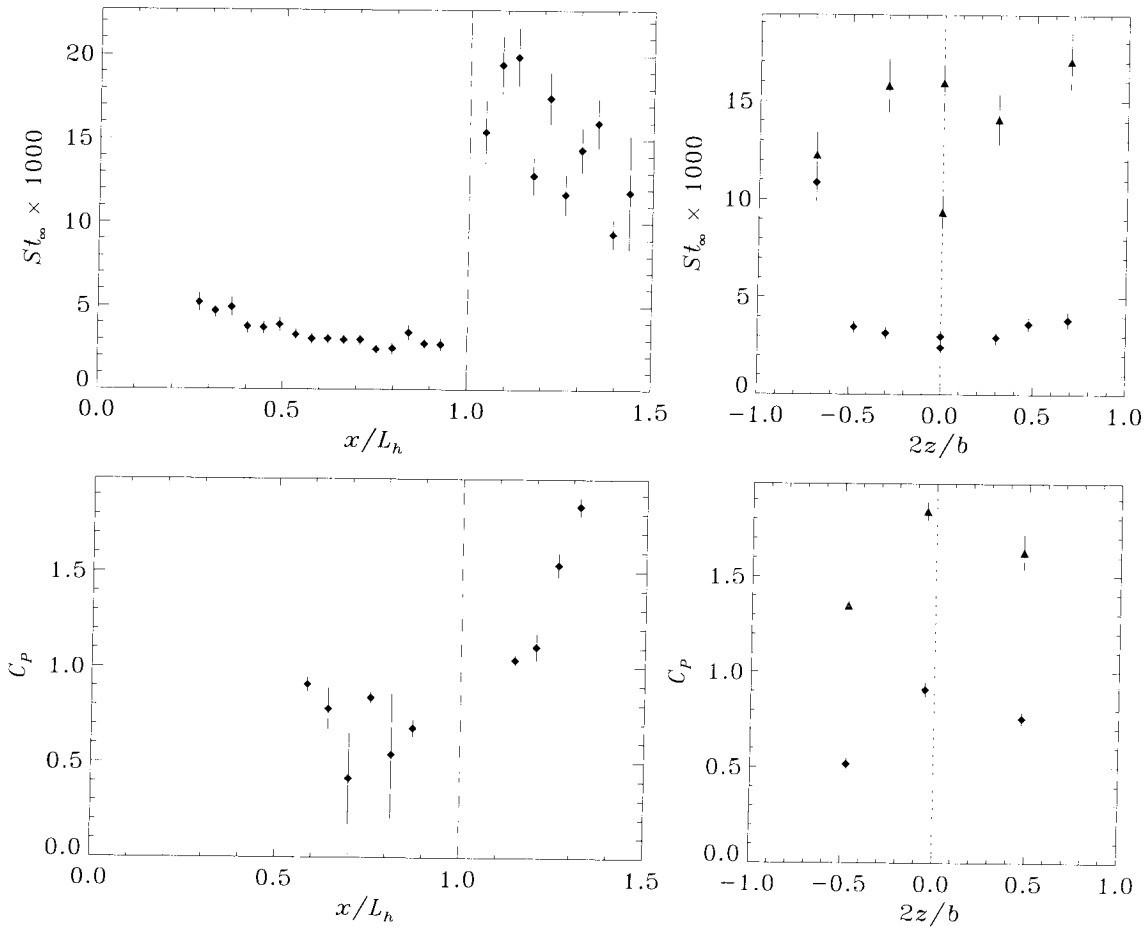

Shot 1749 (condition B2, $A_e/A_* = 100$, $\theta_1 = 30°$, $\theta_w = 15°$)

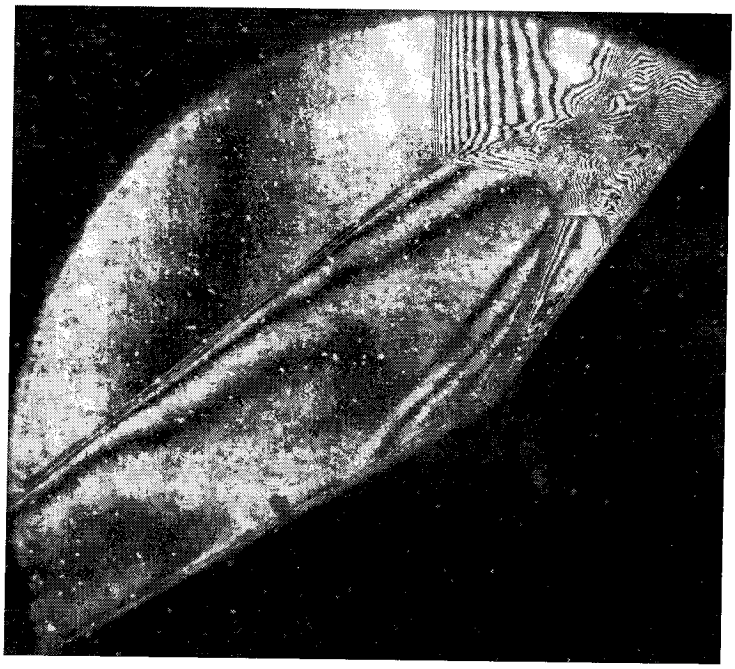

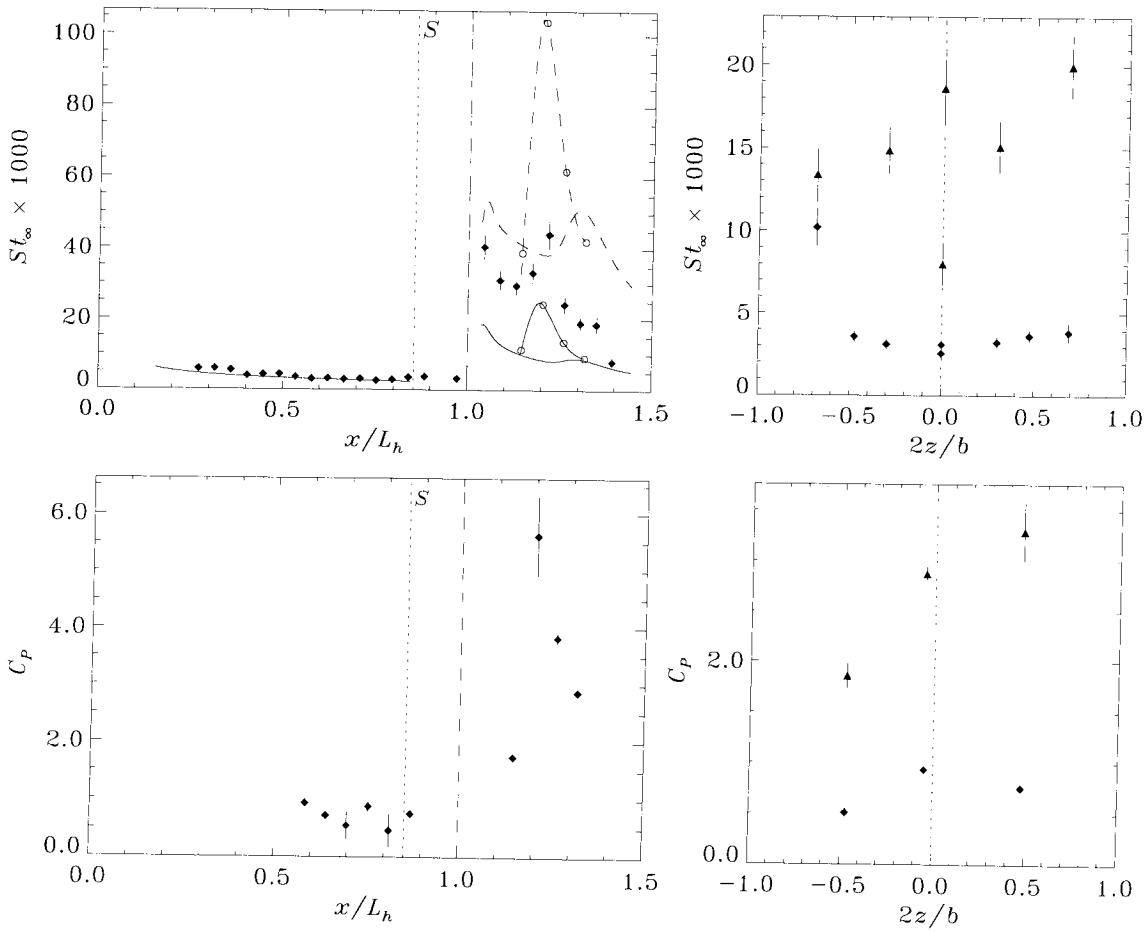

Shot 1750 (condition B2, $A_e/A_* = 100$, $\theta_1 = 30°$, $\theta_w = 25°$)

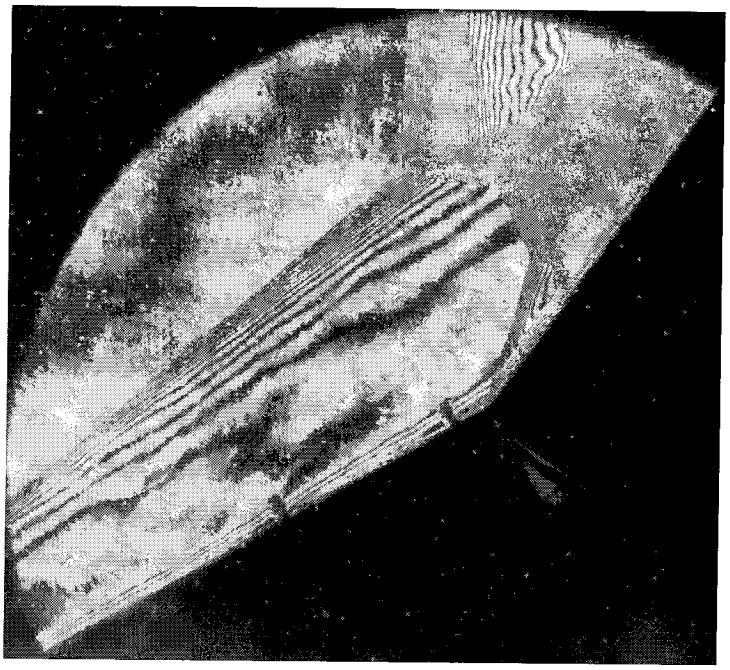

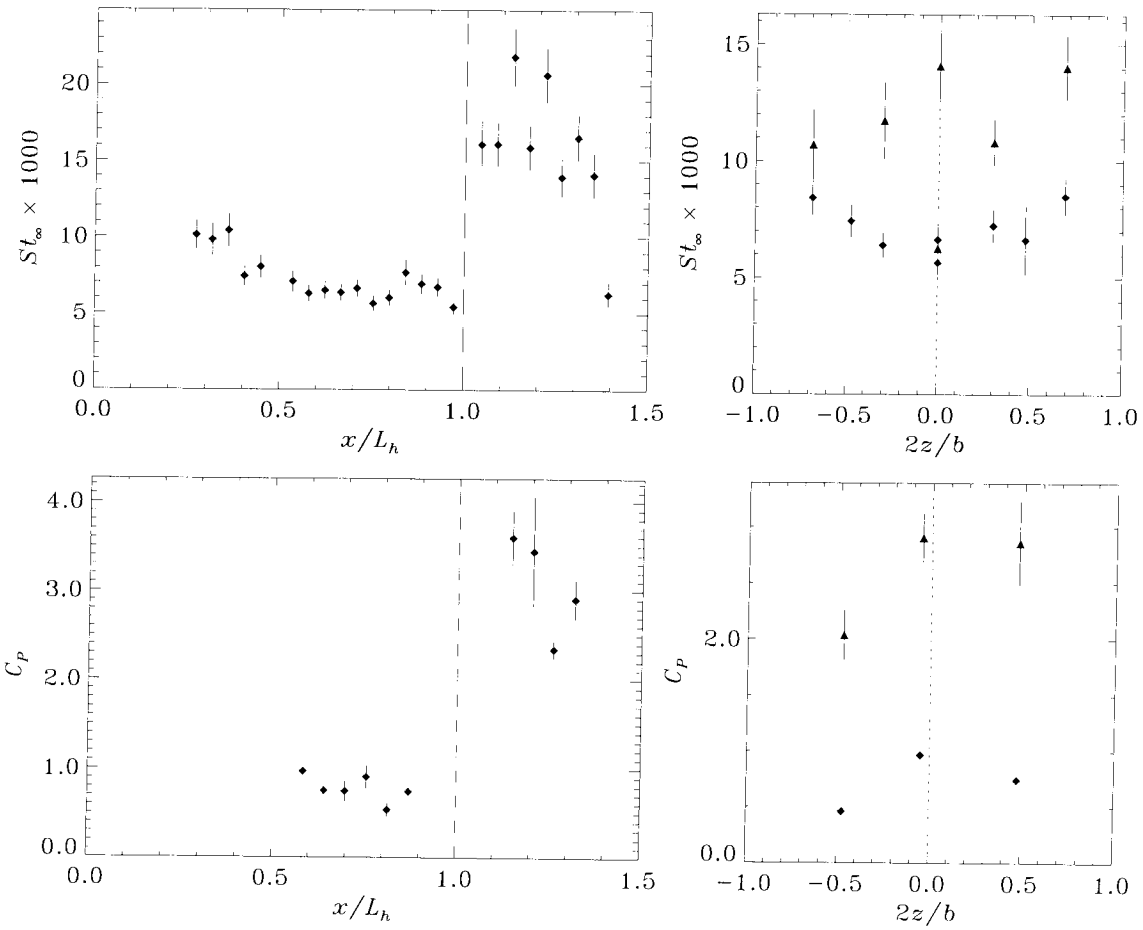

Shot 1751 (condition A3, $A_e/A_* = 100$, $\theta_1 = 30°$, $\theta_w = 25°$)

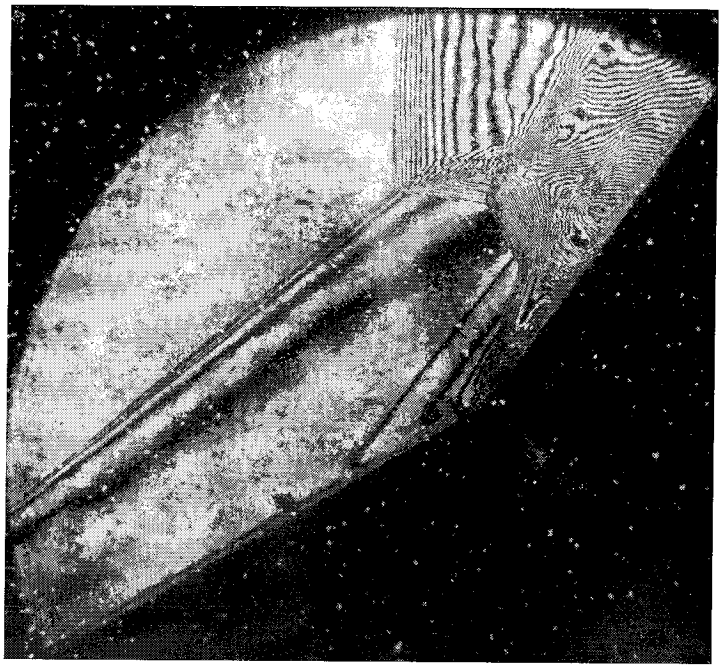

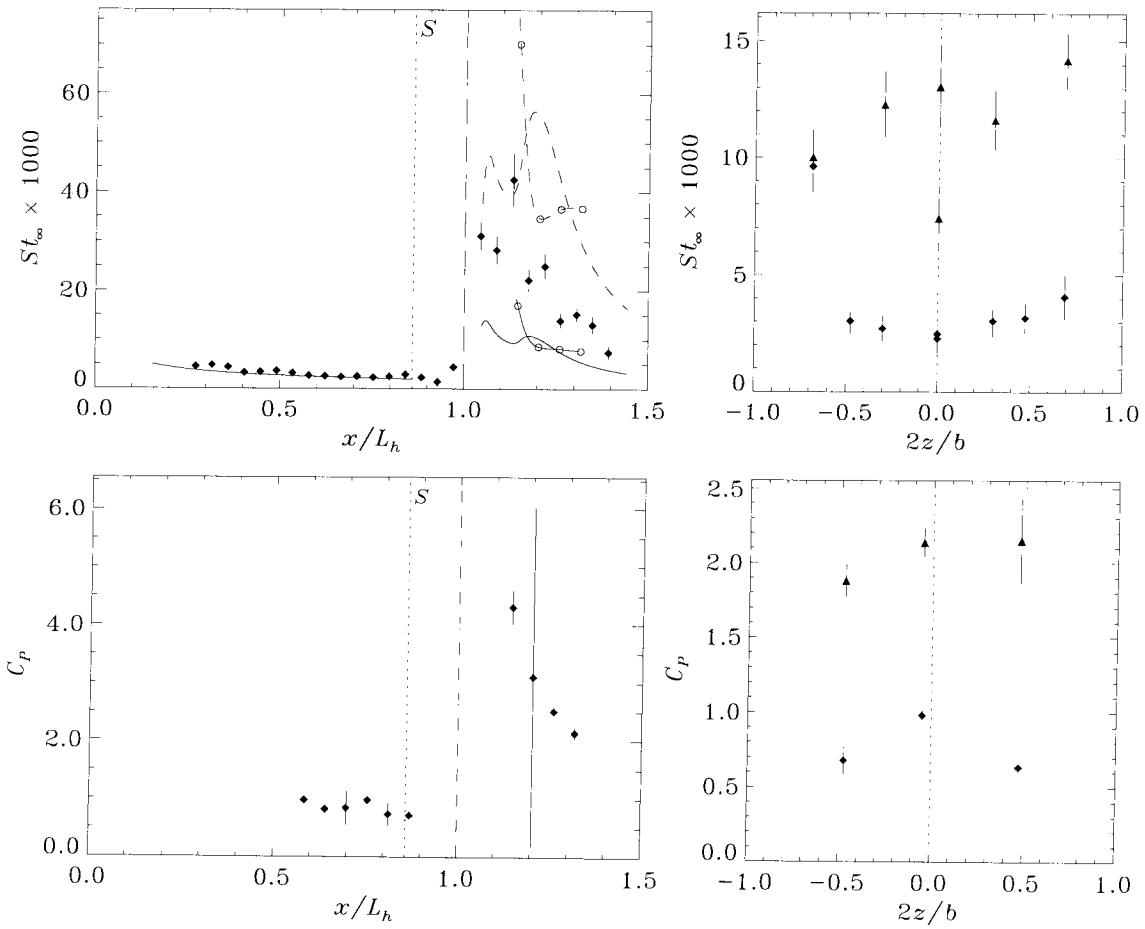

Shot 1752 (condition A1, $A_e/A_* = 100$, $\theta_1 = 30°$, $\theta_w = 25°$)

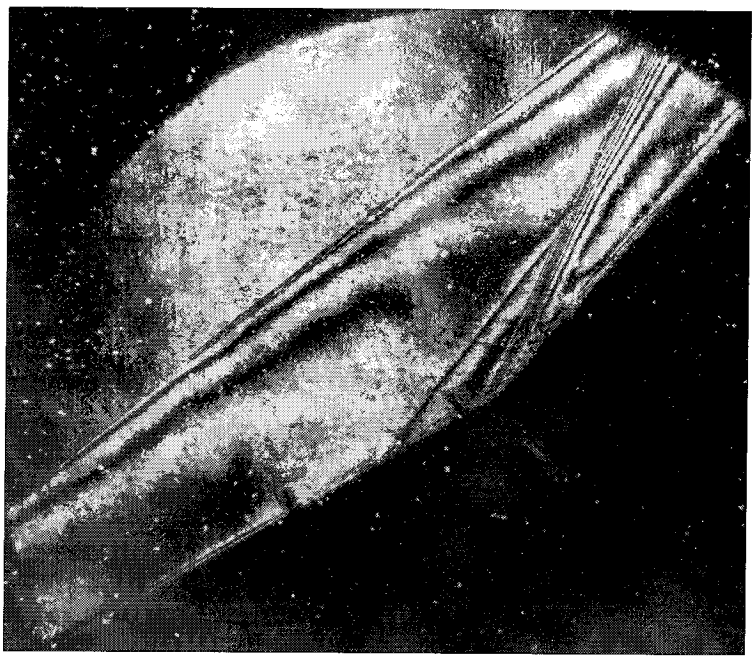

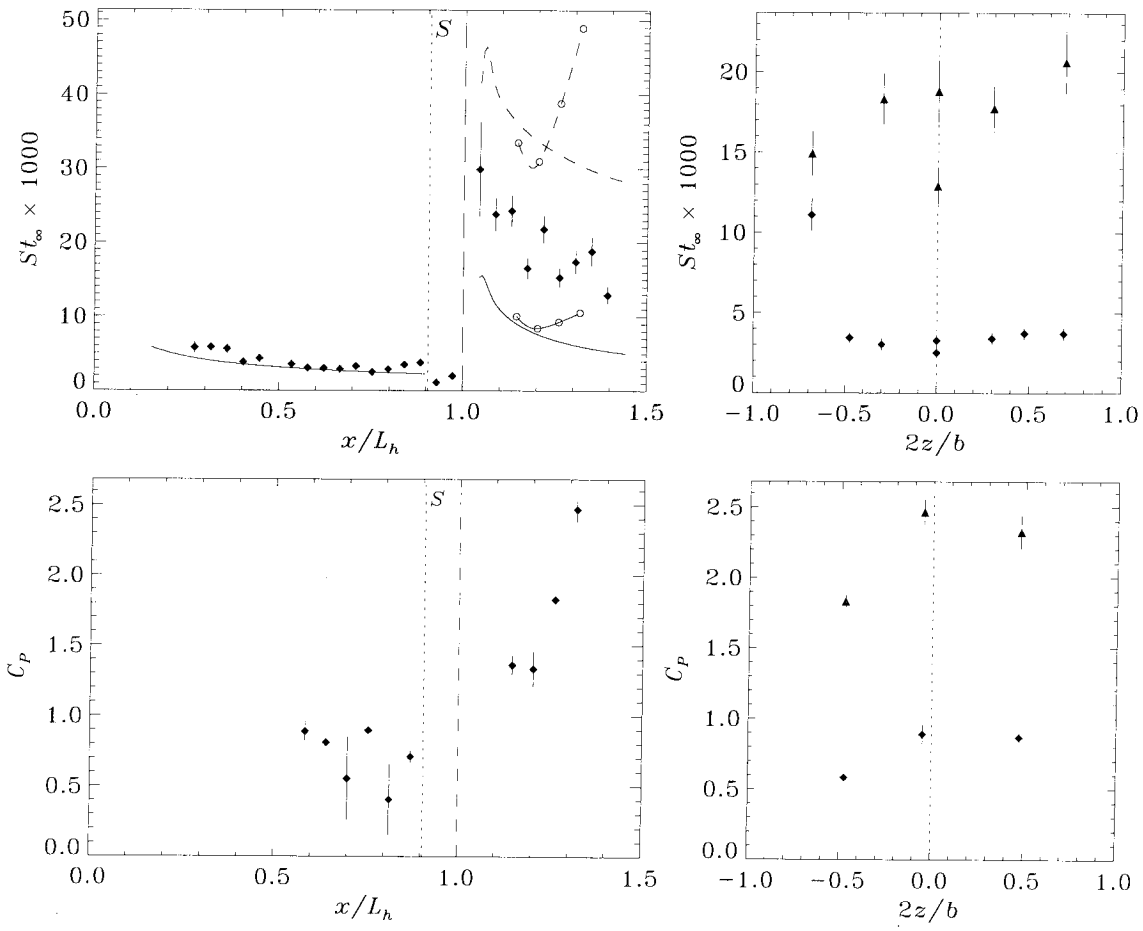

Shot 1753 (condition B2, $A_e/A_* = 100$, $\theta_1 = 30°$, $\theta_w = 20°$)

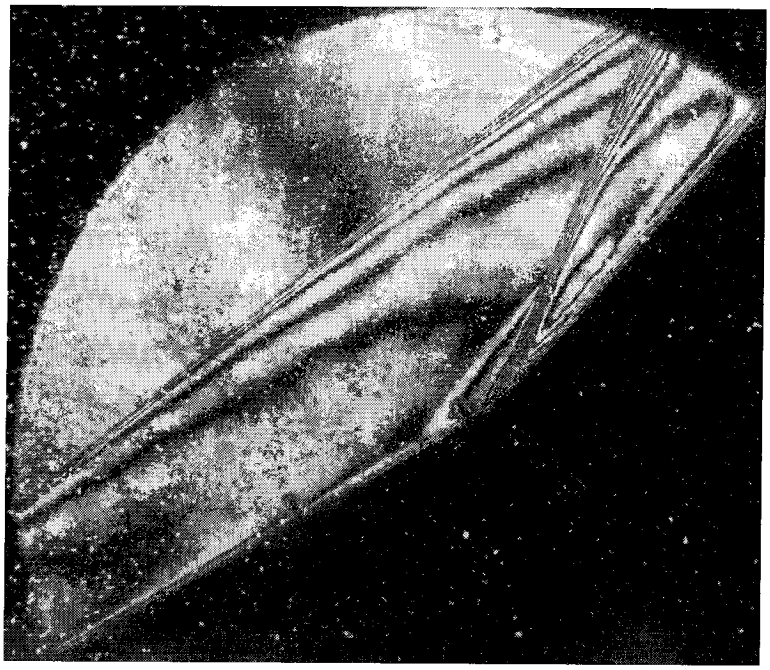

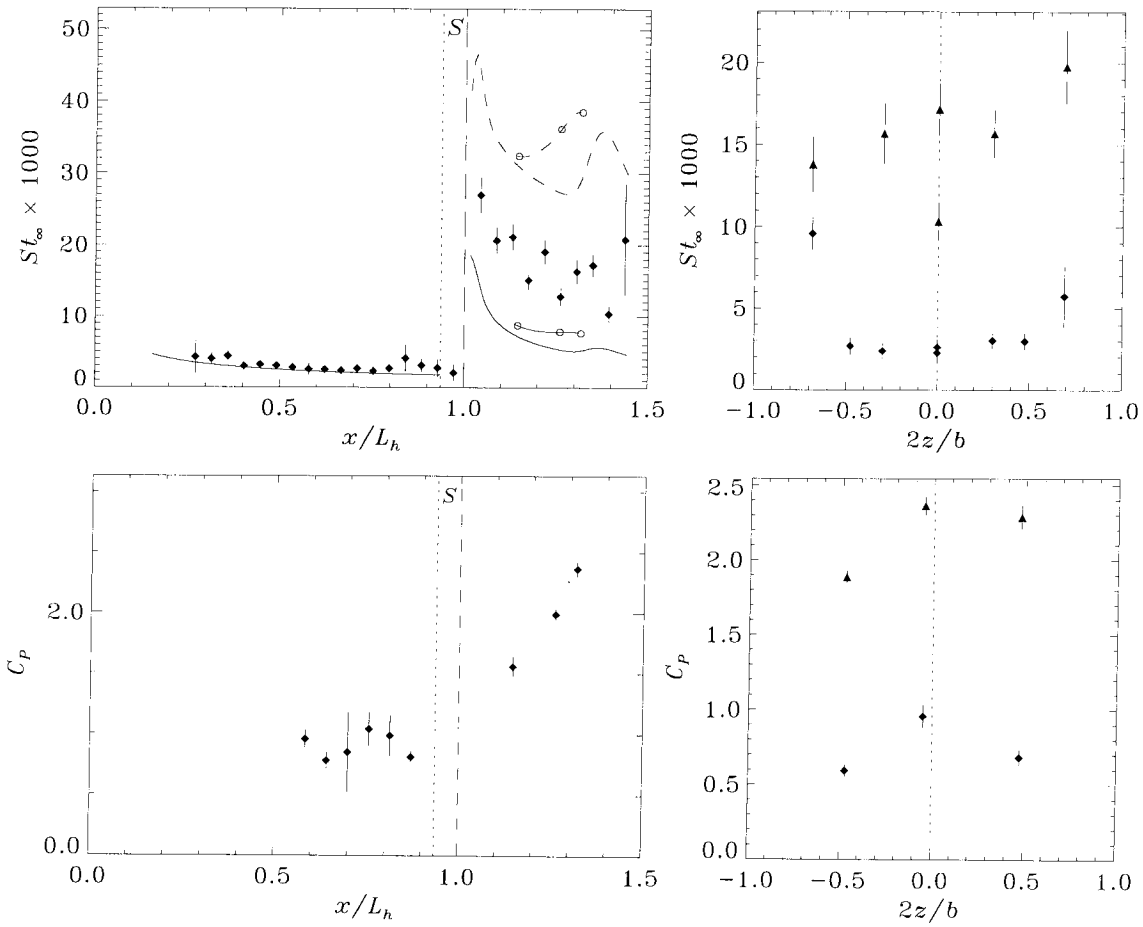

Shot 1754 (condition A1, $A_e/A_* = 100$, $\theta_1 = 30°$, $\theta_w = 20°$)

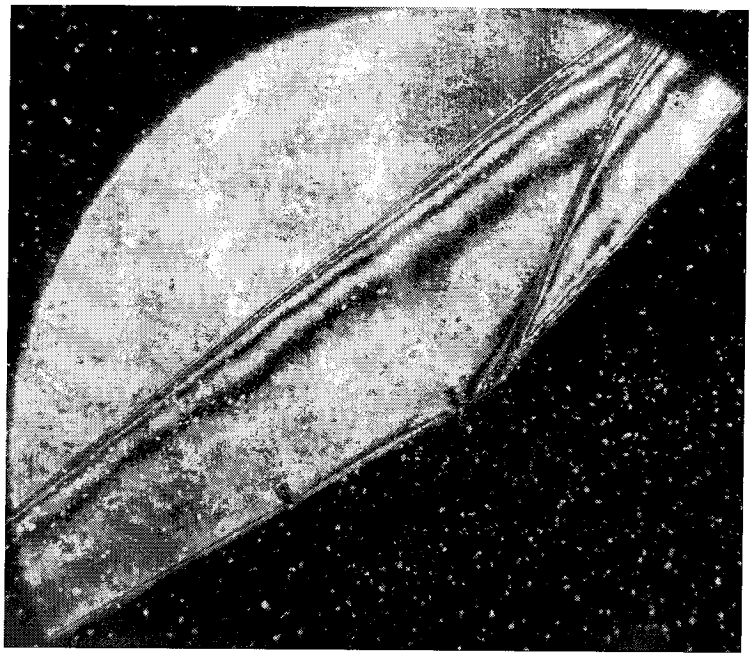

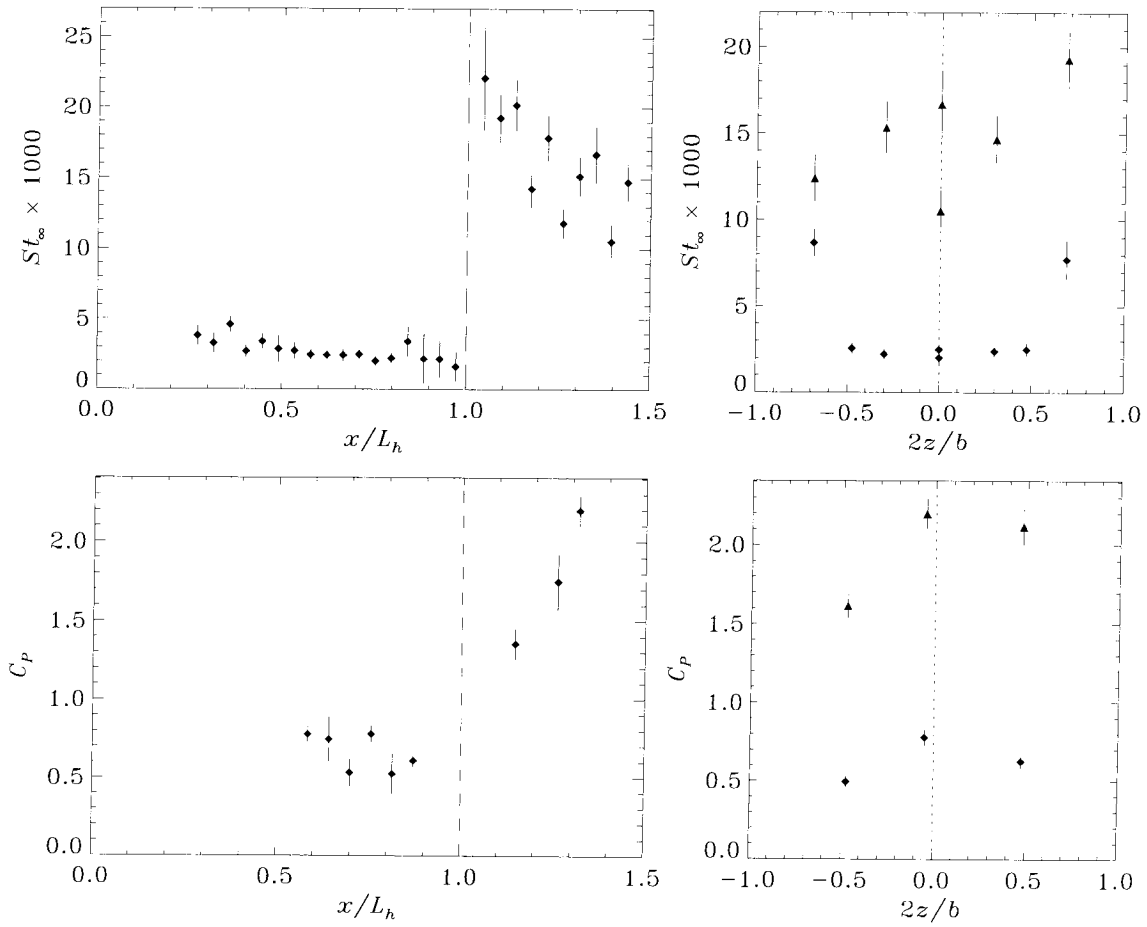

Shot 1755 (condition A2, $A_e/A_* = 225$, $\theta_1 = 30°$, $\theta_w = 20°$)

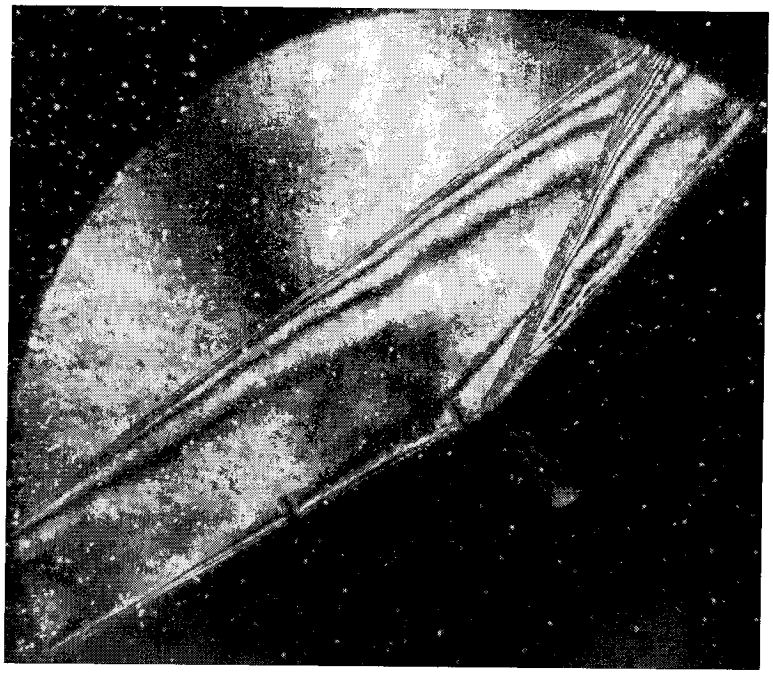

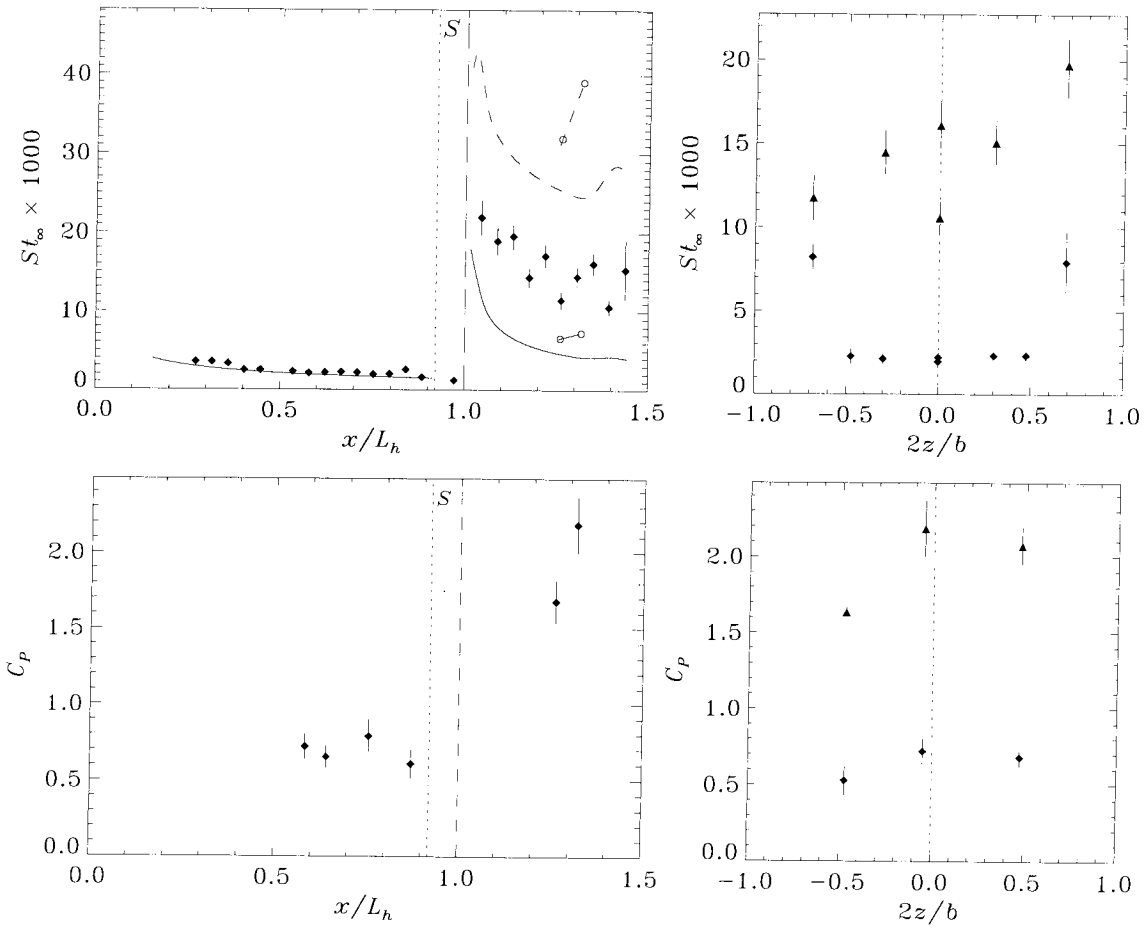

Shot 1756 (condition A2, $A_e/A_* = 225$, $\theta_1 = 30°$, $\theta_w = 20°$)

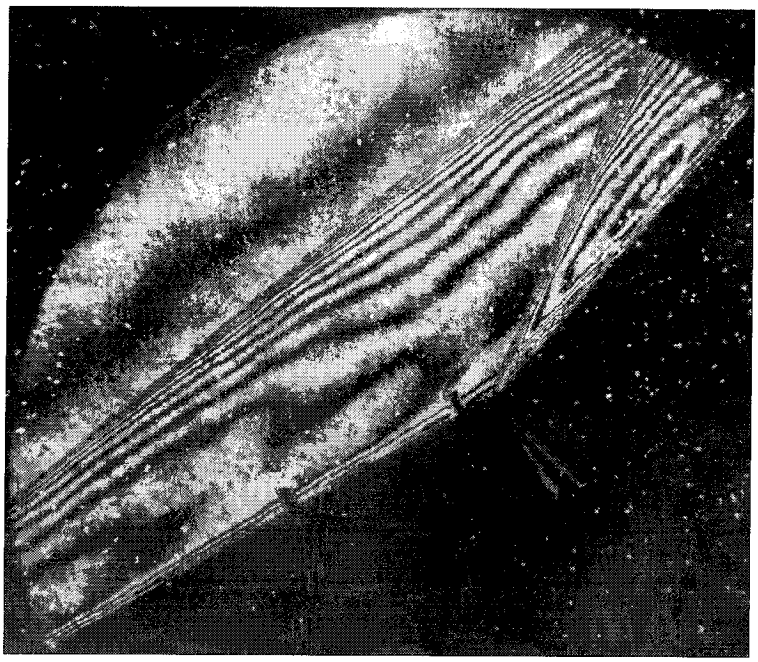

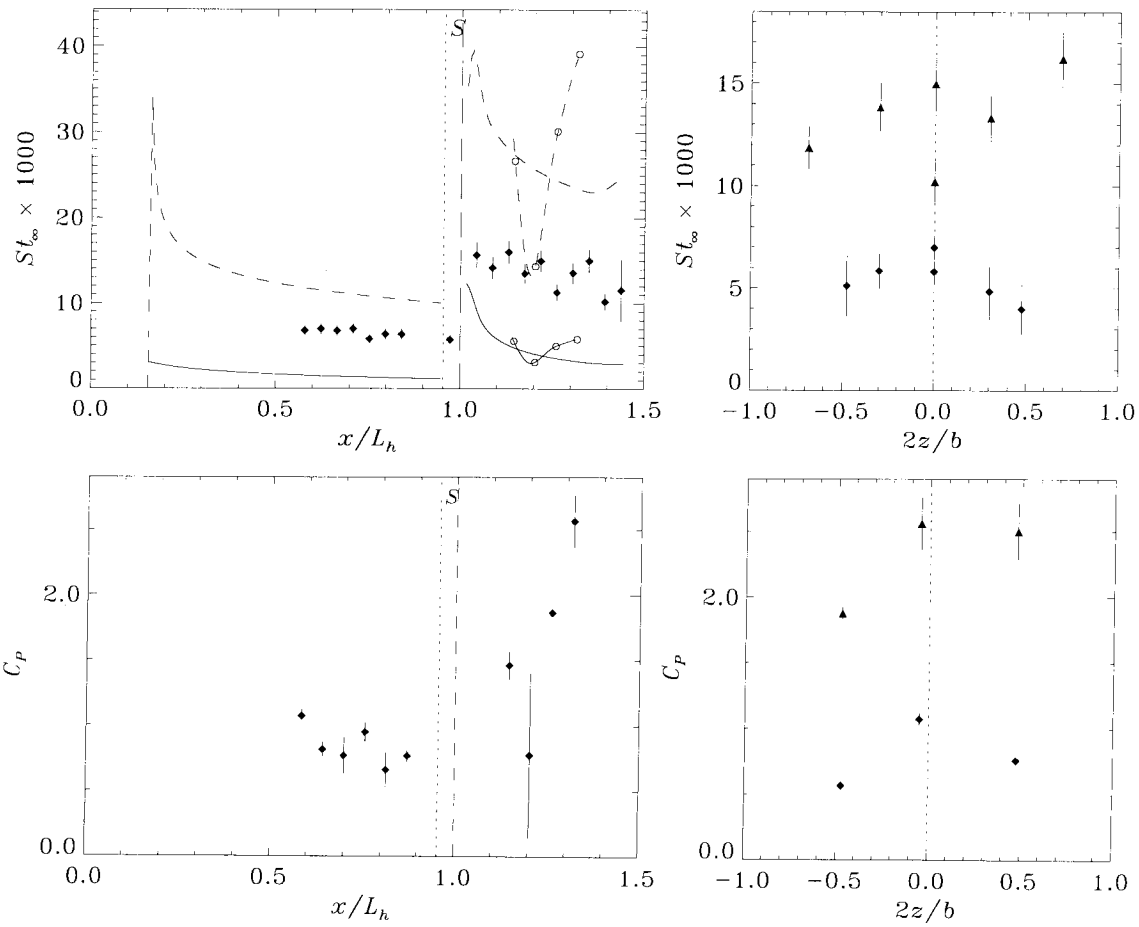

Shot 1757 (condition A2, $A_e/A_* = 100$, $\theta_1 = 30°$, $\theta_w = 20°$)

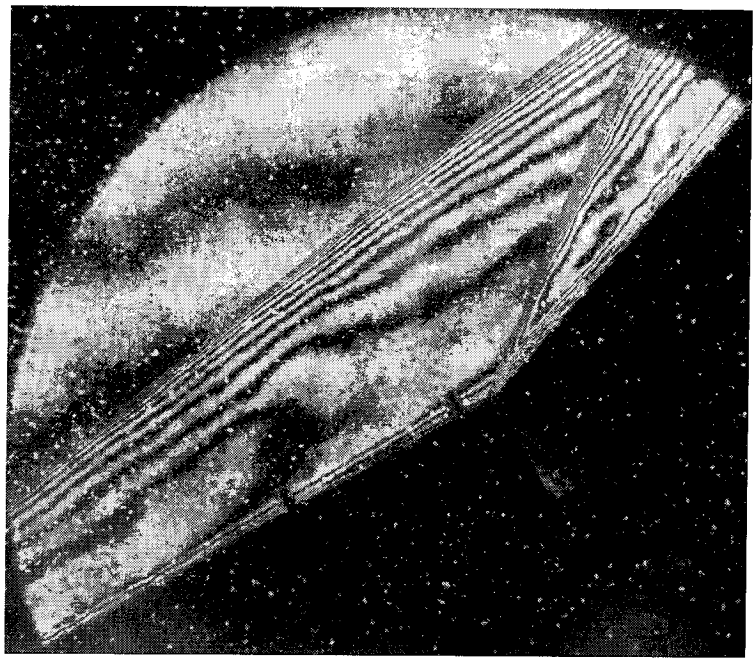

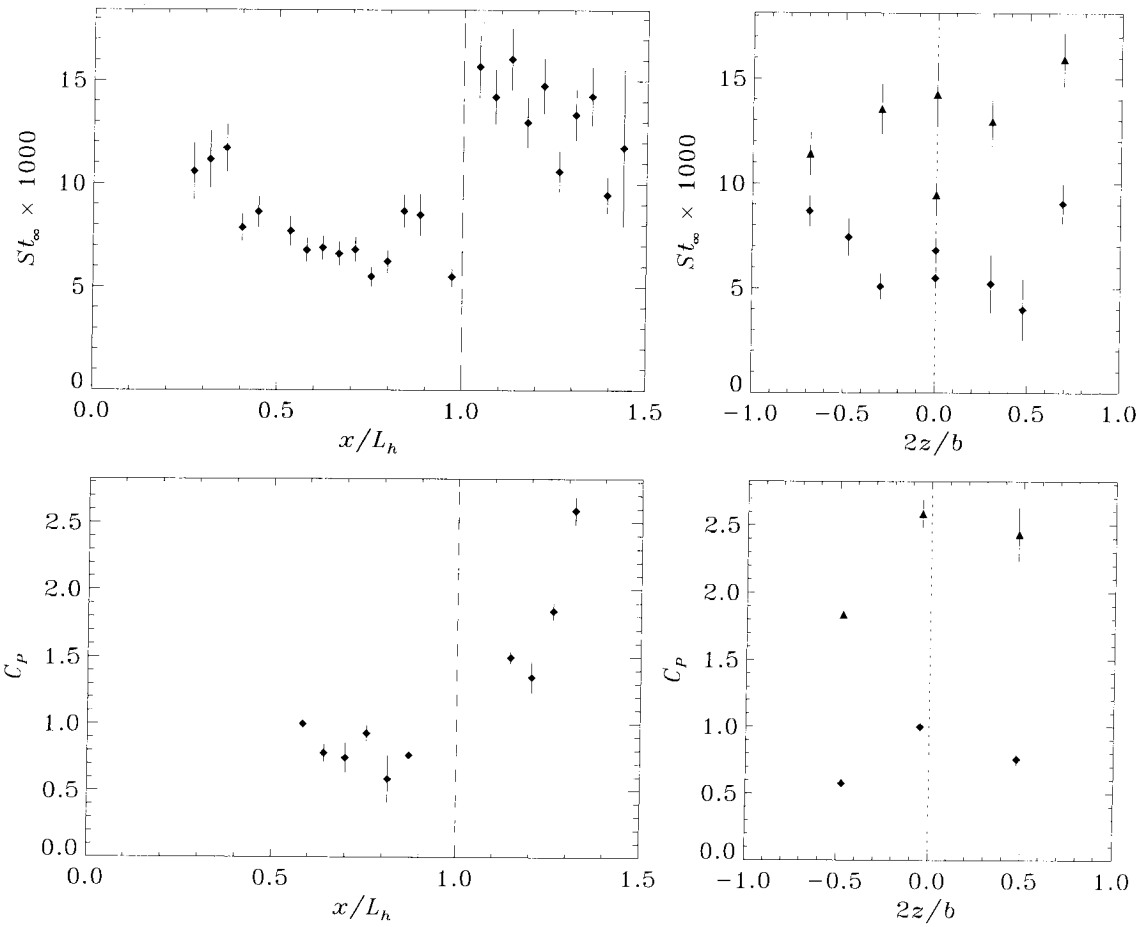

Shot 1758 (condition A2, $A_e/A_* = 100$, $\theta_1 = 30°$, $\theta_w = 20°$)

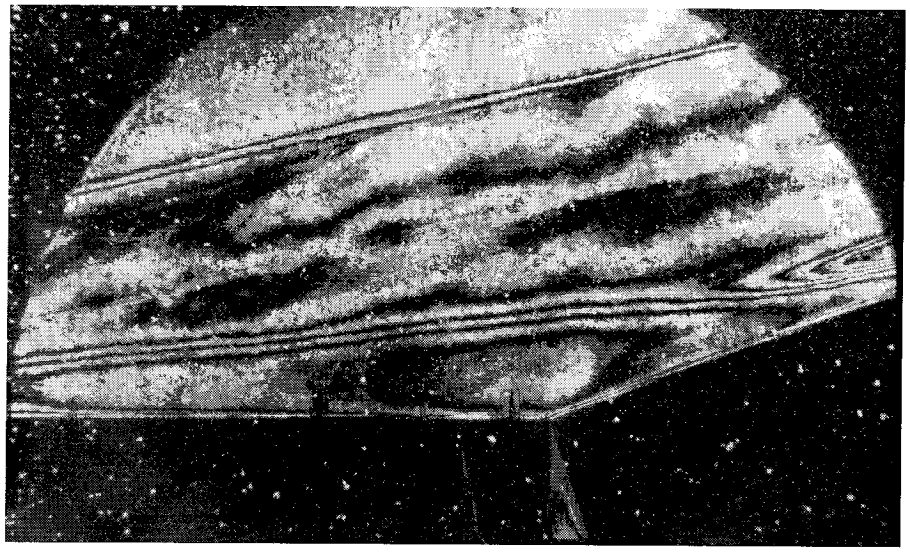

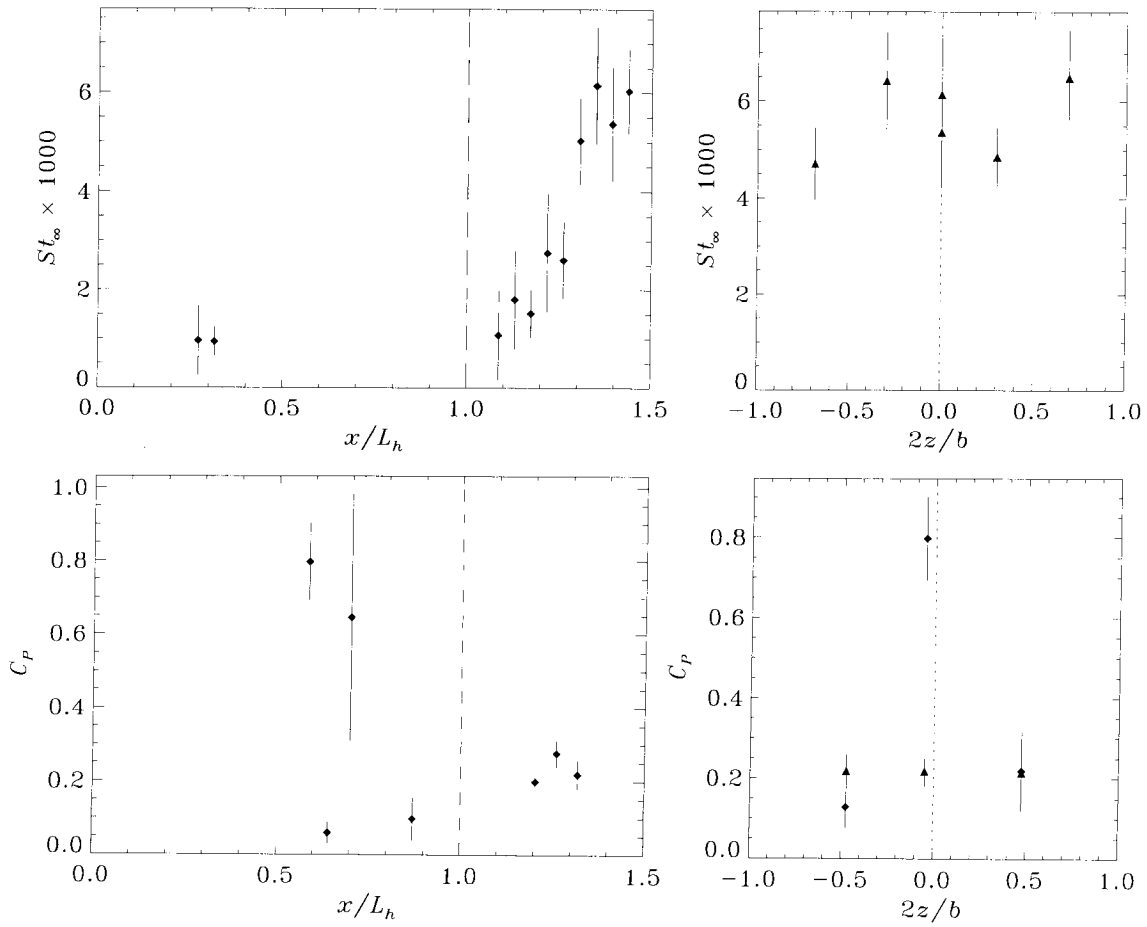

Shot 1759 (condition A1, $A_e/A_* = 100$, $\theta_1 = 0°$, $\theta_w = 20°$)

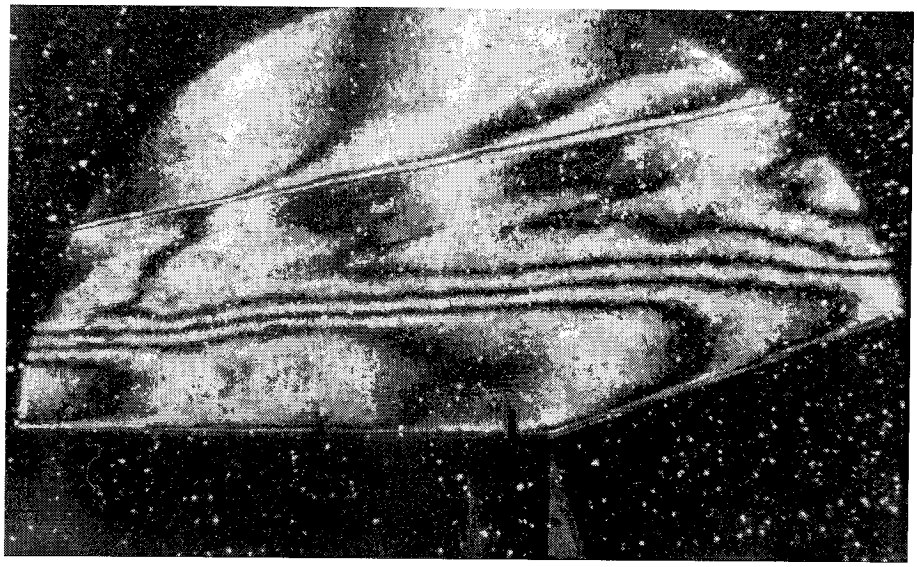

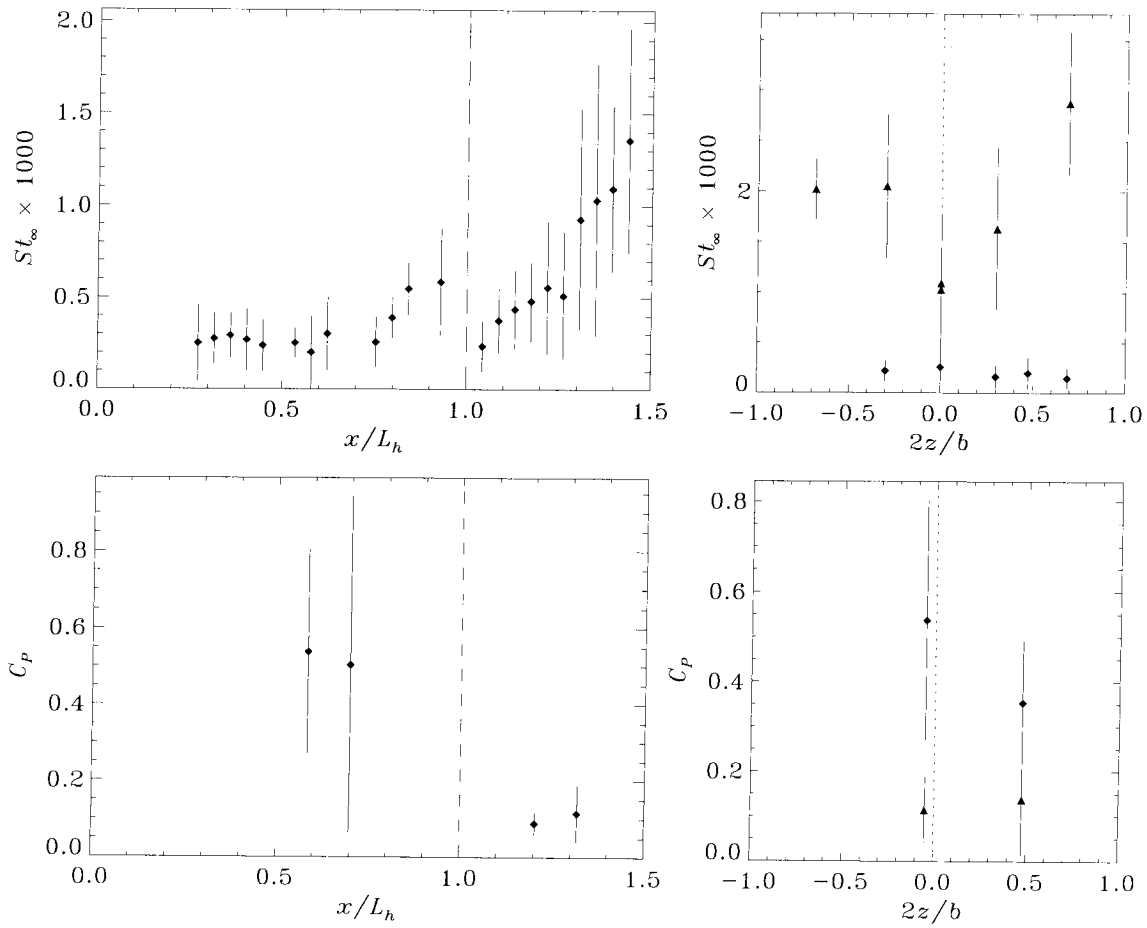

Shot 1760 (condition A2, $A_e/A_* = 400$, $\theta_1 = 0°$, $\theta_w = 20°$)

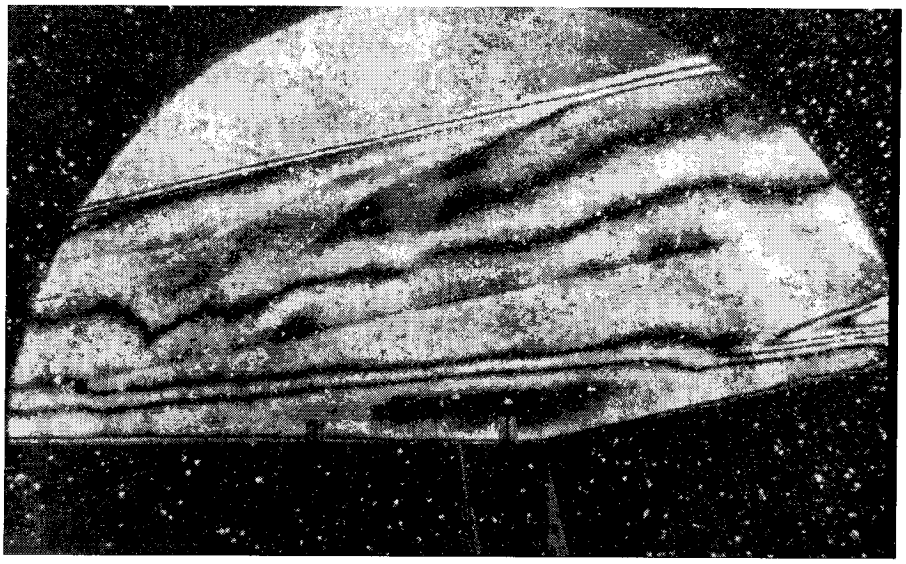

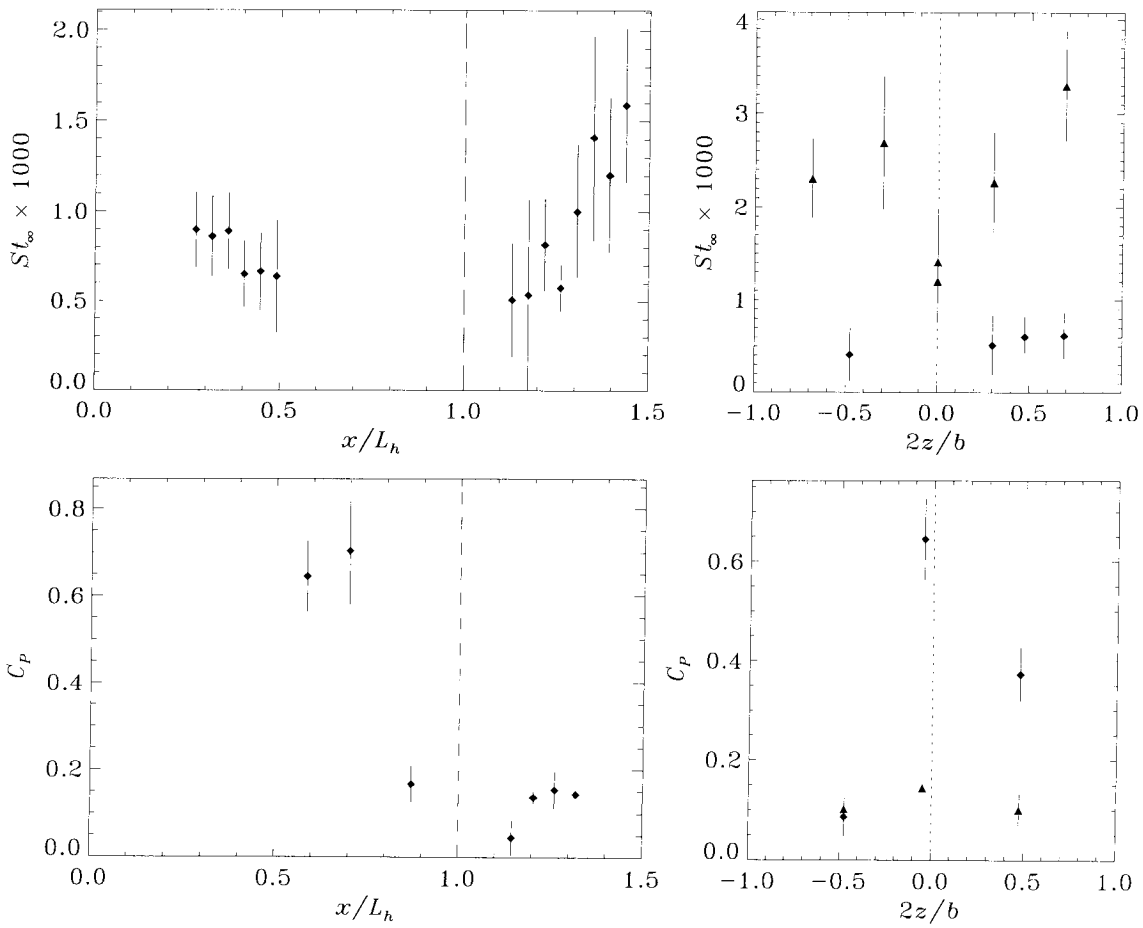

Shot 1761 (condition A1, $A_e/A_* = 100$, $\theta_1 = 0°$, $\theta_w = 10°$)

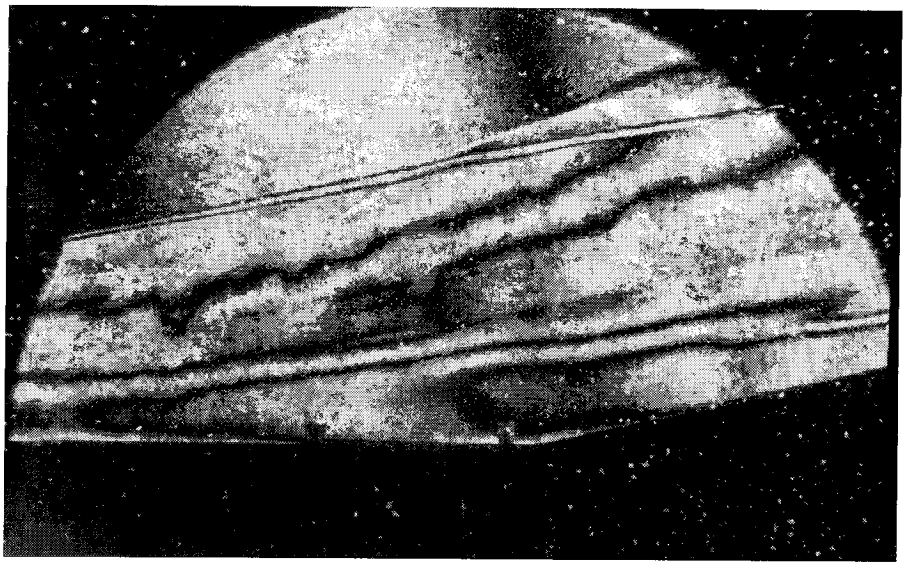

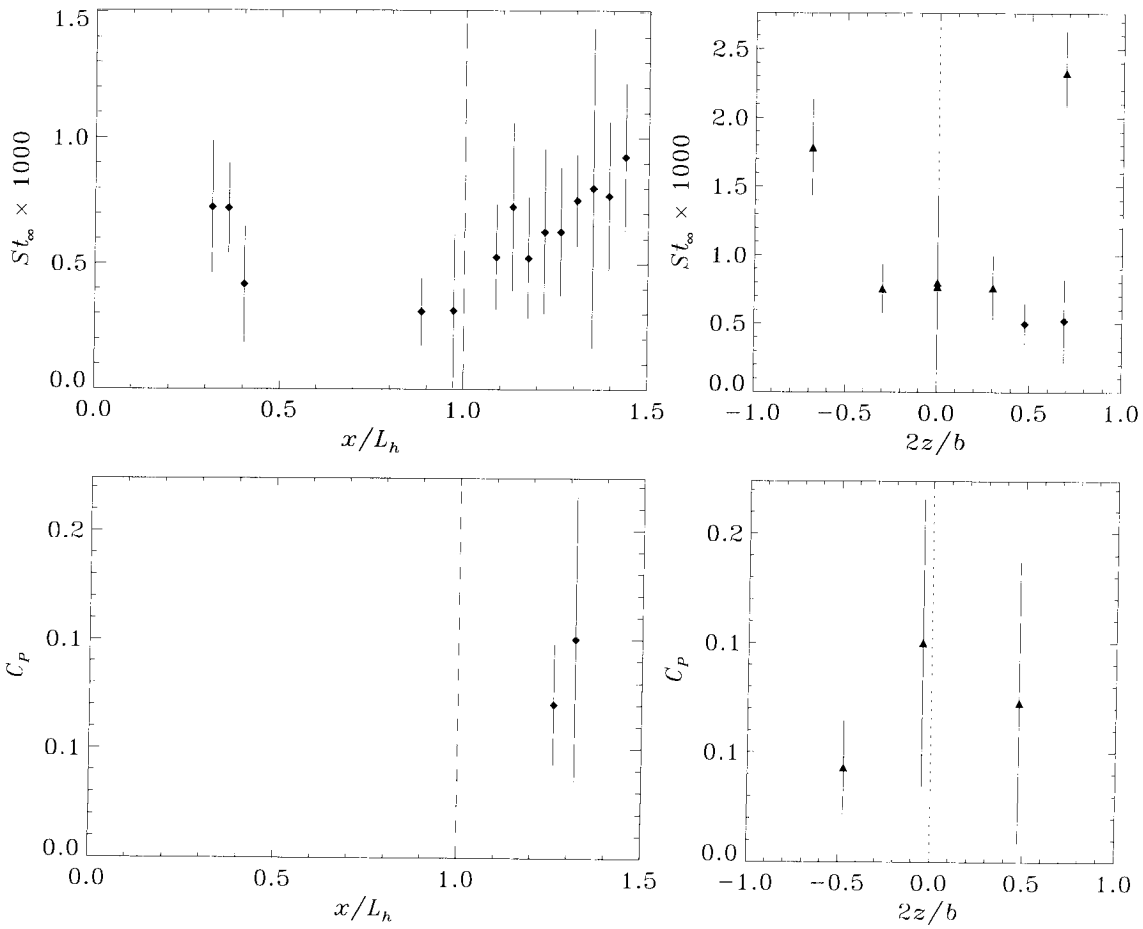

Shot 1762 (condition A2, $A_e/A_* = 400$, $\theta_1 = 0°$, $\theta_w = 10°$)

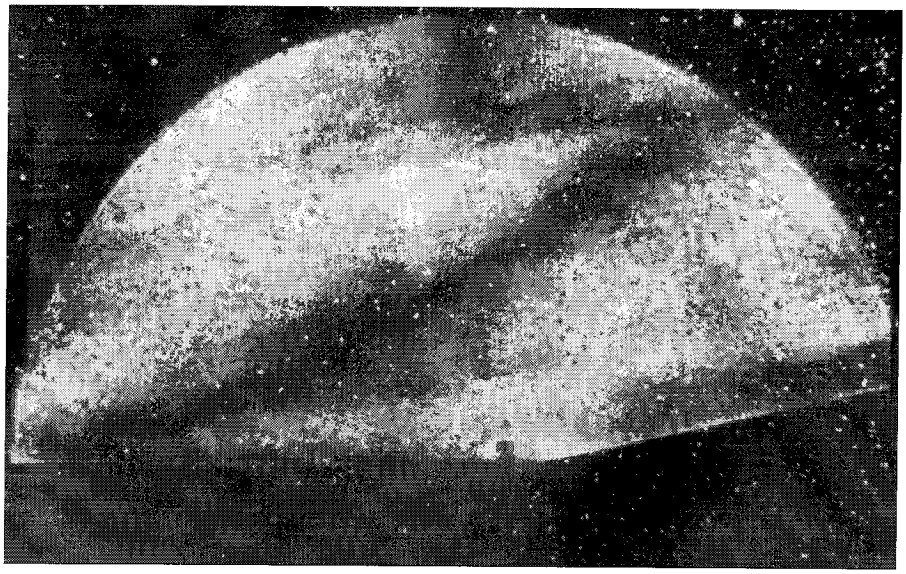

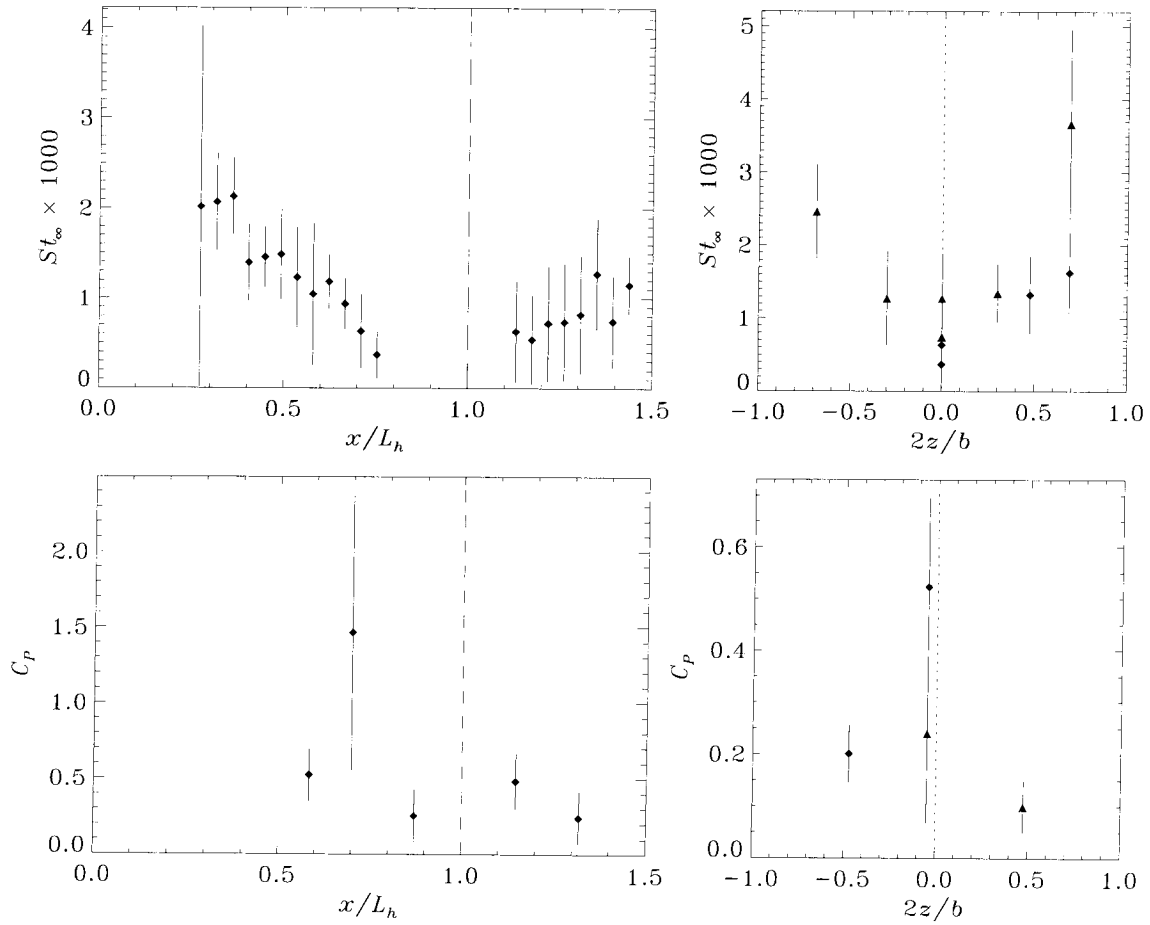

Shot 1764 (condition B1, $A_e/A_* = 225$, $\theta_1 = 0°$, $\theta_w = 10°$)

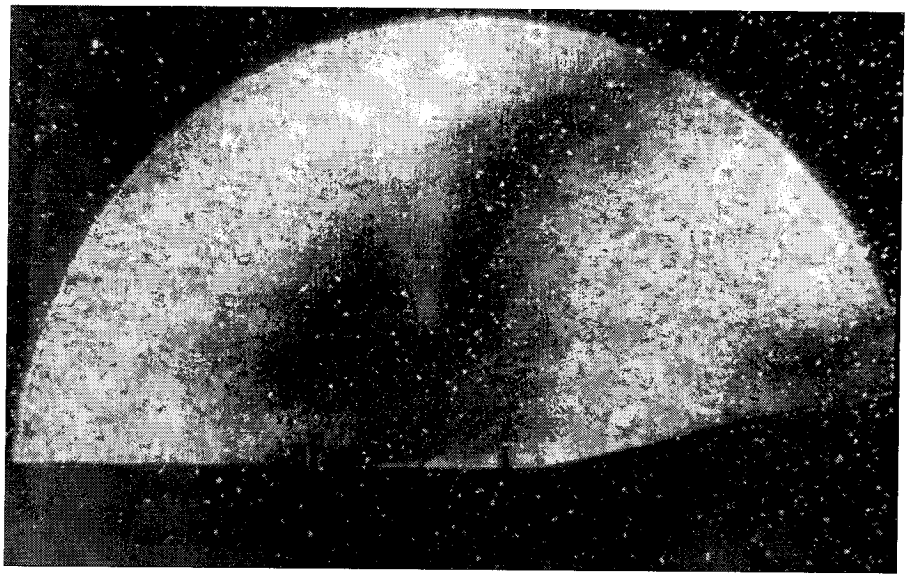

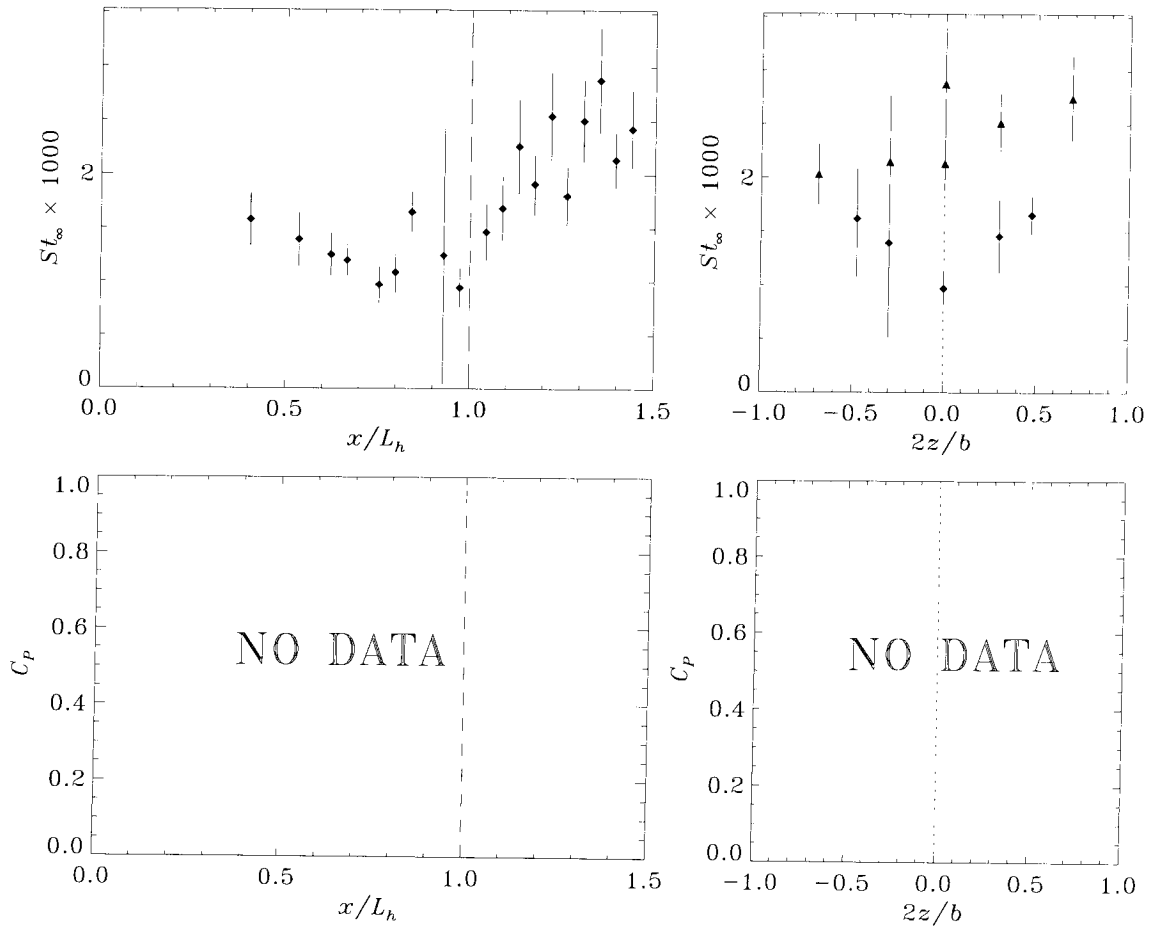

Shot 1765 (condition C2, $A_e/A_* = 400$, $\theta_1 = 0°$, $\theta_w = 10°$)

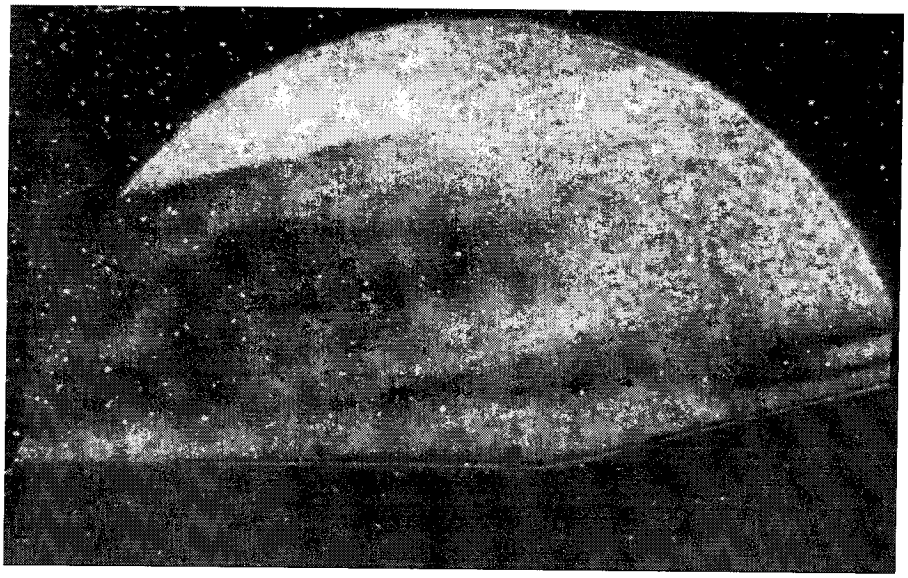

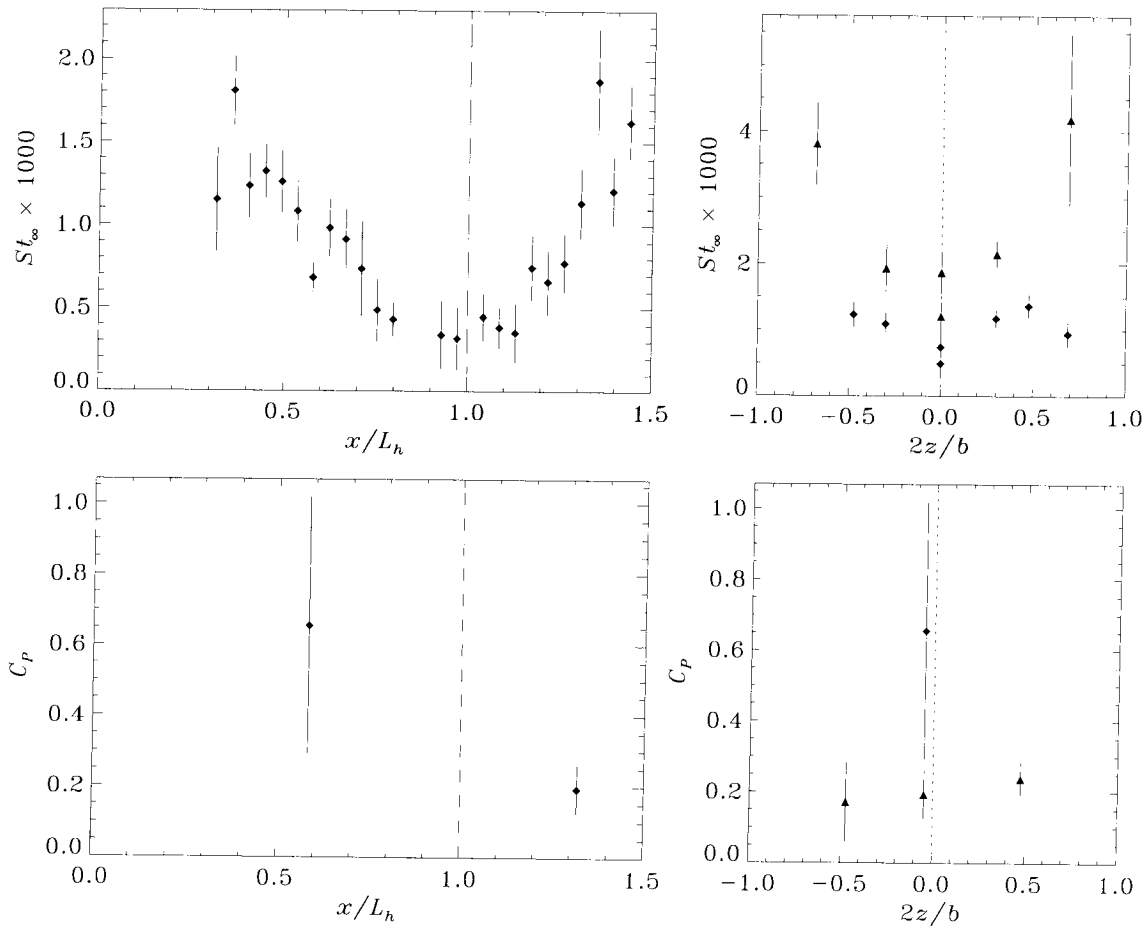

Shot 1766 (condition C2, $A_e/A_* = 100$, $\theta_1 = 0°$, $\theta_w = 15°$)

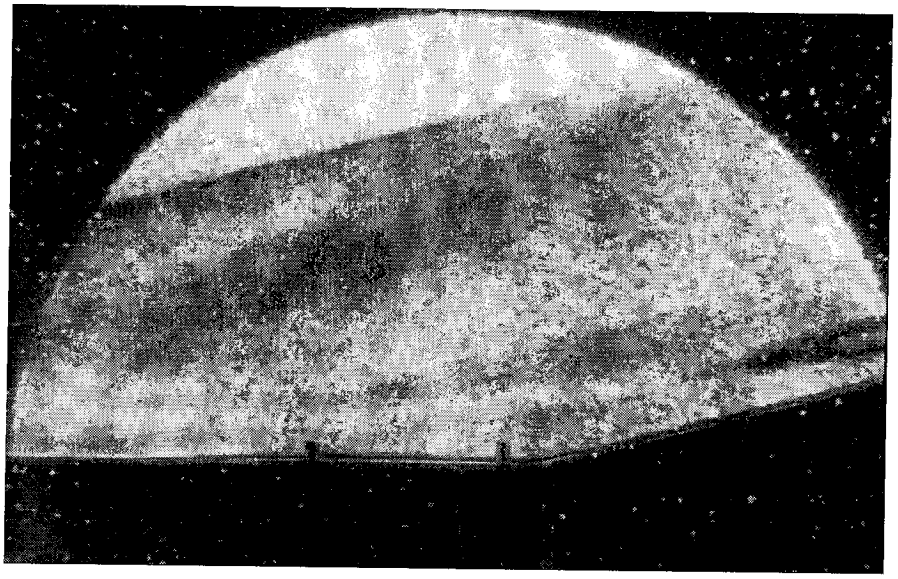

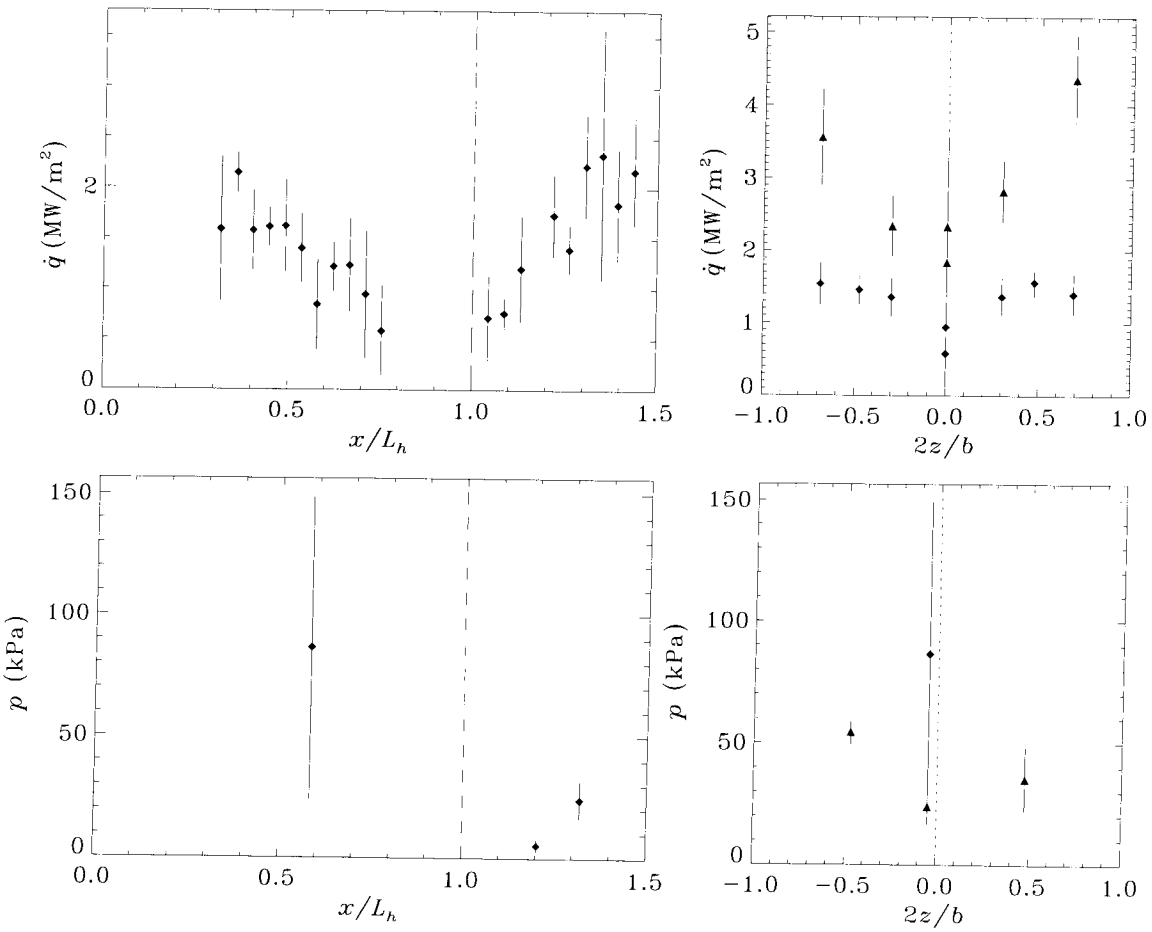

Shot 1768 (condition C0, $A_e/A_* = 100$, $\theta_1 = 0°$, $\theta_w = 15°$)

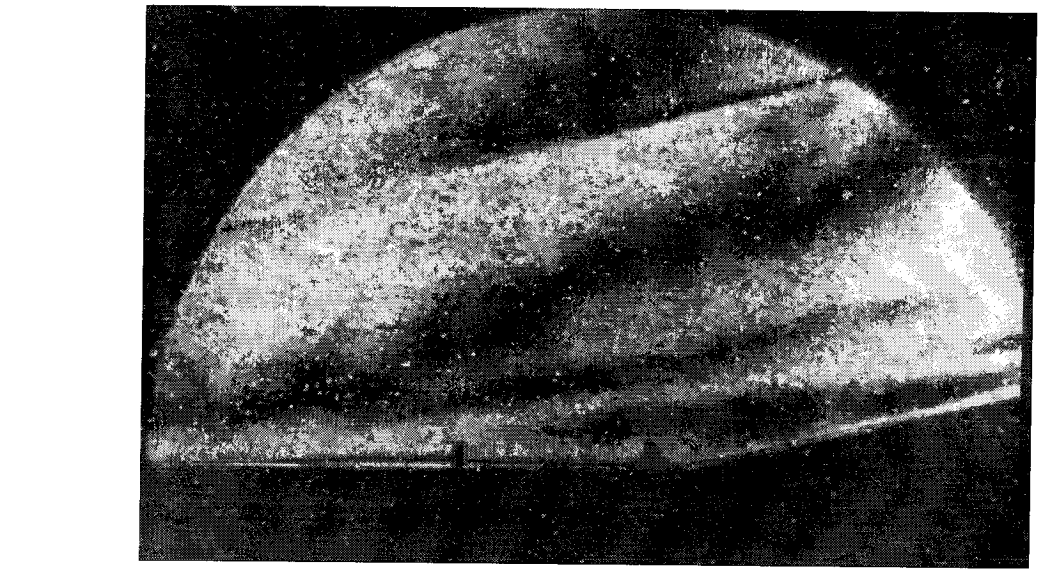

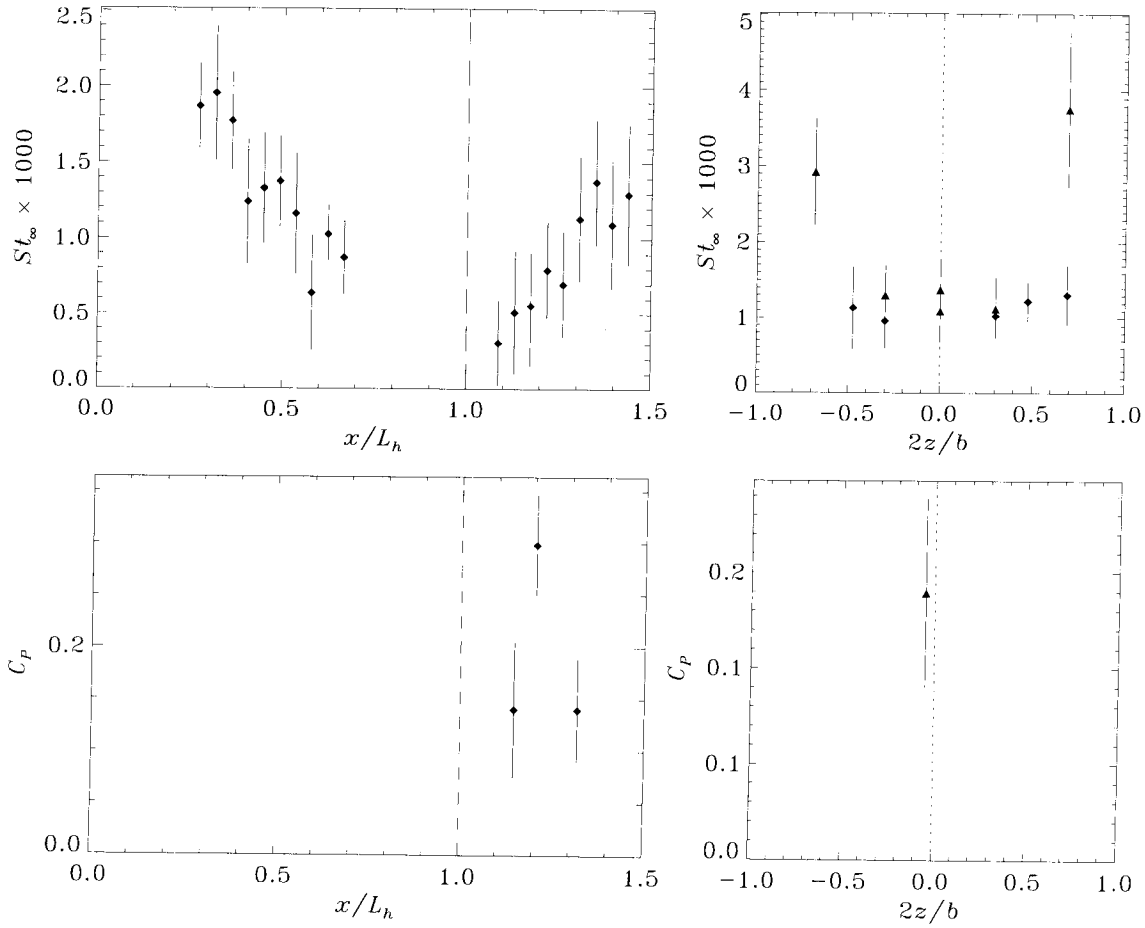

Shot 1770 (condition B1, $A_e/A_* = 100$, $\theta_1 = 0°$, $\theta_w = 10°$)

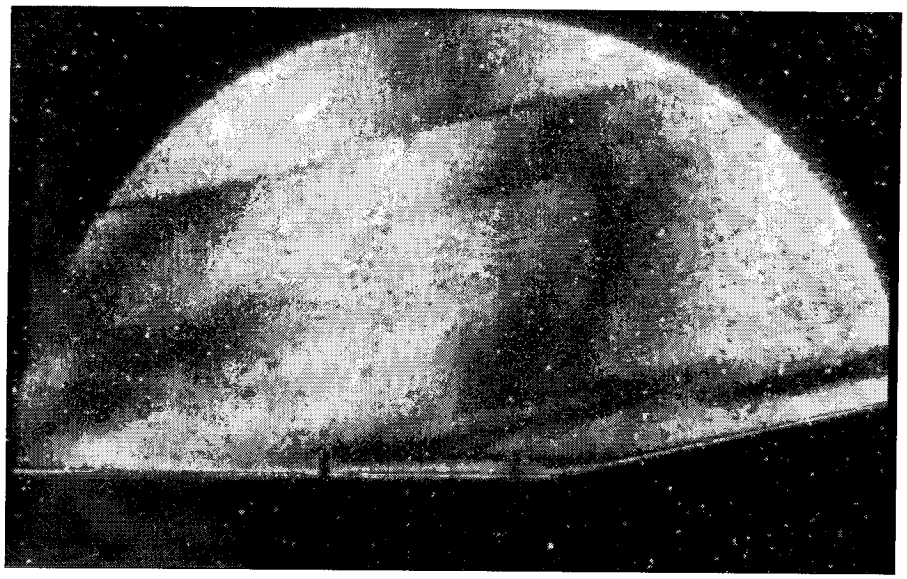

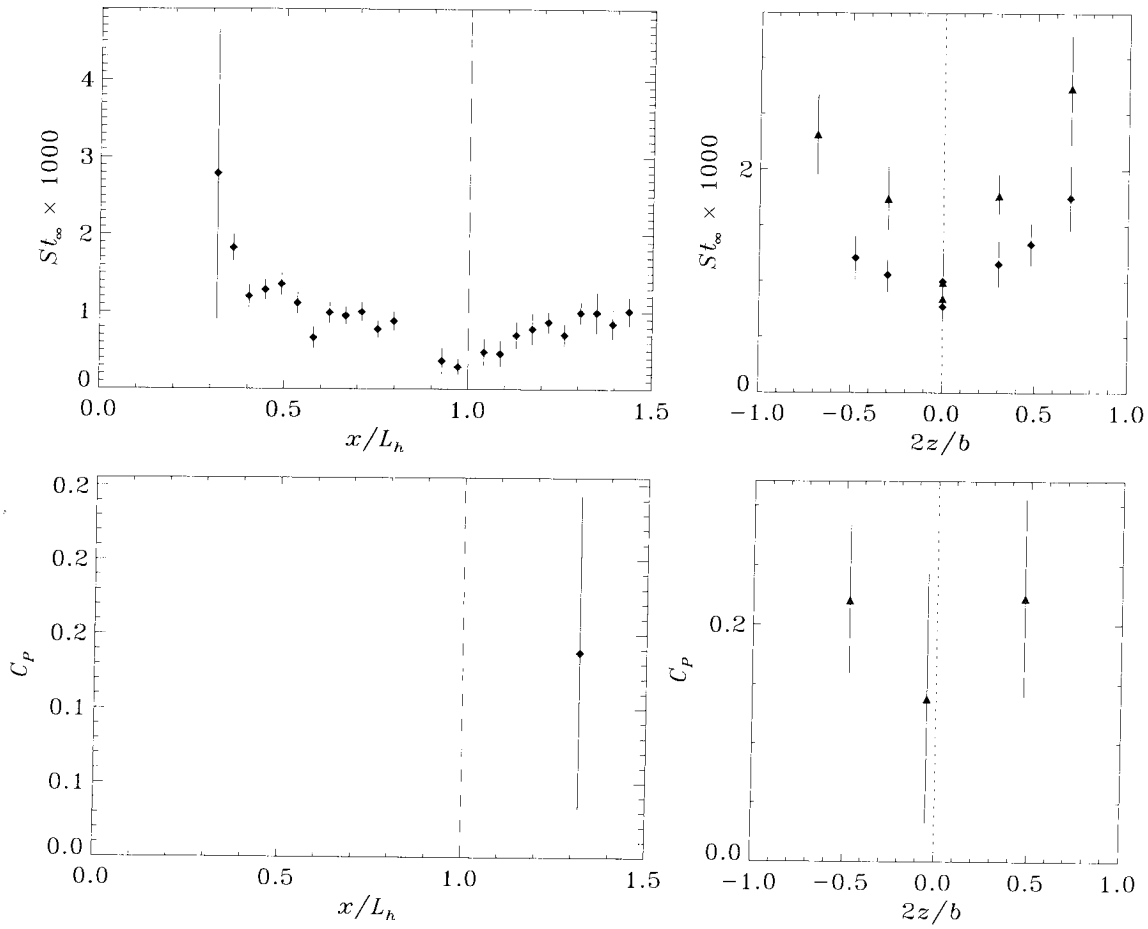

Shot 1772 (condition C2, $A_e/A_* = 100$, $\theta_1 = 0°$, $\theta_w = 10°$)

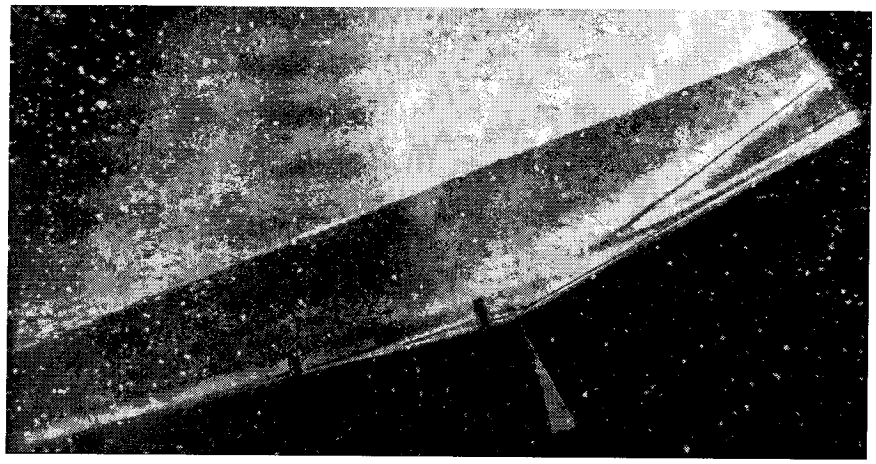

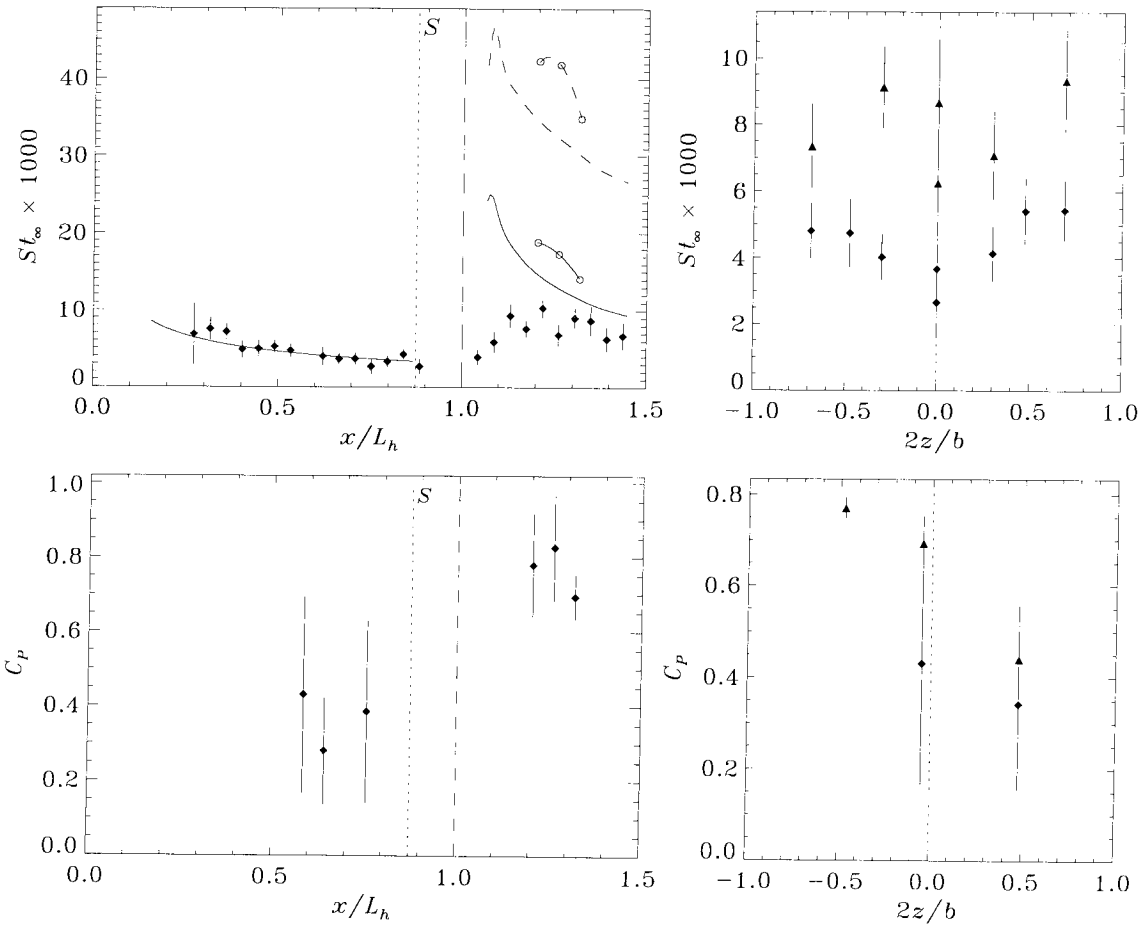

Shot 1774 (condition B1, $A_e/A_* = 400$, $\theta_1 = 15°$, $\theta_w = 15°$)

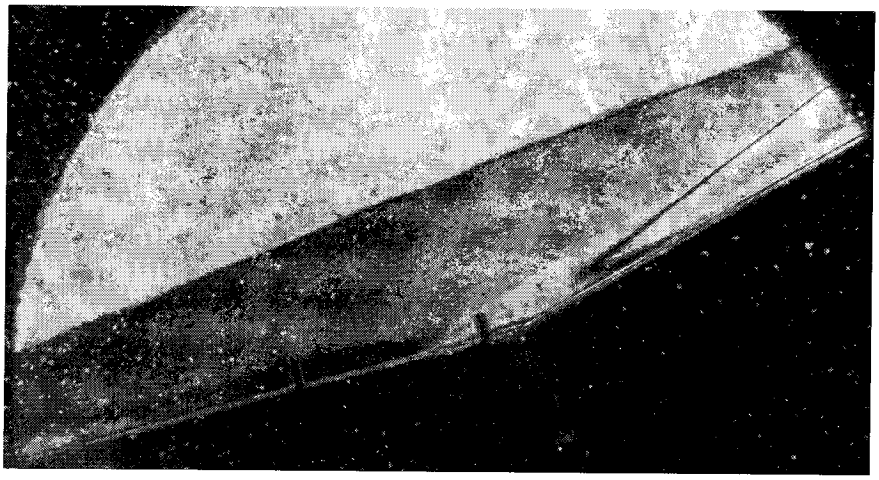

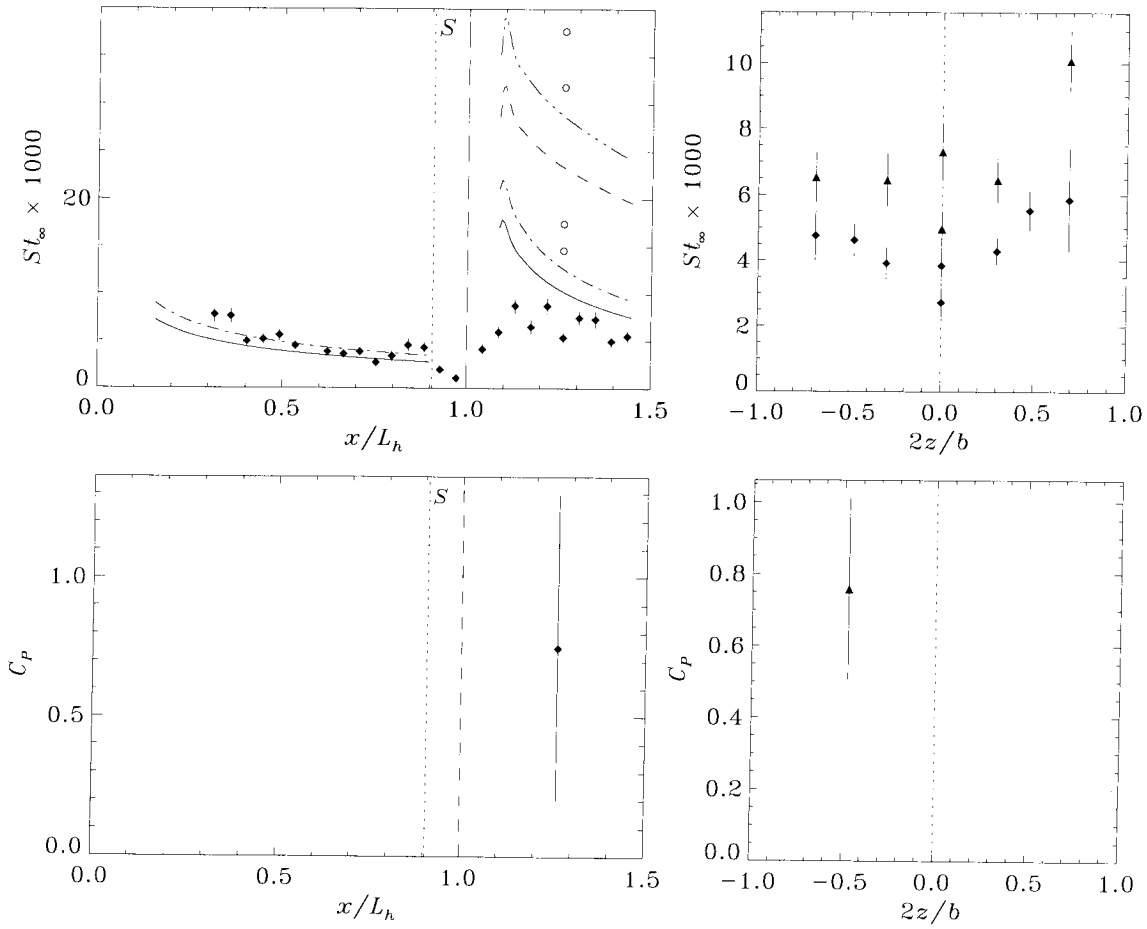

Shot 1775 (condition C2, $A_c/A_* = 400$, $\theta_1 = 15°$, $\theta_w = 15°$)

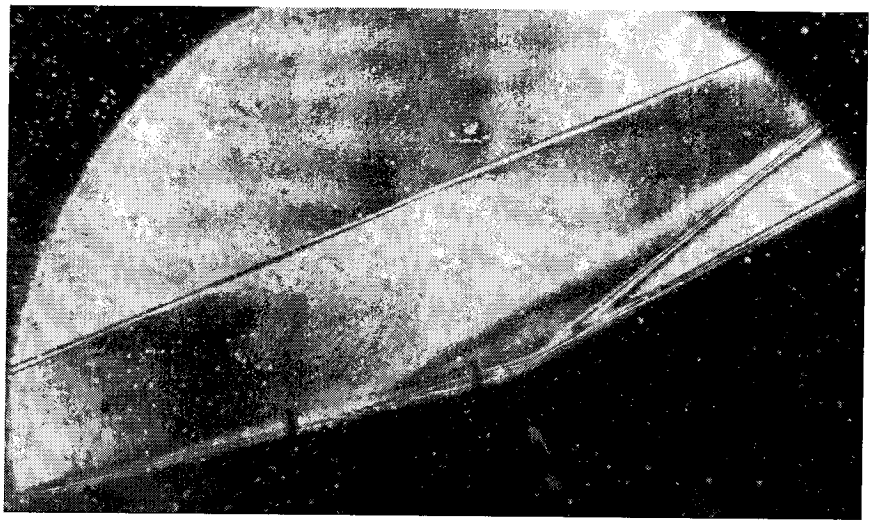

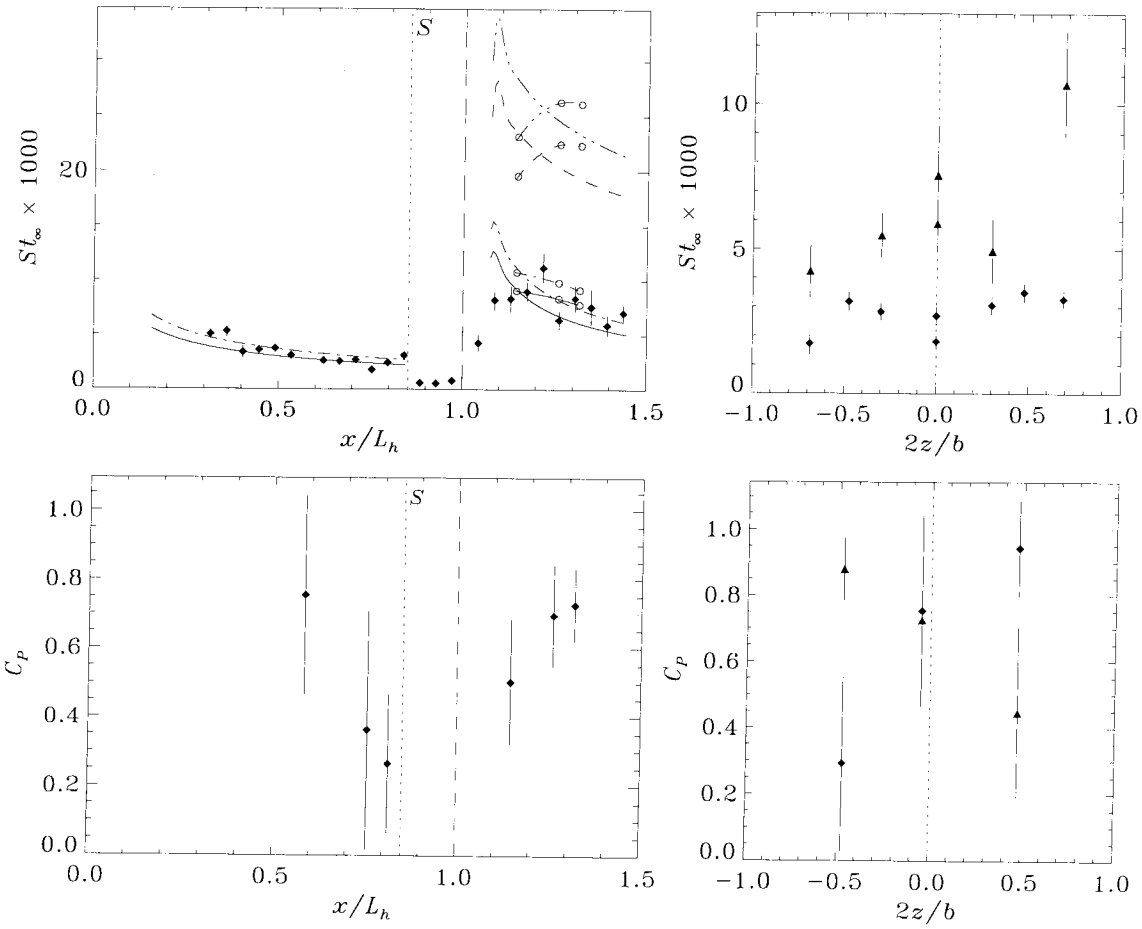

Shot 1776 (condition C2, $A_e/A_* = 100$, $\theta_1 = 15°$, $\theta_w = 15°$)

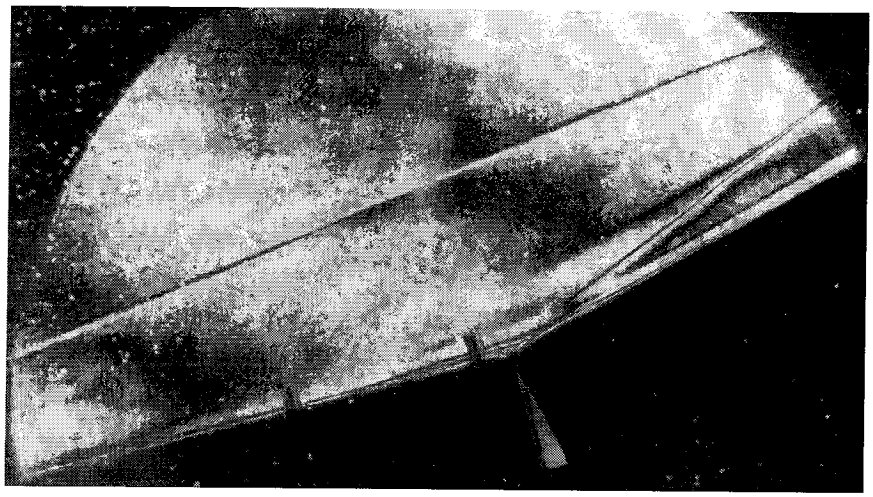

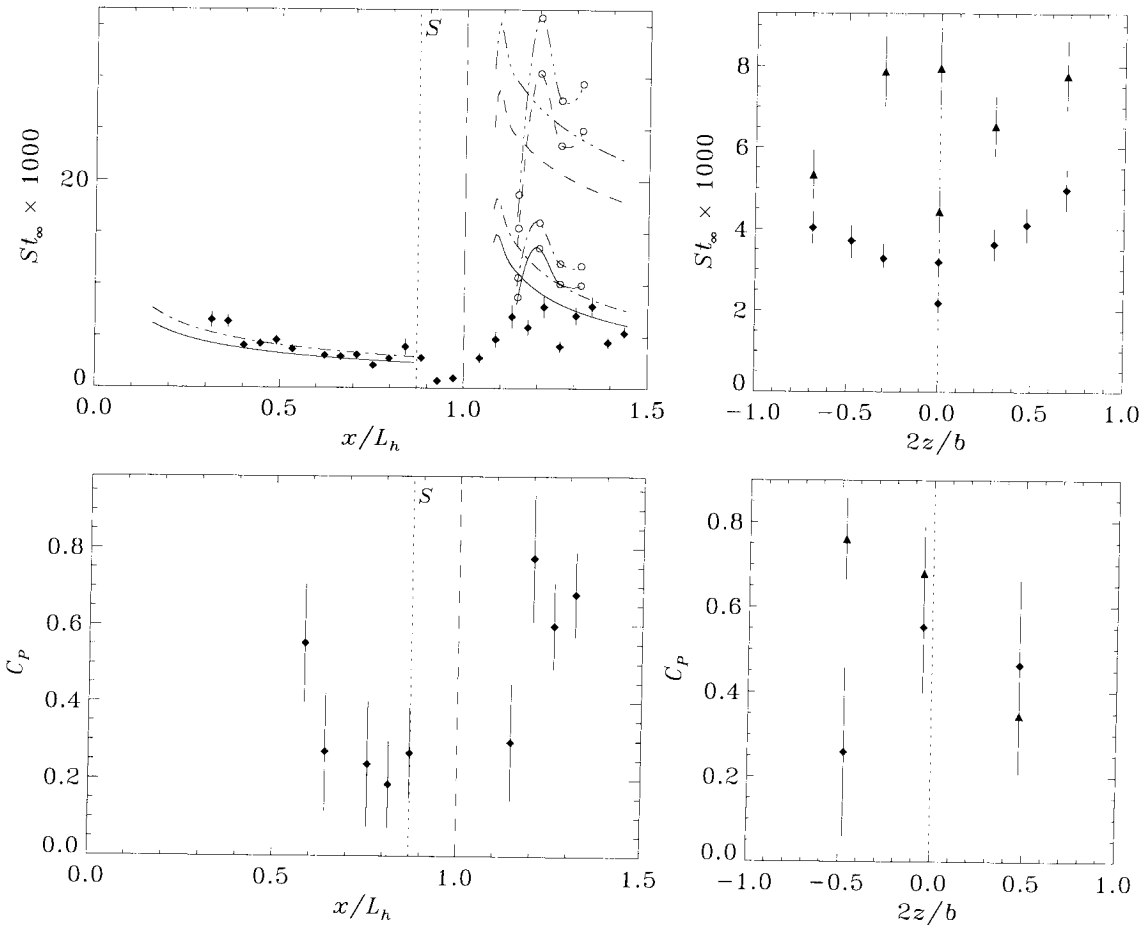

Shot 1777 (condition C2, $A_e/A_* = 225$, $\theta_1 = 15°$, $\theta_w = 15°$)

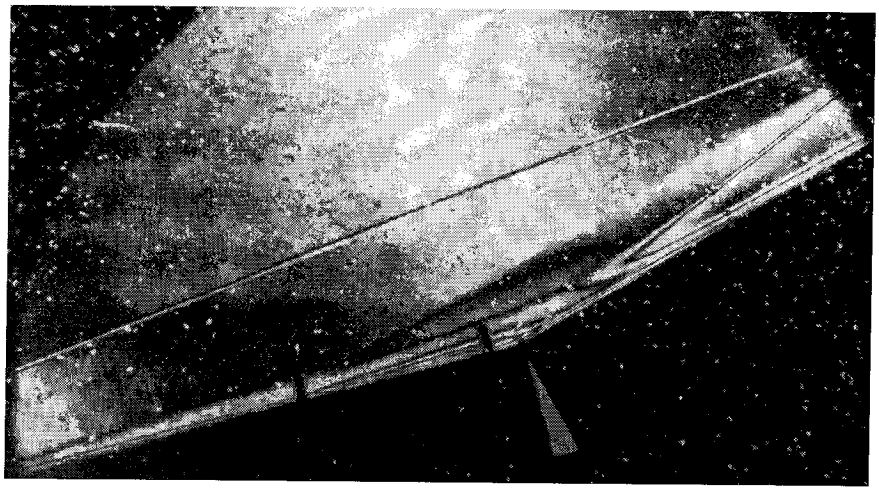

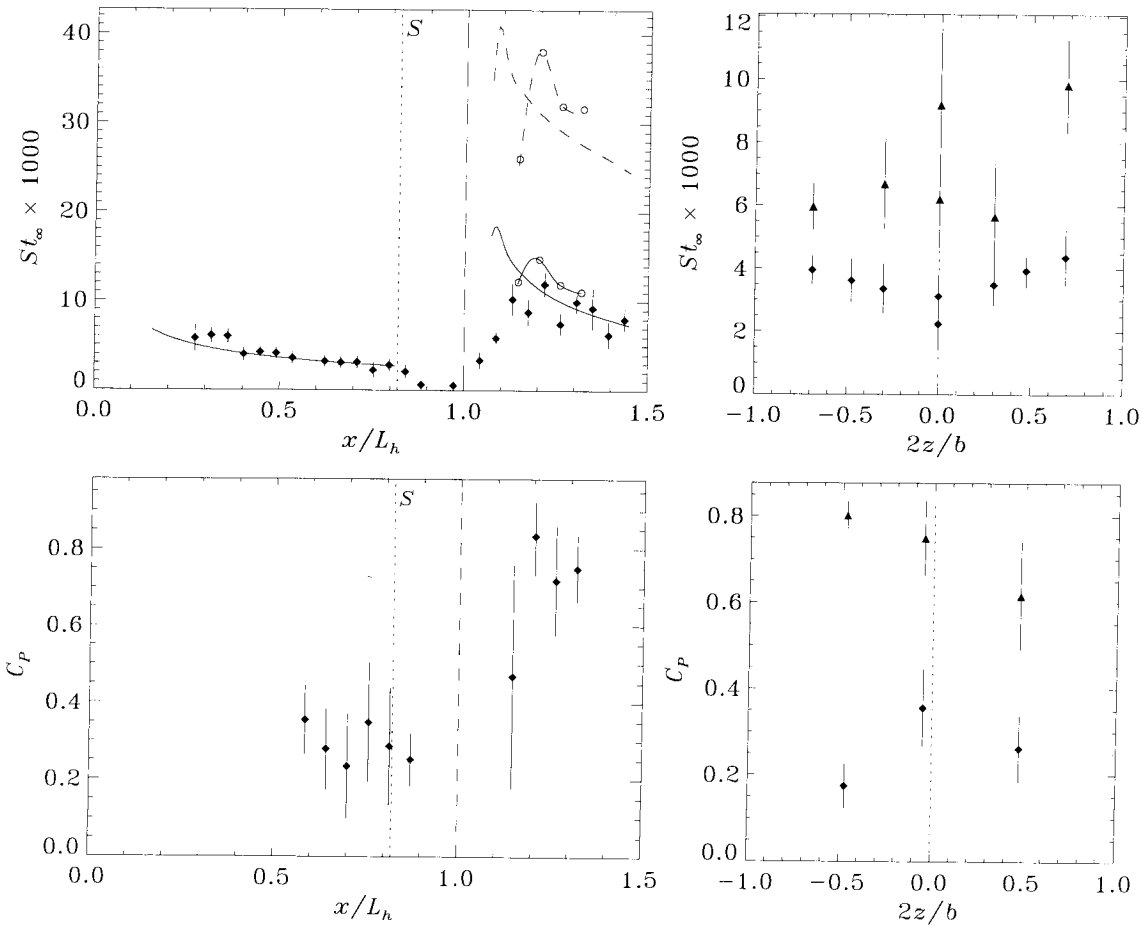

Shot 1778 (condition B1, $A_e/A_* = 225$, $\theta_1 = 15°$, $\theta_w = 15°$)

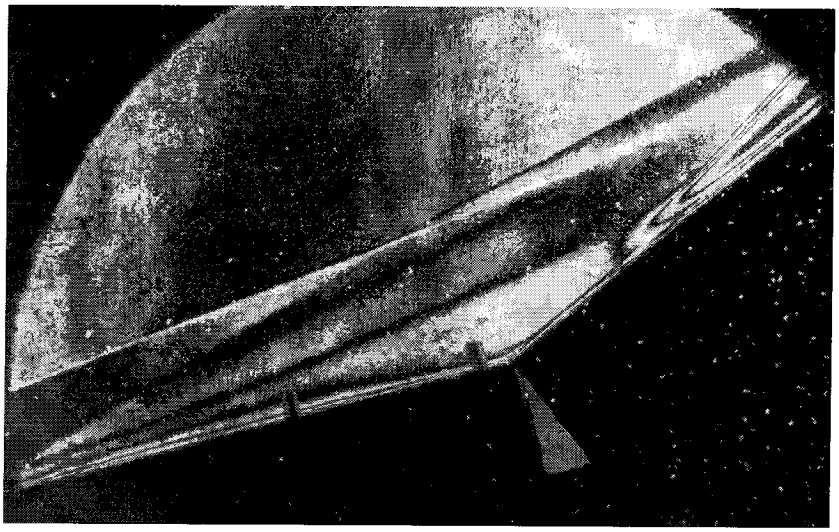

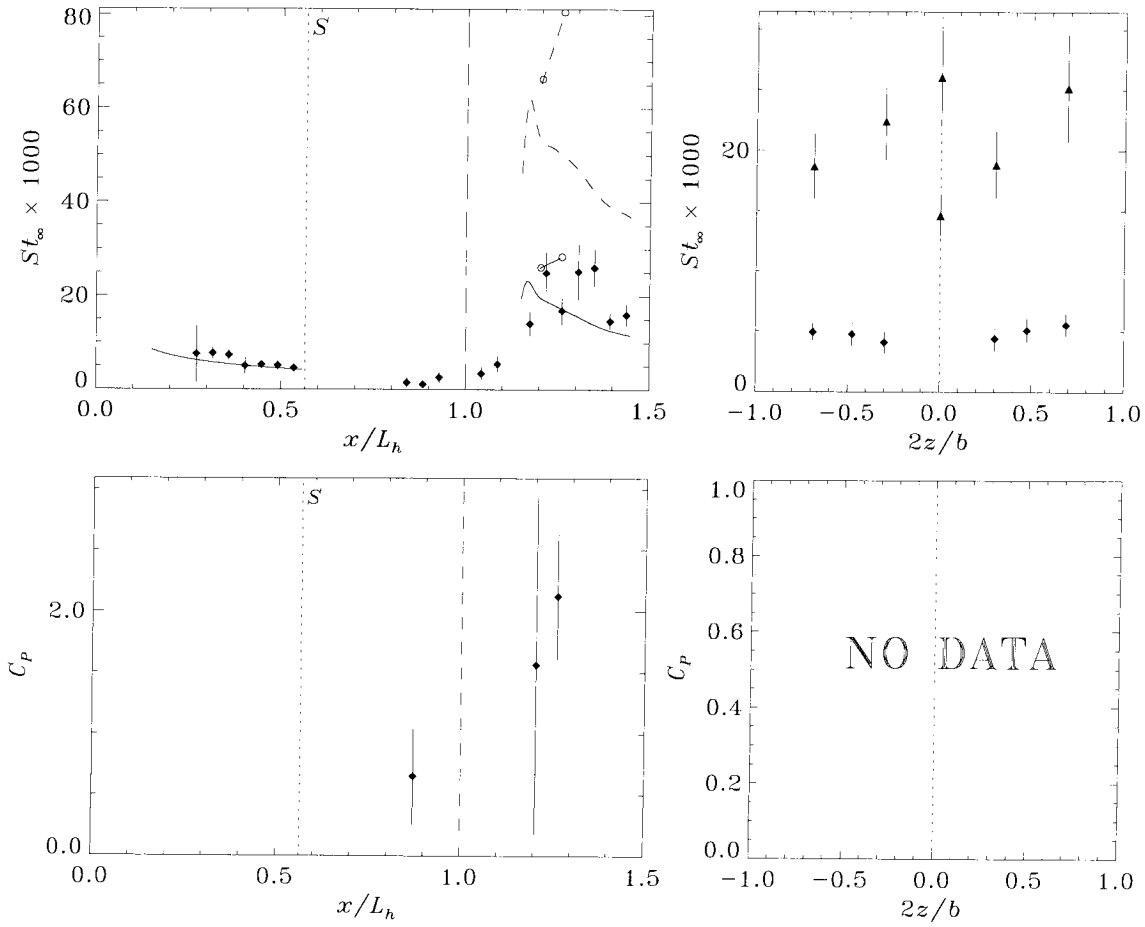

Shot 1779 (condition B1, $A_e/A_* = 400$, $\theta_1 = 15°$, $\theta_w = 25°$)

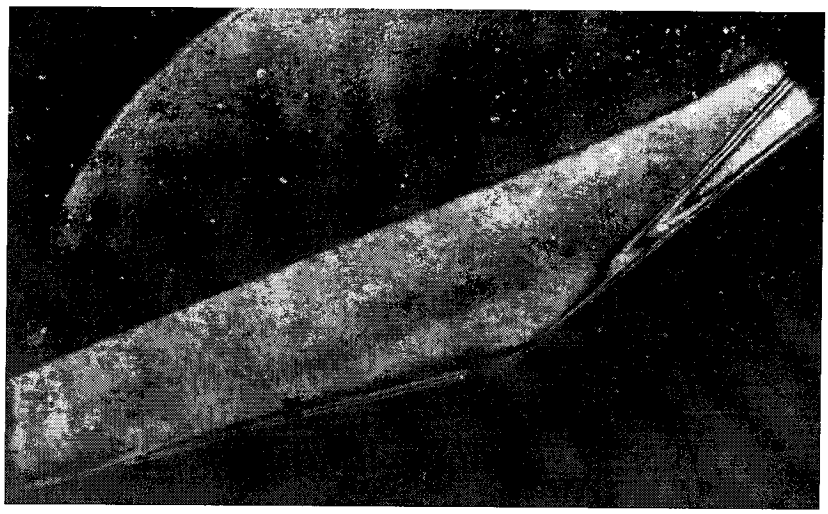

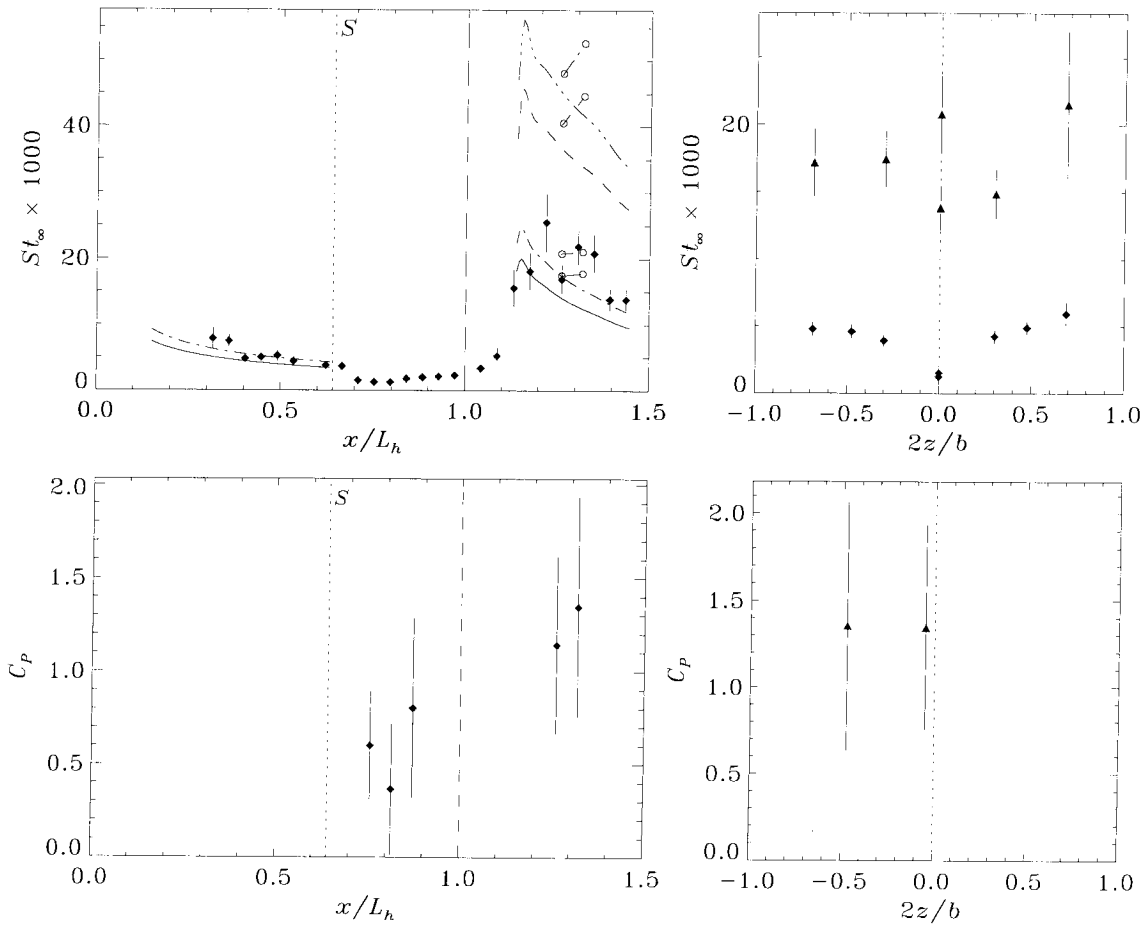

Shot 1780 (condition C2, $A_e/A_* = 400$, $\theta_1 = 15°$, $\theta_w = 25°$)

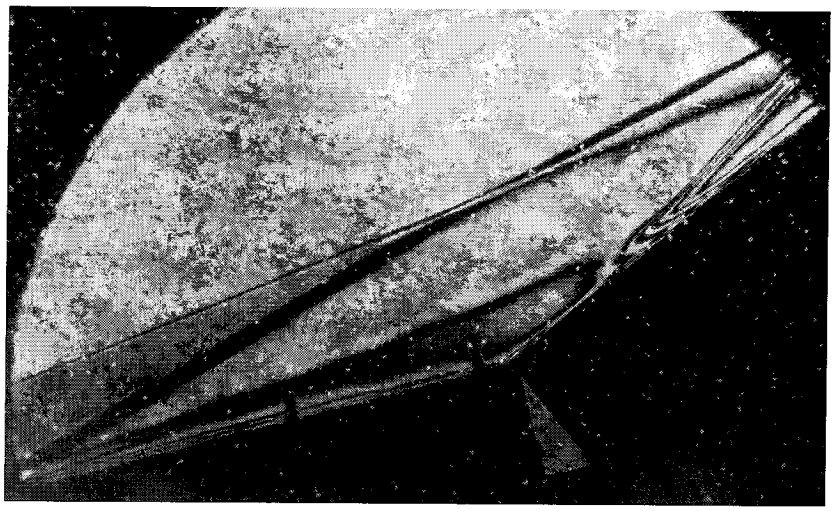

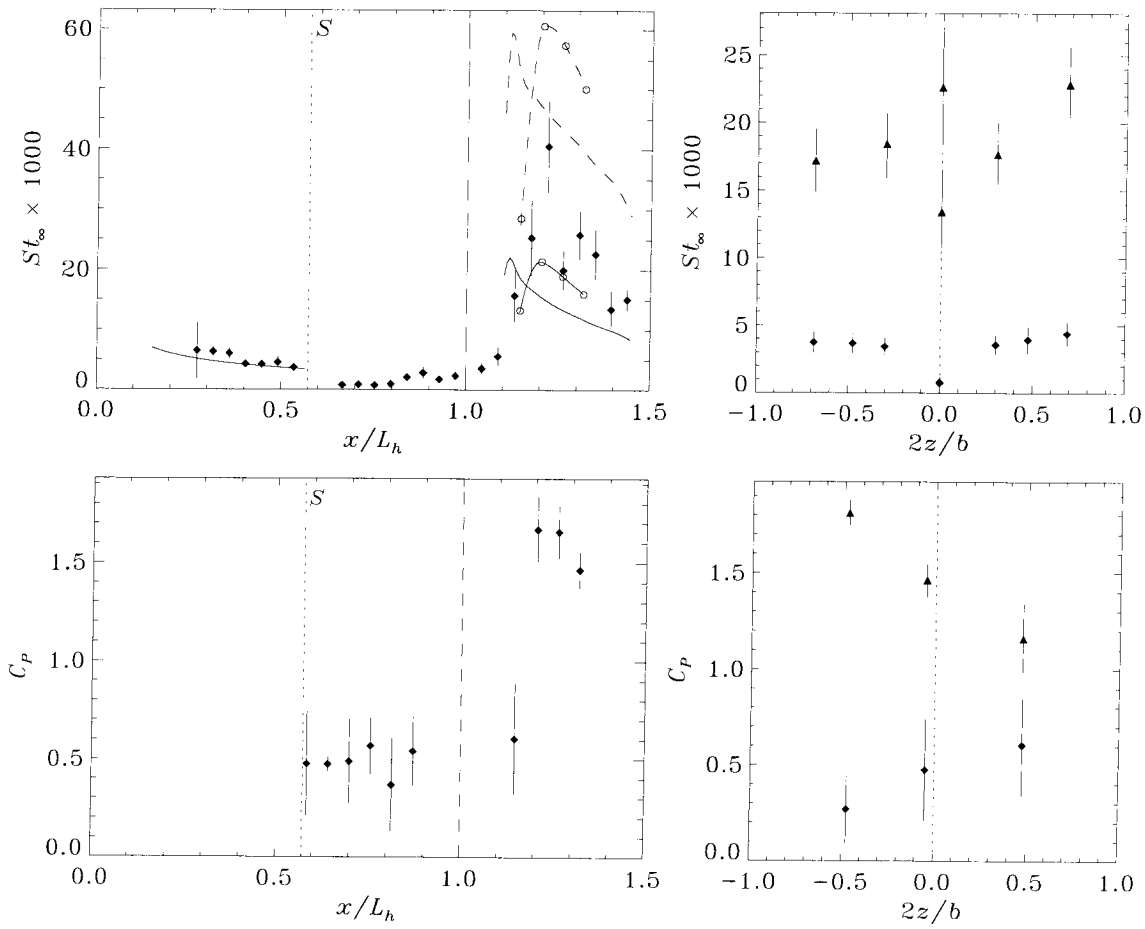

Shot 1781 (condition B1, $A_e/A_* = 225$, $\theta_1 = 15°$, $\theta_w = 25°$)

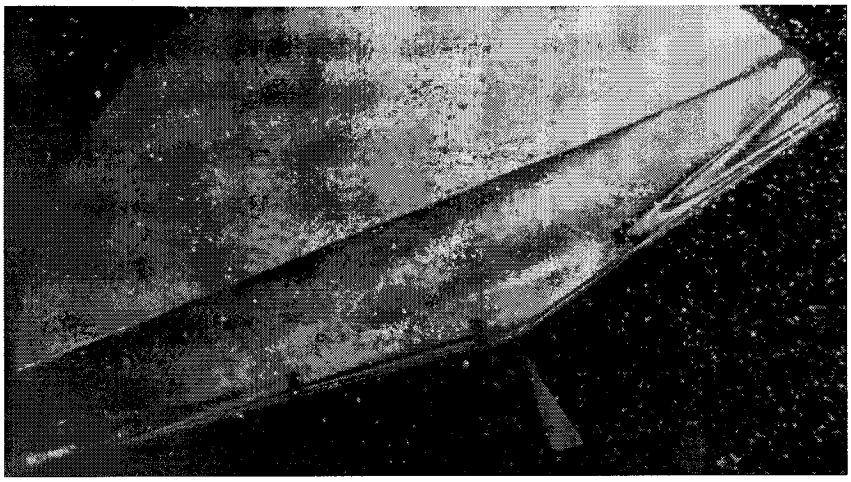

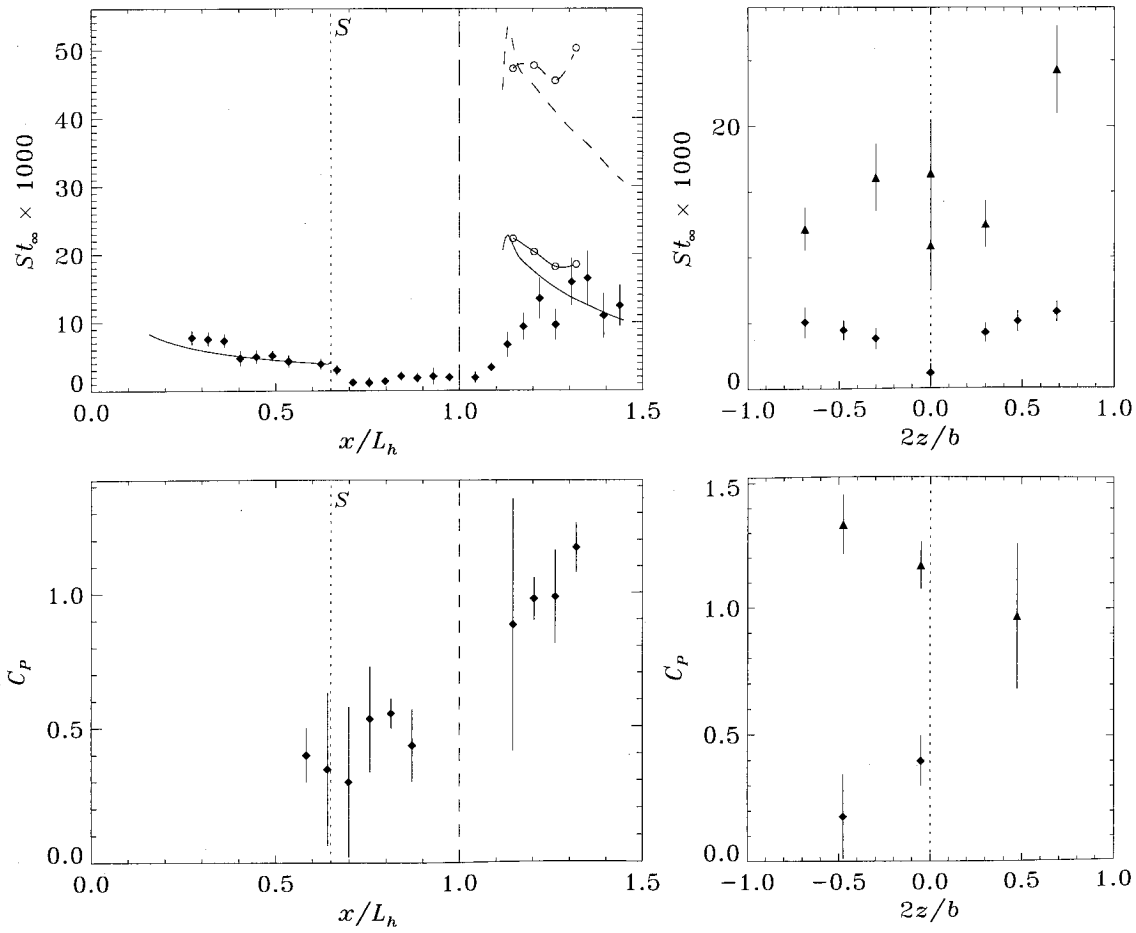

Shot 1782 (condition B1, $A_e/A_* = 400$, $\theta_1 = 15°$, $\theta_w = 20°$)

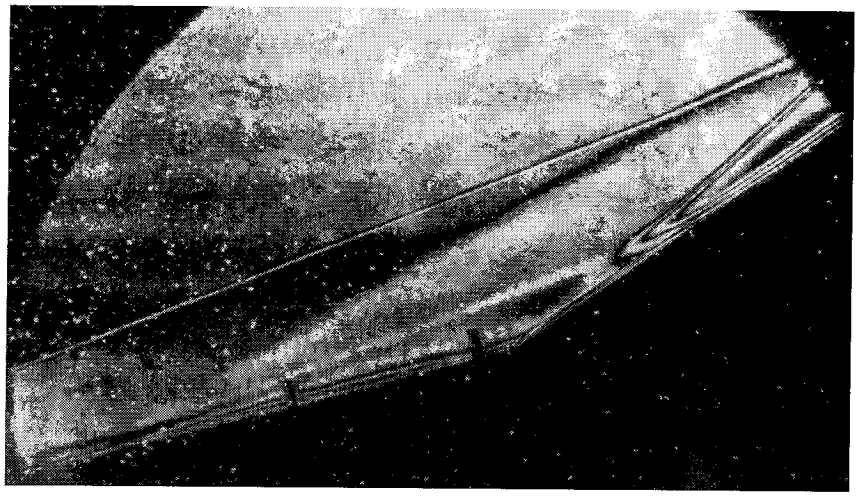

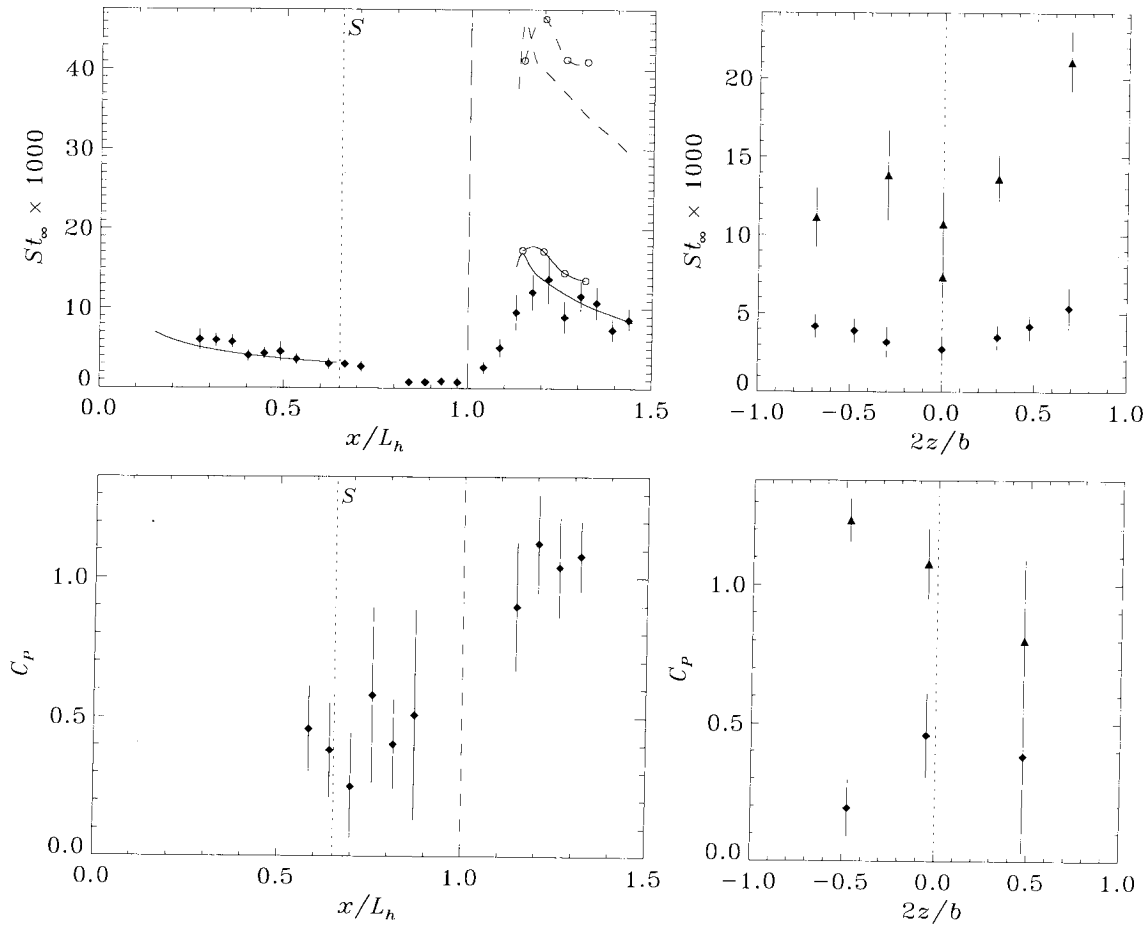

Shot 1783 (condition B1, $A_e/A_* = 225$, $\theta_1 = 15°$, $\theta_w = 20°$)

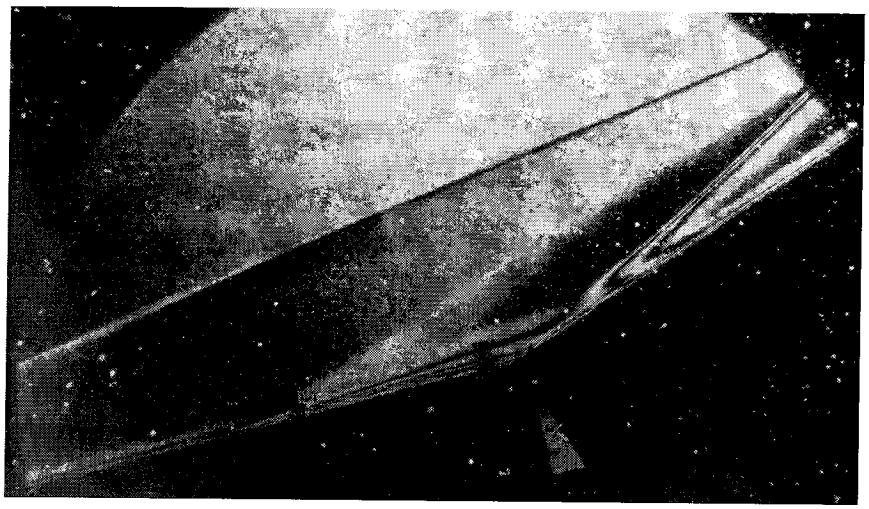

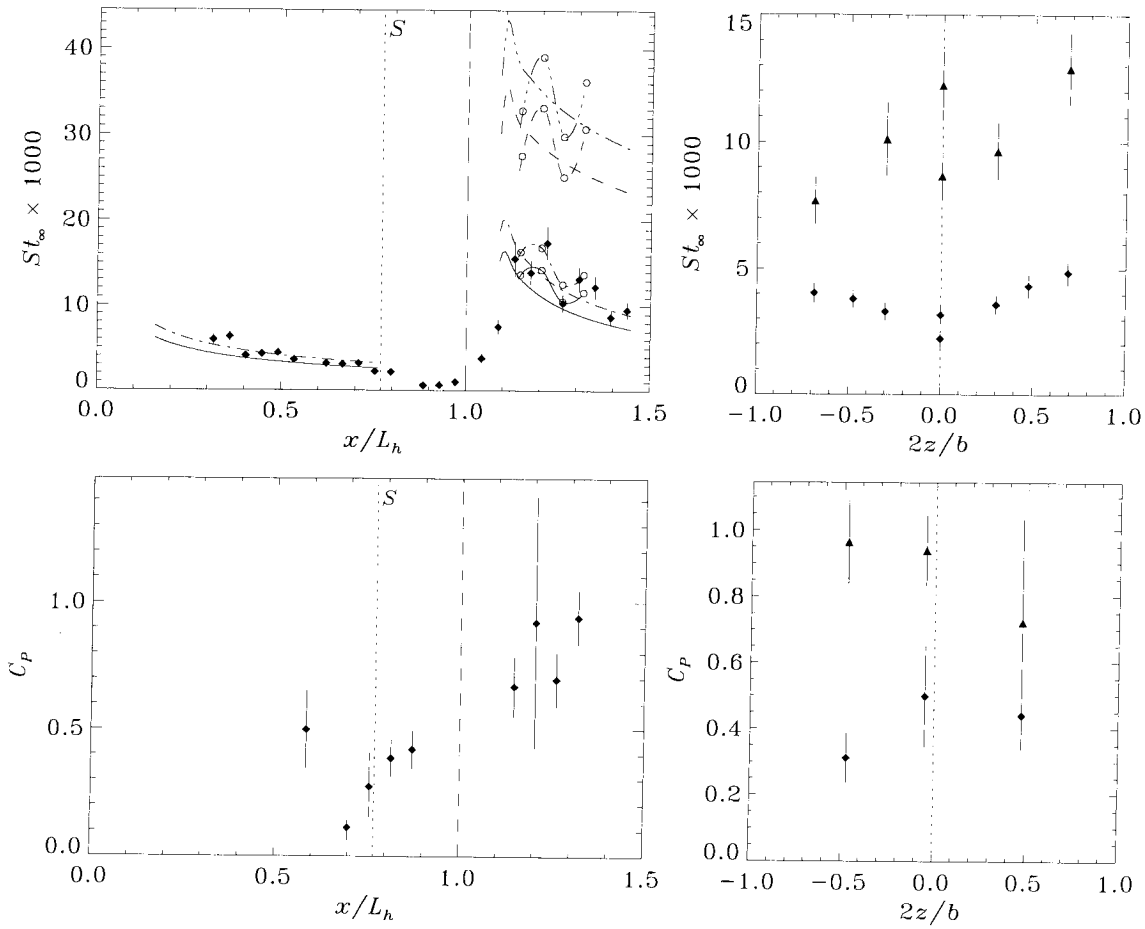

Shot 1784 (condition C2, $A_e/A_* = 225$, $\theta_1 = 15°$, $\theta_w = 20°$)

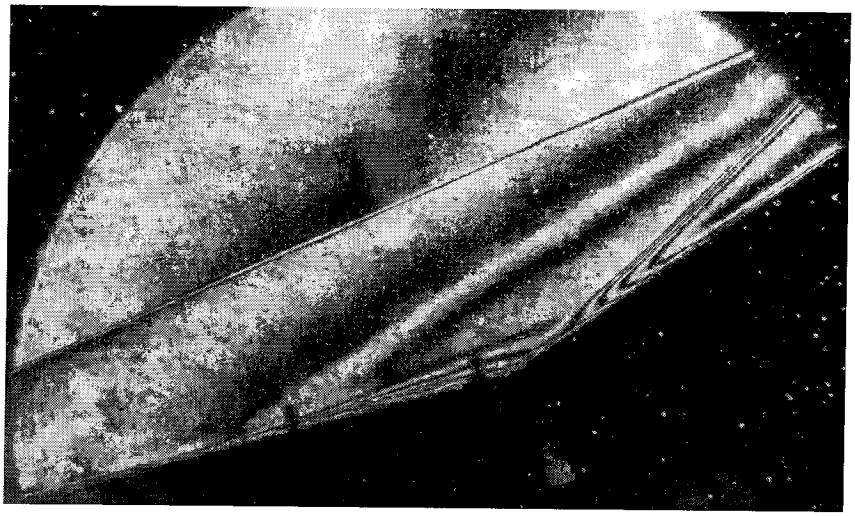

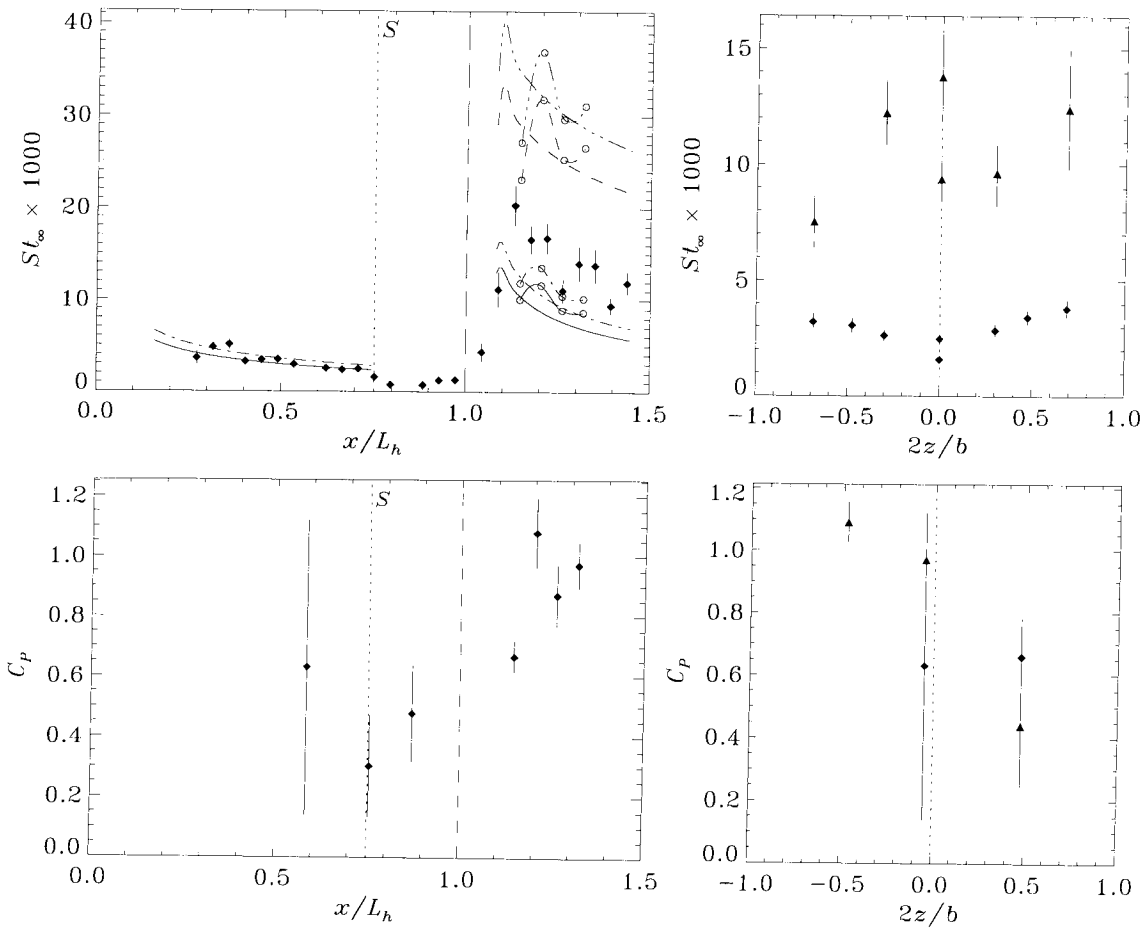

Shot 1785 (condition C2, $A_e/A_* = 100$, $\theta_1 = 15°$, $\theta_w = 20°$)

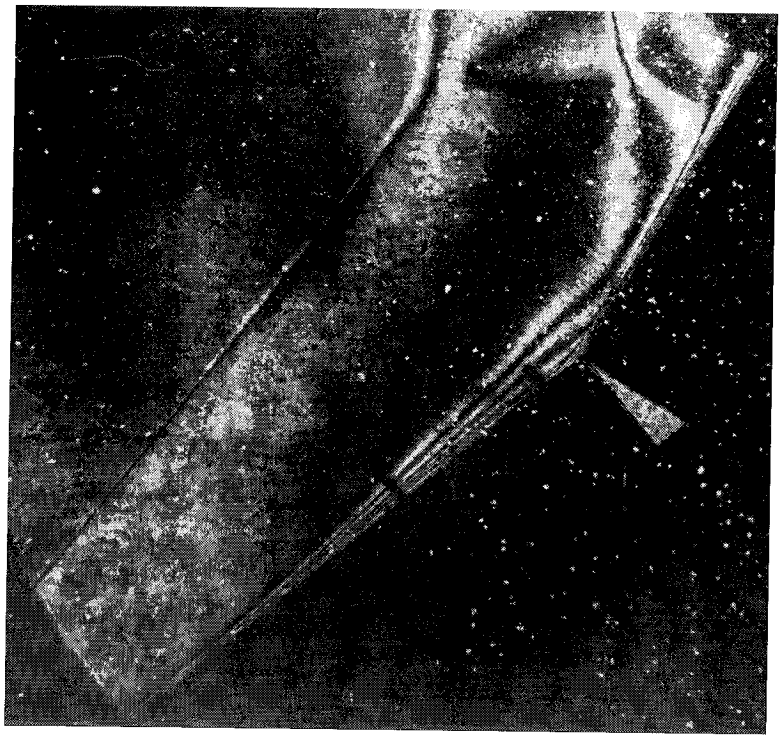

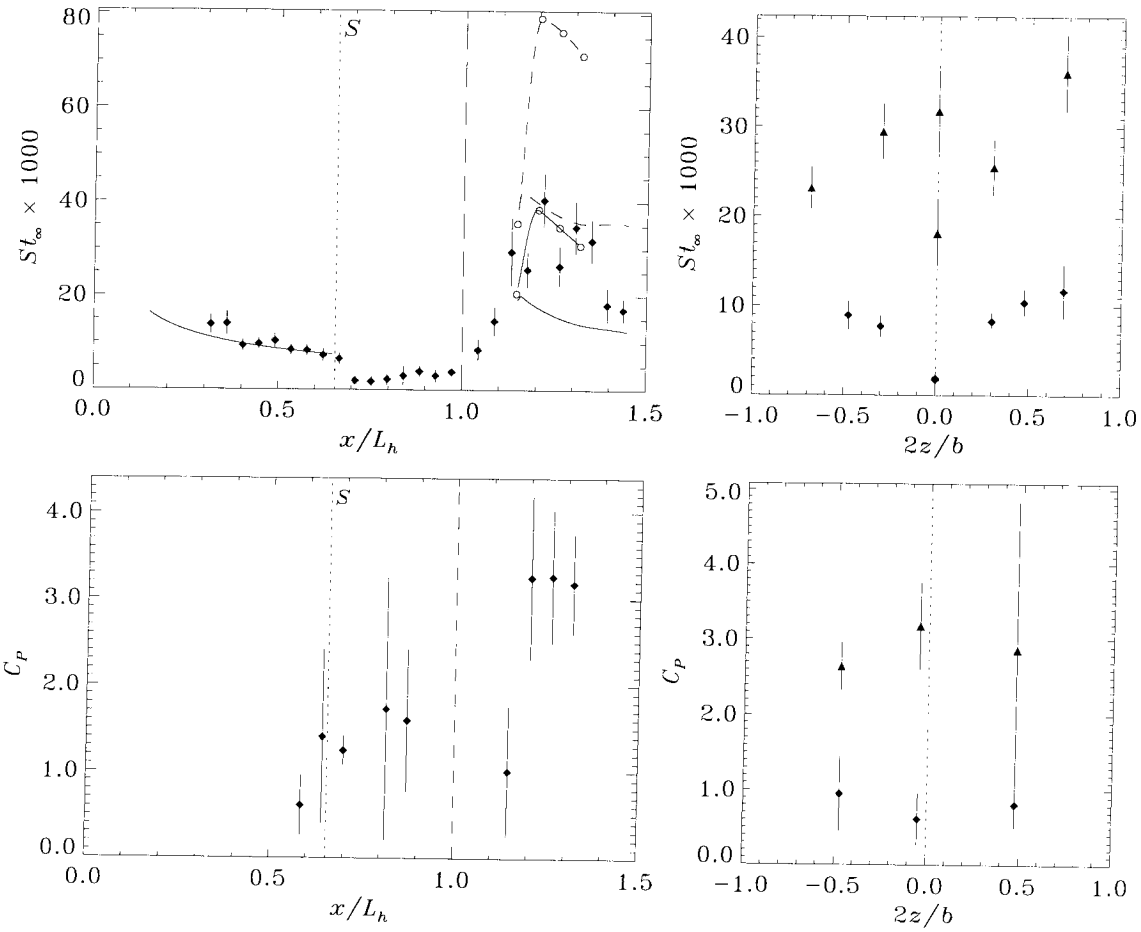

Shot 1786 (condition B1, $A_e/A_* = 400$, $\theta_1 = 40°$, $\theta_w = 20°$)

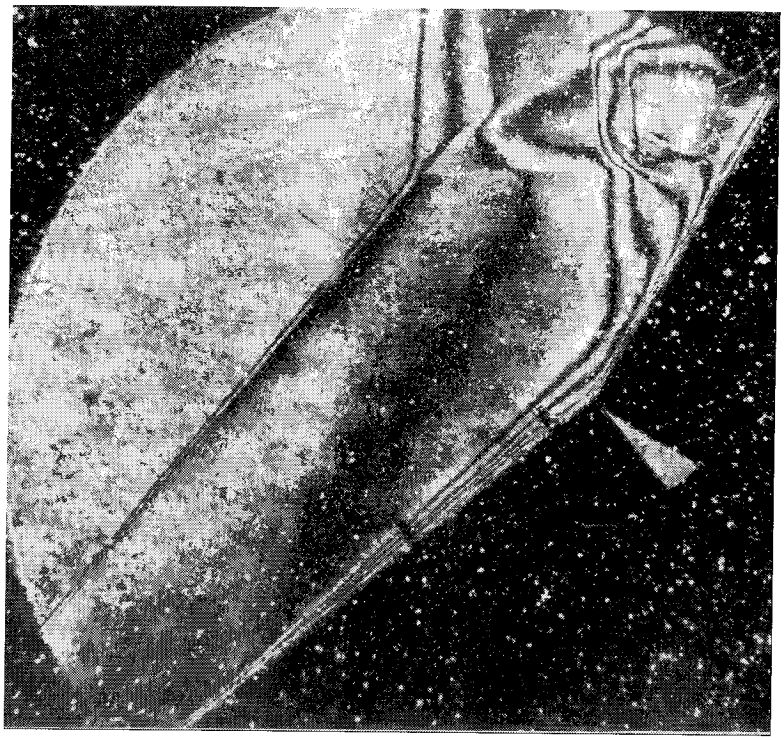

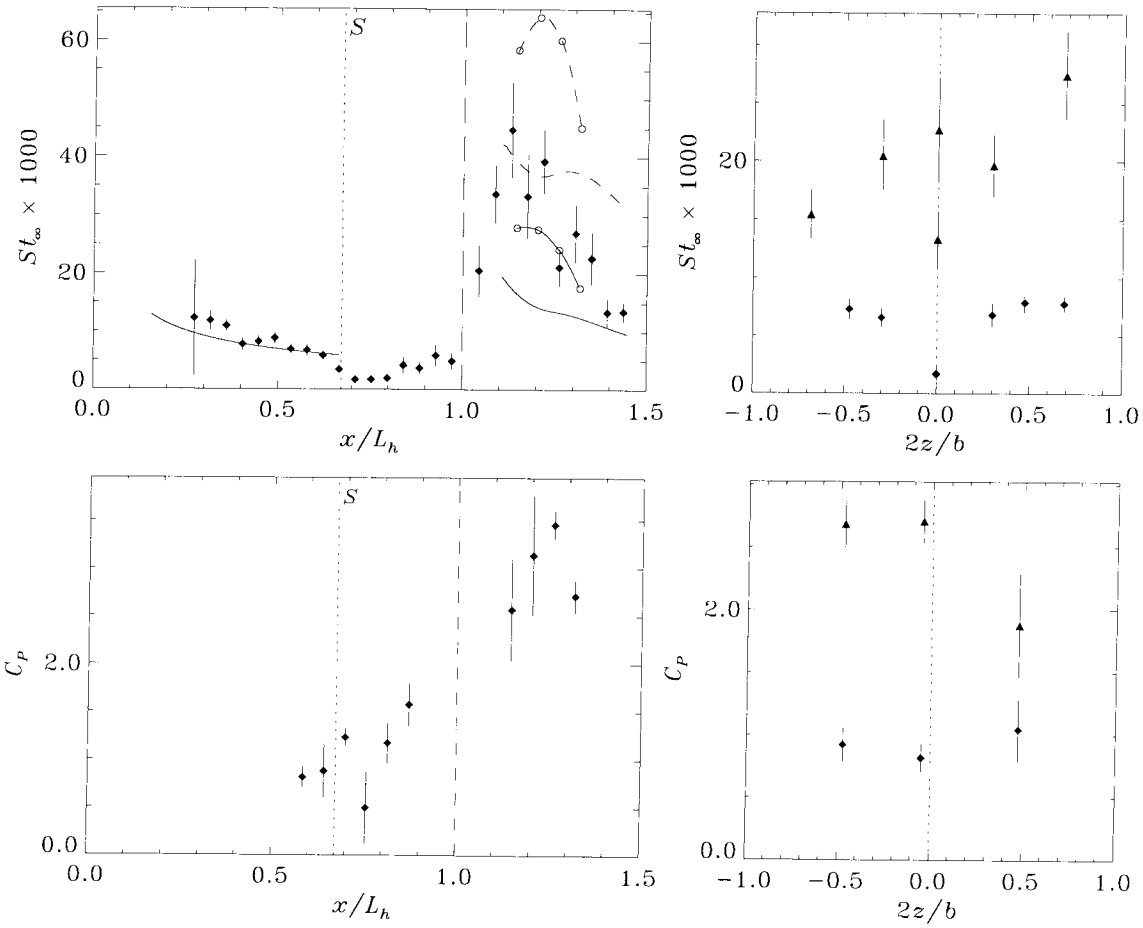

Shot 1787 (condition B1, $A_e/A_* = 225$, $\theta_1 = 40°$, $\theta_w = 20°$)

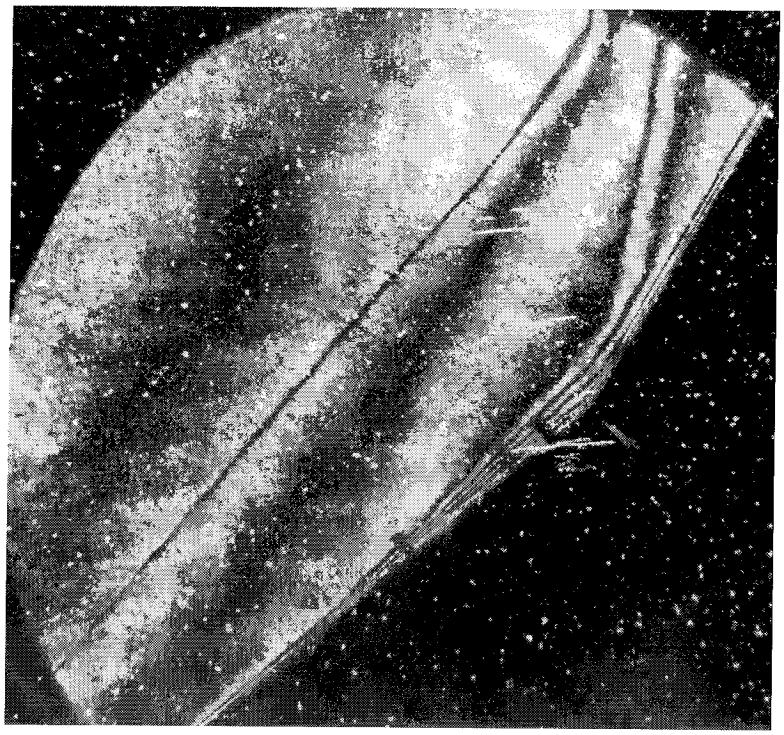

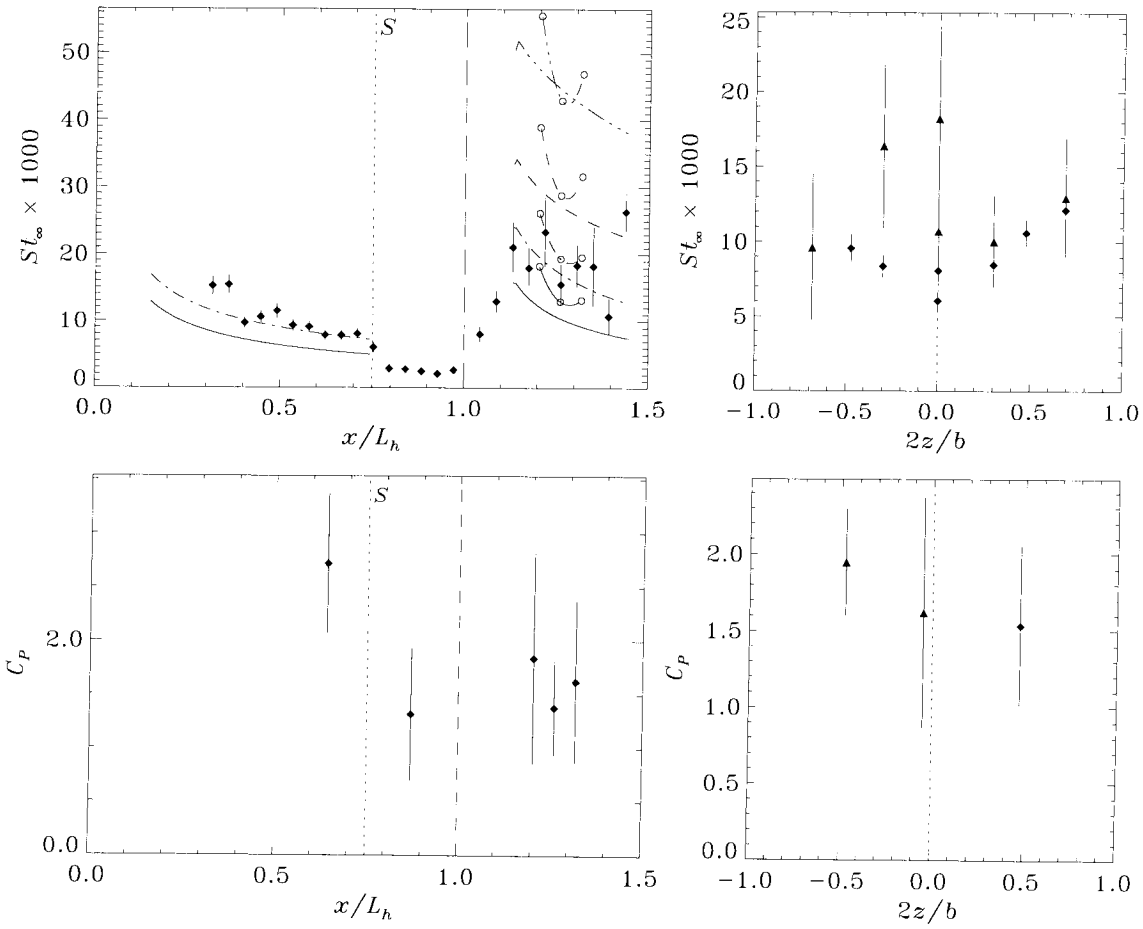

Shot 1788 (condition C2, $A_e/A_* = 400$, $\theta_1 = 40°$, $\theta_w = 20°$)

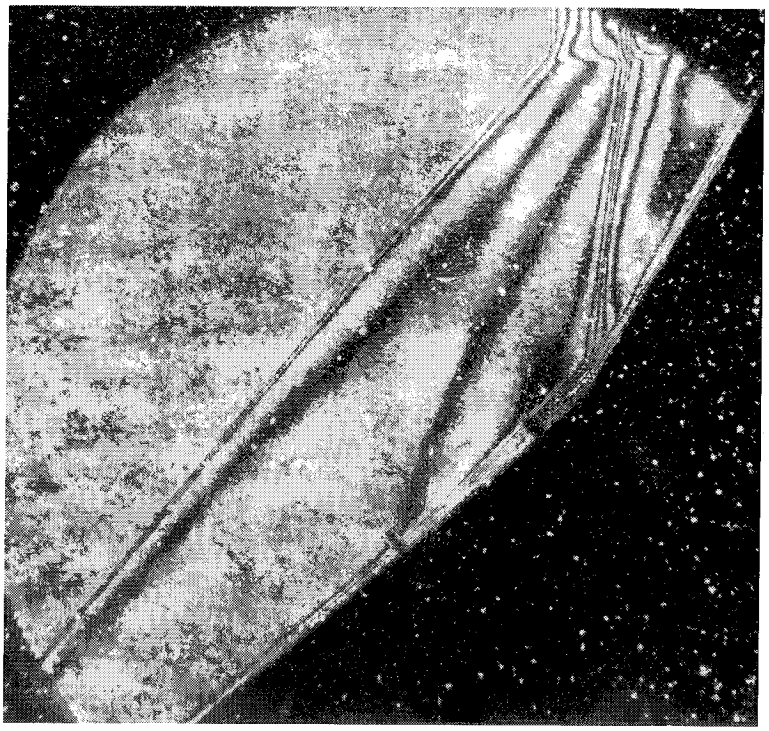

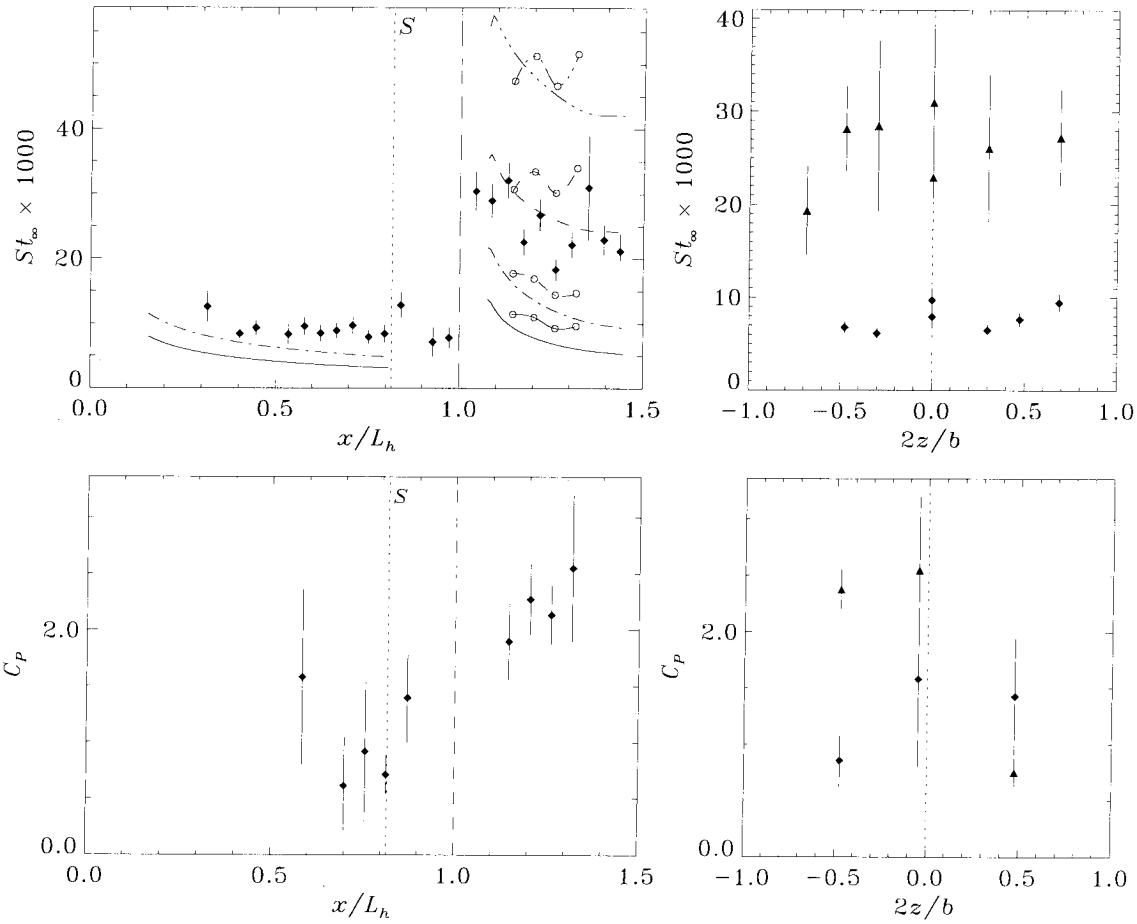

Shot 1790 (condition C2, $A_e/A_* = 100$, $\theta_1 = 40°$, $\theta_w = 20°$)

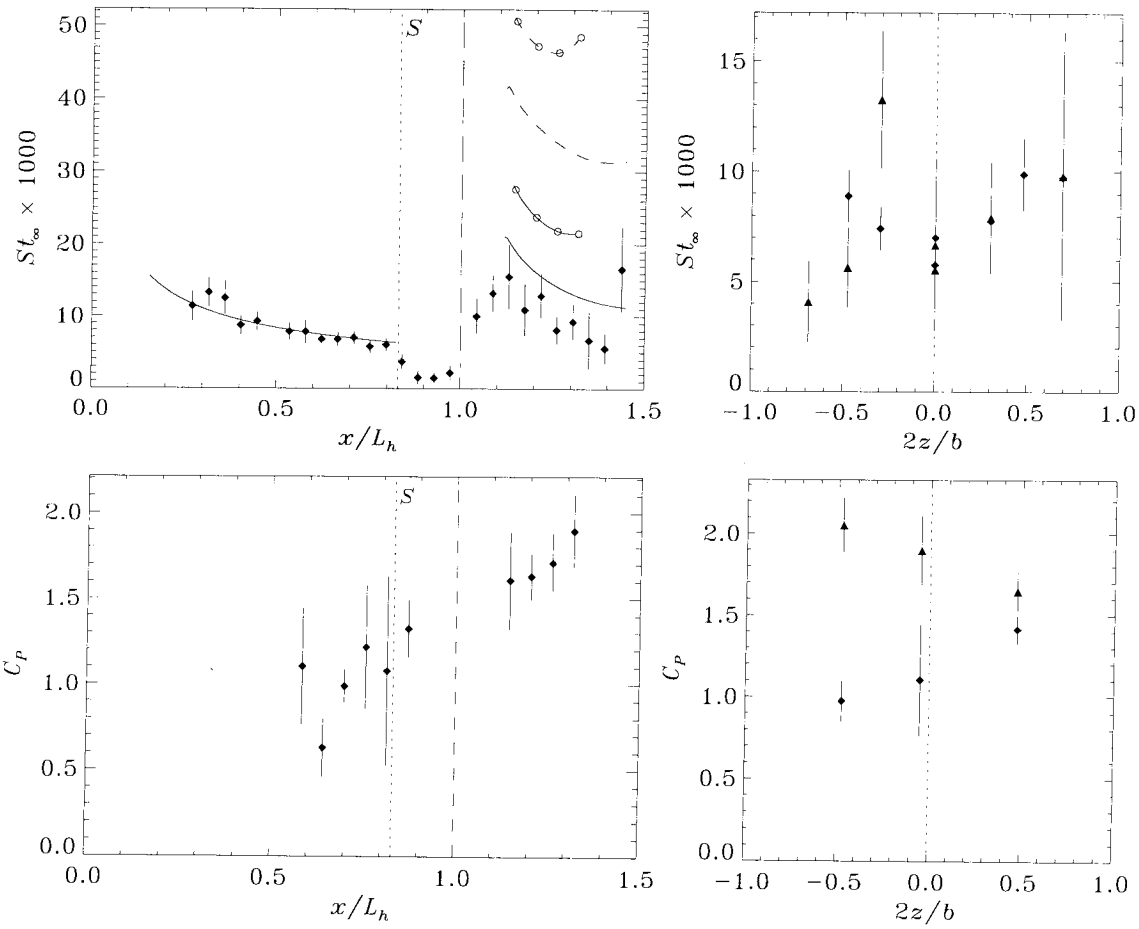

Shot 1792 (condition B1, $A_e/A_* = 400$, $\theta_1 = 40°$, $\theta_w = 15°$)

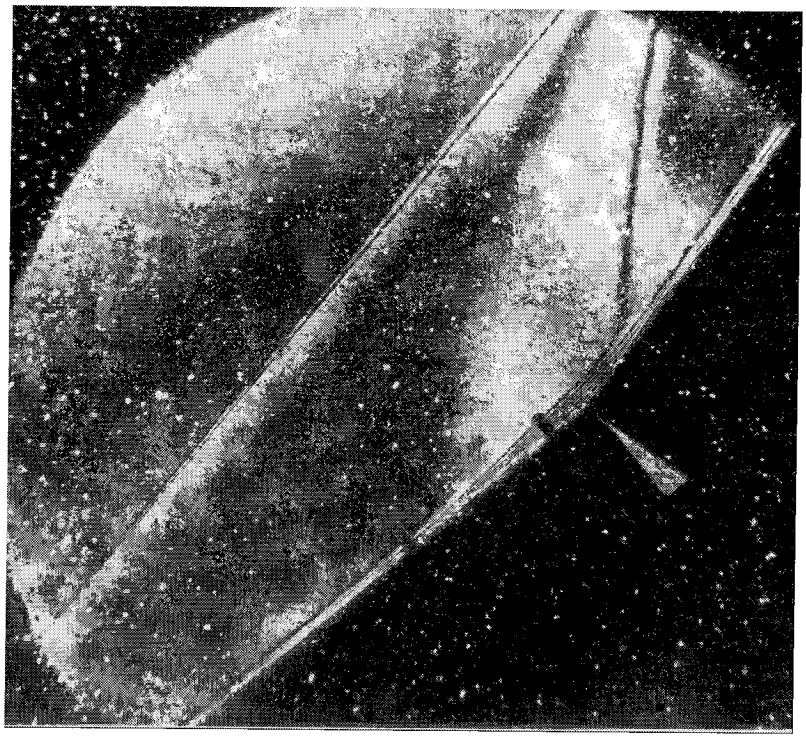

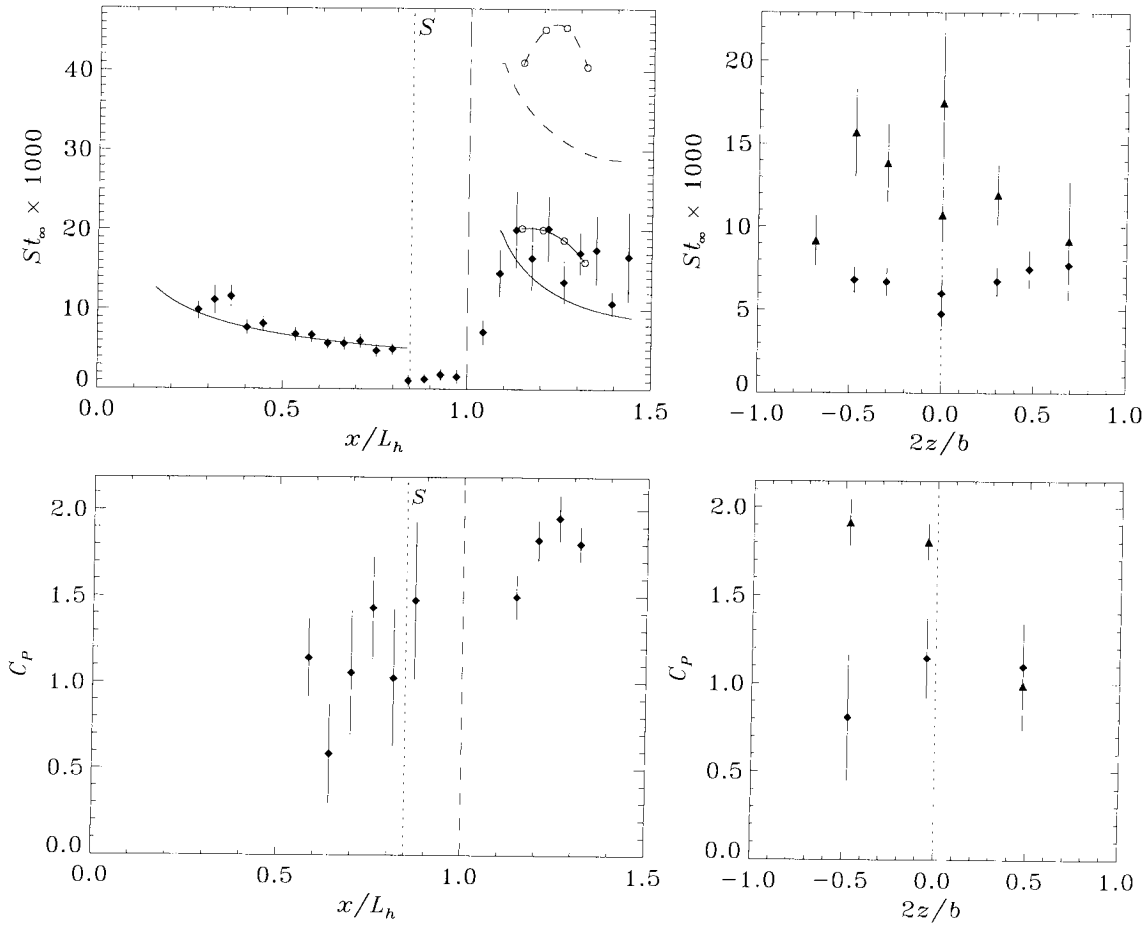

Shot 1793 (condition B1, $A_e/A_* = 225$, $\theta_1 = 40°$, $\theta_w = 15°$)

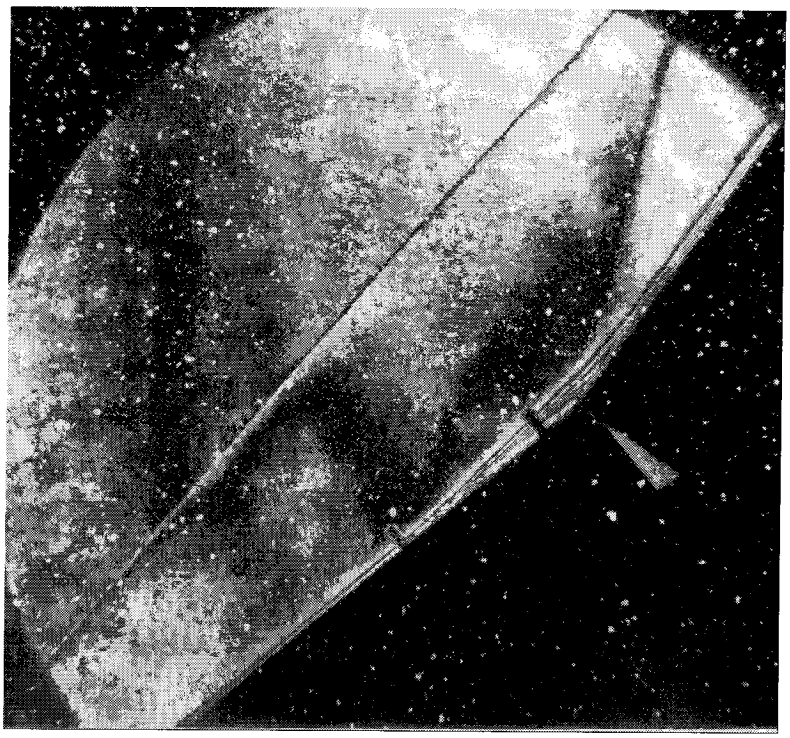

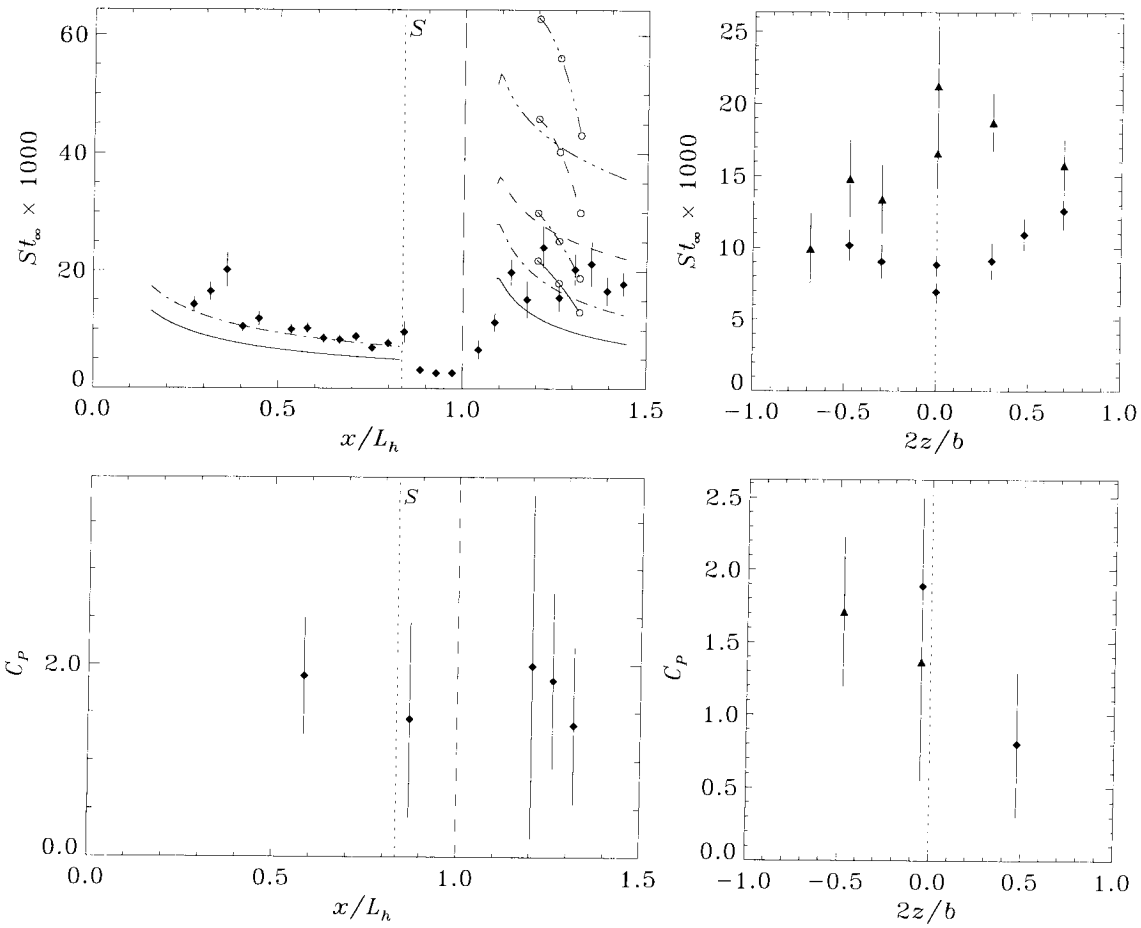

Shot 1795 (condition C2, $A_e/A_* = 400$, $\theta_1 = 40°$, $\theta_w = 15°$)

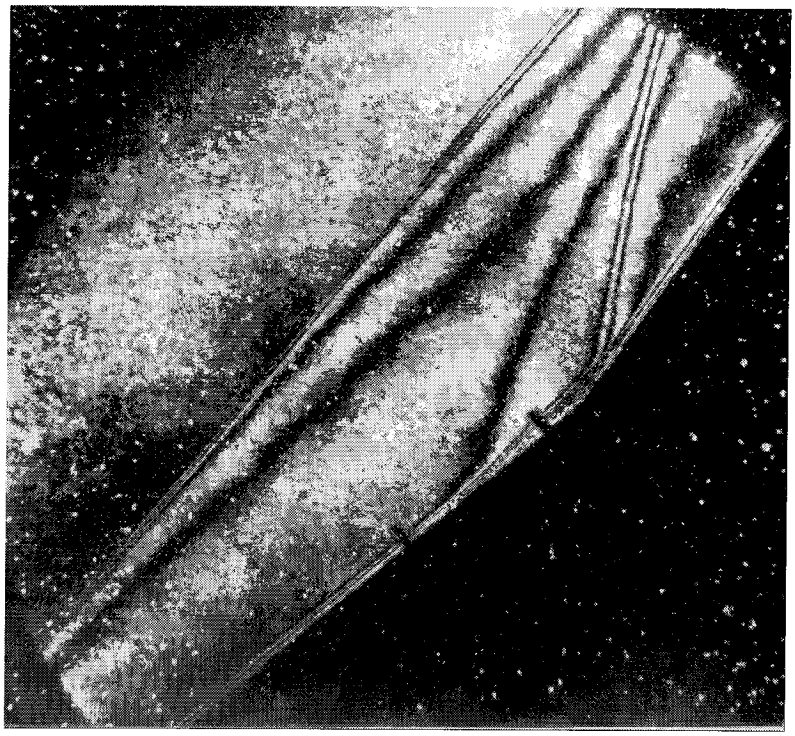

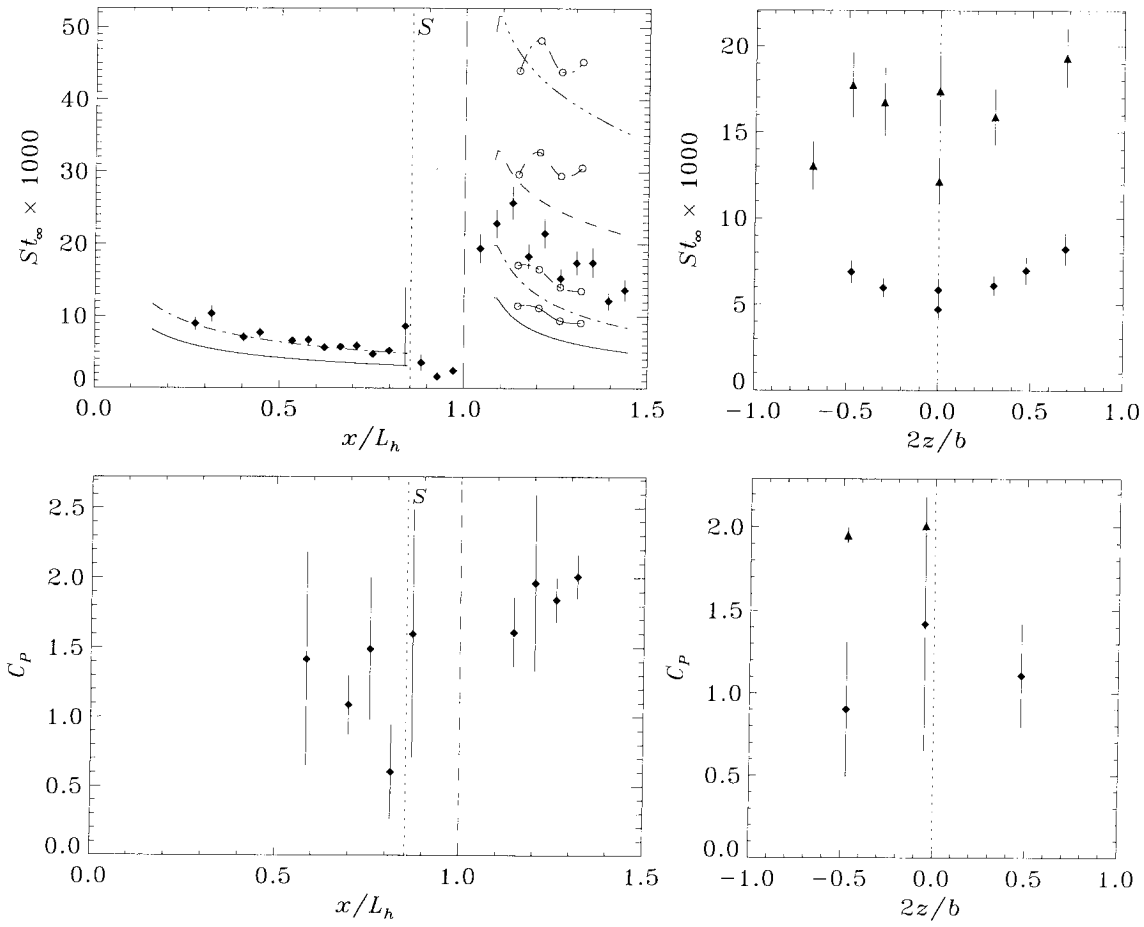

Shot 1796 (condition C2, $A_e/A_* = 100$, $\theta_1 = 40°$, $\theta_w = 15°$)

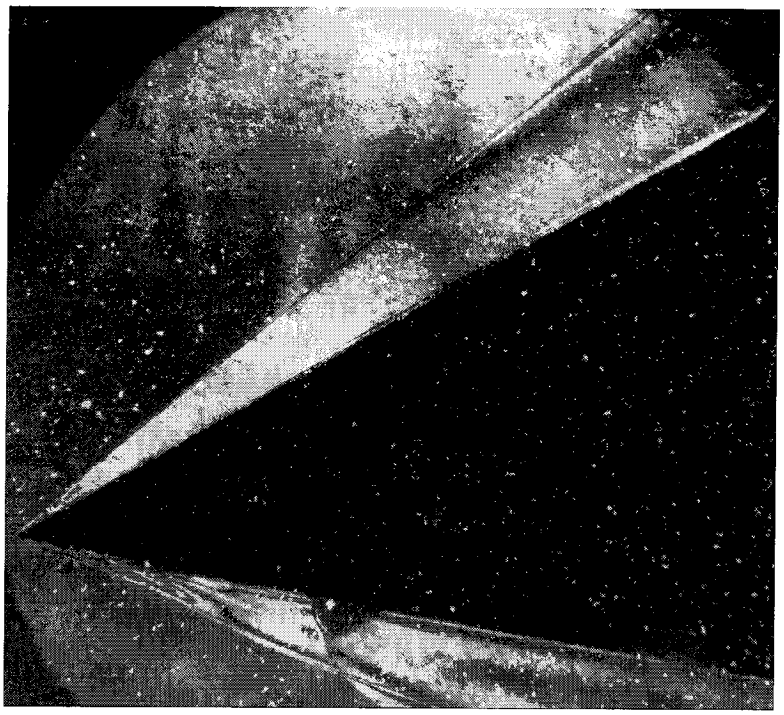

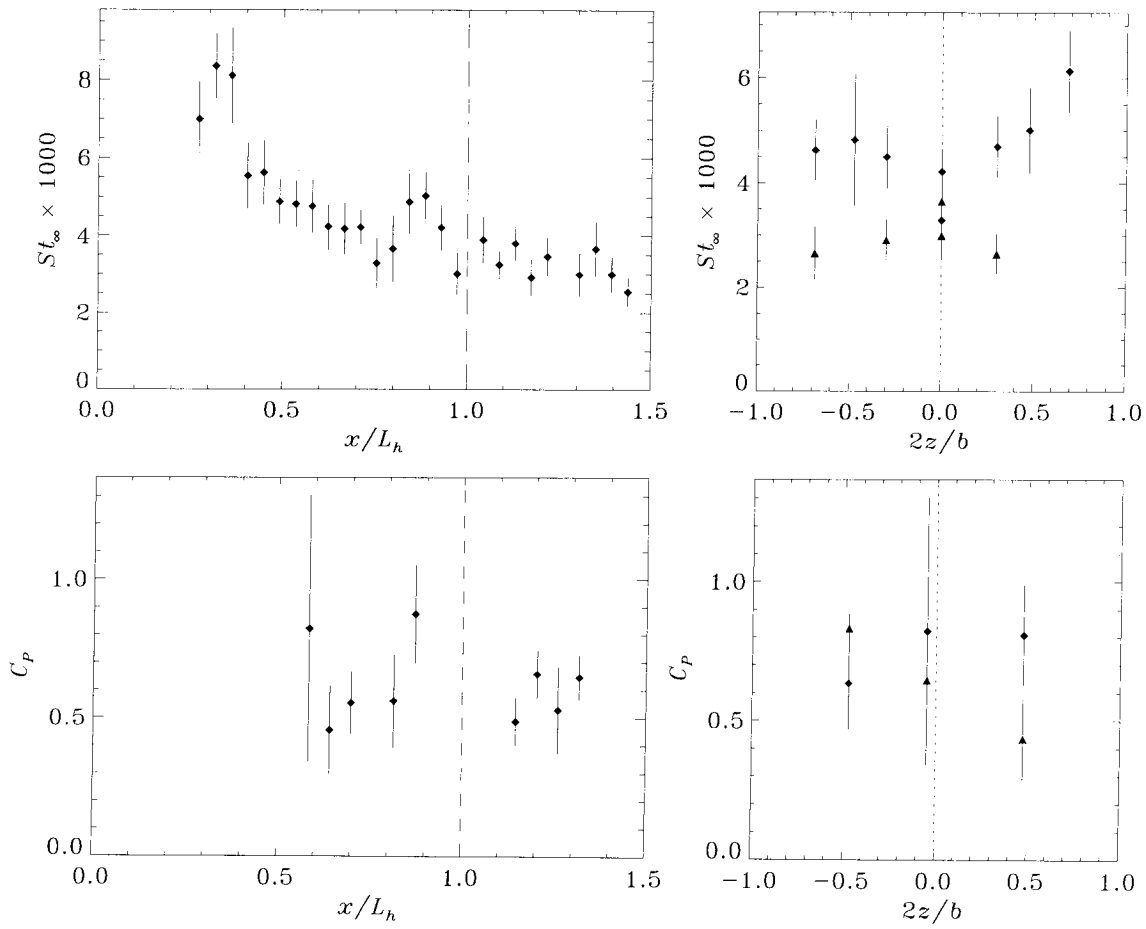

Shot 1798 (condition B1, $A_e/A_* = 100$, $\theta_1 = 30°$, $\theta_w = 0°$)

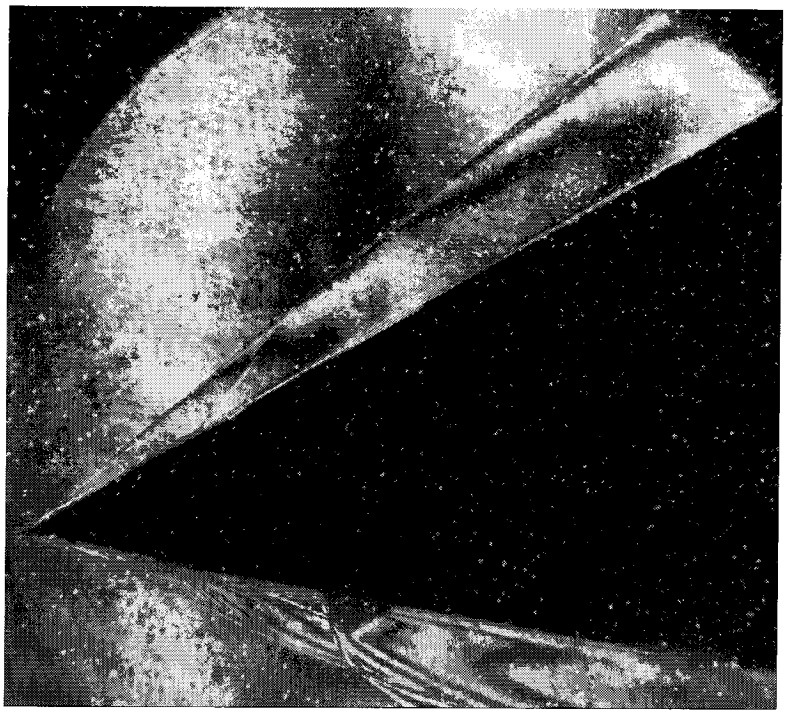

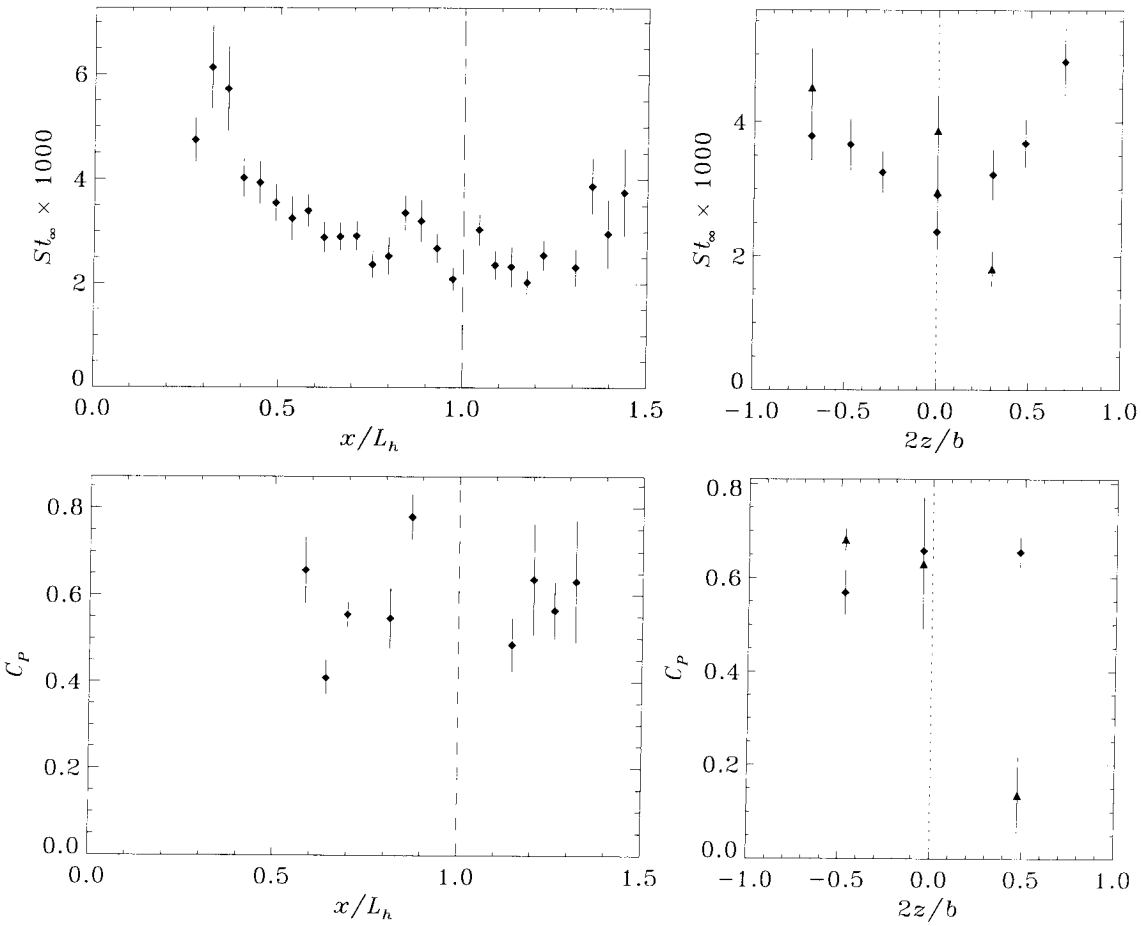

Shot 1799 (condition B2, $A_e/A_* = 100$, $\theta_1 = 30°$, $\theta_w = 0°$)

Appendix G Carbon Dioxide Shots

This appendix documents the eight experiments which were performed using CO_2 test gas, but were not analyzed during the present study due to time constraints. In particular, computations of the nozzle flow and inviscid triple-wedge flow were not undertaken for CO_2 shots. Shock tunnel operating conditions B1 and C2 were modified slightly for use with CO_2 test gas, as shown in Table G.1 which has a format identical to Table 2.1. Table G.2 presents general information regarding each shot, sorted by condition and geometry as in Table D.1. Table G.3 gives flow visualization measurements for the CO_2 shots, sorted by shot number. This is followed by interferograms, measured heat flux distributions, and measured pressure distributions, presented in shot order with one shot per page as was done for the N_2 shots in Appendix F.

	h_0 MJ/kg	p_0 MPa	u_s km/s	p_{ST} kPa	p_4 MPa	p_{CT} kPa	He %	p_{2R} (psig)	m_p (kg)
B1-CO_2	4.89 ±0.24	6.81 ±0.45	2.31 ±0.07	16	18.3 ±2.5	24	78	140	90
C2-CO_2	18.7 ±0.74	15.7 ±0.87	4.58 ±0.11	10	46.1 ±6.7	43	100	325	90

Table G.1: Shock tunnel operating conditions for CO_2 shots. Uncertainties describe only the 2σ variation over each set of shots. m_p is the piston mass.

cond.	A_e/A_*	θ_1	θ_w	h_0 MJ/kg	p_0 MPa	TLR	x_{le} cm	y_{le} cm	t_{las} ms	shot no.
B1-CO_2	225	0°	15°	5.04	6.57	SU	3.2	0.6	1.50	1767
			10°	4.95	6.82	SU	3.2	0.6	1.60	1769
B1-CO_2	400	40°	20°	4.72	6.68	T	3.3	0.5	1.60	1789
			15°	4.84	7.17	T	3.3	0.5	1.60	1794
C2-CO_2	100	40°	20°	19.2	15.8	SU	4.3	0.5	0.89	1791
			15°	18.2	15.4	SU	4.3	0.5	0.89	1797
		0°	15°	18.9	15.3	SU	4.0	0.6	0.94	1773
			10°	18.6	16.4	SU	4.0	0.6	0.94	1771

Table G.2: Reservoir conditions, geometry, *etc.* for CO_2 shots, sorted by condition.

shot no.	θ_{sep}	L_u cm	L_{sep} cm	β_1	cond.	A_e/A_*	θ_1	θ_w
1789	4.92° ± 0.65°	2.22 ± 0.14	2.91 ± 0.22	48.8°	B1-CO_2	400	40°	20°
1791	3.68° ± 0.07°	1.90 ± 0.18	2.31 ± 0.22	48.6°	C2-CO_2	100	40°	20°
1794	5.70° ± 0.45°	1.45 ± 0.13	2.33 ± 0.23	48.8°	B1-CO_2	400	40°	15°
1797	5.60° ± 2.31°	0.71 ± 0.14	1.12 ± 0.36	49.6°	C2-CO_2	100	40°	15°

Table G.3: Flow visualization measurements for CO_2 shots, sorted by shot number.

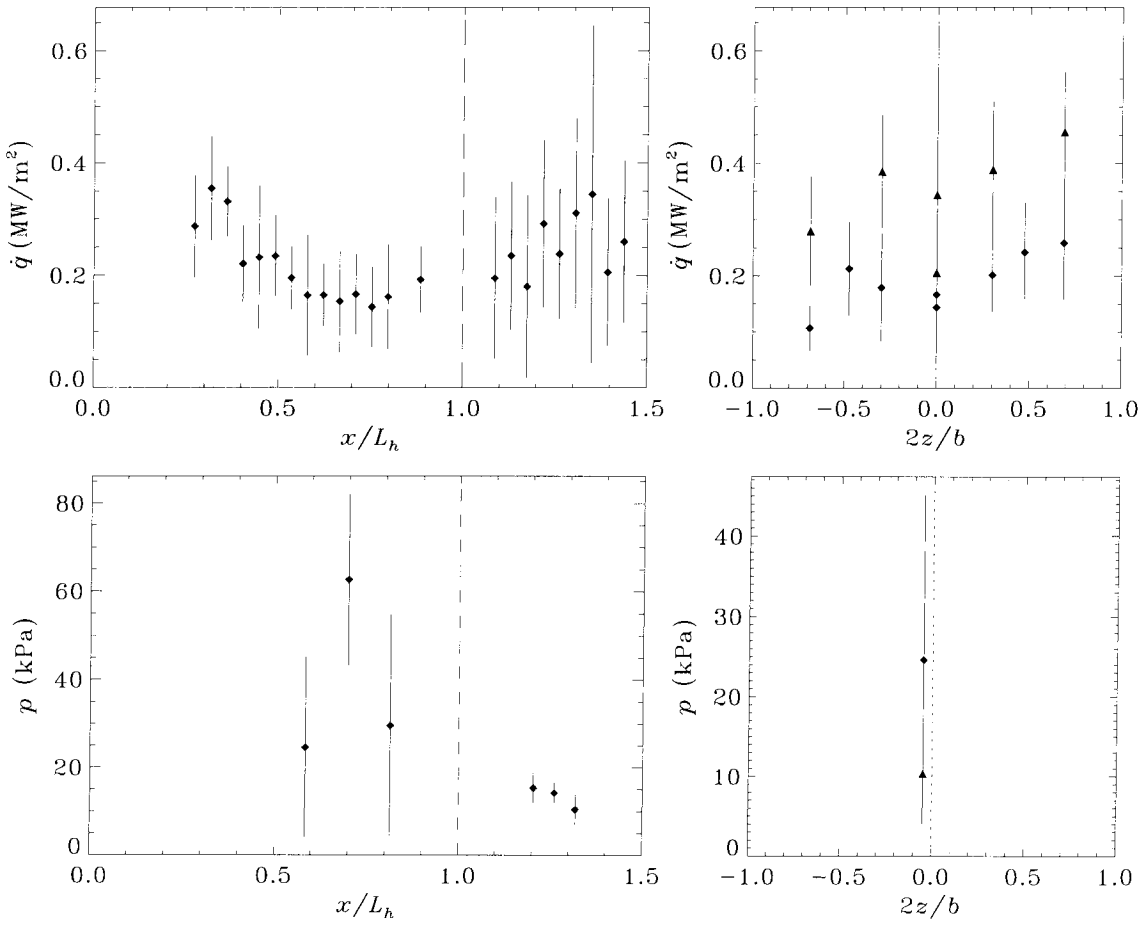

Shot 1767 (condition B1-CO_2, $A_e/A_* = 225$, $\theta_1 = 0°$, $\theta_w = 15°$)

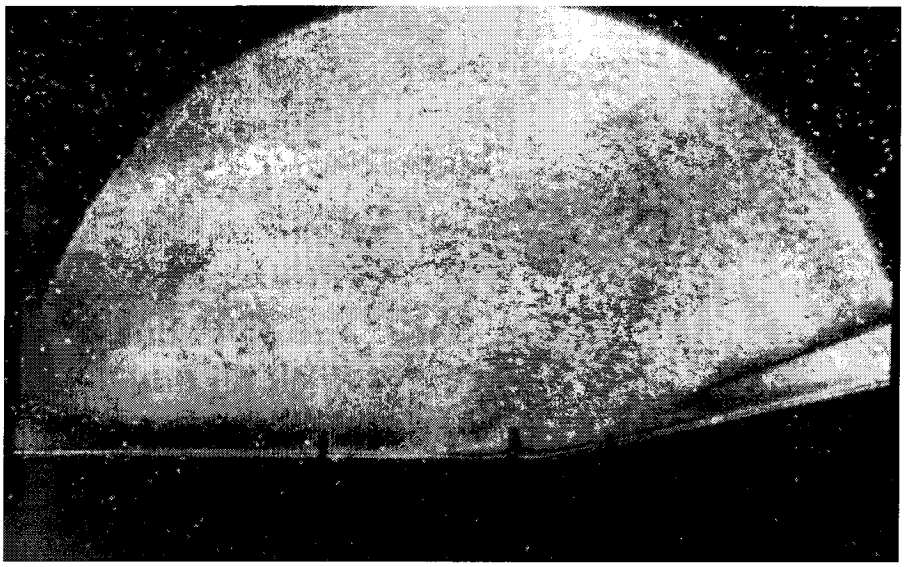

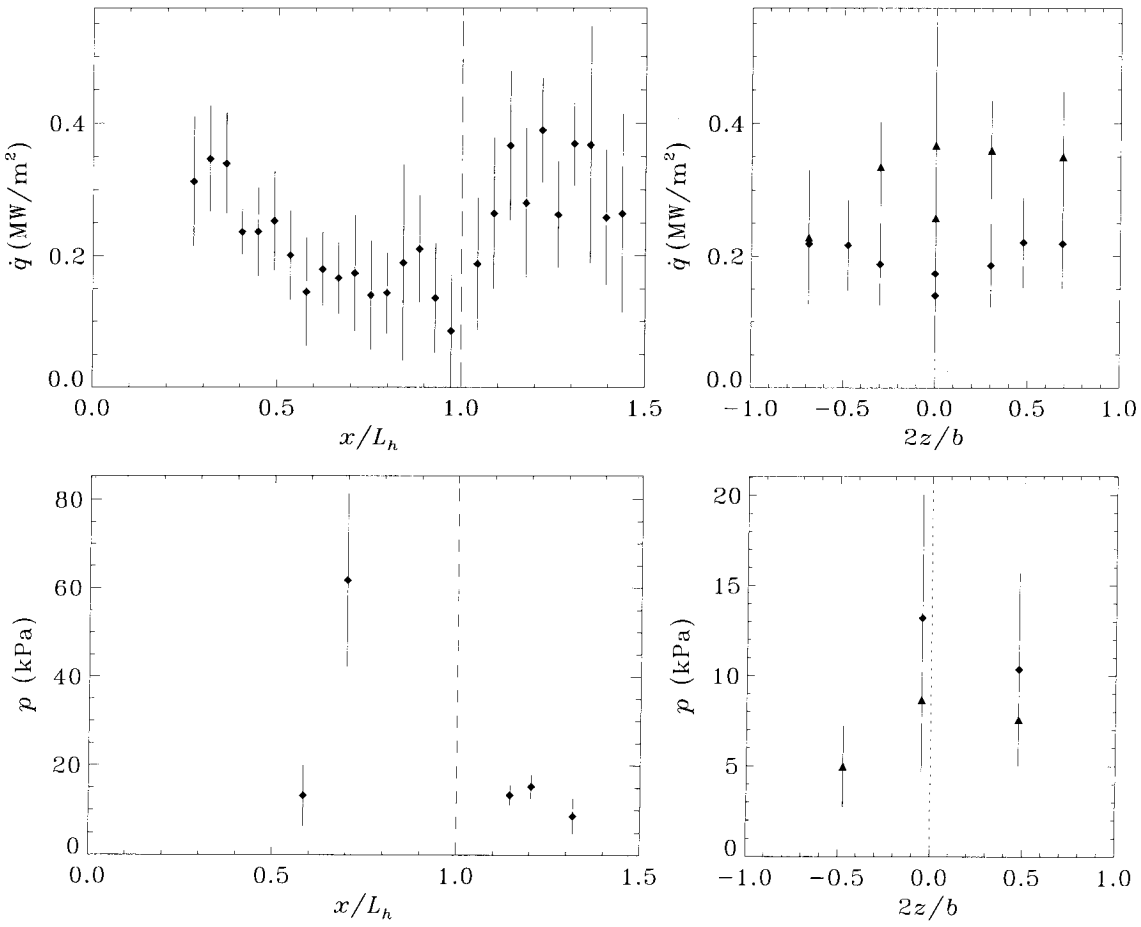

Shot 1769 (condition B1-CO_2, $A_e/A_* = 225$, $\theta_1 = 0°$, $\theta_w = 10°$)

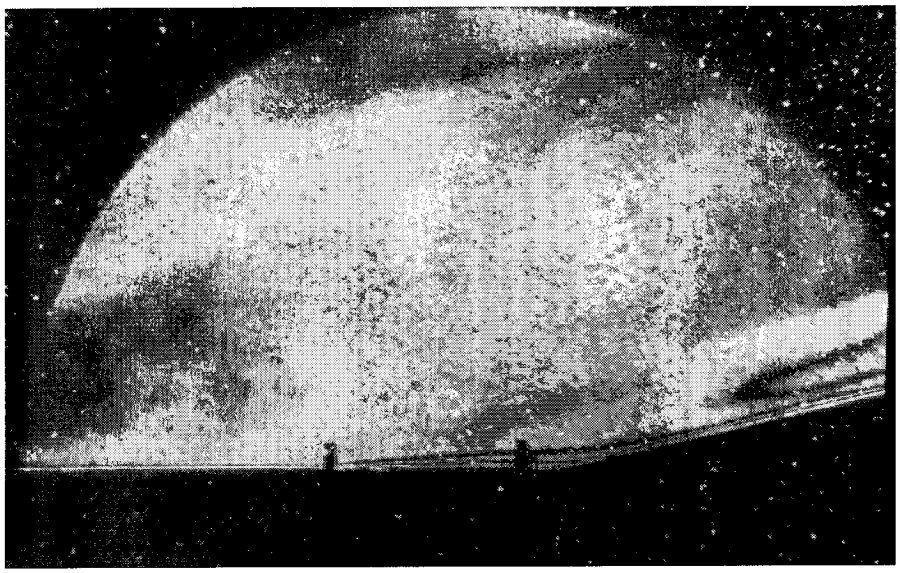

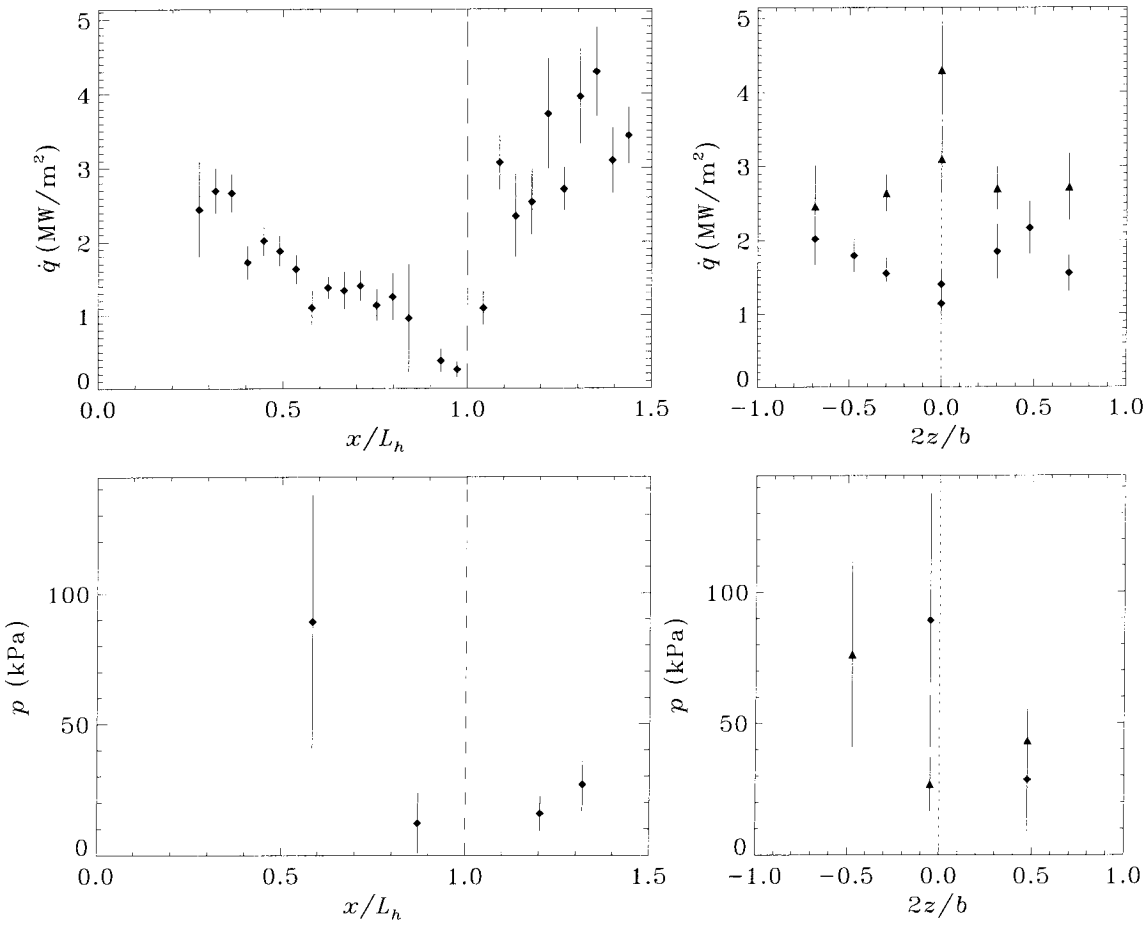

Shot 1771 (condition C2-CO_2, $A_e/A_* = 100$, $\theta_1 = 0°$, $\theta_w = 10°$)

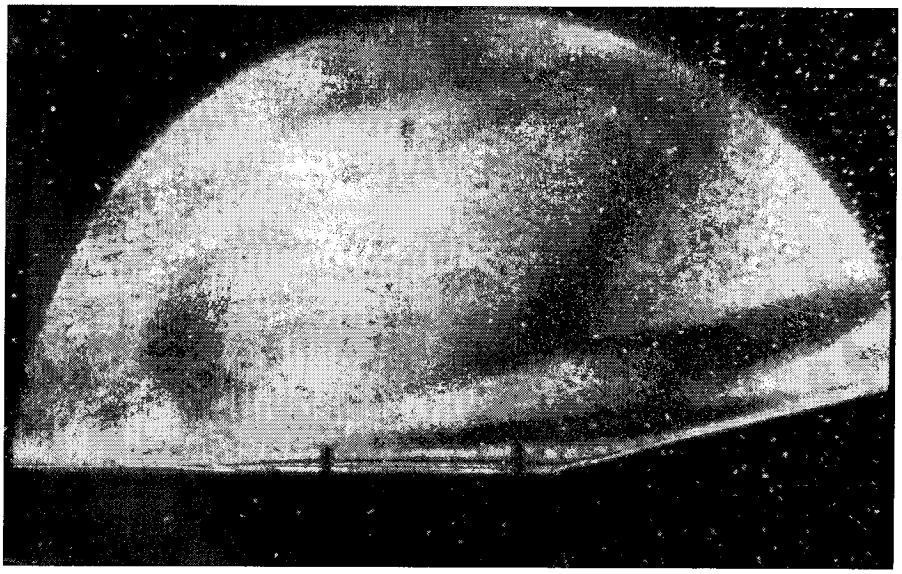

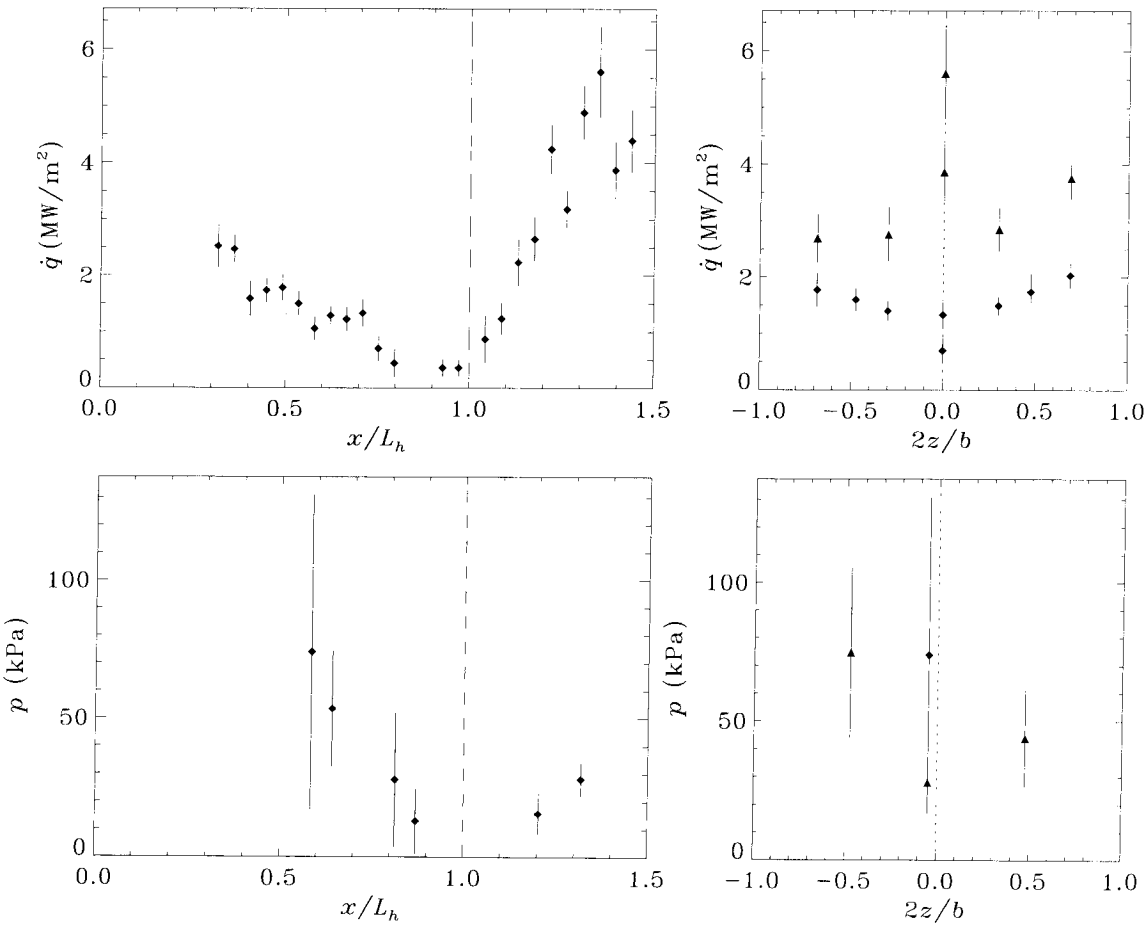

Shot 1773 (condition C2-CO_2, $A_e/A_* = 100$, $\theta_1 = 0°$, $\theta_w = 15°$)

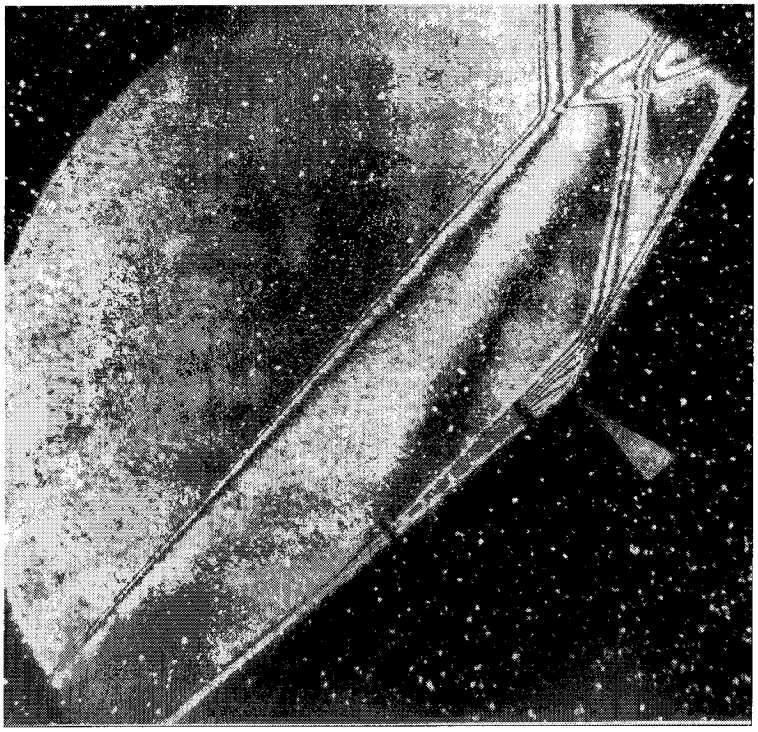

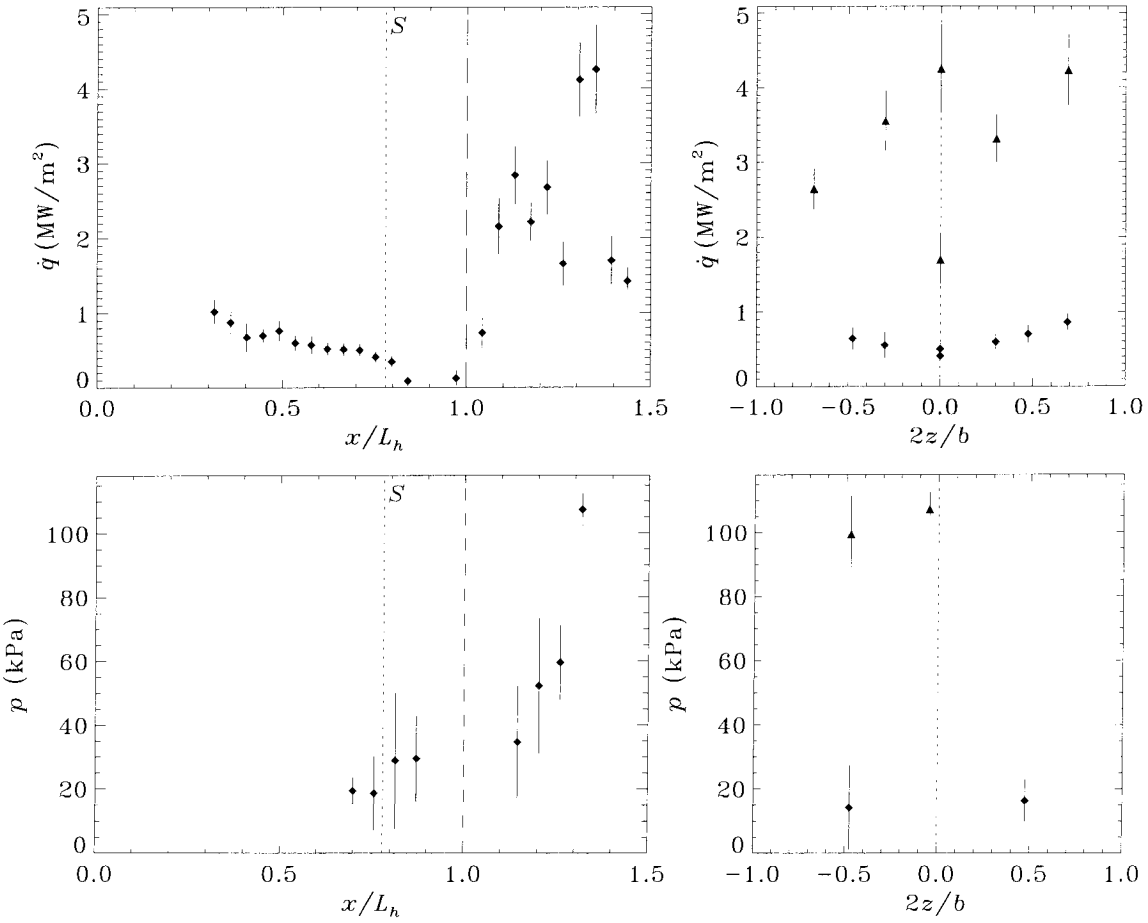

Shot 1789 (condition B1-CO_2, $A_e/A_* = 400$, $\theta_1 = 40°$, $\theta_w = 20°$)

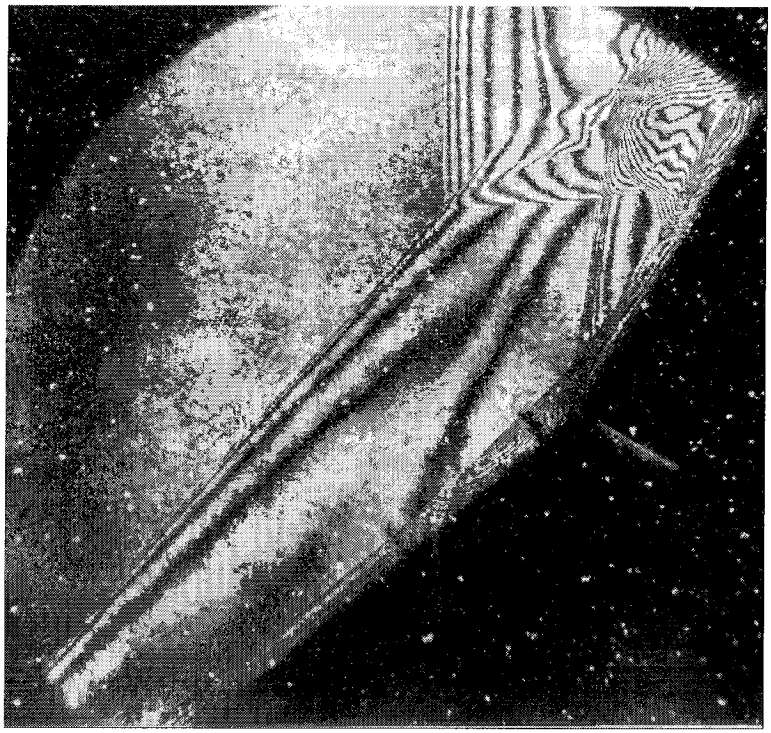

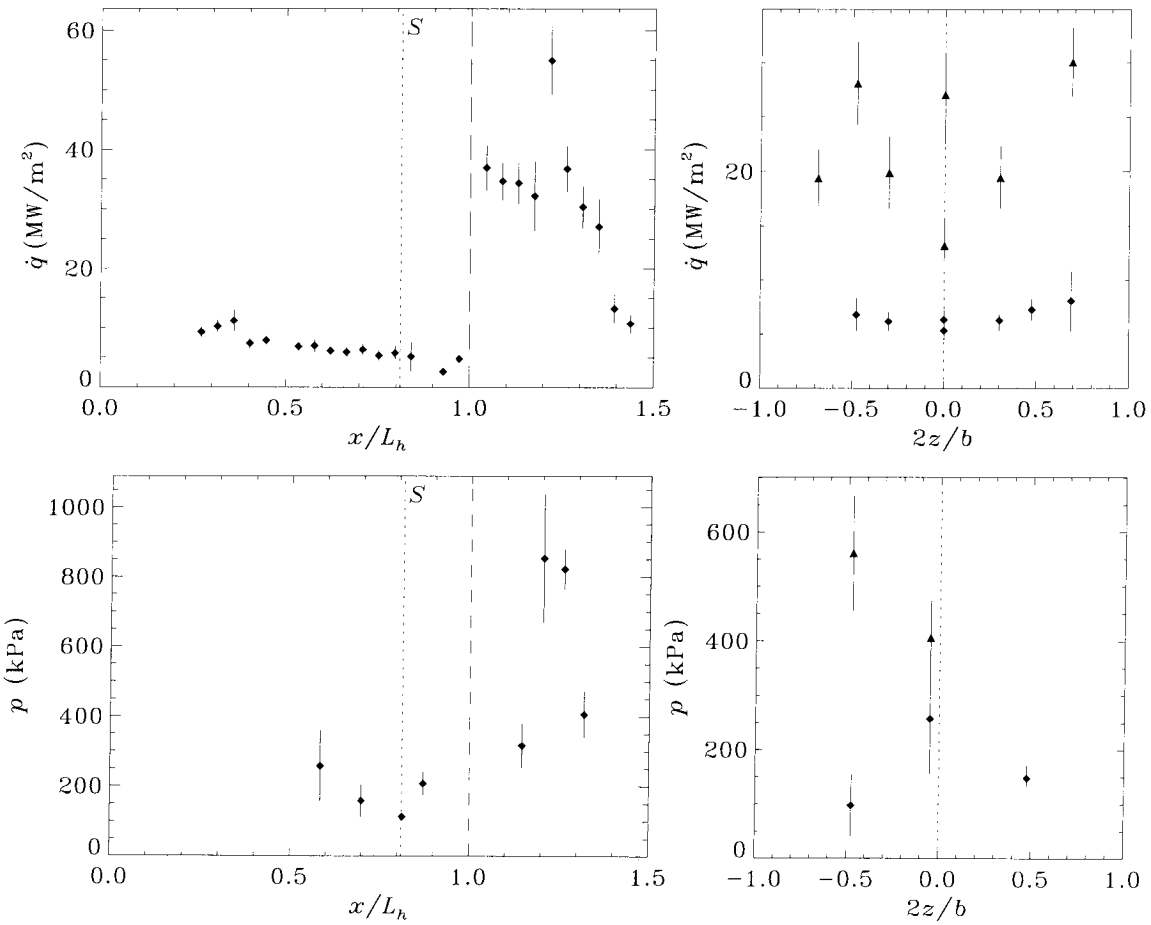

Shot 1791 (condition C2-CO_2, $A_e/A_* = 100$, $\theta_1 = 40°$, $\theta_w = 20°$)

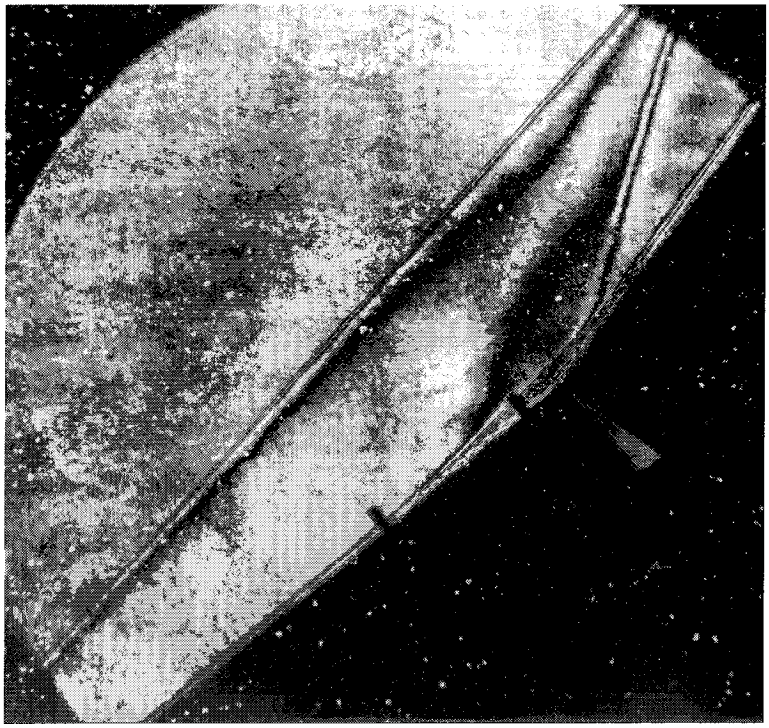

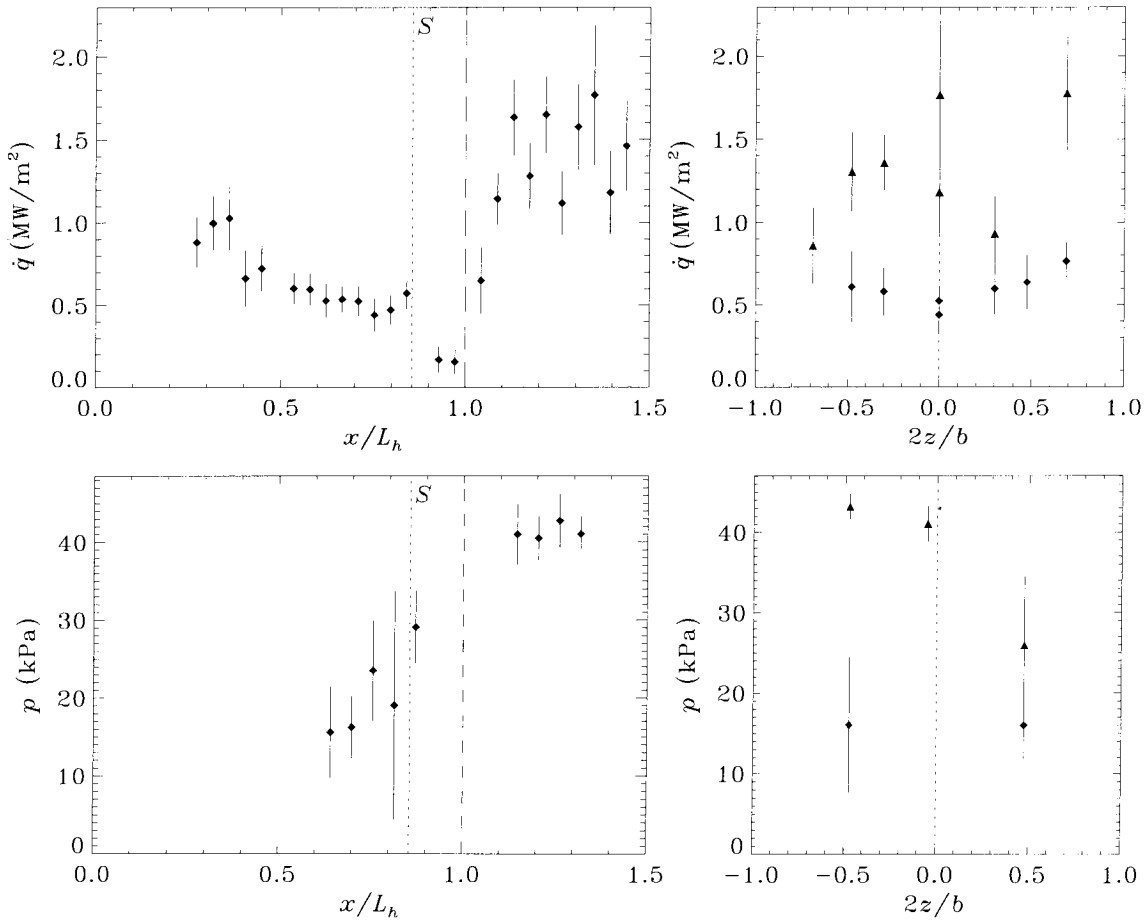

Shot 1794 (condition B1-CO_2, $A_e/A_* = 400$, $\theta_1 = 40°$, $\theta_w = 15°$)

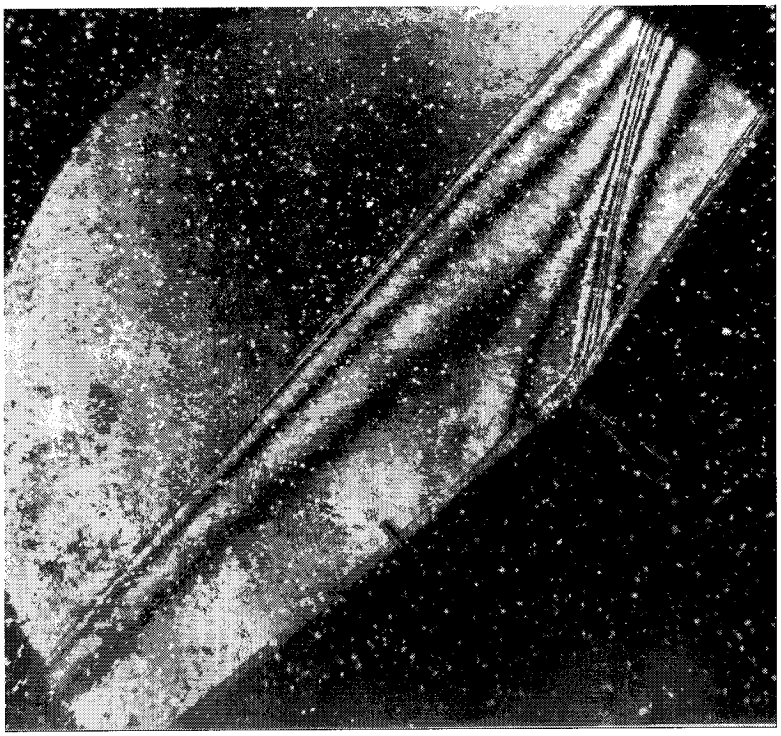

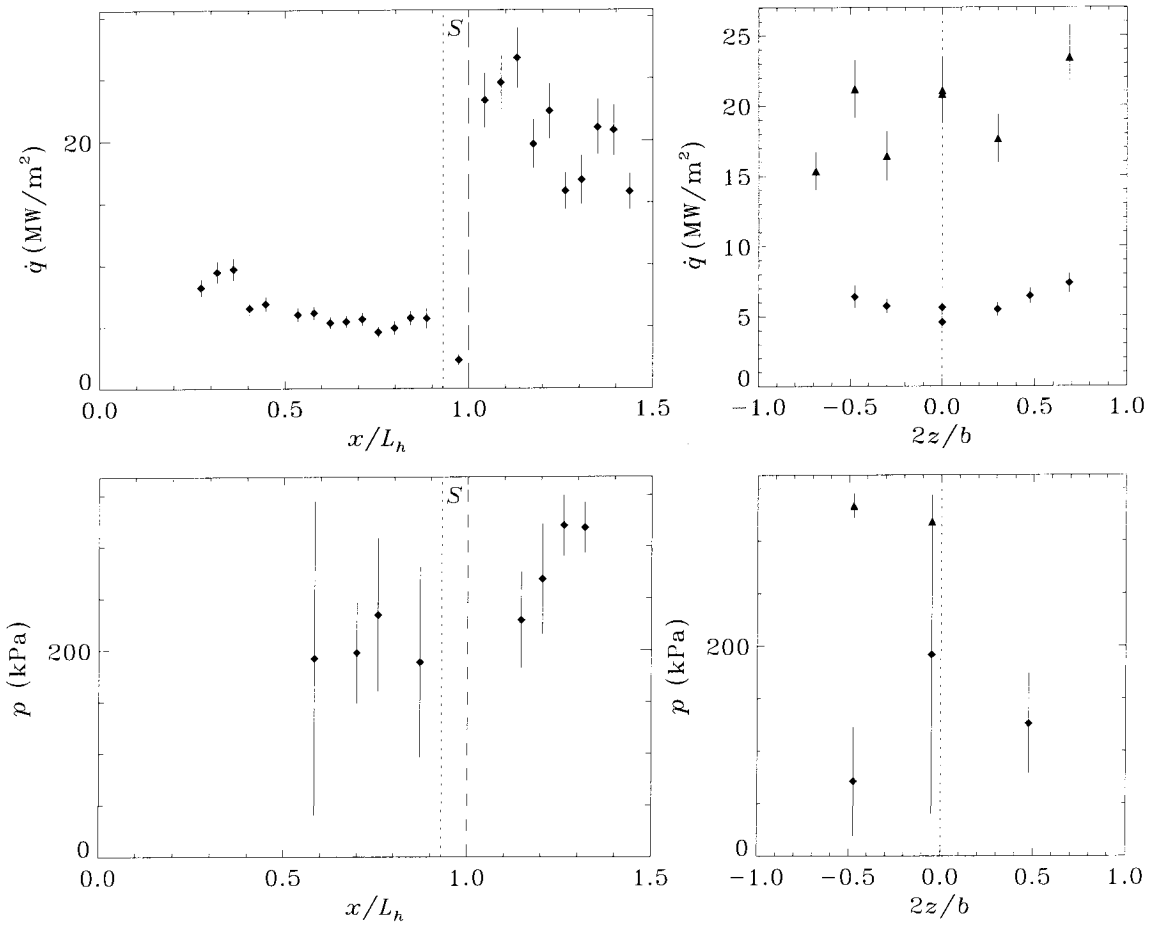

Shot 1797 (condition C2-CO_2, $A_e/A_* = 100$, $\theta_1 = 40°$, $\theta_w = 15°$)